ISSN 1018-5593

INSTITUTE ANNUAL REPORT 95

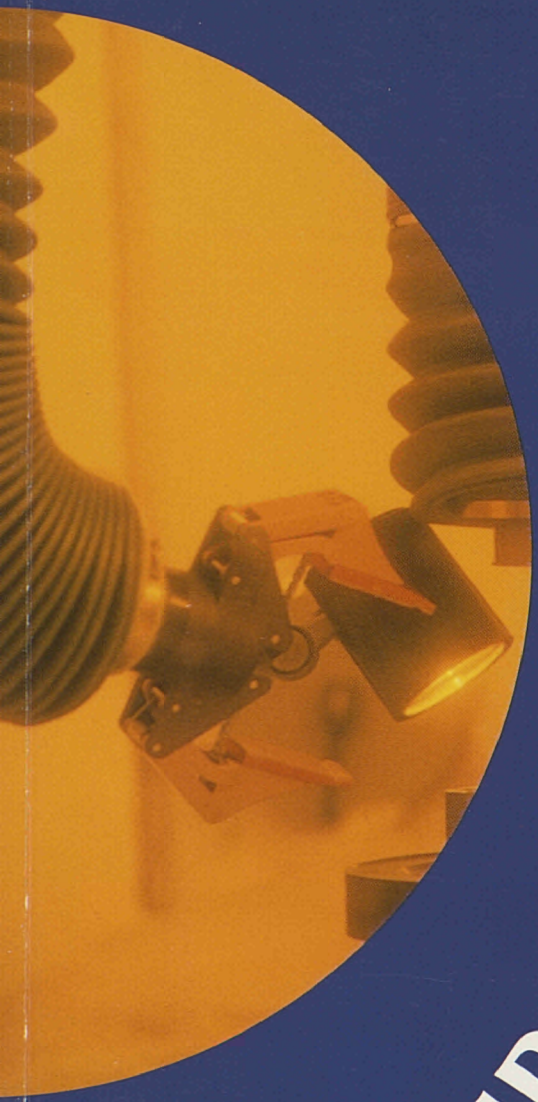

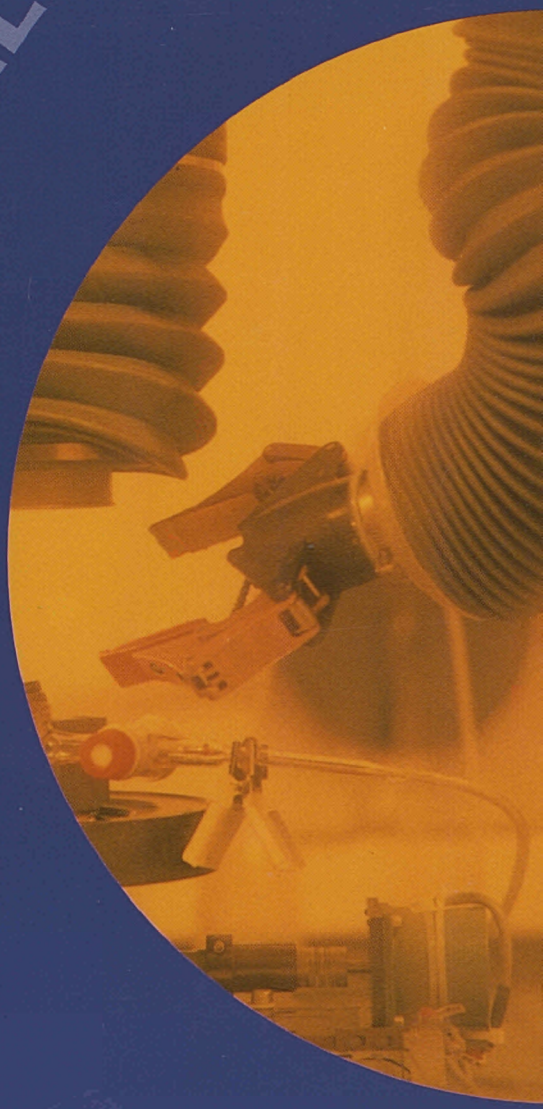

TRANSURANIUM ELEMENTS

TRANSURANIUM ELEMENTS

JOINT RESEARCH CENTRE
EUROPEAN COMMISSION

Report EUR 16368 EN

EUROPEAN COMMISSION

Directorate-General JRC
Joint Research Centre

Institute for Transuranium Elements Karlsruhe

Annual Report 1995

TUAR-95

1995

EUR 16368 EN

Published by the
EUROPEAN COMMISSION
Directorate-General JRC

INSTITUTE FOR TRANSURANIUM ELEMENTS
D-76125 Karlsruhe

LEGAL NOTICE

Cataloguing data can be found at the end of this publication

This report was compiled and edited by R. Schenkel, J. Richter, D. Pel, R. Wellum

Inquiries for more details should be addressed to the Programme Office,
Institute for Transuranium Elements, P.O. Box 2340, D-76125 Karlsruhe,
Phone ++49-7247-951386, FAX ++49-7247-951591

Luxembourg: Office for Official Publications of the European Communities, 1996
ISBN 92-827-6553-9

Printed in Germany

European Commission
Joint Research Centre

TUAR 95

Institute for Transuranium Elements

Annual Report

January – December 1995

Table of Contents

Foreword

by J. van Geel, Director

Difficult years for ITU ...

Attached is the first Annual Report of the new 4th framework Programme period from 1995-1998. While the general layout and structure has not been changed, some minor modifications have been included.

The first modification concerns the table of contents of the report. This simply reflects the new structure as proposed by the Board of Governors, including a more detailed breakdown in particular for the different and new competitive activities. Another modification is the inclusion of a section entitled 'Highlights 1995'. The quick reader finds there a succinct description of some major achievements and events encountered during 1995.

This new framework programme period will be one of the most difficult for ITU. Not as far as the scientific and technical programme as such is concerned. Difficulties will arise as a result of essentially four requirements which will have to be dealt with in this four year period:

- the partial renewal of the nuclear license of the Institute and the corresponding upgradings requested to adapt safety and security systems to the new standards,
- the clean-up and disposal of old glove-boxes and radioactive waste,
- the refurbishment of the Institute's infrastructure, which is now more than 30 years old,
- the need for moderate investments to secure scientific/technical vitality and thus the future of the Institute.

The resolution of these difficulties require above all motivation and engagement of staff but - in addition - financial resources. The Institute has therefore strengthened its own efforts to achieve cost savings in all areas and has increased its efforts in competitive activities. Initial and positive results in both areas are clearly visible. The only larger investment planned for the future of the Institute, the extension of the Minor Actinide Laboratory, again had to be postponed due to the lack of funds.

I trust that the Institute's staff will make a major contribution to the solution of these problems and I am convinced that we will master the challenges in front of us.

J. van Geel

Executive Summary

During 1995 the Institute for Transuranium Elements (ITU) directed its research and development activities towards the objectives defined within the Fourth Framework Programme. The institutional activities of the Institute are in the area of fuel cycle safety, safeguards and fissile material management. Fuel cycle safety comprises basic and applied actinide research, safety of nuclear fuels, mitigation of long lived actinides and fission produkts, and spent fuel characterization in view of long term storage. The Institute participated also in various competitive activities as outlined below.

Fuel cycle safety

Basic actinide research

The overall objective of basic actinide research is to elucidate the electronic structure of the actinides. The highly unusual and unique physical and chemical phenomena observed have indeed attracted the interest of solid state physicists and chemists worldwide. Important results have been obtained for the better understanding of uranium based heavy-fermion superconductors doped with transuranium ions such as neptunium and plutonium. New results have been obtained in the theory of the interaction between light and solids, in neutron experiments of neptunium compounds and in neutron inelastic scattering which provide a better understanding of the uranium and iron inner shell (5f and 3d) electron interaction. Important progress in the understanding of the magnetic behaviour has been made with X-ray synchrotron experiments carried out on uranium oxide single crystals and uranium arsenide crystals. Work on alpha immuno-therapy progressed to the extent that the proof-of-principle for the treatment of acute myelogenous leukaemia is expected for early 1996.

Safety of nuclear fuels

The Institute has continued its work in the area of measuring and modelling fuel properties and fuel-cladding interactions. The objective is to arrive at the turn of the century at fuel claddings with pin failure rates for uranium and uranium-plutonium mixed oxide (MOX) fuels with very high burn-ups similar to that of present-day uranium fuel. Structural investigations of high burn-up fuel continued to be the major activity in 1995. The evolution of the porosity and the grain subdivision process as a function of burn-up was measured with the aid of optical, scanning and transmission electron microscopy.

Fission-product release from irradiated fuel as used in the PHEBUS reactor safety programme was measured up to complete evaporation of the fuel. The new laser flash equipment was successful tested and is now available for experimental investigations. The TRANSURANUS code can now successfully describe high burn-up phenomena (rim effect). High resolution electron microscopy work clearly revealed for the first time dislocation lines in UO_2 and the subgrain boundary formation as first step in the rim-structure formation.

Mitigation of long-lived actinides and fission products

An important objective of the fuel cycle safety activities is to further minimize the radiotoxicity of spent fuel and highly active waste. This is why the Institute continued its collaboration with leading national laboratories, nuclear industry and Member State authorities to prepare, for example, technetium samples for irradiation within the EFTTRA programme (Experimental Feasibility of Targets for Transmutation) and pins with high plutonium and neptunium content and a plutonium-cerium inert matrix based pin within the TRABANT programme (Transmutation and Burning of Actinides in Triox). Extensive studies were done to master fabrication procedures and to measure physical and chemical properties of inert matrix materials for the transmutation of actinides, in particular for americium. A proposal has been made for a method to burn weapon plutonium in a Light Water Reactor with high proliferation resistance. The feasibility of recovering actinides from irradiated fuel targets with 20% americium and 20% neptunium (from the SUPERFACT

experiment) was demonstrated. Extraction chromatography was studied for the separation of uranium and plutonium from such fuels. The involvement of the Institute in international R&D efforts on partitioning and transmutation (P/T) is presented together with initial work on the radiological hazard of high level waste resulting from different P/T cycles.

Spent fuel characterization in view of long term storage

Reactor operators, fuel cycle industry and licensing authorities require safety data including those on radiotoxicity relevant to long-term storage of spent fuel. With this objective in mind, the leaching and corrosion behaviour of natural uranium oxide and irradiated high burn-up fuel was examined with solutions simulating groundwater and salt brine. The mechanisms of leaching and their kinetics are being explored. Extensive leaching studies were also performed on simulated high burn-up fuel in granitic water. The structure of oxidized layers on leached uranium oxide was determined with Rutherford backscattering/channeling techniques. First results on caustic salt dissolution studies of spent fuel are reported and the progress in the area of high temperature fuel cladding interaction and sodium-SUPERFACT fuel compatibility are presented. Finally recent passive neutron and gamma measurements carried out on different spent fuel rods are described together with a theoretical analysis using KORIGEN and isotopic correlations.

Safeguards and fissile material management

Nuclear safeguards on fissile material is performed in the European Union within the framework of the Euratom and the Non-Proliferation Treaty. The Institute contributes to the objectives of these treaties by performing research and development of methods, techniques and instruments, by provision of analytical services and expertise and by direct in-field measurement support.

As part of the support to DG XVII, the pre-on-site laboratory at ITU and the on-site laboratory projects for Sellafield and la Hague progressed with the purchasing and testing of major equipment, such as robots, titrators, alpha spectrometers, detectors and non destructive measurement equipment, the construction of two analytical glove-boxes and continued training of future analysts. As in previous years, ITU staff provided significant analytical in-field support to the Safeguards Directorate in reprocessing plants and in fuel fabrication plants.

A performance evaluation of the Multiple Group Analysis (MA) method for K-edge and neutron-gamma counting applications has been carried out. A comparison of different plutonium assay techniques was performed including a detailed evaluation of isotope correlation techniques for the determination of plutonium-242. Laser ablation optical emission spectroscopy was tested on reference waste glass. In order to cope with safeguards samples with trace amounts of radionuclides, new sample preparation and measurement technology was further tested and refined. The matrices investigated consisted of soils, vegetation and sediments from contaminated areas. The Institute participated in a field test for environmental monitoring techniques.

The Institute continued also in 1995 to provide its facilities and expertise in the area of characterization of vagabonding nuclear materials.

Competitive activities

The Institute participated for the first time in competitive activities under the shared cost action programme. Eight proposals in the field of nuclear fission safety, submitted together with different partners from Member States, were accepted.

A project on the agglomeration and separation of aerosols in industrial off-gases by means of infrasound has been accepted in the framework of competitive support activities, for technology transfer to European industry.

The Institute has started the following projects under the TACIS/PHARE programme of the European Commission:

- transfer of the nuclear safety code TRANSURANUS to the Bulgarian licensing authorities (PHARE)
- measurement of radionuclide release form the Chernobyl reactor debris (TACIS)

As in previous years, the Institute has carried out work for third parties with major contracts in the area of post irradiation examination of irradiated fuels, fabrication and characterization of fuels for transmutation, and examination of high burn-up uranium oxide and mixed oxide fuels for different customers. Taking all competitive activities together, new contracts worth 3.4 MECU have been signed during 1995.

Highlights 1995

Micromechanical Testing of Irradiated LWR Fuels

The mechanical behaviour of LWR fuel and cladding materials plays a fundamental role in the performance of the fuel rods (assemblies) during operational and accidental power transients. Whether the fuel rods withstand the power peaks without failure will depend on the degree of plasticity exhibited by both fuel and cladding materials, i.e. on their capability to diminish rapidly the interaction stresses by creep flow (stress relaxation). Because little information exists concerning the variation of the mechanical properties of fuel and cladding materials at extended burnups (≥ 40 GWd/tM), a programme has been started in the ITU hot-cells to determine these properties for fuel materials.

Due to the heterogeneous nature of the irradiated fuel material, reliable mechanical characterization of the different zones formed along the pellet radius can only be achieved by micromechanical tests on limited fuel areas. For this purpose, a microindentation apparatus for high-temperature applications in hot-cells has been developed and is presently under construction. Complementary to this, room temperature microhardness and fracture toughness determinations of irradiated fuels are being performed with the aid of a remote controlled microscope. Of particular interest appears to be the microporous zone formed at the pellet rim at high burnups, which exhibits a much larger fracture toughness than the rest of the fuel. This unexpected improvement may be due to the combination of the burnup increase effects in the rim zone (i.e., increase of lattice-dissolved fission product concentration, increase of porosity and reduction of grain size), and suggests a possible enhanced plasticity of the region, with consequently a beneficial effect on the pellet-cladding mechanical interaction. For the measurements at high temperatures, special attention will be paid to the determination of the creep and stress relaxation properties under static and dynamic load conditions.

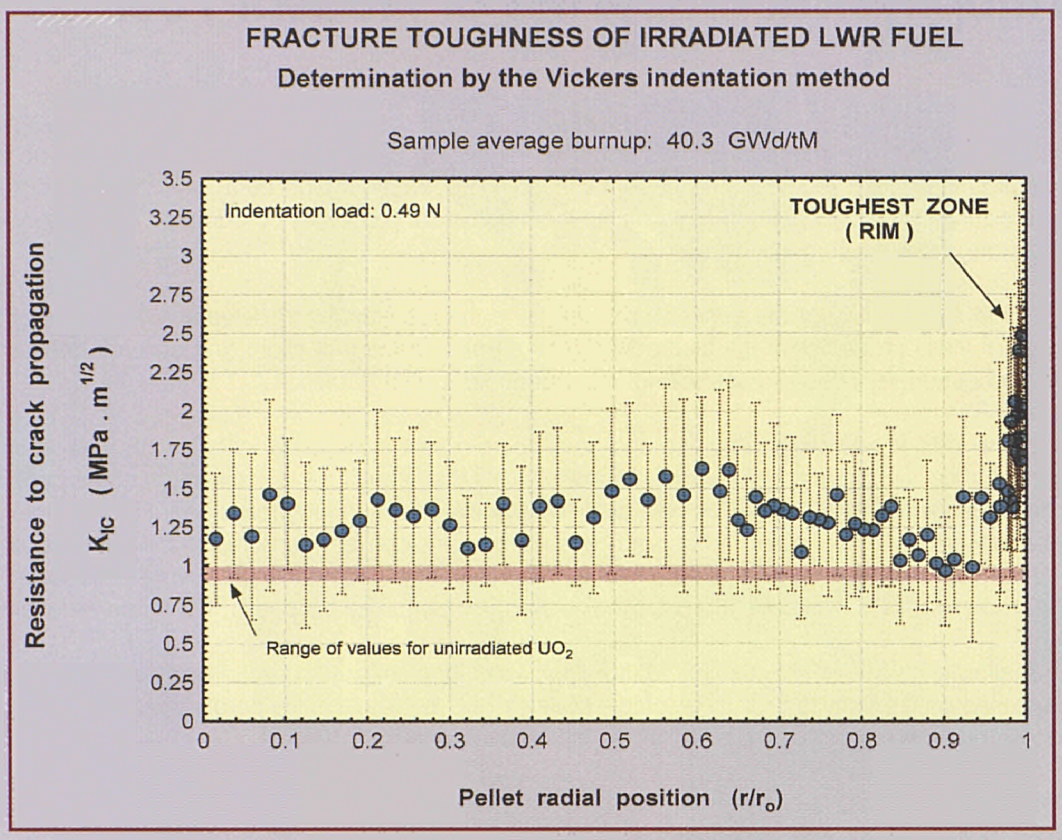

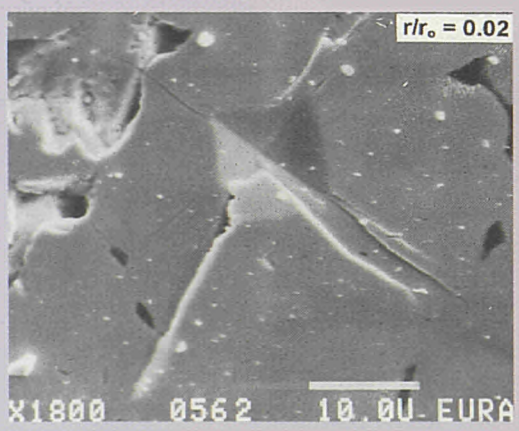

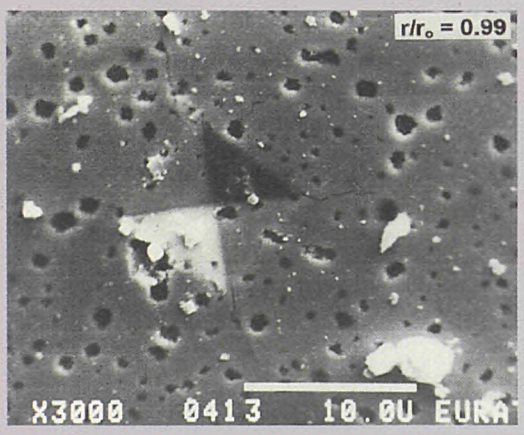

Fracture toughness of irradiated LWR fuel. Determination by the Vickers indentation method.

New Equipment for the Rapid and Accurate Determination of the High Temperature Thermophysical Properties of Nuclear Fuel

The knowledge of the thermodynamic properties of the fuel is of fundamental importance for the safe operation of nuclear reactors. The dependence of these properties on burn-up is still to a large extent merely conjectural. Experimental data on the thermophysical properties of irradiated fuel up to very high temperatures are, therefore, urgently needed.

Due to the high radioactivity of the material, as well as to the requirement to determine the radial and axial dependence of these properties in the fuel rods, it is of great advantage if rapid and accurate measurements can be carried out on very small samples, and with adequate spatial resolution.

Since 1992 the Institute has been designing and developing a new laser flash facility for this purpose. Conceived primarily for the measurement of thermal diffusivity, it will also permit the determination of the heat capacity, and hence the thermal conductivity, as well as melting points and thermodynamic transitions of materials. Two set-ups are presently available: in the first one solid samples can be measured in the temperature range 500 to 1800 K. In a second vessel, in which heating is provided by two continuous wave YAG lasers and in which a high pressure gas atmosphere can be maintained, temperatures of up to 3300 K can be attained.

The thermal diffusity measurement principle is straightforward: a short laser pulse (of approximately 1 ms duration) is deposited on the front surface of a sample platelet, and the resulting temperature increase curve on the rear surface is analysed to obtain the diffusity and the heat capacity.

The outstanding features of this equipment in comparison to others are:

- the highly homogeneous energy distribution in the probe laser beam,
- the extreme sensitivity of the detector which makes it possible to work with extremely low energy inputs, producing rear temperature peaks of less than 1 K.

Based on several tests of standard materials, the major performance data of this instrument are as follows:

- Accuracy: better than 3%
- Temperature Resolution: less than 0.01 K
- Laser Spot Size: variable between 1 and 5 mm
- Spatial Resolution of the Measurement: less than 0.05 mm, with possibility of scanning the surface of the sample for local measurement
- Types of Sample:
  - up to 1800 K: platelets of any shape (transparent support)
  - above 1800 K: disks or non-circular platelets of more than 5 mm size (three-pin mounting)

The instrument is being installed in the gamma-shielded hot-cell for measurements in the framework programme and work for third parties.

A patent proposal for the new equipment has been made. It can be expected that this type of equipment will be of considerable interest in other material science areas, where high temperature properties of composite and anisotropic advanced materials are studied.

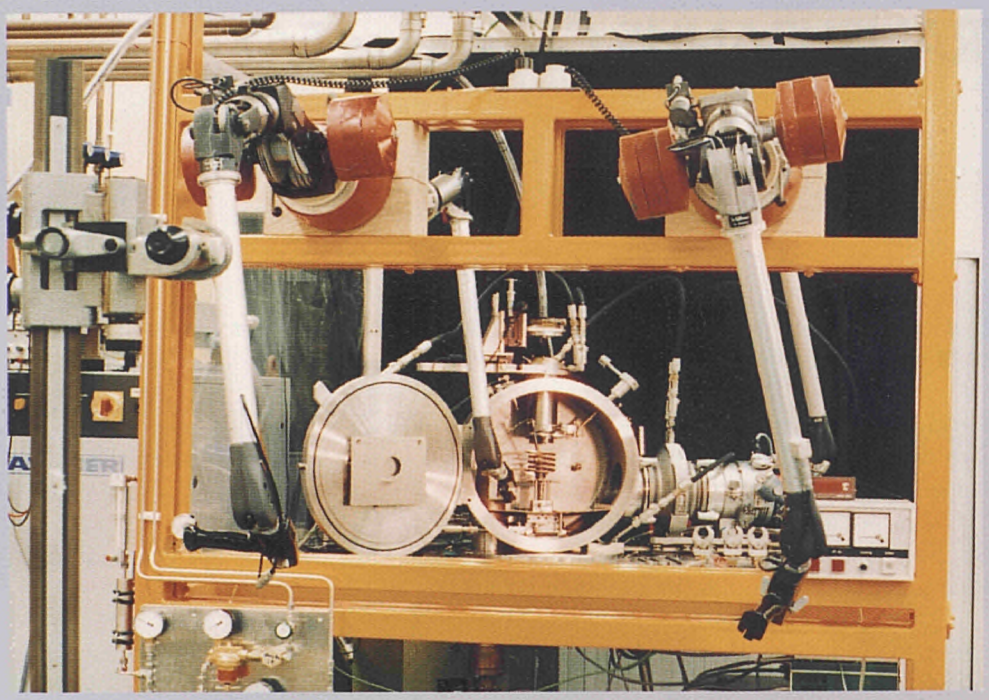

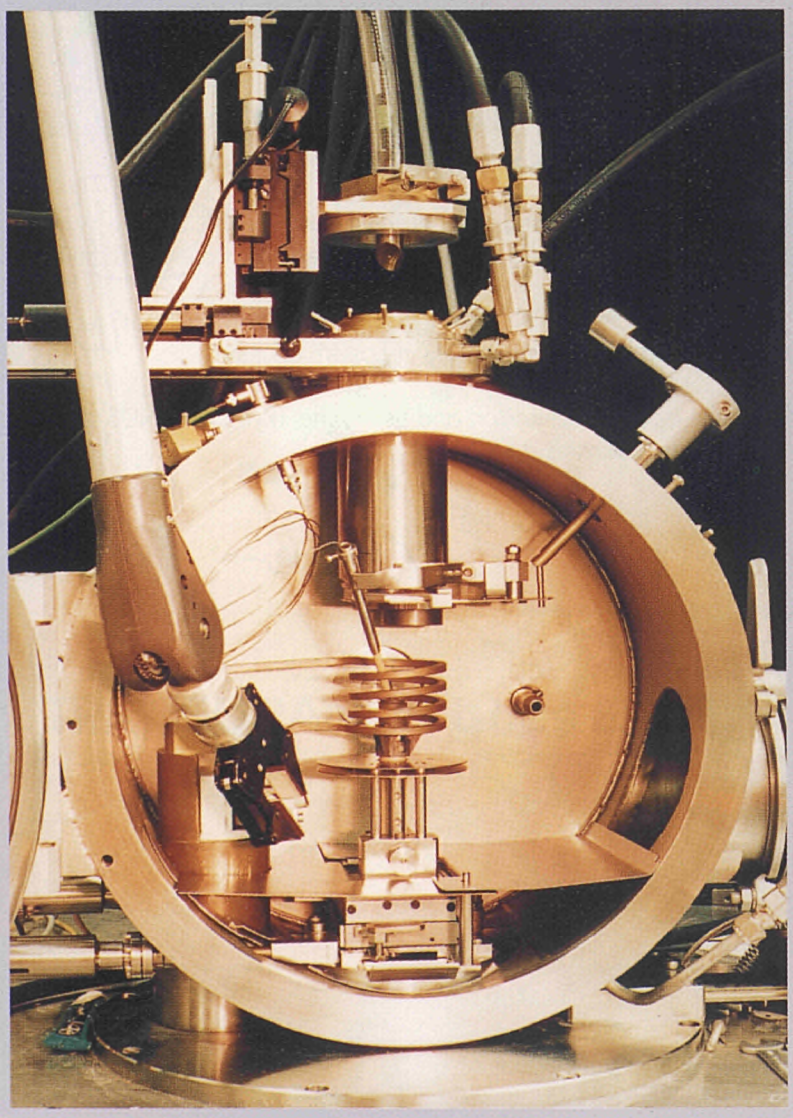

View of the glove-box showing the sample housing of the laser flash apparatus

The TRANSURANUS Code goes EAST

The behaviour of nuclear fuel rods in a nuclear reactor under normal operation or transient conditions, as well as at very high burn-up is a major research and development area of the Institute.

In the framework of the above activities, the computer code TRANSURANUS was developed which permits a comprehensive description of the behaviour of fuel rods for a variety of different reactor operation conditions and different fuel designs.

This code has been and continues to be a real success as it is used by numerous European plant operators, reactor designers, supervising bodies and research institutes.

In addition, the code is improved and updated on a continuous basis with new and proven data obtained for high burn-up fuel.

During 1995 numerous requests have been received to collaborate with ITU on the use and extension of the code to nuclear fuel from Eastern types of reactors.

Within the European Commission's PHARE Programme, the code will be transferred to the nuclear safety authorities and the leading nuclear institutes in Bulgaria and the Czech Republic.

Furthermore, the IAEA is promoting the distribution of the TRANSURANUS code within its regional technical cooperation programme on "Fuel Rod Modelling for WWER Reactors" to eight Eastern countries.

The transfer and the application of the TRANSURANUS code to nuclear fuel from reactors of Russian types will be an essential contribution to improve nuclear safety in Eastern countries.

The attached map shows the existing distribution and use of the TRANSURANUS code together with the new interested customers from Eastern countries.

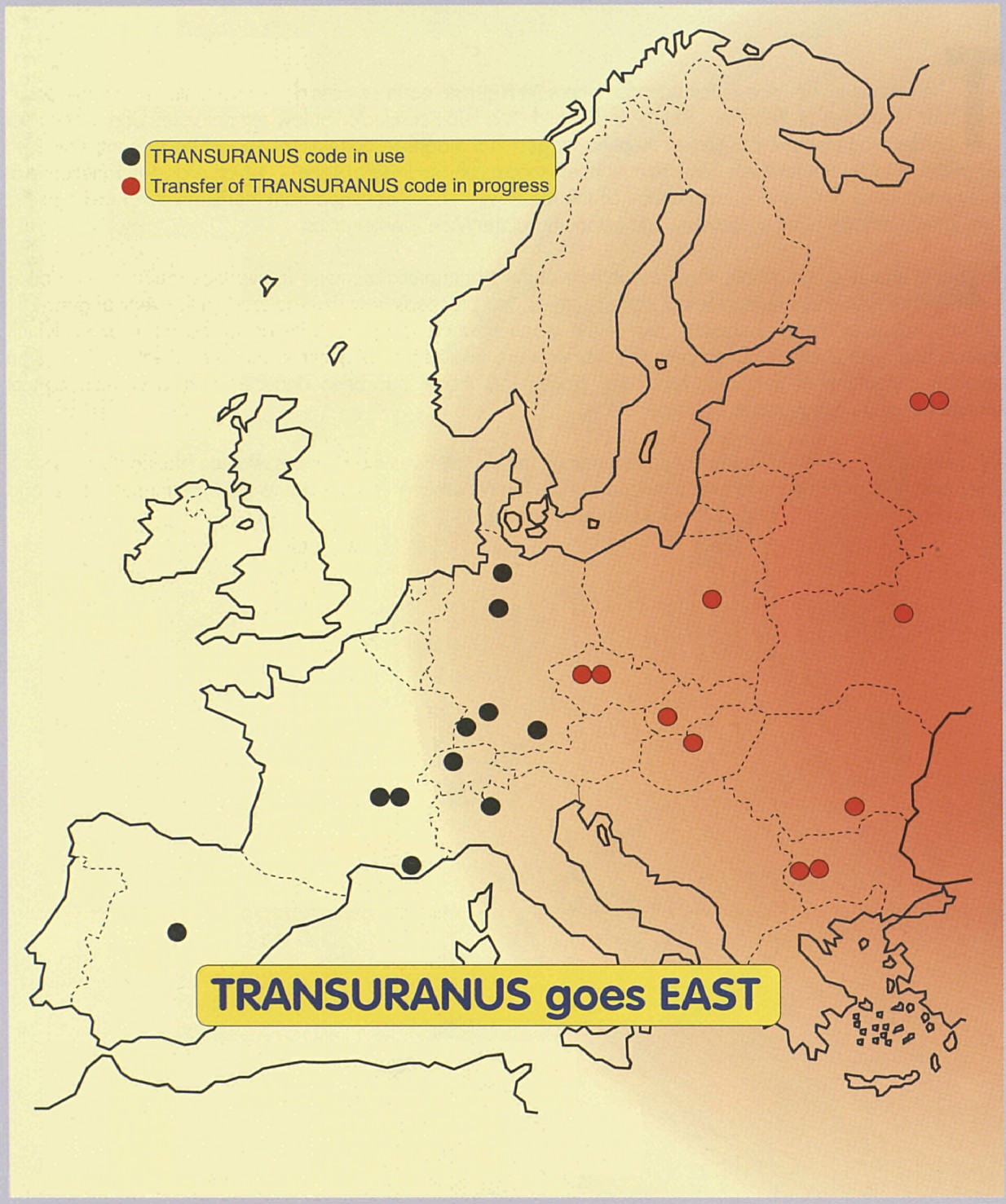
TRANSURANUS code in use
Transfer of TRANSURANUS code in progress
TRANSURANUS goes EAST

New Insights into the Properties of the Actinide B_{13} Compounds

The interest in the MBe_{13} compounds, where M is a rare earth or actinide element, stems from the peculiar properties of the UBe_{13} compound, which is a superconductor at low temperature. UBe_{13} does not order magnetically, but current theories suggest that magnetic correlations should be present; however, experiments to search for them have not yet been successful. Studies of $NpBe_{13}$, which orders magnetically at a temperature of 5 K, and a comparison of the results with those obtained from the isostructural Gd and Ho compounds, allows a more complete understanding of the MBe_{13} systematics.

The figure shows schematically the arrangement of the 5f magnetic moments in the heavy-fermion compound $NpBe_{13}$. The moments are modulated in their size as one proceeds from layer to layer in the vertical direction, – here chosen as the propagation axis of the magnetic modulation. In addition to this modulation, which repeats itself over 3 chemical unit cells, the moments are rotated by 90° when compared with the moments on neighbouring atoms in the same horizontal plane. This model has been deduced from a combination of Mössbauer and neutron scattering experiments.

This research represents a three-way collaboration. The sample was made in Los Alamos National Laboratory, USA, and then annealed and characterized in ITU. The Mössbauer measurements were performed at ITU and the neutron experiments at the CEN-G, Grenoble, France.

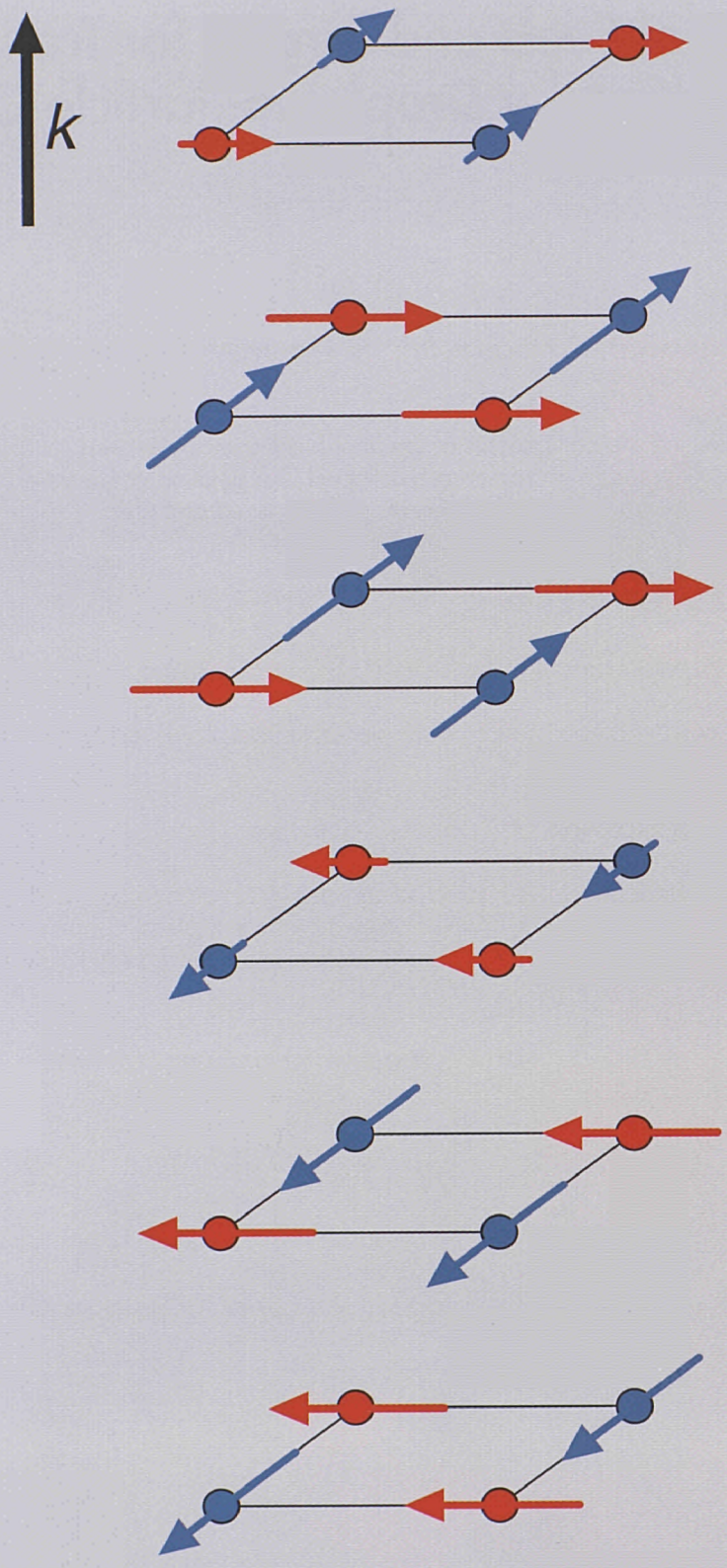

The unusual arrangement of magnetic moments at low temperature (below 5 K) in the cubic material $NpBe_{13}$. These results are deduced from both Mössbauer (at ITU) and neutron experiments in Grenoble, at the CEN-G reactor. Shown is the magnetic sequence of 6 layers of the structure, which is equal to 3 chemical unit cells. The magnitude of the moments have two values, 1.0 and 1.2 μB, with a preponderance of the larger moment as shown in the figure. (The sizes of the magnetic moments are not drawn to scale.)

Fabrication of Fuels and Targets for Transmutation and Incineration by Droplet-to-Particle Conversion

In contrast to generally practised fabrication procedures of mixing and ballmilling the desired fuel in the form of powders, a droplet-to-particle conversion procedure has been developed and successfully tested in the Institute.

Aqueous solutions containing the components of the final product in the desired ratio, are atomized using a high speed rotating cup. The resulting droplets are collected in a gelation bath where they are converted into solid form by a chemical reaction. The resulting beads are then dried and pressed into the desired form before filling the fuel pins. This new process offers several advantages:

- accurate control of composition
- high homogeneity of heavy elements in the fuel
- no dust creation in powder preparation or in the pelletizing steps, i.e. reduced contamination of exposed surfaces
- high degree of automation possible

This process has been successfully used to produce fuels for transmutation and plutonium incineration $(U_{0.55}Pu_{0.40}Np_{0.05})O_2$ and $(Pu_{0.43}Ce_{0.57})O_2$ in the framework of the trilateral cooperation between CEA, FZK and ITU for the irradiation experiment TRABANT (Transmutation and Burning of Actinides in Triox) in HFR Petten.

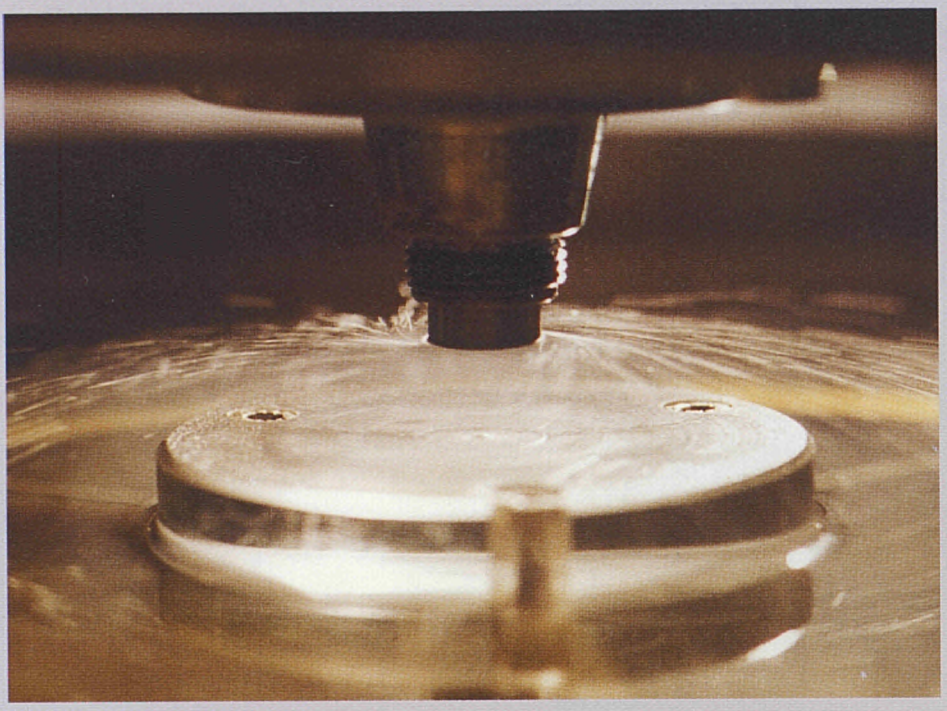

Droplets produced by a high speed rotating cup are collected in a gelation bath

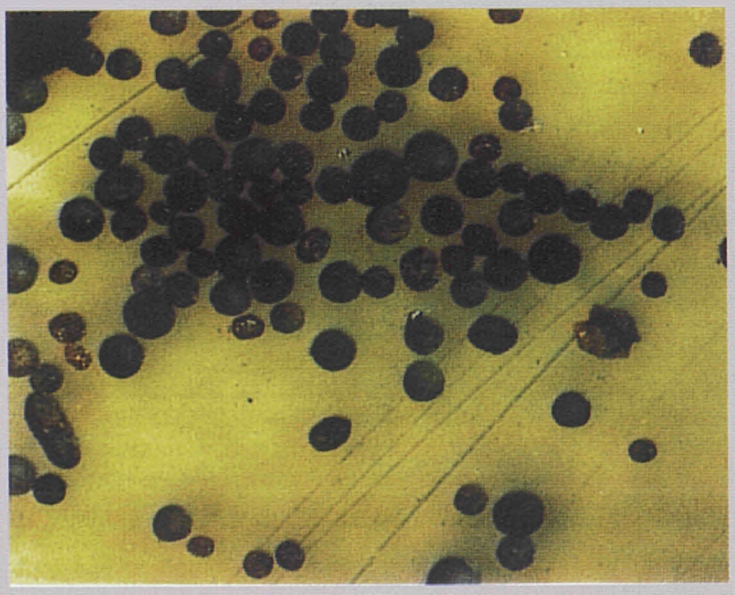

Magnified view of solid beads (x 100) produced by a droplet-to-particle conversion process

Detection of Clandestine Activities by Analyses of Telltale Traces of Radionuclides

On October, 2nd, 1995 ground was broken for the construction of the ARTINA laboratory at ITU Karlsruhe. ARTINA stands for Analyses of Radioisotope Traces for the Identification of Nuclear Activities.

This type of analyses, looking down to femtogram quantities (10^{-15}g) of material corresponding to particle sizes of less than 1 µm is still considered to be an art: the concentrations and particles looked at are so small and sparse, that every precaution needs to be taken to protect the samples against cross-contamination which could occur especially in radiochemical laboratories. The measurements are similar to detecting a needle in a haystack.

The ARTINA laboratory therefore consists essentially of a clean laboratory with associated, specialized equipment for pre-screening, pre-treatment and pre-concentration of radionuclides plus the standard equipment for isotope or element analyses in our analytical laboratories.

During 1995 the Institute participated on request of three Member States of the European Union in a field test of the International Atomic Energy Agency inside and outside a centrifuge enrichment plant. The analyses to be performed included low level bulk analyses of soil and water samples, and particle analyses of swipe samples.

Sample preparation work in the clean laboratory

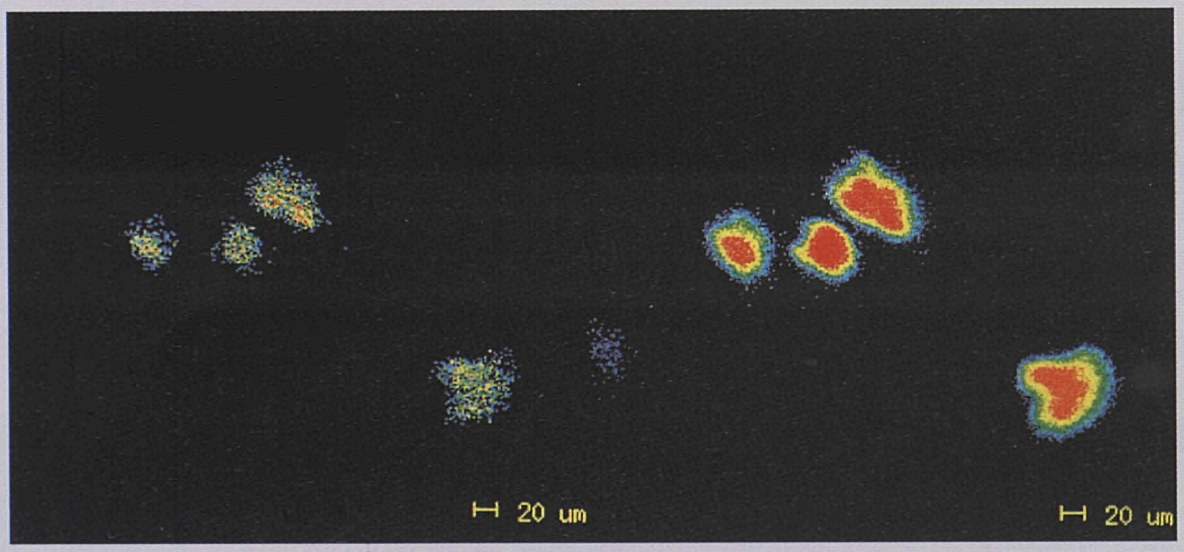

Isotopic analysis of enriched uranium particles from swipe sample

Successful Year for Competitive Activities

For ITU, 1995 was one of the most successful years in the area of competitive activities.

During the year, the Institute has signed new contracts with a volume of about 3.5 MECU. This corresponds to 12% of the ITU annual budget.

The most important contracts have been concluded with the nuclear industry, mainly from Germany, Japan, France and Belgium. Further contracts have been signed with nuclear research centres and with governmental institutions.

As a new area of activity, two contracts were signed under the European Commission's PHARE and TACIS programmes supporting nuclear safety projects in Bulgaria and in the Ukraine (Chernobyl).

The diagram shows the development of the volume of contracts for competitive activities since 1992.

Radioactive Source Term Evaluations related to Mururoa Underground Nuclear Explosions

The European Institute for Transuranium Elements (ITU) was requested by the Commission to examine a part of the documentation supplied by the French authorities to Commission services related to the underground nuclear tests in Mururoa and Fangataufa.

The part of the documentation concerned describes a scenario, in which a fraction of the radioactivity contained in the water of the underground cavities would suddenly be released to the lagoons.

ITU has evaluated the data and conclusions provided in the above document. This appraisal was based on data available from the open literature, own expertise and the application of established scientific methods.

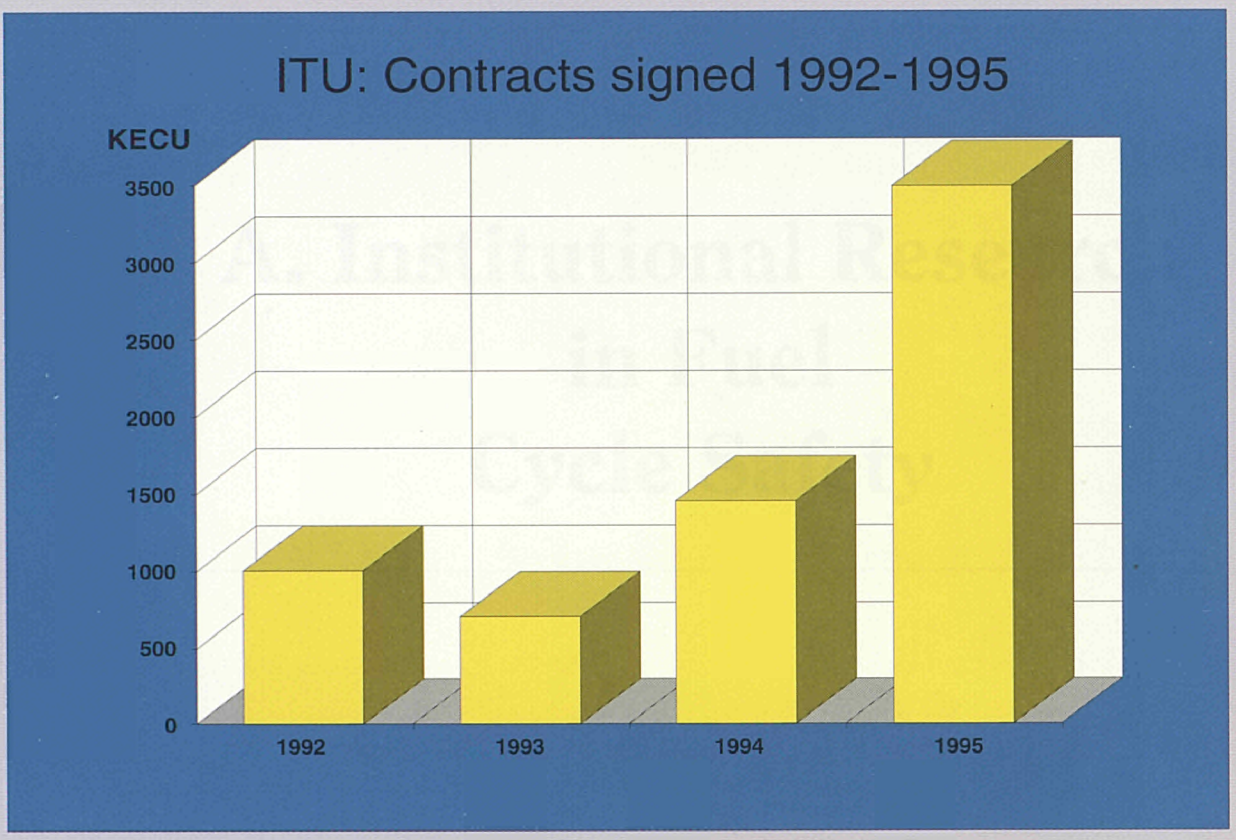

Development of the volume of contracts for competitive activities since 1992.

A. Institutional Research in Fuel Cycle Safety

1. Basic Actinide Research

Introduction

The central objective of actinide research in ITU and in its numerous collaborations is the elucidation of the electronic structure of actinide metals and actinide compounds, in particular of the behaviour of the 5f electrons. The dualism between localized and itinerant characteristics as it is particularly clearly demonstrated in the actinide series, is a key problem in these studies.

These goals are approached by experiment and theory. Experimental studies are either selective investigations on the basis of theoretical or other experimental information which indicates that a particular material and method are promising, or they can involve a systematic approach to a whole class of compounds. Theoretical calculations can indicate to the experimentalist where he can expect to find important results, and theory can on the other hand try to combine experimental evidence from different sources into a general picture. An important basis for the experimental study is the preparation of polycrystalline and single crystal samples of actinides of high specific activity, and their careful characterization by X-ray diffraction, chemical, and electron microprobe analysis. As far as possible, study of physical properties concentrates on the most interesting of the available actinide compounds, and an attempt is made to study them by several different methods to obtain a maximum of information on their physical behaviour. Many of the experimental investigations take place at the special facilities in the Institute, but we also make use of unique large facilities, such as neutron, X-ray synchrotron, and muon sources, in other locations.

As a side line of the above research area the production of ^{225}Ac and ^{213}Bi for alpha immuno-therapy and the conjugation of alpha emitters to antibodies was continued.

1.1 Samples Preparation and Characterization

During the reporting period, preparation and characterization work was divided in four main parts:

- Growth of single crystals
- Preparation of polycrystalline intermetallic compounds
- Encapsulation for collaborative studies
- Organometallic compounds investigation

1.1.1 Growth of single crystals

The new family of U_2T_2X (where T is a transition metal and X is a metalloid, e.g. Sn) compounds offers a possibility to study further the role of the 5f-ligand hybridization and the connection between the shortest inter-uranium distance and the type of magnetocrystalline anisotropy. It is particularly interesting in this family of compounds that, depending on the constituting elements T and X, the shortest inter-uranium distance is found either within the basal plane or along the c axis [1]. Therefore particular attention is given to these compounds, and to further characterize the properties, a large request for single crystals has been expressed by many of our collaborators. We attempted single crystal growth by various techniques. Suitable size crystals were obtained by the mineralization growth technique on U_2Rh_2Sn and U_2Co_2Sn. Crystals obtained were characterized by Laue and single crystal X-ray diffraction, and sent to other groups. Determination of optimal single crystal growth experimental conditions on further systems is in progress.

Another class of compounds for which complete characterization of the basic interactions requires single crystals are the NaCl type compounds. Much work has been done on the monopnictides and monochalcogenides of actinides (AnX) [2] and large single crystals have been obtained by mineralization techniques in our laboratory [3]. Recent developments were to prepare solid solutions, especially $Pu_{1-x}Y_xSb$. Single-crystal growth with x = 0.75, 0.6 and 0.4 was successfully performed and large crystals obtained.

1.1.2 Preparation of polycrystalline intermetallic compounds

To establish systematics within an isostructural family, the investigation of families of intermetallic compounds $An_xT_yX_z$, with An = Th to Am, T = a transition metal and X a metalloid is one of our main activities. Different families were already investigated in the past decade. During this reporting period some of them were selected for further study.

- AnTX or 1:1:1 compounds: were already extensively studied [4]. In the AnTSn systems, some compounds do not form. We completed this family with the synthesis and characterization of new samples, NpIrSn, NpNiSn, PuRhSn and PuIrSn. The measured lattice parameters are given in Tab. 1.1
- $An_4T_7(Si \text{ or } Ge)_6$ or 4:7:6 compounds: In the course of 1:2:2 family study, compounds of the 4:7:6 type

Tab. 1.1 Lattice parameters of new compounds prepared and characterized in the reported period (parameters determined on single crystals).*

Compounds	Structure Type	Crystal Class	Lattice Parameters		
			a (pm)	b (pm)	c (pm)
1:1:1 Compounds					
NpNiSn*	Co_2Si	Orthorhombic	722.8 (2)	447.7 (1)	757.1 (2)
NpIrSn*	Fe_2P	Hexagonal	735.0 (2)	-	397.5 (1)
PuRhSn*	Fe_2P	Hexagonal	740.6 (4)	-	401.7 (3)
PuIrSn*	Fe_2P	Hexagonal	739.4 (6)	-	401.7 (3)
4:7:6 Compounds					
$U_4Ru_7Ge_6$	$U_4Re_7Si_6$	Cubic	829.4 (1)	-	-
$U_4Os_7Ge_6$	$U_4Re_7Si_6$	Cubic	831.5 (1)	-	-
$Pu_4Ru_7Ge_6$	$U_4Re_7Si_6$	Cubic	832.4 (1)	-	-
$Pu_4Ru_7Ge_6$*	$U_4Re_7Si_6$	Cubic	829.9 (2)	-	-
2:2:1 Compounds					
Am_2Ni_2Sn*	U_3Si_2	Tetragonal	731.5 (3)	-	376.5 (2)
Am_2Pd_2Sn*	U_3Si_2	Tetragonal	760.3 (4)	-	385.1 (3)
Am_2Pt_2Sn*	U_3Si_2	Tetragonal	768.5 (5)	-	381.9 (5)
1:2:3 Compounds					
$NpNi_2Al_3$*	$PrNi_2Al_3$	Hexagonal	522.6 (1)	-	400.8 (1)
$U_{0.97}Np_{0.03}Pd_2Al_3$	$PrNi_2Al_3$	Hexagonal	537.5 (1)	-	419.4 (1)
$U_{0.95}Np_{0.5}Pd_2Al_3$	$PrNi_2Al_3$	Hexagonal	536.9 (1)	-	419.1 (1)
$U_{0.92}Np_{0.8}Pd_2Al_3$	$PrNi_2Al_3$	Hexagonal	537.1 (1)	-	419.1 (1)
$U_{0.99}Pu_{0.01}Pd_2Al_3$	$PrNi_2Al_3$	Hexagonal	537.1 (1)	-	419.2 (1)
$U_{0.9}Pu_{0.1}Pd_2Al_3$	$PrNi_2Al_3$	Hexagonal	537.1 (1)	-	419.3 (1)
$U_{0.7}Pu_{0.3}Pd_2Al_3$	$PrNi_2Al_3$	Hexagonal	537.9 (1)	-	419.5 (1)
$U_{0.5}Pu_{0.5}Pd_2Al_3$	$PrNi_2Al_3$	Hexagonal	538.4 (1)	-	419.7 (1)
$U_{0.2}Pu_{0.8}Pd_2Al_3$	$PrNi_2Al_3$	Hexagonal	539.8 (1)	-	420.0 (1)
1:2:2 Compounds					
URu_2Si_2	$ThCr_2Si_2$	Tetragonal	413.1 (1)	-	957.4 (1)
$U_{0.99}Np_{0.01}Ru_2Si_2$	$ThCr_2Si_2$	Tetragonal	413.2 (1)	-	957.6 (1)
$U_{0.9}Np_{0.1}Ru_2Si_2$	$ThCr_2Si_2$	Tetragonal	413.1 (1)	-	957.5 (1)
$U_{0.7}Np_{0.3}Ru_2Si_2$	$ThCr_2Si_2$	Tetragonal	413.2 (1)	-	957.8 (1)
$U_{0.5}Np_{0.5}Ru_2Si_2$	$ThCr_2Si_2$	Tetragonal	413.4 (1)	-	958.3 (1)
$U_{0.3}Np_{0.7}Ru_2Si_2$	$ThCr_2Si_2$	Tetragonal	413.6 (1)	-	958.4 (1)
$U_{0.1}Np_{0.9}Ru_2Si_2$	$ThCr_2Si_2$	Tetragonal	413.5 (1)	-	958.8 (1)
$NpRu_2Si_2$	$ThCr_2Si_2$	Tetragonal	413.7 (1)	-	959.3 (1)

were isolated for some U and Np systems [5]. Among them, $Np_4Ru_7Ge_6$ was found interesting due to possible superconductivity at low temperature [6]. We proceeded to a systematic exploration on U and Pu systems to increase and determine the limit of stability of this new family. Our success in this way was limited and only some samples could be obtained as single phase. They are summarized in Tab. 1.1. Full characterization is still in progress, but our preliminary results let us argue that the stability range of 4:7:6 phases is quite restricted, and that the thermodynamical and kinetical stability of 1:2:2 phases strongly competes with the possibility of formation of the 4:7:6 type.

- An_2T_2(Sn or In) or 2:2:1 compounds: Attempts to synthesize Pu_2T_2X compounds were reported previously (TUAR-94, p. 122). Only seven compounds could be obtained. In this reporting period we investigated the Am_2T_2Sn system and we report here about three new pure phase samples obtained (Tab. 1.1). We show that the degree of stability of 2:2:1 phases decreases with the substitution of the actinide element in the order U → Np → Pu → Am as illustrated in Fig. 1.1

	U			Np			Pu			Am		
Sn	**Fe**	**Co**	**Ni**	*Fe*	**Co**	**Ni**	*Fe*	*Co*	**Ni**	?	?	**Ni**
	Ru	**Rh**	**Pd**	**Ru**	**Rh**	**Pd**	*Ru*	*Rh*	**Pd**	?	?	**Pd**
	Os	**Ir**	**Pt**	*Os*	*Ir*	**Pt**	*Os*	*Ir*	**Pt**	?	?	**Pt**
In	*Fe*	**Co**	**Ni**	*Fe*	**Co**	**Ni**	*Fe*	*Co*	**Ni**	?	?	?
	Ru	**Rh**	**Pd**	*Ru*	**Rh**	**Pd**	*Ru*	**Rh**	**Pd**	?	?	?
	Os	**Ir**	**Pt**	*Os*	**Ir**	**Pt**	*Os*	*Ir*	**Pt**	?	?	?

*Fig. 1.1 Limit of stability of An_2T_2 (Sn or In) phases for An = U, Np, Pu and Am (**Bold:** stable phases, italic: 2.2.1 phase not obtained, ?: system not explored).*

Recently, we have begun a new area of investigation devoted to the doping of Np or Pu into uranium heavy-fermion compounds [7] and have started some investigations on $U_{1-x}Np_xPd_2Al_3$. In this reporting period we particularly concentrated on isostructural $U_{1-x}Pu_xPd_2Al_3$ and $U_{1-x}Np_xRu_2Si_2$:

- $U_{1-x}Np_xPd_2Al_3$: Results on this system with x = 0.01, 0.1 and 0.8 were reported previously (TUAR-94, p. 124). During this study, some anomalies were suspected for low Np dilution and following this we investigated systems with $0.01 \leq x \leq 0.1$. The lattice parameters for these new samples are summarized in Tab. 1.1. A rather surprising anomaly in regard to Vegard's law was found for low concentration, as illustrated in Fig. 1.2. Anomalies were also observed in resistivity properties as reported below.
- $U_{1-x}Pu_xPd_2Al_3$: $PuPd_2Al_3$ is non-magnetic [8] and a similar study to that performed on Np analogue gives us the possibility to mix two magnetically different compounds. Synthesis and characterization on eight different $U_{1-x}Pu_xPd_2Al_3$ compounds were started and new compounds are reported in Tab. 1.1. Studies of the physical properties are planned for next year.
- $U_{1-x}Np_xRu_2Si_2$: this system was also investigated to relate it to the behaviour of the heavy-fermion URu_2Si_2. Six samples were prepared and characterized (Tab. 1.1) and results of preliminary Mössbauer studies are reported below.

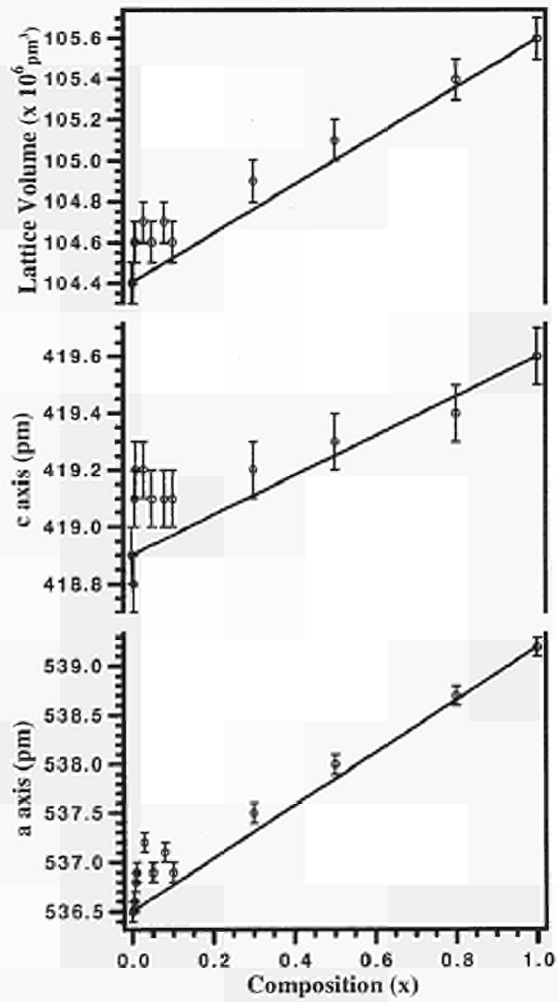

Fig. 1.2 Crystallographic parameters of $U_{1-x}Np_xPd_2Al_3$ versus x. Note the deviations from Vegard's law (straight line) at low neptunium concentrations, x.

References

[1] H. Nakotte, K. Prokes, E. Brück, N. Tang, F. R. de Boer, P. Svoboda, V. Sechovsky, L. Havela, J. M. Winand, A. Seret, J. Rebizant, J. C. Spirlet; Physica B **201** (1994) 247-250

[2] G. H. Lander, P. Burlet; Physica B **215** (1995) 7

[3] J. C. Spirlet; in "Topics in f-Element Chemistry: Synthesis of Lanthanide and Actinide Compounds", eds., G. Meyer and L. R. Morss (Kluwer Academic Publishers) Vol. **2** (1991) 353-367

[4] Y. Kergadallan; Thèse de doctorat, Université de Paris XI Orsay, 1993

[5] F. Wastin, J. Rebizant, J. P Sanchez, A. Blaise, J. Goffart, J. C. Spirlet, C. T. Walker J. Fuger; J. Alloys Comp. **210** (1994) 83-89 and references therein

[6] C. Jeandey, J. P. Sanchez, J. L. Oddou, J. Rebizant, J. C. Spirlet, F. Wastin; submitted to J. Phys., Condens. Matter

[7] J. G. Park, B. R. Coles; Physica B **186-188** (1993) 795-797

[8] A. Seret, F. Wastin, J. C. Waerenborgh, S. Zwirner, J. C. Spirlet, J. Rebizant; Physica B **206 & 207** (1995) 525-527

1.1.3 Encapsulation of active samples for collaborative studies

For studies in collaboration with external organizations, samples are required to be suitably encapsulated for specific measurements. The different samples encapsulated in the reporting period for collaborative studies are listed in Tab. 1.2.

Tab. 1.2 Samples prepared, characterized and encapsulated in 1995 for the indicated measurements.

Measurements	Laboratories	Compounds	Form
Resistivity	ITU-Karlsruhe	Np_2T_2In (T = Ni, Co, Ru, Rh, Pd, Pt ,Ir) $U_{1-x}Np_xPd_2Al_3$ (x = 0.03 0.05, 0.08,) $U_{1-x}Pu_xPd_2Al_3$ (x = 0.01, 0.1, 0.3, 0.5) $Np_4Ru_7Ge_6$	AcM
Mössbauer Spectroscopy	TU-München	$U_{1-x}Np_xPd_2Al_3$ (x = 0.03) $U_{1-x}Np_xRu_2Si_2$ (x = 0.1, 0.3, 0.5, 0.7, 0.9, 1)	AcM
Synchrotron X-ray Scattering	BNL-Brookhaven and ESRF-Grenoble	UAs UPtGe UPd_2Al_3 UO_2 PuSb	SC
Neutron Scattering	CEN Grenoble	U_2Co_2Sn U_2Rh_2Sn	SC
	ILL-Grenoble	U_5Sb_4	SC
Magnetic Properties	ITN Sacavém	U_2T_2Sn (T= Co, Ru, Ir, Rh)	AcM-SC
	ITC-FZK Karlsruhe	$NpRu_7Ge_6$ Tc, Np, Pu metals	AcM
Muon Spectroscopy	TU-München	$NpCo_2$ NpO_2	P
High Pressure X-ray Diffraction	ITU-Karlsruhe DESY-Hamburg	$NpIn_3$, $NpSn_3$, NpS, PuS USn_3	G-SC

AcM = arc melting SC = single crystal P = powders, polycrystalline sample
G-SC= grinding single crystals

1.2 Measurements of Bulk Physical Properties

1.2.1 Electrical resistivity of $U_{1-x}Np_xPd_2Al_3$ with low actinide concentrations

Resistivity and Mössbauer results in $U_{1-x}Np_xPd_2Al_3$ systems with x = 0.1, 0.3 and 0.5 have been previously presented and discussed [1]. We have extended our study to systems with x = 0.03, 0.05 and 0.8. New resistivity curves are consistent with the following scheme: for $0.1 \leq x$ or $x \geq 0.6$, the systems behave as Kondo lattice systems and for $0.3 \leq x \leq 0.5$ as dilute Kondo impurity systems. However, for samples with low dilution (x = 0.03 and 0.05), a new type of resistivity minimum appears at low temperatures (7 K for x = 0.03 and 10 K for x = 0.05) as shown in Fig. 1.3. This minimum is similar to that observed in $U_{1-x}Ln_xRu_2Si_2$ for small Ln concentration [2]. Its origin is far from understood, but could be attributed to the so-called Kondo hole effect [3] or insulating type transition as observed in UCu_5 [4].

References

[1] A. Seret, F. Wastin, J. C. Waerenborgh, S. Zwirner, J. C. Spirlet, J. Rebizant; Physica B **206 & 207** (1995) 525
[2] J. G. Park, S. B. Roy, B. R. Coles; J. Phys, Condens. Matter 6 (1994) 5937
[3] A. Lopez de la Torre, P. Visani, Y. Dalichaouch, B. W. Lee, M. B. Maple; Physica B **179** (1992) 208
[4] J. D. Thompson, private communication

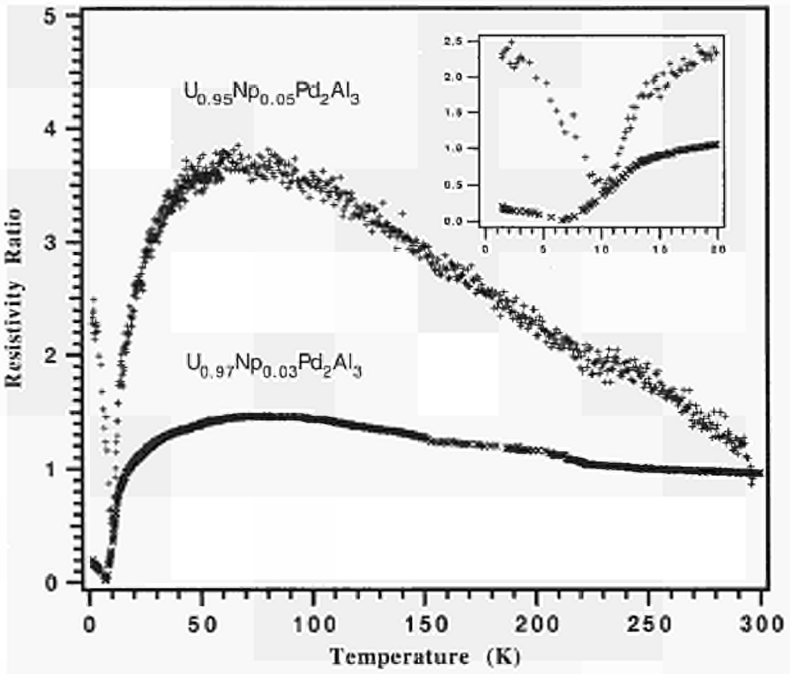

Fig. 1.3 Temperature dependence of the resistivity ratio (r/r_{300K}) of $U_{0.95}Np_{0.05}Pd_2Al_3$ (+) and $U_{0.97}Np_{0.03}Pd_2Al_3$ (x). The insert shows the resistivity minimum observed at low temperature.

1.2.2 Magnetization experiments on U_2T_2Sn compounds

The magnetization measurements of some U_2T_2Sn (T = Co, Ir, Ru and Rh) single crystals grown at the Institute were performed at the Physics Dept. of the University of Lisbon, on a Quantum Design SQUID magnetometer employing the temperature range 2-400 K under magnetic fields up to 5.5 T.

The magnetic results of the U_2Ir_2Sn and U_2Ru_2Sn single crystals were not reproducible. It appears that an extra phase may be present in the crystals. For U_2Co_2Sn, in both *a* and *c* directions, the magnetization curves are similar showing higher magnetization values for the c direction. From these curves *a* paramagnetic behaviour is detected, as was previously reported on oriented powder magnetization measurements [1]. However, in the M(T) curves a small kink is observed at T around 70 K which could indicate a small ferromagnetic component. Finally, for the U_2Rh_2Sn single crystals, magnetization values in both *c* and *a* directions were obtained. The results confirm the presence of an antiferromagnetic transition at around 28 K. The magnetization in a field is slightly higher when the field is parallel to the *a* axis, which suggests that the magnetic moments of the uranium atoms are aligned parallel to the *c* axis, as was found by neutron diffraction.

1.2.3 Magnetization experiments on Np_2T_2Sn compounds

The low-temperature magnetic susceptibility measurements of three Np_2T_2Sn compounds were performed on a SQUID machine at the CEN Grenoble. Np_2Ni_2Sn has a magnetic transition around 55 K, as observed from ^{237}Np Mössbauer spectroscopy measurements [2]. Np_2Pd_2Sn shows an antiferromagnetic transition at 18 K and for Np_2Pt_2Sn two transitions are present, at around 35 K and 20 K (Tab. 1.3).

Tab. 1.3 Ordering temperatures of Np_2T_2X compounds estimated from electrical resistivity (r), Mössbauer spectroscopy, and magnetic susceptibility (c) measurements.

Np compound	T_{ord}(K) from ρ measurements	T_{ord}(K) from Mössbauer spectroscopy	T_{ord}(K) from χ measurements
Np_2Ni_2Sn	≈ 55	≈ 55	≈ 55
Np_2Pd_2Sn	≈ 18 $\rho \propto T^2$ (<9 K)	≈ 18	≈ 18
Np_2Pt_2Sn	≈ 32	≈ 32	≈ 35 / ≈ 20
Np_2Co_2Sn	non-magnetic $\rho \propto T^2$ (<11 K)	non magnetic	
Np_2Rh_2Sn	non-magnetic $\rho \propto T^2$ (<9 K)	non magnetic	
Np_2Ru_2Sn	non-magnetic	non magnetic	
Np_2Ni_2In	≈ 45	≈ 44	
Np_2Pd_2In	≈ 15	≈ 18	
Np_2Pt_2In	≈ 40	≈ 39	
Np_2Co_2In	≈ 20	≈ 21	
Np_2Rh_2In	≈ 50 / ≈ 12	≈ 49	
Np_2Ir_2In	≈ 30		

1.2.4 Electrical resistivity measurements of Np_2T_2X compounds

The electrical resistivity measurements of the Np_2T_2X series with T = Ni, Pd, Pt, Co, Rh, Ru, and Ir and X = Sn and In were concluded (Tab. 1.3). The measurements were performed at the Institute over a temperature range from 1.4 and 295 K. In some of these compounds, the resistivity data suggest a magnetic ordering at temperatures corresponding to the magnetic ordering detected by ^{237}Np Mössbauer spectroscopy [2, 3]. The increase of the resistivity below the magnetic ordering temperature for Np_2Pd_2Sn, Np_2Pd_2In and Np_2Pt_2In compounds is probably due to the anisotropic gapping of the Fermi surface due to an increase of the magnetic unit cell compared with the crystallographic one. This fact suggests antiferromagnetic behaviour. Np_2Co_2Sn, Np_2Rh_2Sn and Np_2Ru_2Sn present a significant decrease of the electrical resistivity as the temperature decreases, but no hint of magnetic ordering was observed down to 1.4 K. These results are consistent with the ^{237}Np Mössbauer results [2]. Additionally, in Np_2Co_2Sn, Np_2Rh_2Sn, and Np_2Ni_2Sn, the resistivity curve at low temperatures follows a T^2 law that normally indicates a spin-fluctuation behaviour. The temperature dependence of the resistivity ratio for three Np_2T_2In systems, are shown in Fig. 1.4. These curves illustrate the different magnetic behaviour present in this family of compounds very well.

Most of these results are consistent with the results from ^{237}Np Mössbauer spectroscopy, which suggests a magnetic ordering for all the In compounds and only the Sn compounds belonging to the Ni group [2-4].

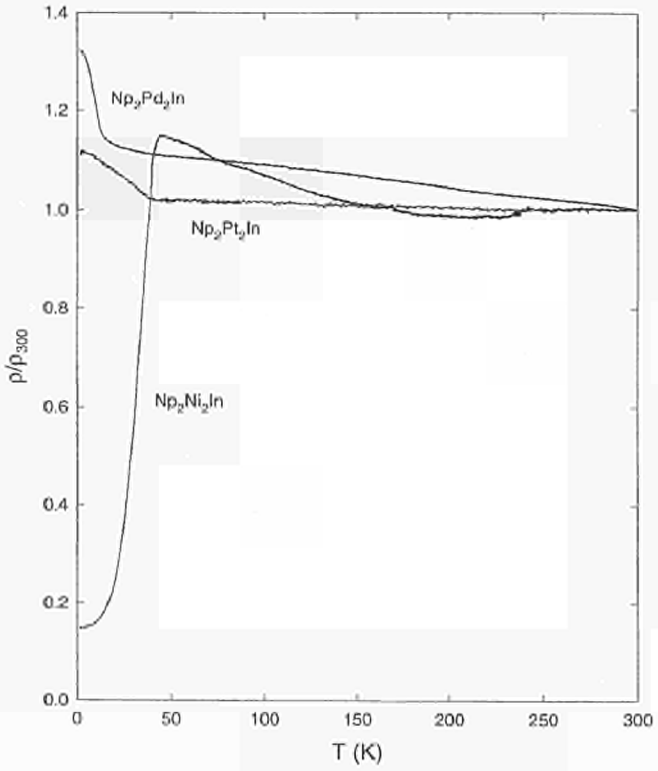

Fig. 1.4 Temperature dependence of the resistivity ratio for Np_2Ni_2In, Np_2Pd_2In and Np_2Pt_2In.

This trend is different from that in the analogous uranium compounds, in which only the Sn-series for the Co and Ni groups are magnetically ordered [4, 5].

This work was the subject of collaborative research between ITU Karlsruhe, ITN Sacavém, Universidade de Lisboa, CEN Grenoble, University of Coimbra, Charles University of Prague and Van der Waals-Zeeman Laboratory of the University of Amsterdam.

References

[1] L. Havela, V. Sechovský; P. Svoboda, H. Nakotte, K. Prokeš, F. R. de Boer, A. Seret, J. M. Winand, J. Rebizant, J. C. Spirlet, A. Purwanto, R. A. Robinson; J. Magn. Magn. Mater. **140-144** (1995) 1367
[2] J. P. Sanchez, E. Colineau, C. Jeandey, J. L. Oddou, J. Rebizant, A. Seret, J. C. Spirlet; Physica B **206 & 207** (1995) 531-533
[3] J. P. Sanchez, private communication (1994)
[4] M. N. Péron et al.; J. Alloys Comp. **201** (1993) 203-208
[5] F. Mirambet et al.; J. Alloys Comp. **203** (1994) 29-33

1.2.5 High-temperature resistivity measurements on Pu monochalcogenides

The electrical resistivity of Pu monochalcogenides (Fig. 1.5) was measured between room temperature and 800-1000 K. The resistivity data show a clear semiconductor behaviour between 440-590 K for PuS, 380-510 K for PuSe and 330-460 K for PuTe (Fig. 1.6, a-c). The obtained energy gaps are 248, 185 and 178 meV, respectively, and are in agreement with the energy gaps calculated by Brooks [1] considering delocalization of the 5f electrons of Pu and using relativistic self-consistent calculations.

However, a logarithmic dependence of the resistivity with temperature (Fig. 1.7, a-c), typical of Kondo systems, is also observed for short but significant temperature ranges, from 310-450 K for PuS, and from room temperature up to 400 K for PuSe, and 340 K for PuTe. This logarithmic dependence was also observed for the low-temperature resistivity measurement of PuTe. The b/a factor, defined according to:

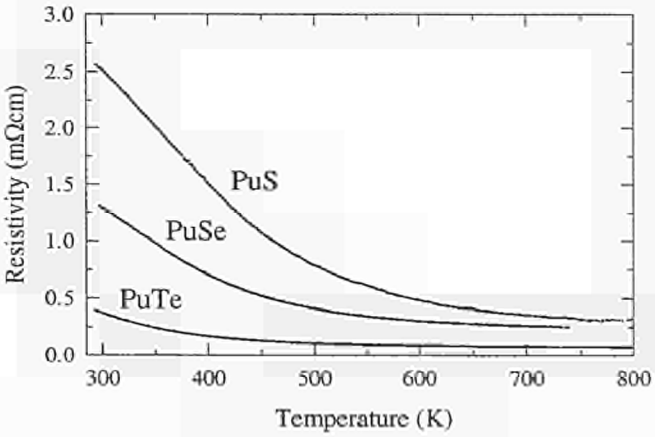

Fig. 1.5 Resistivity curves of plutonium monochalcogenides at high temperature.

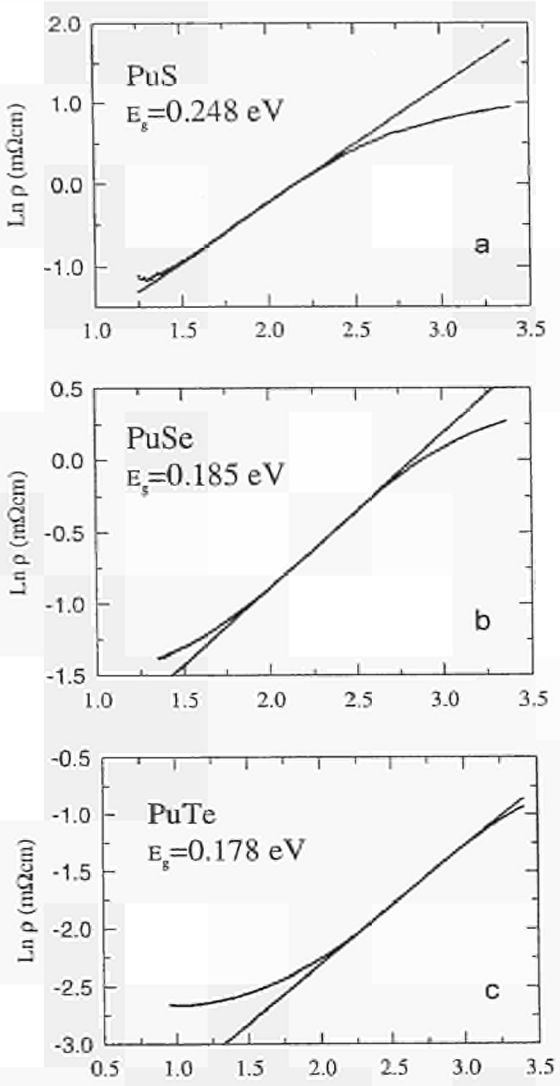

Fig. 1.6 Log of resistivity of PuS (a), PuSe (b) and PuTe (c) versus reciprocal of the temperature.

$$\rho = \rho_M \left(1 - \frac{3ZJ}{E_F} \ln T\right) = a - b \ln T,$$

Z the atomic number, J the exchange integral and E_F the Fermi level, was calculated for PuTe at high temperature. The value found of b/a = 0.163 agrees with that obtained at low temperatures (0.165) [2-3]. Thus, considering both high and low temperature resistivity data, a quite extended temperature range is also found in PuTe for which Kondo behaviour is observed. It follows that the interactions between the 5f electrons of Pu and the conduction electrons cannot be neglected in these compounds.

Simultaneous Kondo and semiconducting behaviour are difficult to reconcile, since the former implies the localization of the 5f electrons, and the latter assumes the 5f electrons to be itinerant. A transition from localized to itinerant behaviour as a direct result of increasing temperature would be unusual. However, all results obtained on these compounds up to now [4-9] suggest a localized model for the measurements carried out at about room temperature and below, and a delocalized model at higher temperatures.

The resistivity of the solid solution $Pu_{1-x}Am_x$ will be measured next at low and high temperatures using foil samples. These are prepared by arc-melting using a new technique specially developed for this purpose. Foils of between 100 and 500 μm wide can be obtained. This technique has already been successfully tested for Pt and Pu metal.

References

[1] M. S. S. Brooks; J. Magn. Magn. Mater. **63 & 64** (1987) 649-651

[2] E. Pleska; Thèse (1990) Université Joseph-Fourier Grenoble (France)

[3] M. Amanowicz; Thèse (1995) Université Joseph-Fourier Grenoble (France)

[4] J. M. Fournier, E. Pleska, J. Chiapusio, J. Rossat-Mignod, J. Rebizant, J. C. Spirlet, O. Vogt; Physica B **163** (1990) 463-495

[5] O. L. Kruger, J. B. Moser; J. Chem. Phys. **46** (1967) 891-900

[6] G. H. Lander, J. Rebizant, J. C. Spirlet, A. Delapalme, P. J. Brown, O. Vogt, K. Mattenberger; Physica **146B** (1987) 341-350

[7] F. Marabelli, P. Wachter; 17èmes Journées des Actinides (1987) Lausanne.

[8] J. R. Naegele, F. Schiavo, J. C. Spirlet; 19èmes Journées des Actinides (1989) Madonna di Campiglio

[9] P. G. Therond; Thèse (1987) Université Joseph-Fourier Grenoble (France)

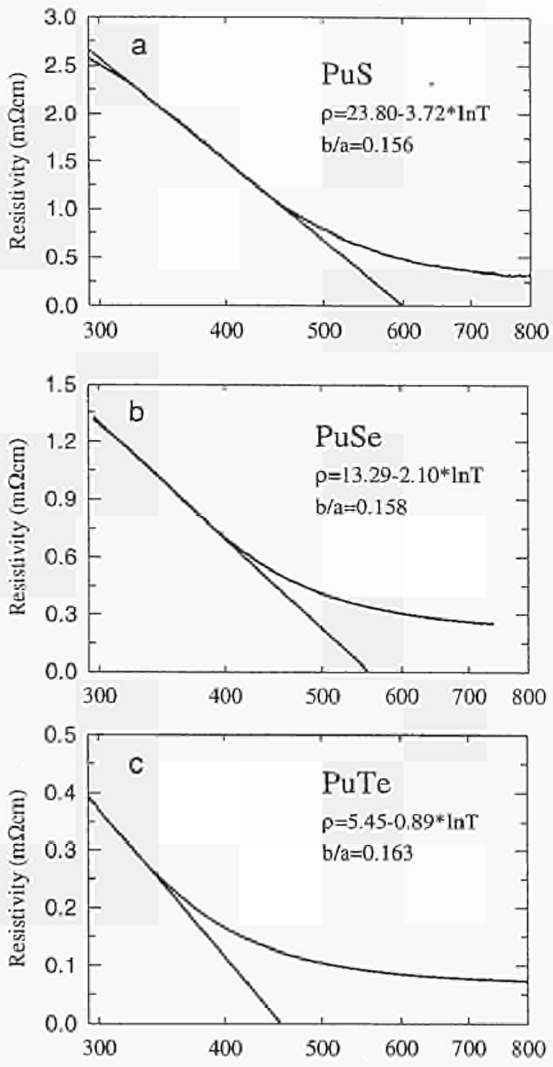

Fig. 1.7 Resistivity of PuS (a), PuSe (b) and PuTe (c) versus temperature in a log scale.

1.3 Mössbauer Studies

In cooperation with the Physik-Department E15, Technische Universität München, ^{237}Np Mössbauer measurements on the solid solutions $U_{1-x}Np_xRu_2Si_2$ (x = 0.1, 0.3, 0.5, 0.7, 0.9) have been prepared.

$NpRu_2Si_2$ is the Np analogue of the isostructural heavy fermion superconductor URu_2Si_2 [1]. The main motivation for the experiments was a comparison with previous results on the $U_{1-x}Np_xPd_2Al_3$ systems (TUAR-94). In the latter group the saturated magnetic moment of Np μ_{ord} decreases from 1.7 μ_B at x = 1 to 0.3 μ_B at x = 0.03. The ordering temperature T_{ord} decreases from 38 K at x = 1 to 3 K at x = 0.3 and increases again between x = 0.3 and x = 0 up to 14 K. These effects have been tentatively attributed to a different magnetic coupling of the Np and the U 5f moments. In $NpPd_2Al_3$ μ_{ord} is aligned along the crystallographic c-axis, in UPd_2Al_3 along the ab-plane. With decreasing x a rotation of the Np moments out of the c-axis accompanied by a strong suppression of μ_{ord} has been observed. The electric hyperfine interactions, i.e. the isomer shift S and the electric quadrupole coupling constant e^2qQ are insensitive to a variation of x down to x = 0.03.

Some results for $U_{1-x}Np_xRu_2Si_2$ are listed in Tab. 1.4. In contrast to $U_{1-x}Np_xPd_2Al_3$, μ_{ord} lies along the c-axis between x = 0 and x = 1. Although μ_{ord} strongly differs between $NpRu_2Si_2$ (1.5 μ_B) and URu_2Si_2 [2] (0.03 μ_B), in the doped compounds the Np moment (1.5 μ_B) does not vary from x = 1 down to x = 0.1.

Our experiments show that mixing isostructural compounds in which the magnetic moments point in *different* directions, as in $U_{1-x}Np_xPd_2Al_3$, can strongly suppress magnetic order, i.e. the U and Np moments interact "destructively". On the other hand mixing the compounds $NpRu_2Si_2$ and URu_2Si_2 with the *same* easy magnetization axis does not affect the Np moment (down to x = 0.1) and T_{ord} starts to decrease only below x = 0.5. In this case the "stronger magnet" seems to dominate the "weaker magnet".

The mechanism of the electric hyperfine interactions in the pure compounds $NpPd_2Al_3$ and $NpRu_2Si_2$ is not well understood. It is usually assumed that the 5f electrons strongly influence S and e^2qQ. In $U_{1-x}Np_xRu_2Si_2$, the isomer shift is nearly independent of x and e^2qQ slightly increases from -71 mm/s for x = 1 to -65 mm/s for x = 0.1. Since S does not vary with x it can be concluded that the Np charge state is not influenced by the doping with uranium. Since the value of S corresponds to a Np^{3+} state it is likely that the U state is also 3+, otherwise the number of conduction electrons would considerably change with x, which in turn would lead to a stronger variation of S than observed. The variation of e^2qQ is probably rather due to the conduction (e.g. 6d) than to the 5f electrons because a change of the electric 5f state leads in most cases to a considerable change of μ_{ord}, which was not found in our observations.

References

[1] V. Sechovsky, L. Havela; in Ferromagnetic Materials, edited by E. P. Wohlfarth, K. H. J. Buschow (North-Holland, Amsterdam, 1988), Vol. 4, chap. 4, pp. 445-461

[2] C. H. Bohom et al.; Phys. Rev. B **43** (1991) 12809

Tab. 1.4 Magnetic ordering temperature T_{ord}, saturated magnetic moment μ_{ord}, electric quadrupole coupling constant e^2qQ and isomer shift S relative to $NpAl_2$ for the solid solution compounds $U_{1-x}Np_xRu_2Si_2$. Errors in parenthesis refer to the least significant figure.

compound	T_{ord} (K)	μ_{ord} (μ_B)	e^2qQ (mm/s)	S (mm/s)
$NpRu_2Si_2$	26(1)	1.5(1)[a]	-71(1)	12.9(3)
$U_{0.1}Np_{0.9}Ru_2Si_2$	25(1)	1.5(1)[a]	-69(1)	13.0(3)
$U_{0.3}Np_{0.7}Ru_2Si_2$	25(1)	1.5(1)[a]	-71(1)	12.9(3)
$U_{0.5}Np_{0.5}Ru_2Si_2$	25(1)	1.5(1)[a]	-67(1)	12.5(3)
$U_{0.7}Np_{0.3}Ru_2Si_2$	22(1)	1.5(1)[a]	-66(1)	13.1(3)
$U_{0.9}Np_{0.1}Ru_2Si_2$	19(1)	1.5(1)[a]	-65(1)	13.3(3)
URu_2Si_2	17.5(8)[b]	0.003[b]	---	---

[a] Np moment derived from the magnetic hyperfine field

[b] U moment measured from neutron diffraction [2]

1.4 Structure of Organometallic Compounds

The crystal structures of two organo-neptunium compounds have been determined to establish their molecular structure. This work is performed in collaboration with the Institut für Technische Chemie (ITC), FZK, which supplies the crystals. These materials play important roles in actinide separation chemistry and/or in problems concerned with handling of actinide wastes.

Neptunocene [$Np(C_8H_8)_2$] is isostructural with thorocene and uranocene. The molecular structure consists of a central Np atom symmetrically π-bonded by two aromatic cyclooctatetraene dianion rings related by a crystallographic inversion center. Neptunocene has D_{8h} symmetry: the molecular eightfold axis passes through the centre of the two rings and the Np atom. This compound is the first π-sandwich structure of neptunium to be published.

Tris(η^5-cyclopentadienyl)phenolatoneptunium(IV) belongs to the class of the mixed-ligand complexes $Cp_3M(XR)$ where M = U or Np, R = alkyl or aryl substituent, X = Group 6 donor atom. This compound is isostructural with the uranium homologue: it consists of one Np atom coordinated by the O atom of the phenoxide and by three η^5-coordinated cyclopentadienyl rings. If the coordination polyhedron is considered to be formed by the O atom and the centres of the cyclopentadienyl rings, the coordination about the Np atom displays approximate C_{3v} symmetry with the O atom at the apex and the cyclopentadienyl rings at the base of a flattened tetrahedron (Fig. 1.8).

Comparison of the frequencies of crystallographic space groups in organo-lanthanide and -actinide compounds

This work was undertaken for the following three reasons: (1) determination of space-group frequency tables for routine structure diffraction measurements; (2) to find out if a difference exists between 4f and 5f-element compounds on one hand, and between these compounds and those having no f-electrons on the other hand; (3) possibilities in crystal engineering: for a number of physical properties (pyroelectricity, piezoelectricity, non-linear optical materials) where the absence of a centre of symmetry is a prerequisite.

The data of 1540 organo-lanthanide and 895 organo-actinide crystalline compounds were derived from the Cambridge *Structural Database*. 10.0% of the lanthanide and 8.4% of the actinide compounds fall in space groups of tetragonal or higher symmetry. Approximately two thirds crystallize in only three space groups: 34.1% of the lanthanides in $P2_1/c$ (actinides: 38.5%), 22.1% (20.5%) in $P\bar{1}$ and 8.3% (9.0%) in $C2/c$.

The distribution of the lanthanides into the different crystal families is similar to that of the actinides. If the data are compared with a study on the space-group frequencies for organic compounds [1], there are a number of important differences: lanthanides and actinides tend to crystallize more in the triclinic crystal family and less in the orthorhombic crystal family than organic compounds. There is an increase in the number of compounds crystallizing in one of the centrosymmetric space groups and a decrease for the enantiomorphic space groups. The number of organo-lanthanide and -actinide compounds which crystallize in space group $C2/c$ is higher and the number which crystallize in space groups $P2_1$ or $P2_12_12_1$ is lower than for the organic compounds, which indicates that the inherent molecular symmetry of f-element compounds is higher than for organic compounds as a whole. No conclusions can be drawn with respect to the difference between 4f- and 5f-element compounds.

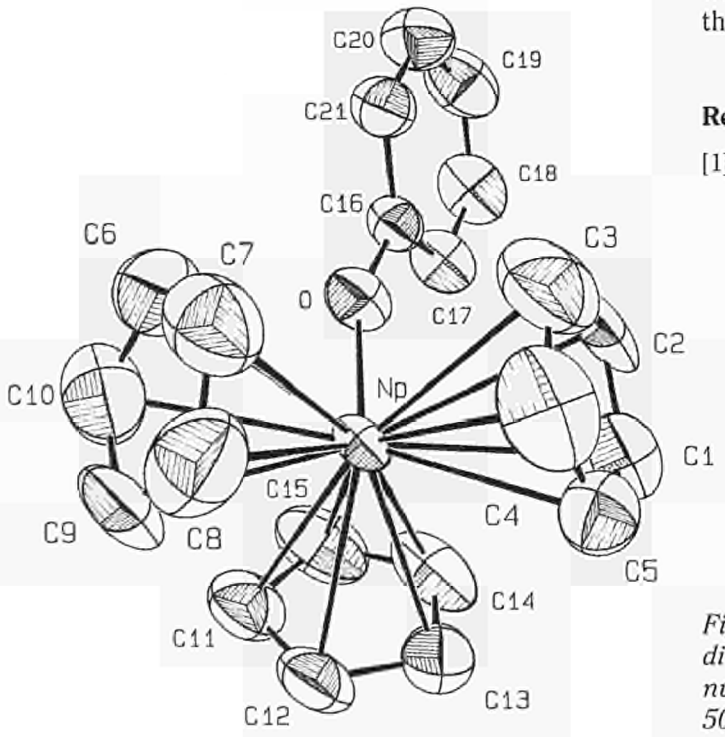

Fig. 1.8 ORTEP drawing of tris(η^5-cyclopentadienyl)phenolatoneptunium(IV) showing the numbering system with thermal ellipsoids at the 50% probability level.

References

[1] A. D. Mighell, V. L. Himes, J. R. Rodgers; *Acta Crystallogr.* **A39** (1983) 737-740

1.5 Spectroscopic Studies of Solid Surfaces

Current surface science activities concentrate on the synthesis and analysis of actinide thin layer systems. Thin layers are interesting both from a fundamental and applied point of view: on the one hand they enable us to investigate further the electronic structure of actinides, and on the other hand they allow a study of the reactivity of actinides and their interactions with their surroundings. Especially in the latter field, there are opportunities for collaborations with other groups in research applied to nuclear safety. The production of thin layers allows a study of interfacial reactivity on minute amounts of material, and they may be characterized and studied under well defined in situ conditions. Examples of collaborations are given below.

1.5.1 Study of the electronic structure of thin U layers on Mg and Al

When prepared in thin layers, actinide properties can be studied in a situation intermediate between the solid-state and the isolated atomic or molecular environment. The lowered coordination in thin layers generally results in a narrowing of the valence bands. For the 5f electrons of the early actinides (U, Np, Pu), which sit in narrow bands even in the bulk form, the presence in thin layers may result in a break-down of the itinerant behaviour. Thus decreasing the thickness of thin layers should, in principle, result in the transition from delocalized to localized behaviour. In this context interactions between the surface layer and the substrate play an important role because they influence the local electronic structure of the actinide atoms (chemical effects): even single dispersed atoms are expected to show extended solid-state properties if they are bound strongly enough to the substrate. It has been proposed recently that delocalization is to be expected on strongly interacting substrates [1], while on weakly interacting materials chemical isolation of the actinide surface atoms favours 5f localization [2].

During the last year we compared the U/Mg and U/Al systems. While U and Mg are completely immiscible, and thus can be regarded as a weakly interacting system, U and Al interact strongly forming well defined intermetallics (UAl_2). U4f spectra for U layers on Mg and Al are compared in Fig. 1.9. The results partly confirm the above hypotheses. The U4f spectra for U/Mg are similar to U metal, except for the suppression of the high binding energy (BE) background, which can be understood in terms of the small surface layer thickness. The U/Al system, on the other hand, shows strong satellites which are generally interpreted as correlation satellites [3], thus indicating band narrowing of the 5f states. One explanation may be that on the weakly interacting Mg substrate, U atoms agglomerate in large clusters, which have properties similar to bulk

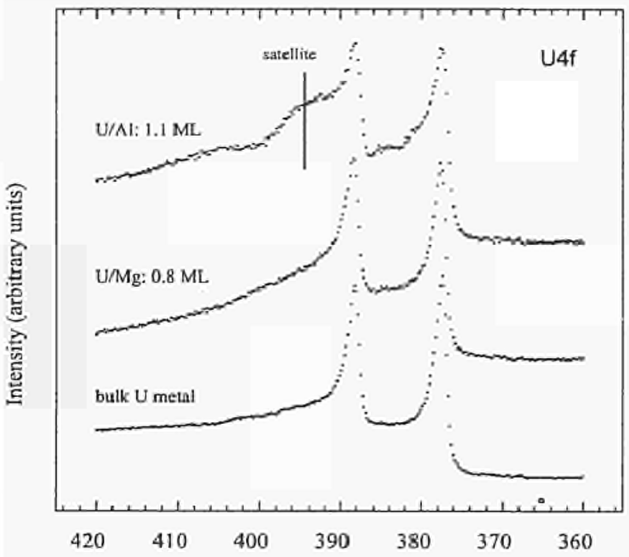

Fig. 1.9 U4f spectra of bulk U metal, U/Mg and U/Al. Surface coverage is measured in monolayers (ML).

U metal. However, contrary to expectations, chemical interactions themselves may favour 5f localization under certain conditions, e.g. by increasing the nuclear potential felt by the outer 5f electrons ("oxidation effect"). Fig. 1.10 compares valence band spectra for U/Mg and U/Al. In spite of the different behaviour of the U4f spectra (Fig. 1.9), the valence band spectra are strikingly similar. This shows that appearance of localization and correlation effects strongly depends on the analysis technique used, and in particular on the energy of the perturbation (which is two orders of magnitude higher in XPS than in UPS). It is interesting that despite the absence of correlation satellites in UPS

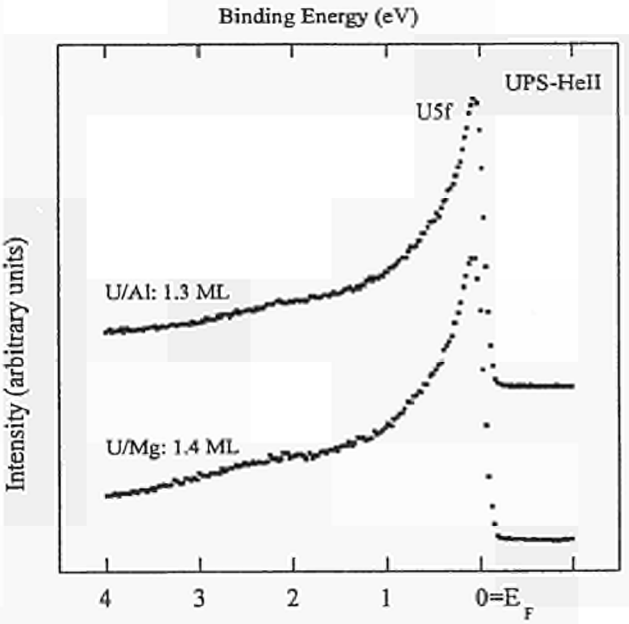

Fig. 1.10 UPS-HeII spectra of U/Mg and U/Al.

spectra, 5f band narrowing is nevertheless observed by this technique: the 5f bandwidth, as observed by photoemission, decreases with overlayer thickness (Fig. 1.11).

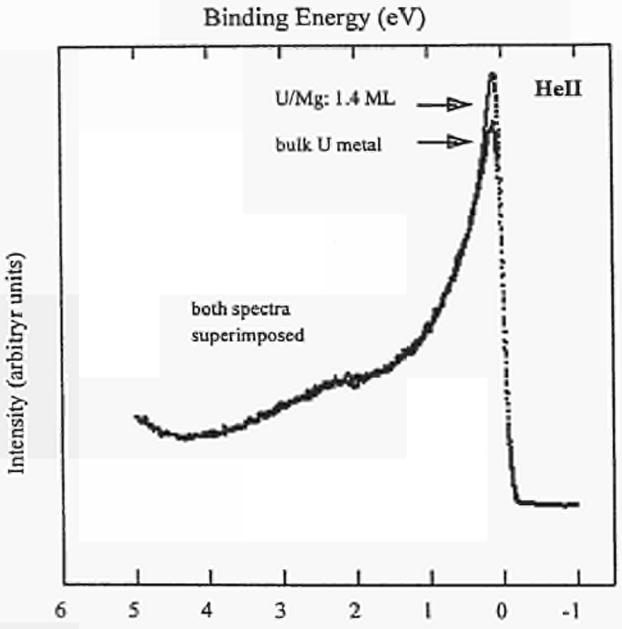

Fig. 1.11 UPS-HeII spectra of U/Mg: 1.4 ml and 15 ml ≈ U-bulk.

Thin layers for this study were prepared using an actinide sputter source, designed and built in house [4], which has run reliably for several months, and is ready to be mounted in the glove-box. Next year Pu systems will be examined, which should be especially interesting for observing 5f localization effects, because Pu lies right at the threshold of 5f localization. Thus, we hope to be able to cross the localization threshold for small overlayer thicknesses, e.g. in the submonolayer range.

1.5.2 Thin layer related activities

Preparation of thin UO_2 layers for electrochemical studies

Thin layers of UO_2 can be used to study the electrochemical behaviour of UO_2 surfaces in the presence of ground water. They may avoid problems associated with the high electrical resistance of UO_2 bulk samples. In addition, the concentration of defects, the average crystal size and oxygen stoichiometry may be easily varied in thin layers by adjusting the deposition conditions. Thin layers of UO_2 on various substrates such as Cu, ..., have been prepared. Electrochemical studies of these systems are under way. Future work should include doped UO_2 systems produced by co-sputtering, to model the electrochemical dissolution behaviour of fuel and fission products.

Preparation of thin UO_2 layers for Rutherford backscattering spectroscopy studies at Orsay

Samples for studies of fission product diffusion in thin layers at the "Centre de spectrométrie nucléaire et de spectrométrie de masse", Orsay, have been prepared. Studies of the interaction of the surface with particle beams showed a particle bombardment related growth of the nano-crystallites. This result is interesting because it reveals that under certain conditions particle bombardment may lead to the healing of surface defects.

References

[1] T. Gouder, C. A. Colmenares; Surf. Sci. 341 (1995) 51
[2] T. Gouder, C. A. Colmenares, J. R. Naegele; Surf. Sci. 342 (1995) 299
[3] A. Grassmann; Physica B **163** (1990) 547
[4] T. Gouder, N. Nolte; to be published

1.6 Resistivity under Pressure

1.6.1 Resistivity study of NpBi under pressure

We have measured the electrical resistance R(T) of NpBi from 300 K down to 1.5 K at pressures up to 22 GPa. This study allows us to compare the magnetic behaviour of the Np monopnictides (NpAs, NpSb, NpBi) under pressure. Figs. 1.12 and 1.13 show a selection of resistance versus temperature curves for two different pressure ranges:

- Below the ordering temperature (T_{ord}) and between 0.2 GPa and 3.9 GPa (Fig. 1.12) the resistance strongly increases with decreasing temperature. The derivative of this increase with pressure dimin-

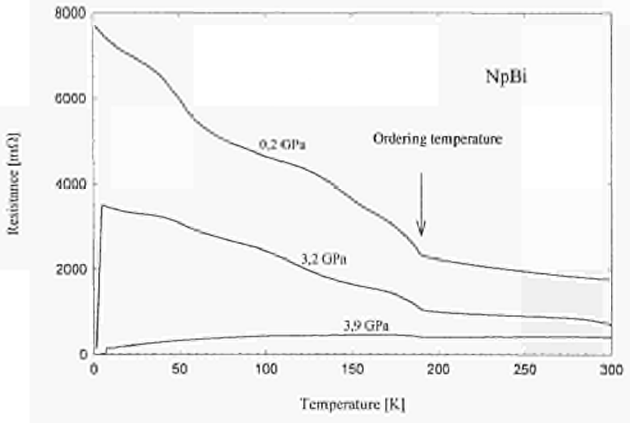

Fig. 1.12 Resistance versus temperature for NpBi between 0.2 GPa and 3.9 GPa.

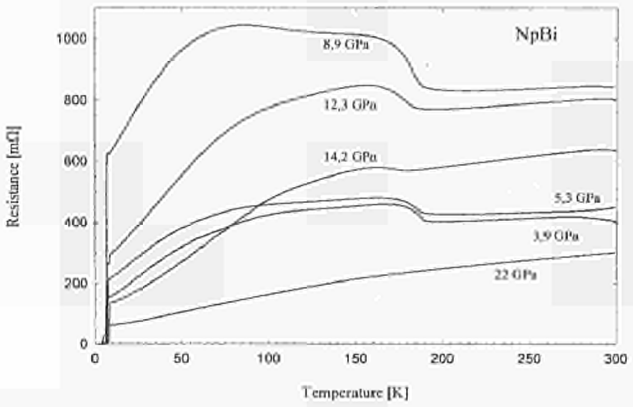

Fig. 1.13 Resistance versus temperature for NpBi between 3.9 GPa and 22 GPa.

ishes with pressure and totally disappears at 3.9 GPa. For NpAs and NpSb, we have previously observed a similar effect below T_{ord}, which diminishes already at 0.4 GPa and 2.3-2.7 GPa respectively. According to previous theoretical models, we assume that the 5f-ligand hybridization decreases when one proceeds down in group V of the periodic table (As→Sb→Bi). Therefore, it is possible that the change of the derivative between NpAs to NpBi is associated with the hybridization of the 5f states.

- T_{ord} decreases from 190 K at ambient pressure and zero pressure down to 166 K at 16 GPa. For NpAs and NpSb, we observed a larger decrease of the ordering temperature with pressure.
- Above 16 GPa (Fig. 1.13), the resistance shows a quasi-linear variation similar to the behaviour of a metallic compound. This can be interpreted as a drastic 5f delocalization effect. The same effect was found for NpSb at ~8 GPa but not for NpAs. This is surprising because one would expect a higher hybridization of the 5f states in NpAs where the distance between the Np and the ligand atom is the smallest.
- Between 1.5 K and 10 K, and above 1.6 GPa, we observe a sharp decrease of R(T) (Fig. 1.12 and 1.13). At 3.9 GPa, the resistance approaches zero at ~4 K. The pressure variation of this superconducting transition shows similarities to that of polymorphic phases of bismuth under pressure. In addition, photoemission measurements on a single crystal from the same batch revealed the presence of metallic Bi. Thus the superconducting transition could be due to traces of free Bi in the NpBi sample.

1.6.2 Extension of the resistivity measurements to lower temperatures

A new apparatus is being set up to perform resistivity measurements below 1.5 K, at ambient and at high pressure. We hope to achieve 300 mK by pumping liquid ^{3}He with an internal charcoal adsorption pump. The insert is a sealed system which retains the ^{3}He over many cooling cycles. The goal is to investigate certain Np compounds such as $NpPd_2Al_3$, $NpRu_2Si_2$ and the heavy fermion system $NpBe_{13}$ at ambient pressure. These studies are motivated by the discovery of superconductivity in their U-based counterparts below 2 K. Our previous investigations on Am metal above 1.5 K revealed an unusual pressure variation of the superconducting transition temperature. It is therefore planned to study Am metal at high pressure and below 1.5 K.

1.7 Structural Studies under Pressure

1.7.1 High pressure X-ray diffraction studies of UGa_3, UIn_3, UAl_3 and $NpIn_3$

Continuing our studies of AnX_3 compounds previously reported [1, 2] high pressure X-ray diffraction experiments were performed on UIn_3 and UAl_3 using the synchrotron radiation source at Hasylab DESY, Hamburg, and $NpIn_3$ was studied in the Institute. As with the previous UX_3 compounds, the same type of anomalous compression curves was found (Fig. 1.14).

The anomalies found all occur in the same range of pressure of between 8 - 12 GPa which corresponds to the solidifying pressure of the silicone oil pressure-transmitting medium used. To examine if this medium could be the cause of these anomalies UGa_3 was stud-

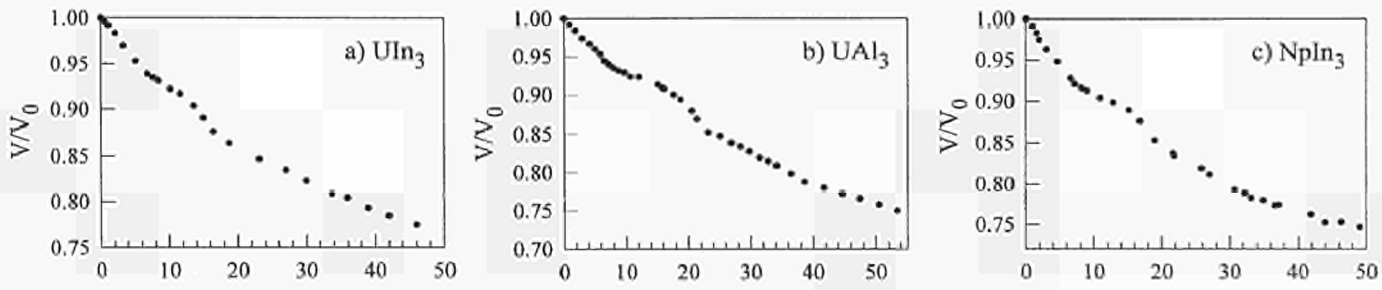

Fig. 1.14 Relative volume as a function of pressure for UIn_3 (a), UAl_3 (b), $NpIn_3$ (c).

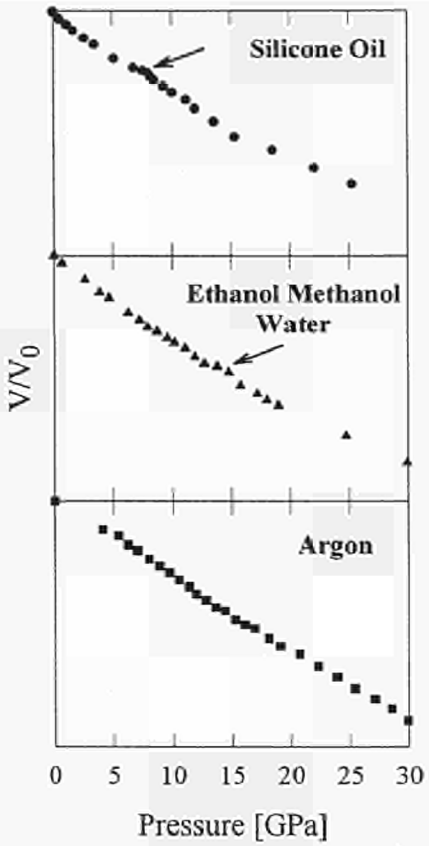

Fig. 1.15 Relative volume as a function of pressure for UGa_3 (pressure transmitting fluid: ● silicone oil, ▲ ethanol-methanol-water, ■ liquid argon).

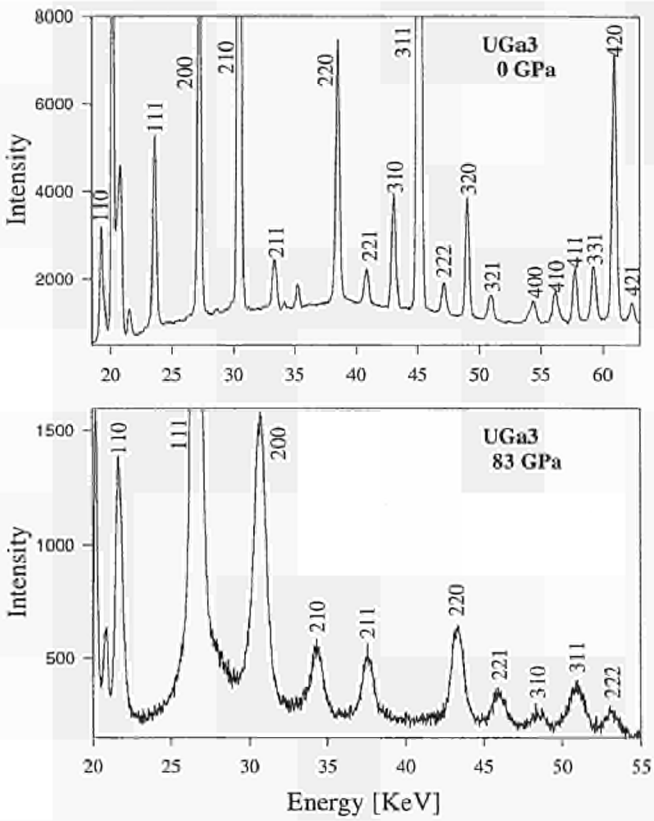

Fig. 1.16 X-ray diffraction spectra of UGa_3 at 0 and 83 GPa (θ = 6.147 °).

ied again using an ethanol methanol water mixture in the ratio 16:3:1 and liquid argon.

As can be seen in Fig. 1.15 the compression curve anomaly using the ethanol methanol water mixture shifted to a higher pressure of between 14 - 17 GPa which corresponds to the higher solidifying pressure of this mixture. To remove all ambiguity the use of liquid argon which remains hydrostatic to around 30 GPa gave a compression curve with no anomaly. The effects with silicone oil were especially evident on the UGa_3 sample because of the high quality of the spectra, and thus the excellent accuracy of the data. It should be noted that this phenomenon has been observed previously in studies of $ThSe_2$ and ThS_2 [3] and is probably present in most high pressure data but masked by the inherent measurement errors.

UGa_3 was also studied using a megabar type diamond anvil high pressure cell to very high pressures to look for a crystallographic phase transition. Such a transition has not been observed for any of the UX_3 compounds studied so far up to 50 GPa and even at the highest pressure of 83 GPa attained with these measurements the $AuCu_3$ type cubic structure was conserved as can be seen in Fig. 1.16.

The figure demonstrates clearly the quality of data which can be obtained with micro samples in a pressure cell under ideal operating conditions with the synchrotron. At 83 GPa the sample thickness is only about 2 to 4 microns after being compressed from its original 70 microns thickness at ambient pressure.

1.7.2 High pressure behaviour of TmTe

Because this material has an interesting phase transition involving f electron delocalization, we have studied TmTe up to a pressure of 49 GPa, using the energy dispersive X-ray diffraction technique and synchrotron radiation [4]. The NaCl type phase found at ambient pressure was conserved up to 8 GPa where a phase transition started to occur which was completed at 12 GPa (Fig. 1.17).

The high pressure phase corresponds to a tetragonal structure using the space groups *P4* or *P4*mm with atoms at 0,0,0 and 1/2,1/2,0.2 whereby the best indexation of the high pressure structure occurs using a tetragonal unit cell with lattice parameters $c_{tetragonal} \approx 1/2\ c_{cubic}$ and $a_{tetragonal} \approx a_{cubic} / \sqrt{2}$. The tetragonal lattice parameters at 12 GPa are a = 408 pm and c = 297 pm. Above 35 GPa this structure undergoes a further distortion. All the transformations observed were found to be reversible upon releasing pressure.

The compressibility curve before the phase transition is anomalous due to a 4f to 5d electronic collapse. The effect is less obvious than for SmS, SmSe, and SmTe [5], although still noticeable, as can be seen in Fig. 1.18. The bulk modulus B_0 and its pressure derivative B_0' were determined for the low pressure phases by fitting the pressure-volume data to both the Birch and Murnaghan equations of state, and gave values of

B_0 = 30.0 GPa, B_0' = 1.7, and B_0 = 31.6 GPa, B_0' = 0.6, respectively.

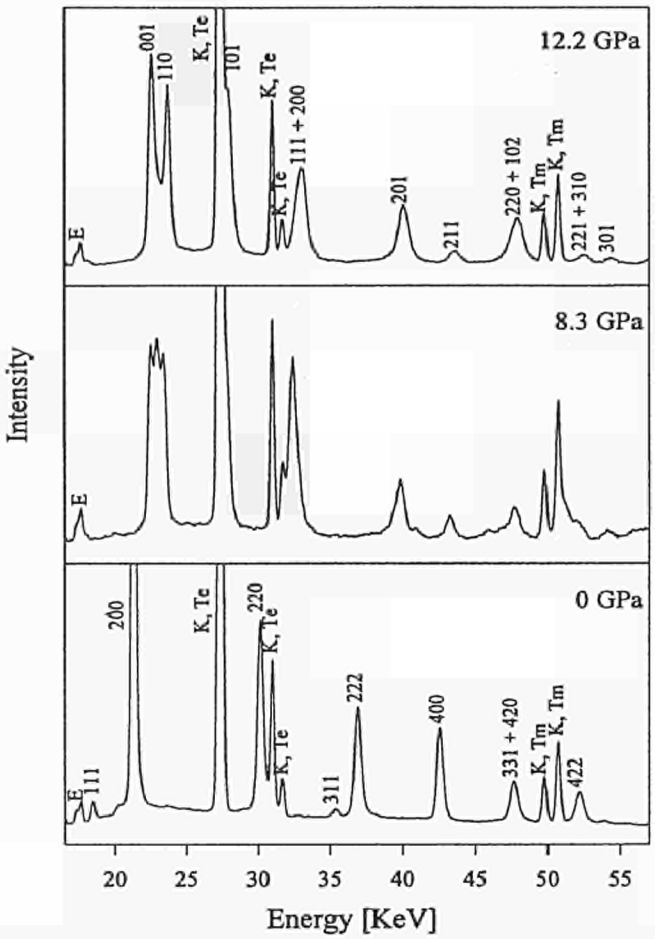

Fig. 1.17 Diffraction spectra of TmTe showing NaCl to tetragonal phase transition.

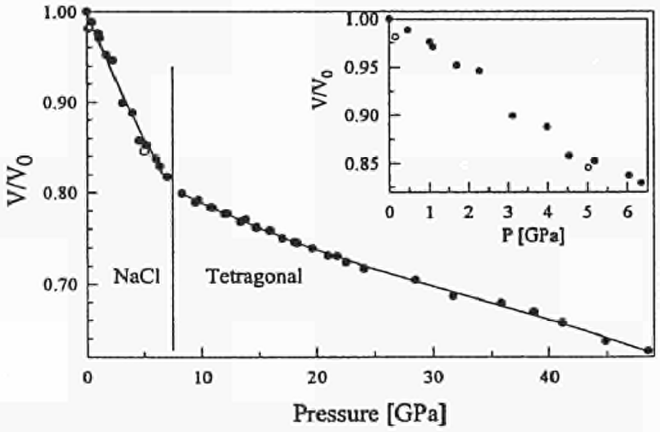

Fig. 1.18 Relative volume of TmTe as a function of pressure.

1.7.3 Einsteinium metal

As part of long standing collaborative efforts between ITU and Oak Ridge National Laboratory, attempts were made to study einsteinium metal under pressure. These experiments were conducted at Oak Ridge. The most important goal was to determine experimentally if the 5f electrons of this first divalent actinide metal would delocalize under pressure like those in the Am - Cf metals, or whether promotion of these electrons would lead to a valence change in the metallic bonding.

The scarcity of einsteinium isotopes and the high specific activity of the most abundant isotope ^{253}Es (5.6×10^{10} $\alpha \cdot min^{-1}$ μg^{-1}, 6.6 MeV α) require that micro techniques be used for preparing and studying einsteinium [6, 7]. The thermal energy associated with the radioactive decay (1 watt·mg^{-1}) is also detrimental to the sample's composition. We were successful in both setting up the required facilities and in preparing the einsteinium metal (Fig. 1.19). This was the first time both for the preparation of this large quantity (200 µg) of einsteinium metal and for obtaining the element in metal form.

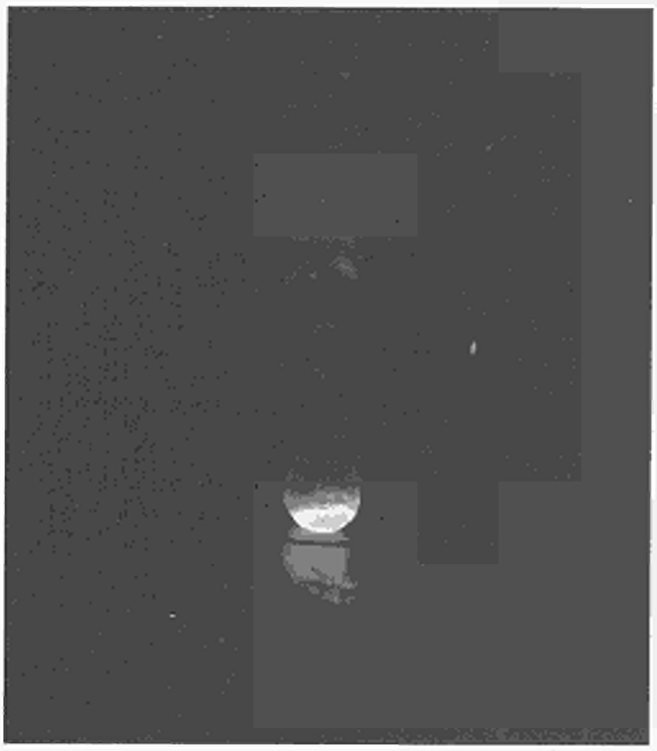

Fig. 1.19 306 micrograms of ^{253}Es used in the preparation of Es metal.

Approximately 70 µg of Es metal was vapour deposited on a small 0.5 mm spot on a platinum gasket. The metal was also loaded directly into an Inconel gasket of a diamond anvil cell. Unfortunately, crystallographic data could not be acquired, as damage to the crystal occurs rapidly due to a significant fraction of the einsteinium's alpha particles releasing their energy within the crystallites. The HPXRD analysis of Es metal therefore creates a considerably more difficult situation for the experimentalist than previously encountered with the other actinides. Because of these reasons Es must be examined immediately after preparation and even under ideal conditions the ^{253}Es sample will contain 3% of ^{249}Bk after only 1 day due to its short 20.4 day half-life.

1.7.4 Perovskites Ba_2CoUO_6 and $Ba_3Co_2UO_9$

These compounds were synthesized in the "High Pressure and Materials" group of the "Institut de Chimie de la matière Condensée de Bordeaux" and crystallize in the cubic type (Fm3m) structure with lattice parameters of a = 8.374Å and a = 8.325Å respectively. The cobalt in Ba_2CoUO_6 is divalent, whereas in $Ba_3Co_2UO_9$ it is in the trivalent state. In the latter case magnetic measurements have demonstrated the coexistence of the diamagnetic trivalent cobalt ion Co^{III} and the paramagnetic trivalent cobalt ion Co^{3+} which is in the majority.

High pressure X-ray diffraction experiments were performed on these oxides to reveal a possible spin transition

H.S. $(t_{2g}^4 e_g^2) \rightarrow$ L.S. $(t_{2g}^6 e_g^0)$

for the trivalent cobalt ion and whether this is affected by the presence of uranium. No structural transitions were observed (Fig. 1.20) although anomalous compression curves were obtained which appear not to be due to the same pressure transmitting medium phenomenon as described previously with the UX_3 compounds. Other hypotheses are possible: it could be a spin transition in both cases (for Co^{2+} in the first and Co^{3+} in the other) or the influence of the structure. Studies are continuing on other compounds.

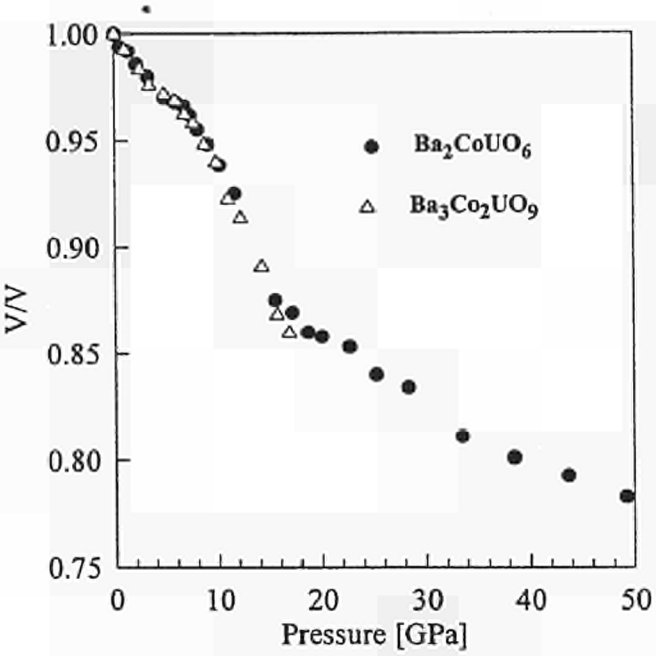

Fig. 1.20 Relative volume as a function of pressure for Ba_2CoUO_6 and $Ba_3Co_2UO_9$.

References

[1] TUAR-93, p. 162-163
[2] TUAR-94, p. 144-145
[3] L. Gerward, J. Staun Olsen, U. Benedict, H. C. Abraham, F. Hulliger; High Pressure Research **13** (1995) 327-333
[4] S. Heathman, T. Le Bihan, S. Darracq, H. C. Abraham, D. J. A. De Ridder, U. Benedict, K. Mattenberger, O. Vogt; J. Alloys Comp. **230** (1995) 89-93
[5] T. Le Bihan, S. Darracq, S. Heathman, U. Benedict, K. Mattenberger, O. Vogt; J. Alloys Comp. **226** (1995) 143-145
[6] R. G. Haire and R. D. Baybarz; J. Phys. **40** C4 (1979) 101-102
[7] R. G. Haire; J. Less Common Met. **121** (1986) 379-398

1.8 Neutron Scattering

Neutron experiments were performed this year at Siloë (Grenoble), Institut Laue-Langevin (ILL, Grenoble), which came back into operation after a 4-year shutdown, Risø (Denmark), Saclay (Paris), and Brookhaven (NY, USA) reactors, and at the ISIS (UK) spallation source.

1.8.1 Neutron studies of intermetallic compounds

Structural studies

A number of compounds were examined this year with neutron diffraction. A major interest was in the magnetic structures, since this is needed to interpret other experiments. Single crystals of U_2Rh_2Sn, UFe_4Al_8 and its rare-earth analogue $DyFe_4Al_8$, were examined, and the spin densities of the materials CeNiSn and $YbAl_3$ were determined. These latter compounds have anomalous properties not unlike those found in a number of actinide materials. In addition two difficult experiments on small (~1 mg) single crystals of $NpBe_{13}$ and $NpPd_2Al_3$ were performed at the Siloë reactor. The normal crystal size for such neutron experiments is 10 - 20 mg, so this effort set a new standard and opened up further possibilities when the higher flux of the ILL is used.

Neutron scattering experiments were performed at the Siloë reactor of the CEN-Grenoble on a U_2Rh_2Sn single crystal grown at the Institute by the mineralization technique. A previous neutron diffraction experiment on a polycrystalline sample [1] could not determine unambiguously the magnetic structure. The results show that the U atoms order in the collinear Γ_8 irreducible representation of the magnetic group, with the antiferromagnetic moments aligned parallel to the unique tetragonal axis. The propagation vector is $\mathbf{k}$ = (0, 0, 1/2) and the ordering temperature is about 28 K.

The value of the ordered magnetic moment of the uranium atoms refined from the neutron scattering intensities is small, around $0.53\mu_B$, suggesting that the f-electrons are strongly hybridized with the conduction band.

UPd_2Al_3 is an interesting heavy-fermion superconductor and a programme, which is described on other pages of this report, exists at the Institute to study the evolution of the properties when Np is doped into UPd_2Al_3. In such a study we need to know the properties of the compound $NpPd_2Al_3$, and the neutron determination of the magnetic structure is thus a key contribution. Experiments on both polycrystalline and single-crystal samples of this material have shown the same complicated phase diagram, which is illustrated in Fig. 1.21. At the ordering temperature T_N (= 38 K) the material is an antiferromagnet with an ordering wavevector characterized by $\mathbf{q}_m = (1/3, 1/3, 1/2\text{-d})$. The incommensurability d = 0.135 c* is independent of temperature down to T = 25 K, at which temperature a further phase transition occurs that results in a partial loss of intensity at the point d = 0.135 c*, and an appearance of intensity at the position d = 0. Normally such an unusual occurrence would be ascribed to a multiphase sample. However, exactly the same ratios of the d = 0.135 and d = 0 peaks were found in polycrystalline and single-crystal samples, so that such an explanation for the presence of two modulations seems unlikely. It will be interesting to try neutron experiments on samples with a small dilution of U into $NpPd_2Al_3$.

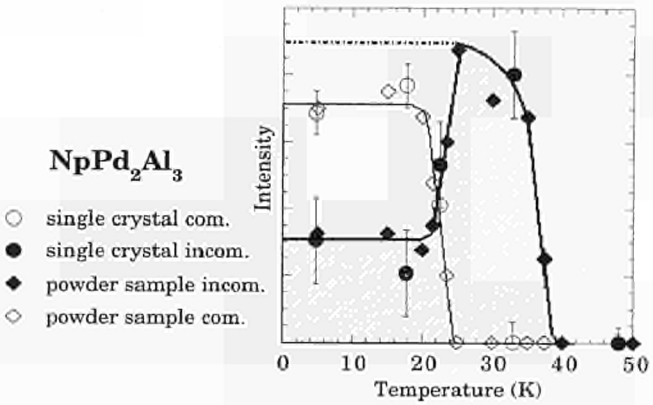

Fig. 1.21 Magnetic phase diagram of $NpPd_2Al_3$ as determined by neutron diffraction on both polycrystalline and single-crystal samples. The initial ordering (T_N = 38 K) is with a wave-vector $\mathbf{q}$ = (1/3, 1/3. 1/2-d) where d = 0.135 c.d is independent of temperature. At T = 25 K, a transition occurs in which the intensity of the d = 0.135 peak decreases by ~1/3, and intensity appears at the d = 0 position. Both modulations coexist at low temperature. Experiments performed at the Siloë and ILL reactor in Grenoble.*

In a third example of a structural study we examined the spin density of the "Kondo insulator" CeNiSn. There has been much interest in this compound as it is thought that the 4f electrons and the conduction states interact at low temperature so as to open a gap in the magnetic density of states, and, as a result, the material becomes insulating. Although this compound is paramagnetic at all temperatures, we have applied a magnetic field and induced a small magnetization, and then used neutrons to examine the induced spin density of the "magnetic" electrons. The resulting induced spin density in a projection of CeNiSn is shown in Fig. 1.22. The largest induced moment is, as expected, on the Ce site. However, a small, but significant, induced moment also resides on the Ni site. Moreover, this nickel signal appears only at low temperature - for temperatures above 30 K it is absent. Present theories for CeNiSn, and similar actinide compounds, consider only the interaction between the f and conduction states. Our experiments show the important role that the 3d states play in the hybridization process, and illustrate that, contrary to expectations, the Ni 3d band is not full at low temperature in this material. These results have to be included into any proposal for the ground-state wavefunction of the Kondo insulator CeNiSn.

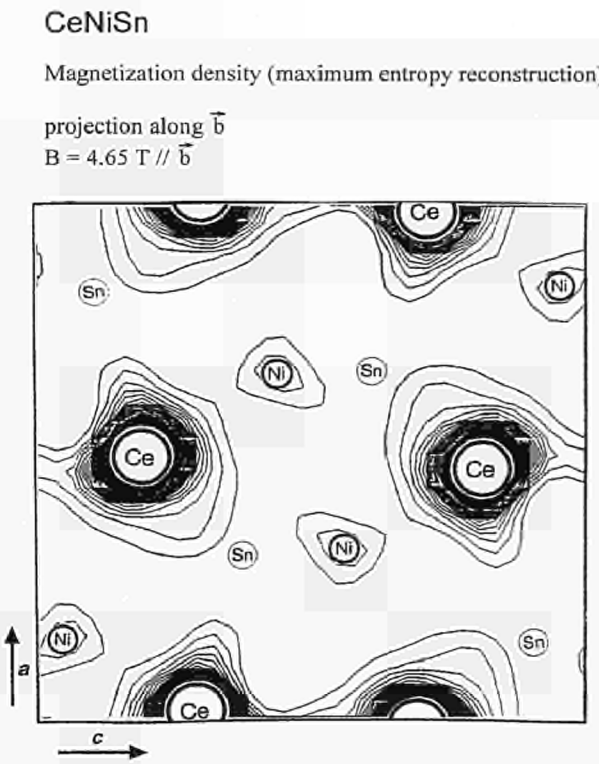

Fig. 1.22 The spin density of the compound CeNiSn as shown projected along the b axis at low temperature (T = 4K). Experiments performed at the Siloë and ILL reactor in Grenoble. The induced moment on the Ce atom is the largest, as expected, but notice also the small density at the Ni site. This shows that the Ni 3d band is not full in this material, an assumption that is always made in theoretical models for the behaviour of CeNiSn.

References

[1] H. Nakotte, A. Purwanto, R. A. Robinson, K. Prokes, J. C. P. Klaasse, P. F. de Châtel, F. R. de Boer, L. Havela, V. Sechovský, L. C. J. Pereira, A. Seret, J. Rebizant, J. C. Spirlet; submitted to Phys. Rev. B. (1995)

Dynamical studies

We reported last year on the first neutron inelastic experiments observing the dynamical response from the ferromagnet UFe_2. Further important experiments were performed in 1995. In particular, a complete characterization of the Fe-like spin wave was obtained for energies up to 5 meV. Fig. 1.23 shows the results of experimental scans at low energy using the IN14 triple-axis spectrometer with full polarization analysis at the ILL, Grenoble.

This technique allows the unambiguous separation of the magnetic and non-magnetic contributions to the scattering, and shows that the Fe-like mode has a gap at q = 0, where q is the momentum transfer. The value of this gap (~0.4 meV) is in good agreement with that deduced indirectly from bulk measurements on this compound.

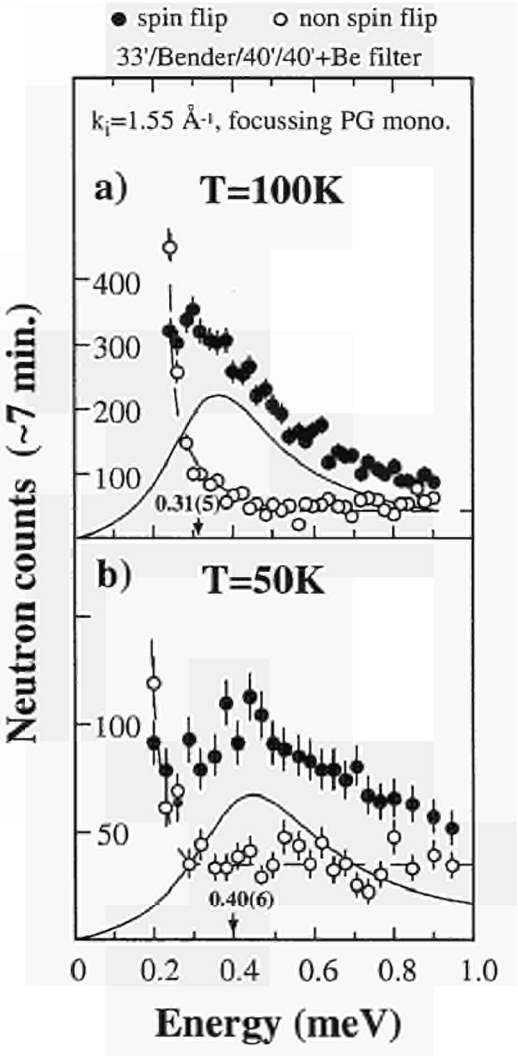

*Fig. 1.23 Constant-**Q** scans from UFe_2 at the (111) reciprocal lattice point with the IN14 triple-axis spectrometer at the ILL. The open (closed) points are those that correspond to non-spin flip (spin flip) neutron scattering, and isolate unambiguously the non-magnetic (magnetic) scattering. At 50 K there is clear indication for a gap in the Fe-like spin wave of 0.40 meV. This gap is reduced on warming the sample.*

There are two unusual and interesting aspects of this study:

The first is the discovery of strong Fe-Fe interactions that may be deduced from the dispersion of the Fe-like spin wave. At low q the energy of a spin wave in a ferromagnet is given by $E = DE + Dq^2$, where DE is the energy gap, and D is the so-called "spin-wave stiffness" constant. D may be determined by plotting the value of energy of the mode versus q^2, and such a plot is shown in Fig. 1.24. Surprisingly, although one can regard the Fe-Fe interactions as being diluted by uranium in UFe_2, the Fe-Fe interaction is actually *stronger* in UFe_2 than it is in pure iron. The D value at 50 K is almost double that found in pure Fe. This observation has interesting implications for efforts to make high-T_C compounds containing uranium, since it suggests that the hybridization between the uranium 5f and iron 3d electrons results in an enhanced ferromagnetic interaction. Unfortunately, the strong temperature dependence of D (see Fig. 1.24) is almost certainly due to higher-order interactions induced by this process, and has a deleterious effect on any effort to raise T_C. More experiments with other materials are needed to explore the significance of this result.

The second unusual aspect of the UFe_2 results is that the lowest energy acoustic-like spin wave involving the spins of both the uranium and iron sites is *not* observed. Our polarization analysis experiments have searched exhaustively for evidence of this mode, but

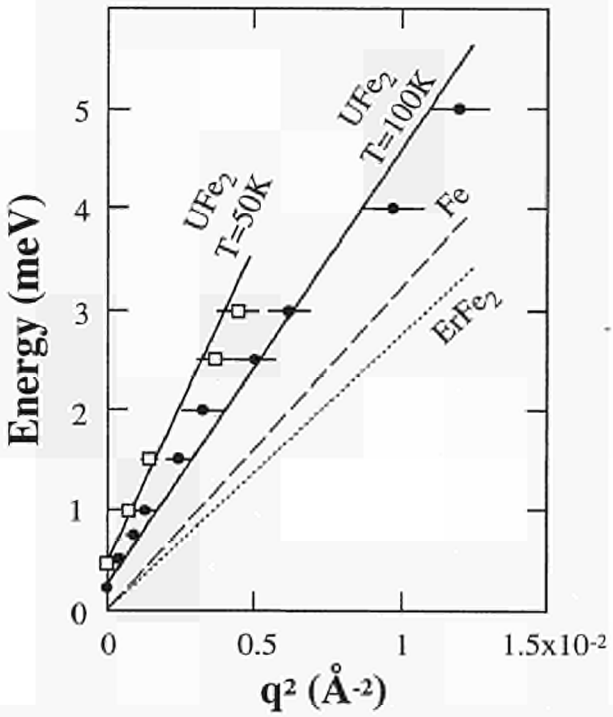

Fig. 1.24 Analysis for the low-q region for various materials according to the formula $E = DE + Dq^2$. Dashed line is best fit Fe-data giving D = 325 (10) meV-Å^2. The dotted curve corresponds to D = 280 meV-Å^2 as given in the literature for $ErFe_2$ at 295 K. The gap, DE = 8 meV, is suppressed in presenting this value of D for $ErFe_2$. The two solid lines are fits to UFe_2 at 100 and 50 K where D values of 440 (30) and 630 (50) meV-Å^2, respectively, are found.

without success. The only reason we can presently advance for this absence is that the mode has become very broad and our instruments are incapable of sensing it. This situation has been observed previously in actinide compounds involving 5f moments [1].

References

[1] E. Holland-Moritz and G. H. Lander; in "Handbook on the Physics and Chemistry of the Rare Earths", edited by K. A. Gschneidner, L. Eyring, G. H. Lander, G. R. Choppin, Vol. **19** (1994) 1

1.9 X-ray Magnetic Scattering

The magnetic scattering with X-rays continued at the Brookhaven (NY, USA) synchrotron with experiments on a number of uranium compounds. The security arrangements for running samples containing transuranium elements were successfully completed and in November 1995 a single crystal of PuSb was examined. Disappointingly, although all the safety procedures worked, we did not observe magnetic scattering. A successful experiment was performed at the European Synchrotron Radiation Facility (ESRF, Grenoble) to separate the spin and orbital contributions in an actinide compound.

1.9.1 Non-resonant magnetic X-ray scattering

We reported last year on our first efforts to observe the weak non-resonant magnetic scattering from a single crystal of $USb_{0.8}Te_{0.2}$ at the new 3rd generation X-ray synchrotron source the ESRF in Grenoble. In principle, this scattering contains valuable information about both the magnetic structure and the spin (S) and orbital (L) contributions to the magnetism of the material. However, the magnetic scattering is weak, ~10^7 times weaker than the normal charge (Thomson) scattering, so that these experiments are difficult. Furthermore, to extract the maximum information we need to analyse the linear polarization of the scattered radiation, adding further difficulty. After a number of efforts, we finally concentrated on UAs for our studies, and have now succeeded in obtaining reliable non-resonant X-ray magnetic intensities with polarization-analysis of the scattered radiation.

Fig. 1.25 shows the results of the determination of L/S as a function of momentum transfer, Q. The theoretical values (assuming Russell-Saunders coupling that applies to the rare-earths) at Q = 0 for a $5f^2$ and a $5f^3$ configurations are -5 and -4, respectively. The value changes as a function of Q because the spin and orbital magnetization densities have a different spatial dependence. The experiments are consistent with a $5f^3$ configuration for UAs.

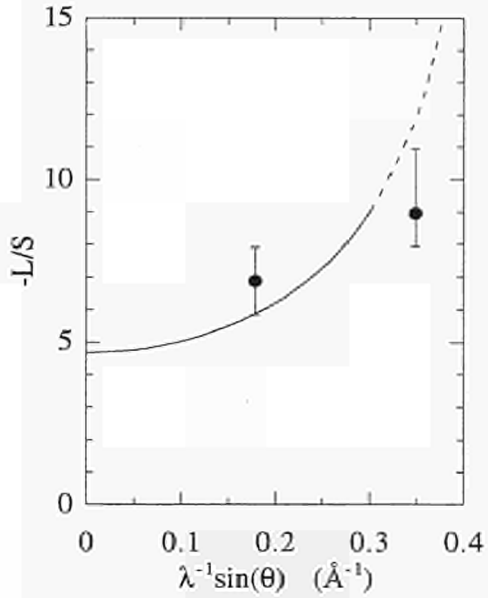

Fig. 1.25 Variation of the ratio L/S as a function of Q (momentum transfer) for the compound UAs. These results have been determined by analysing the non-resonant X-ray magnetic scattering from the Troika beamline at the ESRF, Grenoble.

1.9.2 Resonant magnetic X-ray scattering

We have performed a number of experiments this year on uranium compounds. Samples such as UPd_2Al_3 and UPtGe were examined, and towards the end of the year an experiment was performed on a thin (1500 Å) film of UPd_2Al_3 prepared in Mainz. Magnetic scattering was observed from all these materials. In contrast, our attempts with a PuSb crystal were not successful. The latter results are still being evaluated, but it seems likely that the experiment failed because there was a layer of non-magnetic (oxide?) material on top of the PuSb single crystal. The resonant technique is very surface sensitive because of the large absorption at the M edges.

In collaboration with Brookhaven staff, our effort continues to characterize the resonant scattering from the surface of a highly polished single crystal of UO_2. Our

first observation of such scattering was reported last year. Because the surface of a material is two dimensional in nature, the scattering from it shows a characteristic intensity profile that reflects the abrupt termination of the crystal at the vacuum. Any roughness on an atomic scale will strongly attenuate the scattering from the surface layer. Scans along the so-called magnetic "truncation rod" are shown in Fig. 1.26. The shape of this scattering, and its energy and temperature dependence, all confirm that it comes from the surface (~20 Å) of the UO_2 crystal. Our experiments so far have followed the temperature dependence of the surface scattering and we have found that it is quite different from that coming from the bulk of the crystal, which is known to be 1st-order in nature. Our initial interpretation of these results [1] was that we had observed "surface melting" [2]. This is a phenomena in which the surface disorders at a lower temperature than the bulk, and has been observed in structural phase transitions, for example, at the surface of a $AuCu_3$ crystal [3]. However, a more complete analysis does not totally agree with the theoretical predictions [2], and more modelling is currently in progress.

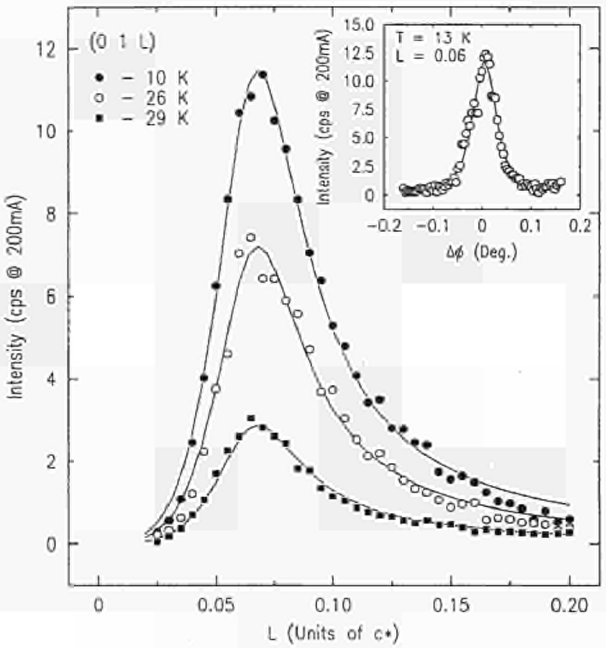

Fig. 1.26 Scans along the (01L) truncation rod as a function of L (the surface normal is [001]) for three different temperatures from a single crystal of UO_2 taken at the X25 Wiggler beam line at the NSLS, Brookhaven National Laboratory, NY, USA. For UO_2 the antiferromagnetic T_N = 30.2 K. These profiles, as a function of L, are characteristic of scattering from a 2-dimensional surface. Lines are guides to the eye. The intensity is peaked when the angle of incidence is equal to the critical angle, which happens in UO_2 when L ~ 0.06 c. The insert shows a scan perpendicular to the truncation rod, i.e. keeping L fixed and varying K, and this peak is sharp, as expected.*

References

[1] G. M. Watson, D. Gibbs, G. H. Lander, Hj. Matzke, B. D. Gaulin, L. E. Berman, W. Ellis; Physica B (in press)
[2] R. Lipowsky; Phys. Rev. Lett. **49** (1982) 1575
[3] H. Dosch, L. Mailänder, H. Reichert, J. Peisl, R. L. Johnson; Phys. Rev. B **43** (1991) 13172

1.10 Theory: *Ab Initio* Calculations of Ground State and Spectroscopic Properties

1.10.1 Calculated elastic constants of UC, US, and UTe

We have studied the elastic constants and inter-atomic forces for three selected compounds, UC, US, and UTe. In UC a combination of the smallness of the anion and the bonding 5f states of the U atom leads to a small lattice constant and high bulk modulus. *Ab initio* calculations with bonding 5f electrons yield the correct lattice constant, bulk modulus, temperature independent Pauli paramagnetism and the calculated Fermi surface agree well with experiment. Both US and UTe are ferromagnets. *Ab initio* calculations for US reproduce the measured lattice constant and bulk modulus within a few percent. The Curie temperature of UTe increases under pressure up to 5 GPa, after which it decreases whereas in US it decreases at all applied pressures [1]. Magnetic excitations are observed in UTe [2] whereas there is no sharp response in US. The measured elastic constants are anomalous in UTe - the Poisson ratio being negative whereas it is positive in UC and US [3]. In US the elastic constant C_{12} is only just positive whereas for UTe it is negative. A negative C_{12} leads to a negative Poisson's ratio since one can write $C_{12} = B - 2/3\ C'$ where B is the bulk modulus. The magnitude of C' is a reflection of how stable the crystal is with respect to a tetragonal shear. A negative C_{12} thus means that it costs more in energy to distort the crystal structure (in a tetragonal way) than to modify the volume.

We used a full-potential, fully relativistic, self-consistent calculations. The charge density and potential was allowed to have any shape. The quantum mechanical basis set, charge density, and potential were expanded in spherical harmonic series within the nonoverlapping atomic spheres and in a Fourier series in the interstitial region of the crystal.

In Tab. 1.5 we compare the calculated lattice constant, bulk modulus, and tetragonal shear constant with measurements for UC, US, and UTe.

Tab. 1.5 Calculated and measured lattice constants, bulk modulus and tetragonal shear constant, for UC, US, and UTe.

	UC		US		UTe	
	Exp.	Theory	Exp.	Theory	Exp.	Theory
Lattice Constant	4.96	4.77	5.49	5.30	6.15	5.96
C' (GPa)	118	137	144	140	82	141
Bulk Modulus (GPa)	158	168	109	130	34	109

Theory and experiment differ by between 6 to 11% for UC. The calculations overestimate the bulk modulus - a common feature of this type of calculation and not restricted to actinides. The calculated lattice constants are within 10% of measurements for all three compounds. The agreement for the bulk modulus and the tetragonal shear is fairly good for UC and US.

In contrast, for UTe our calculations fail to reproduce the experimental data. For this compound the calculated bulk modulus is more than three times too large and the calculated tetragonal shear constant is 72% too large. The failure to reproduce the experimental bulk modulus for UTe suggests that UTe is a mixed valence system [3]. Tab. 5 shows that the tetragonal shear constant for UTe is not dramatically different from that of UC and US, whereas the bulk modulus is very different and that the negative C_{12}, and therefore Poisson's ratio, is caused by the very low bulk modulus. In US, C_{12} is not negative but the measured C_{12} = 1.3 GPa is very low. The calculated C_{12} = 3.7 GPa for US is also very low and close to the experimental value, indicating of US is a borderline compound, where the 5f states are on the boundary between being bonding and non-bonding.

References

[1] P. Link, U. Benedict, J. Wittig, H. Wühl; J. Phys., Condens. Matter **4** (1992) 5585;
P. Link, U. Benedict, J. Wittig and H. Wühl; Physica **B190** (1993) 68

[2] T. M. Holden, W. J. L. Buyers, E. C. Svensson, J. A. Jackman, A. F. Murray, O. Vogt, P. DuPlessis; J. Appl. Phys. **53** (1982) 1967

[3] J. Neuenschwander, H. Boppart, J. Schoenes, E. Voit, O. Vogt, P. Wachter; in Proceedings 14èmes Journées des Actinides, ed. J. Schoenes, ETH, Zürich (1984) 30; J. Neuenschwander, E. Voit, O. Vogt, P. Wachter; Physica **144B** (1886)

1.10.2 *Ab initio* theory of the magneto-optical spectra of UAsSe

The magneto-optical (MO) Kerr effect in uranium and cerium compounds is normally very large and for that reason alone of exceptional interest. In addition the theory of the electronic structure of such compounds is unusually difficult because there is some doubt about how the 5f electrons should be treated - as transition metal electrons as the 3d electrons in iron or as localized electrons such as the 4f electrons in gadolinium. There have been a number of recent studies of magneto-optical properties of uranium compounds that are disturbing because the results were worse than for transition metals. It is possible that the standard theory might be breaking down - especially for excited states.

UAsSe crystallizes in the tetragonal PbFCl crystal structure and is a ferromagnet below 110 K. Magnetic susceptibility measurements [1] and photo-emission experiments [2] suggest localized 5f electrons in UAsSe whereas reflectivity and magneto-optical spectroscopy [3] reveal a pronounced spectral intensity at small photon energies which suggest bonding 5f electrons located at the Fermi energy.

Ab Initio theory has failed to give a satisfactory description of the optical spectra of the uranium monochalcogenides. This failure is thought to be due to an insufficient treatment of f-electron correlation [4]. Correlation can be important for the proper description of ground state properties, but should be even more important for describing optical excitations when strong Coulomb repulsion between electron and hole quasiparticles may dominate.

The crystallographic and magnetic structure of the UAsSe is different from that of the monochalcogenides as it is not cubic and the c-axis is the easy axis of magnetization. The unit cell of UAsSe in this structure is shown in Fig. 1.27. The uranium atoms are arranged in layers

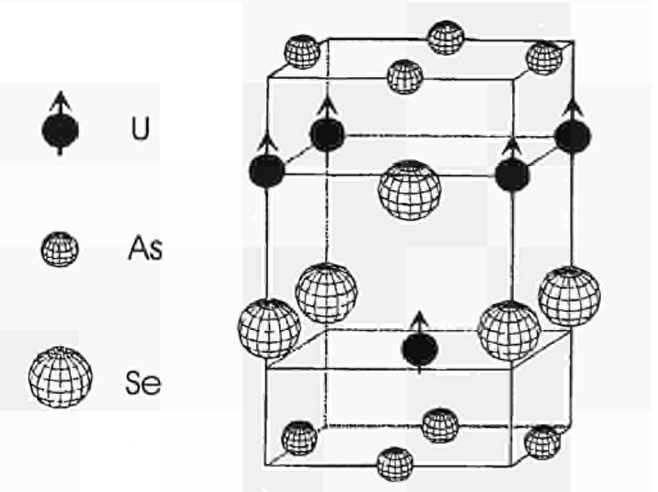

Fig. 1.27 The crystallographic unit cell of UAsSe in the PbFCl (also called ZrSiS) crystal structure. The magnetic moments on the uranium sites are depicted by the arrows.

which leads to both anisotropic bonding and magnetic properties due to hybridization of 5f and p or d states. It is possible that the 5f electrons are delocalized in the planes but localized along the c-axis. The uranium planes are perpendicular to the axis of the polar Kerr measurements, so that the polar MO Kerr effect selectively probes these.

We have calculated the optical conductivity spectra, by employing the usual linear-response formalism and a computational technique which we developed previously [5]. The calculated and measured polar Kerr spectra of UAsSe are shown in Fig. 1.28. Agreement between the theory and experiment is excellent.

We believe that this is because the 5f electrons are bonding in the uranium planes and that it is these planes that are selectively probed by the MO spectroscopy. The present result suggests the interesting possibility of measuring the anisotropy of the polar MO spectra in UAsSe or similar compounds. We would expect the MO spectra to be highly anisotropic if the 5f states are bonding only in the planes.

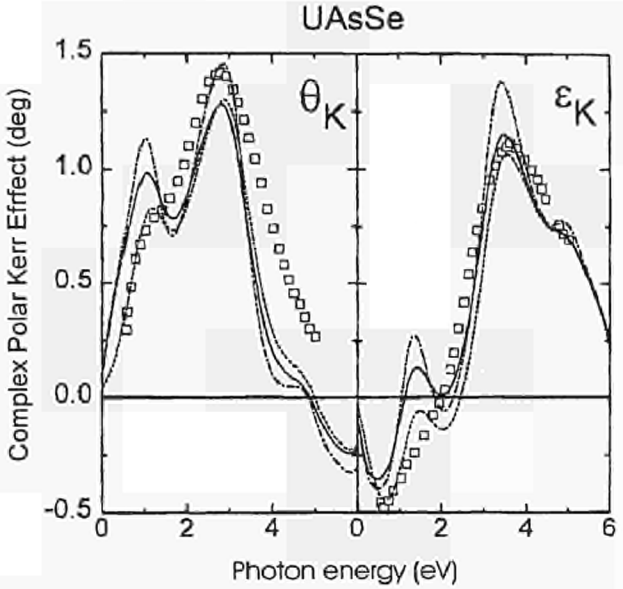

Fig. 1.28 Theoretical and experimental polar Kerr rotation and Kerr ellipticity spectra of UAsSe. The experimental data are after Reim [3].

References

[1] F. Hulliger; J. Less-Common Met. **16** (1968) 113; J. Leciejewicz, A. Zygmunt; Phys. Status Solidi A **13** (1972) 657; A. Zygmunt, M. Duczmal; Phys. Status Solidi A **9** (1972) 659; K. P. Belov, A. S. Dmitrievsky, A. Zygmunt, R. Z. Levitin, V. Trzebiatowski; Zh. Ehksp. Teor. Fiz. **64** (1973) 582

[2] J. Brunner, M. Erbudak, F. Hulliger; Solid State Commun. **38** (1981) 841

[3] W. Reim; J. Magn. Magn. Mater. **58** (1986) 1

[4] A. B. Kunz, C. P. Flynn; Phys. Rev. Lett. **50** (1983) 1524

[5] T. Kraft, P. M. Oppeneer, V. N. Antonov, H. Eschrig; Phys. Rev. B **52** (1995) 3561

1.11 Production of ^{225}Ac and ^{213}Bi for Alpha Immuno-Therapy and Conjugation of Alpha Emitters to Antibodies

1.11.1 Methods of production of ^{225}Ac and ^{213}Bi for alpha immuno-therapy

The "proof of principle" in applying ^{213}Bi -therapy to cure acute myelogenous leukaemia will begin early next year at the Memorial Sloan Kettering Cancer Center, New York. The available ^{229}Th at the Institute can produce about 35 mCi of ^{225}Ac every two months, which is not enough to treat several patients at the same time. For this reason, possible methods to produce larger amounts are being looked at.

There are several ways to either obtain ^{229}Th, from which ^{225}Ac can be milked, or produce ^{225}Ac directly. All methods of production of ^{229}Th are lengthy and cumbersome, but once this nuclide is obtained, it will yield ^{225}Ac for "ever". Direct ^{225}Ac production, however, has to be repeated regularly, but would yield high quantities within a short time, thus suitable for meeting high demand on short notice as may occur after the application has been proven clinically.

^{229}Th from ^{233}U decay

With a half-life of 159000 years for the parent, ^{233}U, the build-up of ^{229}Th is slow. Old stocks of ^{233}U at ORNL contain a few Curies of ^{229}Th with about an equal activity of ^{228}Th stemming from ^{232}U contained in the material. Because of the low concentration of ^{229}Th, in the part-per-billion range, together with precautions to be taken because of the critical mass of ^{233}U, separation will involve considerable costs.

$$^{233}\mathrm{U} \xrightarrow[159100\mathrm{y}]{\alpha} {}^{229}\mathrm{Th}$$

^{229}Th by sequential neutron capture of ^{226}Ra

Irradiating ^{226}Ra in a high thermal flux will yield an equilibrium concentration ratio of ^{228}Th to ^{229}Th of about 1:1. Because of high energy gammas emitted from ^{228}Th daughter ^{208}Tl, the handling requires heavy shielding and the maximum quantities that can be handled in our chemical hot-cells are limited to

37 mg ^{228}Th. The ^{225}Ac product after purification would be only 8 mCi.

^{226}Ra (n, γ) ^{227}Ra (n, γ) ^{228}Ra (n, γ) ^{229}Ra

$\xrightarrow[4.0\,m]{\beta^-}$ ^{229}AC $\xrightarrow[62.7m]{\beta^-}$ ^{229}Th

Neutron capture by ^{228}Ra

The short-lived ^{228}Ra (5.76 y) can be isolated rather easily during the processing of ^{232}Th. However, during target preparation, irradiation and processing, the build-up of ^{228}Th will be considerable. Therefore, the same difficulties are faced as for the previous irradiation process described.

^{228}Ra (n, γ) ^{229}Ra

Fast neutron irradiation of ^{230}Th

The neutrons of a fast reactor would produce ^{229}Th by a (n, 2n) reaction in a rather pure form compared to the previously described processes. The ^{231}Pa formed by (n, γ) reaction as well as the decay products from ^{230}Th can be easily separated. However, the ratio $^{230/229}$Th will be high requiring large ion-exchange columns to prevent Th breakthrough. If neutron spallation sources could be used, the ^{229}Th concentration would be considerably increased.

^{230}Th (n, 2n) ^{229}Th

Irradiation of ^{226}Ra with protons

Using cyclotron-accelerated protons, Curie amounts of ^{225}Ac can be produced within a day from about 1 g of ^{226}Ra. This seems the most promising way to meet a short demand for ^{225}Ac. Cyclotrons for this purpose exist at many places and the chemistry involved is not complicated. The ^{226}Ac formed simultaneously by the (p, n) reaction, will decay quickly ($t_{1/2}$ = 29 h) during the processing of the target after irradiation. A test irradiation is under preparation for January 1996.

^{226}Ra (p, 2n) ^{225}Ac

Irradiation of ^{226}Ra with gamma rays

Irradiating ^{226}Ra with Bremsstrahlung from an electron-accelerator would yield the nuclide ^{225}Ac. However, installations where this can be carried out are scarce. Nevertheless, this possibility should be tried out.

^{226}Ra (γ, n) ^{225}Ra $\xrightarrow[14.8d]{\beta^-}$ ^{225}Ac

Fast neutron irradiation of ^{226}Ra

Just to complete the possibilities, we have included this reaction, too. Due to the lengthy procedures in handling irradiations in fast reactors, the prospects for putting it into practice are low. Again, a spallation source would be a more promising approach.

^{226}Ra (n, 2n) ^{225}Ra $\xrightarrow[14.8d]{\beta^-}$ ^{225}Ac

1.11.2 An experimental study on the radiolabelling of BB4 antibody with ^{213}Bi

Introduction

In the construction of a specific α-radioimmunoconjugate to attack a given type of cancer cells, a sequence of steps is required to come to a successful product. First a suitable α-radioisotope needs to be chosen. ^{213}Bi was selected in this case for reasons indicated in the related contributions to this annual report. Secondly, a suitable chelate needs to be found which efficiently complexes the radioisotope. Based on a literature review, four different types of ligands were investigated in this study. Finally, the antibody must be determined to be selective for the antigen of the target cells. The antibody used for the myeloma cell lines is the BB4 IgG. The cytotoxicity of the radioimmunoconjugate is then tested on real cells using an incubator.

The work reported here was carried out together with the 'Institut de la Santé et de la Recherche Médicale' (INSERM), Nantes, France under the guidance of Prof. J. F. Chatal.

Labelling of BB4 antibody with ^{213}Bi

In the search for a suitable chelate to complex ^{213}Bi, 3 macrocyclic ligands (AK 23, AK 29 and AK 33) and one polyaminocarboxylic ligand (Benzyl DTPA) were investigated (Fig. 1.29). Each ligand was dissolved in 0.1 M hydrochloric acid and then adjusted to pH 5. The ^{213}Bi was eluted from the ^{225}Ac cow with 0.2 M hydrochloric acid, evaporated to dryness and redissolved in 0.1 M sodium chloride. An aliquot of the ^{213}Bi solution was allowed to react with each ligand and the resulting solutions deposited on cation-exchange columns. Each column was eluted with 0.1 M NaCl, and the eluated radioactivity was measured. Under these conditions, only DTPA appeared to complex ^{213}Bi efficiently.

In a related analysis, BB4 IgG antibody was coupled to the 4 chelates, which gave 4 modified antibodies: BB4-AK 23, BB4-AK 29, BB4-AK 33 and BB4-BenzylDTPA. To radiolabel these modified antibodies, ^{213}Bi was eluted from a generator and after adjustment of pH, added to a known amount of antibody. After a 15 minute incubation at room temperature, the radioactive solution was purified on Sephadex G-100 or PD-10 exclusion-diffusion gel. Under these conditions, 30 to 50% of the labelling activity was found in the BB4-BenzylDTPA antibody and less than 3% in the other antibodies test-

DTPA

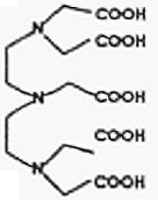

AK 23

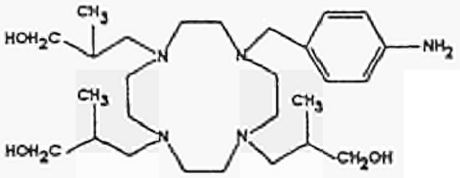

AK 29

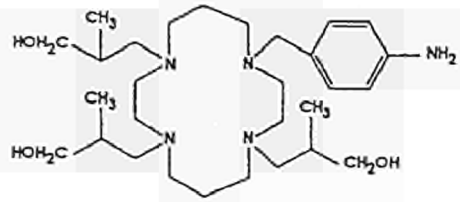

AK 33

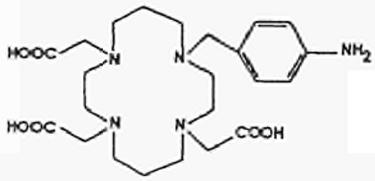

Fig. 1.29 Ligands coupled to the BB4 IgG antibody.

ed. Thus, under the test conditions, only BenzylDTPA seemed usable for radiolabelling BB4 antibody with ^{213}Bi. The specific activities obtained with this antibody (4 ligands/antibody) were 1.5 to 4.8 mCi/mg depending on the procedures used.

Uptake and cytotoxicity studies on cells

The intention was to test the different radioimmunoconjugates on 3 myeloma cell lines (LP1, RPMI and U266) as well as on a control line (RAJI) not expressing the antigen recognized by BB4 antibody. The lines were to be incubated with the same activity of free ^{213}Bi.

However, transport problems and poor cell-culture conditions (breakdown of the CO_2 incubator) prevented the uptake and cytotoxicity tests being carried out. A very high non-specific uptake of ^{213}Bi was found because of passive incorporation of Bi into the dead cells.

The entire uptake and cell cytotoxicity investigation will need to be repeated under more satisfactory conditions.

Conclusions

- The radiolabelling of BB4 antibody with ^{213}Bi appears feasible.
- Hydroxylated ligands do not seem favourable for complexing this radionuclide.
- Polyaminocarboxylic ligands are good candidates, showing complexing kinetics more favourable to open than macrocyclic ligands.

The study needs to be completed by a study on the influence of temperature and incubation time on radiolabelling and a study of radiolabeled antibody stability in a serum medium for the BB4-Benzyl DTPA antibody and for the ligand AK 33 a study of the influence of temperature, incubation time and pH on complexing. Cytotoxicity studies on human myeloma cell lines should also be carried out.

1.11.3 Cytotoxicity of ^{213}Bi and ^{225}Ac-immunoconjugates

Because of their extremely high cytotoxicity, short-lived α-emitting radionuclides are attractive candidates for application in radioimmunotherapy. ^{225}Ac and ^{213}Bi have been proposed as a source of α-particles for this purpose [1]. ^{225}Ac has a half-life of 10 days and decays into a cascade of short-lived β^- and α-emitters. One of the last a-emitters of this series, ^{213}Bi, has a half-life of 47 minutes. This isotope might be a useful alternative for ^{212}Bi, which has been proposed for the treatment of blood-borne cancers. ^{225}Ac may be employed in radiotherapy with immunoconjugates of monoclonal antibodies that show a long residence time at the tumour site, such as the human IgM 16.88, either using a one-step approach or via pretargeting schemes.

The efficient use of a ^{213}Bi - labelled immunoconjugate against the human epidermoid tumour cell line A431 was reported earlier (TUAR-93, p. 215-216). The cytotoxicity of the Bi-conjugate, coupled to a selective murine monoclonal antibody 2D11, was found to be high in comparison to the coupling with an irrelevant antibody.

In this project, the cytotoxic effects of the ^{213}Bi and ^{225}Ac labelled immunoconjugates were studied on multicell spheroids, a realistic model for the *in vitro* situation. Spheroids of SW 1398 cells were incubated with the labelled immunoconjugates (SC-20, a murine IgG) directed against the tumour antigen CEA for 4 hours. After washing, the spheroids were incubated in a cell culture, after which period the rate survival was determined. The results are shown in Fig. 1.30. For ^{213}Bi, no specific cell-killing was observed, which is an indication of the limited applicability of this radionuclide in the treatment of solid tumours. For ^{225}Ac on the other hand, specific cell-killing was measured under identical conditions (same amount of radioactivity/spheroid), suggesting possible applications of ^{225}Ac immunoconjugates in the treatment of solid tumours (metastases). In view of the limited stability of ^{225}Ac chelation, the

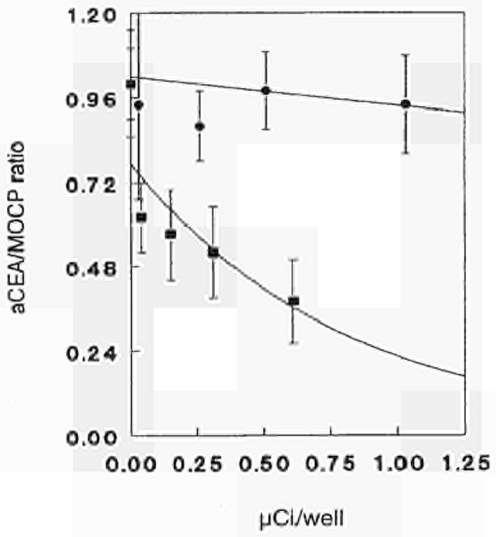

Fig. 1.30 Cytoxicity of ^{213}Bi and ^{225}Ac immunoconjugates on SW 1398 spheroids. The cytotoxicity is expressed as the ratio of survival on treatment with a relevant (aCEA) and an irrelevant (MOPC) antibody. ● ^{213}Bi; ■ ^{225}Ac.

cytotoxicity observed cannot be explained by the longer half-life of ^{225}Ac but suggests an additional effect of the Ac-daughters in areas distal from the immunoconjugate binding site (field effect). Because of the recoil energy associated with the α-decay, the Ac-daughters will diffuse away from the original target cells, but decay within the spheroids is likely (because of their relatively short half-lives). Further experiments using a better Ac-chelator will be performed to prove this point.

Conclusions

^{225}Ac is a candidate for the treatment of solid tumours, since problems of α-treatment in this type of tumour, due to the heterogeneity of antigen expression, may be overcome by the field effect of the daughters of ^{225}Ac. For a therapeutic effect in humans, an injected dose of 5 mg of antibody would suffice, assuming an antigen density of 5 x 10^4 antigens per cell, a specific activity of 10 mCi mg^{-1} and a targeting efficiency of 0.01% g^{-1}.

For successful application of the above radioimmunoconjugates, optimal pharmakinetics will be required, in particular for the ^{213}Bi conjugates, in view of the short half-life of the radionuclide. For ^{225}Ac the design of a suitable chelator is essential for such an application.

References

[1] F. M. Kaspersen, E. Bos, A. V. Doornmalen, M. W. Geerlings, C. Apostolidis, R. Molinet; Cytotoxicity of ^{213}Bi and ^{225}Ac-immunoconjugates; Nucl. Med. Commun. **16** (1995) 468-476

1.11.4 Recovery of ^{213}Bi from a ^{225}Ac cow: Application to labelling of antibodies with ^{213}Bi

Alpha particle-emitting radionuclides are amongst the most promising nuclides for the treatment of metastatic cancers [1]. Because of their short range (60 to 100 µm) and higher linear energy transfer (LET) values, alpha-emitters can deliver a very large radiation dose over the distance of a few cell diameters. When alpha-emitters are linked to tumour seeking monoclonal antibodies (mAbs), the resulting product is a powerful cancer therapeutic.

In recent years, ^{212}Bi has been considered to be the alpha-emitter of choice [2]. One disadvantage of the ^{212}Bi system is the need to shield the 2.2 MeV gamma-ray of the ^{212}Bi daughter, ^{208}Tl. An alternative to ^{212}Bi is offered by the use of ^{213}Bi. ^{213}Bi is available using a ^{225}Ac cow; this system has been developed at the Institute (TUAR-94, p. 199). ^{213}Bi has fewer hard gamma rays than ^{212}Bi. It has a single gamma ray emission at 440 keV which can also provide images similar to those using ^{131}I.

The radiochemistry and labelling chemistries of ^{213}Bi have been investigated in this study. There were three main goals: 1) to establish the elution patterns of ^{213}Bi from the ^{225}Ac cow; 2) to determine if there are any radiochemical impurities in the generator; 3) to optimize the labelling of ^{213}Bi into a mAb CHXA-DTPA system.

Experimental

The full details are reported elsewhere [3]. The ^{213}Bi was eluted from a ^{225}Ac cow with either HCl, HI or a mixture of both. The M195 antibody and CHXA chelating agent were available from earlier studies and purified as previously described.

The appropriately conditioned immunoconjugate (mAb and CHXA-DTPA reagent) was radiolabelled and the non-bound radioisotopes were separated using a high-pressure liquid chromatography column (HPLC). Analyses are performed at different stages to check both for radiochemical impurities (gamma- and alpha-spectrometry) and the efficiency of the radiolabelling. Activities of ^{225}Ac, ^{221}Fr or ^{217}At were not detected in the ^{213}Bi elution products.

Results

^{213}Bi was eluted rapidly and quantitatively with various concentrations of HCl and HI. All of the ^{213}Bi activity can be obtained within 5 to 10 minutes after start of the elution. The radiochemical purity of the ^{213}Bi was assayed by a HPGe detector system. A sample spectrum after elution with 2M HCl from the ^{225}Ac column is shown in Fig. 1.31.

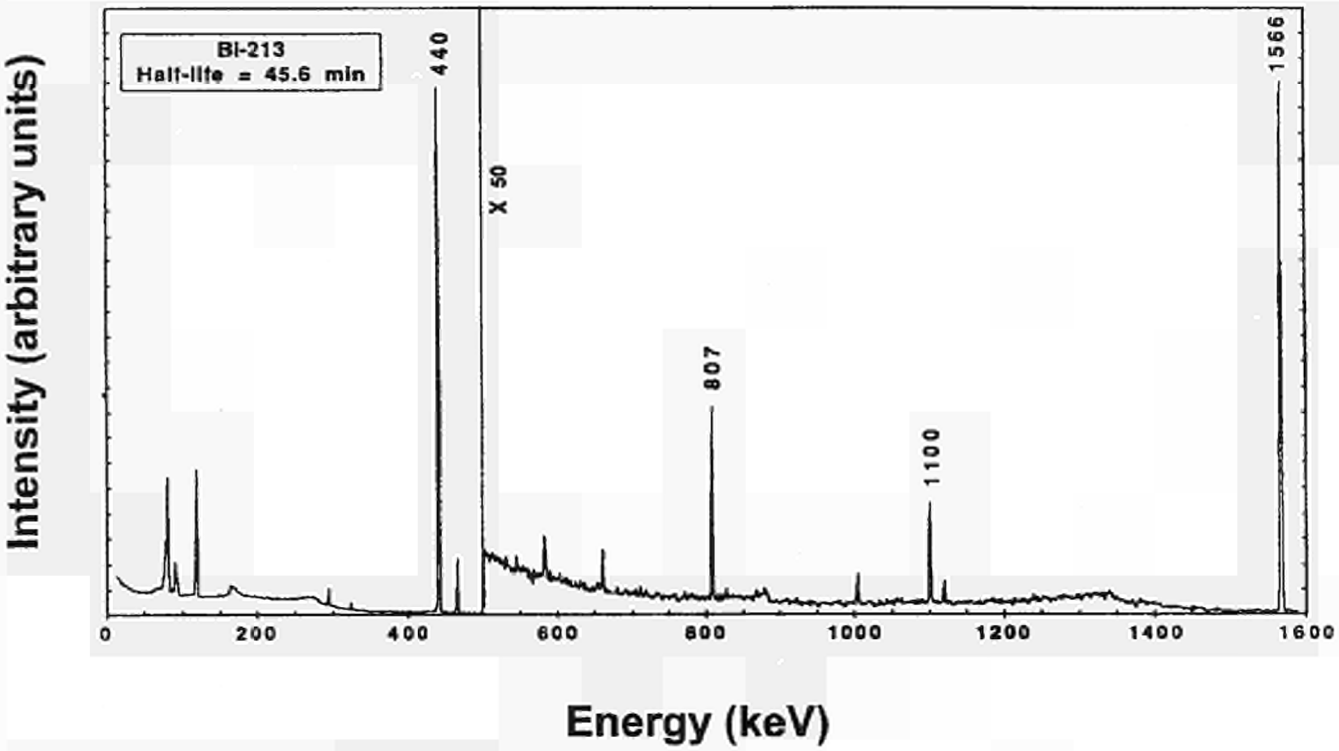

Fig. 1.31 Gamma spectrum of ^{213}Bi fraction from column.

The major peak at 440 keV is from ^{213}Bi. Several TLC experiments were carried out. A sample chromatogram is shown in Fig. 1.32. This result indicates that most of the ^{213}Bi is available for complexation by DTPA.

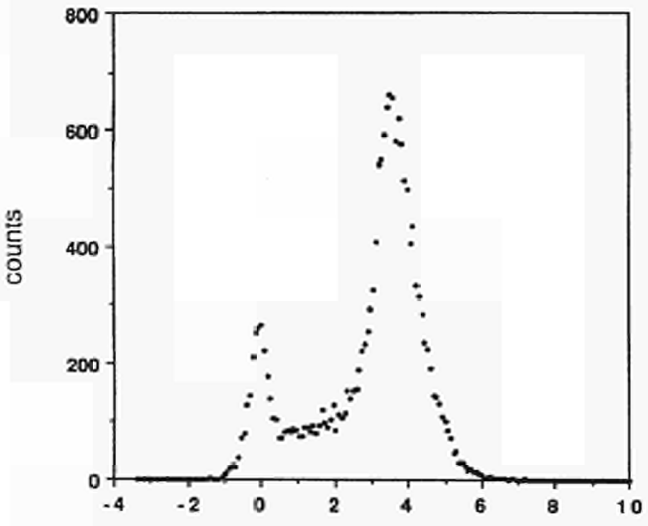

Fig. 1.32 TLC chromatogram for ^{213}Bi in 4.13 µM DTPA at pH 5.

The recovery of ^{213}Bi was optimal when a mixture of 0.1M HCl and 0.1M HI was used as eluant. The eluant volume is kept low and the acidity is suitable for radiolabelling mAbs. Using these conditions the ^{213}Bi was found to be radiochemically pure. No breakthrough of ^{221}Fr or ^{217}Ac was observed in more than 20 elutions of the ^{225}Ac cow. This feature is necessary if scale-up to the multi-millicurie level is to be achieved. The ^{213}Bi eluted from the ^{225}Ac column gave a high specific-activity mAb product, limited by the amount of ^{225}Ac currently available. Preliminary cell-binding studies show that this nuclide is taken up rapidly by cells. Cell-killing studies are currently being planned.

References:

[1] T. A Walfmann; Monoclonal Antibodies in Diagnosis and Therapy; Science **252** (1991) 1661

[2] D. S. Wilber; Potential Use of Alpha Emitting Radionuclides in the Treatment of Cancer; Antibody, Immunoconjugates and Radiopharmaceuticals **4** (1990) 85

[3] C. G. Pippin, O. A. Gansow, M. W. Brechbiel, L. Koch, R. Molinet, J. van Geel, C. Apostolidis, M. W. Geerlings, D. A. Scheinberg; Chemists' Views of Imaging Centers; Ed.: A. M. Emran; Plenum Press, New York, 1995

2. Safety of Nuclear Fuels

Introduction

The work to improve the safety of nuclear fuels was continued along the lines defined in the 1995 workschedules. Major emphasis was placed on the investigation of phenomena occurring at very high burn-up and which may limit the lifetime of Light Water Reactor (LWR) fuel.

This was achieved by performing work in three major areas:

- structural investigations and basic studies on high burn-up fuels
- studies of high temperature properties of nuclear fuel and
- continuation of fuel performance code development (TRANSURANUS)

As in previous years, important results were obtained, evaluated and published within the reporting period.

These include the following:

- the evolution of porosity in UO_2 fuel as a function of burn-up
- study of grain subdivision by electron microscope
- thermal conductivity and radiation damage creation in irradiated UO_2
- thermal diffusivity and heat capacity measurements of spent fuel by laser flash application
- application of double pulse thermoanalysis technique to study high temperature phase transitions
- fission product source term and redeposition measurements and
- advances in fuel performance code development (TRANSURANUS code)

The relevance of the work performed is underlined by the success of the Institute in competitive activity involving know-how established in the above R & D areas.

2.1 Structural Investigations and Basic Studies on High Burn-up Fuels

2.1.1 Porosity of high burn-up UO_2 fuel

Introduction

Irradiated UO_2 at burn-ups upto 60.000 MWd/t displays a strong increase of the porosity as a function of irradiation time. There is a need for a better characterization of this structural feature because swelling, thermal conductivity and mechanical properties are influenced by this restructuring mode and could limit the life time of the fuel rod. To study how the microstructure changes seven samples with burn-ups between 40.3 and 66.6 GWd/tU (see Tab. 2.1) were examined by optical microscopy. The sample with a burn-up of 66.6 GWd/tU was analysed additionally with scanning electron microscopy (SEM). In all investigations, the radial distribution of the porosity was determined by means of a Quantimet image analyser.

The optical microscopy examinations focused on the outer rim of the fuel pellets. Near the pellet surface the local burn-up can be a factor of two higher than the average pellet value due to the formation of fissile ^{239}Pu after neutron resonance capture by ^{238}U. It has been found that for local burn-ups above 70 GWd/tU, corresponding to an average cross-sectional burn-up of approximately 40 GWd/tU, structural changes lead to the formation of a highly porous and fine grained microstructure at the pellet edge. This often referred to as outer rim structure. Because the burn-up is maximal in the rim, this restructuring first occurs there (see also Fig. 3.38, TUAR-94, p. 111). The occurrence of the outer rim and its potential consequences on the fuel behaviour, both for the reactor operation and the storage of spent fuel have to be investigated.

Tab. 2.1 Samples for which quantitative image analysis was performed. The burn-up values are cross sectional average values. 800 x and 1600 x refer to optical microscopy (OM) photographs printed at magnifications of 800 x and 1600 x, SEM to scanning electron microscopy photographs at a magnification of 4500 x.

burn-up (GWd/tU)	OM 800 x	OM 1600 x	SEM 4500x
40.3	x	x	
50.2	x		
50.3	x		
51.4	x		
56.9	x		
63.1	x	x	
66.6	x	x	x

Experimental

Both, optical microscopy and SEM examinations were performed on polished cross sections. Photographs taken of these cross sections were analysed with a quantitative image analyser (Quantimet). In the case of optical microscopy the photographs had a magnification of 800 x, in the case of the scanning electron microscopy of 4500 x. The Quantimet analysis yields directly the porosity, the two-dimensional pore density (pores/mm^2), the mean pore area, and the pore area distribution. From these results the three-dimensional pore density (pores/mm^3), the mean pore diameter, and the pore diameter distribution can be calculated by using the Saltykov-method. This correction method takes into account that a pore is statistically not cut by the plane at its maximum cross section. If this correction would not be applied, the number of pores with small pore size would be overestimated. For three samples (see Tab. 2.1) extra prints with a magnification of 1600 x were made. All pores visible on these photographs were traced over onto transparent paper and the resulting black-and-white drawings were analysed with the Quantimet. The purpose of this procedure was twofold: first, to reduce the influence of the contrast of the photographs, and, second, to study the influence of the magnification on the results. In the analysis of the SEM photographs this method had to be applied anyway, because their contrast was too poor to do the measurements directly on the photographs themselves.

Results

Optical microscopy

In Fig. 2.1 the dependence of the porosity on the relative radial position r/r_0 is displayed for the (representative) samples with burn-ups 40.3, 50.3, and 66.6 GWd/tU. For the 50.3 GWd/tU sample the results were obtained at a magnification of 800 x, for the other two samples at a magnification of 1600 x. In general, the agreement between the porosity values

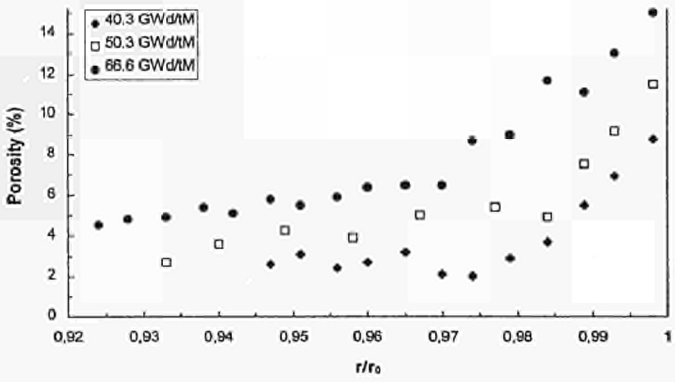

Fig. 2.1 Dependence of the porosity on the relative radial position r/r_0 in the rim region for the samples with burn-up 40.3 GWd/tU (◆), 50.3 GWd/tU (□), and 66.6 GWd/tU (●). The results for the sample with a burn-up of 50.3 GWd/tU were obtained at a magnification of 800 x, for the other two samples at a magnification of 1600 x.

determined at 800 x and 1600 x was good, while the number of pores per unit area, as measured at a magnification of 1600 x, was higher than that measured at a magnification of 800 x. The latter is an obvious consequence of the improved resolution and contrast at 1600 x, which permits the detection of pores that were too small and/or had a too poor contrast with the background to be detected at a magnification of 800 x. Consequently, the mean pore size at a magnification of 1600 x was smaller than at a magnification of 800 x. The contribution of these small pores to the total porosity is relatively small (typically < 15% of the total porosity), which implies that also at a magnification of 800 x it is possible to obtain a reliable value for the porosity.

Fig. 2.1 covers the range $0.92 \leq r/r_0 \leq 1.0$, i.e. the outer 380 μm of the fuel pellet. On approaching the pellet edge, the porosity shows an exponential rise. The r/r_0 range, over which this exponential rise occurs, grows with the burn-up. In other words, the increase of porosity starts at smaller r/r_0 for higher burn-up and the zone, where the rim effect occurs, grows with the burn-up. Also the maximum porosity, which was in all cases observed at the outermost radial position examined, increases with the burn-up: from 8% for the 40.3 GWd/tU sample to 15 for the 66.6 GWd/tU sample. Measurements on three samples with a burn-up of approximately 50 GWd/tU showed that similar burn-ups yield similar results for the porosity.

Fig. 2.2 shows the volume pore density, as calculated from the measured two-dimensional pore size distribution (magnification 1600 x) using the Saltykov-method, for the samples with burn-ups 40.3 and 66.6 GWd/tU in the range $0.92 \leq r/r_0 \leq 1.0$. The pore density in the former sample shows the same trend with r/r_0 as the porosity does: an exponential increase on approaching the pellet edge, which starts at the same radial position as the start of the porosity increase.

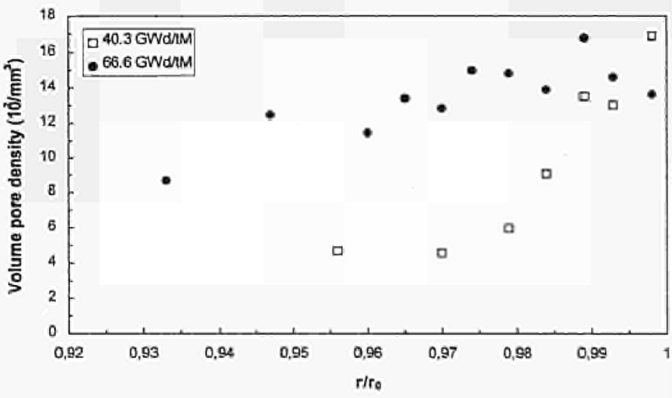

Fig. 2.2 Dependence of the volume pore density on the relative radial position r/r_0 in the rim region for the samples with burn-ups of 40.3 GWd/tU (□) and 66.6 GWd/tU (●). The results were obtained at a magnification of 1600 x.

For the sample with a burn-up of 66.6 GWd/tU, the radial dependence of the three-dimensional pore density is somewhat different from that of the porosity. The maximum value, which is approximately identical for all samples, is not found at the outermost radial

position, but at r/r_0 = 0.989, i.e. some 50 µm away from the pellet edge. The same inwards shift (up to 100 µm) $0.975 < r/r_0 < 1.0$ of the pore density maximum was observed for all samples except that with the lowest burn-up. The curve rises to a plateau at r/r_0 = 0.975 which is approximately 125 µm away from the pellet edge.

The pore density of the 66.6 GWd/t burn-up sample decreases more gently from the pellet edge to the center than the porosity. This means at constant r/r_0 the volume pore density increases with the burn-up, except at the outmost radial position.

In Figs. 2.3a and b the pore diameter distributions corresponding to the total volume pore density from Fig. 2.2 are plotted for a few radial positions for the samples with burn-ups 40.3 and 66.6 GWd/tU, respectively. For the 40.3 GWd/tU sample the distribution has a log-normal like character at all radial positions. As far as the statistics in some cases are too poor (because of the small number of pores in the analysed area), a definite conclusion cannot be drawn. The position of the maximum in the distribution is located at a pore diameter of about 0.7 µm. The distribution profiles of the 66.6 GWd/tU sample have a different form, especially at the outermost edge of the pellet. At the positions r/r_0 = 0.998 and r/r_0 = 0.993 (not shown) the distributions have a bimodal character with a sharp maximum at a diameter of 0.7–0.8 µm and a broader maximum at 1.4-1.5 µm. For $r/r_0 < 0.97$ the distribution has a log-normal like character with a single maximum at a diameter of 0.6-0.8 µm. At positions corresponding to $0.97 \leq r/r_0 \leq 0.99$ in some cases it seems that there is a shoulder visible on the tail at the larger diameter side of the log-normal like distribution. This shoulder might be the remainder of the second maximum observed at larger r/r_0 values.

Summarizing the optical microscopy results, the restructured zone at the pellet rim grows with the burn-up and the porosity and the pore density in this zone increase with the burn-up. For the mean pore size (not shown) no clear trend with the average burn-up was observed. At fixed burn-up, the mean pore area shows an exponential rise similar to that of the porosity on approaching the pellet edge, but this rise starts at larger r/r_0. For all samples the maximum pore area in the rim region was observed at the outermost position studied.

Scanning electron microscopy

In the scanning electron microscopy analysis of the sample with 66.6 GWd/tU burn-up measurements were not only made at positions in the rim area, but also at a few points in the pellet interior. These points were chosen on basis of an analysis of the complete pellet radius by optical microscopy (magnification 500 x), the results of which were presented earlier (TUAR-94, p. 110). Visual inspection of the optical microscopy photographs revealed the existence of six zones with different types of porosity on going from the pellet centre to the rim. In each of these zones at least one SEM photograph was taken and subjected to quantitative image analysis. The resulting volume pore density and the mean pore diameter are displayed versus r/r_0 in Fig. 2.4. The dashed lines indicate the boundaries between the different porosity zones.

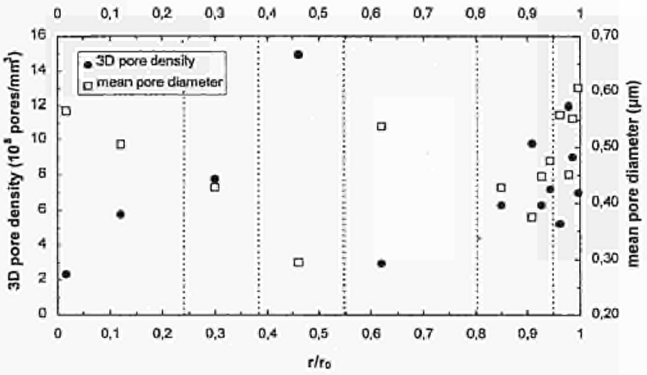

Fig. 2.4 Dependence of the volume pore density (left axis) and the mean pore diameter (right axis) on the relative radial position r/r_0 for the sample with a burn-up of 66.6 GWd/tU. The results were obtained from scanning electron microscopy photographs at a magnification of 4500 x. The dashed lines indicate zones with different types of porosity.

At the rim area, the trends of the porosity, the pore density, and the mean pore size as a function of r/r_0 were the same as observed in the optical microscopy analysis

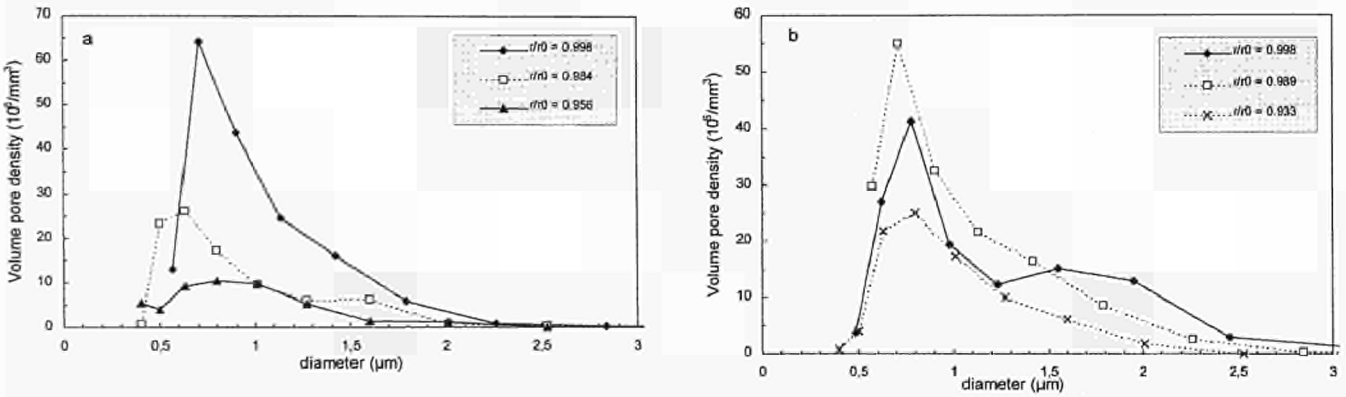

Fig. 2.3 Pore size distributions at various radial positions in the rim region for the samples with burn-ups of 40.3 GWd/tU (a) and 66.6 GWd/tU (b). The lines drawn are to guide the eye. The results were obtained at a magnification of 1600 x.

described above. As the analysed area was smaller in the SEM analysis, the results exhibit more scatter than those from the optical microscopy investigations. Due to the detection of pores that are too small to be observed at lower magnification, the pore density is larger and the mean pore size is smaller in the measurements at high magnification. The maximal pore density inside the rim is observed 100 μm from the pellet edge, whereas the mean pore size has its maximum at the pellet edge. Outside the rim the porosity varies between 2% and 4%, i.e. the porosity in the pellet interior is smaller than in the rim. The radial porosity profile is rather flat outside the rim in comparison to the volume pore density and mean pore diameter profiles displayed in Fig. 2.4. These profiles reflect the different natures of the porosity in the different zones. On going from the pellet centre towards the rim, in the first zone ($0.00 \leq r/r_0 \leq 0.24$) the porosity consists of large, coalesced intergranular pores. The pore density achieves its lowest value in this zone, while the mean pore diameter is large. In the second zone ($0.24 \leq r/r_0 \leq 0.38$) not only intergranular, but also intragranular pores are visible. Their number increases with r/r_0. The next zone ($0.38 \leq r/r_0 \leq 0.54$) shows many small intragranular pores, resulting in the maximum pore density and minimum mean pore size in Fig. 2.4. The mean pore diameter is a factor two smaller than in the pellet centre and in the rim. In the fourth zone ($0.54 \leq r/r_0 \leq 0.80$) only coalesced intergranular pores are visible. The fifth zone ($0.80 \leq r/r_0 \leq 0.94$) contains both inter- and intragranular porosity. In the last zone, i.e. the rim, the original grain structure has changed into a very fine grained structure and no distinction can be made between inter- and intragranular pores.The observed porosity radial distribution is a kinetic process involving two major phenomena, nucleation and pore growth, which depend on the gas concentration and the fuel temperature. The pore growth depends on fuel temperature and vacancy availability. The fuel temperature varies strongly with the linear power which decreases with irradiation time, and improvement of heat exchange as fuel swelling increases. Modelling of these phenomena and processes is underway.

Further work

A first extension of the present work comprises the extension to higher magnifications by electron microscopy of prepared replicas. In this way the porosity in the submicron range can be studied to a smaller scale than in the scanning electron microscopy on the sample itself. Increasing the magnification results in a shift of the measured pore size distribution to smaller pore sizes. Linking the distributions, that are obtained at different magnifications, to each other is a point of interest, for both technological and for scientific reasons e.g. the knowledge of the absolute value of the porosity is important, for example for modelling of the thermal and mechanical behaviour of the fuel rod. Therefore, the porosity values from the quantitative image analysis should be verified by other techniques, e.g. mercury picnometry or density measurements. A point of concern for quantitative image analysis is the contrast of the photographs. The drawing method, used in the analysis of the SEM photographs described in the previous paragraph, is very time consuming and should be avoided where possible. To improve the contrast of the photographs a better sample preparation and/or other photographic technique might be helpful.

2.1.2 Investigation of the "High Burn-up Structure" – the observation of an HBS-type pore inner surface structure in an advanced plutonium-uranium carbide fuel

It has been known for some time [1, 2, 3] that the rim regions of high burn up (average pellet burn up > 40.000 MWd/tU) LWR UO_2 fuel pellets, where the local burn up can be very high, show a structure quite different from that observed towards the centre of the fuel or at lower burn up values. This structure is characterized by a transformation of the initial large grained (typically 10 μm) UO_2 sintered structure into a "cauliflower-type" microstructure produced by grain subdivision to produce sub-grains with typical grain sizes of 0.1 to 0.3 μm. This transformation is usually only seen to a marked extent in the first 150 to 200 μm depth from the pellet surface, and is usually referred to as the "Rim Effect".

This grain subdivision can be observed by Transmission Electron Microscopy of small fuel fragments extracted from the fuel rim [4, 5], and by Scanning Electron Microscopy [4, 5] of fractured fuel surfaces. In the latter case the sub-grain formation is often particularly clearly visible on the inner surfaces of pores or large fission gas bubbles, leading to micrographs such as that in Fig. 2.5.

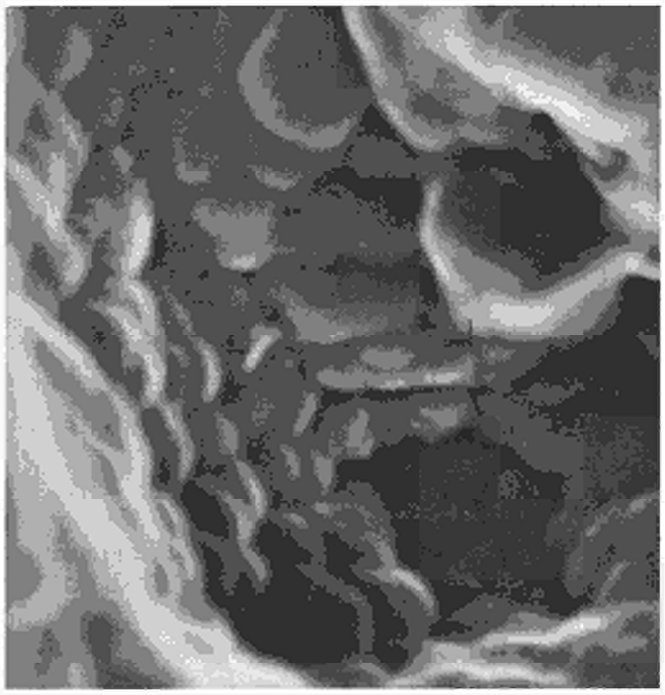

Fig. 2.5 Scanning Electron Micrograph of a fractured fuel surface at the rim of a high burn-up LWR UO_2 fuel sample, showing the sub-grain structure, which is particularly clearly visible on the surfaces of large pores.

This is a Scanning Electron Micrograph of the structure inside a pore from the first 200 μm of an LWR UO_2 fuel pellet with an average burn up of 7.6% FIMA, but a local burn-up at the position examined estimated to be about 20% FIMA. The average grain size in this fuel rim region was measured to be 0.15 μm from such micrographs.

It was originally thought that this type of microstructure was unique to the rim region of high burn up LWR UO_2 fuels. This, however, is not the case because similar pore surface structures have been found in samples of the advanced fuel $(Pu_{0.2}U_{0.8})C$. Figs 2.6, 2.7 and 2.8 show examples of such structures observed on the inner surfaces of a large bubble and on irregular shaped pores.

These images were recorded at a mid-radial position of the fuel pin DFR 330, with a constant radial burn up value of about 8.3% FIMA. Similar structures were also observed in nitride fuels.

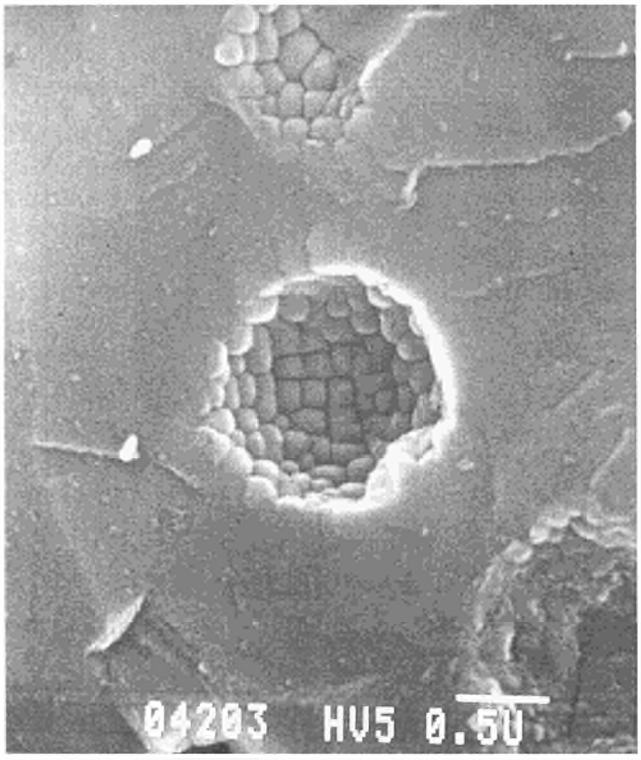

Fig. 2.6 Scanning Electron Micrograph of a fractured fuel surface at a mid radial position of the Fast Breeder advanced fuel $(Pu_{0.2}U_{0.8})C$, from the fuel pin DFR 330, showing a very similar structure of sub grains within a large fission gas bubble.

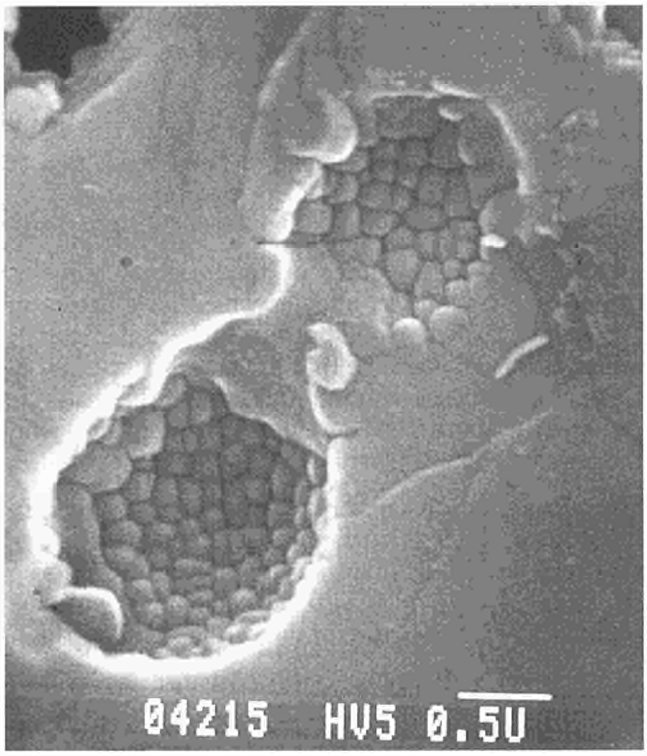

Fig. 2.7 Scanning Electron Micrograph of a fractured fuel surface at a mid radial position of the Fast Breeder advanced fuel $(Pu_{0.2}U_{0.8})C$, from the fuel pin DFR 330, showing the sub-grain structure within an exposed pore.

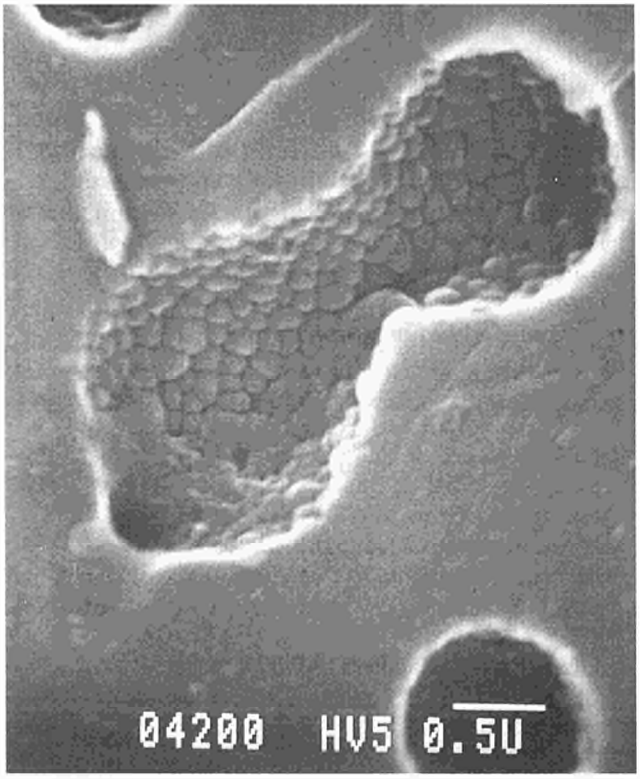

Fig. 2.8 A similar structure observed on the surface of a pore which, from its shape, is more likely to be present from the original porosity rather than to have grown as a fission gas bubble.

Fig. 2.9 shows the sub-grain size histogram measured on subgrains revealed on pore faces at a mid-radial position on the sample.

The average sub-grain size and the form of the distribution are very closely similar to those measured at the rim of high burn up LWR UO_2 fuel [4].

The irregular form of the pores in Figs 2.7 and 2.8 indicate that these represent the original porosity, rather than fission gas bubbles which have grown in the matrix, which would normally be spherical. It seems also most probable that the pore surfaces reveal a structure which is continuous through the material, rather than a structure developed in association with the pore or bubble formation, as has been proposed.

The relevance of this observation on advanced fuels to the study of the high burn-up structure is that the process responsible for grain sub-division in the fluorite structure of UO_2 must also be compatible with the sodium-chloride structure of the carbides and nitrides.

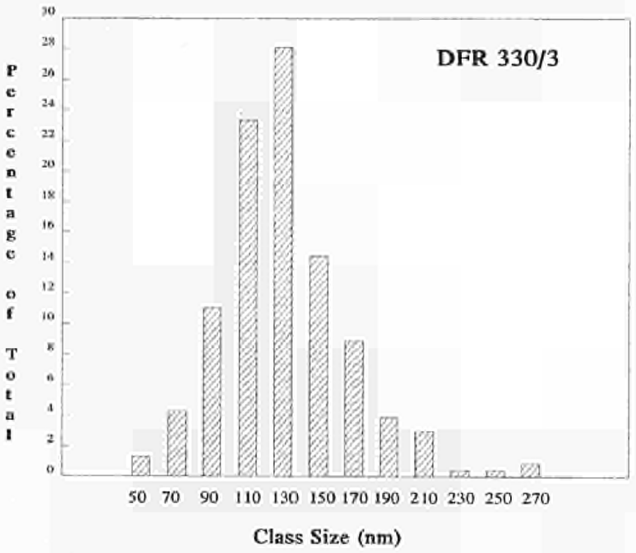

Fig. 2.9 The grain size distribution measured on the sub grains observed in the porosity of the carbide fuel pin at a mid-radial position.

References:

[1] M. L. Bleiberg, R. M. Berman and B. Lustman; Proc. Symp. on Radiation Damage in Solids and Reactor Materials (IAEA, Vienna, 1963) p. 319

[2] H. Stehle; J. Nucl. Mater. **153** (1988) 3

[3] Hj. Matzke, H. Blank, M. Coquerelle, K. Lassmann, I. L. F. Ray, C. Ronchi, C. T. Walker; J. Nucl. Mater. **166** (1989) 165

[4] I. L. F. Ray, Hj. Matzke; TUAR-92, p. 17–23

[5] Hj. Matzke, I. L. F. Ray, H. Thiele, M. Kinoshita; J. Nucl. Mater. (to be published)

2.1.3 High resolution electron microscopy of UO_2

A cooperation has been started with the Department of Geology, University of New Mexico, Albuquerque to study radiation damage and polygonization in UO_2 with High Resolution Transmission Electron Microscopy (HRTEM). In first scoping investigations using unirradiated UO_2 achieving lattice plane resolution, an edge dislocation could be directly observed in UO_2 for the first time [1]. Fig. 2.10 shows in part A the edge dislocation in the middle in the framed region. Part B is the Fourier transform of the framed image in (A). With the inverse Fourier transform using the two <111> spots, shown in part C, the filtered picture D is obtained showing the dislocation line very clearly.

First results in HRTEM on UO_2 implanted with 1.5 MeV Xe^+-ions at either 20 K, 300 K or 773 K to doses in the range of 0.5 to $1x10^{16}$ ions/cm^2 confirmed that UO_2 does not become amorphous under ion impact, in contrast to many other materials such as e.g. Al_2O_3 or U_3O_8. These investigations were supported by the Office of Basic Energy Sciences, USDOE, under grant DE-AC06-76RLO 1830. The work will be continued in 1996 to observe fission tracks and polygonization in UO_2 in more detail.

References

[1] Hj. Matzke, L. M. Wang; J. Nucl. Mater. (in press)

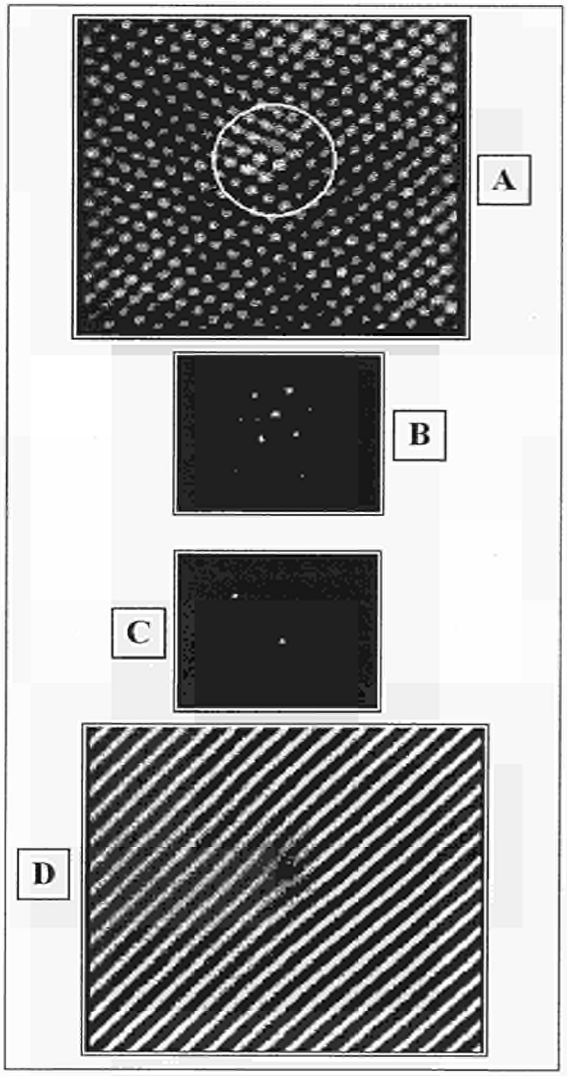

Fig. 2.10 HRTEM of UO_2 showing lattice plane image resolution and an edge dislocation, made more clear via Fourier transformations.

2.1.4 A pragmatic approach to model the thermal conductivity of irradiated UO_2 fuel

The extensive measurements of thermal properties (thermal diffusivity α, thermal conductivity λ, specific heat C_p) in SIMFUEL (simulated UO_2 fuel with different burn-ups) performed in cooperation with Drs. P. G. Lucuta, R. A. Verrall and I. J. Hastings of Chalk River Laboratories, AECL Canada, and reported in TUAR-91, p. 26, TUAR-92, p. 24, TUAR-93, p. 30 and TUAR-94, p. 27 as well as in refs. [1-3] were used to derive an analytical expression for the thermal conductivity λ of irradiated UO_2. The thermal conductivity is one of the most important properties of the fuel since it determines the fuel operating temperatures, thus directly affecting fuel performance (e.g. fission gas release, grain growth etc.). It is generally agreed that λ of irradiated UO_2 differs from the λ_0 of unirradiated UO_2 due to the changes that take place in the fuel during irradiation: build-up of fission products, formation of pores and fission gas bubbles, possible deviations from stoichiometry and radiation damage. We now suggest an expression to describe the dependence of λ on burn-up.

Theoretical considerations

The thermal conductivity of UO_2 consists of two dominant contributions, i.e. conduction through lattice vibrations and conduction by electronic processes (conduction by radiation through the lattice can be neglected). The first one (a hyperbolic term) plays the major role for temperatures below 1900 K and the second (an exponential term) is responsible for the observed increase in conductivity above 1900 K. We will mainly deal with the first one.

The expression for the parametric dependence of the thermal conductivity, λ, of irradiated UO_2 can be written in a form of contributing factors for each individual effect:

$$\lambda = \lambda_1(\beta) \cdot \lambda_2(p) \cdot \lambda_3(x) \cdot \lambda_4(r) \cdot \lambda_0(T) \quad (W/m\cdot°C) \qquad (1)$$

where $\lambda_1(\beta)$ is the burn-up (β) dependence factor, $\lambda_2(p)$ is the porosity/bubble (p) contribution, $\lambda_3(x)$ describes the effect of O/M ratio (deviation from stoichiometry), $\lambda_4(r)$ refers to the radiation damage and λ_0 is the analytical expression for thermal conductivity of unirradiated UO_2. An analytical expression as the one in Equation (1) can be easily adapted into fuel performance codes.

The expression for each factor λ_1 to λ_4 was derived from the available experimental data obtained by studying single effects. The resulting analytical expression for the thermal conductivity of the irradiated UO_2 was validated against published data on irradiated fuel from Bettis-WAPD [4], early AECL data [5], and recent High Burn-up Chemistry (HBC) [6] and Halden data [7-9].

Thermal conductivity of unirradiated UO_2

The data for *unirradiated* UO_2 were critically analysed and reviewed in the literature [e.g. 10, 11]. The current knowledge leads to an analytical expression for the thermal conductivity of the fresh fuel including four parameters:

$$\lambda_0 = \frac{1}{A + BT} + \frac{C}{T^2} \exp\left(-\frac{D}{T}\right) \text{ for } T \le T_0 \qquad (2)$$

Changes of the exponential term of the polaron contributions were the main difference suggested in the various formulations. We suggest to use the expression by Harding and Martin [10] as best describing the thermal conductivity of the UO_2 including our own data [1, 3]

$$\lambda_0 = \frac{1}{0.0375 + 2165 \cdot 10^{-4} T} + \frac{4.715 \cdot 10^9}{T^2} \exp\left(-\frac{16361}{T}\right) \qquad (3)$$

For fuel operating temperatures (T< 1900 K), the hyperbolic term $\lambda = 1/(A+BT)$ is important. To indicate the experimental uncertainties, due to manufacturing differences, porosity corrections, impurities and possibly small deviations from stoichiometry, the A- and B-values in Equation (2) are given here for refs. [10, 11, 2]:

	Harding & Martin [10]	MATPRO [11]	Lucuta, Matzke and Verrall [2]
$A \cdot 10^{-2}$	3.75	4.38	3.53
$B \cdot 10^{-4}$	2.17	2.29	2.20

This causes a difference in λ_0 at e.g. 1000 K of about ± 5%.

Effect of fission product buildup

The fission products formed during irradiation (dissolved and precipitated) impact on the fuel thermal conductivity by changing the lattice contribution. Measurements of SIMFUEL (see TUAR-92, p. 24, and [1]) thermal conductivity allowed to quantify the effect as function of the simulated burn-up. It was shown that a degradation in fuel conductivity occurs with increasing burn-up. An analysis of these results showed that the effect of build-up of fission products can be quantified and separated into two components (except for the fission gases and volatiles which are not present in SIMFUEL): fission products dissolved in the UO_2 fluorite matrix (e.g. rare earths) and fission products precipitated as discreet dispersed phases (e.g. Mo, Pd, Ru, Rh).

Thus the fission product factor, λ_1, consists of these two contributions:

$$\lambda_1(\beta) = \lambda_{1d}(\beta) \cdot \lambda_{1p}(\beta) \qquad (4)$$

where λ_{1d} describes the effect of the dissolved fission products and λ_{1p} accounts for the effect of the precipitates.

The effect of dissolved fission products

The dissolved fission products lower the thermal conductivity and this degradation could be well described by the phonon heat current theory [2]. The analysis showed that the mass difference alone was enough to explain the experimentally observed degradation. The

reduction in fuel thermal conductivity due to the solute fission products is described by the Equation:

$$\lambda_{fp} = \lambda_0 \frac{\varpi'}{\varpi_D} \arctan\left(\frac{\varpi_D}{\varpi'}\right) \quad (5)$$

where ϖ'/ω_D is defined as a burn-up dependent scattering parameter. Introducing the burn-up dependence for the scattering parameter in Eq. (5), the factor λ_{1d} that describes the effect of the solute fission products in the fluorite matrix is given by

$$\lambda_{1d}(\beta, T) = \left(n(\beta) + m(\beta)\sqrt{T}\right) \arctan\left(\frac{1}{n(\beta) + m(\beta)\sqrt{T}}\right) \quad (6)$$

where the parameters m and n contain the burn-up dependence. Their expressions were derived from the SIMFUEL data and are given by the Eqs.(6a) and (6b):

$$m(\beta) = \frac{0.0643}{\sqrt{\beta}} \quad (6a)$$

$$n(\beta) = \frac{1.09}{\beta^{3.265}} \quad (6b)$$

where β is the burn-up expressed in a/o. The fit of the SIMFUEL data with the Equations (6a) and (6b) is shown in Fig. 2.11. Equation (6) accounts for the effect of all solute fission products within the fluorite matrix, including fission-gas atoms and Pu build up through the fission process.

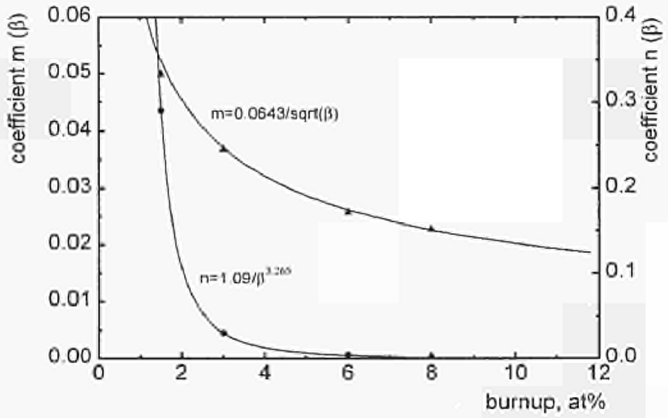

Fig. 2.11 The burn-up dependence of the two constants from the expression of the factor for dissolved fission products fitting the SIMFUEL results.

The effect of precipitated fission products

The effective thermal conductivity of inhomogeneous media is a problem difficult to solve in general. The precipitated fission products (mainly metallic precipitates, i.e. five-metal particles) are dispersed throughout the matrix as discrete, small particles. Their conductivity is much higher than that of the matrix and they have therefore a positive contribution to the fuel thermal conductivity.

A "Maxwell type" correction factor [2] is the suggested approximation for λ_{1p} (β):

$$\lambda_{1p} = \frac{1+2q}{1-q} \approx \frac{1}{(1-q)^3} \quad (7)$$

where q is the volume fraction of the precipitated phases (metallic and $BaZrO_3$-type ceramic-precipitates), which can be related to burn-up with the relation $q = 0.0038\beta$ (β in a/o).

During irradiation metal atoms (Pd, Ru, Mo, Tc, Rh) are formed as fission products uniformly across the fuel pellet. However, most of the metal fission products precipitate outside of the fluorite matrix in the high temperature region (central part) of the pellet. At the pellet periphery, in the cool region of the fuel, the metal precipitates are small and are confined within the matrix, without affecting practically the fuel conductivity. This aspect can be taken into account by a transition function applied to the correction factor λ_{1p}. The distribution is temperature dependent and can be expressed by a function with the transition height at 1200 K. Consequently, in irradiated fuel, the contribution from the precipitated fission products to the thermal conductivity, in the 600 to 1900 K temperature range can be expressed by a modified Klemens factor:

$$\lambda_{1p} = 1 + \frac{0.019\beta}{(3 - 0.019\beta)} \cdot \frac{1}{1+\exp\left(-\frac{T - 1200}{100}\right)} \quad (8)$$

We use Equation (8) to allow for precipitated fission products.

Porosity/gas-bubbles effect

The effective conductivity of a porous (sintering porosity and gas bubbles) fuel is related analytically to the conductivity of the solid matrix, λ_m and of the pores, λ_p. In the UO_2 fuel, where $\lambda_p < \lambda_m$, the form of this relation is simplified as the heat transfer through the pores will take place by conduction through the fission gases or by radiation. The effect of porosity on UO_2 thermal conductivity has been extensively investigated and there are quite a few analytical expressions suggested to calculate the porosity dependence. A brief review of porosity aspects for nuclear fuels can be found in the monograph on advanced LMFBR fuels [12].

The pore/bubble factor $\lambda_2(p)$ in Equation (1) depends on the volume fraction and the shape of the pores/bubbles. For small spherical pores/bubbles, uniformly dispersed, a modified Loeb expression, which includes the temperature dependence can be used:

$$\lambda_{2p} = 1 - (2.58 - 0.58 \cdot 10^{-3} T)\, p \quad (9)$$

where p is the pore/bubble volume fraction. This expression holds up to p ~ 9 v/o but it is clearly inadequate for high porosities: it thus cannot be generally used for irradiated fuel, despite the fact that it is often applied for unirradiated UO_2.

In irradiated fuel, two groups of pores/bubbles exist: sintering pores and intragranular fission gas bubbles which are "immersed" in the matrix, and intergranular bubbles close to interlinkage or tunnel formation. Qualitatively, for the same amount of porosity,

pores/bubbles from the first group will have less thermal resistance than the pores/bubbles of the second group. Along the pellet radius, the distribution and morphology of the pores/bubbles is changing during irradiation and is practically switching from the first group to the second as temperature and burn-up increase. This points out that a single formula for porosity is not sufficient to describe the thermal conductivity of the pores/bubbles in irradiated fuel.

The gas content of the pores/bubbles influences the thermal conductivity as well if conduction through the pores is assumed. However, the conduction is significant only in well defined situations with respect to the size, shape and gas content of the pores. Departure from conduction appears for large, unpressurized pores and/or from radiation heat transfer.

All these aspects have to be considered in a model that accounts for the effects of pores/bubbles on thermal conductivity of irradiated fuel. It is outside of the scope of the present work to develop a new model or adopt one of the many existing models on pores/bubbles in irradiated fuel. Any final model shall include the initial porosity, the burn-up, the linear power and power history as input data and ought to be validated against systematic experimental statistics on population, size, morphology and distribution of pores/bubbles in irradiated UO_2 fuel. In the present work, Eq. (9) with the volume fraction p for bubbles/pores is used to account for the effect of porosity/gas-bubbles on λ.

Deviation from stoichiometry

Deviation from stoichiometry affects thermal conductivity of the fuel as well. The reduction in conductivity is strong in UO_{2+x} and the decrease can be related to the deviation from stoichiometry [13]. Recent results on SIMFUEL [3] showed that at high oxygen potentials (large deviation from stoichiometry) the effect of the buildup of fission products is less significant and the excess of oxygen plays the major role in the reduction of the fuel conductivity.

Analysing the effect of deviation from stoichiometry on irradiated fuel conductivity, two distinct regimes should be considered:

- normal operating conditions (NOC), and
- accident conditions and fuel defects.

Normal operating conditions

Excess of oxygen might occur in irradiated UO_2 from the fission process. Nevertheless, recent measurements of oxygen potentials in irradiated fuels [14] showed that in practice the fuel remains stoichiometric even at extended burn-up when the RIM effect is observed. Based on this available information, *the factor λ_3 to account for the effect of the deviation from stoichiometry* on irradiated fuel thermal conductivity, *under normal operating conditions* ought to be taken as $\lambda_3(x) = 1$.

Accident conditions and fuel defects

The effect of deviation from stoichiometry on thermal conductivity is important for defected fuels and under accident conditions. In both cases the fuel becomes hyperstoichiometric and the thermal conductivity will decrease accordingly. The reduction in thermal conductivity observed experimentally in hyperstoichiometric UO_{2+x} and SIMFUEL (see TUAR-94, p. 27, and [3]) has to be analysed based on the existing theoretical models in order to obtain an adequate analytical expression. For SIMFUEL, at extended simulated burn-ups, samples annealed at the same oxygen potential had practically the same thermal conductivity as the UO_{2+x} [3]. Based on an additive effect on thermal resistivity, $R = 1/\lambda$, the effect of the deviation from stoichiometry can be quickly quantified. Fig. 2.12 shows the measured thermal conductivity of UO_2 and 8 a/o burn-up SIMFUEL annealed at different oxygen pressures. Linear T-dependencies of R were obtained. Consequently, the thermal conductivity of the oxidized fuel can be expressed by the Equation:

$$\lambda_{2+x} = \frac{1}{0.0257 + 3.336x + (2.206 - 6.85x)10^{-4}\,T} \qquad (10)$$

for deviations from stoichiometry up to $x = 0.10$. Eq. (10) will replace the intrinsic thermal conductivity of the UO_2 for defected fuel or accident conditions. Nevertheless, additional experimental data should be obtained for larger deviation from stoichiometry ($x > 0.1$) when U_4O_9 could form in SIMFUEL, or in defected fuels as it does in UO_2.

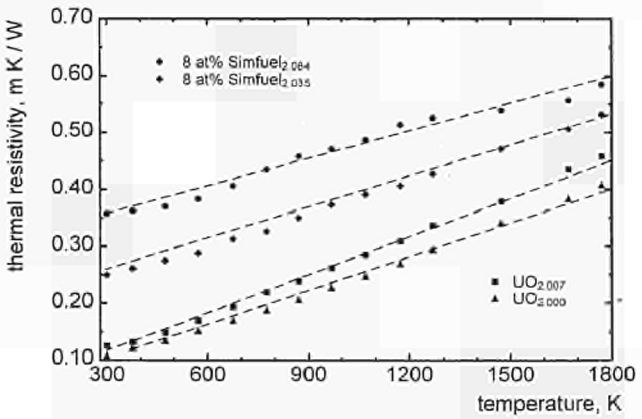

Fig. 2.12 The effect of deviation from stoichiometry on UO_{2+x} and oxidized SIMFUEL for the thermal resistivity plotted as a function of the temperature.

Radiation damage

Radiation damage from neutrons, α-decay and fission increases the number of lattice defects and consequently reduces the thermal conductivity of the fuel. Early work at Chalk River e.g. [5] showed that reactor radiation damage, in rather short irradiations, and below 1000 K, caused a significant decrease in λ. The decrease was very rapid at the beginning of the irradiation. A limiting value of 3.5 W/mK was reported for longer irradiations. Saturation was also reached very fast in a study of α-decay damage in AmO_2 and PuO_2 [15]. The decrease in λ was up to 60% in both cases. Saturation in $\Delta\lambda$ occurs thus faster than saturation in

lattice parameter change, Δa, indicating that the defect concentrations affect λ and a in a different way.

We see thus that the radiation induced decrease in λ occurs very fast. It is large at low temperatures, since damage is stored in the lattice. Oxygen defects are known to anneal at around 500 K (hence below fuel operating temperatures) and uranium defects anneal at higher temperatures, up to around 1000 K. This explains why most changes are seen below 1000 K. Fig. 2.13 shows the relative reduction of UO_2 thermal conductivity due to radiation damage: the first step is due to the oxygen defects and the second to the uranium defects.

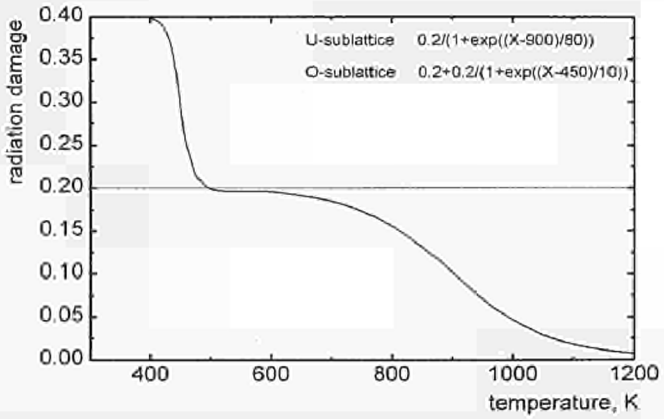

Fig. 2.13 The effect of radiation damage on UO_2 thermal conductivity as a function of the temperature.

The distribution function for the second step (top of Fig. 2.13) is the analytical expression considered for the radiation damage effect during reactor irradiation. (The first step may also be important for fuel storage due to α-decay damage of Am and Cm formed during irradiation). However, even at higher temperatures, above 1000 K, a certain reduction in λ during irradiation is expected, due to the large Frenkel-defect production rate by the fission process. Since no results are available so far on this phenomenon, it is not included in the present treatment. Whereas fuel performance codes presently take radiation damage into account by a cut-off value for thermal conductivity at 800 K, we suggest the physically more sound picture given in Fig. 2.14 that is taking into account the variation of the effect of radiation damage with the temperature. We do not suggest to include fission dose (or fluence) as a parameter since saturation is reached very fast in the fuel life.

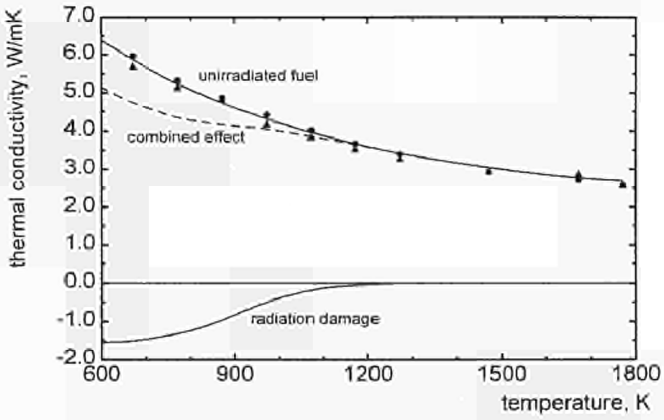

Fig. 2.14 Estimated effect of radiation damage on fuel thermal conductivity as a function of the temperature.

Validation based on thermal conductivity data of irradiated fuel

There are five sources [4-9] of data on thermal conductivity of irradiated fuel which were used for validation: early data from Bettis [4], evaluated by Marchandise [16], and from Chalk River e.g. [5], and more recent data from the HBC program [6], from JAERI [8] and from AEA [9]. The full results of this validation will be published in J. Nucl. Mater. [17]. Here, only one example is shown. The others could be fitted in a similar way. Fig. 2.15 shows the recommended data for unirradiated UO_2, our data for 1.5 a/o burn-up SIMFUEL, the experimental results from the work at Bettis [4] and the evaluation by Marchandise [16].

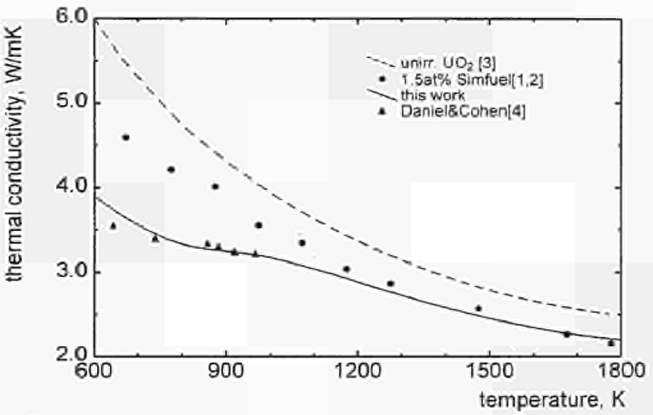

Fig. 2.15 Experimental results from Bettis [4] for UO_2 irradiated to 1.5 a/o burn-up compared with the expression suggested here (full line). The suggested curve for unirradiated UO_2 [3] and the measured values for 1.5 a/o SIMFUEL [1, 2] are also shown.

Clearly, the measured SIMFUEL data (for the same porosity) represent the upper limit for the fuel thermal conductivity degradation, especially for temperatures below 1200 K where the effect of the precipitated fission products is small in the real fuel and since radiation damage is absent in SIMFUEL. Our proposed analytical expression describes the experimental data typically within ±5% whereas the use of results for virgin UO_2 would cause errors of up to 50%.

Summary & recommendations for thermal conductivity of irradiated UO_2

In summary, thermal conductivity of irradiated fuel is affected by:

- fission products:
  - dissolved, and
  - precipitated,
- pores and fission-gas bubbles,
- deviation from stoichiometry,
- radiation damage.

The effects due to fission products, deviation from stoichiometry and radiation damage (three out of four parameters) were well quantified and described as function of burn-up and temperature (from room temperature to 1900 K). The uncertainties related to pores/fission-gas bubbles were also discussed.

Based on the analytical expressions describing these effects, the thermal conductivity of irradiated UO_2-fuel, for normal operating conditions (NOC) up to 1900 K, can be expressed by

$$\lambda = \lambda_{1d} \cdot \lambda_{1p} \cdot \lambda_{2p} \cdot \lambda_{3x} \cdot \lambda_{4r} \cdot \lambda_0 \qquad (11)$$

where the different factors are given in Eqs. (3), (6), (8), (9), (10) and in Fig. 2.13.

Fig. 2.16 shows calculated curves of λ for 6 different burn-ups as a function of temperature. The reduction in thermal conductivity is significant especially in the low temperature region of the fuel where radiation damage builds up. A large reduction is predicted in the 600 to 700 K range at extended burn-up. Note that above 7 a/o burn-up the RIM structure forms in LWR fuels [18], which – due to the increased porosity – may give a further contribution to the thermal conductivity reduction. This is not treated here.

The cracks formed in irradiated fuel and their effect on thermal conductivity were omitted. However, this aspect is important especially if circumferential cracks are developed in the fuel pellet which will act as a gap for the heat transfer.

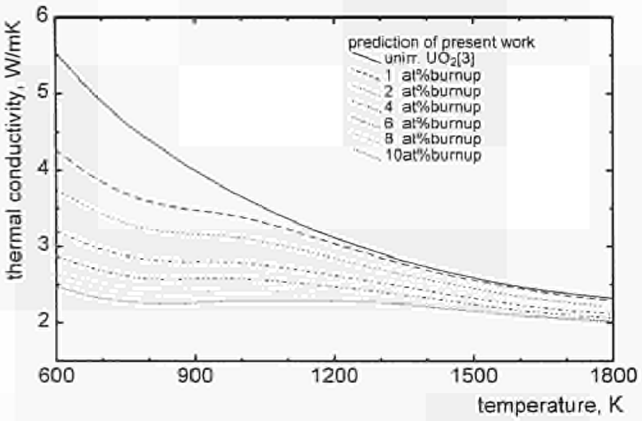

Fig. 2.16 Predicted thermal conductivity of irradiated UO_2 for six different burn-ups and for 5% pores/bubbles, as a function of temperature.

For defected fuel and/or accident conditions, the expression for the intrinsic conductivity λ_0 has to be replaced by Equation. [10], which describes for the time being the effect of the deviation from stoichiometry based on the data for UO_{2+x} and hyperstoichiometric SIMFUEL. However, a better understanding of the effect of excess oxygen is required to be able to quantify the data in a factor form.

References

[1] P. G. Lucuta, Hj. Matzke, R. A. Verrall, H. A. Tasman; J. Nucl. Mater. **188** (1992) 198

[2] P. G. Lucuta, Hj. Matzke, R. A. Verrall; J. Nucl. Mater. **217** (1994) 279

[3] P. G. Lucuta, Hj. Matzke, R. A. Verrall; J. Nucl. Mater. **223** (1995) 51

[4] R. C. Daniel, I. Cohen; Bettis Atomic Power Report WAPD-**246** (1964)

[5] J. A. L. Robertson, A. M. Ross, M. J. F. Notley, J. R. MacEwan; J. Nucl. Mater. **7** (1962) 223

[6] S. Shibab; HBC topical report, HBC 91/34 (1991)

[7] W. Wiesenack; IAEA Technical Committee Meeting on Fission Gas Release and Fuel Rod Chemistry Related to Extended Burnup, 1992 April 27 - May 1, Pembroke, Canada

[8] J. Nakamura, H. Uetsuka, N. Kohno, E. Oheda, T. Sukegawa, T. Furuta; Enlarged Halden Programme Group Meeting, Bolkesjø, Norway, 30 October - 4 November 1994

[9] J. C. Carrol, R. A. Gomme, N. A. Leech; Enlarged Halden Programme Group Meeting, Bolkesjø, Norway, 30 October - 4 November 1994

[10] J. H. Harding, D. G. Martin; J. Nucl. Mater. **166** (1989) 166

[11] MATPRO - A Handbook of Materials Properties for Use in the Analysis of Light Water Reactor Fuel Rod Behaviour, TREE-NUREG-1005, EG&G Idaho, Inc.

[12] Hj. Matzke; Monograph on Science of Advanced LMFBR Fuels, North-Holland, Amsterdam-Oxford-New York-Tokyo (1986) p. 176

[13] R. C. Hawkings, A. S. Bain; report AECL-1790 (1963)

[14] Hj. Matzke; J. Nucl. Mater. **223** (1995) 1

[15] H. E.. Schmidt, J. Richter, Hj. Matzke, J. van Geel; 22nd Int. Conf. on Thermal Conductivity, Nov. 7-10, 1993; Tempe, Arizona, Proc. Thermal Conductivity 22, Ed. T. Tong, Technomic (1994) p. 920

[16] H. Marchandise; CEC report EUR - 4568f (1970)

[17] P. G. Lucuta, Hj. Matzke, I. J. Hastings; J. Nucl. Mater. (in press)

[18] Hj. Matzke; J. Nucl. Mater. **189** (1992) 141, and in "Ceramics Charting the Future", Advances in Science and Technology 3D, ed. P. Vincenzini, Techna Srl. (1995) 2913

2.1.5 Studies on the mechanism of damage creation and track formation in UO_2 induced by fast heavy ions

Introduction

In nuclear reactors, the main source of heat production is the slowing down of energetic heavy ions (fission products) in the UO_2 fuel. A thorough knowledge of this process is helpful to understand the performance of the fuel and its behaviour at long operating times.

As explained in the last report (TUAR-94, p. 37), the damage produced by energetic heavy ions obtained from different large accelerators is studied, mainly with transmission electron microscopy (TEM). Ions of energies up to several MeV per nucleon are used.

The aim of the study has also been outlined in TUAR-94, p. 37. In brief: the energetic heavy ions produce point defects and defect clusters along their path. If a given threshold energy deposition is surpassed, a track is

formed which may be directly visible in TEM or made visible by chemical etching (latent track). By using different ions of different energy (velocity), this threshold energy and the properties of the tracks (e.g. diameter as a function of mass and energy) can be determined. Also, by using the same ion at two different energies (velocities), at the two sides of the Bragg peak, but with the same energy deposition (or stopping power, dE/dx), one can determine whether velocity or stopping power is the important parameter for track formation.

The techniques to produce samples suitable for TEM have been developed in the reporting period. The TEM observations of the specimens described in Tab. 2.2 have been used to correlate implantation parameters and track formation.

Tab. 2.2 Typical parameters of irradiated samples. The energies at Gesellschaft für Schwerionenforschung (GSI) Darmstadt were 11.4 MeV/amu, thus giving mass-dependent energies for Au, Xe and U. At Hahn Meitner Institut (HMI) Berlin, a constant energy nearer to the fission energy was used. The electronic stopping powers dE/dx are for the original energy, i.e. for surface near layers of the specimens. The nuclear stopping powers are much smaller at these high energies (range 0.03 to 0.16 keV/nm).

Ion implanted	Energy (MeV)	Dose (ions/cm^2)	$dE/dx_{elec.}$ (keV/nm)
^{129}Xe HMI	173	7.10^{10}	29.1
^{129}Xe HMI	173	7.10^{11}	29.1
^{129}Xe HMI	173	7.10^{12}	29.1
^{129}Xe HMI	173	7.10^{13}	29.1
^{129}Xe GSI	1470	5.10^{10}	31.8
^{197}Au GSI	2265	5.10^{9}	53.3
^{238}U GSI	1300	5.10^{10}	56.0
^{238}U GSI	2713	5.10^{10}	59.2

Experimental

A number of new samples were irradiated at GSI Darmstadt and HMI Berlin (Some typical examples are given in Tab. 2.2). In order to increase the range of energies of the implanted ions, some samples were covered with polycarbonate or steel foils of different thickness. These thicknesses were chosen to slow very energetic ions down to energies close to the Bragg peak, i.e. the maximum energy loss. In this way, different effective energies can be obtained in one implantation with one beam energy. All implantations were performed at room temperature.

After implantation, the samples were thinned in order to be transparent to the electron beam of a transmission electron microscope (Hitachi 200 kV). Previous experiments had shown that when thinning UO_2, surface damage is very easily produced, masking the tracks to be observed. The conditions for sample preparation had therefore to be optimized in order to provide good specimens for TEM.

Two techniques were chosen and optimized for the thinning of the samples. In the first, the samples, consisting of discs of three millimeter diameter were ground and dimpled, and finally ion milled (Ar^+, 6 kV, 2.5 mA, 6°). In the second, the specimens were thinned using electropolishing (electrolyte: acetic acid + chromic acid). Both techniques are suitable to produce specimens transparent to the electron beam of TEM, and both methods yield good surfaces whether or not the specimens were annealed after thinning.

The ion milling attacks only one side of the sample. This constitutes a clear advantage compared with the electropolishing technique, because ion milling leaves the implanted side unetched, while the electropolishing procedure available at the Institute attacks both sides of the sample. Even when electropolishing is performed from one side only, the second side may be attacked as soon as a hole is formed. This could cause the implanted surface to be etched as well, thus leading to uncertainties on the actual depth of the layer observed by TEM and consequently on the corresponding energy loss.

Thinning before implantation (using one of these two techniques), followed by annealing to 1400 °C, has the advantage to produce samples with very good surfaces and hence without background in TEM. The disadvantage is that only one energy loss value can be observed in the very thin material obtained with this method, whereas the energy losses continuously vary in bulk materials.

In order to avoid this disadvantage, cross sectional TEM should be used (see TUAR-94, p. 38). Progress was made in preparing specimens with this method and we plan to use it in future work.

Calculations with the TRIM code

Calculations of the expected range profiles and of the expected damage distributions were performed for each implantation condition with the TRIM 95 code [1]. This code was also used to calculate the thickness of absorber necessary to vary the energy of the incoming ions. A useful tool of this program is the calculation of the electronic energy losses as a function of the penetration depth. The plot of energy loss by ionization of Xe ions in UO_2 and the range profiles are shown in Fig. 2.17 as an

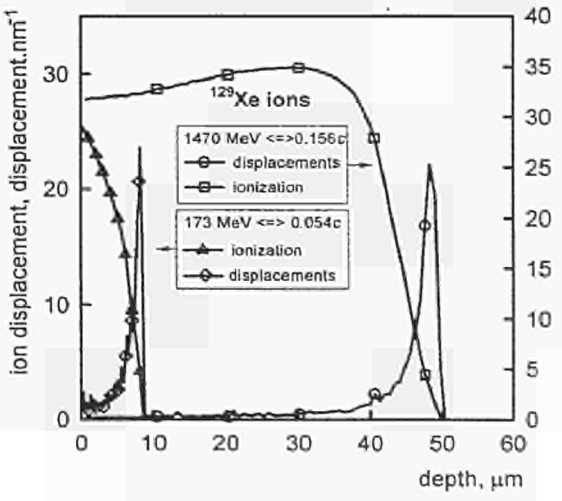

Fig. 2.17 Energy loss and displacements produced in UO_2 by Xe ions of 173 and 1470 MeV. The results shown in Fig. 2.19 are for the first 0.1 µm of the depth scale.

example for two widely different energies. Similar calculations are shown in Fig. 2.18 for U-ions. The energy loss of 2.713 GeV U ions in UO_2 (velocity: 0.158 *c*) is 59.2 keV/nm. With a cover of 20 µm steel, the calculated energy of the U-ions after passing through the foil is ~1.3 GeV. While the velocity (0.108 *c*) is smaller than at 2.713 GeV, the stopping power dE/dx is practically the same for both energies.

TEM observations

All the samples described in Tab. 2.2 were analysed by TEM. Fig. 2.19a shows as reference an unimplanted UO_2 specimen, which was dimpled, then annealed at 1400 °C for two hours and finally ion milled to produce thin areas. Fig. 2.19b shows a sample irradiated with 7.10^{10} Xe ions/cm^2 of 173 MeV at HMI: surface defects are visible, apparently constituted by defect clusters, distributed in good correlation with the dose (see inset in Fig. 2.19b).

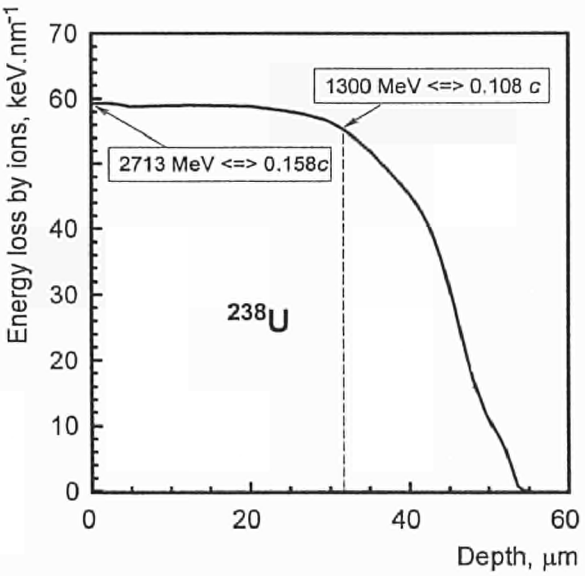

Fig. 2.18 Electronic energy loss of U-ions in UO_2.

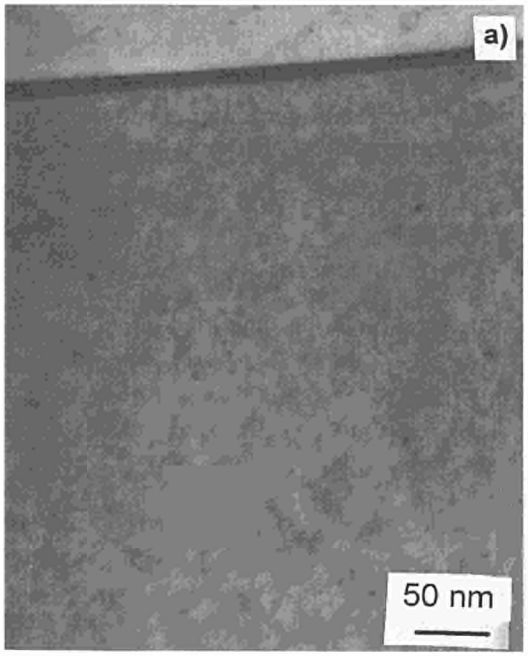

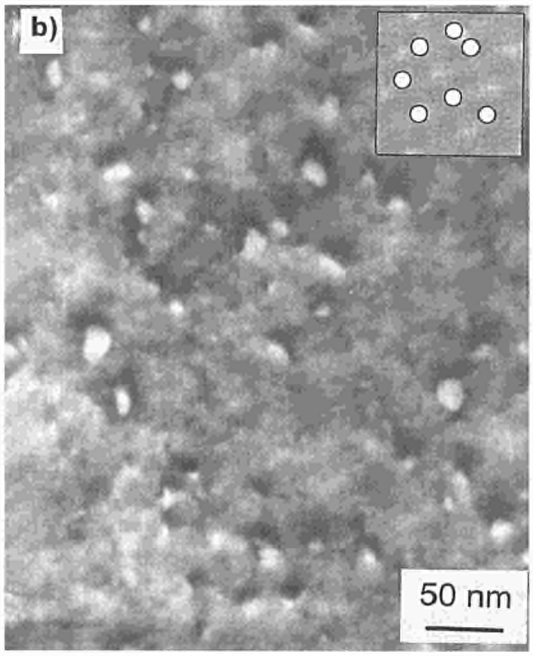

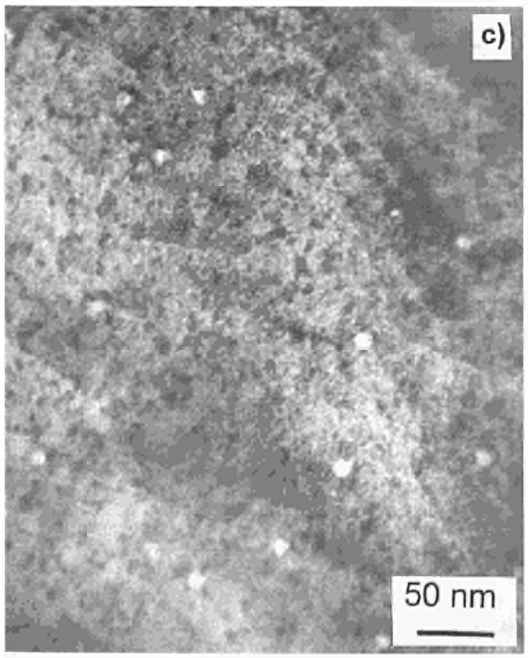

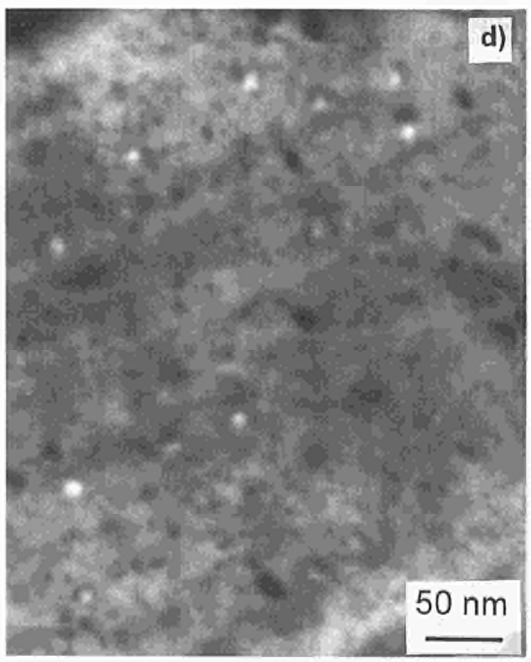

Fig. 2.19a-b Transmission electron micrographs of a) an unimplanted UO_2 specimen thinned by ion milling and annealed b) implanted with 7.10^{10} ions.cm^{-2} 173 MeV Xe ions. The expected track distribution is shown in the upper right

Fig. 2.19c-d Transmission electron micrographs of UO_2 specimens implanted with 11.4 MeV/amu U ions. c) covered by a 20 µm steel foil, leading to a decrease in the energy of the incoming ions to 1300 MeV. d) without foil, i.e. the energy of the incoming ions was 2.713 GeV. Both samples were implanted with a dose of 5.10^{10} ions.cm^{-2}.

Fig. 2.19c shows a UO_2 specimen irradiated with 10^{10} U ions/cm^2 of 11.4 MeV/amu (2.713 GeV energy) with an energy loss of 59.2 keV/nm, mainly by ionization. Tracks are visible on photo c as white dots of 10±2 nm in diameter. The implantation dose at GSI is less well known than at HMI, because of the low beam currents and the high energy used. Nevertheless, the distribution of the spots fits with the indicated dose (5 spots per 0.01 μm^2). Fig. 2.19d shows another sample irradiated at the same time but covered with a stainless steel foil of 20 μm thickness in order to decrease the energy of the incoming ions. The visible tracks in this case are comparable to those of Fig. 2.19c.

For the specimens implanted with higher doses of 173 MeV Xe (7.10^{11}-7.10^{13} ions/cm^2) the damage density was, as expected, too high to resolve small features by TEM. These specimens will be used for measurements of changes in lattice parameter and surface topography. Note that with a track diameter of 10 nm, overlap of the damaged regions is expected at a dose of ~10^{12} ions/cm^2. The specimen with 7.10^{13} ions/cm^2 has therefore been subjected to multiple overlap. A very high density of defect clusters was seen using TEM.

Discussion

The samples studied in the reporting period can be divided into two sets. Those implanted with ions of very high energy (in the range of 1.3 to 2.7 GeV), and those irradiated with ions of an energy comparable with fission energy.

For the high energy U-implants in UO_2, we had two energies: The electronic energy deposition was practically the same (56 and 59.2 keV/nm) while the velocity differed by a factor of 1.5. The nuclear energy deposition (nuclear collisions leading to displacements of the target atoms) is about two times greater for the ions of lower energy, but it is still much smaller than the electronic energy losses (0.1% for 2.7 GeV and 0.2% for 1.3 GeV-U ions). Comparable track sizes are observed, thus leading to the conclusion that the velocity, within the (small) range studied, has only a small effect on track diameters in UO_2. Actually, for the lower energy, the tracks were, on average, some 10% larger than at high energy. For Xe implants, we had also two energies (1470 and 173 MeV) with similar dE/dx (31.8 and 29.1 keV/nm) but of course different velocities, varying by a factor of $(1470/173)^{1/2}$ ~ 2.9.

The specimens implanted with Xe ions of 1470 GeV showed no evident tracks but some dislocation loops. On the samples implanted with 173 MeV Xe ions one can observe larger damaged spots with a density corresponding to the implantation dose. This is not unexpected, since at lower velocity the volume in which the electronic energy is deposited is larger [2] and since there is more damage creation by production of collision cascades (nuclear energy loss).

Various models have been proposed to explain track formation in insulators e.g. [3, 4]. In the thermal spike model of Szenes [5], the latent tracks, produced in the wake of an energetic ion, can be related to the electronic stopping power, S_e.

The model does not include velocity effects, but is used nevertheless, since it was rather successfully applied to a number of insulators [5].

Szenes assumes an initial Gaussian temperature distribution with a width a(0), and identical radii of the molten zone of the thermal spike. For the threshold energy loss, S_{et}, he arrives at the formula

$$S_{et} = \rho \cdot \pi \cdot c \cdot a^2(0) \cdot T_0 / g \qquad (1)$$

Here, ρ, T_0 and c are the density (10.96 g/cm^3 for UO_2), the difference between melting and irradiation temperature (2850 K for UO_2) and the average of the specific heat over this temperature range (0.33 J/gK for UO_2 [6]). Szenes reported a remarkably uniform behaviour for 8 (magnetic) insulators. For a(0), a constant value of 4.5 nm was deduced, and for g, the fraction of S_e deposited in the phonon system in the thermal spike, a constant value of 0.17 was deduced. Note that this simple model allows neither for ion velocity nor ion mass or differences in thermal conductivity of the insulators. If we apply it to UO_2, the threshold energy loss for track formation is S_{et}=24 keV/nm. We can use this value as a first guideline.

Szenes derived also relations for the radius R of (latent) tracks. For our cases, the one for the range $S_{et} \leq S_e \leq 2.7\ S_{et}$ is relevant:

$$R^2 = a^2(0) \cdot \ln[(gS_e) / (\rho \cdot \pi \cdot c \cdot a^2(0) \cdot T_0)] \qquad (2)$$

Since the above values for a(0), r, c and T_0, yield S_{et}=24 keV/nm, Eq. (2) can be simplified to

$$R^2 = (4.5\ \text{nm})^2 \cdot \ln[S_e/24\ \text{keV/nm}]$$

We obtain thus for the track radius R for the high energy U-ions a value of R = 4.3 nm, in acceptable agreement with the measured diameter of 10±2 nm. For the Xe-ions the predicted diameter is very small, i.e. only 1 nm. This is in disagreement with the experimental results, possibly because velocity effects are not taken into account in Eqs. (1, 2). We will attempt to use other theoretical models in the future.

References

[1] J. F. Ziegler, J. P. Biersack, U. Littmark; The Stopping and Range of Ions in Solids, Pergamon Press (1985)

[2] M. Toulemonde, S. Bouffard, F. Studer; Nucl. Inst. and Meth. **91** (1994) 108

[3] Hj. Matzke; Radiat. Eff. **64** (1982) 3

[4] R. L. Fleischer, P. B. Price, R. M. Walker; Nuclear Tracks in Solids, University of California Press (1975)

[5] G. Szenes; Phys. Rev. B **51** (1995) 8026

[6] C. Ronchi, J. P. Hiernaut, R. Selfslag, G. J. Hyland; Nucl. Sci. Eng. **113** (1993) 1

2.1.6 Effect of inhomogeneity on the level of fission gas and caesium release from optimized co-milling (OCOM) MOX fuel during irradiation

In this report electron probe microanalysis (EPMA) results for two OCOM fuels are compared. In one fuel (OCOM 30), the MOX agglomerates contained a high concentration of fissile plutonium, but had a low volume fraction; in the other (OCOM 15), the agglomerates contained a low concentration of fissile plutonium, but had a high volume fraction. EPMA was used to measure the concentrations of xenon, caesium, neodymium and plutonium in the MOX agglomerates and their radial distributions in the UO_2 matrix. The agglomerates analysed were located at different radial positions in the fuel, including the pellet rim, and varied in size from 40 to 160 μm. To obtain a comprehensive picture of the behaviour of the above elements, point analysis and area analysis, which included both agglomerates and the UO_2 matrix, were performed.

Fuel characteristics and irradiation history

The design characteristics of the two OCOM fuels are given in Tab. 2.3. Both fuels contained about 4.5 w/o plutonium. Recycled material from MOX fuel pellet production (rejected pellets, grinding swarf etc.) constituted 5-10% of the total weight of fuel. As a result of the addition of MOX scrap, about 0.2 w/o plutonium was present in the UO_2 matrix of the fuel before irradiation. The OCOM 15 fuel contained 34 v/o of MOX agglomerates with a fissile plutonium concentration (^{239}Pu + ^{241}Pu) of 9 w/o. The OCOM 30 fuel contained 17 v/o of MOX agglomerates with a fissile plutonium concentration of 18 w/o.

Tab. 2.3 Fuel pellet and pin segment design characteristics.

Design Parameter	OCOM 15	OCOM 30
Fissile Pu [a] (w/o)	3.06	3.06
Total Pu (w/o)	4.43	4.47
PuO_2 in agglomerates (wt%)	15	30
v/o of agglomerates	34	17
U enrichment (% ^{235}U)	0.72	0.72
Grain size [b] (μm)	5-6	5-6
Stoichiometry (O/M)	1.994	1.992
Fuel density (%TD)	95	95
Pellet diameter (mm)	9.13	9.13
Diametrical gap (mm)	0.17	0.17
Fill gas [c]	He (2.25)	He (2.25)
Cladding material	Zircaloy-4	Zircaloy-4

a $^{239}Pu+^{241}Pu$.
b Linear intercept.
c Figure in parenthesis is the pressure in MPa at room temperature.

The fuels were irradiated under normal PWR conditions in the KWO reactor at Obrigheim in Germany. The irradiation spanned four reactor cycles and lasted 1260 effective full power days (EFPD). During the irradiation the average linear power was 19.4 kWm^{-1} for the OCOM 15 segment and 20.4 kWm^{-1} for the OCOM 30 segment. In both cases, the linear power during the first reactor cycle was around 16 kWm-1 and did not exceed 23 kWm^{-1} in the second, third and fourth cycles. Therefore, the fuel centre temperature probably barely exceeded 1300 °C. The fuel cross-sections on which EPMA was carried out had burn-ups of 43.6 GWd/t (OCOM 15) and 44.5 GWd/t (OCOM 30).

Methods

EPMA was carried out at an electron acceleration potential of 25 keV and a beam current of 250 nA. The matrix correction was carried out using the QUAD2 program of Farthing et al. [1]. Xenon was analysed using the approach pioneered at the Institute [2]. This gives the concentration of xenon in solution and trapped in intragranular gas bubbles smaller than 0.1 μm. Plutonium was analysed using the Mβ X-ray line. The measured intensity of this line was corrected for X-ray contributions from the U $M\beta_2$ line as described elsewhere [3].

Analysis of the UO_2 matrix

The radial distributions of Pu, Nd, Xe and Cs in the UO_2 matrix of the OCOM 30 fuel were obtained by point analysis at radial intervals of 50 to 250 μm. At each location six determinations for Xe, Cs and Nd, and four determinations for U and Pu were made. These were up to 10 μm apart and the point of measurement was chosen to avoid grain boundaries, pores and cracks.

In the OCOM 30 fuel the concentrations of Pu and Nd in single grains of the UO_2 matrix were measured at three radial positions; r/r_o= 0.82, 0.36 and 0.14. At each location six grains were analysed. In the OCOM 15 fuel the concentrations of Pu, Nd, Xe and Cs were measured in the UO_2 matrix. In this case, however, the determinations were restricted to the cold outer region of the fuel at r/r_o= 0.98, 0.90, 0.80 and 0.70.

Analysis of the MOX agglomerates

The MOX agglomerates in both fuels were analysed in detail. In the OCOM 15 fuel, agglomerates at the pellet rim, at r/r_o= 0.85 and 0.35 were analysed. The agglomerates analysed in the OCOM 30 fuel were situated at the pellet rim, at r/r_o= 0.86, 0.76, 0.58 and 0.28. At each radial position except 0.76 and 0.28, one large and one small agglomerate was selected for analysis.

The concentrations of Pu, Nd, Xe and Cs in the MOX agglomerates were determined by point analysis at intervals of 5-10 μm along a line traversing the agglomerate. The specimen current image was used to obtain information about the distribution and mor-

phology of the pores and gas bubbles in the agglomerates and to position the electron beam.

Integral analysis of the fuel cross-section

The integral concentrations of Pu and Nd in the OCOM 15 fuel and of Pu, Nd, Xe and Cs in the OCOM 30 fuel were measured using area analysis along the fuel radius. A raster measuring 300x300 µm was employed and the distance between the mid-planes of adjacent rasters was also 300 µm. In this way an unbroken radial strip of fuel containing both matrix and MOX agglomerates was analysed. At each of the sixteen steps along the radius three determinations were made.

Results

Burn-up in the MOX agglomerates and the UO_2 matrix

The local concentration of neodymium was taken as a measure of the local burn-up in the MOX agglomerates and the UO_2 matrix. For this purpose, 0.106 w/o neodymium was assumed to correspond to 10 GWd/t. As seen from Tab. 2.4, neodymium concentrations of 0.46 and 0.47 w/o were measured in the OCOM 15 and OCOM 30 cross-sections, respectively. These concentrations correspond to 43.4 and 44.3 GWd/t which are very close to the reported burn-up values of 43.6 and 44.5 GWd/t.

Tab. 2.4 Integral concentrations of Pu, Nd, Xe and Cs in the fuel cross-section and in the UO_2 matrix.

Fuel	Concentration, w/o			
	Pu	Nd	Xe	Cs
	MOX Agglomerates + UO_2 Matrix			
OCOM 30	3.6	0.47	0.52	0.53
OCOM 15	3.2	0.46	...	...
	UO_2 Matrix			
OCOM 30	1.9	0.33	0.51	0.28
OCOM 15	...	...	...	...

The burn-up in the MOX agglomerates was considerably higher in the OCOM 30 fuel. Fig. 2.20 shows the burn-up in a number of agglomerates at different radial positions in the OCOM 15 and OCOM 30 fuels. The burn-up reported is based on the highest neodymium concentration measured in each case. It is seen that at the fuel surface the burn-up in the OCOM 30 agglomerates was about 270 GWd/t whereas in the OCOM 15 agglomerates it was about 160 GWd/t. Similarly, in the central region of the fuel, the burn-up in the

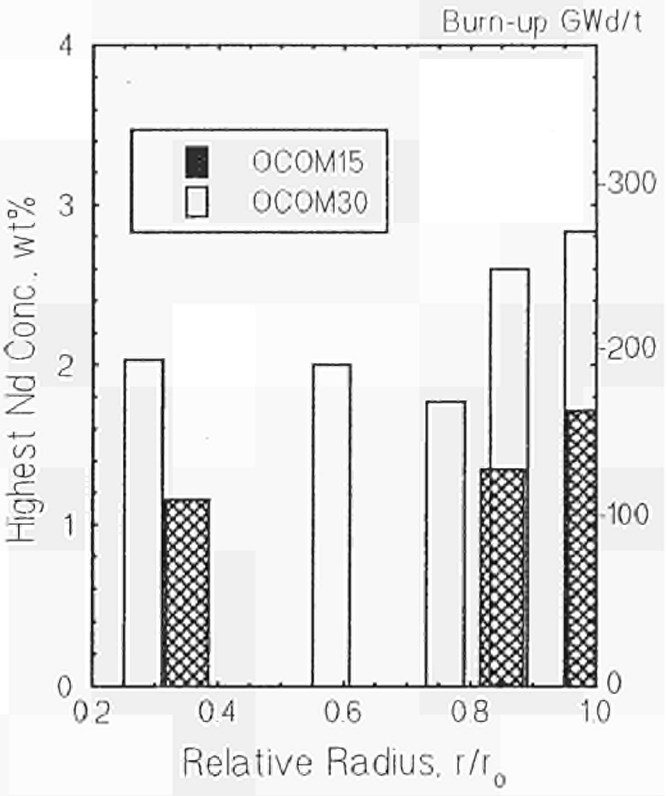

Fig. 2.20 Burn-up in the MOX agglomerates in the OCOM 15 and OCOM 30 fuels as derived from their neodymium content. A much higher burn-up was reached in the OCOM 30 agglomerates.

OCOM 30 agglomerates was around 190 GWd/t, but did not exceed 110 GWd/t in the OCOM 15 agglomerates. It is also evident from these figures that the MOX agglomerates in the outer region of the fuel had accumulated more burn-up than those in the central region of the fuel.

As in conventional UO_2 fuel, the radial burn-up profile in the UO_2 matrix of the MOX fuel was quite flat in the body of the fuel, but increased sharply near the fuel surface. The radial distribution of neodymium in the UO_2 matrix of the OCOM 30 fuel, which represents the radial burn-up profile, can be seen in Fig. 2.21 Over most of the fuel radius, the local concentration of neodymium is slightly less than 0.3 w/o, which corresponds to about 28 GWd/t, but at $r/r_0 = 0.90$ it increases abruptly from this level to 0.66 w/o at the pellet rim. This concentration is equivalent to a burn-up of 62 GWd/t. The average concentration of neodymium in the UO_2 matrix was 0.33 w/o, giving a burn-up for the cross-section of 31.1 GWd/t.

Although, the neodymium profile in Fig. 2.21, indicates that the burn-up in the UO_2 matrix of the OCOM 30 fuel was rather uniform, the analysis of single grains revealed that in truth the burn-up varied widely from grain to grain. Fig. 2.22 shows the burn-up in single grains at $r/r_0 = 0.82$, at $r/r_0 = 0.36$ and $r/r_0 = 0.14$ in the OCOM 30 fuel.

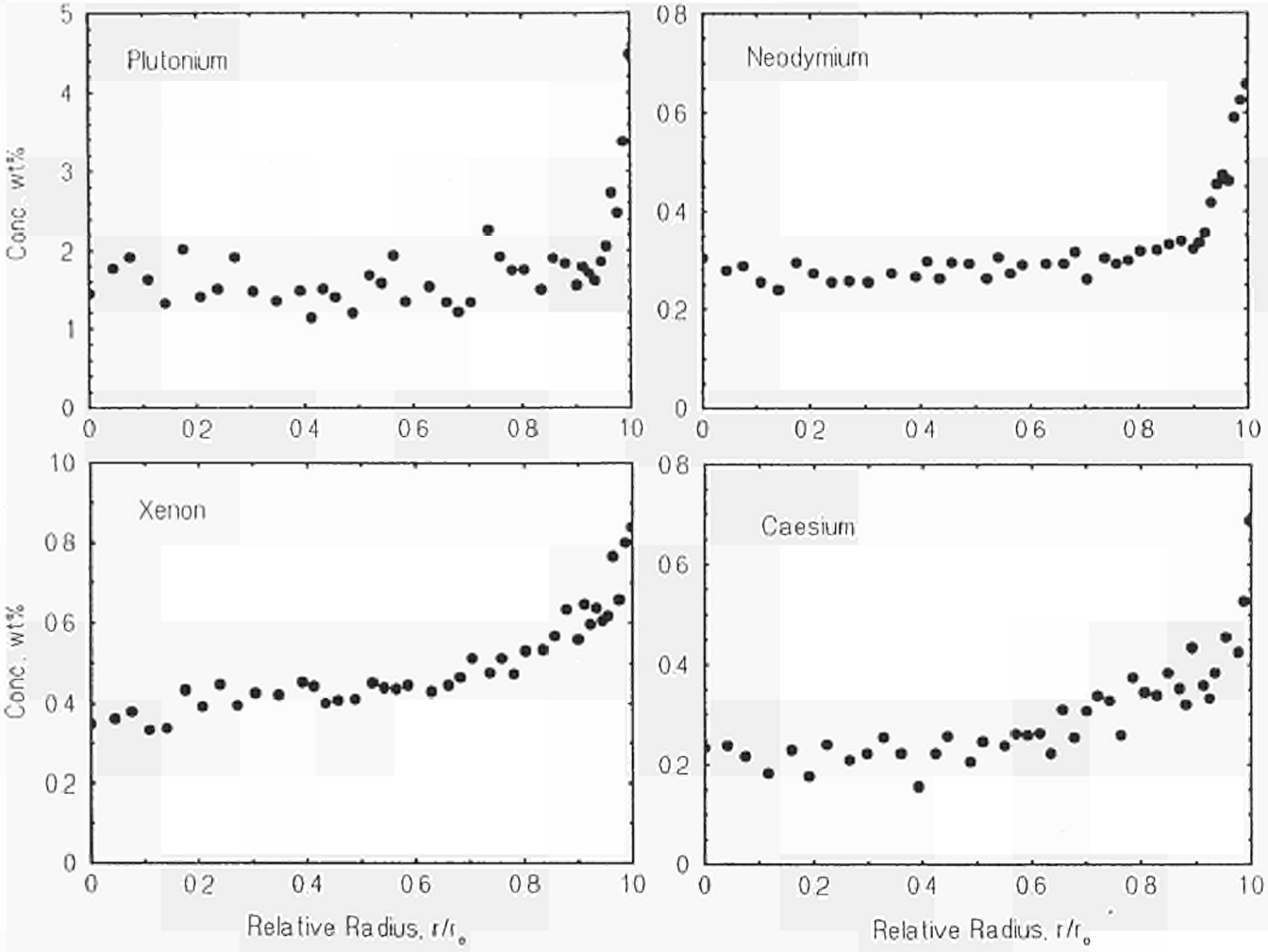

Fig. 2.21 Radial distributions of Pu, Nd, Xe and Cs in the UO_2 matrix of the OCOM 30 fuel.

At each of these radial positions, the burn-up in six grains is seen. The burn-up in the grains was found to vary between 13 and 88 GWd/t. The large variation in burn-up is due to the different concentrations of fissile plutonium in the grains, which represent different materials: i.e., UO_2, MOX fuel scrap and the MOX agglomerates (see below). It is assumed that 13 GWd/t is representative of the burn-up in areas of the UO_2 matrix that were unspoilt by plutonium from agglomerate particles or plutonium from MOX fuel scrap. The neodymium profile in Fig. 2.21 indicates a uniform burn-up distribution, because the data points used to draw concentration profile are the average of six determinations made on different grains.

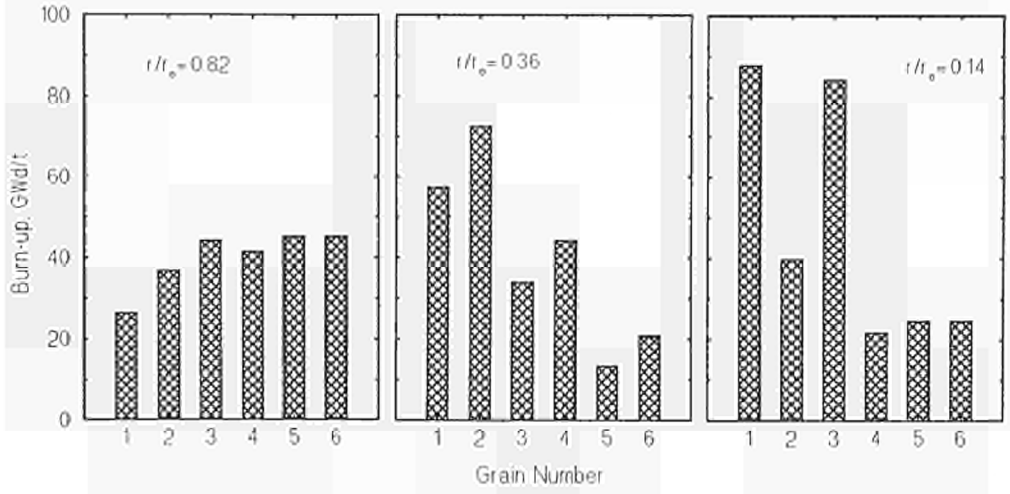

Fig. 2.22 Burn-up in single grains in the UO_2 matrix of the OCOM 30 fuel at three radial positions.

Plutonium burn-out in the MOX agglomerates

In Fig. 2.23 the concentration of Pu in the MOX agglomerates in the two fuels is plotted against the neodymium concentration (i.e., the burn-up). Included in the plot are data from MOX agglomerates of different size (50 to 185 µm) and from agglomerates at different radial positions, including the fuel rim. The plutonium concentration in the OCOM 30 agglomerates had decreased from 26.5 to approximately 13 w/o at a burn-up above 140 GWd/t, while in the OCOM 15 agglomerates it had decreased from 13.2 to roughly 6.5 w/o at a burn-up higher than 55 GWd/t.

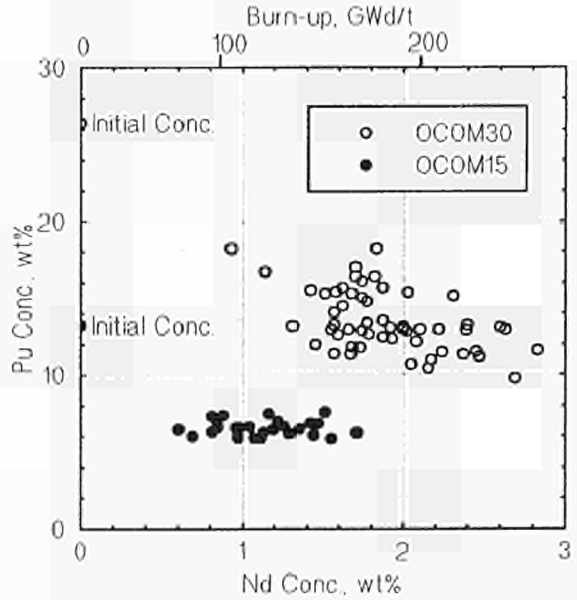

Fig. 2.23 Plutonium concentration in the MOX agglomerates related to the neodymium concentration (representing the burn-up) at the same location. In both fuels approximately 50% of the plutonium in the agglomerates was burnt.

Plutonium in the UO_2 matrix

The radial distribution of Pu in the UO_2 matrix of the OCOM 30 fuel can be seen in Fig. 2.21. Like the neodymium concentration profile, the plutonium concentration profile exhibits a steep rise close the pellet surface due to enhanced neutron capture. Volume integration of this profile gives an average plutonium concentration of 1.9 w/o.

The plutonium in the UO_2 matrix was far less homogeneously distributed than one would be led to believe from the plutonium concentration profile in Fig. 2.21. Results from analysis of single grains in the OCOM 30 fuel are shown in Fig. 2.24. It is seen that the measured plutonium concentrations ranged from about 1.0 to 14.5 w/o. It is also seen that with the aid of the neodymium concentration it seems possible to identify the source of the plutonium in the grains. That is to say, whether the plutonium resulted from small particles of agglomerate material, or came from the addition of MOX fuel scrap, or resulted from neutron capture by ^{238}U during the irradiation.

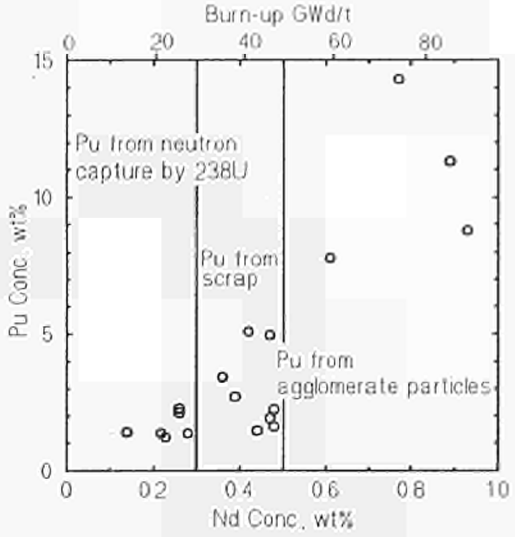

Fig. 2.24 Concentration of plutonium in single grains in the UO_2 matrix in the OCOM 30 fuel related to the concentration of neodymium (representing the burn-up) in the same grains.

Fission gas release

The EPMA data for fission gas release from the OCOM 30 fuel is summarized in Tab. 2.5. As can be seen, the integral release from the fuel cross-section was approximately 12%. In the case of the MOX agglomerates, however, about 90% of the fission gas had been released from the mixed oxide lattice.

Tab. 2.5 Fission gas release data for the OCOM 30 fuel.

Radial Position	Xe created	Xe measured [a]	%
	(w/o	(w/o)	Release
MOX Agglomerates + UO_2 Matrix			
	0.59	0.52	11.9
MOX Agglomerates			
$r/r_o = 0.86$	2.59	0.20	92.3
$r/r_o = 0.28$	2.18	0.28	87.2
UO_2 Matrix			
	0.42	0.51	...

[a] Average values.

It is clear from Fig. 2.25 that an extremely high percentage of gas had been released from (U, Pu)O_2 lattice of the MOX agglomerates. From this figure, it is evident that the concentration of xenon measured in the OCOM 15 and OCOM 30 agglomerates was generally less than 0.6 w/o, and on average about 0.25 w/o, regardless of the neodymium concentration. This reveals that gas release increased with the agglomerate burn-up, which implies that OCOM 15 agglomerates released less gas from the oxide lattice than the OCOM 30 agglomerates, and that MOX agglomerates close to the fuel surface, where the burn-up is higher, released more gas than those further in.

The analyses which provided the data in Fig. 2.25 were performed on MOX agglomerates of different size and on agglomerates at different radial positions in the

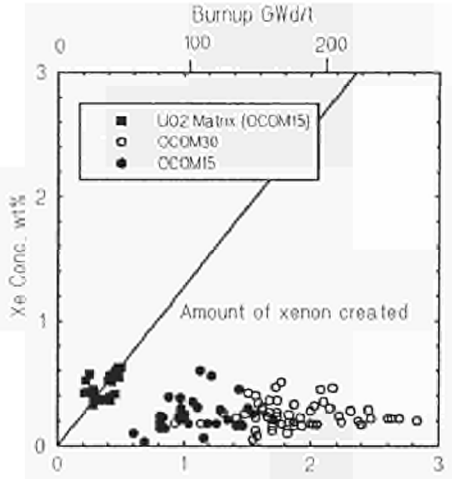

Fig. 2.25 Concentration of retained xenon in the MOX agglomerates related to the local concentration of neodymium (representing the burn-up). The local concentrations of xenon and neodymium in the UO_2 matrix in the outer region of the OCOM 15 fuel between r/r_0= 0.7 and the fuel surface were used to position the line giving the created amount of xenon, and are included for comparison.

fuels. In Fig. 2.26 the average concentration of xenon measured in the OCOM 15 and OCOM 30 agglomerates is plotted as a function of the radial position and agglomerate size. It is seen that the concentration of xenon measured did not vary significantly with the size of the agglomerate or its radial position in the fuel.

It is not clear what percentage of fission gas was released from the UO_2 matrix. As seen from Tab. 2.5, EPMA measured 0.51 w/o xenon in the matrix, which is considerably more than the amount produced during irradiation to 31.1 GWd/t (0.42 w/o). The cause of this inconsistency is not known, but it does not appear to be due to recoil or diffusion from the MOX agglomerates. Consideration of the fuel temperature during the irradiation, however, reinforces the view that little gas was released from the UO_2 matrix. This assumption is supported by the radial xenon profile shown in Fig. 2.21, which indicates that at the most 11% release may have occurred locally in the central region of the fuel, between approximately r/r_0= 0.15 and the centre

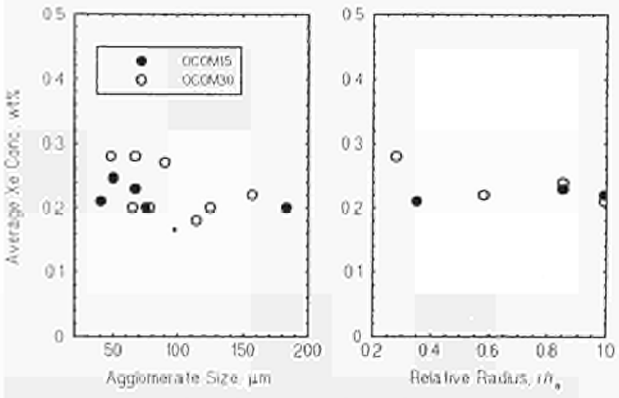

Fig. 2.26 Graphs showing that the concentration of xenon measured in the MOX agglomerates did not change significantly with the size of the agglomerate or its radial position in the fuel.

of the pellet. This translates to an average cross-section release of just 0.2%.

The behaviour of the fission product caesium

Caesium behaved very differently from xenon in that it was almost completely retained by the MOX agglomerates. In Fig. 2.27 the concentration of caesium in the MOX agglomerates of the OCOM 15 and OCOM 30 fuels is plotted as a function of the neodymium concentration. Despite the scatter in the data it is clearly seen that at neodymium concentrations up to 2.3 w/o (burn-ups up to 215 GWd/t) the concentration of caesium increased linearly with the neodymium concentration indicating complete retention by the MOX agglomerates. At neodymium concentrations above 2.3 w/o, however, the measured caesium concentrations lie below the line drawn through the data indicating some release of caesium from the agglomerates at the very highest burn-ups (215–270 GWd/t).

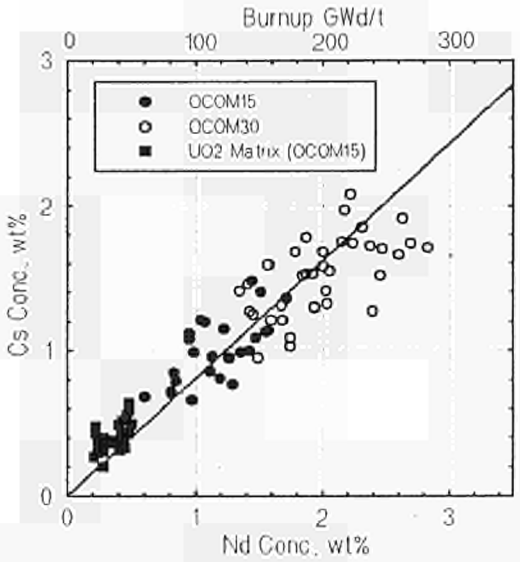

Fig. 2.27 Concentration of retained caesium in the MOX agglomerates related to the local concentration of neodymium (representing the burn-up). Over most of the range of neodymium concentrations measured, the caesium concentration increases linearly, indicating full retention. Data for the UO_2 matrix in the outer region of the OCOM 15 fuel are included for the purposes of comparison.

In the UO_2 matrix of the OCOM 30 fuel a caesium concentration of 0.28 w/o was measured. This corresponds to the caesium inventory calculated using the fission yield value of 0.17 a/o caesium per 1 a/o burn-up derived from the EPMA data plotted in Fig. 2.27. It would appear, therefore, that caesium was not released from the UO_2 matrix.

Discussion

Fission Gas Release

The release of fission gas to the rod free volume requires a system of escape tunnels along the grain

boundaries in the UO_2 matrix. Because the fuel irradiation temperature was low, such a tunnel system did not develop in the OCOM 15 and OCOM 30 fuels. Hence, the UO_2 matrix behaved like a hard shell enclosing the agglomerates and preventing the gas released there from escaping to the rod free volume. Most of the released gas, therefore, precipitated in the pore structure of the agglomerate.

Around 90% of the fission gas was released from the lattice of the MOX agglomerates and most of this gas had precipitated in the agglomerate pore structure. Although the burn-up in the OCOM 30 agglomerates was almost twice as high as that of the OCOM 15 agglomerates, the percentage of fission gas released from the oxide lattice of the agglomerates was not significantly different (90% compared with 85%). In absolute terms, however, considerably more gas was lost from the lattice of the OCOM 30 agglomerates, because these had a much higher burn-up. At the end of the irradiation, generally around 0.25 w/o xenon remained in the agglomerate lattice. Evidently, the high gas release is due to a profound transformation in the agglomerate microstructure (recrystallization) caused by the high local burn-up.

For the OCOM 30 fuel an average cross-section release value of about 12% was obtained from area analysis by EPMA. Most of this gas must have come from the MOX agglomerates because apparently less than 0.5% of the fission gas inventory was released from the UO_2 matrix. However, the puncturing result for this segment (see Fig. 2.28) revealed that only around 2.5% of the fission gas inventory was released to rod free volume at an average burn-up of 44.5 GWd/t. This indicates that almost 80% of the gas released from the fuel lattice was retained in the fuel, presumably in pores and at grain boundaries.

The puncturing result for the OCOM 15 segment with an average burn-up of 43.6 GWd/t was 1.7%. Thus, despite the difference in the pore structure of the OCOM 15 and OCOM 30 agglomerates, the percentage of gas released to rod volume in both segments is practically the same.

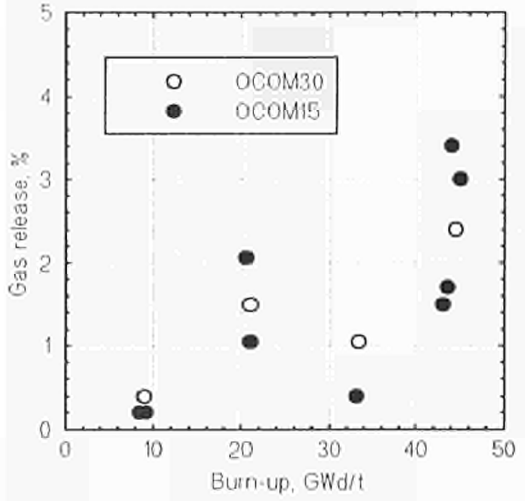

Fig. 2.28 Puncturing results for percentage of fission gas released to the free volume in the OCOM 15 and OCOM 30 fuel segments.

Effect of fuel inhomogeneity

During the irradiation of the OCOM 15 and OCOM 30 fuels low temperatures prevailed and consequently U/Pu interdiffusion was minimal. As a result both fuels remained inhomogeneous on the microscopic scale. The MOX agglomerates in the central region of the fuel did not lose Pu to the UO_2 matrix, and initial variations in the plutonium concentration of the grains in the UO_2 matrix were not smoothed out. In both fuels, however, the concentration of plutonium in the MOX agglomerates decreased by about 50% as a result of fission, whereas owing to neutron capture by ^{238}U the plutonium content of the UO_2 matrix increased ten-fold to about 2 w/o. Consequently, from an initial average of 4.5 w/o, the total concentration of plutonium fell to 3.6 w/o in the OCOM 30 fuel (a decrease of 20%) and to 3.2 w/o in the OCOM 15 fuel (a decrease of 29%).

Although the volume fraction of the MOX agglomerates and the burn-up in the agglomerates were entirely different in the OCOM 15 and OCOM 30 fuels, there was no significant difference in the level of release from the two fuels. This is evident from the puncturing data in Fig. 2.28, which reveal that for both fuels the percentage of gas released to the rod free volume increased from less than 0.5% at 10 GWd/t to a maximum of 3.5% at 45 GWd/t. Perhaps the low percentage of gas measured is surprising in view of the extremely high percentage that had escaped from the MOX agglomerate lattice. The puncturing results, however, reflect the fact that most of the gas released from the agglomerate lattice remained in the agglomerates, being unable to penetrate the dense UO_2 matrix, and that a large fraction (80%) of the gas that did manage to escape from the agglomerates was retained in the fuel.

About twice as much caesium was produced in the OCOM 30 agglomerates as in the OCOM 15 agglomerates due to the difference in the burn-up, and apparently all this was retained. However, since the volume fraction of the agglomerates was twice as high in the OCOM 15 fuel as in the OCOM 30 fuel and the average burn-up of the two fuels was almost the same, both probably contained approximately the same total amount of caesium.

Summary and conclusions

The burn-up in the OCOM 30 agglomerates was almost twice as high as in the OCOM 15 agglomerates (e.g., at the fuel surface, typically 270 GWd/t compared with 160 GWd/t). As low temperatures prevailed during the irradiation, U/Pu interdiffusion did not occur. Because of this, both fuels remained inhomogeneous on the microscopic scale. The concentration of plutonium in the MOX agglomerates decreased by about 50% as a result of fission, whereas owing to neutron capture by ^{238}U the plutonium content of the UO_2 matrix increased ten-fold to about 2 w/o. Consequently, the total concentration of plutonium in the fuel fell to 3.6 w/o in the OCOM 30 fuel (a decrease of 20%) and to 3.2 w/o in the OCOM 15 fuel (a decrease of 29%).

Around 90% of the fission gas h0ad been released from the oxide lattice of the MOX agglomerates in both fuels leaving at the most 0.6 w/o and on average 0.25 w/o in solution. A very large fraction of the gas released from the lattice precipitated and remained in the pore structure of the agglomerates. Although the burn-up in the OCOM 30 agglomerates was considerably higher than in the OCOM 15 agglomerates, the percentage of fission gas released from the oxide lattice of the agglomerates was not significantly different (90% compared with 85%).

The puncturing results for the OCOM 15 and OCOM 30 were very similar. For both fuels the percentage of gas released to the rod free volume increased from less than 0.5% at 10 GWd/t to a maximum of 3.5% at 45 GWd/t. This reveals that the percentage of gas released by MOX fuel manufactured by the OCOM process is largely independent of the level of inhomogeneity of the fuel.

References

[1] I. Farthing, G. Love, V. D. Scott, C. T. Walker, Mikrochim. Acta Suppl. **12** (1992) 117

[2] C. T. Walker, J. Nucl. Mater. 80 (1979) 190

[3] K. Lassmann, C. O'Carroll, J. Van de Laar, C. T. Walker, J. Nucl. Mater. **208** (1994) 223

2.1.7 Study of the ternary plutonium-uranium-oxygen phase diagram

Introduction

The aim of this investigation is the extension of the present knowledge of the U-Pu-O phase diagram and especially the determination, in the O/M range between 1.6 and 2.0, of the plutonium concentration, above which a two-phase system exists.

While the uranium oxygen [1] and plutonium oxygen [2] phase diagrams are fairly well established, relatively little work has been reported on plutonium-uranium-oxygen equilibrium [3, 4]. In the miscibility gap, at high Pu concentrations and for substoichiometric compositions, contradictory data exist. This is all the more problematic as it is important for technological applications.

Literature overview

The uranium plutonium oxygen system has been studied mainly by Markin [3] and Sari [4], whose results are described as follows:

1. Using high temperature X-ray diffraction, Markin determined the U-Pu-O phase diagram between the compositions $UO_{1.88}$-U_3O_8 and PuO_2-$PuO_{1.5}$ for all concentrations of plutonium from room temperature to 800 °C. At room temperature, the material with the general formula $U_{1-z}Pu_2O_{2\pm x}$, reduction of oxides with $z > 0.4$ to a substoichiometric composition results in the formation of two phases with compositions $MO_{2.0}$ and MO_{2-x}. Upon heating this two phase-product, a single phase material is formed at a temperature which depends on the value of z. Reduction of oxides with $z < 0.4$ results in a single phase material at all temperatures (Fig. 2.29).
2. Sari [4] has studied uranium plutonium oxides with plutonium concentrations between 5% and 97% with an O/M ratio less than 2.0. His constructed ternary phase diagram at room temperature is shown in Fig. 2.30. In contrast to Markin [3], Sari's results indicate that only mixed oxides containing

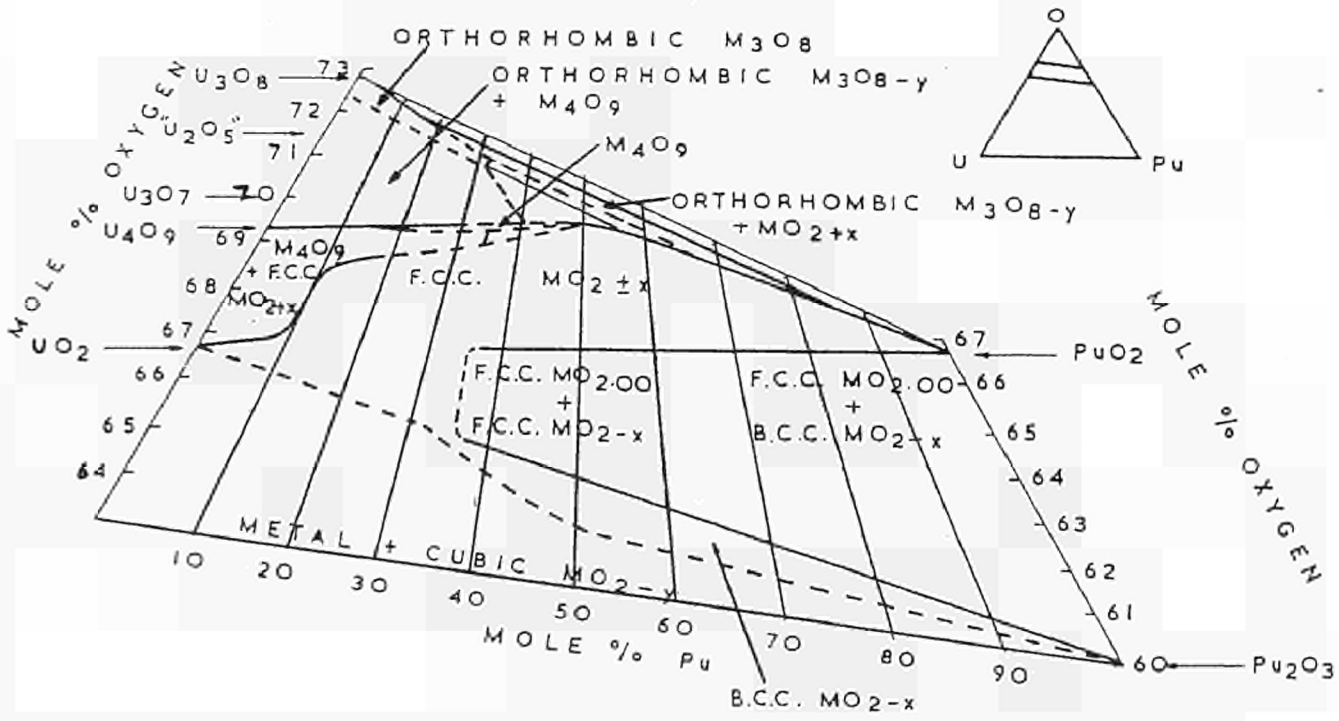

Fig. 2.29 Ternary phase diagram for uranium plutonium oxygen for all concentrations of plutonium.

less than 20% of plutonium remain in a single phase (fcc) until all the plutonium has been reduced to the trivalent state. Above this Pu concentration, and for $1.6 < O/M < 2.0$, a large two-phase region extends up to the binary plutonium-oxygen system. In the range of plutonium concentrations between 20% and 50% two fcc structures are formed. At higher plutonium concentrations (> 50%), a bcc phase and a fcc phase are formed (Fig. 2.30) [4].

Experimental

The crucial point of this study is the preparation of understoichiometric mixed oxides. This preparation is particularly difficult due to the low reduction rate of the MOX specimens. Experiments were carried out in several furnaces under different reducing atmospheres and at different temperatures up to 1700 °C. Due to the difficulties in sufficiently reducing the MOX fuel material under these conditions, development of a high frequency furnace for very high-temperature applications in a glove box was necessary.

As shown in Fig. 2.31, a double chamber design was used to prevent hydrogen losses. The heating was performed via a Mo-susceptor, within which the sample was placed in a Al_2O_3 crucible. Both, susceptor and sample were supported by a Al_2O_3 ceramic tube, through which the hydrogen gas was passed directly over the sample surface. The design of the induction coil was based on empirical data [5] and previous experience.

Materials

The materials used were MOX fuel pellets with different concentrations of plutonium. The preparation of the MOX fuel pellets was achieved using standard cold pressing and sintering procedures. The O/M ratio was determined from the lattice parameter and thermogravimetry. All MOX fuel pellets were brought to stoichiometric ratio by equilibrating with CO/CO_2 (10:1) mixtures at 850 °C.

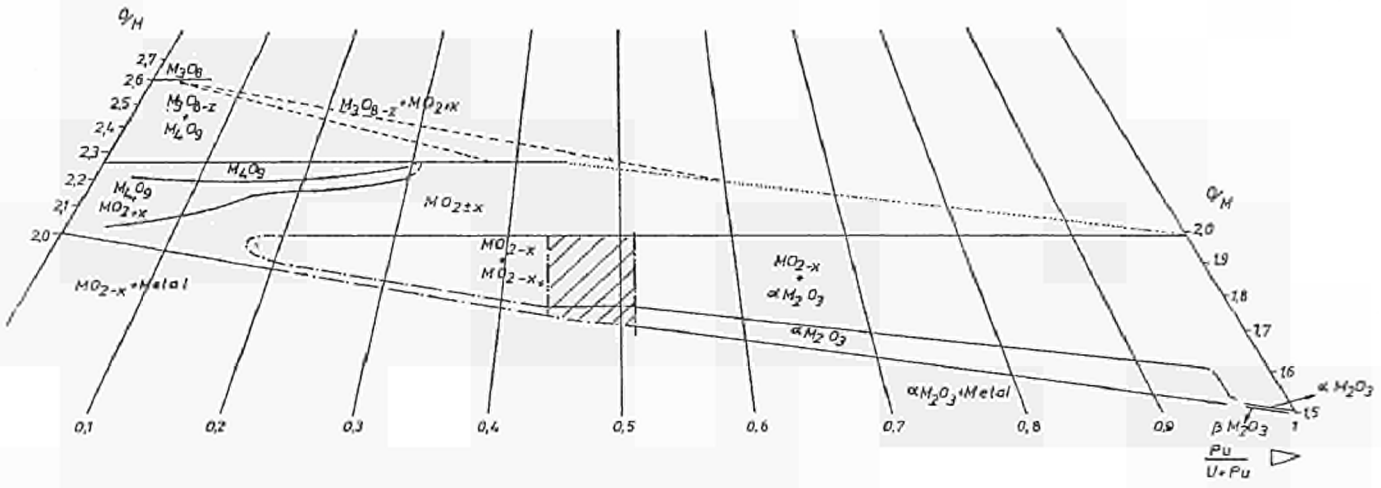

Fig. 2.30 Ternary phase diagram for uranium plutonium oxygen.

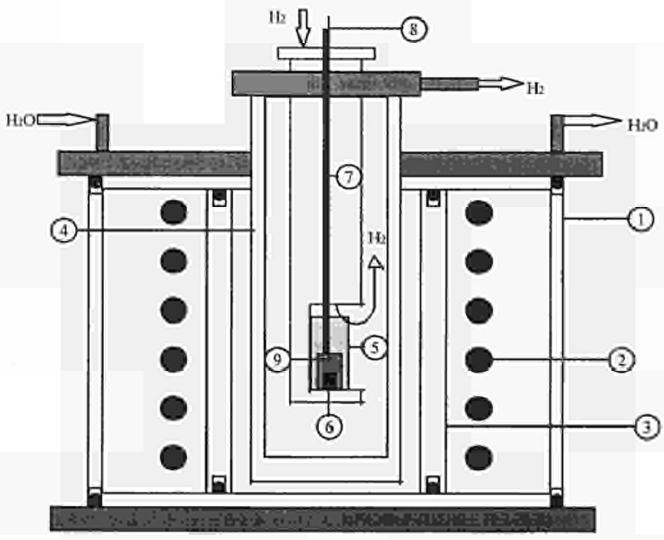

Fig. 2.31 Schematic drawing of the shielded high frequency furnace:
(1) quartz protection chamber;
(2) induction coil;
(3) ceramic chamber (under argon);
(4) ceramic chamber (under hydrogen);
(5) molybdenum susceptor;
(6) MOX fuel sample;
(7) Al_2O_3 capillary;
(8) Tungsten-rhenium thermocouple;
(9) Al_2O_3 crucible.

Work in progress

The first phase of this work was concerned with the development of the experimental equipment and the preparation of stoichiometric mixed oxides with 30, 40 and 50% of plutonium. The next step will involve the production of different understoichiometric-oxygen compositions, and the study of the corresponding phase transformations by different characterization techniques. Optical and scanning electron microscopy (SEM) will be used for microstructural characterization. Thermogravimetry, dilatometry and X-ray diffraction techniques will be employed for structural identification and the determination of phase boundary transitions.

References

[1] I. A. E. A.; Thermodynamic and transport properties of uranium dioxide and related phases; Technical Report Series N° 39 (1965)

[2] E. R. Gardner, T. L Markin and R. S Street; J. Inorg. Nuclear Chem. **27** (1965) 541

[3] T. L Markin and R. S Street; J. Inorg. Nuclear Chem. **29** (1967) 2265

[4] C. Sari, U. Benedict, H. Blank; J. Nucl. Mater. **35** (1970) 267-277

[5] S. Zinn, S. L Semiatin; Elements of induction heating; ASM International. Metal Park Ohio 44073 (1980), ISBN 0-87170-308-4

2.2 Studies of High Temperature Properties of Nuclear Fuels

2.2.1 Advances in laser-flash applications for thermal diffusivity measurements of irradiated nuclear fuel

A project was initiated for the construction of advanced laser-flash devices for the measurement of the thermal diffusivity of highly radioactive materials to be operated in a γ-shielded cell. The design and construction of these apparatus, called LAF-1 and LAF-2 (Laser-Flash 1 & 2), started in 1992, the most pertinent design criteria being the requirement to measure the thermal diffusivity of ceramic nuclear fuels, particularly of UO_2 irradiated in Light-Water Reactors up to high burn-ups.

The technological interest of these measurements is focused on two aspects:

The change of the thermal diffusivity, α, under stationary reactor irradiation conditions caused by uranium fission and formation of fission products, whereby the significance limit of these possible variations is approximately 10% of the original value of α.

Investigation of latent burn-up effects which, though they do not manifest themselves at the reactor operating temperature, could affect heat transport in the fuel during off-normal or accident conditions.

The method of thermal diffusivity measurement

The laser-flash method for the measurement of the thermal diffusivity is conceptually straight forward, and presents advantages with respect to the various methods used in the past. When the front face of a disk-shaped specimen is subjected to a very short burst of radiant energy with an irradiation time of the order of one millisecond, the resulting temperature rise, measured on the rear surface, is used to compute the materials thermal diffusivity with the aid of suitable models. These models are based on mathematical solutions of the heat conduction equation expressed in a form which provides a sufficiently realistic description of the given transient event.

The ideal case is that of the simple one-dimensional adiabatic propagation of a temperature spike of infinitesimal duration applied on the surface of an effectively infinite medium at constant initial temperature. Under these conditions a simple analytical solution enables the diffusivity to be expressed in terms of the sample thickness, l, and of $t_{1/2}$, (the time corresponding to the 50% transient temperature increase), i.e.,

$$\alpha = 0.1388 \frac{l^2}{t_{1/2}}$$

However, in practice, several additional factors affect the temperature transient. The various thermal losses, (radiative and conductive), represent the most significant factors. These losses are mainly influenced by the design of the specimen holder and on the pulse energy spot size relative to the sample size. Other deviations from the ideal case are caused by the finite duration of the laser pulse and by the non-homogeneity of the spatial profile of the pulsed laser beam. An additional source of uncertainty is the presence of optical and electrical noise, and the possible drift of the baseline sample temperature during the shot. Finally, the axial temperature gradient in the sample must also be considered. In some cases the front temperature peak can rise to as much as several hundred degrees. Though this front temperature rise decays quickly due to heat

propagation into the specimen depth, the evaluation of the diffusivity should also take into consideration this additional bulk temperature increase caused by the shot itself.

When the flash method was first applied in the sixties it was soon recognised that even under optimal experimental conditions, correction coefficients were necessary to compensate for the major systematic errors which, in some cases, can be as large as tens of percents of the measured diffusivity value [1, 2, 3]. These models are used in error correction procedures, and their performance and validity limits are well known by experimentalists. In the last three decades a number of papers dealing with methods of improving the systematic error corrections, based on analytical solutions obtained for a two-dimensional model diffusion equation, as well as on various other data evaluation methods have been published [4, 5, 6, 7, 8, 9, 10, 11]. Other approaches have been pursued using numerical, statistically weighted fitting of integrals of the temperature diffusion equation, along with the development of computer programs for comparative studies of the various techniques [12, 13, 14].

Accuracy limits are mostly due to the inadequacy of the analytical application of the temperature diffusion equation to real experimental conditions, and to the uncertainty of parameters used with more complex approaches. In fact, in customary experimental set-ups the recorded data provide the necessary and sufficient conditions for the integration of the temperature diffusion equation only for symmetrical diffusion and distinct conjectural boundary conditions. From the experimental data however it cannot be inferred whether these hypotheses are actually satisfied.

Presently, with a view to ensure higher reliability of measurement and correction procedures, the improvement of the quality of key system components was essential to producing experimental conditions which can be realistically described by analytical models.

Two aspects of the project design were believed to be of particular importance:

1. The first concerns the quality of the laser beam. In a recent article presenting a new laser-flash apparatus [15], an examination of the error sources is made, from the most trivial to the most significant. It is reported that the non-uniform heating effect can contribute up to an 8% deviation in the measured α. In the instrument described in this paper, a high quality laser, mounted with a long fibre optic cable (which has a mixing effect on the spatial pulse energy profile), provides a homogeneous energy deposition on the specimen surface. This ensures the absence of more or less erratic hot spots and consequent formation of irregular thermal gradients. The beneficial effects of this feature have been recently recognised [16], and this point is examined in more detail in the next paragraph.
2. The second improvement regards the temperature peak. The lower this temperature, the weaker are the temperature perturbation effects brought about in the sample front-layer by possible variations of the local, temperature dependent, thermal conductivity. This effect is particularly important in the case of irradiated fuel where high temperature peaks produce a dramatic restructuring. Normally, high input energy levels are imposed by the sample properties and by the required precision of the temperature measurement on the rear surface. With the equipment described it is possible to decrease the input energy to levels which generate a rear-face temperature increase of less than 1 K, and still produce reliable results.

The laser-flash 1 (LAF-1) apparatus

This first system has been tested and characterized, and is now ready for introduction into a standard hot-cell. A second machine, with similar characteristics is being constructed for use in an alpha-glove-box for thermal diffusivity measurements of transuranium element compounds.

As mentioned above, the requirements for experimental investigations of the thermal properties of irradiated fuel are very stringent. Firstly, the measurements must be carried out on sufficiently large samples to represent local evolving features which occur during fuel burn-up. Due to the relatively small size of the nuclear fuel pellets ($\cong$10 mm in diameter) and also due to extensive cracking produced during irradiation, plane parallel samples can only be prepared with sizes and shapes which vary from sample to sample.

Secondly, the measurements must be rapid, precise and statistically significant, in order to detect real variations of α related to the evolution of the irradiation effects.

The design of the first apparatus, called LAF-1, was conceived with these experimental difficulties in mind. The strong γ-activity of the specimens necessitated a design suitable for remote handling.

The equipment is based on conventional HF heating, producing temperatures above 2000 K. The choice of an HF furnace was dictated by the requirement for easy access and maintenance under remote handling conditions. The measurement chamber was constructed as a double-walled water cooled horizontal cylinder with a door opening at one end (Fig. 2.32).

The vessel is pumped down with roughing and turbomolecular pumps, and its atmosphere can be regulated with a gas-inlet system within the range 10^{-4}–10^{-7} torr. The pumping and vacuum valve system is protected against volatile fission product contamination with suitable shields.

Centrally located within the vacuum chamber is the furnace and sample holder assembly. The graphite sample holder itself is positioned inside the HF heating coil, and can be raised and lowered by remote manipulators to allow mounting of the sample. The complete assembly is then positioned by precision DC-motors according to the location in which the sample was laid down by the remote manipulators, thus allowing the operator to select the optimum measurement

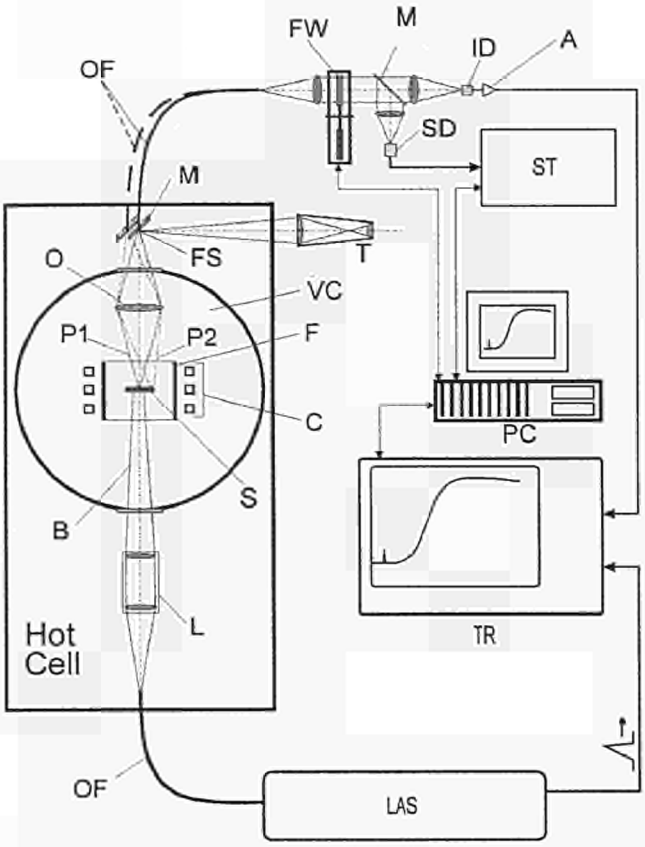

Fig. 2.32 Schematic of the LAF-1 laser flash system.

LAS = probe laser; OF = optical fibre; L = lenses; B = focused laser beam; S = sample; C = HF heating coil; P1, P2 = variable observed surface areas; VC = vacuum vessel aperture; M = movable mirror; T = telescope; FEW = pyrometer optical filters; ID = pyrometer photodiode; A = amplifier; SD = transient pyrometer photodiode, ST = steady-state pyrometer; PC = computer; TR = transient recorder.

point on the sample surface. Measurements can therefore be made at different points across the sample surface with a view to determining the thermal diffusivity profile of the sample. Thermal shields are situated such as to provide protection for the delicate mechanical and optical components.

Two methods of specimen mounting are employed. The first is a conventional three-point mounting, providing good thermal isolation of the sample. This is used for standard calibration tests on prepared samples of a regular circular shape.

The second method incorporates a sapphire disk onto which the sample is laid down. This method is used to overcome the difficulties associated with supporting non circular, arbitrarily shaped, irradiated fuel specimens. The sapphire disk, which is transparent to the Nd-YAG pulse laser beam, can be easily replaced as required or when it becomes damaged or discoloured.

Located above the heating coil and sample holder, is the water-cooled objective lens assembly which enables a 0.5 to 1 mm^2 large spot of the specimen upper surface to be focused onto the signal collecting optical fibre. The lenses are placed in a water-cooled and vertically adjustable housing, which is contained within the measurement chamber. Protection for the lenses from γ-radiation, (which can cause glass darkening), is provided by a tungsten cylinder which is removed only during measurements.

This lens and optical fibre combination form the front end signal collection section of the system pyrometer. The collecting optical fibre then delivers the transient temperature signal to InGaAs and Si photodiode detectors which are located outside the hot-cell.

These detectors were chosen to allow a sufficiently broad measurement temperature range to be covered. The detector diode signals are subsequently amplified using low-noise pre-amplifiers at the point of signal delivery outside the hot-cell. The background temperature, (Planck radiation in the range 600–2500 K), is compensated for by injecting an offset current at the amplifier inputs. A grey filter wheel is located immediately before the diode detectors to further improve and linearize the range of temperature of operation. Because the detectors are placed outside the hot-cell, (the light being transmitted through the optical fibre), they are not subject to radiation damage. The fibre itself, which can easily be plugged in and out, can thus be replaced as required.

The Nd-YAG pulse laser is also placed outside the hot-cell, and the beam is transmitted to a second focusing system via a second optical fibre. This beam enters the measurement chamber from underneath. The beam size can be varied between 2 and 5 mm diameter, without significant changes in the radial power profile, which remains essentially flat over the beam cross section.

After amplification, the detector signals are then digitized with a resolution of 12-bits, and further transmitted over a GPIB interface to a 486DX-PC for data analysis. The software for data storage and screening was written with a fourth generation package, and is operated via a user-friendly WINDOWS-interface.

Numerical signal analysis and quantification

If the laser energy deposition on the sample is homogeneous, we expect that the classical analytical solutions of the temperature diffusion equations are suitable for a direct numerical fitting, using all the parameters which can be reasonably accounted for in a mathematical model, namely radiation losses from the front surface, radiation losses from the rear surface, and radial conduction losses.

Two models have been chosen representing, respectively, laser pulse spots covering the whole sample, and cases where the sample diameter is larger than the laser spot.

For the first case, an integral of the temperature diffusion equation was adopted corresponding to an infinite cylindrical plate of thickness, l, and thermal diffusivity, α, subject to radiation heat losses from the surfaces, and also, to radial heat losses. In the second case it is assumed that the sample is not completely covered

by the pulse laser beam and, furthermore, that the applied pulse is of a higher energy, so that large conductive radial losses have to be accounted for, and the radiative losses on the front surface are expected to be markedly larger than that on the rear surface.

2

This model corresponds to the "microprobe mode" discussed in the next sections. The one-dimensional solution of the problem, (different radiative losses on the two faces of the sample), is available for an infinite solid whose origin plane is heated by an instantaneous homogeneous source [17]. In our case the laser power profile is effectively constant, so that the theoretical temperature integral depends on four or five parameters, depending on the assumed theoretical model. The approach followed is based on the fitting of the experimental temperature measurements T_{exp} (t) with one of the theoretical functions, depending on the case examined, whereby a variable number (<5) of parameters can be considered as free variables in each case.

Actually, only the first two parameters, the diffusivity, α, and the temperature scaling factor are a-priori unknown, whilst the Biot numbers, and the laser spot size can be either estimated in advance, or used as fitting parameters together with the former parameters.

This task requires an efficient searching strategy as well as adequately accurate experimental data. A powerful algorithm is also necessary, since multidimensional non-linear fitting is a delicate operation which must cope with the sometimes counteracting effects of maximum attainable numerical precision and overfitting. The technique employed is a combination of Newton-Raphson, Marquardt and Steepest Descent methods to find the least square of the sum of the functions:

$$f_m = \left[1 - T_{(r=\bar{r},t_m,x)} \Big/ T_{\exp}(t_m)\right]$$

m = 1,.....M = total number of measurements

where t_m are the measurement times, and

$$\vec{x} = \{x_1,x_2,x_3,x_4,(x_5)\} = \{\alpha, T_0, Y_x(Y_1), Y_r(Y_2), (R)\}$$

represents the vector of the above mentioned fitting parameters.

Calculation starts with a reasonable guess of the heat loss parameters, the choice of the number of fitting parameters then being dictated by the quality of the available experimental information, which includes temperature and time measurement precision, number of points, and range of the variables. The suitability of the experimental data to be fitted by the maximum number of parameters x_i, i = 1 ... N, $N \leq 5$, cannot be appraised a-priori, so that one must proceed by evaluating the confidence limits of the results. This analysis is only feasible if the function f in the vicinity of the minimum is approximately linear in $\vec{x}$, i.e. if it is sufficiently regular with respect to continuity and derivability, allowing an expansion into a Taylor's series. In this case the covariance matrix ||b||,

where $b_{rs} = \sum_{i=1}^{m} \frac{\partial T_i}{\partial x_r} \frac{\partial T_i}{\partial x_s}$ can be calculated.

Finally, if the experimental data, can be regarded as the observed values of a normally distributed random variable, the variance of x_i is expressed as:

$$\sigma_i = \sigma' \sqrt{\frac{M}{M-N} \frac{B_{ii}}{B}}$$

where B is the determinant of ||b||, and B_{ii} is the cofactor corresponding to the element b_{ii}, and where

$$\sigma' = \sqrt{\left(\frac{1}{M} \cdot \sum_{m=1}^{M} f_m^2\right)}$$

is the MLSQ fitting error.

There are various aspects of this fitting worth mentioning:

The fitting is aimed at minimising σ' over the full experimental curve, or segments of it, with the least number of free parameters.

Operatively, the minimum attainable value of σ' should not be forced to decrease below some a-priori undefined weighted average of the (random) individual errors of T_{exp}(t), with weights determined by the partial derivatives of the theoretical spline function with respect to the fitting parameters calculated at the corresponding times. This uncertainty entails some equivocal results, since increasing the number of fitting parameters may lead to a decrease of σ', with an apparent, but in fact illusory, precision improvement. This is normally reflected by a possible decrease of one (or more) of the σ_i, but by a conjoined increase of others.

It should be noted that σ_i represents the errors of x_i only in the case where the local residuals are normally distributed; whilst in the presence of systematic deviations these errors may become meaningless. This danger is often faced when high experimental accuracy's of T_{exp}(t) are encountered. In these cases it is advisable to determine the extent and the location of possible systematic errors on the fitted curve. This can be easily done by a variance analysis of different segments of the temperature curve as described by Fischer [18]. For instance, a suitable method is to compare the residuals in the ascending flank of the pulse, in the zone of the maximum, and also in the tail. In cases where the systematic error is larger than the temperature accuracy, the sum of squared residuals must be replaced by $\sigma'_{(systematic)} > \sigma'$.

The problem of overfitting is illustrated in the following example.

A sample, (a UO_2 disk of 12 mm diameter, and 1.5 mm thickness), was submitted to a pulse with a homogeneous laser beam of 5 mm diameter. The radial heat losses were, therefore, expected to be predominant. The experimental temperature curve, shown in Fig. 2.33, was fitted with five free parameters.

The fitting result was good, giving a residual MLSQ deviation of less than 1%. The fitted parameters are reported in the first column of Tab. 2.6. The order in which they appear from the top to the bottom reflects their hierarchical rank as it was recognised by the fitting algorithm. It can be seen that, after α and T_0,

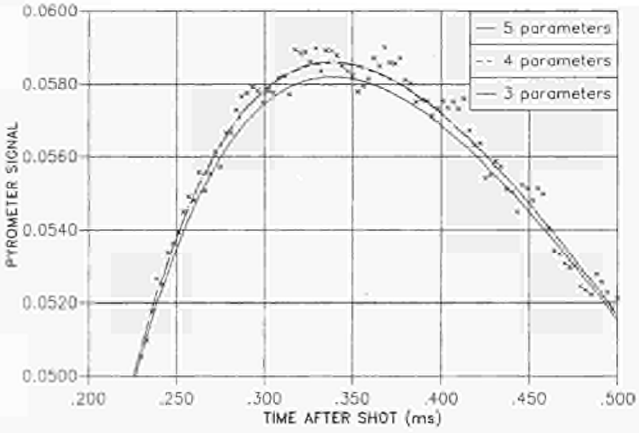

Fig. 2.33 Fitting of a measured temperature pulse with five parameters.

follows the effective laser beam radius R, whose value is very close to the measured one.

A calculation experiment was then carried out. These parameters were used to calculate the ideal curve; this was subsequently perturbed with a random-number generator which was used to apply to the calculated values an error of between 0 and 5% (i.e. with an upper limit more then three times greater than the actual experimental error). The perturbed curve was then re-fitted with, respectively, three, four and five parameters, taken in the same order as in Tab. 2.6, with guessed initial values equal to zero. The results with the respective uncertainties are reported in the other three columns of the table. It can be seen that the fitting precision increases weakly with an increasing number of parameters, indicating a permanent large uncertainty in the Biot numbers $Y_{1,2}$. However, whilst the uncertainties decrease from three to four-parameter fitting, a further attempt at improving the results by using five free parameters fails, resulting in a better fitting, but also in a larger uncertainty in two parameters of high rank. The improvement of the Y_1 precision and the evaluation of Y_2 cannot be seen as a compensation, since the radiation losses described by these parameters evidently play a minor role compared to the much larger radial losses, and the data accuracy allows here only a very approximate evaluation of the Biot numbers. This finally suggests that for this experiment the four-parameter fitting would provide the best results, and this is indeed confirmed by the fact that the values obtained are closest to the "true" ones.

Instrument characterization

POCO-AMX 5Q graphite, (a well investigated and documented material), and as-fabricated 95% theoretical density UO_2 sintered pellets have been used. Various different sample sizes, (which varied in both diameter and thickness), were used for the measurements. Laser-pulse parameters were also widely varied. Fig. 2.34 shows the measured thermal diffusivity of POCO-graphite compared with previously published data. The results agree to within better than 5%, which is within the average error of the reference values.

Uranium dioxide, though being also one of the most studied compounds, presents a more complex thermal diffusivity behaviour, especially at low and moderately high temperatures, where the oxide stoichiometry and impurity concentration markedly affect thermal diffusivity (which is maximum in the pure stoichiometric compound).

Measurements were carried out on the same sample with two different holders, the first is constructed using the three point mount, and the second using the sapphire plate, (0.5 mm thickness), supported in the graphite sample holder, the sample being laid down in approximately the centre of the sapphire disk.

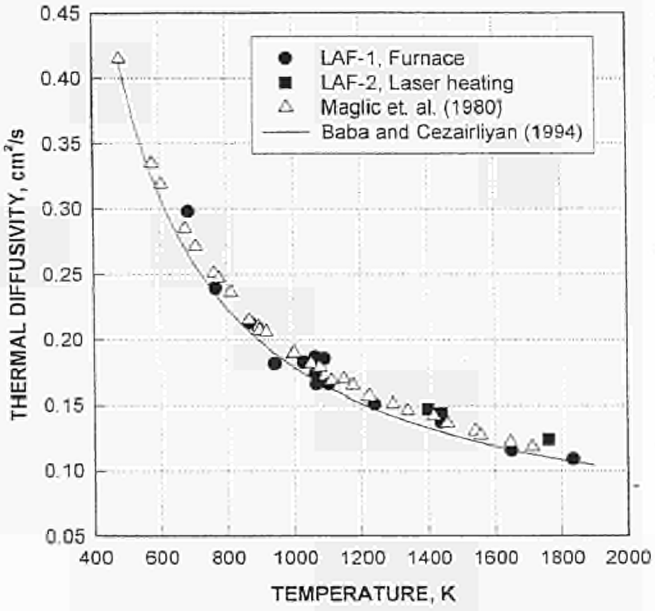

Fig. 2.34 Thermal diffusivity of POCO 5Q AMX graphite measurements compared with literature data.

		3-Parameter Fitting prec. 2.98%		4-Parameter Fitting prec. 2.97%		5-Parameter Fitting prec. 2.96%	
	true values	values	±%	values	±%	values	±%
Th.diff. x100	1.500	1.544	3.668	1.521	2.396	1.551	2.479
To(K)	3.420	3.322	2.592	3.260	1.748	3.197	1.417
R	0.250	0.252	5.620	0.250	5.160	0.259	5.516
Y1	0.010	0.000	*****	0.018	*****	0.013	40.000
Y2	0.010	0.000	*****	0.000	*****	0.131	*****

Tab. 2.6 Fitted parameters from the data plotted in Fig. 2.33. The asterisks denote an uncertainty of more than 100%. The non-fitted parameters are taken equal zero.

It was demonstrated that the measured value of the thermal diffusivity is not affected by the presence of the sapphire support. Fig. 2.35a shows a set of measurements of UO_2 with the two holders, in the temperature range 580 K–1100 K. Fig. 2.35b shows the measured standard deviations versus temperature; the error increase at lower temperatures is typical for $UO_{2.00}$, since the thermal diffusivity at low temperature is markedly affected even by very small changes in structure and composition, so that from 1200 down to 500 K the thermal diffusivity accuracy decreases in our case by a factor of two, as a consequence of heterogeneities in the fabricated (5.3 mm diameter) pellet.

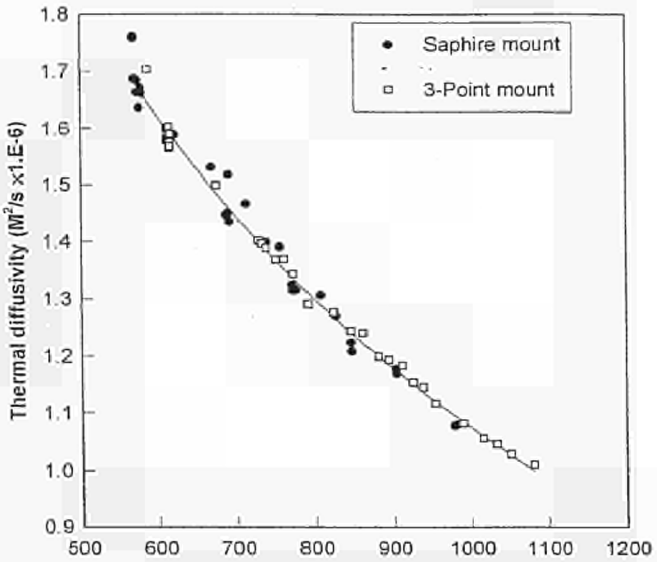

Fig. 2.35a Comparison of thermal diffusivity measurements of as-fabricated (95% theoretical density) sintered uranium dioxide, using both sapphire and 3-point mounts.

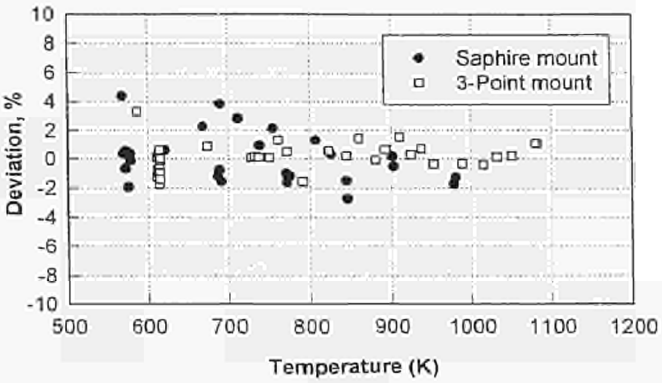

Fig. 2.35b Local errors for the thermal diffusivity measurements plotted in Fig. 2.34.

The effect of the laser pulse energy was also studied. Fig. 2.36 shows the variation of the measured diffusivities at constant temperature and for different energies. In the explored range the apparent diffusivity decreases monotonically with the input energy. The effect is due to a change in the state of the sample produced by the laser pulse. As mentioned in the preceding section, increasing the input energy increases the effective bulk sample temperature, producing an apparent decrease in α. For this reason, the pulse height is normally kept as low as allowed by the signal-to-noise ratio of the measured signal.

Further device characterization tests deal with the effect of the position of the measured rear-surface area with respect to the pulse laser beam centerline (see scheme of Fig. 2.37). Here, the pulse laser beam was aligned and centred on the axis of the sample, which was mounted on the sapphire support (Fig. 2.37, case a). On the rear surface a 1 mm-large circular zone was measured by the pyrometer.

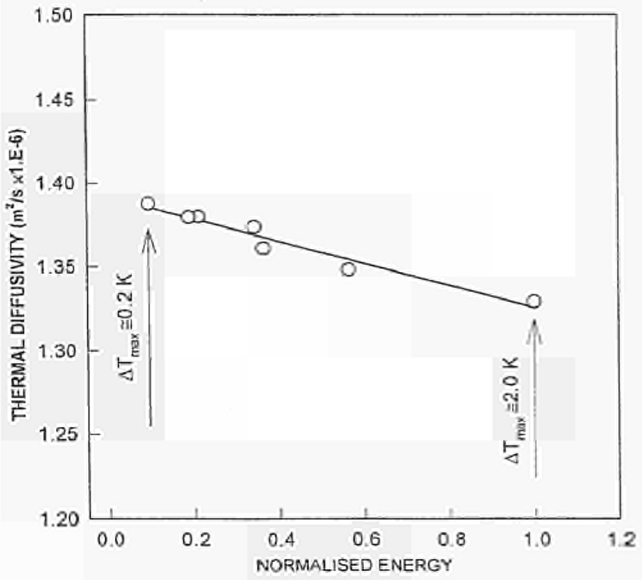

Fig. 2.36 Change of the apparent thermal diffusivity in UO_2 due to a tenfold increase in the laser-probe energy. The lowest applied energy corresponds to the sensitivity limit of the transient pyrometer.

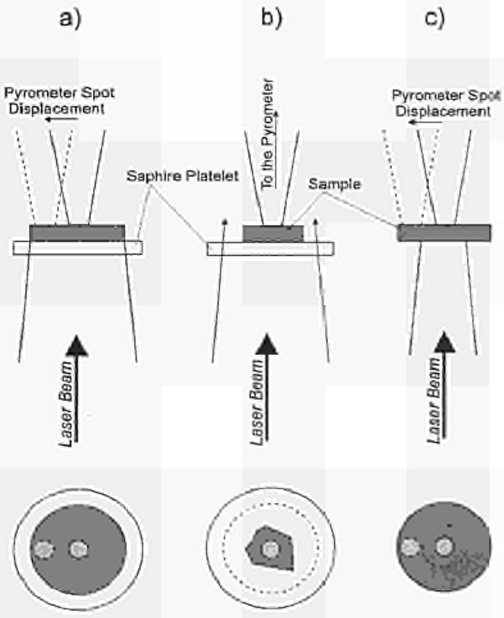

Fig. 2.37 Physical arrangements of laser beam/sample/pyrometer spot. Case a) is the normal measurement regime, and the least sensitive to beam heterogeneities, however, also arrangements b) and c) produced acceptable results, with errors below 5%.

A sequence of shots, (of varying energies), were then applied, and for each shot the pyrometer signal collection fibre optic assembly at the top of the instrument was moved on its x-y mounting, so that the rear-face temperature signal was measured at different radial positions with respect to the pulse laser beam, (and sample), central axis. Fig. 2.38 shows the results of one of these experiments on POCO graphite.

At the top of the figure the fractional rear-temperature peaks, (normalized), are plotted for different radial positions. It can be seen that the measured thermal diffusivities (plotted at the bottom as fractions of the value measured in the centre of the disk) are effectively independent (within $\cong$ 3%) of the radial position of the measured area.

Similar tests were repeated under pronounced symmetrical radial heat loss conditions (Fig. 2.37, case c). A disk of the same material, of 5 mm diameter was pulsed with a laser beam covering only a central circular area of 3 mm diameter of the specimen. Despite the presence of a strong radial heat flow, the diffusivity measurements resulted in an accuracy of better than 5% (Fig. 2.39), even in off-centre positions up to a 0.5 mm distance from the pulse beam contour, (although the rear temperature rise at external radial positions was about four times lower than in the centre).

Further tests were carried out to get a measure as to what accuracy the thermal diffusivity can be determined at local points on a sample where the diffusivity varies across the specimen. To simulate this effect, a graphite specimen of approximately 2.5 mm thickness was taken and machined over half its surface area to reduce the thickness by 200 µm. As the half-time, $t_{1/2}$, is directly proportional to the square of the thickness, its measured value should also exhibit this dependence. Fig. 2.40 shows the results of the test, by plotting the "apparent" diffusivity for 11 positions across the sample diameter. The measurement spot was in this case only 200 µm in diameter. As can be seen, the results reflect the correct apparent diffusivity change to within approximately 5%, and although this sample is not an ideal model of an heterogeneous sample, the experiment indicates the possibility of mapping the thermal diffusivity across a real heterogeneous sample, and also gives an indication of the quality of the data analysis procedure.

The same type of measurements have been performed on non-circular UO_2 samples, with the laser beam entirely covering their surface. In some cases the samples were obtained by breaking previously measured disks and repeating the experiments on fragments as small as 2 mm across. The measurement accuracy was again found to be within satisfactory limits.

When measuring the thermal diffusivity of irradiated fuel samples, it is important not to keep the specimen at high temperatures for too long a period as significant restructuring of the material can lead to incorrect diffusivity results. On the other hand it takes time for the temperature of the furnace assembly to stabilize at the measurement temperature of interest. In order to overcome this difficulty, the baseline temperature is

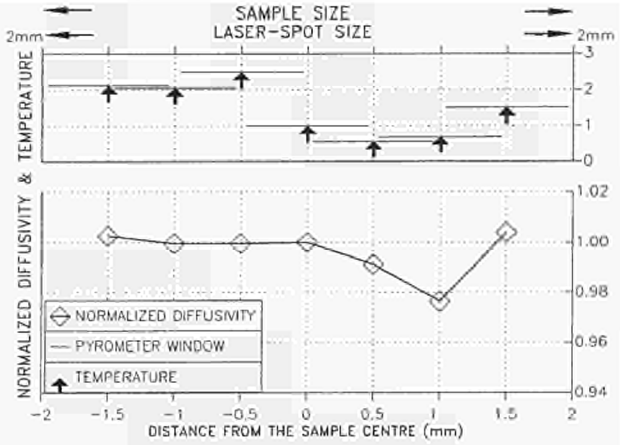

Fig. 2.38 Radial thermal diffusivity measurements at 773 K across the sample (POCO 5Q AMX graphite). The arrows represent the level of the rear-face temperature rise and the horizontal bars the width of the pyrometer window. The laser spot covered entirely the sample surface. The deviation of the measured diffusivity is less than 3%.

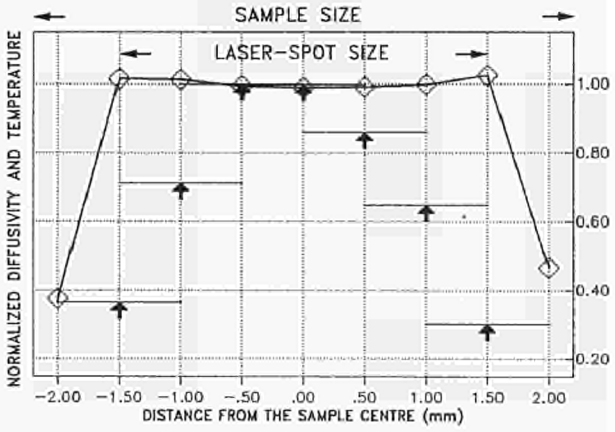

Fig. 2.39 The same as in Fig. 2.38, but with the arrangement c). The sample is here a UO_2 specimen.

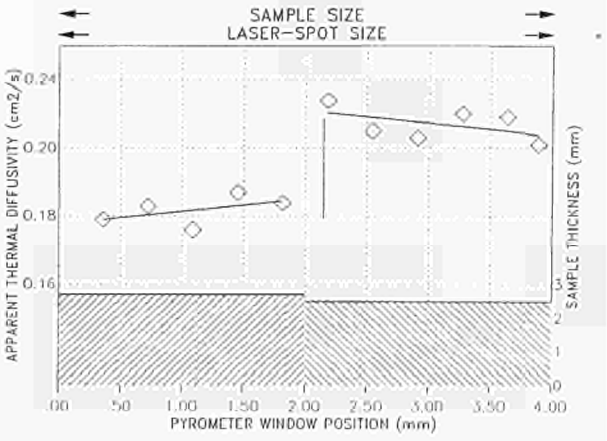

Fig. 2.40 Local diffusivity measurements simulating a heterogeneous material. The sample has here two different thicknesses, sketched at the bottom, which produce two different apparent diffusivities. The vertical bar indicates the expected change. Using a pyrometer field stop aperture of 200 µm enabled a better resolution of the spatial measurements than in the case of Fig. 2.38.

measured immediately before the shot, interpolated, and then used to compensate the measured signal for this temperature drift.

Fig. 2.41 shows an example of a measurement where the sample temperature is purposely made to increase at a rate of approximately 10 K/s during the measurement period. This method of drift compensation proved to be satisfactory, enabling an acceptably short time window of measurement for irradiated fuels.

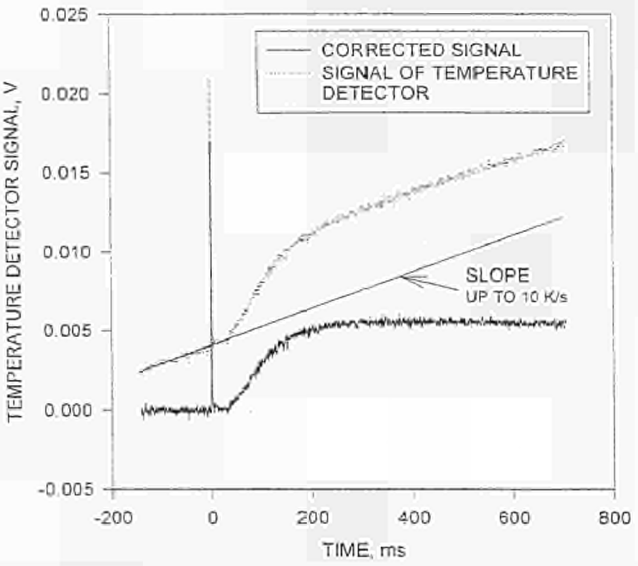

Fig. 2.41 Measured temperature transient under non-stationary temperature conditions. The linearly increasing baseline temperature is extrapolated and subtracted from the raw data.

Finally, the performance of the instrument satisfies the criteria required for the investigation of the thermal conductivity of irradiated fuel, since:

a) Measurements can be carried out delivering relatively low laser pulse energies on the samples front surface thus avoiding a bulk temperature increase of the sample during the shot.

b) The problem of having only irregularly shaped samples of varying dimensions from spent nuclear fuel pins for measurement has been fully investigated with the results proving to be accurate and reliable.

c) Diffusivity measurements can be made locally over the whole sample. This is an important feature, as the thermal diffusivity often varies radially outwards from the centre of the fuel pin towards the peripheral regions.

d) The measurement accuracy, (3%), is below the threshold of relevance for thermal diffusivity variations occurring, or expected to occur, during reactor irradiation.

e) The requirement to hold the sample at the measurement temperature for only short periods of time has been investigated and solved using a compensation technique already described.

f) The use of fibre optic cables along with carefully designed protected and replaceable optical and mechanical components has resulted in the production of an instrument suitable for installation and continued operation in a radiation hot-cell.

Further progress in design and set-up of the LAF-2

Further work is being carried out to produce the equipment which can operate at higher temperatures, i.e., up to 3000 K and higher. This work is being carried out in parallel with the development of the LAF-1 instrument described above.

These devices are built using small cylindrical metallic vessels, (130 mm x 130 mm), incorporating quartz windows at either end. The vessel is provided with a single gas inlet/outlet connection which allows the environment within the chamber to be regulated to various buffer gas pressures and mixtures. This feature is important in the investigation of the effects of stochiometric changes in the materials which inevitably result in changes of the materials thermodynamic properties.

The sample is supported centrally inside the chamber by a three pin refractory ceramic mounting. Heating of the sample is achieved by directing the continuous wave (CW) laser energy on the sample from both sides simultaneously, as can be seen in the prototype set of Figs. 2.42a and b. The two laser heating beams are produced by splitting a Nd-YAG continuous wave laser beam, and delivering the energy via a fibre optic cable and lens system. The proportion of the intensities of the beams can also be varied. A third beam from a Nd-YAG pulsed laser impinges the specimen front face. Two high speed pyrometers simultaneously measure the temperature on both faces of the specimen disk.

As with the instrument described in the preceding section, great care was taken in producing very homogeneous laser beams. Stationary temperature conditions in the sample can be reached very rapidly, the only limiting factor being the thermal shock resistance of the sample. The temperature in the sample is almost uniform, except for the three small contact regions around the supporting pins, where the temperature is lower.

Thermal diffusivity measurements are then performed in a similar manner as described for the LAF-1 machine above. The peak temperature produced on the front surface heated by the pulsed laser is also measured.

Among the various requirements, relating to the measurement of irradiated samples, were the ability to characterize specimens of irregular shape and size, to make these measurements in a sufficiently short experimental time frame and to maintain good experimental accuracy while keeping pulse laser energies at low levels.

Along with these requirements, the apparatus has been built to specifications peculiar to operation in radioactive environments, necessitating remote preparation and handling of samples, remote specimen heating and laser pulse excitation, coupled with the requirement to remotely collect the resulting optical signal.

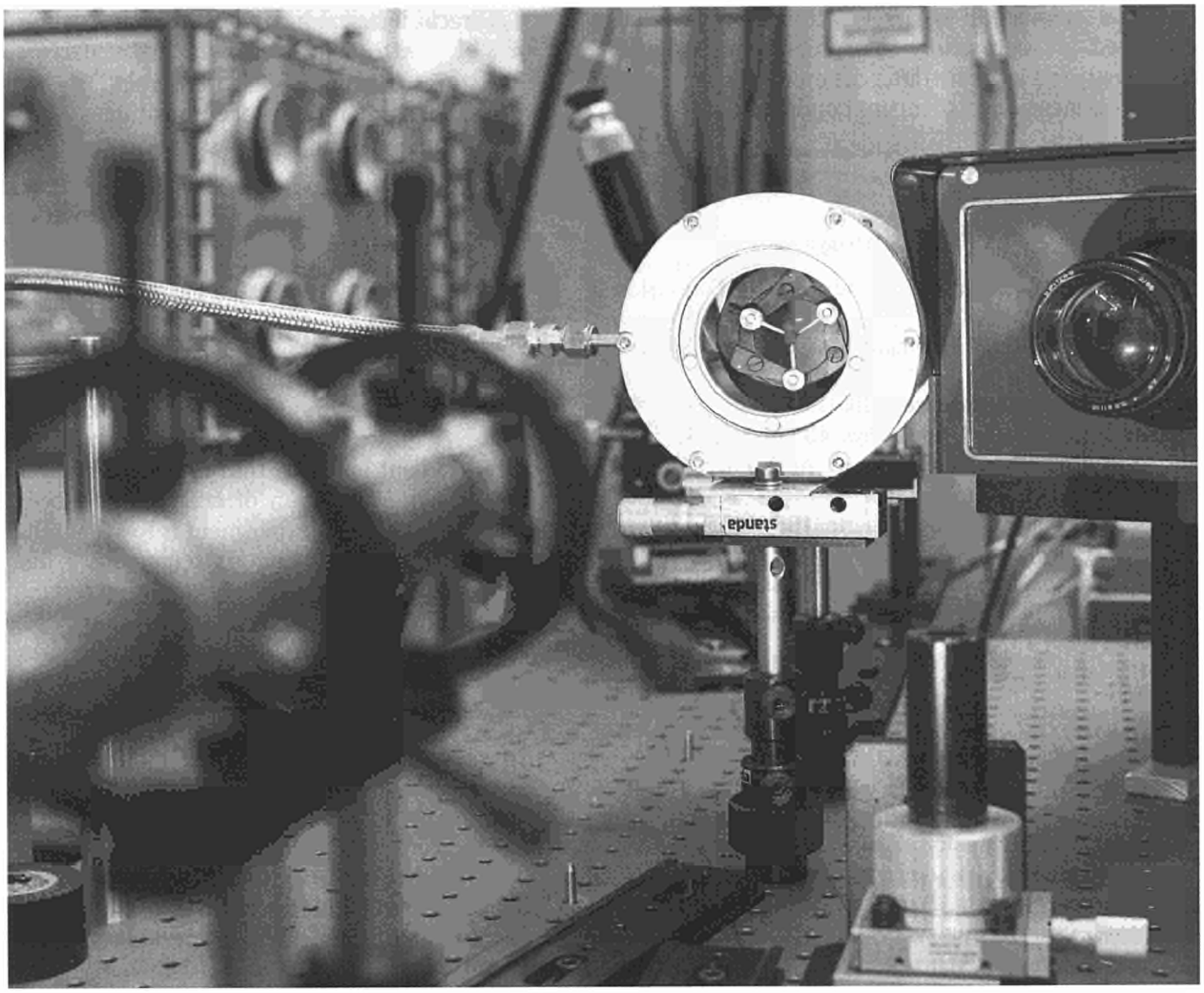

Fig. 2.42a Picture of the sample chamber with three-pin sample mount and two-face laser heating. One of the two laser heads can be seen in the immediate foreground to the left.

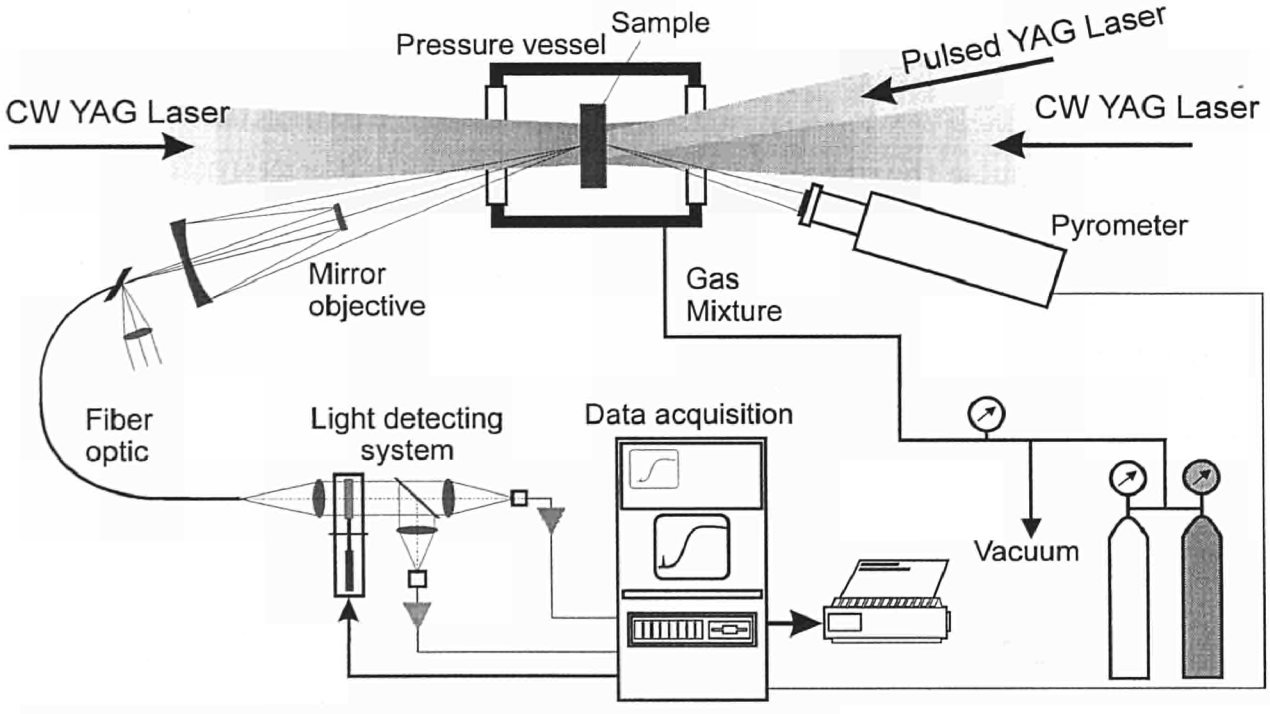

Fig. 2.42b Schematic layout of the experimental set-up of Fig. 2.42a.

Powerful numerical analysis techniques have been employed to successfully interpret the experimental data measured in many different modes as imposed by the above mentioned stringent conditions.

2

References

[1] W. J. Parker, R. J. Jenkins, Adv. Energy Conversion **2** (1962) 87
[2] J. A. Cape, G. W., Lehman, J. Appl. Phys. **34** (1963) 1909
[3] R. D. Cowan, J. Appl. Phys. **34** (1963) 926
[4] A. B. Donaldson, J. Appl. Phys. **43** (1975) 4226
[5] A. B. Donaldson, R. E. Taylor J. Appl. Phys. **45** (1975) 4584
[6] A. Degiovanni, Rev. Gen. Therm. **185** (1977) 420
[7] D. L. Balageas, Rev. Phys. Appl. **17** (1982) 227
[8] A. Degiovanni, High Temp.-High Press. **17** (1985) 683
[9] F. I. Chu, R. E Taylor, A. B. Donaldson, J. Appl. Phys. **51** (1980) 1
[10] H. Bauer, L. Dusza, B. Schulz, Interceram **41** (1992) 489
[11] L. Vozar, J. Gembarovic, V. Majernik High Temp.-High Press. **25** (1993) 593
[12] L. M. Clark, R. E. Taylor, J. Appl. Phys. **46** (1975) 714
[13] J. Gambarovic, R. E. Taylor J. Appl. Phys. **65** (1994) 3535
[14] F. I. Chu, R. E. Taylor, A. B. Donaldson, Proceedings Of The 7th Conference On Thermophysical Properties (Asme New York 1977), pp 148-154
[15] A. Cezairliyan, T. Baba, R. Taylor, Int. J. Thermophys. **15** (1994) 317
[16] T. Baba, M. Kobayashi, A. Ono, J. H. Hong, M. M. Sulyianti Thermochim. Acta **218** (1993) 329
[17] H. S. Carlslaw, J. C. Jaeger "Conduction of Heat in Solids", Chap. XIV, Sect. 14.3, Clarendon Press, Oxford (1971)
[18] R. A. Fisher "Statistical Methods for Research Workers", Oliver & Boyd Publ. Edinburgh (1950)

2.2.2 Double pulse thermoanalysis technique for the study of high temperature transitions of actinide oxides

Introduction

The scope of this work is the development of methods and corresponding equipment for the study of high temperature phase transitions in non stoichiometric uranium dioxide and other actinide oxides.

The general behaviour of refractory materials under different environmental and temperature conditions is also studied.

A number of problems have to be solved in order to perform accurate measurements of high temperature phase transitions in oxide ceramics due to various limitations, namely:

- Direct electrical heating of the materials is not possible due to their low conductivity.
- Saturated vapour pressure is relatively high at the temperature of the phase transitions.
- The materials under investigation are prone to thermal shock damage.
- There is a lack of well established methods for the monitoring of phase transitions under non homogeneous heating conditions.
- Finally, all operations must be carried out under the protection of α/γ-shielded glove boxes.

The use of laser heating for the study of the melting points of refractory materials is well known [1, 2]. However, pulse laser heating creates a high temperature gradient across a thin molten surface layer, and leads to the formation of cracks. Therefore, a major problem of such an experiment is to satisfy the requirement for an homogeneous temperature distribution across this surface layer of molten material, in which both solid and liquid phase transitions coexist. The application of CW (continuous wave) laser heating alone however is problematic, due to the high vaporization and chemical decomposition rates produced.

To reduce these effects to a minimum, three laser beams are employed. Two beams deliver CW laser heating energy to either side of the sample raising the temperature to a point just below melting. The third laser beam, from a pulsed laser, is then fired which launches a thin surface layer of the materials surface into a molten state for a short period of 20 milliseconds or so.

Following the melting shot, this molten layer then cools and solidifies, while the dual beam CW laser heating is maintained.

This procedure, along with minimizing the detrimental effects mentioned above, also reduces axial temperature gradients and leads to a long and stable temperature arrest plateau.

Hence, a regime of operation is created, that allows the measurement and analysis of the dynamic thermophysical behaviour of materials under investigation.

The apparatus used for these experiments is an adapted version of the existing continuous wave laser sample heating apparatus. This apparatus was developed at ITU for the laser flash measurement of thermal diffusivity.

Among the materials used for experimental analysis was a disk shaped uranium oxide sample, of 0.75 mm thickness and 5.5 mm diameter, mounted in a three pin, zirconia support. Each of the three laser beams were then focused to a diameter of 5 mm on the sample surface, and their heating energy distribution was monitored with a CCD camera, triggered such as to allow analysis of the individual video field line profiles. Preliminary melting experiments were conducted by heating the UO_2 up to a temperature of approximately 2800 K, in buffer gas environments of Ne and Ar +2% H_2 at pressures of 2-3 bar. The third pulse laser was then applied to lift the surface into a molten state. The temperature of the molten surface was measured using a high speed monochromatic optical pyrometer, calibra-

ted against a standard tungsten lamp, and true temperatures were determined using published values of UO_2 spectral emissivity in the vicinity of the melting point.

The thermal arrest curves obtained from these experiments are shown in Fig. 2.43. Long and stable cooling plateaux were only achieved when the pre-melting temperature was carefully maintained just below melting, before application of the final pulse laser shot.

Curve No. 6 (Fig. 2.43) exhibits a well formed, long cooling plateau of over 125 milliseconds, at a temperature of 3162 ± 1 K, which can be considered to be the congruent melting temperature of this sample. It is worth noting that the maximum and minimum deviation from the average plateau temperature did not exceed 2K.

Attempts were made to improve thermal arrest plateaux by changing the materials stoichiometry using the buffer gases mentioned. It was found however that better plateaux occurred after the second and third shots, due to the prior melting of earlier shots bringing the surface layer closer to 100% density.

On the ascending part of the curve, as melting begins, a "knee-point" was observed. Although a consistent correlation existed between this knee-point temperature and the cooling plateau temperature, the temperature interval over which the knee occurred was considered too large, for determination of the melting temperature.

Post-experimental examinations of specimens were carried out using both optical and SEM (scanning electron microscopy) techniques. It was found that the typical thickness of the molten zone was in the order of 0.1 mm, with a diameter of about 4 mm. The molten profile observed was indicative of a reasonably isometric temperature distribution, and as the area actually measured by the pyrometer was only 0.5 mm in diameter, any small thermal gradients can be safely assumed to be insignificant. SEM micrographs of the molten surface, and break-through of the molten surface, are shown in Fig. 2.44a and b.

On the basis of the foregoing results it can be concluded that:

- The method of thermoanalysis described here is suitable for the determination of melting points (or the study melting behaviour in general) of high melting point ceramics.
- Special attention must be paid to crack formation and vaporization of the samples rear surface. (Laser vaporization non-homogeneous materials is important as this results in "channel vaporization" leading to axial temperature gradients across the pellet.)
- The density of the materials was found to play a significant role in the production of good solidification plateaux.
- The temperature knee point is correlated to both solidification plateaux, and undercooling swings, with some consistency.

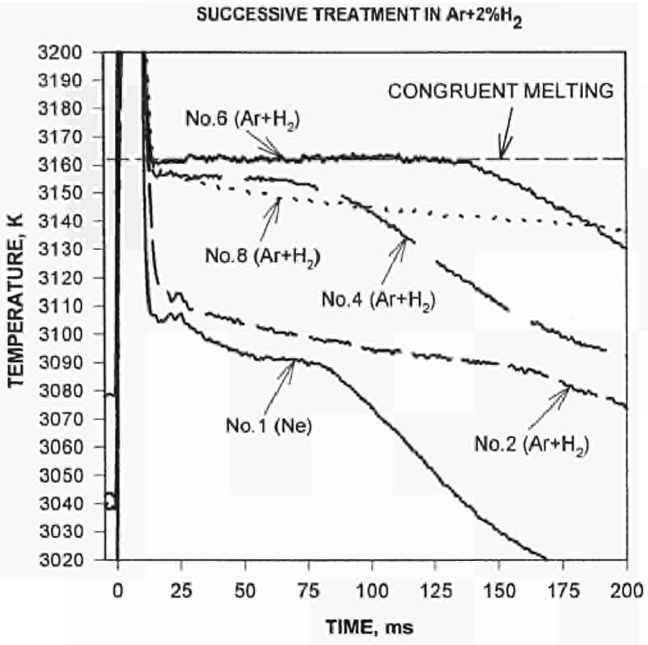

Fig. 2.43 Melting thermal arrest curves of UO_2.

References

[1] C. Ronchi et al., Nucl. Sci. Eng. **113** (1993) 1-19

[2] V. L. Vinogradov, A. V. Konstanovski, A. V. Kirillin, High Temp. - High Pressures **23** (1991) 685-688

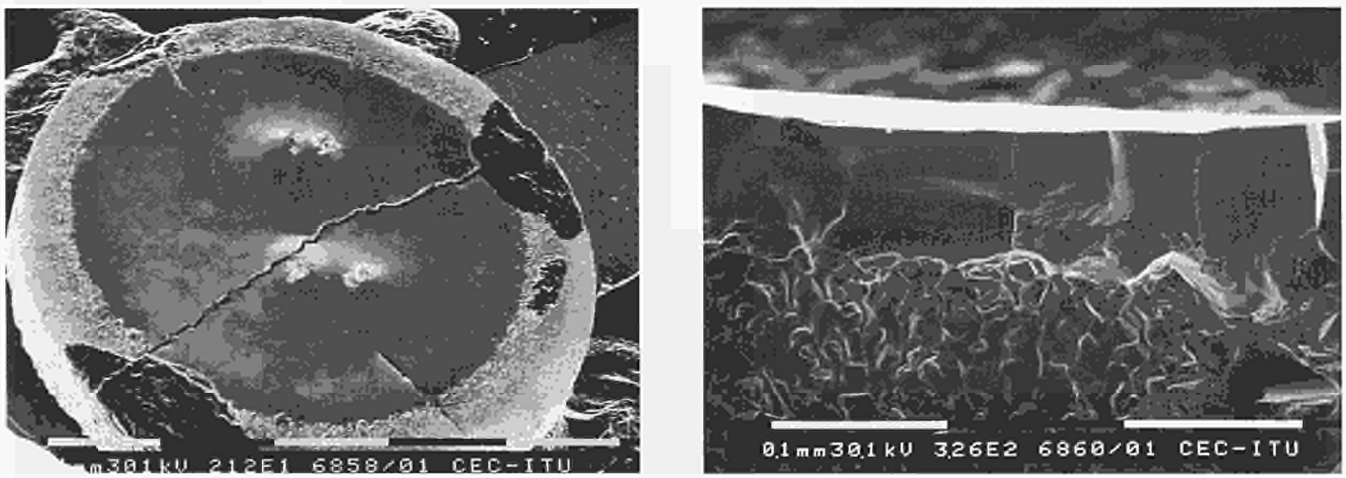

Fig. 2.44 a) Uranium dioxide specimen after laser heating, b) axial section showing the molten layer thickness.

2.2.3 Heat capacity measurements of irradiated fuel using the laser-flash 1 (LAF-1) apparatus

2

Introduction

The heat capacity of irradiated fuel, C_p, is needed to obtain the thermal conductivity value from measured thermal diffusivity. There are several methods of measuring heat capacity but they cause problems for the measurement of irradiated fuel samples.

By definition, heat capacity is defined as, $C_p = \partial H/\partial T$, where H is the enthalpy, and T the temperature. Instead of the usual calorimetric method of measuring the H(T) function, and subsequent differentiating, (which can lead to uncertain errors), the proposed method is based on the direct measurement of the mean C_p in a very small temperature interval. To implement this technique, the laser-flash apparatus for thermal diffusivity measurements has been utilised. In the laser-flash apparatus, a very short energy pulse is deposited into the specimen which causes a bulk temperature increase of several K. Therefore, when the absorbed heat, Q, and the specimen temperature increase, ΔT, are known, heat capacity can be calculated as:

$$C_p = Q/\Delta T$$

Use of LAF-1 for heat capacity measurements

In order to make use of the already existing laser-flash apparatus, LAF-1, for these measurements, a number of technical problems must first be solved. Measurement of ΔT is clearly possible after absolute calibration of the pyrometric system. Absorbed heat is more difficult to determine for several reasons. First, a certain absorption coefficient must be introduced which may be done with the assumption, that its value is equal for both, irradiated and "fresh fuels". Second, possible heat losses during the pulse must also be taken into account. Finally, since the deposited energy can only be calculated from the laser energy pulse, the problem is further complicated in cases where the size of the irradiated fuel sample is less than the diameter of the laser beam. Here, the portion of the laser energy which is not trapped by the specimen must also be measured in order to deduce the value of the absorbed energy.

The method can be simplified by using a reference fresh fuel sample. In this case there is no need for the absolute calibration of the pyrometer or laser energy, provided of course, that the irradiated fuel specimen is large enough to absorb the total energy. However, the reference sample method is still useful even when the probe sample is small. Heat capacity can then be derived according to the following equation:

$$C_p^s = C_p^r \left(\frac{M_r}{M_s}\right) \left(\frac{\rho T_r}{\rho T_s}\right) \left(1 - \frac{E_{sc}}{E_{las}}\right) \quad (1)$$

where:

C_p^s = specimen heat capacity,
C_p^r = reference sample heat capacity,
M_s = mass of the specimen,
M_r = mass of the reference sample,
ρ = density,
E_{las} = total laser energy,
E_{sc} = residual laser energy which has not been absorbed by the specimen,
T_v = specimen temperature increase,
T_r = reference sample temperature increase.

However, a heat loss correction must be introduced in Eq. (1). This can be performed by mathematically fitting the temperature curve, taking C_p as an additional fitting parameter.

The measurement procedure entails the temperature increase measurement of both the sample and of the reference, for a given energy E_{las}. E_{sc} is then measured by a precision calorimeter, which is placed on top of the vessel.

In order to measure E_{las} a special detector and an integrating amplifier have been constructed. The output of the detector was calibrated using a precision, volume absorbing, calorimeter. During calibration, the pyrometer optics were removed and the calorimeter was installed on the top of the vessel. The calibration of the detection system is performed over a wide energy range (0-3 J), using different pulse lengths, (1, 1.5 and 2 ms.). The calibration showed very good detector/amplifier linearity over the required range, and did not show any particular dependence on the laser pulse length.

To permit precise measurements of the absolute value of the temperature increase, the InGaAs pyrometer was first calibrated. A grey filter wheel with carefully selected absorbance values, was placed in front of the detectors in order to enable coverage of a wide temperature range, while still maintaining sufficient sensitivity. Each filter covers a temperature range of approximately 70 K which corresponds to a signal output swing of about 2 V. In this region, the detector/amplifier linearity is within the required experimental accuracy.

A uranium oxide specimen was taken for C_p measurements at a temperature of approximately 1000 K using the direct method. These tests were important as they rely on an accurate absolute calibration of both energy absorption, and temperature increase measurements, (which is not the case using the reference method). The laser energies applied were in the range of 50 mJ, resulting in a bulk temperature rise of less than 2 K. A non-linear curve fitting procedure was then applied to evaluate C_p from the resulting data, and was in agreement to within 15% of previously published values.

Clearly, greater precision can be expected from improved calibration, and, with the reference method, further gains in accuracy can be achieved.

2.2.4 Fission product source term measurements from high burn-up LWR fuel

Samples and experimental set up

The investigation of the vaporization and the release of fission products and actinides from high-burnup irradiated LWR fuel described in TUAR-93, p. 40 was continued.

A KWU fuel (10B2 segment 6) was chosen for comparison with the BR3 fuel used for the PHEBUS experiments, which was the object of a set of effusion measurements, whose results have been published in TUAR-94, p. 75.

The sample was taken from a fuel rod (UO_2) with an initial enrichment of 3.8% ^{235}U. The burn-up was approximately 60 GWd/t and the cooling time 4.5 years. The samples were in the form of spontaneously detached pellet fragments of sub-millimetre sizes, which were originally located in the peripheral pellet annulus.

The effusion tests were performed in a tungsten Knudsen-cell, clad on the inner side with thoria, and heated by resistance coil. The vaporizing molecular beam was measured by mass spectrometry.

The sample temperature was step-wise increased up to 2500 K in a time interval of approximately 4 hours. The spectrometer (Balzers Q500 quadrupole) was operated with pre-fixed window mode, in order to maximize the detection sensitivity for the selected masses. Two β-γ-counters placed in the vacuum pump pipeline provided measurements of the flow rate and of the released amount of ^{85}Kr.

Results obtained

Rare gases

The release of rare gases reveals four distinct stages, against the three stages observed in the lower burnup fuel of BR3 (TUAR-94, p. 75). The differences can be summarized as follows:

The high burnup fuel exhibits a net release stage (IA), corresponding to a few percents of the inventory, already at temperatures as low as 1200 K. This release is abrupt and non interpretable in terms of diffusion mechanisms (Fig. 2.45, 2.46). The features of the second stage (IB) are similar to those of stage I in the low burnup fuel. The release was analysed in terms of the de-convolution function

$$Z(1/T) = \ln\left(\frac{d}{dt}(-\ln(L - F))\right) \simeq -\frac{\Delta H}{RT} + \ln(D_0(k_{sc}^2 + k_{sg}^2)) \quad (1)$$

where F is the fractional release, and the indexed k represents the sink strengths of bubbles and grain boundaries, respectively indicated with the subscripts sc. and sg. Eq. (1) provides the means for deducing the parameters D_0 and ΔH, which define the diffusion coefficients which rule the various examined stages. L represents the asymptotic limit of release for the analysed stage.

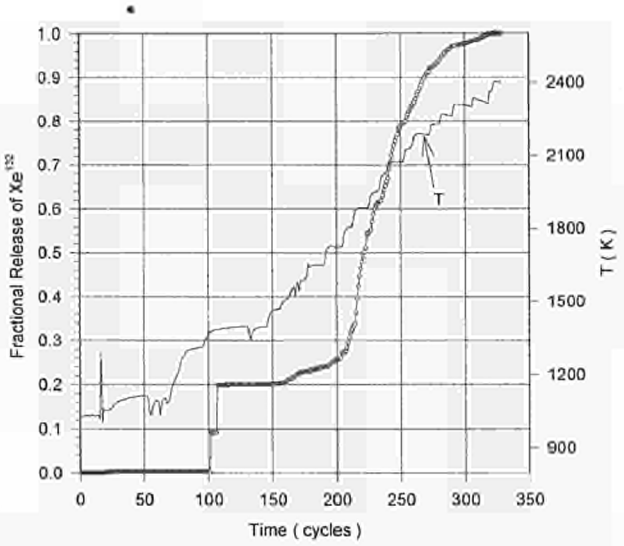

Fig. 2.45 Fractional release of ^{132}Xe and corresponding temperature as function of time (1 cycle corresponds to 26 s).

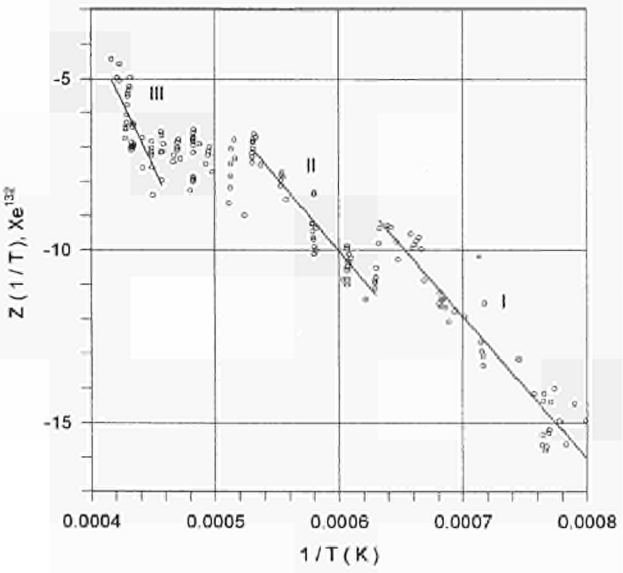

Fig. 2.46 Arrhenius plot of the de-convolution function Z(1/T) of ^{132}Xe.

Different to the low burnup case, where stage I was characterized by a low diffusion enthalpy, the high burnup fuel, stage IB has effectively the same ΔH as stage II (90±5 kcal/mole). This implies that:

- the gas previously collected at the grain boundaries, after release at lower temperatures (stage IA) created a completely open porosity network;
- in the following stage (IB) the gas diffusing from the interior of the grains was immediately released by fluid percolation, without intermediate grain-boundary diffusion processes.

The passage from stage I and II is simply characterized by a decrease of the logarithmic term at the right-hand side of Eq. (1). Calculation of the sink strengths, k, shows that the passage from stage I to stage II is due to an increase in bubble size and intragranular swelling, entailing a decrease of k_{sc}. Actually, independent experi-

ments show that in the temperature interval 1600-1750 K the fuel undergoes drastic bubble growth and coalescence, perturbing the diffusion flux of fission gas atoms. Further precipitation and bubble coalescence during the annealing stages do not substantially change the diffusion enthalpy, but only the *effective* pre-exponential factor of the diffusion coefficient.

The amount finally trapped in larger bubbles, and eventually released in stage III (> 2250 K) amounts to approximately 20%. The release rate in this stage is proportional to the vaporization rate of the matrix; the measured enthalpy is 150 kcal/mole, equal to the value measured in the BR3 fuel.

Interesting isotopic effects were observed in rare gas release at moderate temperatures. Bursts have been observed with duration of several minutes at temperatures around 1400-1500 K. The released xenon is almost only ^{132}Xe, an isotope with a relatively long-lived tellurium mother ($\cong$ 3 days). The concomitant presence in these bursts of the long-lived ^{137}Cs and ^{129}I (Fig. 2.47) indicates the presence on grain boundaries of caesium telluride and iodides. Interestingly, these compounds (very likely Cs_2Te and CsI) contain only a small fraction of the formed ^{133}Cs, whose nearest precursors are, in the order, ^{133}I (10h) and ^{133}Xe (5 days). It can be, therefore, inferred that the stable ^{133}Cs-isotope was formed in-pile after previous trapping of the mother in gas bubbles, and hence it was finally released, during the annealing stages, at much higher temperatures than ^{137}Cs.

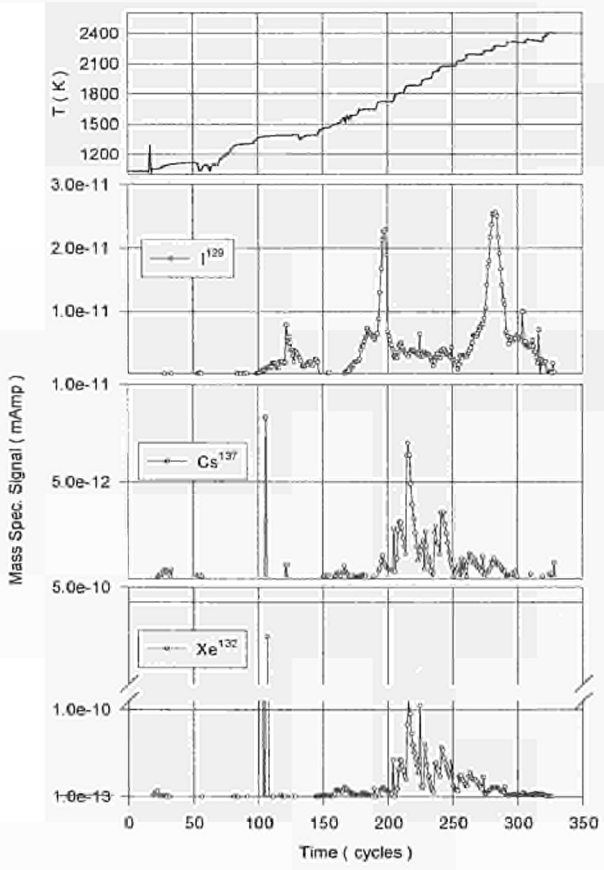

Fig. 2.47 Temperature and effusion's mass spectrometric measurement of ^{129}I, ^{137}Cs, ^{132}Xe as function of time.

Iodine

Due to the long cooling time of the examined fuel, only ^{129}I could be measured. The release of this isotope occurs in three stages with activation enthalpies similar to those of xenon, however, the diffusional stage II starts for iodine already at 1430 K (1850 K for xenon), and terminates at approximately 1800 K (2250 K for xenon). Fig. 2.48 shows the plotted Z-curve: Except for the low temperature burst mentioned above (whose non-diffusional nature clearly results from the almost vertical position of the corresponding Z-values), the stages are well separated. Both stage I and II terminated with a marked burst, followed by a silent annealing interval.

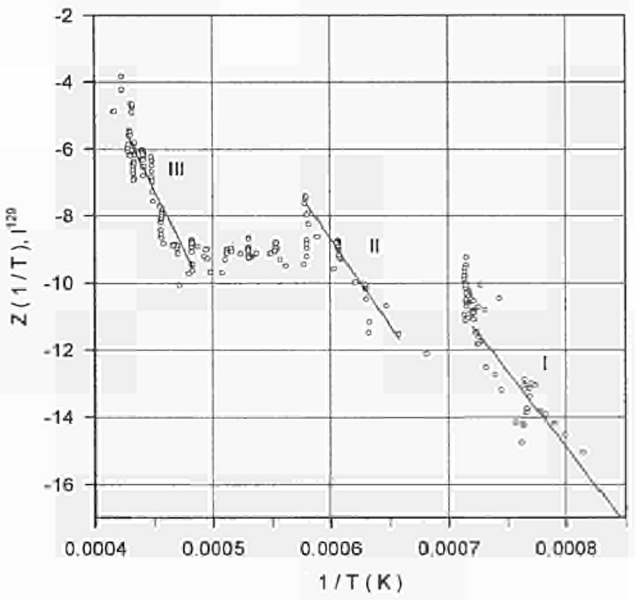

Fig. 2.48 Arrhenius plot of the de-convolution function Z(1/T) of ^{129}I.

These results indicate that iodine has a much higher entropy coefficient than rare gases. This means that its associated defect configuration and preferential trapping are different to that of rare gases.

Strontium and Barium

The strontium isotopes ^{88}Sr and ^{90}Sr were measured. The release rate in stage I is very irregular, involving less than 5% of the created strontium. Stage II is observed, starting at 1700 K and merging into the vaporization stage III at circa 2100 K. The enthalpy of diffusion is approximately 70 kcal/mole, significantly lower than that of caesium and the rare gases. It can be seen that 40 to 50% of the strontium inventory is released in stage II.

The relatively low diffusion enthalpy leads us to deduce that the chemical activity of strontium in UO_2 has a non negligible influence on diffusion. Trapping of this element in intragranular precipitates is less evident than in the case of xenon: the fractional release as well as the Z-curve as functions of time/temperature increase rather regularly up to the vaporization temperature (Fig. 2.49). The slope of stage I, though very imprecisely defined, is not very different from that of stage II

and, furthermore, the transition between stage I and stage II does not exhibit large entropy variations.

^{138}Ba was detected both in the elemental form and as BaO. Ba is released already at temperatures around 1100-1200 K with rates having the form of erratic, but non-negligible peaks (4-5% of the inventory at the end of stage I). Stage II starts at circa 1500 K with an enthalpy of 80 kcal/mole (Fig. 2.50), whilst the onset temperature of the BaO diffusional stage is above 1850 K, and ΔH is lower (58 kcal/mole) than for the elemental form.

Other oxides

Three other fission-product oxides have been identified in the effusion vapour during stage II: LaO, NdO and CeO (Fig. 2.51). Since their corresponding solid sesqui- and di-oxides have higher oxygen potentials, and lower melting points than UO_2, their vaporization at temperatures lower than those characterizing stage III is to be expected.

Zirconium, though especially searched for, could not be detected, neither as element nor as oxide. Actually, independent effusion experiments on zirconia showed that this compound starts vaporizing in vacuo at detectable rates only above 2600 K.

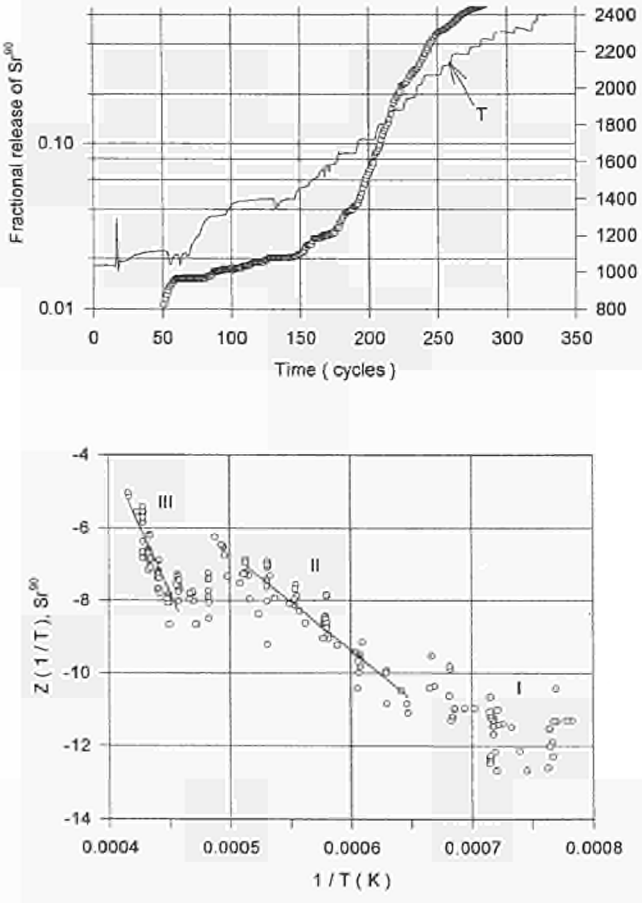

Fig. 2.49 Fractional release and de-convolution function Z(1/T) of ^{90}Sr as function of time and inverse temperature.

Fuel stoichiometry

As in the preceding experiments on BR3 fuel, the fuel vapours can be quantitatively analysed with sufficiently accuracy only at T > 1900 K, at which temperature the ratio of the equilibrium pressure of UO(g) to that of U(g), (UO_2(g) was found to be a minor species over the whole measurement range), indicate a slight sub-stoichiometry of the specimen.

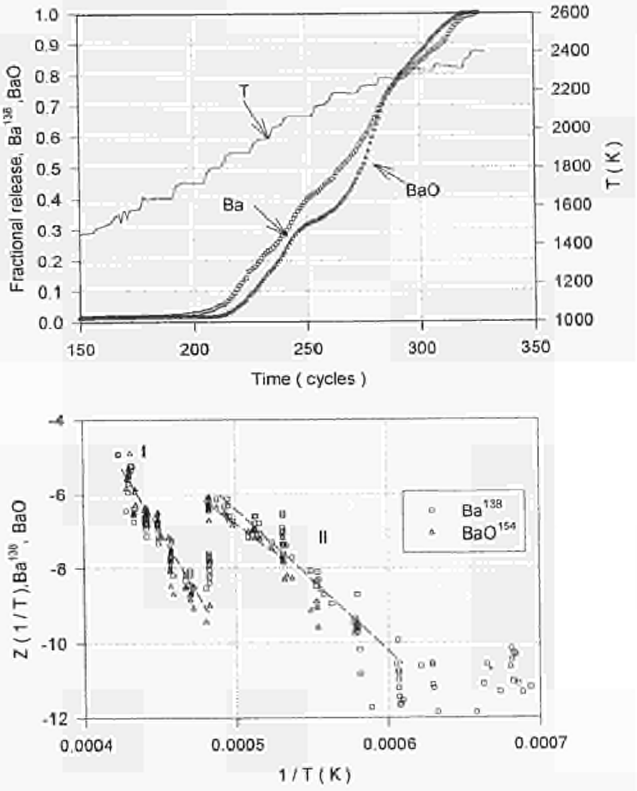

Fig. 2.50 Comparison of the Z-functions and of the fractional release of ^{138}Ba and BaO.

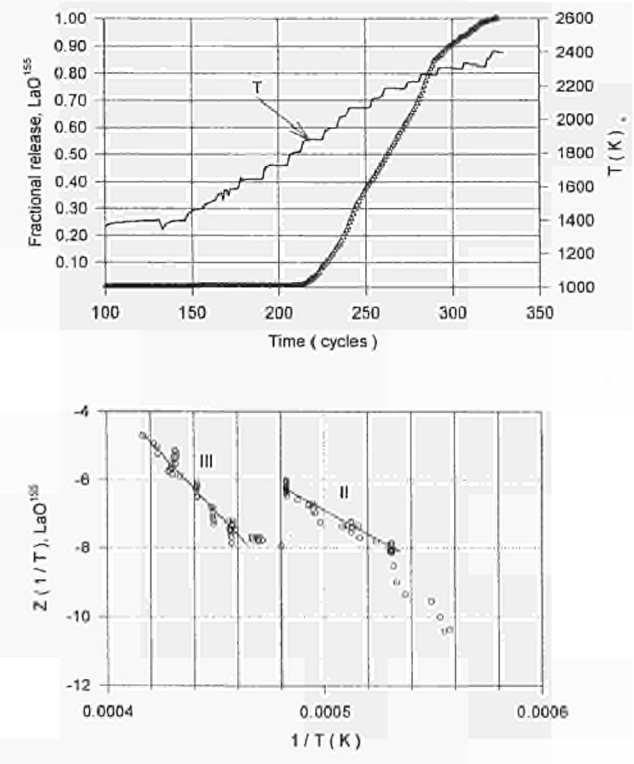

Fig. 2.51 Idem as in Fig. 2.50 for LaO.

Interestingly, during stage II the ratio UO(g)/U(g) in the vapour increases with temperature, whilst during the following stage III (T > 2100 K) the fuel displays a marked tendency to reduction (Fig. 2.52). One can therefore infer that massive release of fission products (mostly in the form of elements or monoxides) during the diffusional stage II leads to an increase of the oxygen activity in the fuel (this effect has been observed in samples of different origin and burnups).

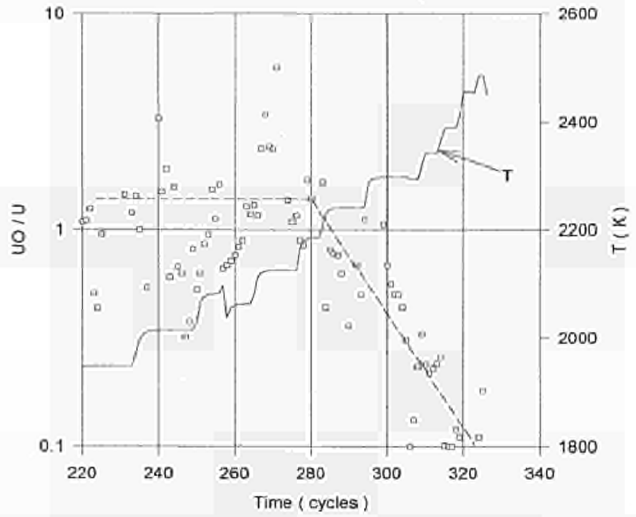

Fig. 2.52 Evolution of the UO/U fraction in the vapour phase as a function of time and temperature.

Conclusions

The effusion experiments on the high-burnup KWU fuel basically confirm previous results on lower burnup fuel, performed under similar annealing conditions, namely:

- Intragranular fission products, independently of their chemical nature, diffuse and escape to free surfaces via matrix diffusion or with diffusion enthalpies which approach that of cations in UO_2. The latter is 130 ± 8 kcal/mole [1].
- The release rate is proportional to structural factors depending on both the *intra-* and *inter-*granular sink strengths, which are submitted to important changes during distinct thermal annealing steps.
- Intragranular sinks retain fission gas and volatile fission products up to fuel vaporization temperatures. As for the relevant differences observed between the high burnup and the low burnup fuel, it was observed that:
- Volatile fission products are present in *intergranular* pockets, and are released at much lower temperatures (1100-1200 K). A few percent of the amounts of Cs, I and Te formed migrated and reacted in these pockets during reactor irradiation, and are immediately released in the first annealing steps.
- Part of the grain boundary porosity becomes effectively vented at *lower* temperatures as the burnup increases, so that release during thermal annealing is rate-controlled by matrix diffusion over a broad temperature range. Yet, since grain separation does not completely occur, volatile fission products have a short, but finite residence time on the grain boundaries; this makes the measured release rate rather discontinuous up to relatively high temperatures. However, the burst sequence is sufficiently rapid to obtain the significant temperature dependence from annealing experiments of a few minute time-steps.
- The effect of the radiochemical precursors is in some cases determinant for the release behaviour of a nuclide, so that the isotopic composition of a fission product element may vary in the different release stages.

  This aspect, which can be even more important for short-lived fission products, is being further investigated.

Reference

[1] Hj. Matzke, 'Diffusion Processes in Nuclear Fuels', in Diffusion Processes in Nuclear Materials', Ed. R. P. Agarwale; Elsevier (1992) p. 9

2.2.5 Revaporization studies on fission product deposits

Introduction

Thermal resuspension of fission products is a possible mechanism of material transfer in the primary circuit during a severe reactor accident. Volatile fission products released from the overheated core will condense on cooler parts of the primary circuit for example. The decay heat evolution would cause reheating of the deposit and its revaporization, with ultimate deposition further downstream. This phenomenon could significantly affect the source term release of a nuclear accident. The revaporization mechanism can be analysed experimentally in two possible ways:

a) Resuspension tests can be carried out on active samples coming from the reactor ramp tests. They can be considered as very close to reality. Unfortunately, these will be complex in nature and the samples limited in number and availability.

b) Simulation tests can be done which basically reproduce the experimental conditions in a simplified form aiming to understand the main mechanisms. This can be both inactive tests in the laboratory as well as tests on active samples in the hot-cells.

Within the frame of this work:

a) deposits taken from the vertical line of the PHEBUS fp FPTO test will be used in order to obtain quantitative revaporization phenomena on realistic samples and

b) small-scale simulation studies of deposition and release of inactive fission compounds on stainless

steel coupons will also be performed. The latter studies will concentrate on caesium compounds (CsOH, CsI, $CsBO_2$), since caesium is predicted to be among the fission products that would dominate the consequences of a severe accident [1].

Further simulation studies can be envisaged by annealing irradiated UO_2 and collecting the released fission products on foils positioned downstream.

Previous studies

The release of caesium from stainless steel coupons which were previously exposed to vapour of Cs compounds has already been studied [2, 3, 4, 5]. These experiments showed that the temperature at which revaporization of caesium occurred depends on the chemical form of caesium deposited on the coupons, which in turn depends on the temperature at which the coupons were exposed to the vapour. Previous experiments [6, 7, 8] did not give sufficient information on the form of the Cs compounds deposited on the samples. The formation of a caesium silicate at the oxide-metal interface has been postulated as bonding part of the Cs deposit on a 316 stainless steel. Isolated Cs ions were detected in the chromium oxide layer, with no evidence for the formation of other compounds such as chromates or silicates [7]. According to [3] it has been found that the caesium release from stainless steel, previously exposed to CsOH vapour at high temperature, occurred in two stages associated with caesium chromate and caesium silicate respectively. It has also been shown that stainless steel is attacked by gaseous CsOH at 780 °C [8]. Although these studies were carried out at different experimental conditions (different temperature or atmosphere), it can be concluded that the stainless steel oxidation, which takes place during the exposure, strongly affects the caesium stabilization on the stainless steel [3, 4]. Studies of the oxidation of stainless steel have shown that the type and the amount of the oxide formed are influenced by the atmosphere, temperature and the time of exposure [9, 10, 11, 12].

Experimental

The above results indicate that the experimental conditions can affect the chemical state of the stainless steel. Therefore an experimental programme will include:

a) Exposure of the stainless steel samples to the Cs compound vapour under a wide temperature range (200-1000 °C) and several atmospheres (Ar, Ar/H_2, $Ar/H_2/H_2O$).

b) Release tests of caesium from the exposed samples using thermogravimetry. Deposition tests of caesium on stainless steel samples after volatilization of the Cs.

c) Repeat of a) and b) with pre-oxidized stainless steel coupons.

d) Characterization of the stainless steel samples in each treatment step by using the following methods:

- X-ray diffraction (XRD) to obtain information about the structure and composition of the stainless steel samples and the determination of caesium or Cs-compound deposits.
- Optical microscopy and scanning electron microscopy (SEM) for the examination of the surface topography of the coupons before and after exposure, as well as after the release tests.
- Weight measurements to determine the amount deposited.
- Auger electron spectroscopy (AES),
- X-ray photoelectron spectroscopy (XPS) and
- Ion scattering spectrometry (ISS) to obtain the nature of the oxides formed on the stainless-steel coupons and the deposition of caesium.

Preliminary tests

For the preparation of the samples a set-up including two individually controlled furnaces has been constructed, as illustrated in Fig. 2.53.

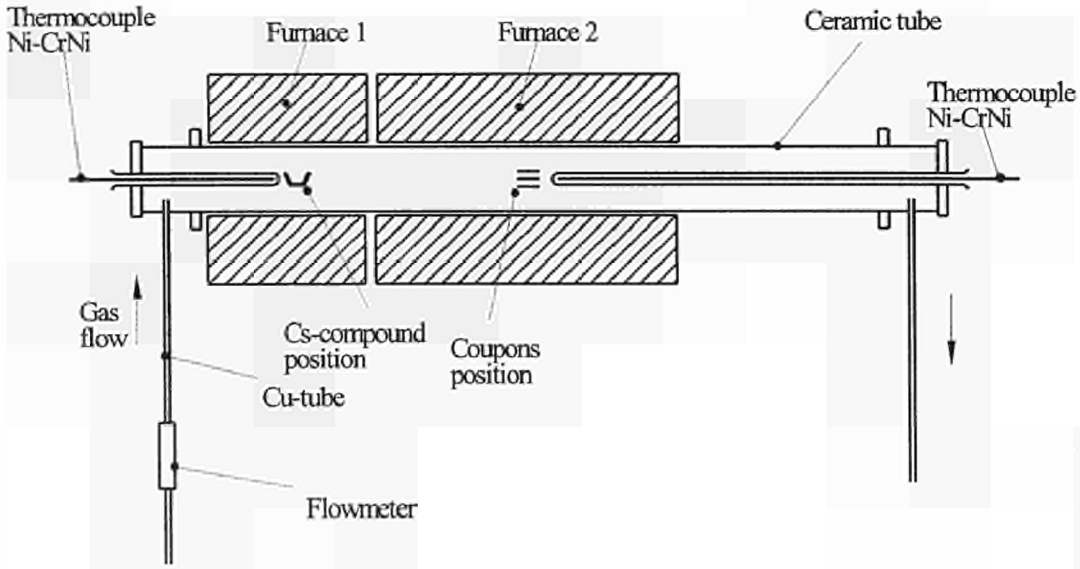

Fig. 2.53 Set-up for the preparation of the deposition samples.

The following preliminary tests have been performed:

a) Samples have been prepared in order to examine the effect of an *Ar 4.8 (9.998%)* atmosphere on the stainless steel type DIN 1.4301 at different temperatures. The composition of this stainless steel type is similar to stainless steel AISI 304 (C≤0.10; Si≤1.00; Mn≤2.00; Cr:17.00-19.00; Ni:8.00-10.00 S:0.25, P:0.20). To minimize the amount of air present, Ar was passed at 100 ml/min, 12 h before each experiment, through a ceramic furnace tube with the stainless steel sample (10 x 10 x 0.5 mm) mounted at a preselected position. The sample was heated to its final temperature within ca. 60 min and the temperature held stable for another 60 min. The samples were analysed by XRD after they had cooled down to room temperature in a Ar stream. In Tab. 2.7 are collected the interplanar spacing or d values, resulting from the XRD spectra. The final thermal treatment temperature is also given in the table.

b) Samples were prepared in order to examine the effect of *air atmosphere* on the stainless-steel 1.4301 at different temperatures. A ceramic tube was used to hold the 10 x 10 x 0.5 mm stainless steel samples in the furnace tube. The thermal treatment was the same as described above and the samples were analysed with XRD. Tab. 2.7 also shows the XRD d values from these air treated samples. The final thermal treatment temperature is referred in the sample code.

c) Stainless steel coupons 10 x 10 x 0.5 mm have been exposed in *CsOH-vapour* as an initial reference test to select the experimental conditions. The carrier gas (argon 4.8) was flowing at 100 ml/min through the furnace tube. When a sample temperature of 200 °C was reached, the CsOH was heated up to 450 °C during a 60 min. period and held at temperature for a further 60 min. The CsOH heating was then interrupted by removing the furnace 1 and cooled down to room temperature in ca. 30 min. After cooling of the coupons and their removal from the furnace 2, they were analysed with XRD, SEM and by weight measurement.

Conclusions

From these preliminary tests it can be concluded that all thermally treated stainless steel samples under Ar and air atmosphere at temperatures of 200, 400, 600 and 800 °C give the same XRD spectra as the as-received sample (Tab. 2.7). The different peaks appeared in sample Ar/700 correspond, according to the Powder Diffraction Index of the "International Centre for Diffraction Data" to Iron Nickel Chromium (Ni-Cr-Fe) or Iron Nickel Kamacite and to Iron Oxide Magnetite ($FeFe_2O_4$) (Tab. 2.7). Although XRD only penetrates to a depth of approx. 10 µm, the interference surface colour changes above 400 °C simply (assuming these are 1st order interference phenomenon) that the oxide layer is of the order of 0.2-0.4 µm. Thus the substrate stainless steel dominates the spectra despite the presence of any oxide. XRD is therefore an insensitive technique for the lower annealing temperatures.

However at 1000 °C the stainless steel coupons show some changes in the XRD spectra, unfortunately since many peaks are small and cannot be easily assigned to a compound, it is difficult to interpret these changes.

The weighing of the samples before and after their exposition to CsOH vapour at 200 °C, showed no weight change within the accuracy of the balance used (±50 µg). Additionally, no Cs has been identified on this coupons surface with SEM analysis.

For the future work a balance with higher accuracy will be used. SEM analysis accompanied by EDX analy-

Tab. 2.7 Results of the XRD-measurements.

sample symbol (atmorphere/ Temperature [°C])	d [A]	%	d[A]	%	d[A]	%	d[A]	%	d[A]	%	d[A]	%	d[A]	%	d[A]	%
common spectra peaks																
as received	1,267	100	1,789	89,88	1,082	85,81			2,064	77,12	0,824	76,23	1,079	77,12	0,822	
Ar/200	1,268	100	1,792	86,26	1,082	70,36	1,266	68,97	2,068	58,88	0,824	54,97	1,080	54,50	0,822	45,39
Ar/400	1,270	100	1,794	87,13	1,082	65,74	1,267	68,57	2,071	62,06	0,824	51,51	1,081	52,17	0,822	41,93
air/400	1,270	100	1,795	92,66	1,083	67,47	1,267	70,79	2,071	73,05	0,824	53,28	1,080	54,06	0,822	44,68
Ar/600	1,270	100	1,795	73,15	1,083	71,29			2,070	65,14	0,824	60,97				
air/600	1,269	100	1,793	83,08	1,083	62,74	1,265	69,64	2,068	65,36	0,824	53,02	1,080	49,65	0,822	44,86
Ar/700	1,269	100	1,794	85,83	1,083	78,31	1,266	81,.13	2,07	70,79	0,824	69,38			0,822	61,89
air/700	1,268	100	1,791	85,63	1,082	67,51	1,266	73,33	2,069	68,49	0,824	50,72	1,080	53,58	0,822	44,25
Ar/800	1,268	100	1,791	76,76	1,082	68,72	1,265	67,75	2,067	58,22	0,824	49,56	1,080	50,66	0,822	40,51
air/800	1,269	100	1,792	97,56	1,082	72,48	1,265	77,69	2,069	76,53	0,824	58,55	1,080	57,66	0,822	47,39
Ar/1000	-		-		-		-		-		-		-		-	
air/1000	1,268	90,44	1,791	88,12									1,080	82,26	0,823	87,01
different spectra peaks																
Ar/700	2,026	78,47	1,171	63,90	1,439	62,41	: Iron Nickel Chromium or Iron Nickel (Kamacite)									
	2,533	70,71	1,490	64,21	2,967	48,63	: Iron Oxide (Magnetite)									
Ar/1000	2,540	100	1,487	76,09	2,975	70,23	: Iron Oxide (Magnetite)									
	2,028	80,75	1,171	84,89	1,435	76,03	: Iron Nickel Chromium or Iron Nickel (Kamacite)									
air/1000	2,025	100	1,171	86,22	1,437 ?	80,99 ?	: Iron Nickel Chromium or Iron Nickel (Kamacite)									

sis, will be carried out on selected positions on the coupons exposed to other atmospheres and/or higher temperatures.

References

[1] Reactor Safety Study. An Assessment of Accident Risks in US Commercial Nuclear Power Plants. WASH-1400, NUREG-75/014, (1975)
[2] B. R. Bowsher, S. Dickinson and A. L. Nichols, UKAEA Report AEEW-R 1697 (1983)
[3] A. M. Beard, I. R. Beattie, E. R. Buckle, EUR 12844 EN (1990)
[4] N. E. Freemantle, A. T. Tuson, M. S. Newland, B. R. Bowsher, UKAEA Report AEA TSD-0267 (1994)
[5] N. E. Bennet, C. G. Benson, N. Beatham, UKAEA Report AEA RS 3353 (1993)
[6] R. M. Elrick, R. A. Sallach, A. L. Quellette, S. C. Douglas, NUREG/CR-3197, Vol.1 (1984)
[7] G. C Allen, B. R. Bowsher, S. Dickinson, G. M. Fotios, A. L. Nichols and R. K. Wild, Oxid. Met. **28** (1987) 33
[8] O. Götzmann, C. E. Johnson and D. C. Fee, J. Nucl. Mater. **74** (1978) 68
[9] A. S. Khanna, P. Kofstad, Proc. 11th Int. Corrosion Congress, Assoc. Ital. Met., p. 4.45-4.52 (1990)
[10] F. R. Mertens, Corrosion **34** (1978) 359
[11] J. T. Bittel, L. H. Sjodahl and J. F. White, Corrosion **25** (1969) 7
[12] G. C. Allen, J. M. Dyke, S. J. Harris and A. Morris, Oxid. of Metals **29** (1988).391

2.3 Fuel Performance Code Development (TRANSURANUS)

2.3.1 Maintenance work

TRANSURANUS is a computer program for the thermal and mechanical analysis of fuel rods in nuclear reactors which was developed at the Institute [1]. The TRANSURANUS code is fully described in the literature and was outlined in previous Annual Reports. The code is in use in several European organizations, both research and private industry. Preparatory work continued to release TRANSURANUS and the related know-how to several Eastern countries which requested this transfer. One contract was signed within the PHARE programme.

2.3.2 Specific model development

At high local burnups, typically above a threshold burnup of 75 GWd/tU, microstructural changes occur in UO_2 fuel [2]:

1. Marked decrease in the UO_2 grain size; development of a subgrain microstructure with a typical grain size of 0.2 to 0.3 μm within the original coarse grain structure.
2. Development of pores with a typical diameter of 1-2 μm. The pore density increases with increase in the local burn-up.
3. Xe-depletion of the matrix (athermal release of Xe from the UO_2 grains).

Since the local burnup is highest on the surface regions of LWR fuel because of build-up of Pu, these microstructural changes (High Burnup UO_2 Structure, HBS) were first observed at the fuel rim and are therefore usually referred to as the "RIM effect". Interest of researchers and technologists in these microstructural changes has increased because of the strong commercial interest in raising the burnup achieved of LWR fuel.

The scope of the work was to analyse experimental data from different sources and to review the concept of a burnup threshold. For the analysis the TRANSURANUS burnup model TUBRNP [3] was used.

The simplest model for the Xe depletion is the assumption that above a threshold burnup the loss term of Xe from the matrix to the pores is proportional to the Xe concentration:

$$\frac{d\,Xe}{d\,bu} = a\,Xe + \dot{c}_{Xe} \qquad (1)$$

where $\dot{c}_{Xe}$ is the Xe creation rate and a is a fitting constant.

An integration of Eq. (1) gives

$$Xe\,(bu) = \dot{c}_{Xe}\left[\frac{1}{a} + \left(bu_0 - \frac{1}{a}\right) e^{-a(bu-bu_0)}\right] \qquad (2)$$

$bu \geq bu_0$

where bu_0 is the threshold burnup. Xe equilibrium for $bu \rightarrow \infty$ is given by

$$Xe_\infty = \frac{\dot{c}_{Xe}}{a} \qquad (3)$$

The result is shown in Fig. 2.54.

Two trends are clearly visible:

1. At about 1 w/o Xe, which corresponds to a burnup of 60-75 GWd/tU, the Xe concentration deviates from the generated Xe concentration.
2. At high burnup above 120 GWd/tU the Xe concentration does not fall below a concentration of

approximately 0.25 w/o and approaches an equilibrium between generated and released Xe. From this value the fitting parameter a is obtained.

A more detailed look at Electron Probe Micro-Analysis (EPMA) results revealed that there is a transition from the original grain structure to the fully developed HBS. The beginning of the transition zone (at a burnup of approximately 60 GWd/tU) is characterized by single HBS spots which are formed at pores and surfaces. The density of these spots increases until a homogeneous HBS has formed, which is the case at about 75 GWd/tU (see also TUAR-94, p. 211).

It is seen from Fig. 2.54 that equations (2) and (3) explain the data reasonably well. With few modifications this model can also be applied in the transition zone.

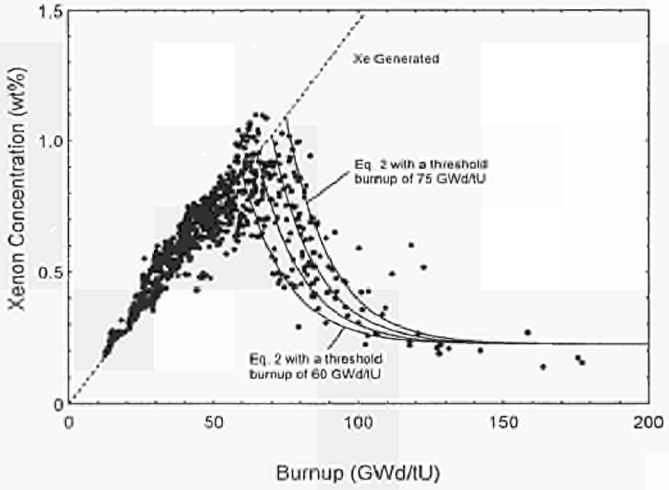

Fig. 2.54 Comparison between predicted and measured local xenon concentrations as a function of the local burnup; the threshold burnup was varied between 60 and 75 GWd/tU in steps of 5 GWd/tU.

Fig. 2.55 shows the available experimental data on the thickness of the fully developed HBS zone obtained from EPMA measurements. Because the end of the transition zone, i.e. the boundary of the HBS zone, is uncertain, error bands are given. The data originate from different fuel geometries, different enrichments and different irradiation conditions. It seems that the TUBRNP model is able to predict correctly the trend of the data.

The concept of a threshold burnup is valid only if the local temperature is sufficiently low. At present we do not know what this temperature limit is. However, from Fig. 2.54 one must conclude that the threshold concept can be applied up to an average cross-section burnup of 70 GWd/tU for standard LWR conditions. The dashed line of the prediction in Fig. 2.55 indicates that the model is probably no longer applicable above this burnup level. More details are given in reference [4].

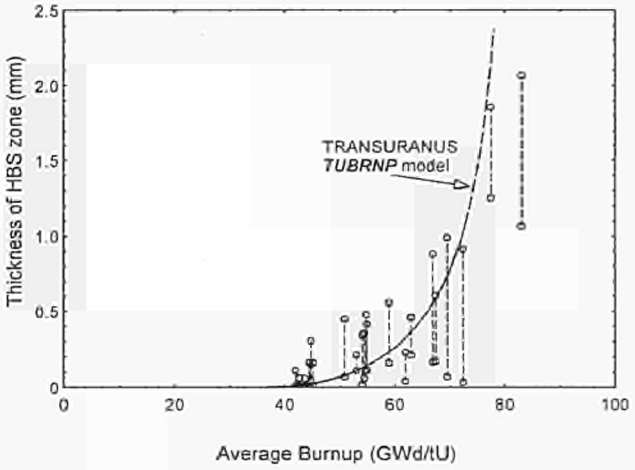

Fig. 2.55 The thickness of the HBS zone (rim zone) as a function of the cross-section average burnup as revealed by Xe measurements performed by EPMA. The prediction of the TRANSURANUS TUBRNP model serves only to demonstrate the theoretical trend. It is not known whether the model is valid at burnups above 75 GWd/tU and hence the line of the model predict is shown dashed.

References

[1] K. Lassmann; J. Nucl. Mater. **188** (1992) 295-302
[2] Hj. Matzke, H. Blank, M. Coquerelle, K. Lassmann, I. L. F. Ray, C. Ronchi, C. T. Walker; J. Nucl. Mater. **166** (1989) 165
[3] K. Lassmann, C. O'Carroll, J. van de Laar, C. T. Walker; J. Nucl. Mater. **208** (1994) 223
[4] K. Lassmann, C. T. Walker, J. van de Laar, F. Lindström; J. Nucl. Mater. **226** (1995) 1

3. Mitigation of Long Lived Actinides and Fission Products

Introduction

The Institute continued its work in the area of partitioning and transmutation (P + T) of minor actinides and long lived fission products.

A major pre-requisite for a successful P + T strategy is the development of an effective chemical separation technology. The contribution on the recovery of minor actinides from irradiated SUPERFACT fuels demonstrates the status of the development in this area.

Of similar importance is the development of advanced fabrication technologies for fuels containing minor actinides. The contribution on design and fabrication of fuel pins for the TRABANT irradiation element provides an update on the status of fabrication technology in this area.

In view of the recycling of americium, thermodynamic data and phase diagram studies have been performed on americium oxide and on the americium oxide-magnesium oxide system. Magnesium oxide is considered to be an interesting candidate for an inert matrix.

Initial work is reported to assess the radiological hazard of the long term storage of highly active waste produced by potential P + T fuel cycles.

The report on the Minor Actinide Laboratory shows, that the extension did not really progress due to budget restrictions.

In a final contribution a strategy for plutonium destruction in a pressurized light water reactor is described which does not lead to a net plutonium generation.

3.1 Recovery of Minor Actinides from Irradiated SUPERFACT Fuels with a View to their Recycling for Transmutation

Introduction

A successful transmutation option for the reduction of the long term radiological risk of disposed nuclear wastes can only be envisaged, if it includes as a head-end step the separation of relevant isotopes from spent nuclear fuels and at the tail-end of the transmutation process, the separation of the remaining long lived isotopes. A recovery rate of the long-lived radiotoxic isotopes as close as possible to 100% is imperative for the application of the transmutation option [1, 2].

In the case of a homogeneous, self-generated recycling [3], the minor actinide (MA) content in the fuel is in the order of a few percent only; thus the partitioning process to be applied could be the same as for the usual fast breeder reactor (FBR) fuels.

In the heterogeneous concept the high MA content requires modifications of the partitioning scheme. For the SUPERFACT fuels a valency state adjustment in the feed is required to avoid, especially for Np, a distribution into different process streams. In the present study, target fuel with an initial content of 20% Am and 20% Np has been reprocessed.

Experimental

After dissolution and clarification of the feed some main constituents of the fuel are separated by extraction chromatography under PUREX type conditions [4]. For Np with its well-known complex redox behaviour [5], two routes are possible; either reduction or oxidation of all Np to the extractable states Np(IV) or Np(VI), leading to a complete co-extraction with U and Pu or stabilization of the Np(V) state, in which case the Np stays together with Am in the HLLW. In order to avoid high loadings of the organic phase in the subsequent partitioning process, it was decided to extract as far as possible the Np together with U and Pu.

The partitioning was carried out in a continuous extraction process by means of trialkyl phosphine oxide using 12 centrifugal extractors. A successful demonstration of this process has already been described previously [6, 7]. Unfortunately lanthanides cannot be separated from Am/Cm with the present separation scheme.

The oxide fuel sample (2.21 g) was dissolved in 120 ml 7 M HNO_3. The actinide content in the dissolver solution determined by TIMS is given in Tab. 3.1.

Tab. 3.1 Actinide content in the dissolver solution.

actinide	content g/l
Np	2.40
U	9.76
Pu	1.93
Am	2.52
Cm	0.03

The oxidation state distribution of the actinides was controlled by spectrophotometry (CARY 17D equipped with optical fibres). Extraction chromatography was used to separate U, Pu and as far as possible Np from the HLLW. The resin used for this purpose was an Amberlite XAD-7 impregnated with diamyl amylphosphonate [8], now commercially available from EIChroM (Darien, IL, USA) as U/TEVA.Spec resin. The distribution factors for the actinides are considerably higher (sometimes more than an order of magnitude) than for tributylphosphate (TBP).

Preliminary tests using the resin packed into miniature glass columns (20 x 4 mm) allowed the elution parameters (Tab. 3.2) to be optimized for the separation process itself which was carried out on a larger column (280 x 20 mm). The resin was pre-equilibrated with 5 M HNO_3.

Tab. 3.2 Elution parameters for the U, Pu, Np separation (flow-rate: 1 ml/min.).

fraction	eluent	volume ml
HLLW	5 M HNO_3	172
Pu	5 M HNO_3 / 0.2 M NH_2OH*HCl	315
Np	2 M HNO_3 / 0.2 M $H_2C_2O_4$	420
U	5 M HNO_3	580

In order to adjust the HNO_3 concentration of the HLLW fraction for the subsequent partitioning, the solution was concentrated by evaporation down to about 15 ml and diluted again 10 times with distilled water.

The separation scheme used for the partitioning process has been described previously (TUAR-92, p. 80). However, instead of TRPO, the very similar extractant with the tradename CYANEX 923 purchased from CYTEC Industries (Rungis, France) was used. This extractant is applied on a large scale for Nb/Ta separations and for the removal of impurities from copper electrolytic solutions. For the present experiment it was used without further purification in a mixture containing 70% dodecane.

In the feed, the adjustment of the Np(IV) oxidation state is achieved with Fe(II) sulfamate. The analyses were carried out by ICP-MS.

Results

Despite its very unusual composition, the fuel did not show any anomaly upon dissolution. As mentioned above Np was expected to be the most problematic element in the subsequent reprocessing. The knowledge of the ratio of extractable (IV and VI) to not extractable (V) oxidation states of this element allows the feed adjustment prior to extraction. Well-defined extraction behaviour is only possible if each element is present in a single extraction stage. The absorption spectrum shown in Fig. 3.1 demonstrates, that this is not the case in the dissolver solution.

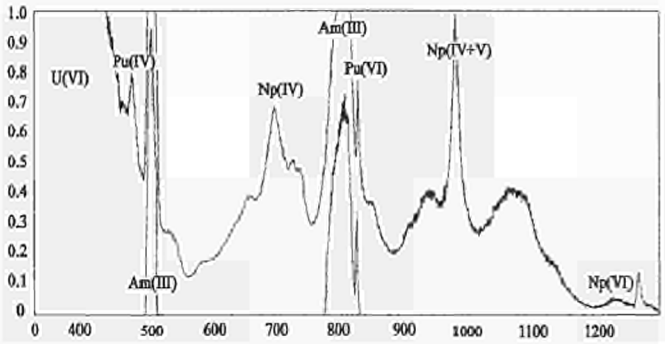

Fig. 3.1 Absorption spectrum of the dissolver solution.

Knowing the absorption coefficients it was possible to determine the concentrations in g/l for the different oxidation states of U, Pu and Np by complete oxidation by means of AgO followed by complete reduction by means of Fe(II)-sulfamate. The quantitative evaluation of the spectrum is given in Tab. 3.3.

Tab. 3.3 Actinide composition of the dissolver solution.

element (oxidation state)	wavelengt h nm	absorption coefficient l/g.cm	ref.	content g/l	oxidation state(s) content %
U(VI)	419	11	[9]	9.74	100
Pu(IV)	476	58	[9]	0.18	11
Pu(VI)	831	381	[9]	1.62	89
Np(IV)	700	53	[10]	2.33	84
Np(V)	981	250	[10]	0.11	4
Np(VI)	1222	36	[10]	0.33	12
Am(III)	811	60	[11]	2.78	100

As only 4% of the Np was in the unextractable oxidation state V, no feed adjustment was made. This avoided the introduction of additional chemicals in the process, and also allowed to test the capabilities of the subsequent partitioning process for Np.

Chromatographic extraction of U, Pu and Np

Preliminary tests with microlitre amounts of solution were used to develop the reaction scheme (Tab. 3.2) to be applied for the large scale separation.

The remaining HLLW fraction contains, as expected, all the Am and Cm but no Pu nor U. The Np content of this fraction corresponds, as could have been predicted, to the Np(V) content in the dissolver solution.

The elution of the columns gave a pure Np fraction, which however contains less than 15% of the extracted Np. 34% of the Np is eluted together with Pu and 51% with U. Thus, redox reactions of Np must have occurred during the elution and, consequently, improvements are necessary to obtain a clear elution behaviour of Np in the chromatographic process. Another problem could be the precipitation of Np(IV) oxalate on the column, which might occur with the present high Np concentration. Additional tests on the microcolumns were therefore carried out in order to improve the elution scheme. As a result of these test, after elution of Pu as Pu(III), the Np is first oxidized to Np(VI) by AgO / 1 M HNO_3 and then eluted as Np(V) by 0.1 M $(NH_3OH)^+(HSO4)^-$ /1 M HNO_3.

Advanced partitioning

The continuous counter-current partitioning of the remaining actinides from the HLLW was conducted according to the TRPO separation scheme (TUAR-92, p. 80). The HNO_3 concentration in the feed, determined by titration, was found to be 1.41 M. In the raffinate the concentration of Am and Np could be decreased down to the background level of the hot-cell environment. For Am the back-extraction was also complete after almost 4 stages, only for Np two additional stages seem to be necessary to achieve complete back-extraction. The material balance for the chromatographic reprocessing and the liquid-liquid extraction partitioning of the actinides from an irradiated $(U_{0.6}Np_{0.2}Am_{0.2})O_2$ fuel is summarized in Tab. 3.4.

These results show that, except for Np, a very clear distribution into the various process streams is found.

Discussion

The feasibility of recovering actinides from irradiated $U_{0.6}Np_{0.2}Am_{0.2}O_2$ fuel from the point of view of recycling and transmutation could be demonstrated. At the laboratory scale, extraction chromatography with diamyl-amylphosphonate is a suitable technique to separate the main bulk elements U and Pu. A pure Np product would be obtained, if adjustment of the oxidation state to Np (IV) by for instance Fe(II)-sulfamate and, as shown on the microscale, elution after oxidation to Np (VI) were carried out. If some Np were to remain in the HLLW, it would be possible to obtain complete recovery with 6 instead of 4 back-extraction stages as in the present experiment.

Fibre-optics spectrophotometry is a very good tool for valency control. Excellent agreement could be obtained between the actinide content determined by this technique (Tab. 3.3) and that found by IDMS (Tab. 3.1). Spectrophotometry would also be an excellent elution monitor in the reprocessing campaigns of larger amounts of the 4 SUPERFACT fuels, planned for the near future.

References

[1] C. Prunier, A. Chalon, M. Boidron, M. Coquerelle, J. F. Gueugnon, L. Koch, K. Richter; FR '91 Int. Conf. on Fast Reactors and related fuel cycles, Kyoto, Japan, Oct.-Nov. 91

[2] L. Koch, G. Nicolaou, Comparison of Possible Partitioning and Transmutation Schemes when added to the existing nuclear fuel cycle, Proc. Technical Committee Meeting on Safety and Environmental Aspects of Partitioning and Transmutation of Actinides, IAEA , 29.11.-2.12 1993

[3] C. Prunier, F. Boussard, L. Koch and M. Coquerelle, in GLOBAL '93 - Future Nuclear Systems: Emerging Fuel Cycles and Waste Disposal Options, Seattle, Washington, September 12-17, 1993, Proceedings pp. 158-163

[4] J.-P. Glatz, H. Bokelund, M. Ougier, Development of a Multipurpose Unit for the Separation of Actinides, J. Less-Common Met. **122** (1986) 419-423

[5] C. Apostolidis, H. Bokelund, M. Ougier, A. Moens, Inorg. Chim. Acta **140** (1987) 253

[6] J.-P. Glatz, C. Song, X. He, H. Bokelund, L. Koch, Partitioning of Actinides from HAW in a Continuous Process by Centrifugal Extractors, Proc. of the Special Symposium on Emerging Technologies in Hazardous Waste Management, September 27-29, 1993, Atlanta, Georgia, D. W. Tedder ed., ACS , Washington, DC

[7] C. Song, J.-P. Glatz, X. He, H. Bokelund, L. Koch, Actinide Partitioning by Means of the TRPO Process, Proc. of the Fourth Int. Conf. on Nuclear Fuel Reprocessing and Waste Management, "RECOD '94", April 24-28 1994, London, UK

[8] E. P. Horwitz, M. L. Dietz, R. Chiarizia, H. Diamond, Anal. Chim. Acta **266** (1992) 434

[9] H. Schmieder, E. Kuhn, W. Ochsenfeld, report KFK 1306 (1970)

[10] C. Apostolidis, H. Bokelund, M. Ougier, 18èmes Journées des Actinides, April 20-24 1988, Paris, France

[11] W. W. Schulz, The Chemistry of Am, ERDA CRS, USA (1976)

process	process stream	Np	U	Pu	Am	Cm
dissolution	fuel	0.2922	1.1888	0.2359	0.3070	0.0035
extraction chromatography	HLLW	0.0093	0.0000	0.0000	0.3055	0.0034
	Pu fraction	0.0438	0.0000	0.2371	0.0003	0.0000
	Np fraction	0.0993	0.0000	0.0001	0.0000	0.0000
	U fraction	0.1490	1.1864	0.0001	0.0001	0.0000
liquid-liquid extraction	raffinate	0.0000	-	-	0.0000	0.0000
	Cm,Am fraction	0.0000	-	-	0.3082	0.0037
	Np fraction	0.0079	-	-	0.0001	0.0000
	organic	0.0012	-	-	0.0001	0.0000

Tab. 3.4 Material balance for the actinides in the reprocessing and partitioning of actinides from irradiated $(U_{0.6}Np_{0.2}Am_{0.2})O_2$ fuel, values in grammes.

3.2 Design and Fabrication of Fuel Pins for the HFR Experiment TRABANT

Introduction

The irradiation experiment TRABANT (Transmutation and Burning of Actinides in TRIOX) was planned and executed in a trilateral cooperation CEA, FZK and ITU within the framework of the project CAPRA (Consommation Accrue de Plutonium dans les Rapides), to study the transmutation of actinides and long-lived fission products and the behaviour of the new fuel types in a fast neutron flux. The fuels are either defined by a very high content of plutonium (> 40 w/o), together with uranium and minor actinides (MA) or by the complete absence of uranium (in order to avoid additional breeding).

Irradiation of the mixed $(U,Pu)O_2$ fuel with 45 w/o Pu, fabricated by CEA-Cadarache, started in July 1995 at HFR Petten and has reached 6 cycles and 3% burn-up. The $(U,Pu,Np)O_2$ and $(Pu,Ce)O_2$ fuel pins were fabricated at ITU, transported to Petten in August 1995. Irradiation at the HFR started in December 1995. The irradiation of the PuO_2-MgO fuel has been postponed.

Fuel and fuel pin fabrication

In order to assure a solid solution of the $(Pu,Ce)O_2$ and the $(Pu,U,Np)O_2$ fuel the starting oxide powders were prepared by a droplet-to-particle processing technique based on aqueous processes. This technique allows an excellent control of composition for multi-component materials, as each droplet contains precursors of the same stoichiometry as desired in the final product. The pellet fabrication technique used is a "hybrid" process, combining Sol-Gel with powder metallurgy. Based on an ammonia precipitation of actinide hydroxides, with or without uranium, small droplets of weak nitric acid solutions are formed by dispersion from a high speed rotating cup. The droplets are collected in a NH_4OH gelation vessel and the resulting small spheres (beads) are dried in an organic solvent by an azeotropic distillation (Fig. 3.2).

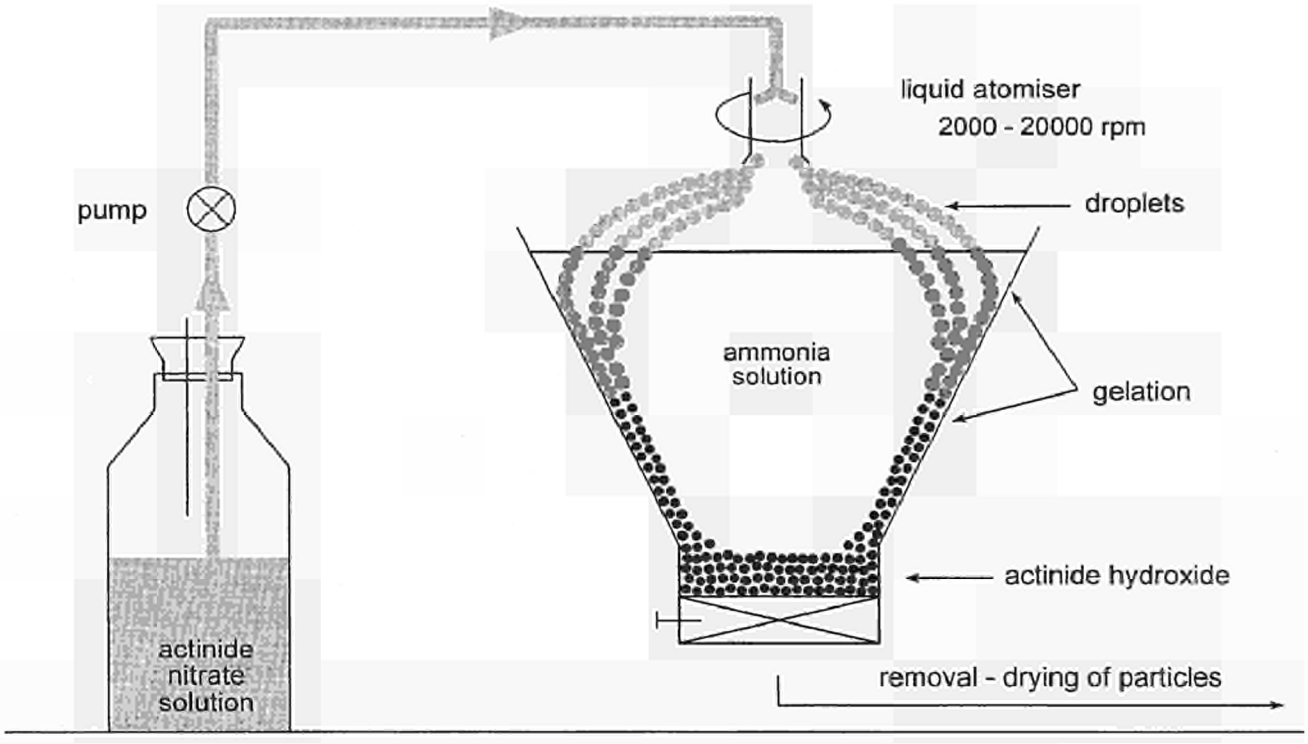

Fig. 3.2 Schematic representation of the droplet-to-particle processing technique.

Two types of pellets were prepared, annular pellets for the $(U,Pu,Np)O_2$ fuel and solid pellets for the $(Pu,Ce)O_2$ fuel. Both fuels were sintered at 1600 °C under a flowing Ar-5% H_2 atmosphere to maintain a substoichiometric composition. A part of the $(Pu,Ce)O_2$ fuel was sintered under air, in order to obtain an O/M ratio of 2.0.

Destructive and non-destructive controls were made in accordance with the specifications and the quality assurance plan. Afterwards pellet columns were assembled and filled into stainless steel tubes, flooded with He and closed by TIG-welding of the end caps. Tab. 3.5 summarizes fuel and fuel pin data and Fig. 3.3 shows the fuel pin design and position relative to core centre line.

Tab. 3.5 TRABANT 1: Fuel and cladding compositions and dimensions.

	Fuel pin No. 2	Fuel pin No. 3 (upper part)	Fuel pin No. 3 (lower part)
Manufacturer	ITU	ITU	ITU
Composition	$(U,Pu,Np)O_2$	$(Pu,Ce)O_{2-x}$	$(Pu,Ce)O_2$
Pu/M	0.40	0.41	0.41
U/M	0.55	-	-
Np/M	0.05	-	-
Ce/M	-	0.59	0.59
O/M	1.98	1.70	2.00
Pellet density (% th.d.)	96.2	-	-
Pellet density (g/cm³)	11.16	7.24	7.75
Pellet O.D. (mm)	5.42	5.45	5.44
Pellet I.D. (mm)	2.3	0.0	0.0
Fuel lengths (mm)	340,0	106,0	106,0
Fuel cladding	austenitic 15/15 Ti	austenitic 15/15 Ti	austenitic 15/15 Ti
Outer diameter (mm)	6.55	6.55	6.55
Inner diameter (mm)	5.65	5.65	5.65

Fuel characterization

Fuel structure

Fig. 3.4 shows a micrograph and an autoradiograph of the $(U_{0.55}\ Pu_{0.40}\ Np_{0.05})O_2$ fuel pellet. The perfect Pu distribution revealed by the autoradiograph was confirmed by X-ray analysis (see Fig. 3.5).

The $(Pu_{0.43}\ Ce_{0.57})O_{2-x}$ fuel, shown in Fig. 3.6, was also very homogeneous with respect to Pu distribution, however, X-ray revealed 2 phases (Fig. 3.7) in contrast to the stoichiometric fuel version (Fig. 3.8).

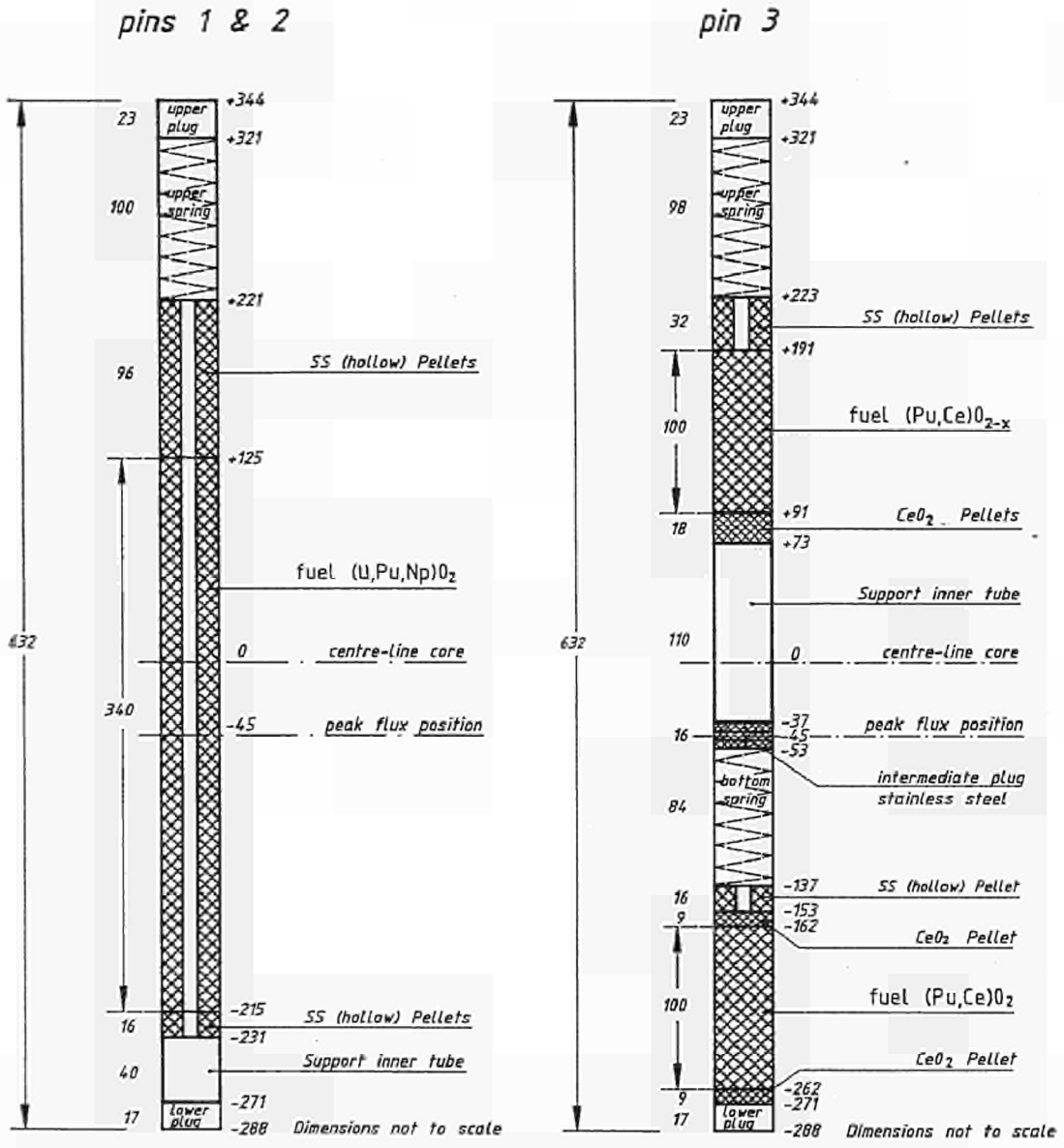

Fig. 3.3 TRABANT 1: Fuel pin design and position relative to core centre-line.

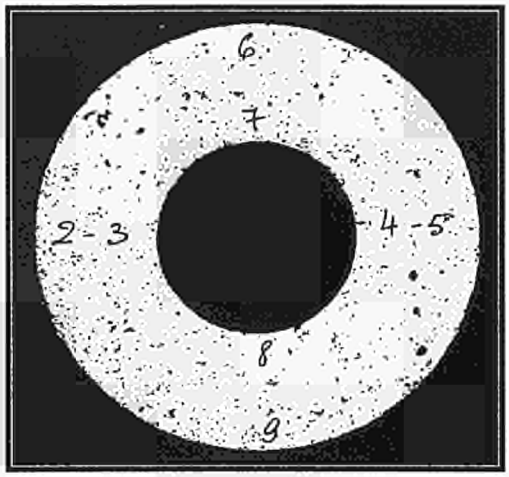

Micrograph x 20

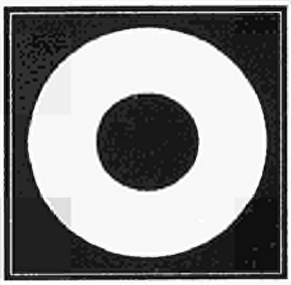

Autoradiograph x 10

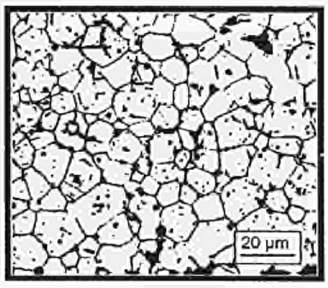

Micrograph

Fig. 3.4 TRABANT - Fuel pin 2 ($U_{0.55}$ $Pu_{0.40}$ $Np_{0.05}$)O_2 - micrograph.

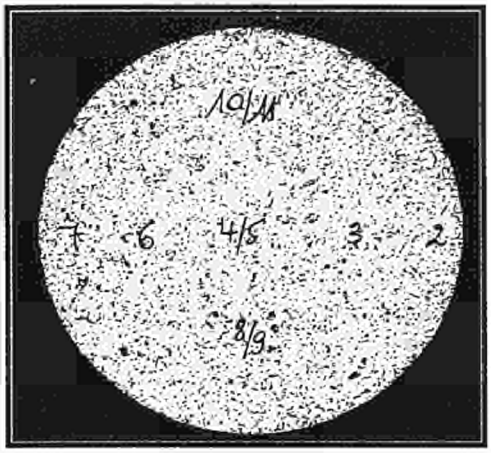

Micrograph x 20

Autoradiograph x 10

Fig. 3.6 TRABANT - Fuel pin 3 ($Pu_{0.43}$ $Ce_{0.57}$)O_{2-x} - micrograph.

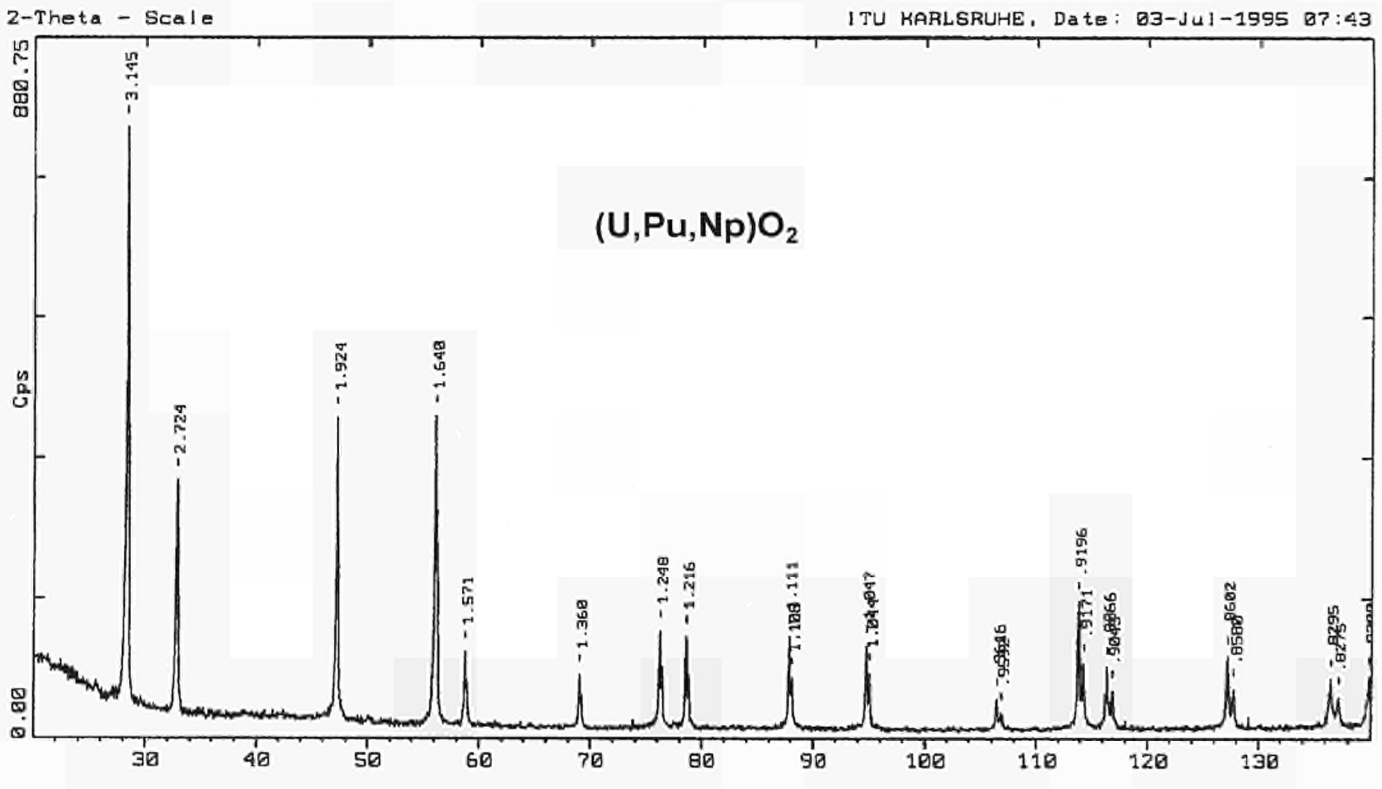

Fig. 3.5 X-ray analysis ($U_{0.55}$ $Pu_{0.40}$ Np0.05)O_2 fuel.

Solubility in boiling nitric acid

Dissolution tests of the TRABANT fuel and other Pu bearing fuels were made on sintered pellets in 10 molar nitric acid under reflux. For each test a complete, not crushed pellet of about 2 g was used. This variation of the standard dissolution test was chosen as a single and fast (intermediate weighing of samples with the same surface area) approach to compare the solubility of different fuel types. Fig. 3.9 shows the dis-

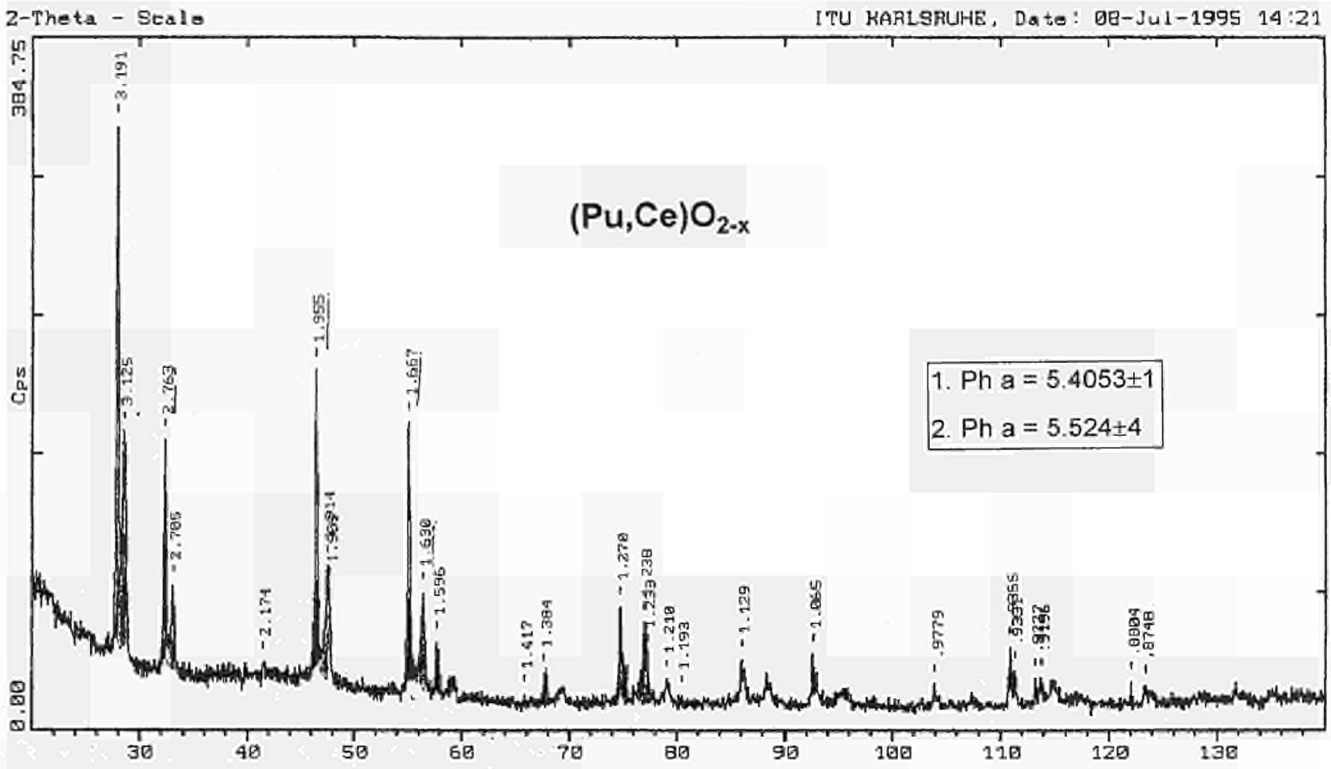

Fig. 3.7 X-ray analysis of 2 phases ($Pu_{0.43}$ $Ce_{0.57}$)O_{2-x} fuel.

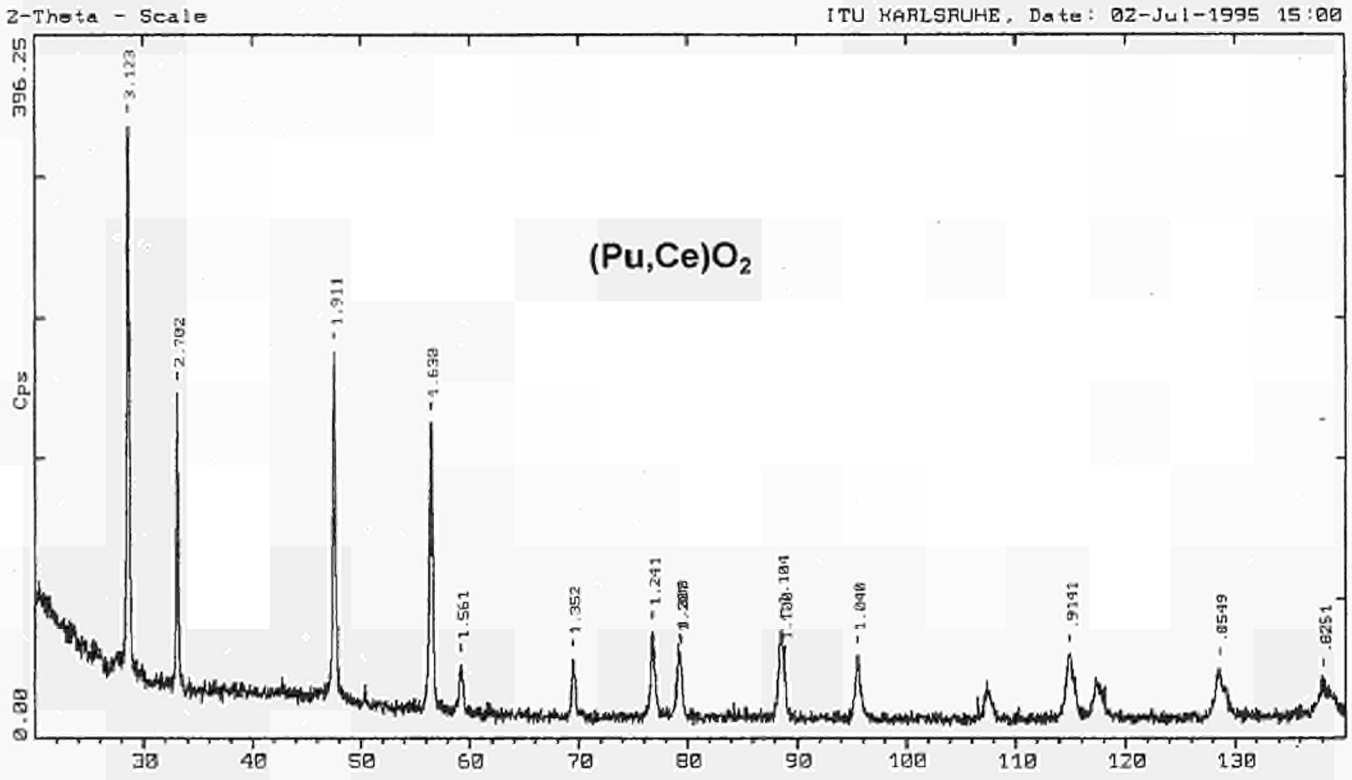

Fig. 3.8 X-ray analysis of stoichiometric ($Pu_{0.43}$ $Ce_{0.57}$)O_2 fuel.

solved quantity versus time and gives a first information on solubility and kinetics for these fuel types. X-ray analysis of the non-dissolved fuel rests proved that the composition of the fuel was not changed, i.e. no selective dissolution occurred.

Compatibility with sodium

Pellets of the two fuel types and a standard fast breeder (U,Pu)O_2 fuel were heat treated in immerged sodium. The fuel pellets were heated in a capsule filled

with sodium at 550 °C for 6 hours. Fig. 3.10 shows a radiograph of the different fuels after heat treatment. The uranium-plutonium-neptunium oxide fuel did not react with the sodium. However, the $(Pu_{0.43}\ Ce_{0.57})O_{1.70}$ fuel pellet revealed an increase in diameter. The reaction was increasing with oxygen content, until a complete destruction of the stoichiometric $(Pu,Ce)O_2$ pellet.

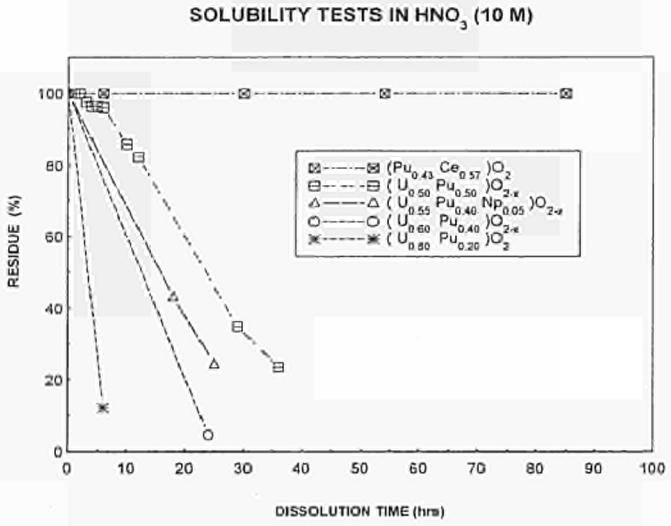

Fig. 3.9 Solubility tests 'TRABANT' fuel and other Pu bearing fuels in HNO_3 (10 M).

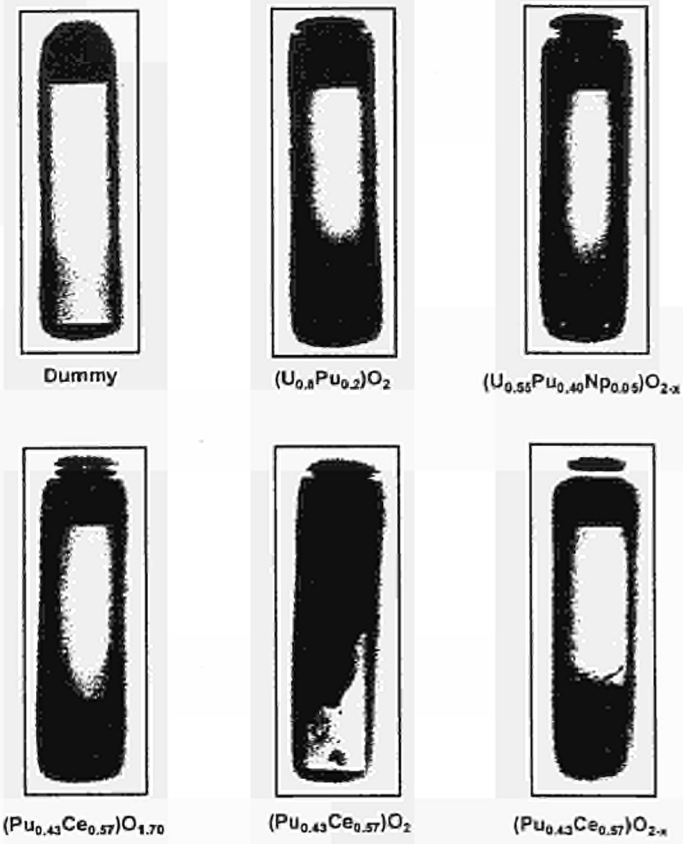

Fig. 3.10 Sodium-compatibility of Pu-fuels.

References

[1] A. Conti, T. d'Aletto; The TRABANT experiment, presentation report, Note technique SDC/LEMC 94.2006 and SIS-CAPRA 941002

[2] G. Mühling; TRABANT-1, Irradiation Experiment in HFR, Specifications

[3] R. L. Moss, M. P. W. Beers; PROJECT 291 TRABANT, Design and Safety report, Technical Memorandum HFR/95/4191

[4] J. F. Gueugnon, K. Richter, G. Mühling, H. Plitz; Design and fabrication of fuel pins for the HFR experiment TRABANT, Global 1995; Int. Conf. on Evaluation of Emerging Nuclear Fuel Cycle Systems; September 11-14, 1995, Versailles, 1293-1299

[5] J. F. Babelot, H. Bokelund, P. Gerontopoulos, J. F. Gueugnon, K. Richter; New fabrication techniques for the nuclear fuels of tomorrow; Global 95; Int. Conf. on Evaluation of Emerging Nuclear Fuel Cycle Systems, September 11-14, 1995, Versailles, 1663-1666

3.3 EFTTRA Collaboration

EFTTRA-T1 irradiation experiment in HFR-Petten

The irradiation of 3 Tc samples, fabricated at the Institute (TUAR-94, p. 62), and of 6 iodine compounds, fabricated at ECN, was completed, and the post-irradiation examinations started at ECN, CEN Cadarache and ITU. One of the Tc samples is being prepared for further irradiation to a higher burn-up (EFTTRA-T2) in the HFR-Petten.

EFTTRA-F2 irradiation experiment in Phenix reactor

A long-term irradiation of 3 Tc samples, identical to the samples of the HFR irradiation will be performed in Phenix from 1996 to 1998 (ANTICORP 1 irradiation). The fabrication and encapsulation of these 3 samples has also been performed by ITU. As a result of the good behaviour of the Tc samples during the irradiation experiment in the HFR, the same casting procedure as used for the HFR samples was applied for this fabrication. At a later stage, however, an alternative fabrication technique, such as pressing of powder and sintering, will be investigated.

3.4. Studies on the Am-O and the AmO_2-MgO Systems for Transmutation of Am

Introduction

To reduce the long-term radiotoxicity of minor actinides, two concepts of transmutation of actinides are proposed: the homogeneous and heterogeneous mode. The aim of this present project is to look at the recycling of the americium-241 contained in spent fuels by heterogeneous transmutation in fast reactors. We chose to develop oxide targets for the heterogeneous mode with Am and furthermore without U or Pu to avoid fresh actinide production during irradiation; the oxide should therefore be an inert matrix for Am transmutation.

Amongst the simple metal oxides, a good inert matrix for heterogeneous transmutation seems to be magnesia. The physical properties of MgO (low thermal neutron absorption cross-section, relatively high thermal conductivity and high melting point) and its compatibility with sodium make it of interest as a matrix for fuel applications.

Besides studying the MgO-AmO_2 system, an effort was made to fill the existing gaps in the knowledge of the Am-O system. AmO_2 and MgO are insoluble in the solid state. A good knowledge of the Am-O system is therefore necessary to understand its solid state chemistry in the AmO_x-MgO system.

Thermodynamic study of the Am-O system

The Am-O system was investigated between room temperature and 1500 °C using X-ray and ceramographic methods. The miniaturized galvanic cell used before to measure oxygen potentials of high burn-up UO_2 fuel [1] was employed to measure the oxygen dissociation pressure of stoichiometric AmO_2 and of substoichiometric AmO_{2-x}. Tab. 3.6 gives the impurities in the available AmO_2 powder, as determined by ICP-MS analysis.

Tab. 3.6 Impurities in AmO_2 as determined by ICP-MS.

Element	Concentration (10^{-6})	Element	Concentration (10^{-6})
Ca	25	Gd	30
Fe	135	Ta	67
Ni	11	W	40
Zr	25	Pb	655
Ba	18	Bi	11
La	30	U	644
Ce	61	Np	8945
Nd	13	Pu	2179

From this powder, pellets were pressed and sintered to theoretical densities of 85-90%. Reduction of the black AmO_2 to AmO_{2-x} with varying x-values was achieved by high temperature anneals under different atmospheres. The O/M-ratios were determined gravimetrically by annealing in air at 900 °C which yields stoichiometric AmO_2.

The oxygen potential measurements are shown in Fig. 3.11. Data points are given for AmO_2 and lines for 12 different compositions of AmO_{2-x} with O/Am-ratios between 1.98 and 1.58, as well as for the (red, hexagonal) sesquioxide Am_2O_3. Data for UO_2 [1] are shown for comparison.

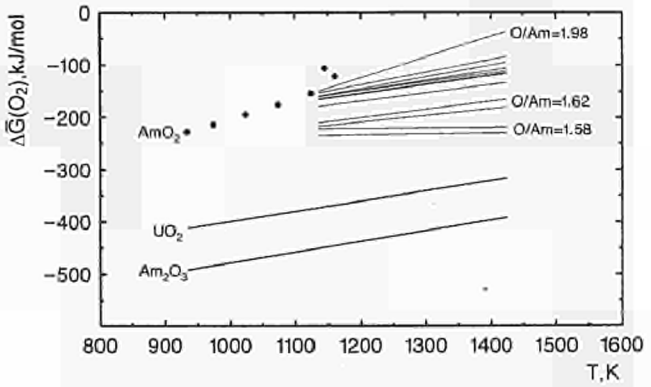

Fig. 3.11 Oxygen potential $\Delta G(O_2)$ as a function of the temperature for AmO_2, the red hexagonal Am_2O_3 and for AmO_{2-x} with different O/Am-ratios of 1.98, 1.96, 1.90, 1.85, 1.80, 1.75, 1.65, 1.63, 1.62, 1.59 and 1.58.

X-ray diffraction, ceramography and thermogravimetry showed that AmO_2 is stable between room temperature and ~ 850 °C in inert atmosphere. At higher temperatures, it looses oxygen and forms AmO_{2-x} phases. An example is shown in Fig. 3.12 for annealing AmO_2 in vacuum at 1071 °C.

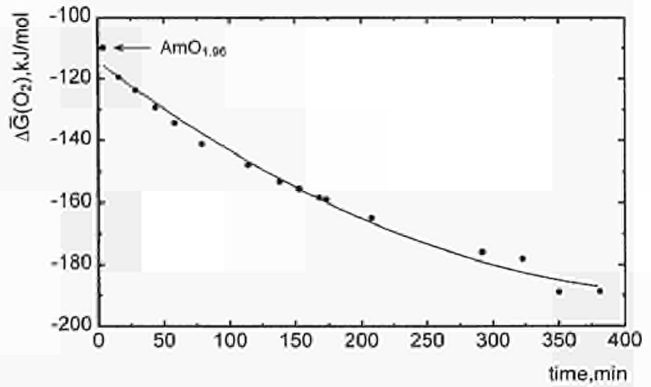

Fig. 3.12 Development of $\Delta G(O_2)$ with the time for annealing of AmO_2 in vacuum at 1071 °C. Reduction to AmO1.62 occurs within about 6 h.

Reduction to $AmO_{1.62}$ occurs within about 350 min, and the oxygen potential follows the relation (t in min)

$\Delta G(O_2) = -206.3 + \exp(4.543 - 0.00415\ t)$ kJ/mol

At this time and O/Am-ratio, $\Delta G(O_2)$ reaches a stable value.

The linear relations between $\Delta G(O_2)$ and temperature T allow to deduce the relative partial molar enthalpy and entropy for different O/Am-ratios from the measured $\Delta G(O_2)$ values, using the relation

$\Delta G(O_2) = \Delta H\ (O_2) - T\Delta S(O_2)$

Tab. 3.7 gives the results for four O/Am-ratios.

Tab. 3.7 Calculated values of $\Delta G(O_2)$ and $\Delta S(O_2)$ for four different O/Am-ratios.

O/Am	$-\Delta G(O_2)$ (kJ/mol)	$-\Delta S(O_2)$ (J/deg/mol)
1.98	493	401
1.62	334	163
1.58	234	188
1.50	631	205

Whereas a good knowledge exists in the literature on the U-O and Pu-O phase diagrams, this is not the case to the same extent for the Am-O phase diagram. In particular, at high temperatures and near Am_2O_3, data are missing. Partial phase diagrams were previously published by Sari and Zamorani from ITU [2] and by Okamoto [3]. The phase field $1.5 \leq O/Am \leq 2.0$ contains AmO_2 and AmO_{2-x} phases of the cubic fluorite structure, hexagonal Am_2O_3 and two oxygen-rich sesquioxides Am_2O_{3+x}, one being cubic and one assumed to be monoclinic [4]. On annealing above ~ 850 °C in vacuum, in inert or reducing atmospheres, AmO_2 looses oxygen by formation of O-vacancies (see Fig. 3.12). For charge compensation, two Am^{4+}-ions are reduced to Am^{3+} for each O-vacancy. Since the Am^{3+}-ion is larger than the Am^{4+} ion, lattice expansion occurs.

In the present study, some observations on the phase behaviour in the field $1.5 \leq O/Am \leq 2.0$ were made up to temperatures of ~ 1400 °C. After the different thermal anneals, the samples were examined by X-ray diffraction and by ceramography. Typical X-ray results obtained soon after the anneals (hence before radiation damage occurred) are given in Tab. 3.8.

The Am_2O_3 phase assumed to be monoclinic could not be found. However, a phase not corresponding to any of the Am_2O_3 phases reported so far was found when quenching $AmO_{1.63}$ from 1200 °C to room temperature. Though X-ray diffraction data were obtained [5], the structure could not be identified. It did not correspond to any of the Am_2O_3-type phases reported so far. However, this region of the Am-O phase diagram has not really been examined before in detail. Previous results by Sari and Zamorani [2] show that in the region of about $1.50 \leq O/Am \leq 1.56$, there is a single phase at low temperature. At temperatures above 1450 °C, samples with $1.5 < O/Am < 1.54$ consisted of two phases. The phases implied are the hexagonal phase Am_2O_3 with the lattice constants of a = 0.3810 nm and c = 0.5957 nm, and a high temperature form of Am_2O_3. This latter phase is cubic of bcc-type with a lattice constant of 1.100 nm. This phase seems to correspond to the cubic β-Am_2O_3 reported by Sari and Zamorani.

Two phases were observed at low temperature, one is the fluorite AmO_2 and the other is the cubic Am_2O_{3+x}. The lattice parameter of this last phase has been found to increase from 1.077 to 1.099 nm with decreasing x.

We see that the Am-O phase diagram is very complex. AmO_2 is easily reduced and in the T-$\Delta G(O_2)$ region of operating fuels, a number of phase changes can occur. This point has to be kept in mind when designing fuel for Am-transmutation.

A study of the AmO_2-MgO system

As mentioned in the introduction, a study was started to investigate the AmO_2-MgO system as target for americium transmutation in fast reactors.

The first step of the development for actinides to be transmuted is to know the basic chemical and physical data of the target as constrained by the fuel requirements:

- Phase diagram
- The region of the structural stability
- Melting point
- Thermodynamic stability
- Thermal conductivity
- Reaction with the coolant (sodium)
- Target-cladding interactions
- Radiation stability against neutrons, fission and α-decay

Phase	Composition a/o O	Pearson symbol	Prototype	Lattice parameters, nm a	c	Comment
AmO_2	66.7	cF12	CaF_2	0.53897		
Am_2O_{3+x}	61.5-62.5	cI80	Mn_2O_3	1.077-1.099		
Am_2O_3	60.6			1.100		at T > 1450 °C
Am_2O_3	60	hP5	La_2O_3	0.3810	0.5957	
Am_2O_3	61.9					Unidentified phase at T > 1200 °C

Tab. 3.8 X-ray diffraction results for different americium oxides.

Fabrication of MgO-AmO_2 specimens

Samples were prepared from MgO and AmO_2 powders. After mixing and pressing, the pellets were sintered in a dilatometer. Different heating/cooling rates and atmospheres were used up to 1620 °C to achieve densities ranging from 85 to 90% of the theoretical value. After each treatment, the phases of the mixture MgO-AmO_2 were determined by ceramography and X-ray diffraction.

Phase diagram studies:

Both experimental work and calculations were done. The binary phase diagrams of magnesia with plutonium oxide and uranium oxide was already examined. Both systems are simple eutectics with no intermediate compounds. The compositions and temperatures of the eutectics were determined experimentally. They are remarkably similar to values calculated assuming that the solution in the liquid phase is ideal and applying the laws of ideal solution:

for UO_2-MgO - predicted eutectic temperature 2160 °C at 41 mol% UO_2;

experimental values 2275 °C and 47 mol% UO_2.

for PuO_2-MgO - predicted eutectic temperature 1923 °C at 53 mol% PuO_2;

experimental values 2100 °C and 43 mol% PuO_2.

In the same way, for AmO_2-MgO an eutectic temperature of 1880 °C at 64 mol% AmO_2 was calculated. In practice, however, we expect deviations from these calculated values since AmO_2 easily looses oxygen as shown above. Different anneals of the AmO_2-MgO targets showed that reduction of AmO_2 occurred. This was indicated by weight losses, and confirmed by X-ray diffraction, ceramography and emf-measurements in the miniaturized galvanic cell used also for the study of the Am-O system (see above). For instance, reduction of AmO_2 to Am_2O_3 was sometimes observed. The loss of oxygen and the structural instability of AmO_2 at high temperatures under neutral atmospheres have to be considered for reactor application. As Am_2O_3 is thermodynamically more stable than AmO_2 (see Fig. 3.11), future work should show whether MgO-Am_2O_3 is suitable as target. A physical and chemical study is necessary to determine whether its properties satisfy all reactor requirements.

References

[1] Hj. Matzke; J. Nucl. Mater. **208** (1994) 18-26
[2] C. Sari and E. Zamorani; J. Nucl. Mater. **37** (1970) 324
[3] H. Okamoto; J. Phase Equ. **12** (1991) 696
[4] T. D. Chikalla, L. Eyring; J. Inorg. Nucl. Chem. **30** (1968) 133
[5] S. Casalta, Hj. Matzke, C. Prunier; A Thermodynamic Properties Study of the Americium-Oxygen System; Proc. GLOBAL 1995, Int. Conf. on Evaluation of Emerging Nuclear Cycle Systems, Sept. 11-14, 1995, Versailles, ENS/IAEA (1995) p. 1667
[6] S. Casalta, K. Richter, C. Prunier; A Study of AmO_2-MgO System for Americium Target Transmutation in Fast Reactors, ibid., p. 1725

3.5 The Involvement of the Institute in International R&D Efforts on Actinide Partitioning and Transmutation

Introduction

In addition to partitioning and transmutation (P&T) studies carried out under the present framework programme, the Institute participates in several other related projects.

From the present 165000 t of accumulated spent fuel worldwide, 65000 t have been reprocessed. 108 t of surplus separated plutonium exist because the present rate of MOX fuel fabrication consumes only 2-7 t of plutonium annually. In addition, there exists ca. 200 t of weapon plutonium which will be dismantled at an estimated rate of 7 t/y. The amount of spent fuel will grow annually by 10000 t of which about 5000 t will be reprocessed, producing 40 t of plutonium. These figures illustrate the enormous investment that would be needed to manage worldwide P&T.

There is, of course, a strong relation between the waste disposal option that a state has chosen and its research effort in partitioning and transmutation (Tab. 3.9). Canada, United States, Sweden and Spain, for example, have not taken the reprocessing option because they do not (yet) consider partitioning and transmutation as a viable option for the future. On the other hand, France, Japan and the Netherlands, which have decided to reprocess their fuel, have an intensive research programme on the technical feasibility of P&T. Because of the huge R&D effort needed, multilateral co-operation programmes have been started, in which the Institute, because of its unique installations and long experience in the field, plays a central role.

A long-term programme will be needed to develop and set up a partitioning and transmutation scheme for actinides (and other long lived radiotoxic fission prod-

reprocessing	Belgium[2] Brazil	*UK*[2,6]	*India*[1]	China[1] *Czech Republic*[1]	France[2,3,4,5] Japan[5,6] Netherlands[2,3]
reprocessing and direct storage	Spain	Germany[3,4]	*Rep. of Korea*[1]	Russian Federation[1]	
direct storage	USA Canada	Sweden			
	low		P&T research effort		high

[1]IAEA-CRP; [2]EU-CSA, [3]EFTTRA; [4]Trilateral co-operation; [5]Metaphix; [6]ISTC

Tab. 3.9 Waste disposal modes (countries which have deferred a decision are shown in italics) Source: IAEA yearbook 1994 p. C69.

ucts). Such a programme cannot solve short-term problems like the present excess of plutonium. Nevertheless, the denaturation of weapon plutonium, by recycling in LWRs for example - which for obvious reasons should be carried out as soon as possible - results in products that can easily be fed later into a partitioning and transmutation scheme.

Because MOX fabrication at present requires considerable operator intervention, the separated plutonium cannot be allowed to age too much in order to limit its 241Am build-up. Because of this, the recycling of plutonium into MOX fuel for LWR is pursued although the plutonium will rarely be recycled more than once. However, the intermediate stored spent MOX fuel is also available for P&T, as is the HAW that was left over from the earlier reprocessing.

International R&D activities

Several international programmes have been set up to study the P&T option.

The OECD concerts the R&D activities of its interested member states. To this end, the organization regularly arranges information exchange meetings and has started an evaluation of the present activities [1, 2]. Although not a formal member of NEA, the Institute actively contributes to the conferences by reporting on work done as part of the Framework programme or under commercial contracts.

There are also R&D activities in this field outside the OECD, and the IAEA has organized meetings to inventory the research activities in the member states: China, Czech Republic, India, Republic of Korea and Russian Federation [3]. With the assistance of the Institute, a status report is in preparation in which a basis for an eventual co-ordinated research programme is proposed. For the evaluation of the environmental safety and non-proliferation aspects of partitioning and transmutation of actinides and fission products, a co-ordinated research programme has already been set up, to which OECD and non-OECD member states contribute [4]. Here the Institute has also been asked to contribute, extending earlier studies on the eventual release of radioactivity to the environment to cover the effect of P&T.

In its cost shared action (CSA) programme, the European Union has supported and co-ordinated activities in several fields of Partitioning & Transmutation. The Institute is involved in some of the tests, mainly in the preparation of irradiation experiments and in pilot partitioning studies:

- The CEA, FZK, ECN, EdF and the Institute co-operate together in EFTTRA to develop and jointly test heterogeneous mixed oxide fuels, which to a large extent are supported in inert matrices, and which are to be irradiated in the HFR and PHENIX.
- In a trilateral co-operation between CEA, FZK and the Institute, mixed oxide fuels under irradiation in the HFR, Osiris and PHENIX are being studied.
- In the frame of a commercial contract with CRIEPI, the Institute has developed a minor-actinide fuel based on Zr alloys which is to be irradiated by CEA in PHENIX (Metaphix).
- The International Science and Technology Centre (ISTC) has accepted a research proposal from RIAR to demonstrate a minor actinide fuel cycle based on mixed oxides obtained by electro-deposition from a NaCl-2CsCl melt. The oxides are vibro-compacted and will be irradiated in Bor-60. The partners are PNC, BNFL and the Institute.

Emerging actinide fuel cycles

In order to be able to perform feasibility studies for different P&T options, international co-operation has to be intensified in a situation of shrinking budgets in nuclear R&D. From the first experimental results and considering the constraints on future fuel cycles (proliferation resistance, reactor safety, compactness and radiotoxic waste), the following technological solutions have emerged:

- a minor-actinide fuel cycle consisting of aqueous partitioning and MOX produced by gel supported precipitation (GSP) which could be vibro-compacted and recycled in fast reactors (trilateral co-operation),
- a dry reprocessing method based on electro-refining from a KCl-LiCl melt that produces material for Zr-based alloys (as has been demonstrated for Pu in the EBR-2 project). The transmutation of MA-containing alloys again will be in a fast reactor (Metaphix),

- the analogue process of electro-refining in NaCl-2CsCl produces MOX fuel which could be milled, vibro-compacted (as demonstrated for plutonium-containing MOX in Bor-60 and BN-600) and be recycled in a future Pb-cooled FBR (ISTC - project).

If in the medium term, a solution involving P&T together with the light water reactor fuel cycle is found, then the waste burner concept with heterogeneous fuel has to be considered. Under this assumption, the further development of the CAPRA project (trilateral co-operation) would lead to fast burning reactors into which the excess of Pu, MA and possibly ^{99}Tc would be discharged. Subcritical fast reactors which are driven by accelerators and fuelled by metal alloys, oxides or even nitrides could play the same role. However, these solutions may soon be superseded by the deployment of a fast reactor economy, or alternatively be rejected because of a public reluctance to accept burner reactors that concentrate radiotoxicity from other power stations and which would need a separate (on-site) fuel cycle. The situation of future fuel cycles is summed up in Tab. 3.10.

Tab. 3.10 Emerging actinide cycles.

Short term	Aqueous partitioning, MOX by GSP
	Partitioning KCl-LiCl, Zr-based alloys
	Partitioning NaCl-2CsCl, MOX vibro-compacted
Medium term	(AD)-MA-burner in symbiosis with LWR
Long term	Self-generated cycle in FBR

Future research

From the different feasibility studies presently under way, only a few demonstration projects will emerge having the necessary intense international co-operation, because of the high costs involved. Before this stage, knowledge gaps in the three fuel cycles (sketched out above) have to be filled. These are mainly in the partitioning process, and especially the separation of actinides from lanthanides. There are a number of partitioning processes already tested that produce a combined actinide and lanthanide fraction. The separation of the two element groups, however, is a difficult task. Moreover, the decontamination factor of Ln in An has still to be defined (it depends on whether a homogeneous or heterogeneous fuel cycle is applied). The same is also true for the dry processes. In the case of the deposition of metals from KCl-LiCl melts, the separation of americium from lanthanides is not solved. The same holds for the analogue process to produce the oxides. It should also be emphasized that any partitioning process has to minimize the losses of radiotoxic nuclides to less than 0.5% per cycle in order to achieve overall hazard reduction factors of about 100. None of the processes discussed (nor even the PUREX process) has reached this goal at present.

The minor-actinide-containing fuels for fast reactors do not require the same degree of separation of fission products as for LWR fuels. The γ- and neutron- doses emitted from minor actinides are already so high, that existing glove-box technology cannot be applied in any case. To ease fuel fabrication under the conditions of shielded glove-boxes or hot-cells, the casting of alloys or the vibro-compacted fuel technology seems to be better suited. There already exists experience of producing fuels by GSP (trilateral co-operation) as well as for granulates from the milled cathodes as obtained by the dry reprocessing method (ISTC).

References

[1] OECD/NEA 2nd General Meeting of the International Information Exchange Program on Actinide and FP Separation and Transmutation, Argonne (Chicago) Nov. 11-13, 1992

[2] OECD/NEA Symposium Cadarache, Sep. 12-14, 1994

[3] Technical Committee Meeting on Status of Programmes on Actinide Transmutation in non-OECD countries, Vienna, Sep. 4-8, 1995

[4] IAEA Technical Committee Meeting on 'Safety and Environmental Aspects of P&T of Actinides and Fission Products', Vienna, Nov. 29 - Dec. 2, 1993

3.6 Evaluation and Comparison of Public and Occupational Radiological Hazard from Intended Waste/Spent Fuel Repositories from Standard and Partitioning & Transmutation Fuel Cycles

3

The PAGIS (Performance Assessment of Geological Isolation Systems) study [1] has defined a group of long-lived nuclides which may be considered to be capable of delayed (hundreds of thousands of years) release from a nuclear waste repository. The radionuclides that were considered to be a potential long-term release risk are: ^{135}Cs, ^{129}I, ^{99}Tc and actinides ^{237}Np, ^{234}U and ^{233}U. PAGIS considered four types of geological deposition areas including salt and granite formations, sub-sea bed sediments and clay formations. Spent nuclear fuel and vitrified nuclear waste destined for waste repositories contain a wide range of nuclides, fission products and activation products produced in reactor construction materials and in the fuel itself. The basic source data for scenarios considered by the PAGIS programme are shown in Tab. 3.11.

The release of nuclides and subsequent rates of migration and mass transport from repositories are influenced by many factors, including the geology, chemical and physical nature of the area enclosing the repository, the hydrology of open and closed systems, dynamic/static equilibrium, the design and construction materials of the repository itself, and packaging of waste containers.

Many influences were modelled in the PAGIS programme but it appears that the effects of isotopic exchange mechanisms on the rates of radionuclide migration have not been addressed. Both ^{135}Cs and ^{129}I have natural analogues, ^{133}Cs and ^{127}I, which will be present in the surrounding area of a waste repository to varying degrees depending on the chemical composition of the geological matrices and the waste containment materials, e.g., ^{135}Cs would have a non-radioactive ^{133}Cs natural counterpart. The natural waters flowing through salt formations contain considerably more Cs and I than granitic waters and would therefore be more susceptible to isotopic exchange. It would be expected that the kinetics of *elemental* migration from a repository would not be affected, however, the overall dilution affecting the emergence of influential *radionuclide* activity will be altered. The isotopic exchange effect may thus be useful in slowing the rate of migration of *radionuclides* which have natural analogues. The effect should be carefully studied and the data applied to observe its influence on the radioactive releases from the waste repository. Following this, the risk to the general public should be re-assessed with regard to ICRP regulations for the Annual Limits of Intake of those particular nuclides [2].

It should be stressed that the isotopic dilution effect should not promote increased emissions of Cs into the environment with respect to the disposal of nuclear waste but should be seen as a rate-influencing effect.

Two of the other main radiotoxic isotopes that can emerge from the nuclear wastes described above are ^{99}Tc and ^{237}Np whose precursors (^{241}Pu, ^{241}Am, ^{245}Cm) are in the original waste. It is necessary therefore, to consider all actinides in any P&T work.

Tab. 3.11 Basic data for computing the radionuclide source terms [1].

Spent Fuel:

Reactor type	LWR
Nominal electric power per reactor	0.9 - 1 GW(e)
Average specific power	33 - 40 MW (th)/t HM
Fuel type	UO_2
Initial average enrichment	3.5 % U-235
Irradiation time	1000 - 1333 days
Burn-up	33 - 40 GWd (th)/t HM
Fuel discharged per years	27 - 33 t HM
Delay before reprocessing	3 - 7 years
Delay before HLW vitrification	1 year
Delay before disposal	30 - 300 years

Vitrified Waste:

Overall volume of container	0.18 m^3
Weight of container (empty)	75 kg
Glass volume	0.15 m^3
Weight of glass	405 kg
Radioactivity inventory (time zero)	
beta and gamma	2.9 E16 Bq
alpha	1.4 E14 Bq
Residual heat at vitrification (time zero)	3000 W
Residual heat after 30 years	680 W
Residual heat after 100 years	165 W
Power reactor energy equivalent	51 MWe·a
Initial Heavy Metal equivalent	1369 kg

Composition of Reference Waste (all data in w/o)

Glass:	87.9					
	SiO_2	45.5	CaO	4.0	P_2O_5	0.3
	B_2O_3	14.0	Fe_2O_3	2.9	ZrO_2	1.0
	Al_2O_3	4.9	NiO	0.4	Li_2O	2.0
	Na_2O	9.9	Cr_2O_3	0.5	ZnO	2.5
Waste residue:	12.1					
		Fission product oxides		11.25		
		Actinide oxides		0.85		

In order to compare the radiological hazard of the long-term storage of HLW produced by the P&T fuel cycles to that generated by present fuel cycles, an investigation on the effects of the reduction of certain selected nuclides on the occupational and public radiological hazards will be undertaken.

References

[1] G. Cottone, S. Orlowski, G. Bertozzi, F. Girardi, A. Saltelli; Performance Assessment of Geological Isolation Systems for Radioactive Waste, Summary, EUR 11775 EN (1988) 270

[2] Annual Limits of Intake of Radionuclides by Workers Based on the 1990 Recommendation, Annals of the ICRP (1990), ICRP Publication 61

3. 7 Minor Actinide Laboratory

The conceptual study of the fabrication chain has been carried on, through contacts with potential manufacturers of the technical equipment. Unfortunately, because of budgetary restrictions, the decommissioning of the old equipment from the future site of the caisson had to be interrupted, and the ordering procedure for new material was postponed. Nevertheless, after a survey of the potential suppliers, three detailed technical studies were made, for the following units to be installed in the boxes:

- the automatic press,
- the sintering unit (with automatic furnace loading),
- the filling/welding unit for fabrication of the pins.

For each study, a supplier with a good experience in the related (corresponding) field and in nuclear applications, was selected; the development was done in close collaboration with ITU, aiming at the definition of specifications suited to our peculiar needs, while taking profit from industrial know-how. These specifications will serve for the next step, i.e. the invitation for tender, as soon as the requested budget will be available.

Due to the budget restrictions, potential external customers of the Minor Actinide Laboratory have been contacted. It appears, that financial contributions, either in the form of a participation in the investment costs or in the form of payment under a third party regime can be expected. These discussions will be intensified during 1996 in order to arrive at a definite decision.

3.8 Particle Agglomeration and Deposition in Turbulence (PADIT)

The PADIT (Particle Agglomeration and Deposition In Turbulence) project was initiated in 1994 (TUAR-94, p. 73) to study the deposition and resuspension of radioactive solid aerosols, and agglomeration phenomena during their transport in duct systems (e.g. ventilation exhaust ducts) with highly turbulent flow conditions (Re >100,000). For the transport experiments, similitude in size to particles generated in the fabrication of nuclear fuel materials was achieved by using particles of natural uranium oxide with a size distribution ranging from 10 to 40 μm.

During the reporting period, the following improvements were made:

- The size distribution of the particle samples before injection into the facility could be better characterized using a CILAS-ALCATEL HR850 granulometer. This device uses the energy spectrum in the diffraction pattern generated by a coherent beam from a low power helium-neon laser, passing through the powder in liquid suspension, to gain information on the size of the diffracting objects,
- the injection of the particle samples into the wind channel (TUAR-91, p. 61) was improved by use of a rotating brush solid particle disperser (PALAS-RBG-1000) which permits reproducible dosing of powder samples to be dispersed. Furthermore, agglomerates present in the original powder could be dispersed by suitable selection of the dispersing air pressure,
- in addition to the transport experiments with particles of natural uranium oxide, attempts were also made with spherical UO_2 particles.

Results and discussion

Earlier experiments (TUAR-94, p. 74) showed that the extent of agglomeration occurring during the transport in highly turbulent conditions is difficult to evaluate due to the pre-existence of aggregates in all size fractions of the original powder in spite of ultrasonic sieving. This "primary" agglomeration is due to interparticle adhesion and thus strongly depends on the shape of the individual particles. For a given material, these adhesion forces are expected to be minimized in the case of spheres. Thus a few experiments were carried out using spherical UO_2 particles (20-40 μm in size). These particles were generated by the sol-gel technique, and had been calcined in air at 800 °C. The

small quantity (7g) of material did not allow an evaluation of the original size distribution with the CILAS-ALCATEL granulometer. The original spherical particles were dispersed with a spray bulb on a glass plate and their size distribution was evaluated using themethod described in TUAR-94, p. 73. Micrographs of such samples, e.g. in Fig. 3.13, show a substantial number of agglomerates, consisting of up to 3 single spheres, in the original material. An histogram of the size distribution is also shown in this figure: 38% of the particulates are agglomerates bigger than 40 µm.

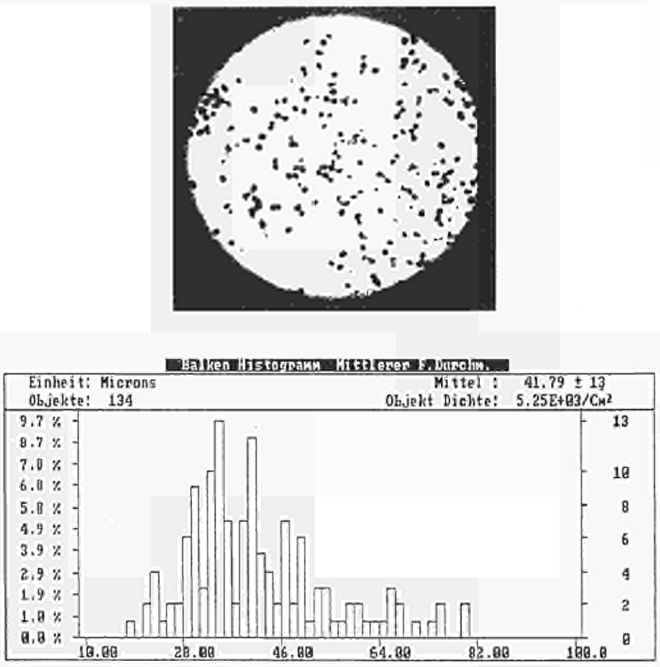

Fig. 3.13 Micrograph (magnification 50 X) and size distribution of original spherical UO_2 particles generated by the sol-gel technique.

Samples were then injected into the turbulent flow using the PALAS particle disperser with the air pressure set to 1.5 bar in order to break up the primary agglomerates. The loaded Nuclepore filters located at the downstream end of the transport channel were investigated. Analysis of the micrographs show broad distribution of particle size, but a significant reduction (30% of the particulates) of the agglomerates larger than 40 µm. An example is given in Fig. 3.14.

It must be noted however that the efficiency of the PALAS disperser to break all primary agglomerates could not be proved, so that those present initially could remain unchanged during the transport. Thus in the case of UO_2 spheres the agglomeration process during the transport in a turbulent flow remains uncertain. This problem can only be solved by direct *in situ* measurement of the particle size in the channel, e.g. using a laser phase doppler anemometer which unfortunately is not available. Nevertheless the absence of particulates significantly lower than 20 µm demonstrates the mechanical stability of the UO_2 single spheres during the turbulent transport.

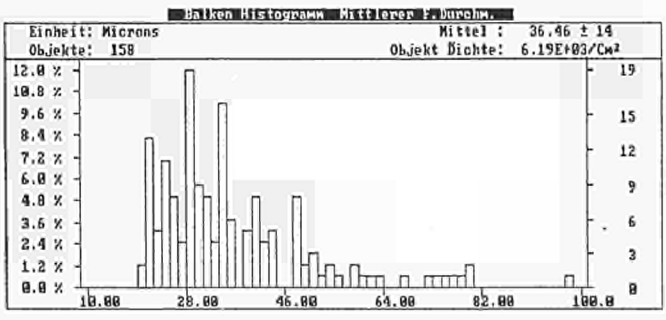

Fig. 3.14 Size distribution of the same spherical UO_2 particles as in Fig. 3.13, but collected on a sampling filter after transport in the turbulent flow.

Numerous transport experiments were carried out with commercial natural UO_2 powder. Particles smaller than 60 µm were selected by ultrasonic sieving. The original size distribution measured with the CILAS-ALCATEL granulometer shows (Fig. 3.15) an almost monodisperse distribution with a count median diameter (CMD) of about 22 µm superimposed on an abroad distribution (0.1 to 60 µm).

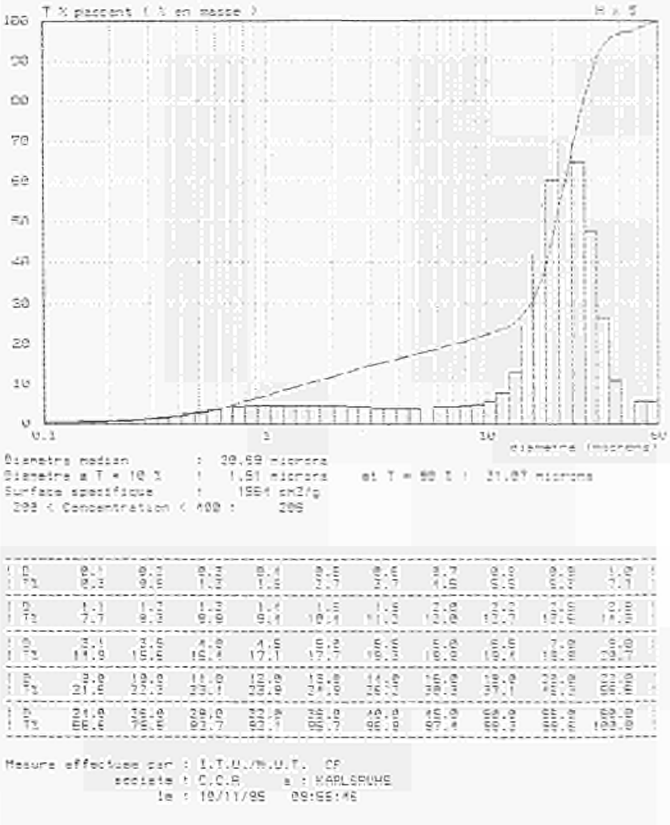

Fig. 3.15 Original size distribution (obtained with the CILAS-ALCATEL HR850 Granulometer) of the commercial UO_2 powder sample before injection into the wind channel.

The samples were injected into the wind channel using the PALAS disperser. After the transport, quantimetric examination of the loaded sampling filters demonstrate the same counteracting processes as precedently observed (TUAR-94, p. 73): The CMD moves to smaller values (12 to 15 µm) suggesting that primary agglomerates have been broken up by the turbulence. On the other hand, the number of agglomerates increased. In a typical experiment (see Fig. 3.16), the percentage of aggregates larger than 30 µm rises from 12% in the case of the original material to 18% in the case of the sample on the collection filter.

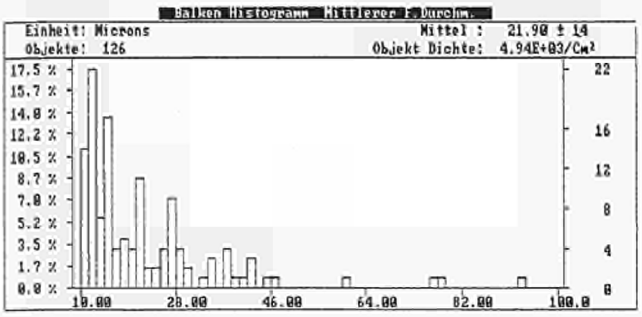

Fig. 3.16 Size distribution of the same UO_2 powder as in Fig. 3.15, but collected on a sampling filter after transport in the turbulent flow.

Conclusion

The investigations on the agglomeration process during transport in a high turbulent flow, indicate that the results obtained with commercial UO_2 powder are not so evident as those obtained with the Bi_2O_3 test aerosol used in early experiments. This could be due to interparticle adhesion which depends on the physico-chemical properties of the materials and on the particle shape. Optical or electron micrographs show that most bismuth oxide particles (TUAR-92, p. 59) are irregularly shaped whereas most of the uranium oxide particles are not far from sphericity.

As expected, the change in size distribution, resulting from both counteracting processes as described above, observed in these experiments is not very pronounced. A more accurate measuring method is necessary to quantify this phenomenon in *situ*. The most suitable would be a laser phase doppler anemometer whose purchase is foreseen.

3.9 A Strategy for Pu Destruction in PWR's

In conventional PWR, fissile ^{235}U is present to a level of about 3.2% in a ^{238}U matrix. Although not directly fissionable, this fertile ^{238}U is transmuted to Pu isotopes in the reactor neutron spectrum. During the lifetime of the fuel in the reactor some of this Pu is burnt. At the end of the fuel lifetime, however, a considerable amount of Pu remains and makes a major contribution to the radiotoxicity of the spent fuel.

Ideally, one would like to use a non-fertile, inert matrix instead of ^{238}U and thereby avoid the main source of radiotoxicity [1]. In practice, however, problems arise when one attempts to do this. One such problem is associated with the Doppler effect in ^{238}U. If for some reason the neutron flux increases in the reactor it results in an increase in temperature. This in turn leads to a thermal broadening of the absorption resonances at 5 eV in ^{238}U, which results in neutrons being lost from the system and thereby acts as a self regulating mechanism to stabilize the reactor.

Various options are available by which one can reduce the net amount of Pu produced while at the same time having a significant amount of ^{238}U present. In one such scheme the spent fuel could be reprocessed to remove the Pu isotopes and then mixed with fresh UO_2 fuel. This is the basis of Mixed Oxide (MOX) fuel fabrication. In this paper, we consider an alternative to this approach, in which the recycled Pu is used in an inert matrix (Pu/IM). Assemblies of such Pu/IM pins would then be mixed with standard UO_2 assemblies.

In a LWR, plutonium is produced by neutron irradiation of the fertile matrix of ^{238}U. In the case of the pressurized water reactor considered below, plutonium is produced at a rate of approximately 9 kg Pu per tonne of fuel during the lifetime (879 EFPD) of the fuel in the reactor (corresponding to approximately 300 kg Pu per GWy_e, see ref. [2]). An inert matrix having the same volume as one tonne of standard fuel and containing initially 50 kg R-Pu (i.e. 10 w/o assuming the density of the inert matrix is half that of the standard fuel) will burn approximately 40 kg Pu in the same neutron spectrum and over the same time, as shown in Tab. 3.12. Hence, in a steady situation where no net Pu is produced, approximately 18% (i.e. 9/49) of the core should contain inert matrix assemblies.

Tab. 3.12 Composition (%) of different types of plutonium.

	^{238}Pu	^{239}Pu	^{240}Pu	^{241}Pu	^{242}Pu
MOX Grade Plutonium (R-Pu)*	1.5	55.7	21.1	16.2	5.5
Weapons Grade Plutonium (W-Pu)	0	94	5.3	0.7	0

*Plutonium recovered from pressurised water reactor fuel (3.2% U^{235}) with burnup 33gwd/t

In a second scenario, the inert matrix assemblies could be kept in the reactor for another 879 days i.e. twice as long as the standard assemblies. Over an irradiation period of 2 x 879 days approximately 46 kg Pu are destroyed. On average, over 879 days 23 kg Pu is destroyed. Using the same arguments as above, in a steady situation where no net Pu is produced, approximately 28% (i.e. 9/32) of the core contains Pu/IM assemblies. Notice in this latter scenario, keeping the inert matrix in the reactor for a further three cycles increases the amount of Pu burnt only from 40 kg to 46 kg. Clearly more Pu would be burnt if after three cycles irradiation, fresh Pu/IM assemblies were substituted since over the next three years irradiation another 40 kg of Pu will be burnt instead of only 46-40 = 6 kg! This does mean, however, that larger quantities of Pu are present in the spent inert matrices i.e. 20 rather than 8 kg Pu per ton of inert matrix.

Calculational details

The calculations were made using the point depletion code ORIGEN2 [3] and checked independently with RADONN [4]. The one group cross section library used, PWRUS.lib [3] as that for a standard pressurized water reactor with 3.2% ^{235}U initial fuel enrichment, power level of 37.5 MW/tonne, and burn-up of 33 GWd/tonne (achieved after 879 EFPD-effective full power days). Details of the calculation have been given elsewhere [5].

3

Pu/Inert Matrix irradiation in PWR neutron Spectrum

We consider the irradiation of an inert matrix based fuel containing 10 w/o reactor grade Pu (R-Pu) in a PWR. It is also assumed that the presence of the inert matrix plus fissile material does not disturb the neutron spectrum of the reactor (in the next section the variation of k_∞ for this fuel is considered). The results of an irradiation over three cycles together with extended irradiation over six and seven cycles are shown in Fig. 3.17 and summarized in Tab. 3.13 for the plutonium isotopes. Here the masses of isotopes present per tonne of inert matrix are given at various irradiation times.

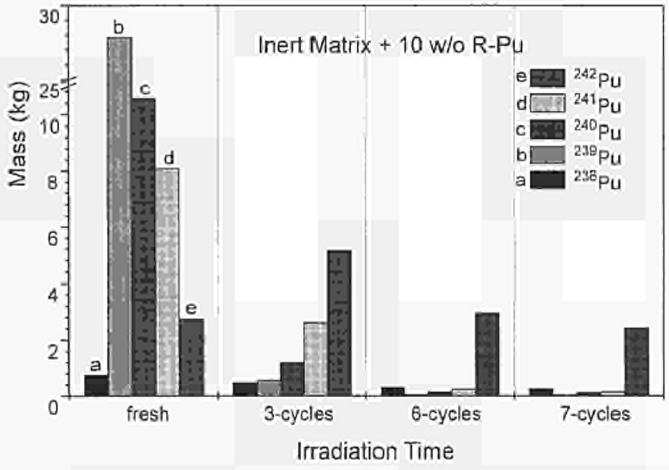

Fig. 3.17 Evolution of an inert matrix containing 10 w/o Pu in the neutron spectrum of a PWR (3 cycles = 879 EFPD). Densities of the inert matrix is assumed to be half of that of the standard fuel.

In Tab. 3.13 results of an irradiation using weapons grade Pu (W-Pu), with composition given in Tab. 3.12, rather than R-Pu, are also given.

Tab. 3.13 Pu isotopic masses in 0.5 tonne of matrix: in fresh fuel, and after 3, 6, and 7 cycles in a PWR (3 cycles = 878 EFPD). Fresh fuel contains 10 w/o R-Pu.

	fresh	3 cycles	6 cycles	7 cycles
total W-Pu	50kg	7.9kg	2.4kg	1.9kg
total R-Pu	50kg	10.0kg	3.8kg	3.1kg

Although the amount of Pu burnt increases with irradiation time (after 7 cycles 94% of the Pu has been destroyed), the rate at which it is being burnt is decreasing. Hence, over the first 3 cycles 40 kg Pu is burnt. Over the next three cycles only 6 kg is burnt. In an additional cycle only 0.7 kg is burnt.

Criticality Aspects of Pu/Inert Matrix Fuel

In the above calculations it was assumed that the presence of inert matrix based fuel pins did not disturb the neutron flux in the reactor. A necessary condition for this to be the case is that the infinite neutron multiplication k_∞ for the standard and inert matrix based fuels are not too different. In this section we consider k_∞ variations from the irradiation of standard and inert matrix based fuels.

In Fig. 3.18. the variation of k_∞ of the standard fuel configuration (described in the previous section) of 3.2% ^{235}U in a natural U matrix is shown over three cycle (i.e. 879 days).

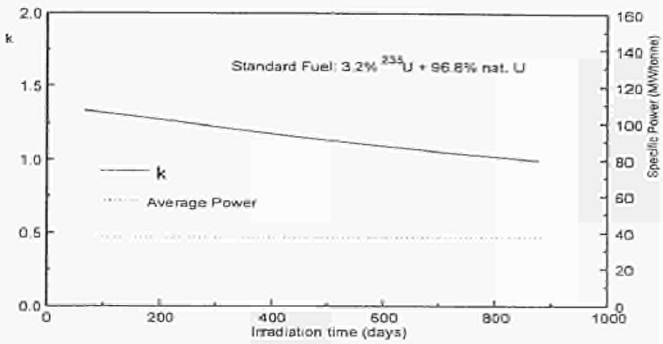

Fig. 3.18 Variation of k_∞ and average power with time for a standard PWR fuel.

Also shown is the average thermal power generated. The variation of k_∞ of an inert matrix containing 10 w/o W-Pu and in a neutron flux of the LWR is shown in Fig. 3.19. The irradiation time extends to 2000 days corresponding to 7 cycles of the LWR. During this time k_∞ from about 1.4 to 0.4 can be seen. After about 900 days irradiation the inert matrix plus fissile material becomes subcritical. Although $k_\infty < 1$, the Pu/IM assemblies still produce power since the multiplication factor $M \infty 1/(1-k_\infty)$.

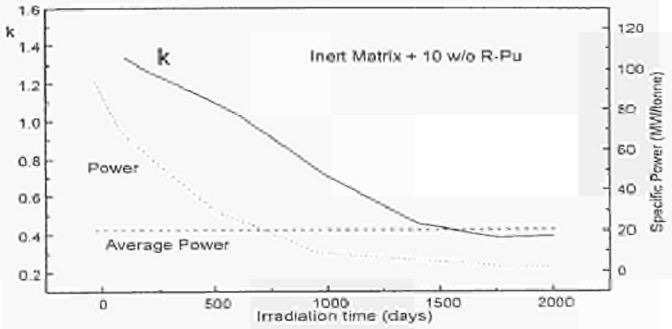

Fig. 3.19 Variation of k_∞ and power with time for inert matrix based R-Pu fuel during extended irradiation in a PWR neutron spectrum.

How can such an irradiation be accomplished within a LWR with a standard fuel life of 879 days? One possible scheme is to consider the core composed of three regions as shown in Fig. 3.20.

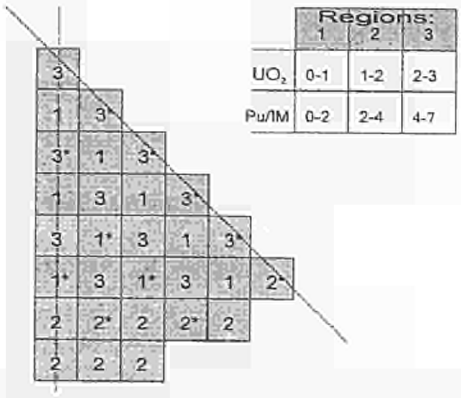

Fig. 3.20 Equilibrium cycle loading pattern for standard UO_2 and Pu/IM fuel assemblies in a PWR. Regions of the core are denoted 1, 2, and 3 and contain fresh, once burnt, and twice burnt standard assemblies. Regions denoted 1, 2*, and 3* contain fresh, once burnt, and twice burnt Pu/IM assemblies.*

In steady operation of the reactor, after each cycle (293 days), one third of the UO2 fuel assemblies (i.e. those which have been in the reactor for 879 days) from positions 3 in Fig. 3.20 are removed from the reactor core and replaced by fresh fuel in positions 1. Fuel assemblies in regions 1 and 2 are moved to regions 2 and 3 respectively. Similarly with the Pu/IM assemblies for a three cycle irradiation. For a six cycle irradiation, the Pu/IM assemblies stay in regions 1, 2, and 3 for two cycles each. For a seven cycle irradiation, the Pu/IM assemblies stay in regions 1 and 2 each for two cycle and in region 3 for three cycle.

The above heterogeneous core layout cannot be investigated with a zero dimensional code such as ORIGEN2. However, an approximate treatment of such a heterogeneous core can be made by considering a homogeneous core containing fuel at different stages of irradiation. Hence a standard core (or a Pu/IM core, three cycle irradiation) can be considered as containing fuel - one third of which is fresh, one third has been irradiated for 293 days and one third irradiated for 586 days. The values of k_∞ for the UO_2 and Pu/IM fuels over one cycle (293 days) given in Fig. 3.21 show generally good agreement. Initially, the value of k_∞ for the Pu/IM fuel is about 10% higher than that for the standard fuel. This could be compensated for, however, by the use of a burnable poison.

For the extended irradiations, the Pu/IM fuel is considered to be in the reactor for seven cycles (≅ 2000 days). As described above, the core can be considered as containing a homogeneous mixture - one seventh of which is fresh, one seventh irradiated to 293 days, one seventh irradiated to 586 days, etc. The results of seven cycle irradiations using R-Pu and W-Pu are shown in Fig. 3.21. It can be seen that the variations in k_∞ are

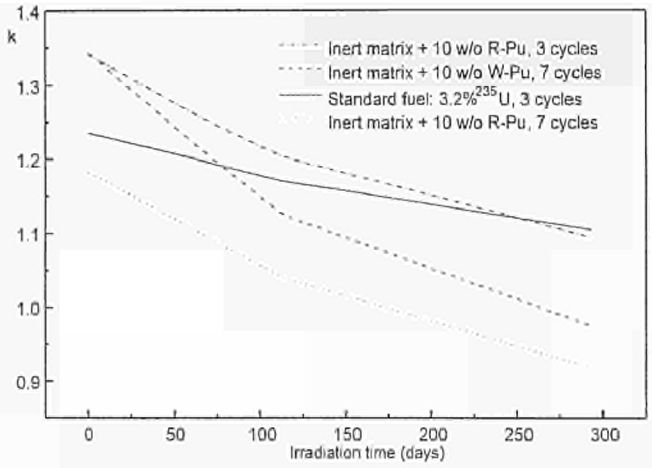

Fig. 3.21 Comparison of k_∞ for standard and inert matrix based fuels in a PWR neutron spectrum accounting for periodic refuelling of fuel bundles.

still relatively large indicating that the use of a PWR neutron spectrum is not a good approximation here.

Conclusions

A strategy is described whereby standard UO_2 fuel assemblies are placed together with Pu/IM fuel assemblies in a PWR such that no net Pu is generated. The amount of Pu generated from the fertile ^{238}U in the standard fuel is equal to the amount burnt in the inert matrix. Following discharge, spent UO_2 fuel is reprocessed to obtain the Pu which is then used to fabricate fresh inert matrix fuel. Spent inert matrix fuel is not reprocessed. Two options are available for burning Pu in the inert matrix: either one can maximize the absolute amounts of Pu which are burnt or one can maximize the burning rates.

Maximizing the amounts of Pu burnt requires an extended irradiation and results in minimum levels of the Pu in the spent inert matrix fuel. A zero net production of Pu requires that approximately 28% of the fuel assemblies to be inert matrix based. The spent inert matrix fuel contains approximately 3 kg Pu in 0.5 tonne of inert matrix (which has the same volume as 1 tonne of standard fuel).

Maximizing the burning rates occurs in a single 3-cycle irradiation, and results in higher levels of Pu in the spent matrix. A zero net production of Pu requires that only 18% of the fuel assemblies are inert matrix based. The spent inert matrix fuel in this case contains approximately 10 kg Pu in 0.5 tonne of inert matrix.

An example of the equilibrium cycle loading pattern for a reactor core containing 180 fuel assemblies in which standard fuel is present in the reactor for 3 cycles whereas the Pu/IM fuel is present for up to 7 cycles is described. An analysis of the infinite neutron multiplication factor k_∞ for homogenous cores containing Pu/IM material at various stages of irradiation in the range of 1-7 cycles shows that extended irradiation results in large variations of reactivity. Over three cycles, however, the reactivity of both the standard and

inert matrix based fuels are fairly similar. The initially higher values of for the Pu/IM fuel can be compensated by the use of a burnable poison. In addition, one may be able to accommodate such fuel within the core without significantly disturbing the Doppler effect since 82% of the core still consists of standard assemblies.

References

[1] J. Magill, C. O'Carroll, P. Gerontopoulos, K. Richter, J. van Geel; *Advantages and Limitations of Thorium Fuelled Energy Amplifiers*, Proceedings of the technical committee meeting on Unconventional Options for Pu Disposition, Obninsk, Nov., 7-11 1994, IAEA to be published

[2] Garwin, R. L., Grubb, M., Mantale, E. (Editors); *Managing the Plutonium Surplus: Applications and Technical Options*, Kluwer Academic Publishers, Netherlands, 1994

[3] Croff, A. G.; *ORIGEN2: A Versatile Computer Code for Calculating the Nuclide Composition and Characteristics of Nuclear Materials*, Nucl. Tech. **62** (1983) 335-353

[4] Magill, J. and Pel, D., *RADONN: – A Software Package for Radionuclide Analysis*, in EUR 15741 EN (1994), Annual Report 1993, Institute for Transuranium Elements, Karlsruhe

[5]. Magill, Hj. Matzke, G. Nicolaou, P. Peerani, J. van Geel; *A Once Through Scheme for Weapons Grade Pu Disposition in LWR´s: Proliferation and Criticality Aspects*, Technical Committee Meeting on the Recycling of Plutonium and Uranium in Water Reactor Fuels, U. K. 3-7 July 1995, IAEA, to be published

4. Spent Fuel Characterization in View of Long Term Storage

Introduction

Long term storage of spent fuel without reprocessing is an option followed in some Member States of the European Union.

The work performed by the Institute in this area has therefore the objective to characterize spent fuel with respect to its behaviour under long term storage conditions, to develop instrumentation to determine the actinide contents of spent fuel, to determine the evolution of the radiotoxicity as a function of time and to investigate corrosion and leaching behaviour of spent fuel under realistic conditions.

Within this overall objective, the Institute has continued work during 1995 in three major areas as follows:

- determination of oxidation, corrosion and leaching behaviour of spent fuel,
- interaction of fuel with structural materials and
- non destructive assay of spent fuel.

The results obtained during 1995 are described in the following sections.

4.1 Characterization of Spent Fuel

4.1.1 Study of UO_2 corrosion in carbonate and chloride solutions by electrochemical techniques

Introduction

Extensive electrochemical measurements have been made on natural (non-irradiated) UO_2 and on SIMFUEL to determine the mechanisms of dissolution or reprecipitation and quantification of the rate-determining steps [1-3]. The interest in verifying these findings is of importance for determining or modelling the effects of ground-water in contact with irradiated fuel in final storage conditions. Shoesmith et al. [4-6] carried out an examination of natural UO_2 electrodes in water, and of the effects of α and γ-sources on the natural UO_2 electrode. Since then this group has prepared active CANDU fuel electrodes for glove-box work [7] and has confirmed their previous findings. Due to the lack of an appropriately designed electrode, higher burn-up and activity levels of irradiated PWR fuel remain to be examined by electrochemical means.

We used both electrochemical measurements, stationary (potential-time) and quasi-stationary (AC impedance) as well as transient techniques (cyclic voltammetry/polarization curves), to assess the reactions and confirm the leach rates measured and electron-optically examined under the Waste Management programme.

Theoretical consideration

The basis for electrochemical determination of corrosion rates is the relationship between measured current density i and potential E or polarization E_p = E - E_{corr} (E_{corr}: free corrosion potential) in the form [8]

$$i = i_{corr} \cdot e^{\left(\frac{\ln 10}{b_a} E_p\right)} \cdot E_p - e^{\left(\frac{-\ln 10}{b_c} \cdot E_p\right)} \cdot E_p \qquad (1)$$

The corrosion current i_{corr} can be obtained by extrapolation of anodic, b_a, and cathodic, b_c, Tafel lines to the corrosion potential or by measurement of the polarization resistance R_p which is defined as

$$R_p = \left(\frac{dE_p}{di}\right)_{E_p = 0} \qquad (2)$$

Differentiation of expression (1) gives:

$$\frac{di}{dE_p} = i_{corr} \cdot \ln 10 \cdot \frac{1}{b_a} e^{\left(\frac{\ln 10}{b_a} E_p\right)} + \frac{1}{b_c} e^{\left(\frac{-\ln 10}{b_c} E_p\right)} \qquad (3)$$

At the corrosion potential this reduces to the well-known Stern-Geary relations [9, 10]:

$$\left(\frac{di}{dE_p}\right)_{E_p} = i_{corr} \cdot \ln 10 \cdot \left(\frac{1}{b_a} + \frac{1}{b_c}\right) = \frac{1}{R_p} \qquad (4)$$

$$i_{corr} = \frac{B}{R_p}; \qquad B = \frac{b_a \cdot b_c}{\ln 10 \cdot (b_a + b_c)} \qquad (5)$$

For higher anodic potentials E_p > 60 mV the second exponential term in Equation (1) can be neglected, and Equation (3) reduces to

$$\frac{di}{dE_p} = i_{corr} \cdot \frac{\ln 10}{b_a} \cdot e^{\left(\frac{\ln 10}{b_a} \cdot E_p\right)} \qquad (6)$$

In this case it is possible to derive the relationship between the measured current density and the differential polarization resistance (R_{dp}) from Equations (1) and (6) by eliminating the exponential term, i.e.

$$\frac{1}{R_{dp}} = \frac{1n\ 10}{b_a} \cdot i \qquad (7)$$

If $E_p < -60$ mV the relation

$$\frac{1}{R_{dp}} = \frac{-1n\ 10}{b_c} \cdot i \quad \text{is valid.} \qquad (8)$$

In potentiostatic experiments it is possible to determine the Tafel slopes b_a and b_c and also the composite Tafel parameter B by measuring the current densities and impedance spectra at various applied potentials. The advantage of this method is that the iR-drop which mainly occurs at the UO_2 bulk resistance, does not have to be taken into consideration. The main limitation of this method lies in the accuracy of the determination of R_{dp}.

Electrochemical equipment and testing

The polarization curves/cyclic voltammetry were carried out using a Sycopel Autostat 251 and the impedance measurements were performed with a CAPCIS Voltech CV 2001 frequency response analyser (FRA) and CAPCIS March interface (potentiostat). Both instruments were linked to a 386 personal computer for data collection, evaluation and presentation. Additional equivalent circuit modelling of the results were carried out using software (IMPEDANZ).

Rest potential measurements were measured with either a Solartron 7151 (discretely) or logged continuously with a Linseis LSB 36II/14 data-logger to the PC for subsequent presentation of results.

In making these impedance measurements, there are substantial effects due to the potentiostat's interaction in the high frequency range (above 1 kHz) where it disturbs the current measurements from the amplifier [11]. These disturbances were analysed and quantified. They could be minimized by the measurement technique itself and also corrected from the measured total impedance.

Further problems in the high frequency region were caused by the high-impedance reference electrodes. This problem was solved by using a dual reference electrode consisting of an inert Pt-wire with a capacitor (0.1 μF) in parallel to the reference electrode [12, 13]. At high frequencies the capacitor short circuits the reference electrode and the sinusoidal applied potential (reference electrode vs working electrode) is imposed through the inert wire. This dual system was tested with very good results for various reference electrodes.

A further effect was found while performing experiments in the concrete cell due to the fact that the hot-cell requires leads of approximately 10 m from the electrode to the potentiostat. Only 1 m inside the cell is effectively protected by the 'Faraday cage' of the inner steel caisson of the hot-cell. The deviation of the measured spectra from the expected ideal behaviour could be simulated by a capacitor of about 3 nF between reference and working electrode. An example of the various effects is shown in Fig. 4.1.

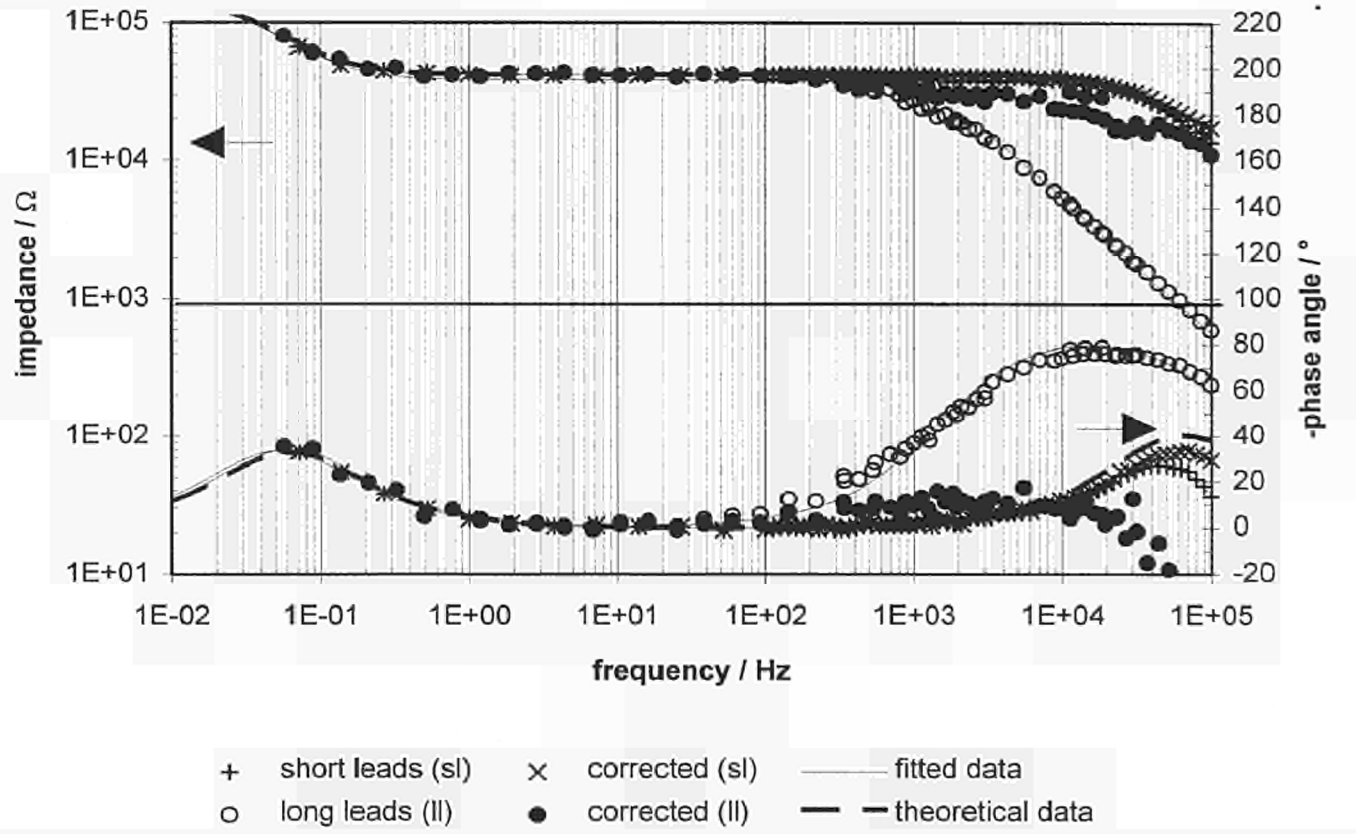

Fig. 4.1 The effect of lead length on impedance spectra is shown by comparing measurements performed with short (sl) and long leads (ll) on a dummy cell.

It can be seen that impedance data collected at frequencies higher than 1 kHz have to be treated very carefully even in the case of hot-cell experiments. The low frequency domain, where corrosion processes are observable, are not affected by these disturbances. The measurements are limited in the 10 mHz - 100 mHz region by the sensitivity of the frequency response analyser (FRA) due to the high impedance values of the electrochemical system at these low frequencies. Reliable measurements in the concrete cell could therefore be obtained from 10/100 mHz up to 1 kHz with the equipment.

Cyclovoltammetry

After preparing and polishing electrodes of natural UO_2 or spent fuel, polarization curves were performed starting with a five minutes pre-cathodization at -2000 mV to reduce the surface to stoichiometric UO_2, and then scanning at a maximum rate of 0.3 $mV.s^{-1}$ up to +1000 mV and then back to -2000 mV. Due to the considerable potential drop across the UO_2 electrode, given its high resistivity, the true potential at the interface is proportionally less. This is given by

$$E = E_{appl} - I \cdot R_{el}$$

where E_{appl} represents the applied potential, I the overall current and R_{el} the electrode resistance.

This in turn, means that the scan rate at the electrode is reduced in proportion to the potential drop ($I \cdot R_{el}$).

These measurements were carried out with natural UO_2 in 0.01 M $NaHCO_3$, 0.1 M NaCl and 95% saturated NaCl solutions to simulate ground-waters and salt brines which may appear in a final storage repository. An example of a measurement obtained in 95% saturated NaCl solution is shown in Fig. 4.2.

On the anodic scan the shallow slope of the 'Tafel line' in the potential range from about -50 mV_{SHE} to +600 mV_{SHE} (oxidation of UO_2 to UO_{2+x}) is surprising. This behaviour was only observable in concentrated salt solutions. In dilute salt solutions these slopes were steeper and also the dissolution reaction, indicated by a strongly increasing current density at lower anodic potentials (above +300 mV_{SHE}).

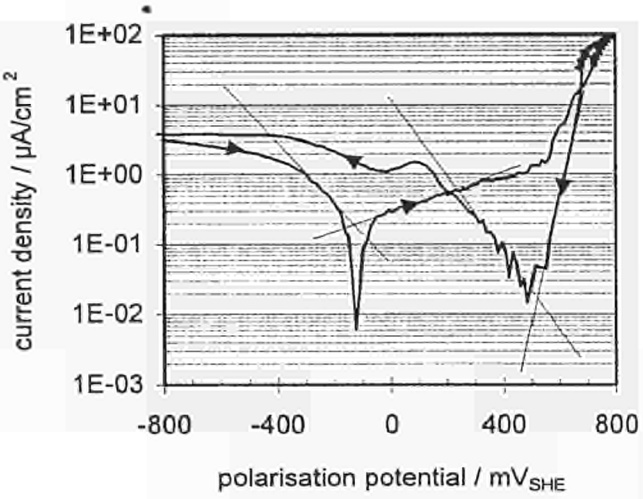

Fig. 4.2 Cyclic voltammogramm of polished natural UO_2 in 95% saturated NaCl solution (max. scan 0.3 $mV.s^{-1}$; initial pH 7.; $[O_2]$ = 8.8 ppm; 22 °C). The straight lines represent 'Tafel lines' which were used to determine b_a, b_c, B, E_o and i_o.

On the reverse scan (Fig. 4.2) an additional reduction peak at +100 mV_{SHE} is also observable. Both of these observations indicate an alternative dissolution behaviour in highly concentrated salt solutions. In Tab. 4.1 the results are summarized. It was found that the current densities were all of the same magnitude (about 0.1 $\mu A/cm^2$) and the samples were mainly attacked at grain boundaries.

Potentiostatic experiments

AC impedance measurements were made approximately 5 minutes after immersion in the solution and then holding it potentiostatically at that potential while superimposing a small (20 mV to 40 mV) sine wave potential in the range from 100 kHz down to 10 mHz frequency. Further impedance tests were performed at various potentials progressing from cathodic to anodic polarization. The electrode polarizations were selected on the basis of previously performed polarization sweeps. In this way the electrode was examined in various states of reduction or oxidation/passivation or dissolution. Each AC impedance frequency sweep was

Tab. 4.1 Current densities and potentials resulting from cyclic voltammetry performed on natural UO_2 in aqueous solutions at 22 °C.

electrolyte	pH	$[O_2]$ ppm	upward				downward			
			b_a ↗ mV	B ↗ mV	$E_{i=0}$ ↗ mV_{SHE}	i_o ↗ $\mu A/cm^2$	b_a ↘ mV	B ↘ mV	$E_{i=0}$ ↘ mV_{SHE}	i_o ↘ $\mu A/cm^2$
0.01 M $NaHCO_3$	8,4	8,8	160 ± 50	39 ± 6	41 ± 17	0.1 ± 0.1	86 ± 10	31 ± 4	318 ± 43	0.12 ± 0.07
0.1 M NaCl	3,6	8,5	220 ± 60	44 ± 6	95 ± 16	0.1 ± 0.1	66 ± 1	23 ± 3	460 ± 52	0.1 ± 0.5
0.1 M NaCl	10,4	8,5	160 ± 40	34 ± 5	-87 ± 15	0.15 ± 0.06	100 ± 4	31 ± 3	432 ± 34	0.1 ± 0.3
95% sat. NaCl	7,1	7,4	710 ± 230	75 ± 10	-132 ± 21	0.19 ± 0.03	56 ± 3	19 ± 2	518 ± 36	0.02 ± 2
95% sat. NaCl	10,3	7,3	230 ± 30	49 ± 4	-89 ± 12	0.11 ± 0.04	117 ± 5	35 ± 2	387 ± 20	0.05 ± 0.05

performed at the selected potential following a 5 to 10 minutes stabilization time. Typical steady state polarization curves (i vs E and R_{dp}^{-1} vs E) resulting from experiments with a high burn-up fuel (79 GWd/tU) in 0.1 M NaCl solution are shown in Figs. 4.3 and 4.4.

A comparison of results obtained from current and impedance measurements performed on non-irradiated and irradiated fuels is given in Tab. 4.2.

In Figs. 4.3 and 4.4 both 'Tafel lines' used for calculating the parameters and the theoretical curves based on these data are outlined. Dotted lines represent error limits for corrosion potentials, and corrosion current density/reciprocal polarization resistance. The errors are rather high because the data are obtained from an extrapolation in the logarithmic scale. The i_{corr} values resulting from potentiostatic

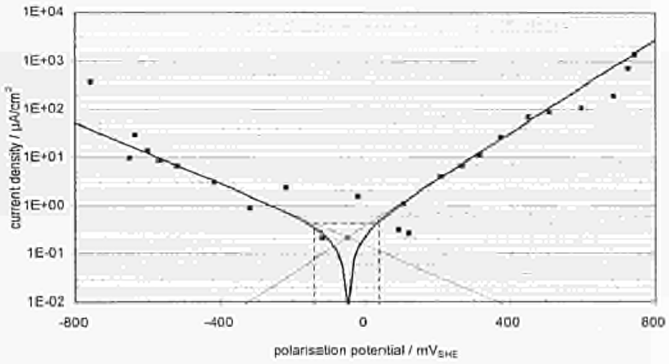

Fig. 4.3 Steady state polarization curve (i vs E) obtained from irradiated UO_2 fuel (79 GWd/tU) in 0.1 M NaCl solution (initial pH 9.9; [O_2] approximately 2 ppm; 26 °C). The dotted lines represent the error limits of corrosion potential E_{corr} and corrosion current density i_{corr}. Full lines represent a theoretical curve obtained from Equation (1).

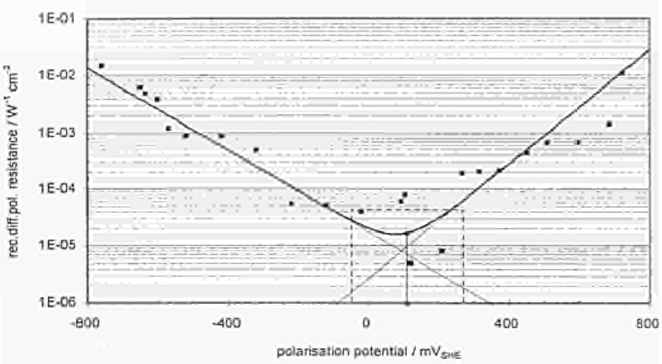

Fig. 4.4 Potential dependence of the reciprocal differential polarization resistances R_{dp}^{-1} obtained from irradiated UO_2 fuel (79 GWd/tU) in 0.1 M NaCl solution (initial pH 9.9; [O_2] approximately 2 ppm; 26 °C). The dotted lines represent the error limits of the corrosion potential E_{corr} and the reciprocal polarization resistance R_{dp}^{-1}. Full lines represent a theoretical curve obtained from Equation (3) combined with Equation (5).

Tab. 4.2 Corrosion currents and Tafel parameters obtained from potentiostatic current and impedance measurements on natural UO_2 and spent fuels at room temperature.

sample	potentiostatic current density measurements				impedance measurements: 1) $R_{dp}^{-1} = f(E_p)$				2) $i = f(R_{dp}^{-1})$	
	b_a mV	B mV	E_{corr} mV_{SHE}	i_{corr} µA/cm²	ba mV	B mV	E_{corr} mV_{SHE}	i_{corr} µA/cm²	b_a mV	B mV
nat. UO_2, 3% Na_2CO_3, pH 10.8, 6 ppm O_2	85 ± 8	26 ± 6	122 ± 75	0.01 ± 0.03	135 ± 31	45 ± 11	131 ± 81	0.2 ± 0.3	81 ± 7	31 ± 2
nat. UO_2, 0.01 M $NaHCO_3$, pH 8.4 , 9 ppm O_2	141 ± 39	35 ± 10	199 ± 78	0.03 ± 0.03	139 ± 13	47 ± 6	367 ± 63	0.3 ± 0.3	144 ± 10	32 ± 9
nat. UO_2, 0.1 M NaCl, pH 3.6, 9 ppm O_2	125 ± 49	32 ± 8	298 ± 85	0.004 ± 0.005	106 ± 72	33 ± 17	408 ± 199	0.02 ± 0.05	80 ± 3	24 ± 1
nat. UO_2, 0.1 M NaCl, pH 10.4, 9 ppm O_2	160 ± 76	38 ± 11	220 ± 89	0.007 ± 0.008	114 ± 116	40 ± 33	493 ± 380	0.2 ± 0.5	129 ± 30	31 ± 6
nat. UO_2, 95% sat. NaCl, pH 7.1, 8 ppm O_2	340 ± 119	63 ± 17	211 ± 77	0.05 ± 0.03	518 ± 1190	95 ± 104	212 ± 254	0.2 ± 0.2	91 ± 18	30 ± 6
nat. UO_2, 95% sat. NaCl, pH 10.3, 7.3 ppm O_2	314 ± 234	53 ± 20	54 ± 113	0.02 ± 0.02	417 ± 371	115 ± 70	341 ± 254	1 ± 1	113 ± 5	23 ± 7
UO_2 (6.85%; 26.4 GWd/tU), 3% Na_2CO_3, pH 11.2, » 2 ppm O_2	89 ± 27	26 ± 8	239 ± 88	0.2 ± 0.4	100 ± 37	35 ± 11	307 ± 113	2 ± 3	126 ± 10	33 ± 7
UO_2 (def., reimp., 20-25 GWd/tU), 3% Na_2CO_3, pH 11.2, » 2 ppm O_2	131 ± 15		155 ± 50	0.9 ± 0.8	129 ± 43			0.8 ± 1	143 ± 17	
UO_2 (68 GWd/tU), 3% Na_2CO_3, pH 11.2 , » 2 ppm O_2	120 ± 330	42 ± 96	172 ± 176	0.4 ± 0.5	142 ± 515	53 ± 164	301 ± 784	4 ± 10	128 ± 24	25 ± 3
UO_2 (79 GWd/tU), 0.1 M NaCl, pH 9.9 , » 2 ppm O_2	207 ± 34	54 ± 12	-50 ± 90	0.2 ± 0.2	199 ± 184	50 ± 28	110 ± 160	0.9 ± 1	296 ± 80	19 ± 5
MOX (21.1 GWd/tU), 3% Na_2CO_3, pH 11.2 , » 2 ppm O_2	281		-8 ± 50	1.4 ± 8	212				233	

current density measurements should be more reliable than those taken from impedance measurements due to the fact that in the former case only the potential has to be corrected for the potential drop across the bulk of the electrode while the current could be measured directly. The differential polarization resistances measured (Fig. 4.4) in the region around the corrosion potential are rather high (100 kΩ to 1 MΩ taking into account a surface area of 0.1 cm^2) however, and are reaching the sensitivity limits of the impedance spectrometer used. Nevertheless the same tendency of the corrosion behaviour as in the current density measurements was found. The lowest corrosion currents arise in dilute NaCl solutions followed by carbonate and saturated NaCl solutions in the case of natural UO_2. The values found were in the 0.01 $\mu A/cm^2$ range. Using spent fuel electrodes the resulting currents were a factor of 10 to 100 higher and lie in the 0.2 $\mu A/cm^2$ to 1 $\mu A/cm^2$ range. A similar behaviour was also found by comparing the current densities resulting from cyclovoltammetric experiments. The values are additionally in good agreement with literature data.

Shoesmith et al. [14] used a surface roughness factor of 3 to convert measured currents to current densities. This means that the current densities given in Tabs. 4.1 and 4.2 would be reduced by one third. Using this assumption they would give corrosion rates for non-irradiated material in the range of 8.55 $ng \cdot cm^{-2} \cdot d^{-1}$ to 302 $ng \cdot cm^{-2} \cdot d^{-1}$ for carbonate-containing solutions. For granite groundwater values of 0.5 $ng \cdot cm^{-2} \cdot d^{-1}$ and 3.53 $ng \cdot cm^{-2} \cdot d^{-1}$ have been reported [14].

Assuming also a surface roughness factor of 3 and using a conversion factor of 106.5 $g \cdot A^{-1} \cdot d^{-1}$ to calculate corresponding corrosion rates from the current densities given in Tab. 4.2 limits of 3.6 and 10.7 $ng \cdot cm^{-2} \cdot d^{-1}$ for natural UO_2 in carbonate-containing solutions were found. For dilute sodium chloride solutions the corresponding values were 1.4 and 2.5 $ng \cdot cm^{-2} \cdot d^{-1}$ and for 95% saturated solutions they range between 7.1 and 17.8 $ng \cdot cm^{-2} \cdot d^{-1}$. In case of irradiated fuel significantly higher corrosion rates between 71 and 370 $ng \cdot cm^{-2} \cdot d^{-1}$, were found.

More reliable data for the composite Tafel factor B were found using the linear relation between i and R_{dp}^{-1} (see Equations 7 and 8) for their determination. These values are only slightly influenced by the different types of samples and are insensitive to the dissolution mechanism occurring. A value 30 ± 5 mV seems to be a suitable choice to estimate corrosion currents of UO_2-fuels from impedance measurements at free corrosion potential during long-term experiments (see Equation 5).

Long-term experiments

Rest potential measurements versus a Ag/AgCl or saturated calomel electrode were taken on non-irradiated and irradiated UO_2 fuel electrodes directly after placing the working electrode in solution and connecting it. The Solartron 7151 or Linseis LSB 36 II equipment were capable of logging measurements at any desired frequency (initially every 10 s, after 12 h every 10 minutes). Additional impedance spectra were taken at various times. Measurements were carried out in aqueous solutions for immersion times of up to 9.5 weeks. Corrosion current densities estimated from impedance spectra and potential curves are shown in Figs. 4.5 and 4.6.

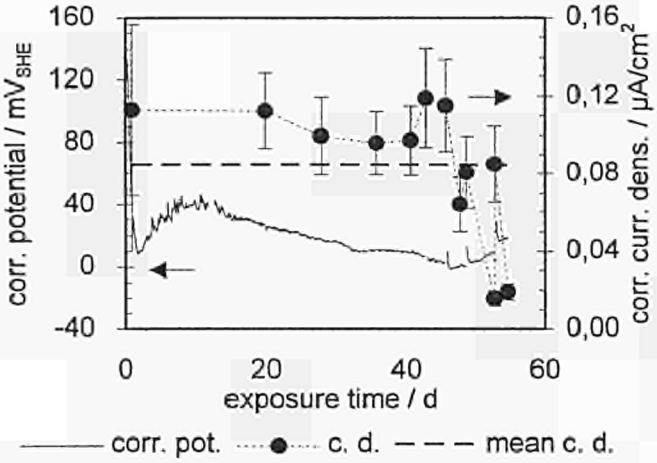

Fig. 4.5 Free corrosion potential and corrosion current densities estimated from impedance spectra of natural nonirradiated UO_2 in 0.01 M $NaHCO_3$ solution (pH 8.8; 21 °C; $[O_2]$ = 9.1 ppm) [c. d.: current density].

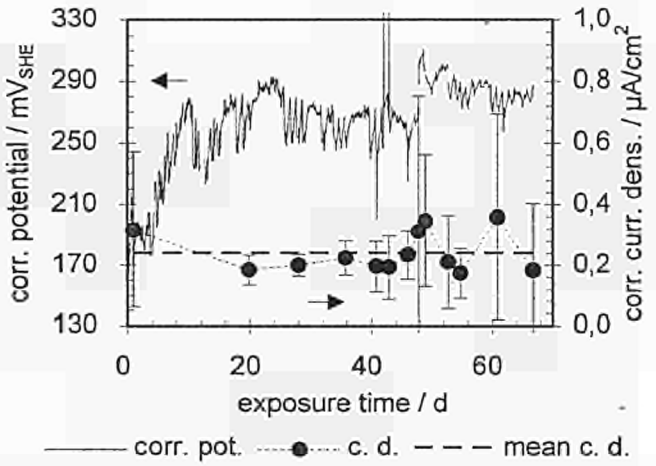

Fig. 4.6 Free corrosion potential and corrosion current densities estimated from impedance spectra of irradiated UO_2 fuel (8.26%^{235}U burn-up 53.1 GWd/tU) in 0.01 M $NaHCO_3$ solution (pH 9.0; 25 °C; $[O_2]$ approximately 2 ppm) [c. d.: current density].

Comparing these data the most striking difference lies in the 200 mV to 250 mV higher corrosion potential for the irradiated fuel (Fig. 4.6). This effect could be caused by H_2O_2 - a result of water radiolysis - causing reduction at the electrode and/or by fission products. Moreover the potential curve of the irradiated sample has much more noise than that of the nonirradiated UO_2. This behaviour could be due to a localized attack at inhomogeneities of the sample. Also the overall mean corrosion current density of the irradiated fuel is somewhat higher (approximately a factor 3 more).

From the corrosion currents the expected amount of uranium in solution was calculated and then compared with experimental results obtained by ICP-MS solution analysis (Tab. 4.3). In 0.01 M $NaHCO_3$ solution the expected U-concentration was 2.6 ppm but nothing was found in solution by ICP-MS. For 3% NaCl solution some U was seen but the results only match in case of 3% Na_2CO_3 solutions (see TUAR-94, p. 85).

Tab. 4.3 Comparison of U solution concentrations obtained from an estimation based on electrochemical data and solution analysis by ICP-MS after long-term immersions.

sample	t h	estimated [U] ppm	ICP-MS [U] ppm	E_{corr} . mV_{SHE}
nat. UO_2, 3% Na_2CO_3	521	0,7	0,44	
nat. UO_2, 3% Na_2CO_3	450	1,8	1,76	
nat. UO_2, 3% NaCl	496	20	< 0.01	
nat. UO_2, 3% NaCl	450	55	0,06	
nat. UO_2, 0.01 M $NaHCO_3$	1312	2,6	< blank	0 - 40
UO_2 fuel (8.26% ^{235}U, 53 GWd/tU)	1608	2,1		250 - 300

Carbonate is a relatively strong complexing agent for U specimens in aqueous media. Hence U remains in solution with a high carbonate content as $UO_2(CO_3)_2^{2-}$ and $UO_2(CO_3)_3^{4-}$ complexes. In chloride solutions or solutions with a low carbonate concentration it seems that the oxidation products of UO_2 remain at or on the surface or that a dissolution/precipitation mechanism occurs. Chloride is a relatively weak complexing agent for UO_2. Micrographs taken after the experiment show slight attack (Fig. 4.7) of these samples.

A further indication for the formation of a surface layer, which could block active sites at grain boundaries and pores is found in the observation that the bulk resistance of natural UO_2 and spent fuel samples sometimes increased during immersion in most experiments performed. This effect was also observed in some 3% Na_2CO_3-tested samples.

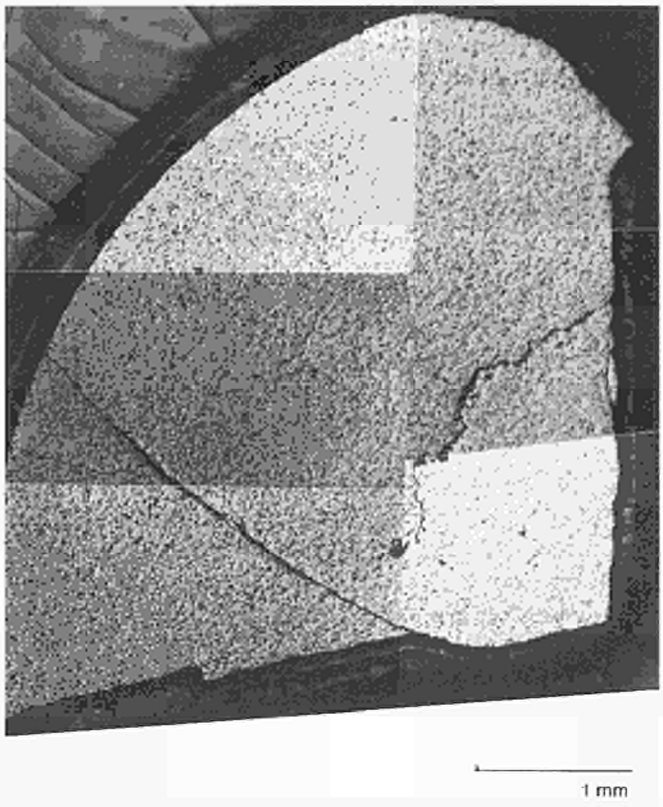

Fig. 4.7 Micrograph of highly enriched (8.26% ^{235}U) UO_2 fuel (burn-up 53.2 GWd/tU) after 69 days immersion in 0.01 M $NaHCO_3$ at free corrosion potential.

References

[1] M. J. Nicol, CRS. Needes, Radiochimica Acta 20 (1975) 585
[2] J. Bruno, I. Casa, Pingdomenach, Radiochimica Acta 44/45 (1988) 11
[3] D. W. Shoesmith, S. Sunder, AECL report -AECL-10488 (1991)
[4] M. G. Bailey, L. H. Johnson, D. W. Shoesmith, Corros. Sci. 25 (1985) 233
[5] S. Sunder, D. W. Shoesmith, L. H. Johnson, M. G. Bailey, G. J. Wallace, Proc. 2nd Int. Conf. on Radioactive Waste Management, Sept. 7-11 (1986), Winnipeg, Manitoba
[7] D. W. Shoesmith, M. G. Bailey, S. Sunder, N. H. Miller, Spent Fuel Workshop '94, Aug. 22-24 (1994), Montebello, Quebec
[8] F. Mansfeld, Corrosion-NACE 32 (1976) 143
[9] M. Stern, A. L. Geary, J. Electrochem. Soc. 104 (1957) 56
[10] F. Mansfeld, Corrosion-NACE 29 (1973) 397
[11] H. Göhr, M. Mirnik, C. A. Schiller J. Electroanal. Chem. 180 (1984) 273
[12] F. Mansfeld, S. Lin, Y. C. Chen, H. Shih, J. Electrochem. Soc. 135 (1988) 906
[13] S. W. Watson, B. W. Madsen, Corrosion 48 (1992) 727
[14] D. W. Shoesmith, S. Sunder, M. G. Bailey, G. J. Wallace, Corros. Sci. 29 (1989) 1115

4.1.2 Oxidation of irradiated UO_2 at low temperatures (< 500 °C)

Long term oxidation tests of irradiated UO_2

Introduction

Oxidation rate experiments of irradiated spent fuel pellet fragments are performed continuously in an autoclave installed in the hot-cells (TUAR-94, p. 96). The

fragments are oxidized in dry air at 268 ± 1 °C for several time intervals and weighed to register their weight gain. The oxidized samples are kept for future X-ray and ceramographic examination in order to determine the influence of the fuel restructuring, porosity and the presence of fission products on the appearing phases and on the oxidation mechanism of the spent fuel. As mentioned in previous reports, the oxidation mechanism for irradiated and unirradiated UO_2 is significantly different (TUAR-93, p. 100-101, TUAR-94, p. 97). In the temperature range 200-300 °C spent fuel oxidizes by rapid growth of U_4O_9 along grain boundaries with, in comparison to unirradiated fuel, delayed (or even no) formation of the phase U_3O_8. As is known, formation of U_3O_8 is strongly undesirable in spent fuel geological repositories, as its 36% volume expansion with respect to UO_2 could dramatically expand small effects initially present in the cladding and thereby increase the fuel area available for leaching.

Results and discussion

In this section, some results from long term oxidation tests, in the form of weight change as a function of time, for two UO_2 and one $(UPu)O_2$ (MOX) spent fuel are represented. The fuel characteristics are listed in Tab. 4.4.

In Fig. 4.8 it can be seen, that no significant difference can be observed in the oxidation rate of two UO_2 spent fuels, with burn-ups of 53.1 and 31.5 GWd/t. Only at oxidation times below 500 h can a slightly more rapid oxidation of the fuel with the higher burn-up be observed. After 3000 h the UO_2 fuel remains with an oxidation level of about O/M = 2.4.

The test is being continued with the aim of determining the second oxidation stage in this temperature range, which would lead to the formation of the U_3O_8 phase (O/M ≅ 2.66). Very interesting, but also a point of concern for the fuel repository, is the higher oxidation rate of MOX fuels compared to UO_2 fuels under the same experimental conditions (Fig. 4.8). The MOX samples, (pellet fragments at the beginning of the test) are partially powdered and exhibit a weight gain of about 3% after an exposure of 800 h in dry air at 268 ± 1 °C, as shown in Fig. 4.8.

Further work

The long term oxidation tests will be continued with representative UO_2 and MOX fuels and will be extended to lower temperatures (around 200 °C) under several oxidizing atmospheres. Some of our already oxidized samples are being examined by optical microscopy and will be analysed also by X-ray diffraction.

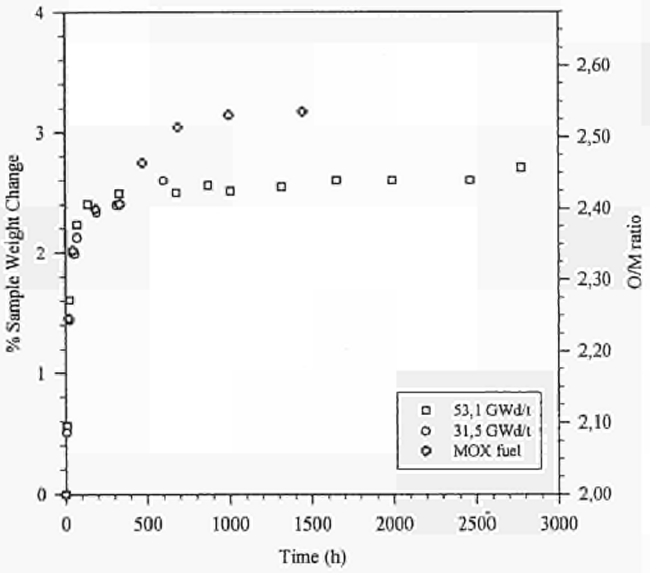

Fig. 4.8 Oxidation of spent fuel pellet fragments in dry air at 268 °C.

Lead shielded X-ray goniometer for microbeam X-ray analysis

A lead shielded glove-box designed for X-ray diffraction and thermogravimetric analysis (see TUAR-93, p. 101-103, TUAR-94, p. 94-96) has been constructed and

	KWU B4	KWU B2	MOX6015
Reactor			
Fuel type	LWR	LWR	LWR
Nominal burn-up (GWd/t)	53,1	31,5	38,8
Fission gas release (%)			9
Initial enrichment (wt% ^{235}U)			0,72
Initial enrichment (wt% ^{239}Pu)	----------	----------	3,2
Initial pellet density (% ID)			94-95
Postirradiation grain size (mm)			5-6
Average linear power (KW/m)	not available	not available	25,3
Irradiation time (EFPD)[a]			877

a: Effective Full Power Days

Tab. 4.4 Fuel characteristics.

installed, as shown in Figs. 4.9 and 4.10. This installation will be used for the phase characterization of irradiated fuel samples.

In parallel, it is planned to equip the goniometer with a microbeam X-ray capillary. Such a collimator condenses the X-ray beam to very small dimensions (below 15 μm), providing an excellent spatial resolution for characterization [7, 8, 9]. In particular, this method can be used for the determination of the eventual oxidation state gradients in the examination of irradiated UO_2 samples.

References

[1] R. E. Einziger, L. E. Thomas, H. C. Buchanan, R. B. Stout; J. Nucl. Mater. **190** (1992) 53-60

[2] L. E. Thomas, R. E. Einziger, H. C. Buchanan; J. Nucl. Mater. **201** (1993) 310-319

[3] R. E. Einziger; Nucl. Technol. **75** (1986) 82-95

[4] P. A. Tempest, P. M. Tucker and J. W. Tyler; J. Nucl. Mater. **151** (1988) 251-268

[5] S. R. Teixeira, K. Imakuma; J. Nucl. Mater. **178** (1991) 33-39

[6] R. E. Woodley, R. E. Einziger, H. C. Buchanan; Nuclear Fuel, **85** (1989) 74-87

[7] D. H. Bilderback, S. A. Hoffman, D. J. Thiel; Science, **263** (1994) 201-203

[8] D. J. Thiel, D. H. Bilderback, A. Lewis; Rev. Sci. Instrum. **64** (1993) 2872-2878

[9] D. H. Bilderback, D. J. Thiel; Rev. Sci. Instrum. **66** (1995) 2059-2063

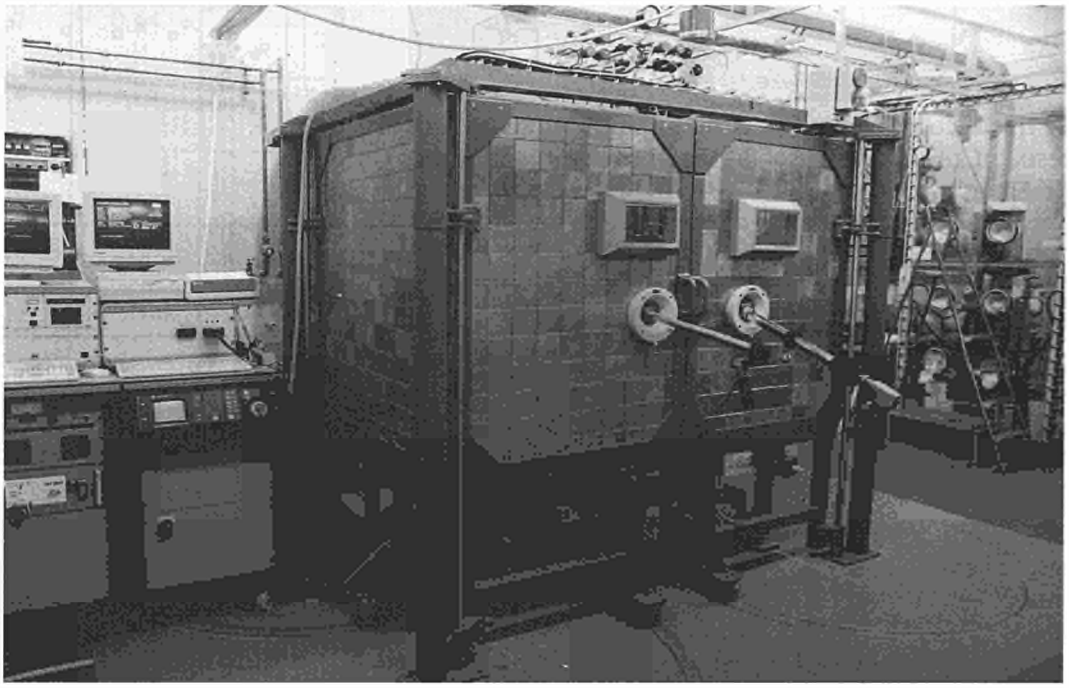

Fig. 4.9
The lead shielded glove-box with the installed X-ray diffractometer and thermobalance.

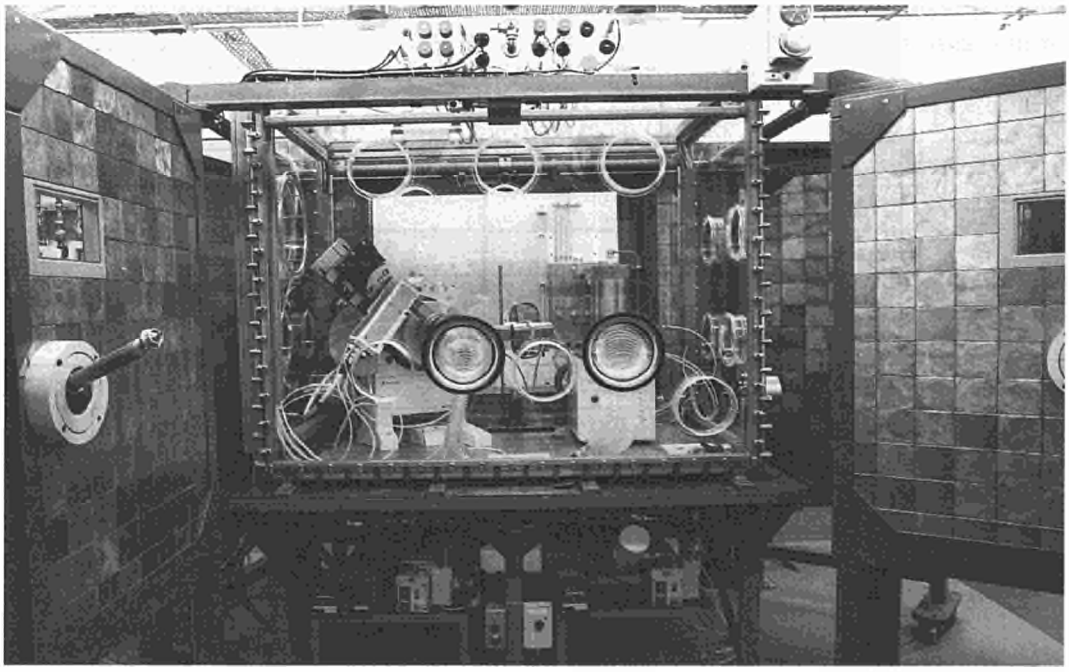

Fig. 4.10
Glove-box with lead walls open to show the installed X-ray diffractometer and thermobalance.

4.1.3 Influence of low temperature air oxidation on the dissolution behaviour of LWR spent fuel

Introduction

In the event of cladding failure in an intermediate repository, contact between spent fuel and air can occur. In this case air oxidation of the fuel is a potential reaction, and it is important to know the influence of the oxidation state of irradiated UO_2 on its dissolution rate should underground water comes into contact with the later phase.

Sequential leaching tests were performed in deionized water at ambient temperature using high burnup (53.1 GWd/t(U)) Light Water Reactor (LWR) spent fuel samples. These samples were oxidized to different O/M ratios, to investigate the effect of low-temperature air oxidation on the dissolution behaviour of LWR spent fuel in water at room temperature.

Experimental

LWR-spent fuel has been used to perform long term oxidation tests [1]. From this material, samples with different O/M ratios were taken to perform leaching tests:

Sample	Sample Weight Change %	O/M
A	2.0080	2.348
B	2.2405	2.389
C	2.5270	2.440

The tests were performed in deionized water (DIW) at room temperature (about 25 °C) in a hot-cell. This temperature was selected assuming that the O/M-ratio is not modified, i.e., further oxidation will not take place or can be neglected. The surface volume ratio S/V was approximately 20.000 m^{-1} (the surface taken corresponds to the geometric surface).

The experimental procedure was as follows:

- The specimens were immersed in 20 ml of DIW in sealed glass bottles, having 50 ml total volume.
- After completion of each intermediate leaching period, the solid specimens were transferred in a new bottle with fresh leachant.
- The empty used bottles were rinsed with 1M HNO_3 and this leachant kept separately for analysis.

The chemical analysis of the leachants was performed by ICP-MS (ELAN 5000, Perkin ElmerSciex), modified in order to handle radioactive samples in a glove-box.

Results

In Fig. 4.11 the ^{238}U concentration normalized to the geometric surface is shown as a function of leaching time. This represents the dissolution behaviour of the matrix. The values obtained are comparable with results published elsewhere [2-6] using similar oxidized materials. The different O/M ratios tested show the same tendency: after an initial relatively high dissolution rate, the uranium concentration in the leachant reaches a plateau. The uranium concentration in the leachants found for the two higher O/M ratios is about two times higher than in the lower oxidized fuel. Ongoing tests using the same material but not oxidized, revealed that the amount of uranium leached is about one order of magnitude lower than oxidized samples.

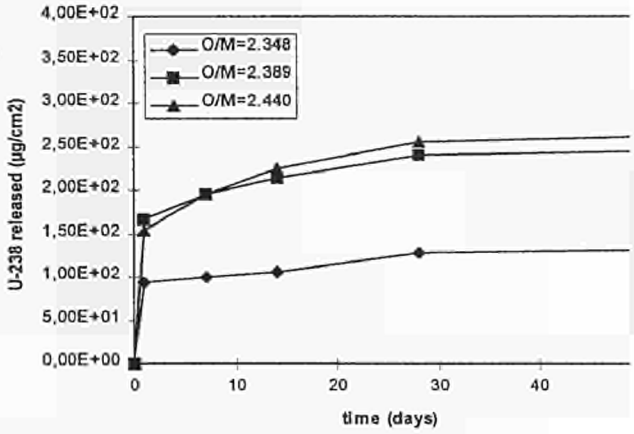

Fig. 4.11 Uranium-238 released vs. time.

In contrast, the measured Pu released (Fig. 4.12) does not show dependence on the dissolution behaviour on the O/M ratio.

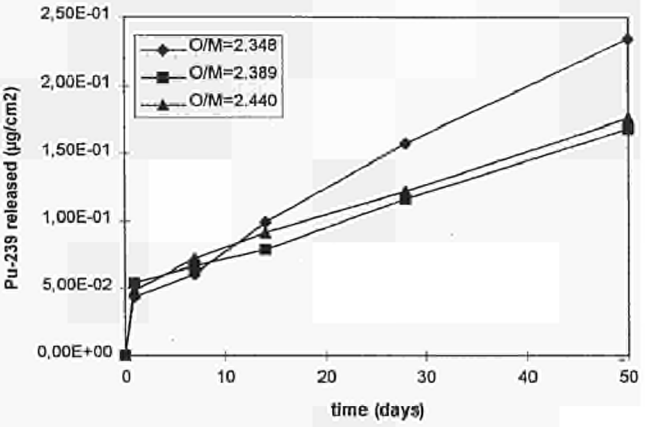

Fig. 4.12 Plutonium-239 released vs. time.

For the dissolution behaviour of the fission products two cases can be distinguished. The first case (see Fig. 4.13),

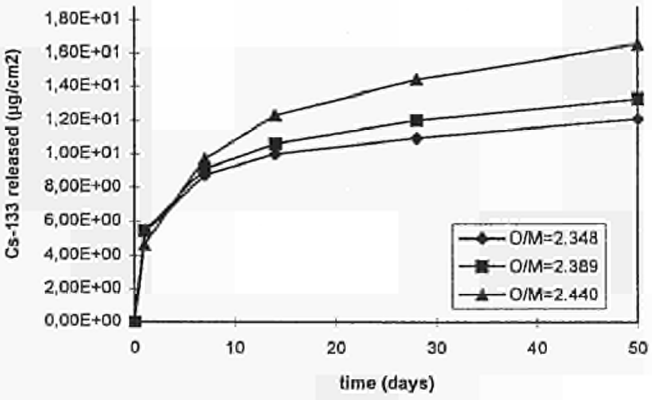

Fig. 4.13 Caesium-133 released vs. time.

represented by ^{133}Cs includes Tc and Mo, and the dissolution behaviour is similar to the matrix with a high dissolution rate at the beginning followed by a plateau.

The second case, represented by ^{138}Ba (see Fig. 4.14), includes Sr also. In this case a slow dissolution rate during the first 15 days is followed by a more rapid rate which is not complete even after 50 days leaching time.

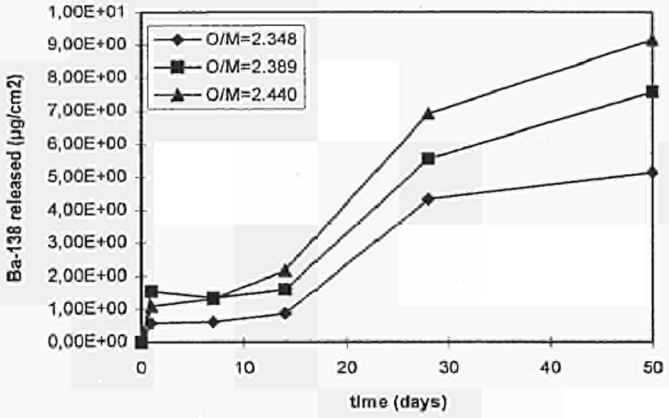

Fig. 4.14 Barium-138 released vs. time.

For the elements analysed (apart from Pu), the overall dissolution rate showed the same behaviour i.e. for higher O/M-ratios a higher leaching rate was observed.

From the geometric surface, already used to calculate the normalized leaching rates, the thickness of the layer leached was obtained. The values are of the order of 0.1 µm for the less oxidized fuel (sample A), and close to 0.2 µm for the highest (sample C). Although these values depend strongly on the assumed geometric surface taken, they can assist in the understanding of the leaching attack, which will be characterized by SEM and XRD.

These results have also been analysed by considering the release of each element as a function of its own concentration in the fuel (Fraction of Inventory, FI_x, see below) versus time or, alternatively, as the fraction of inventory of each element normalized to the fraction of inventory of ^{238}U (FIN_x, see below) versus time. The inventory was experimentally determined by dissolution of the base material and chemical analysis by ICP-MS, whose results were confirmed by code calculations (KORIGEN).

$FI_x = m_x / M_x$;

where: m_x: quantity of the x nuclide released
M_x: quantity of x nuclide in the fuel before leaching test.

$FIN_x = FI_x / FI_{Uranium\text{-}238}$

Considering these two evaluation parameters, three cases can be distinguished:

CASE 1

The nuclide showed an increase of the dissolution rate based on FI with increasing O/M. However, the uranium normalized fraction of inventory (FIN), remains constant as a function of time, indicating that the elements in this group have the same dissolution behaviour as ^{238}U. This is shown in Fig. 4.15 for Tc, but the same trend was observed for Cs and Mo.

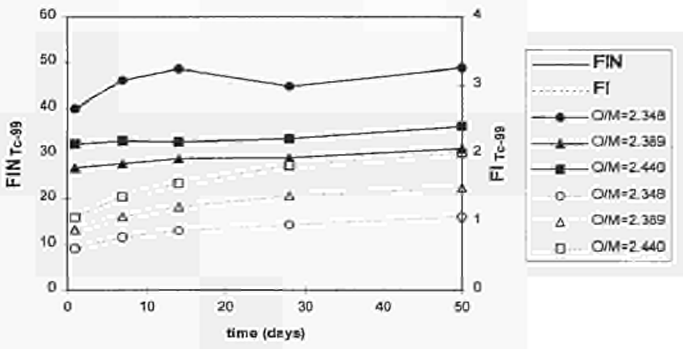

Fig. 4.15 FIN (continuous lines) and FI (broken lines) of Technetium-99 vs. time.

CASE 2

In this case, like in the Case 1, the nuclide shows a significant increase in its dissolution rate as a function of the O/M-ratio (FI vs. time). However, the FIN increases (unlike to the case 1) as a function of time, revealing that the dissolution rate of these elements is higher than that of the matrix. An example of this behaviour is shown in Fig. 4.16 for La. This group includes also Sr and Ba.

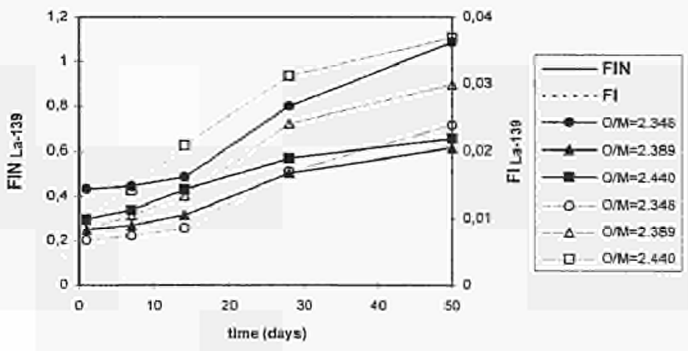

Fig. 4.16 FIN (continuous lines) and FI (broken lines) of Lanthanum-139 vs. time.

CASE 3

In this case, the nuclide dissolution does not show a clear dependence on the O/M ratio. This was observed for ^{239}Pu, as can be also seen from Fig. 4.12. As Pu is soluble in the UO_2 matrix it seems that the major influence is determined by the low solubility of Pu in water.

Conclusions

Oxidized UO_2 fuels corresponding to an intermediate state between U_4O_9 and U_3O_8 (detailed characterization is underway) show an increase of leaching rate for U and for the tested fission products with the O/M ratio; Pu does not obey this behaviour. A further point to be considered is the oxidation state of the fission products in these samples.

By taking account of FI and FIN data, information about dissolution of the elements species with respect to the matrix was obtained. It is possible to distinguish between three different trends (case 1, 2 and 3), which can be used in an attempt to separate physical effects (degradation of the fuel due to oxidation and leaching process) and chemical effects (associated with the solubility constant of the elements in different oxidation states).

Future work

A complete interpretation of the results needs a full characterization of the solid exposed to the solution. Characterization by SEM and X-ray diffraction is underway in order to determine the surface modification - in particular at the grain boundaries - due to the initial oxidation and the leaching process.

Future activities on the dissolution behaviour of oxidized irradiated fuel will include:

- Irradiated UO_2 fuel leaching test at different O/M ratios and at different burnups in simulated groundwater.
- Irradiated MOX fuel at different O/M ratios in simulated groundwater.

References

[1] D. Papaioanou, "Long term oxidation tests of irradiated UO_2", private communication and TUAR-94, p. 96

[2] B. Grambow, "Spent fuel dissolution and oxidation. An evaluation of literature data", SKB-Technical Report, Stockholm, March 1989

[3] W. J. Gray and L. E. Thomas, "Initial results from dissolution testing of various air-oxidized spent fuels", Mater. Res. Soc. Symp. Proc. **333** (1994) 391

[4] R. S. Forsyth, "Spent fuel degradation", Mater. Res. Soc. Symp. Proc. **212** (1991) 177

[5] C. N. Wilson and W. J. Gray, "Measurement of soluble nuclide dissolution rates from spent fuel", Mater. Res. Soc. Symp. Proc. **176** (1990) 489-498

[6] R. S. Forsyth and L. O. Werme, "Spent fuel corrosion and dissolution", J. Nucl. Mater. **190** (1992) 3

4.1.4 Leaching of SIMFUEL in simulated granitic water; comparison to results in demineralized water

Introduction

The final disposal in granite repositories of spent nuclear fuel is one of the options under consideration. Leaching experiments on simulated high burnup fuel (SIMFUEL) have been performed at 200 °C under static and anaerobic conditions in granitic water in the presence of granite monoliths. SIMFUEL with three burnup compositions (3, 6, and 8 a/o) was used. The experimental parameters were chosen to reflect the range of expected conditions in a deep granite repository at the time, when the spent fuel containers will fail (~500 years). The experiments were performed at a temperature of 200 °C to avoid excessively long leaching times. Although a temperature of 200 °C or even higher is reached during interim storage of spent nuclear fuel, it is generally believed that, for the period considered, the maximum temperature of granite in the repository will not exceed 100 °C. Previous investigations [1-3] showed that higher temperatures correspond to accelerated testing conditions.

The leachate, the rinse solutions of container and granite monolith, and the SIMFUEL were analysed after the tests. In particular, the leached SIMFUEL surface was characterized and the results compared to previous work on leaching of SIMFUEL [1] and UO_2 [2, 3] in demineralized water under air (see also TUAR-92, p. 90-93). The aim of these experiments was to investigate the behaviour of the nuclear fuel in contact with relatively small quantities of water in equilibrium with the surrounding granite.

Experimental

Experimental set-up

Electrically heated autoclaves with Teflon liners of 40 cm^3 volume were used. The temperature was kept constant at 200 ± 1 °C. Four leaching periods were used: 1 h, 10 h, 100 h, 1000 h.

In order to maintain anaerobic conditions, a small glove-box with an argon atmosphere was constructed. The leachant was stored inside the glove-box in an air-tight bottle, and before the experiments it was flushed with argon. The configuration of a loaded leaching container is shown schematically in Fig. 4.17.

The SIMFUEL specimen (with a typical mass of a fraction of a gram) was placed in a cup-shaped granite holder, and both specimen and holder were loaded in the Teflon container, and then submerged by synthetic granitic water. The volume of the granite holder was approximately 8 ml and the volume of leachant 25 ml. The loaded Teflon container was then inserted into an autoclave element. After the test, part of the leachate, designated for ICP-MS analysis (performed using a Perkin-Elmer ELAN 5000), was immediately

transferred to a clean bottle. The pH of the remaining leachate was then measured. Subsequently, the container, the granite holder and the specimen were removed from the glove-box. The Teflon container and the granite holder were inspected in order to locate and remove possible fragments broken off the edges of the SIMFUEL specimens during leaching. Thereafter, they were rinsed with 25 ml of 1N HNO_3 for 25 minutes at 40 °C. The rinse solution was also analysed by ICP-MS.

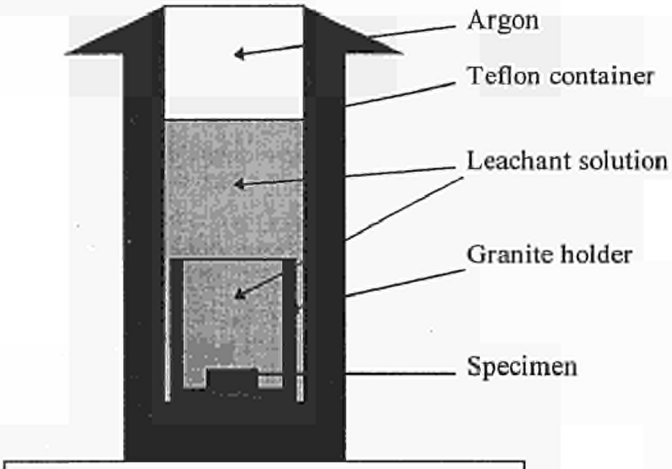

Volume of container: 40 ml
Volume of granite holder: ~8 ml
Leachant solution: 25 ml of granitic water
S/V (specimen/leachant): ~0.1 cm^{-1}
Test parameters: 200 °C, in autoclave.

Fig. 4.17 Schematic illustration of the experimental set-up.

The solid specimen was weighed and observed under an optical microscope. Several techniques were used to characterize the leached surfaces [4]: all the specimens were analysed using Scanning Electron Microscopy (SEM); some were also studied by Electron-Probe Micro-Analysis (EPMA); Rutherford Backscattering Spectrometry (RBS), helium resonance scattering, and Elastic Recoil Detection Analysis (ERDA) were performed using the accelerators at the 'Institut für Nukleare Festkörperphysik', Forschungszentrum Karlsruhe, Germany, and at the 'Istituto Nazionale di Fisica Nucleare', Legnaro (Padova) Italy. Part of the characterization using the nuclear techniques is still in progress.

In parallel, tests in demineralized water [1] were performed at 200 °C using the same autoclaves, but in laboratory air. The leaching times were 4 h, 14 h, 29 h, 54 h, and 102 h. The techniques used for leached surface analysis were the same as described above.

SIMFUEL

SIMFUEL with 3, 6, and 8 a/o burnup was used. The composition is given in Tab. 4.5 [5]. A total of 15 SIMFUEL specimens was prepared. For each test a different specimen was used. One specimen of each composition (burnup) was kept unleached for reference. The specimens of each composition, cut from the same pellet, were polished and annealed. A specific surface area value of ~1.5 cm^2g^{-1} was calculated. The S/V ratio, SIMFUEL surface to the leachant volume, was approximately 0.1 cm^{-1}. The polished face of the SIMFUEL specimen was facing with the leachant solution.

Tab. 4.5 SIMFUEL composition. The amounts of some elements were increased to include other fission products or actinides: the amount of Ru includes that of Tc, that of Ce includes that of Np, that of Sr includes that of Cs, that of La includes those of Am and Cm, Nd those of Pr, Pm, Sm, Eu and Gd; Pu is replaced by U.

Oxide	Amount (w/o)		
	3 a/o	6 a/o	8 a/o
UO_2	97.449	94.866	92.990
ZrO_2	0.336	0.593	0.777
MoO_3	0.356	0.720	0.980
PdO	0.147	0.434	0.652
$BaCO_3$	0.150	0.307	0.433
Y_2O_3	0.040	0.060	0.075
SrO	0.223	0.406	0.531
CeO_2	0.304	0.545	0.717
La_2O_3	0.113	0.254	0.367
RuO_2	0.360	0.754	1.026
Rh_2O_3	0.028	0.034	0.038
Nd_2O_3	0.494	1.027	1.418

Granite

Four granite holders were used with approximately the same dimensions and mass. The material, obtained from Sweden (Tranås Rubin, Askeryd, Sweden), was the same as in the experiments of Glatz et al. [6]. Tab. 4.6 shows the elemental composition of granite [7] according to analysis by Glow Discharge Mass Spectroscopy (GDMS), EPMA, and X-ray Diffraction (XRD) analysis.

Although measurements by GDMS gave a value of ~18 ppm of molybdenum in the granite, EPMA did not detect any Mo on the surface area scanned (~400 x 400 μm^2). This discrepancy may be explained by the fact that GDMS measures the bulk composition, whereas EPMA may miss elements present in isolated mineral inclusions.

All components of the SIMFUEL were also present in the granite (with a possible exception of molybdenum on the granite surface). In particular, Ba was one of the main components of granite, while the other nine elements of SIMFUEL were found among the impurities.

Thus, to take into account the contribution of releases from the granite holder a set of blank leaching tests *without* the SIMFUEL specimens was performed using the same conditions as for the experiments with SIMFUEL. The released amounts of U and fission products measured in the leachate and rinse in the blank tests, resulting from leaching of the granite holder, were subtracted from the corresponding values measured in the experiments with SIMFUEL.

Tab. 4.6 Elemental composition of granite. The amount of O and H are omitted. Ca is missing from the list of the main components because of a detection problem of the GDMS device. However, the presence of Ca was confirmed by electron microprobe analysis and XRD.

Main Components (%)							
Si	Al	K	Na	S	Fe	Ba	Ca
56.1	18.5	17.3	6	0.8	0.5	0.2	

Impurities (ppm)					
Elements present in SIMFUEL		Other Elements			
Sr	11	Li	200	Sb	7
Y	94	B	1	I	27
Zr	410	F	820	Cs	6
Mo	18	Mg	200	W	127
Ru	3	P	24	Pb	12
Rh	8	Ti	400	Co	15
Pd	6	Cr	150	Ni	10
La	60	Mn	108	Rb	630
Ce	117				
Nd	65				
U	20				

Granitic water

The leachant solution was prepared by mixing deionized water with crushed granite powder from the same block that provided the sample holders. The mixture was stirred for ~100 h at room temperature and for ~25 h at 90 °C, and then left to equilibrate for 15 months in a close-tight bottle filled with air. Tab. 4.7 shows the pH and the composition of the water after this equilibration period.

Tab. 4.7 Composition and pH of synthetic granitic water.

Main Ionic species	Conc. (ppm)	SIMFUEL elements (impurities)	Conc. (ppb)
Na	**2.0**	Sr	28
K	**1.4**	Y	0.7
Mg	**1.2**	Zr	0.03
Ca	12.6	Mo	0.6
F	**3.3**	Ru	-
Cl	**2.5**	Rh	-
SO_4	**6.9**	Pd	0.1
NH_4	**0.2**	La	0.05
NO_3	**0.8**	Ce	0.1
HCO_3	40	Nd	0.1
pH	~7.95	U	2

Results

Solution analysis

The following remarks can be made about the measured concentrations of dissolved elements: Ru, Rh, Pd and Zr were either not detected, or measured occasionally in negligible quantities. Nd, which was found essentially in the rinse solutions only, can be considered a granite leaching product. Sr, Y, Ba, La and Ce, found only in the rinse solutions, could not be attributed entirely to leaching from the granite holder. Mo behaved differently from the other elements, because it was present almost only in the leachate and was not detected in the blank test solutions. U was present in all solutions, but it could not be accounted for by considering only the contribution of the granite.

Based on these findings, the analysis of the experimental results was focused mainly on U and Mo. Sr was also considered, because, among the five elements found only in the rinse solution, it was the one with the lowest concentration in the granite. The important contribution of the rinse solutions to the measured concentration is a strong indication that sorption phenomena, especially on the solid granite surface [6], play a significant role in determining the behaviour of this system.

All data points of SIMFUEL in Figs. 4.18 and 4.19 represent the total amount released (from SIMFUEL), i.e. the sum of the quantities measured in the leachate and rinse solutions after subtracting the results of the corresponding blank tests.

The total released amounts of U as a function of leaching time for the three types of SIMFUEL (after subtracting the blank tests results) are shown in Fig. 4.18. Also shown are the total released amounts for the blank tests with granite only, and the amount of U present in the granitic water. The values for leaching of the SIMFUEL were approximately two orders of

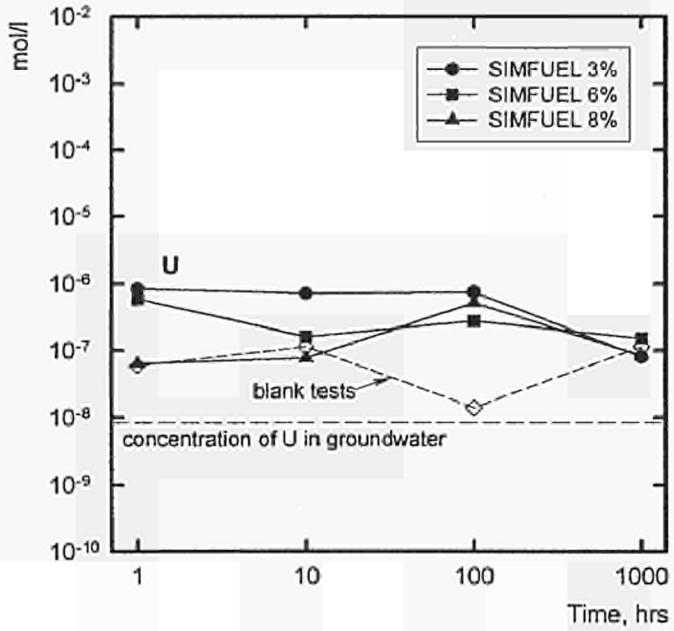

Fig. 4.18 Total released amount of uranium as a function of leaching time. The initial amount of U in the groundwater (straight line) and the total released amount of U measured after the blank tests (open diamonds) are also shown.

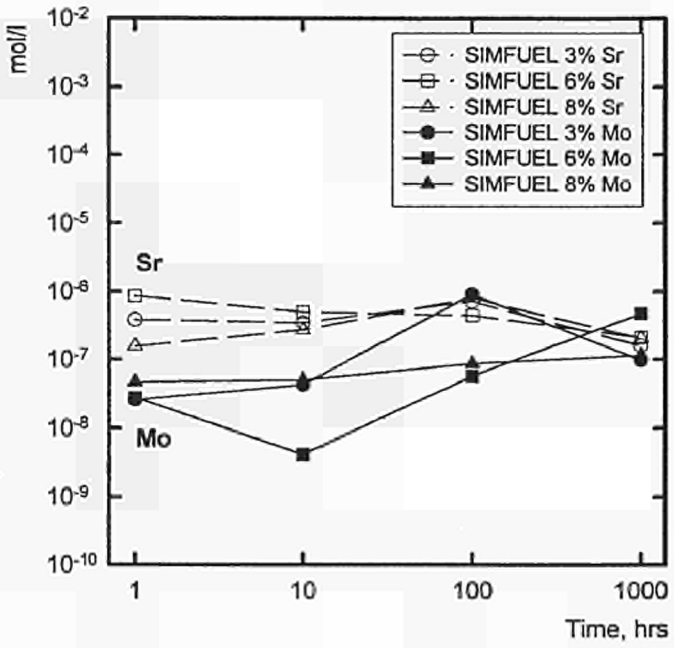

Fig. 4.19 Total released amount of strontium and molybdenum as a function of leaching time.

magnitude higher than the initial concentration in the groundwater, and in most cases they were also higher than the corresponding values of the blank tests (though these show significant scatter). There was no clear effect of burnup (composition) on the leaching behaviour. The values for 8 a/o SIMFUEL, after 1 h and 10 h, were approximately one order of magnitude lower than those for the two other compositions (3 a/o and 6 a/o). The values for 6 a/o SIMFUEL lie between those for 3 and 8 a/o; however, after 100 h and 1000 h, the range of measured concentrations was rather narrow. With increasing leaching times, the total released amount of U leached from SIMFUEL remained essentially at the level reached after 1 h, possibly showing a slight decrease after 1000 h, especially for 3 a/o burnup. Therefore, it seems that 1 h at 200 °C was sufficient to reach equilibrium between dissolution and reprecipitation. In most cases, equal amounts of released U came from the leachate and from the rinse solution.

The total amounts released of Mo and Sr as a function of leaching time are shown in Fig. 4.19. Mo was present only in the leachate, whereas all the Sr was found in the rinse solutions. The released amounts of both Mo and Sr are essentially independent of the SIMFUEL composition (though the concentration of fission products in the SIMFUEL increases with the burnup). The behaviour of Sr was very similar to that of U, with values essentially constant for all leaching times and of the same magnitude as those of U. In the case of Mo, different from the behaviour of U and Sr, an increase with time was observed, from lower values after the short leaching times to values similar to those of U and Sr after 1000 h. The amounts of the fission products measured in the leachate and the rinse were not congruent with the composition ratio in the SIMFUEL. The ratio between atoms of U and atoms of Mo in the SIMFUEL varies approximately between 145, 70, and 50 for, respectively, 3, 6 and 8 a/o burnup; in the case of Sr these ratios are higher (approximately 170, 90 and 65).

SIMFUEL characterization

The weight changes measured after all the leaching experiments are summarized in Tab. 4.8.

Tab. 4.8 Weight changes after leaching. The missing values correspond to specimens with pieces broken off the edges during post-test handling.

Experimental conditions	Weight change (mg)		
	SIMFUEL 3 a/o	SIMFUEL 6 a/o	SIMFUEL 8 a/o
200 °C, granite, groundwater, argon			
1 h	-0.03	-	-0.04
10 h	-0.01	-0.03	+0.07
100 h	-0.11	+0.04	+0.06
1000 h	-0.14	+0.02	+0.06
200 °C, demineralized water, air			
4 h	-0.01	-0.09	-0.04
14 h	0	-0.06	0
29 h	0	-0.06	0
54 h	+0.10	+0.01	+0.13
102 h	+0.10	+0.12	+0.19

One significant problem when weighing the SIMFUEL specimens after leaching was their mechanical degradation, which caused in some cases the edges to break off. While it is not possible to unequivocally attribute the measured weight losses to surface dissolution processes during leaching, it is certain that the measured weight increases are due to deposition of material from the granite, hydration and/or oxidation on the SIMFUEL surface.

It is interesting to compare the weight changes for the two sets of experiments (*i.e.* in granitic environment and in demineralized water) performed at 200 °C and in particular the results for the 6 and 8 a/o SIMFUEL, whose weights increased after longer leaching times under both types of experimental conditions. When leaching in demineralized water, only SIMFUEL and water were present; therefore, the causes of weight increase are hydration and oxidation. Reprecipitation of crystals of higher oxides of uranium was in fact observed on the surface using SEM (see below), as also previously reported for UO_2 leaching (TUAR-92, p. 90-93) [2, 8]. No such phenomenon was evident on the surface of the specimens leached in presence of granite. Here the system is more complex than in the case of demineralized water. Since many species are present in solution, the determination of the causes of weight increase is more problematic.

A Scanning Electron Microscope (SEM) picture of a typical polished unleached surface of a 3 a/o SIMFUEL specimen before leaching is shown in Fig. 4.20, which is representative for the three SIMFUEL compositions used in this work.

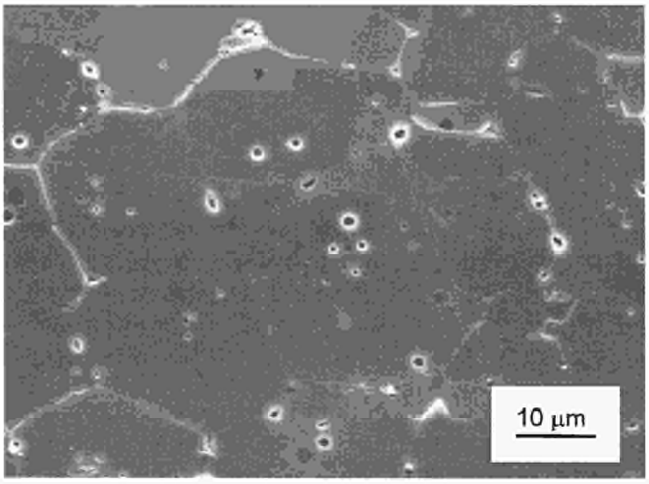

Fig. 4.20 Scanning Electron Microscopy (SEM) image of the unleached SIMFUEL surface.

The surface of a SIMFUEL specimen with 3 a/o, leached for 1 h, is shown in Fig. 4.21.

The effect of leaching on the SIMFUEL surface is evident by comparing Fig. 4.20 and Fig. 4.21 (taken at the same magnification). There is a significant surface etching occurring during the 1 h test. Longer leaching times did not show signs of further etching.

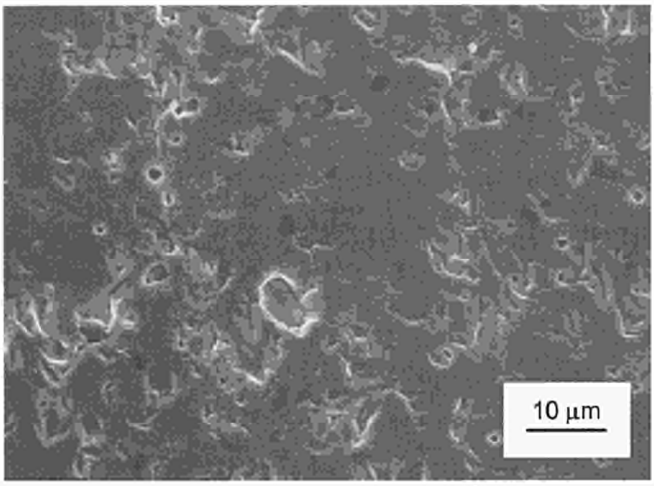

Fig. 4.21 SEM image of a specimen with 3% burnup after 1 h of leaching at 200 °C in granitic groundwater in presence of granite monolith and under an argon atmosphere. The magnification of this figure is the same as Fig. 4.20. The small spheres visible at the grain boundaries are precipated fission products (Mo, Ru, Rh and Pd) in metallic form.

Preliminary results using ERDA on all the 8 a/o SIMFUEL specimens using 2 MeV He^+ ions, shows that essentially no hydrogen is present at or near the surface after leaching in presence of granite. This would suggest that the alteration of the SIMFUEL surface due to water attack, under the experimental conditions used in this work, is small in contrast with what normally is observed when leaching UO_2 or SIMFUEL in demineralized water in air [2, 3, 8].

The surface of 3 a/o SIMFUEL, after leaching for 100 h at 200 °C in demineralized water in air, is shown in Fig. 4.22. The surface appears partially covered with crystals of reprecipitated higher oxides of uranium (e.g. schoepite). The amount of surface reprecipitation increases with leaching time. This was not observed in the case of the granitic environment. Very small precipitates are visible on the surface of SIMFUEL leached in the granitic environment after 1000 h.

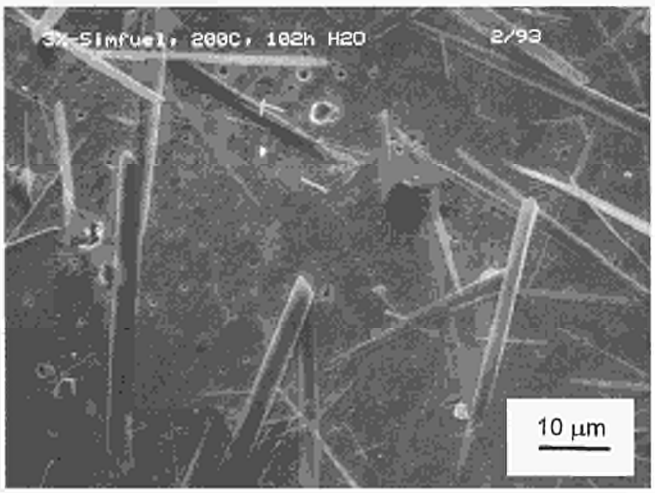

Fig. 4.22 SEM image of a specimen with 3% burnup leached at 200 °C for 100 h in demineralized water in air. The crystals on the surface are mainly constituted by U reprecipitated as higher oxide (schoepite).

These precipitates for a 3 a/o SIMFUEL specimen are shown in Fig. 4.23 (note that the magnification of Fig. 4.23 is approximately 8 times higher than that of Fig. 4.22; this illustrates the different nature of the two precipitation processes).

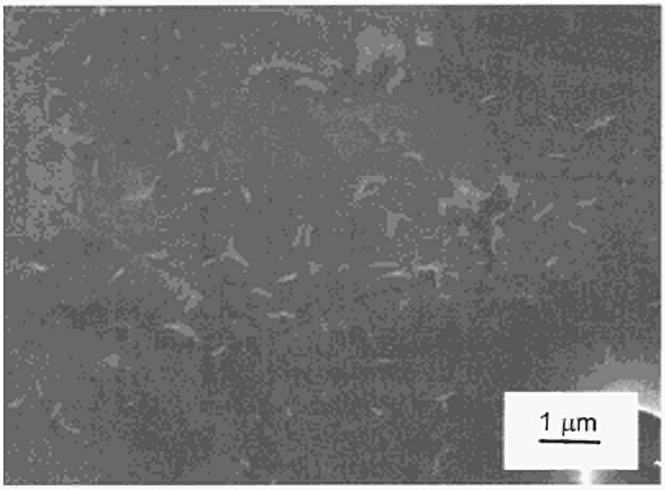

Fig. 4.23 SEM image of a specimen with 3% burnup after 1000 h of leaching at 200 °C in granitic groundwater in presence of granite monolith and under an argon atmosphere. The magnification of this image is ~8 times higher than Fig. 4.22.

The results obtained by Energy Dispersive X-ray (EDX) analysis, did not reveal any element other than U on the surface. However, EPMA, with its lower detection limit, indicated the presence of silico-aluminates on the surface of the specimen. Further investigations are currently going on to determine a possible correlation between the leaching time and the extent of surface deposition by these materials.

Although dissolution also occurred during leaching in granitic groundwater in presence of granite and in argon, as shown by the ICP-MS results described above, and although there is evidence (*i.e.*, the weight increases) that deposition or sorption onto the SIMFUEL surface occurs also in presence of granite, it is evident that reprecipitation of uranium oxides does not occur in the same form as shown in Fig. 4.22.

Discussion

Solution analysis

The amounts of U and simulated fission products measured after leaching using ICP-MS were generally very small. For most elements they were close to or below the detection limits of the instrument. In fact, only U and Mo were clearly detected in the leachate. The concentration of U in both the leachate and the rinse solution was approximately one order of magnitude lower than the values reported in studies of SIMFUEL dissolution in granitic groundwater (but without solid granite) under anoxic conditions and at room temperature [9]. The total released fraction of inventory of U was about one order of magnitude lower than the value reported by Glatz et al. (1995) [6] for leaching experiments with irradiated UO_2 fuel in presence of the same type of granite at 100 °C under dynamic conditions and in the presence of γ-radiolysis. The released fraction of inventory of Sr was similar.

Approximately one half of the total released U was found in the rinse solutions, which means that sorption phenomena on the container walls and especially on the granite holder played an important role in determining the behaviour of dissolved U. The released amounts of U appeared to be unaffected by the leaching time, except for a possible decrease after 1000 h. This suggests that an equilibrium between U dissolution, sorption and reprecipitation processes was reached after the shortest leaching time of 1 h. In support of this consideration, SEM examination of SIMFUEL surfaces showed, at least qualitatively, that the degree of etching did not increase with leaching times longer than 1 h.

The total released amounts of Sr as a function of leaching time overlapped those of U. In terms of fraction of inventory, this corresponded to a release of Sr approximately 2 orders of magnitude higher than that of U. Different to uranium, essentially all the measured Sr was found in the rinse solutions; this means that sorption phenomena played a dominant role in the case of Sr, even more important than for U. A significant contribution to the released fraction of Sr is probably due to grain boundary etching processes. Although Sr is present in irradiated UO_2 fuel as a dissolved matrix oxide, with only a small fraction as a perovskite phase segregated at grain boundaries [10], the SIMFUEL used in this work contains a higher amount of Sr than irradiated UO_2 with the same burnup [5]. The Sr in excess is present as a precipitated grain boundary phase and simulates the Cs at the grain boundaries of irradiated fuel (see Tab. 4.5).

The behaviour of Mo was in sharp contrast to that of Sr. Firstly, almost all the Mo measured by ICP-MS was found in the leachate, thus indicating that sorption phenomena did not play a major role for Mo. Secondly, the concentration of Mo in solution increased with leaching time. Possibly related to this behaviour is the fact that negligible amounts of Mo are present in the groundwater or are leached out of the granite.

The total released amounts of Mo were lower than those of Sr after the shorter leaching times and reached the level of the other fission product after the longest time. This probably corresponded to smaller leaching rates of Mo for the shorter leaching times, compared to the rates of Sr and U. Strontium oxide is more soluble in water than molybdenum trioxide. Furthermore, while Sr is present both in the matrix and at the grain boundaries, Mo is present in SIMFUEL (and in irradiated UO_2 [10]) mainly as rather large (~0.5 to 1 μm) metallic precipitates at grain boundaries, with only a very small fraction as segregated grain boundary perovskite phase [11]. Since Mo as a metal is insoluble in water, its release during leaching is governed by oxidation and subsequent dissolution from metal precipitates reached by grain boundary etching.

Thus, the observed discrepancies between Mo and Sr could be explained either by an overall slower dissolution kinetics for Mo than for Sr, or by the fact that less Mo than Sr is initially available for dissolution. The latter possibility would imply that grain boundary etching did not stop after 1 h of leaching, but instead continued through the increasing leaching times, reaching more metallic precipitates, and thus contributing to increasing concentrations of Mo in solution. This would also explain the observed larger scatter of Mo results than of U and Sr.

Surface characterization

Two points must be considered when comparing the results of the previous experiments performed in demineralized water in air (TUAR-92, p. 90-93) with the present ones performed in groundwater in the presence of granite monoliths in an argon atmosphere. Firstly, a tendency to weight gains of comparable magnitude after longer leaching times was found in both sets of tests; this indicates that material is deposited onto the SIMFUEL during leaching in amounts greater than that dissolved. Secondly, direct observation of the specimen surfaces using SEM shows dramatic differences between the two types of conditions. Increasingly larger amounts of crystals of higher uranium oxides precipitate on the surface leached in demineralized water with increasing leaching time, while leaching in granitic environment produces only very small amounts of precipitates, visible only at high magnifications and after 1000 h leaching. ERDA results support the conclusion that the surface leached with granite undergoes a lower degree of alteration than in demineralized water in air. Furthermore, the EPMA shows that silico-aluminates tend to deposit onto the surface of specimens leached with granite monoliths, particularly at grain corners and edges. This process might have a passivating effect, by reducing the surface of the SIMFUEL available for leaching. Moreover, deposition of elements from the granite might explain the observed weight increase. In demineralized water, oxidation and dissolution at grain boundaries and at sample edges were more pronounced (actually leading to grain pullout in some cases), thus delivering the U for redeposition of the large crystals on the surfaces. Further investigations to quantify the nature and composition of the surface layers of the leached specimens are underway.

Conclusions

The results of static leaching experiments on SIMFUEL with three different simulated burnups at 200 °C in granitic groundwater, in an argon atmosphere and in presence of granite monoliths showed that only very small amounts of uranium and of fission products were released. The fraction of the total released quantity sorbed on the granite or on the container walls was negligible for Mo, significant for U, and close to unity for Sr. After 1 h of leaching, the total release of U and Sr reached a level which remained essentially constant for longer leaching times, and the SIMFUEL surface underwent observable etching that did not visibly increase with further leaching time. The results for Mo indicated either a slower dissolution kinetics for Mo, or the presence of a different leaching mechanism, based on the release of Mo from metallic precipitates at grain boundaries reached by an advancing etching front, which caused increasing amounts of Mo to oxidize and dissolve with increasing leaching time. ERDA results indicated that there was essentially no surface hydration. After 1000 h of leaching, small deposits, possibly silico-aluminates, were visible on the surface. This was in sharp contrast with the behaviour of SIMFUEL leached in demineralized water in air, which showed pronounced grain boundary etching and increasingly large amounts of reprecipitated crystals of higher uranium oxides (schoepite) on the surface. In the presence of solid granite this type of oxidation and reprecipitation was inhibited.

References

[1] Hj. Matzke; presented at the Spent Fuel Workshop 94, Montebello, Quebec, Canada, August 1994
[2] Hj. Matzke, A. Turos; Solid State Ionics **49** (1991) 189
[3] Hj. Matzke; J. Nucl. Mater. **190** (1992) 101
[4] Hj. Matzke; Surface and Interface Analysis **22** (1994) 472
[5] P. G. Lucuta; AECL, private communication (1995)
[6] J. P. Glatz, E. H. Toscano, G. Pagliosa, A. Nicholl; J. Nucl. Mater. **223** (1995) 84
[7] A. B. Muller, B. Fritz, A. Wyman, M. Snellman; Mater. Res. Soc. Symp. Proc. **50** (1985) 165
[8] Hj. Matzke, G. Della Mea, F. L. Freire Jr., V. Rigato; Nucl. Instr. and Meth. B45 (1990) 194
[9] K. Ollila; J. Nucl. Mater. **190** (1992) 70
[10] H. Kleykamp; J. Nucl. Mater. **131** (1985) 221
[11] P. G. Lucuta, Hj. Matzke, R. A. Verrall, B. J. Palmer; J. Nucl. Mater. **178** (1991) 48

4.1.5 Analysis of the structure of layers on UO_2 leached in H_2O

Introduction

The studies of leaching and surface analysis of UO_2 were continued employing the nuclear techniques of Rutherford backscattering/channeling, resonance scattering and elastic recoil detection analysis using energetic He-ions. In the reporting period, the structure of layers of U_3O_7 on UO_2 leached in demineralized water at temperatures up to 200 °C were analysed and the lattice mismatch between the bulk UO_2 and the transformed layer was determined.

Experimental techniques

The material used in the present study was single-crystalline UO_2, with well polished surfaces preannealed to recover polishing damage and to adjust the oxygen-to-metal ratio to the stoichiometric value of 2. Leaching

was performed in demineralized water in autoclaves with Teflon liners, at temperatures between 20 and 200 °C, and times between 1 and 1000 h. The ratio of solution volume to crystal surface area was 10:1 or 20:1 cm^3/cm^2. The pH of the water was varied between pH = 4.5 and pH = 10 using suitable buffers. Following leaching, the surfaces were studied by scanning electron microscopy and analysed with the different nuclear techniques mentioned above (see also TUAR-91, p. 31 and TUAR-92, p. 90).

Results and discussions

Fig. 4.24 shows He-resonance scattering spectra with large signals for both oxygen (channel nrs. 100-400) and uranium (channels 400 to 1000).

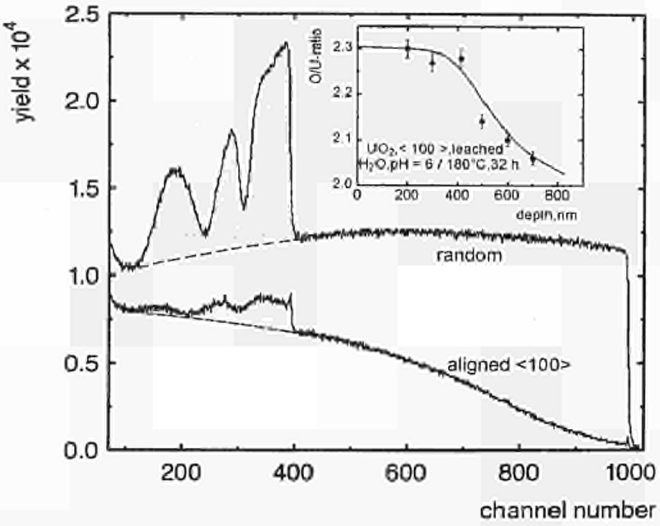

Fig. 4.24 Random and aligned backscattering spectra of 7.6 MeV He-ions from a virgin UO_2 single crystal of <100> orientation. The inset shows a depth profile of oxygen in leached UO_2 determined with this resonance scattering technique.

The figure contains as an inset a typical result of oxygen gradients on leached UO_2, deduced from the spectra, the conditions for this experiment being demineralized water, pH = 6; 180 °C; 32 h. The composition of the layer formed on the UO_2 single crystal is seen to correspond to that of U_3O_7, and the thickness corresponds to that measured with conventional Rutherford backscattering RBS. The sensitivity of the method depends on the counting rate which cannot be increased indefinitely since radiation damage eventually influences the results. The error bars in Fig. 4.24 indicate the typical accuracy in O/U-ratio determination to be ± 0.03. The advantage of the technique is that a depth profile is obtained nondestructively in one (short) measurement. Fig. 4.25 shows typical results obtained with conventional RBS, hence with 2 MeV He-ions, for other crystals leached at 200 °C for 4 and 15 h. Three random spectra are shown together with the corresponding aligned spectra. Only the U sublattice can be analysed with conventional RBS, the signal from O being too small (< 1%). Characteristic

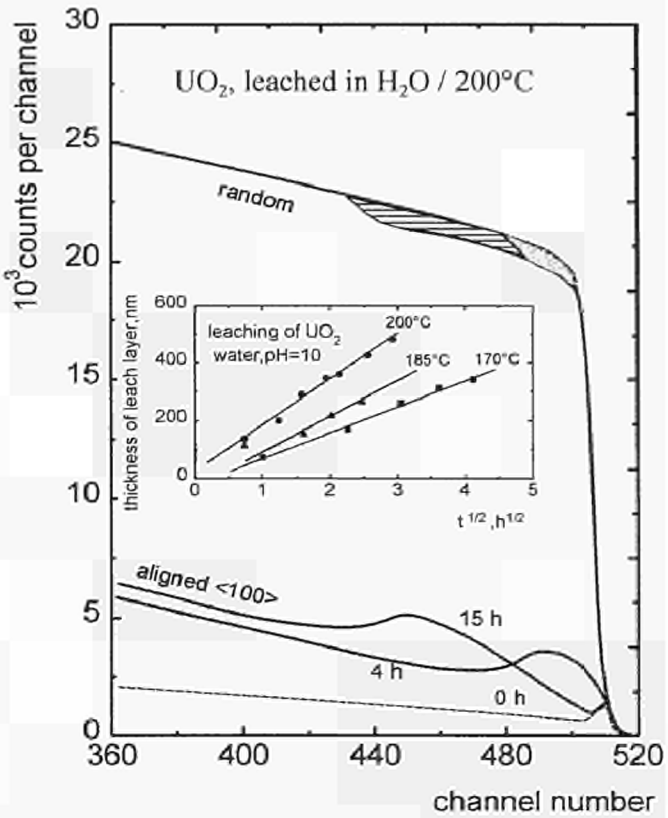

Fig. 4.25 RBS energy spectra for UO_2 single crystals leached at 200 °C for 4 and 15 h, respectively. The inset shows the thickness of the surface layers as a function of time for three temperatures (water, pH = 10).

steps are seen in both random and aligned spectra corresponding to the thickness of the oxidized layers. The lower counting rate in the random spectra is due to a smaller U-atom density, because of the incorporation of additional oxygen, i.e. the random spectra confirm the results deduced from the aligned spectra.

Resonance scattering with 7.6 MeV He-ions was performed both in the surface layer and in the underlying bulk crystal. This showed that the leached layers were misaligned with respect to the bulk by about 0.8° [1]. Clear minima for the aligned condition were seen for both O and U in the bulk, but only for U in the U_3O_7 layer. The minimum for oxygen in the U_3O_7 layer was hardly visible due to the excess oxygen atoms and their structural location, which was indicated to be close to the center of the (100) planar channel, as evidenced by what is called *flux-peaking*, i.e. a higher than random signal for the aligned crystal for this channeling condition. There was no sharp interface between the U_3O_7 layer and the underlying UO_2. This is compatible with oxygen diffusion through the U_3O_7 surface layer and oxidation of UO_2 at the interface. It is suggested that this transition layer located between the bulk UO_2 and the U_3O_7 layer accommodates most of the misfit since the channeling clearly shows that above this transition layer, an almost unstrained crystalline film of U_3O_7 is growing retaining some coherence with the underlying UO_2 single crystal.

Monte Carlo channeling simulations [2, 3] were performed to fit the experimental data. Fig. 4.26 shows schematically the final model of the structure of U_3O_7 layers on leached UO_2.

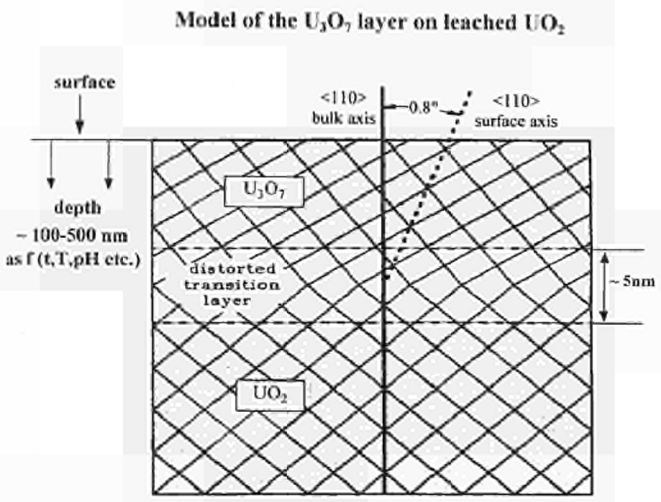

Fig. 4.26 Model of the U_3O_7 layer on leached UO_2.

Conclusions and Summary

The present study shows the potential of applying nuclear techniques to analyse surface-near layers of leached UO_2. The full potential is achieved when single crystals are used and the channeling effect technique can be applied. In this case, kinetics of layer growth, composition of the layers and their structure can be determined for a large variety of leaching conditions.

For the case of leaching in water at temperatures up to 200 °C, for not too long times (≤ 500 h), water-free layers of U_3O_7 are formed, as measured by a number of different nuclear techniques and as confirmed by X-ray analysis. These layers grow by inward diffusion of oxygen, through the U_3O_7 layer. The layer retains some coherence with the UO_2, and a thin distorted transition layer accommodates most of the misfit.

The results show that for the leaching conditions used, and for unirradiated UO_2, any U_4O_9 layer is very thin and likely coincides with the distorted transition layer. It is well known that in irradiated UO_2, as well as in SIMFUEL, the U_4O_9 phase is stabilized by fission products up to O/U ratios larger than those of U_3O_7. However, it is not known whether the layer facing the water is U_3O_7 or stabilized U_4O_9. We plan to investigate this question with the above techniques and with SIMFUEL.

References

[1] A. Turos, R. Falcone, A. Drigo, A. Sambo, L. Nowicki, N. Madi, J. Jagielski, Hj. Matzke; Nucl. Instrum. Methods Phys. Res., in press

[2] A. Turos, O. Meyer, L. Nowicki, J. Remmel, M. Wielunski; Nucl. Instrum. Methods Phys. Res. **B85** (1994) 448

[3] A. Dygo, A. Turos; Phys. Ref. **B40** (1989) 7704

4.1.6 Caustic salt dissolution studies of irradiated fuel

Introduction

Usually the spent fuel inventory is determined after dissolution in strong acid (mainly HNO_3). By using the current equipment housed in a hot-cell "volatile fission products" such as Xe, Kr, I cannot be measured. Furthermore light gases formed in the fuel such as ^3H, ^3He and ^4He, cannot be detected if the conventional method is applied. ^3H is formed either as an activation product [1] according to

$$^{14}N + n \rightarrow {}^{12}C + {}^{3}H$$

or as third fragment in the fission process [2].

In order to determine all these volatile compounds, a new dissolution method was developed and checked, involving fuel dissolution in a sealed capsule by means of a molten salt mixture.

Preparatory experiments

Initial inactive experiments were carried out using a $NaNO_3$, NaOH and Na_2O_2 salt mix alone and with:

1) natural UO_2,
2) U-Pu-Zr alloy and
3) (U, Pu)O_2

under flowing argon to find the most suitable temperature and time.

Differential thermal analysis was carried out on heating up to 350 °C - 600 °C at 10 °C. min^{-1}, and then holding at this temperature for a short (1 min) or long (15 hours) time before cooling (at 10 °C. min^{-1}). Thereafter visual examination, solubility testing and X-ray diffraction analysis were carried out on the reaction products.

Experimental

The low melting point (~ 280 °C) salt mixture selected was composed of $NaNO_3$, NaOH and Na_2O_2 [3]. A zircaloy capsule, filled with this salt mixture (ca. 1.5 g) and a piece of spent fuel of about 250 mg was closed under Ar atmosphere by means of a welded endplug. The capsule is then heated up to 600 °C during approx. 3 hours. A schematic drawing of the melting capsule is shown in Fig. 4.27.

After cooling to room temperature, the capsule was opened by first puncturing it in a closed gas chamber to analyse the gas phase by mass spectrometry. In the next step, the crucible was cut open and the melt cake submitted to a sequence of dissolution steps, using first distilled water, second 1 M HNO_3, and third 7 M HNO_3. Any remaining residues were dissolved in concentrated HNO_3/HF.

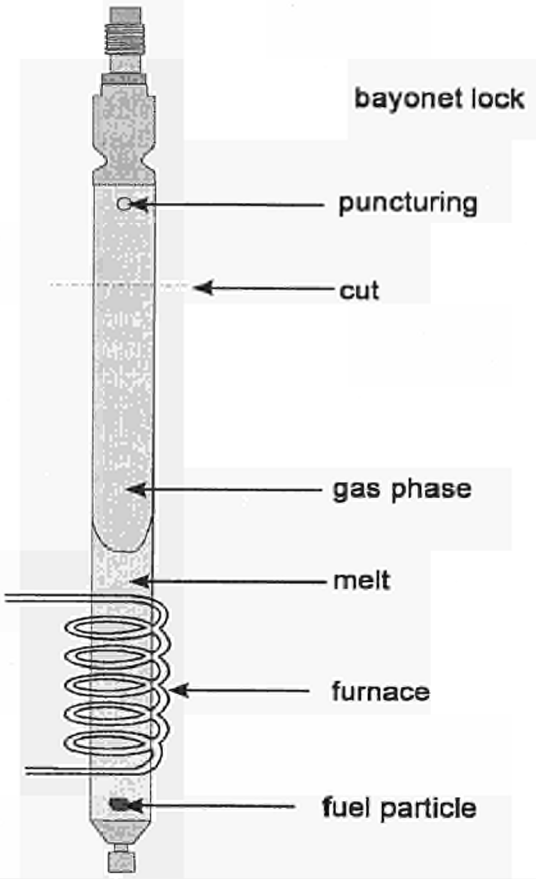

Fig. 4.27 Sealed zircaloy capsule used for dissolution of an irradiated fuel sample with a salt mix.

Results

The results of these tests are given in Tab. 4.9.

The DTA results show that the salt mixture melts above 280 °C (see Fig. 4.28) but commences to vaporize or react above 400 °C, with some evidence from X-ray diffraction of reaction (nitrite formation: $NO_3^- \rightarrow NO$).

With natural UO_2 present, the salt appears to react and to oxidize the fuel to U (VI) with the formation of water soluble orange uranates, most probably by the action of the peroxide. This proceeds rapidly at 600 °C or more slowly (6 h) at 400 °C or even 350 °C. At lower temperatures there is minimal thermal decomposition of the salt. X-ray diffraction (XRD) failed to detect any sodium uranate despite the typical bright orange colouring of these compounds. A possible explanation may be that it is amorphous or microcrystalline and hence not detectable by XRD.

The metallic U-19Pu-10Zr alloy also appears to be oxidized and dissolved in the salt mix. The differential thermal analysis shows that a reaction occurs directly upon fusion. The yellow-brown colour appears to be typical of U (IV) as oxide (UO_3). If it is soluble this may indicate another form or may be due to the presence of brown Pu (IV) nitrate or Zr (IV). The testing of non-irradiated $(U,Pu)O_2$ shows that it is less easily oxidized and dissolved than natural UO_2 requiring 600 °C compared to 350 °C - 400 °C (for 6 hours) for UO_2. The yellow/orange colouring as opposed to the orange colouring, observed for UO_2 alone, is assumed to be due to presence of Pu (as Pu (IV). The poorer solubility (only acid soluble compared with water soluble for natural UO_2) is also consistent with this explanation.

By contrast the irradiated MOX fuel i.e. $(U,Pu)O_2$ with (approx. 7% PuO_2) compared to the non-irradiated $(U,Pu)O_2$ (with 25% PuO_2) was partially dissolved in the salt mix at only 350 °C for 12 hours, instead of 600 °C. This may have been principally due to the attack of the UO_2 matrix as the PuO_2 was present as Pu-rich agglomerate particles (with up to 25% PuO_2 content) in a UO_2 matrix.

Tab. 4.9 Results of caustic salt dissolution tests of UO_2, $(U,Pu)O_2$ and alloys (salt: $NaNO_3$/ Na_2O_2/ NaOH: 55:4.5:6 under Ar).

Fuel	Temperature profile	Product
No fuel salt alone	i) rise to 350°C, descend	melting at 270°C (DTA) but no reaction (XRD)
	ii) rise to 670°C, descend	melting and vaporisation (or reaction) >400°C (DTA), small amount of $NaNO_2$ formed (XRD)
UO_2	i) rise to 600°C, descend	orange product (uranate?) water soluble
	ii) rise to 400°C, hold for 15 h, descend	slow reaction (6h) at 400°C (DTA) orange product-water soluble (uranate?) - XRD detected no uranate
	iii) rise to 350°C, hold for 15 h, descend	orange water soluble product (uranate?)
UPu Zr alloy	i) rise to 720°C, descend	reaction at > 300 °C on fusion (DTA) yellow-brown product - water soluble, U (VI) as $UO_2 NO_3)_2$?
$(U,Pu)O_2$	i) rise to 350°C, hold for 12h, descend	no reaction
	ii) rise to 600°C, descend	yellow/orange product-acid soluble
	iii) rise to 600°C, hold for 40 mins, descend	yellow/orange product-acid soluble
irradiated MOX	i) rise to 350°C, hold for 12 h, descend	some dissolution of fuel (UO_2 matrix) residue as grains

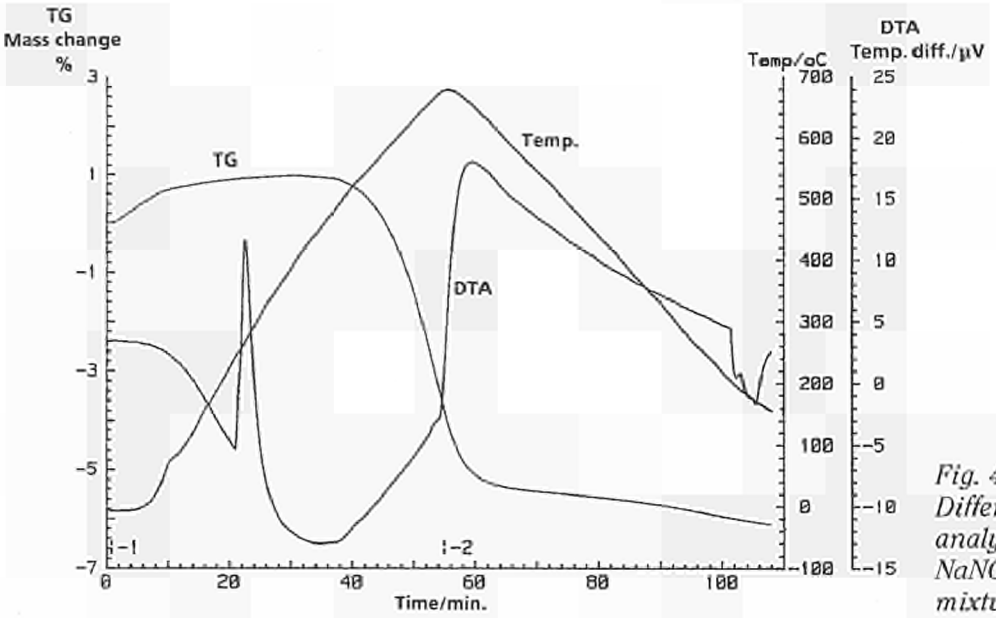

Fig. 4.28 Differential thermal analysis (DTA) trace of $NaNO_3/Na_2O_2/NaOH$ salt mixture.

Irradiated fuel sample testing

The experiment with MOX fuel (burn-up 37 MWd/kg U) was carried out at this temperature for almost 10 h. In contrast to the tests with unirradiated material the dissolution of the melt revealed an incomplete dissolution under these conditions. This is most probably due to the low dissolution kinetics for the irradiated MOX fuel.

It was therefore necessary to raise the temperature to 600 °C and in a second experiment, a complete dissolution was obtained after 8 hours. The qualitative results of the gas analysis by mass spectrometry revealed, apart from Xe and Kr, the presence of NO_x and in the low mass range the presence of H, H_2 ^3He and ^4He as shown in Fig. 4.29.

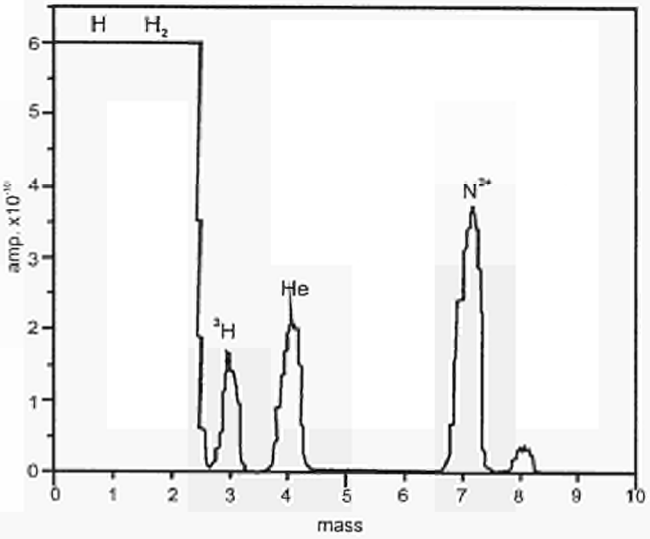

Fig. 4.29 Mass spectrum of light gases released by salt dissolution of an irradiated MOX fuel at 600 °C for 8 hours.

A quantitative analysis of Kr and Xe was also carried out by mass spectrometry by means of a standard mixture, having a similar content of the two gases in the natural isotopic composition (Tab. 4.10).

Tab. 4.10 Quantitative composition of Kr and Xe.

gas	volume, ml	mg/g
Kr 82	5.46E-05	7.90E-04
Kr 83	1.37E-03	2.00E-02
Kr 84	2.32E-03	3.44E-02
Kr 85	1.64E-04	2.46E-03
Kr 86	3.09E-03	4.68E-02
Kr total	**6.99E-03**	**1.05E-01**
Xe 130	1.09E-03	2.51E-02
Xe 131	1.15E-02	2.65E-01
Xe 132	3.39E-02	7.89E-01
Xe 134	4.86E-02	1.15E+00
Xe 136	5.74E-02	1.38E+00
Xe total	**1.52E-01**	**3.61E+00**

In the next step, the capsule was cut open (Fig. 4.27) and submitted to the dissolution procedure mentioned above. Each of the four solutions was analysed by ICP-MS and the result obtained for the total amount of each element is given in Tab. 4.11.

Given the large amounts of Pu detected the rather low levels of Am and Cm found is surprising. It has to be emphasized, of course, that the fuel particle was taken from the centre of the fuel pellet and not from the outer rim. The amount of detected iodine corresponds to that predicted by the KORIGEN code for a UO_2 fuel of the same burn-up.

Tab. 4.11 Composition of the dissolution solutions of the melt by ICP-MS.

element	µg	µg/g
Rb	23	90
Sr	59	233
Y	23	90
Zr	510	2000
Mo	578	2268
Tc	183	718
Ru	524	2055
Rh	102	399
Pd	601	2356
Ag	29	115
Cd	38	149
Sn	234	917
Sb	48	187
I	66	258
Te	34	133
Cs	1144	4485
Ba	884	3465
La	412	1616
Ce	636	2493
Pr	429	1684
Nd	1122	4400
Sm	512	2007
Eu	72	284
Gd	44	172
Np	95	372
U	207198	812542
Pu	11909	46704
Am	79	378
Cm	7	28

The present results show:

- Salt melt dissolution of spent fuel is a suitable method to determine the total inventory, including gaseous fission products or by-products such as He and ^3H.
- Although the Cm content in the present fuel was rather low (^{242}Cm is the main source of He) it was possible to detect significant amounts of He in the gas phase after melting.

Conclusions

The preliminary inactive experiments have defined the conditions for successful dissolution of natural uranium oxide, uranium-plutonium oxide and metallic U-Pu-Zr alloy by caustic salt dissolution. These procedures have been successfully applied to irradiated UO_2 and MOX fuel samples with subsequent analysis of the gas products by mass-spectrometry and of the solutions by ICP-MS. These analyses methods have shown the presence of tritium as well krypton, xenon, and other volatile species such as I, Br and Cs compounds.

Future work will aim of the optimization of the caustic salt dissolution method as a means to analyse volatile fission products.

Combined with micro-coring, the present method could also be used to determine radial profiles of all elements mentioned above. Thus the release of these volatile compounds in the pellet during irradiation could be followed. This method can determine total volatile fission product inventory, while EMPA can deliver local fission product concentrations within grains. The combination of these values could give an estimate of the grain boundary inventory of volatile fission products.

The method could be useful in the measurement of the iodine content in the fuel cladding interaction layer. This is relevant for the understanding of the iodine assisted stress corrosion.

References

[1] A. V. Nero Jr, A Guidebook to Nuclear Reactors, University of California Press (1979)

[2] Plutonium Handbook - A Guide to the Technology, Ed. O. T. Wickes, Amer. Eve (1980)

[3] G. R. Choppin, J. Rydberg, Nuclear Chemistry, Pergamon Press (1980)

[4] M. Coquerelle, D. Bottomley, IAEA TECDOC-697 (1992) p. 145

4.2 Interaction of Fuel with Structural Materials (Fuel Chemistry)

4.2.1 High temperature severe degradation and interactions of structural material with fuel

Introduction

In severe reactor accidents involving prolonged and extreme fuel overheating, fuel and cladding oxidation and interaction occur both with each other and with the structural materials of the reactor. The main structural materials are:

i) silver absorber rods,
ii) 304 stainless steel (type 304) cladding, and
iii) Inconel 718 spacer grids.

The interaction between structural materials, zircaloy cladding and UO_2 fuel is very dependent upon the oxidizing atmosphere. The extent of oxidation has already been studied [1, 2, 3], using non-irradiated UO_2. A further aspect is the influence of irradiation on these interactions. Thus irradiated fuel has more porosity and heterogeneity than the non-irradiated fuel. The structural materials are also more brittle and contain more crystal defects than non-irradiated materials and this will also influence the results. Parallel work has also been carried out with irradiated fuel and structural material using heat treatments up to 1500 °C in pre-adjusted atmospheres. Work on both irradiated fuel and natural UO_2 has been reported previously (TUAR-93, p. 104-112; TUAR-94, p. 102-106).

This year's work has focused on the interactions of structural materials with natural UO_2, particularly the role of the major elements in the steels and Ni-based alloys: Ni, Cr and Fe on zircaloy and the attack of molten reactor materials on UO_2.

Experimental details

Two main techniques were used: dilatometry and differential thermal analysis (DTA). The dilatometry was used to register the liquefaction of a component when the expansion ceased. The DTA could be used to identify exothermic or endothermic reactions or phase formation from the temperature change compared to an inert reference sample.

In both cases, natural UO_2, zircaloy, 304 stainless steel, and also Ni and Fe discs with 5 mm diameter, 1 mm or 5 mm height, were used. Cr was also used but was in the form of chips of irregular thickness that were impossible to machine further. The composition of the materials and their melting points along with the melting points of the elements are given in Tab. 4.12.

The samples were placed as either two 5 mm high discs, one on top of the other (two material interactions) or as a thin 1 mm disc sandwiched between two 5 mm discs of materials (3 material interaction). These were placed in the Al_2O_3 crucible of the dilatometer or in the Al_2O_3 cup of the DTA apparatus, before sealing and filling with an inert He atmosphere. Heating was at 10 °C.min^{-1}, and was halted after a major interaction was noted (either by expansion collapse for the dilatometry, or by thermal evolution in the DTA or at a pre-programmed maximum). The maximum temperature used in the experiments was 1500 °C. The cooling rate was 20 °C.min^{-1}. The interaction temperatures on heating and on cooling were recorded as was the DTA potential developed during the interaction. This is proportional to the heat evolution (absorption) as well as the maximum temperature attained. The samples were then removed and sectioned, embedded and polished for optical microscopy (polished and etched). Selected specimens were further examined by scanning electron microscopy (SEM) with subsequent energy dispersive X-ray (EDX) analysis of the phases formed during the interaction.

Materials	°C
Fe	1538
Ni	1455
Cr	1863
Zry	1760
UO_2	2860
304ss	1450
AIC	800

Tab. 4.12 a) melting points of material and metals employed in the experiment, b) structural material composition.

Zry 4	Zircaloy 4	Zr - 1.65 Sn - 0.2 Fe - 0.13 Cr - 0.1 O - 0.012 C
304 ss	304 stainless steel	Fe -19 Cr - 9 Ni - 2 Mn - 1 Si - 0.08 Co - 0.08 C
AIC	Silver Absorber rod	Ag -15 In - 5 Cd

Results

Dilatometry and DTA

The results of the dilatometry experiments (INT 1 - 9) have already been given in the previously (TUAR-94, p. 102-104). For a summary of the subsequent DTA results (INT 11 - 18), where the steel components have reacted with zircaloy and with or without UO_2, see Tab. 4.13.

The interaction temperature recorded along with the maximum temperature is compared with the lowest melting point of the single components. In Tab. 4.14, the extent of the exothermic (or endothermic) reaction is also noted as μV from the DTA apparatus. It is seen that the strongest reaction occurs between Ni and zircaloy - 210 μV, and furthermore occurs at a much lower temperature of 1160 °C, compared to the reaction temperature of Fe-zircaloy (1325 °C and -27 μV). When the zircaloy - 304 stainless steel couple was tested, the interaction temperature was found to be 1400 °C (effectively that of the Fe-zircaloy couple). A strong exothermic reaction was observed at -175 μV which is nearly as strong as that of the Ni-zircaloy couple (-210 μV). By contrast the reaction of the Cr-zircaloy system, although it gave a poorly stable trace and only a moderate heat evolution (-26 μV), took

4

Tab. 4.13 DTA and metallography results.

Experiment	Materials	Interaction Temp. °C	Max. Temp. °C	Extent of Interaction	lowest T melting °C
INT 11	Zry	880 ($\alpha \rightarrow \beta$)	1500	Zr melted/liquefied	1760
INT 12	Ni/Zry	1060	1250	very strong Ni+Zr interaction Al_2O_3 crucible attacked	1455
INT 13	Fe/Zry/UO_2	1395	1460	very strong Fe+Zr liquefaction. U 0.25 mm penetration	1538
INT 14	--		--		--
INT 15	Cr/Zry	≈ 1375	1450	medium reaction at corners	1760
INT 16	Fe/Zry	1330	1400	strong	1538
INT 17	Ni/Zry/UO_2	1120	1450	strong penetration ≈ 0,5 mm into UO_2	1455
INT 18	Cr/Zry/UO_2	≈ 1390	1450	Zry strong reaction with Cr. Moderate/slight attack of Cr. UO_2 penetration or interaction layer of 0.2 mm	1760

Tab. 4.14 Comparison of different thermal analysis with dilatometry results up to 1500 °C in argon.

Experiment	Interaction degree (μV)	Interaction Temp. (°C)	Interaction Extent (microscopy)	Dilatometry Interaction Temp. (°C)	Lowest Melting Temp. (°C)
Zry	-2/3 μV	900 ($\alpha \rightarrow \beta$)	very slight	-	1760
Zry-304ss	- 175 μV	1) 1400	very strong	1030	1450
	- 5 μV	2) 1280 (cooling)	slight		1450
Zry-Ni	- 210 μV	1160	extremely strong	-	1455
	- 20 μV	1160 (cooling)	slight reaction		
	- 10 μV	1120 (cooling)	slight reaction		
	- 5 μV	1060 (cooling	slight reaction		
Zry-Fe	- 27 μV	1325	strong	< 1400	1538
	- 5 μV	910 (cooling)	slight reaction		
Zry-Cr	- 26 μV (broad)	1330 (cooling)	small reaction	< 1450	1760
	- 5 μV (broad)	1380 (cooling)	small reaction		
Zry-Ni-UO_2	- 200 μV	1115	extremely strong	< 1250	1455
	- 40 μV	1220 (cooling)	medium		
	- 60 μV	1170 (cooling)	medium		
Zry-Fe-UO_2	- 165 μV	1390	extremely strong	< 1460	1538
	- 10 μV	930 (cooling) ($\beta \rightarrow \alpha$)	slight		

place at a high temperature of 1330 °C and appeared to be slow and incomplete compared to the Fe-zircaloy and Ni-zircaloy. During cooling secondary exothermic phase changes (solidification) were noted at different temperatures to the heating stage. This was a clear indication of the completeness of the reaction to form new phases.

The final experiments were sandwich 3-material experiments using UO_2 in addition to zircaloy-stainless component couples, i.e. Ni-Zry-UO_2, Fe-Zry-UO_2 and Cr-Zry-UO_2. Ni-Zry-UO_2 and Fe-Zry-UO_2 gave strongly exothermic reactions at -210 µV and -165 µV (see Figs. 4.30 and 4.31) which are comparable with the Ni-Zry couple and Zry-304 stainless steel couples.

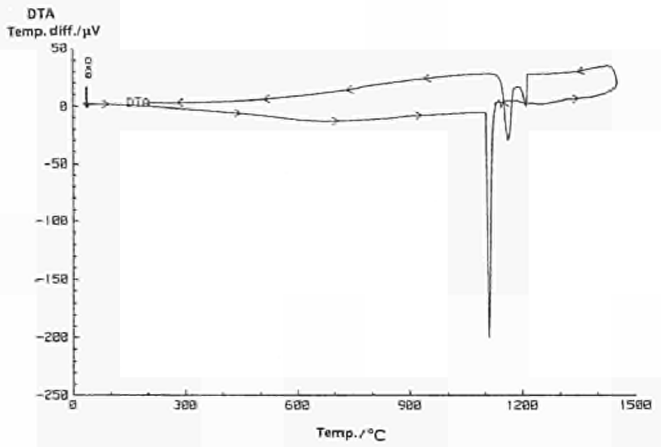

Fig. 4.30 Differential Thermal Analysis (DTA) trace of a Ni-Zry-UO_2 sandwich.

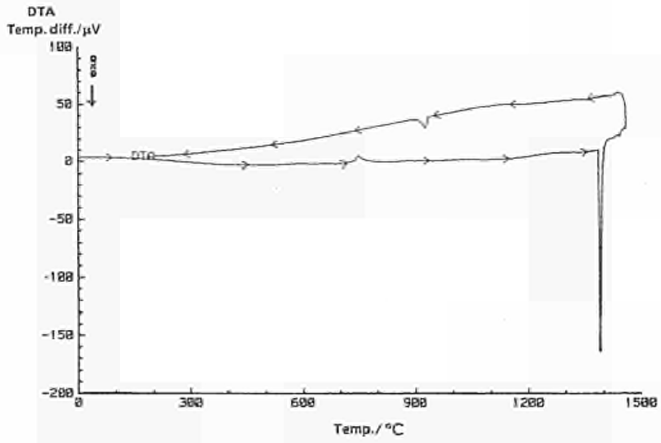

Fig. 4.31 Differential Thermal Analysis (DTA) trace of a Fe-Zry-UO_2 sandwich.

However the Fe-Zry couple yielded only a potential of -26 µV which is at odds with Zry-304 stainless steel and Fe-Zry-UO_2 evolutions (since 304 stainless steel contains 66 w/o Fe). The Ni-Zry-UO_2 and Fe-Zry-UO_2 interaction temperatures are, at 1115 °C and 1390 °C, very similar to the interaction temperatures of the Ni-Zry couple (1160 °C) and Fe-Zry couple (1325 °C) respectively. In addition the Cr-Zry-UO_2 test also gave a similarly high interaction temperature at ~1390 °C in comparison to that of the Cr-Zry couple (1375 °C). The Zry-304 stainless steel couples interaction temperature (~1400 °C) is thus dominated by the Fe and Cr component although the heat evolution is increased by the presence of Ni. The dilatometry results from the previous year however gave an interaction temperature of 1030 °C which indicates a predominant role of the Ni-Zry interaction. Possibly the contact pressure of the dilatometer rod could be the cause for the favouring of this strong interaction and hence the difference compared to the DTA test of the same couple. It is intended to test the Fe-Zry couple again by DTA and also to test this and the Zry-stainless steel couple by dilatometry using different contact pressures of the extensometer rod.

Optical and scanning electron microscopy (SEM)

The optical and SEM examinations of the dilatometry and DTA samples cut in half and embedded gave a good indication of the extent of interaction, both in terms of deformation of geometry or melting, and the penetration depth of the samples. The phases formed could also be analysed by EDX.

Optical microscopy

There was considerable liquefaction of zircaloy in the zircaloy-stainless steel (INT 1) and Zry-stainless-UO_2 (INT 2) couples. It was worth noting that the zircaloy appeared to be particularly fluid and attacked compared to stainless steel (see Fig. 3.24 of previous ITU annual report TUAR-94, p. 104). Despite the low heat evolution of the Cr-zircaloy couple (INT 15) DTA analysis, the optical microscopy (Fig. 4.32) shows again that Cr is slightly attacked but that the zircaloy has been liquefied and flowed away reacting with the Al_2O_3 crucible.

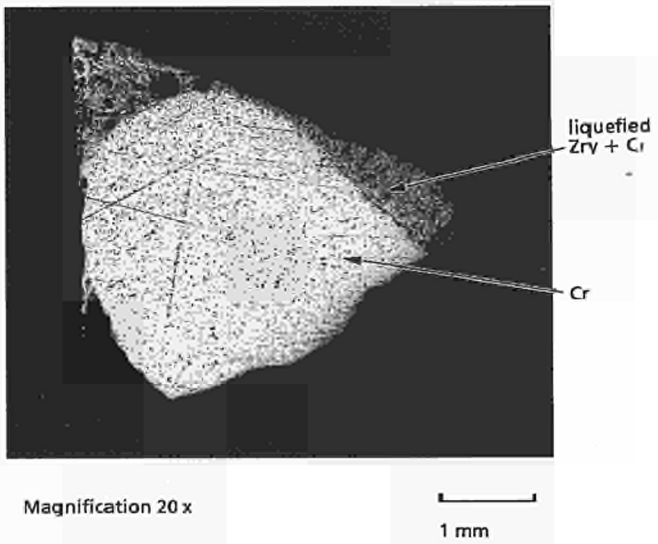

Fig. 4.32 Chromium-zircaloy (Cr/Zry) interaction.

On cooling a lamellar pattern of two phases has been formed. During the Cr-Zry-UO_2 test (INT 18) the UO_2 was also attacked by this Zry-Cr liquid forming at about 1400 °C. However, the biggest interaction between UO_2 and liquefied material appears to be that of the Ni-Zry-UO_2 couple where the Ni-Zry intermetallics have attacked the UO_2 and then on cooling appear to have

precipitated out of the ceramic, leaving a slightly different ceramic matrix appearance (lighter due to compositional differences?) with substantially larger porosity than the underlying unattacked UO_2 matrix. Fe/Zry/UO_2 couples showed a stronger attack of the UO_2 and the Al_2O_3 crucible by liquified material. Penetration was approximately 250 µm for Fe/Zry into UO_2, whereas it was approximately one third of this for Ni/Zry penetration into UO_2 (80 µm) (see Figs. 4.33 and 4.34) - although the latter was at lower temperatures of 1100 - 1250 °C compared to 1400 - 1450 °C for Fe-Zry-UO_2.

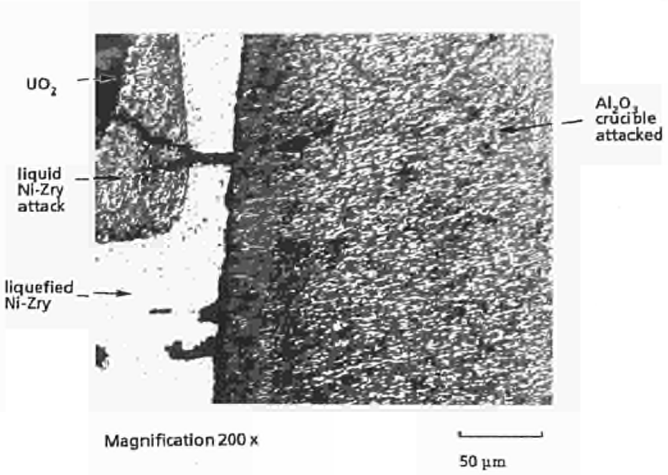

Fig. 4.34 Nickel-zircaloy-uranium dioxide (Ni-Zry-UO_2) interaction showing the liquefied Ni/Zry penetration into the UO_2.

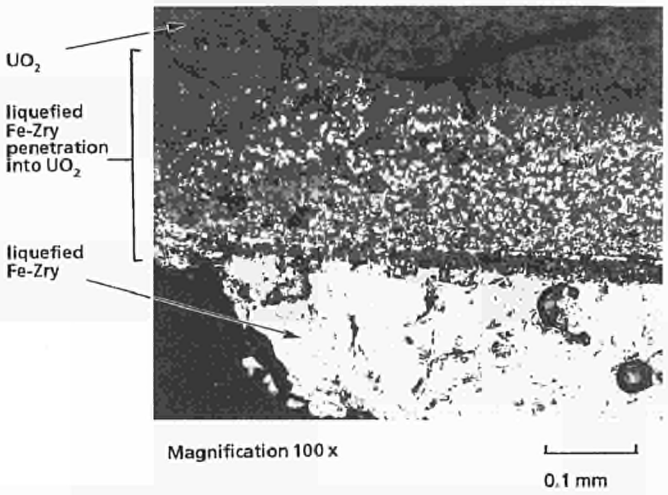

Fig. 4.33 Iron-zircaloy-uranium dioxide (Fe-Zry-UO_2) interaction showing liquefied Fe/Zry penetration into the UO_2.

Scanning electron microscopy

Three selected dilatometry samples were examined by SEM and with EDX for the local phases. In the stainless steel-zircaloy interaction (INT 1) the various phases found at the interface were intermetallics of either Zr-Fe-Cr or Zr-Ni compositions. In Figs. 4.35 and 4.36 porous phases are seen at the interface that are approximately $(Fe,Cr)_3Zr_2$ in composition; Fe_2Cr had also been found in earlier analyses. This compares with compositions of $(Fe,Cr)_2Zr$ found by Hofmann and Markiewicz in Zry/stainless steel reaction at 1150 °C for 5 min. [4].

atomic %

1) Large phase
Zr 43 %
Fe 31 %
Cr 26 %

2) Zircaloy
(circular phase)
pure Zr

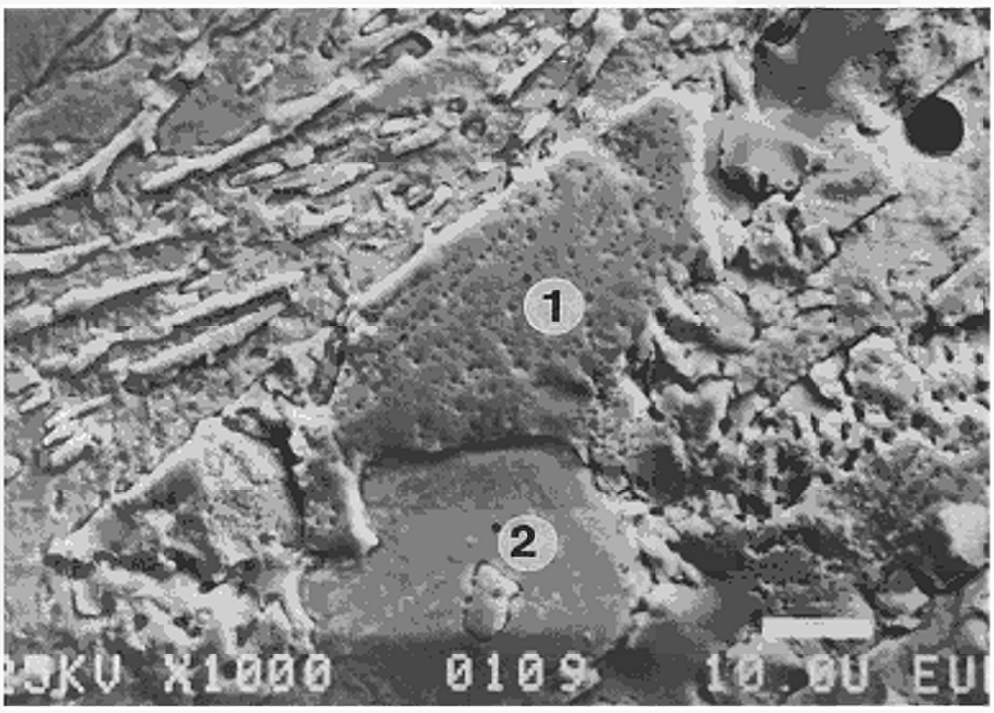

1000 x

Fig. 4.35 304 stainless steel-zircaloy (304ss-Zry) interaction.

atomic %

1) Smooth phase
(Cr-Fe)
Cr 45 %
Fe 38 %
Zr 14 %

2) Porous phase
Zr 40 %
Fe 30 %
Cr 30 %
≈ $(Fe, Cr)_3Zr_2$

3) Stainless steel
Fe 70 %
Cr 20 %
Ni 10 %

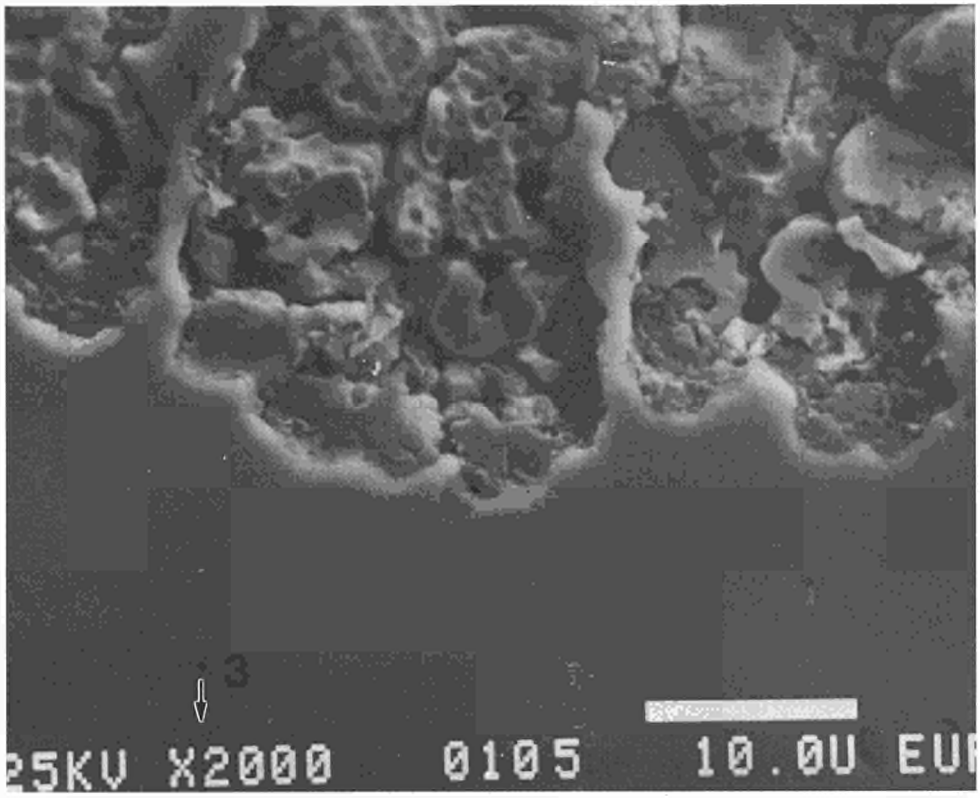

2000 x

Fig. 4.36 304 stainless steel-zircaloy (304ss-Zry) interaction showing edge of interaction zone.

In other areas lamellar structures are evident (Fig. 4.37) resulting from mixing, cooling and then separating out into different phases.

The overall analysis indicates some admixing of the steel to the zircaloy. Fig. 4.38 shows the lamellar structure in close -up and that they are Zr-Fe-Cr mixture in a matrix of practically pure zirconium.

In the 304 stainless-Zry-UO_2 interaction (INT 9) SEM examination of the 304 stainless-Zry interaction zone is shown in Fig. 4.39 (compare with Fig. 3.28 in TUAR-94, p. 106).

atomic %

1) Global analysis
Zr 79 %
Fe 15 %
Cr 5 %
Ni 1.5 %

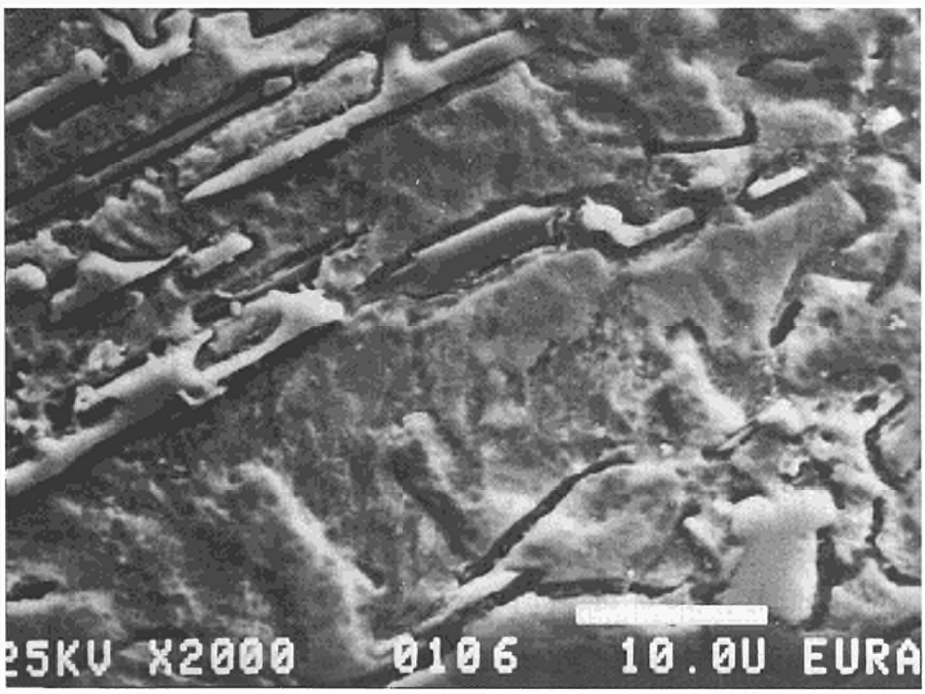

2000 x

Fig. 4.37 304 stainless steel-zircaloy (304ss-Zry) interaction showing the lamellar structure of the interaction zone.

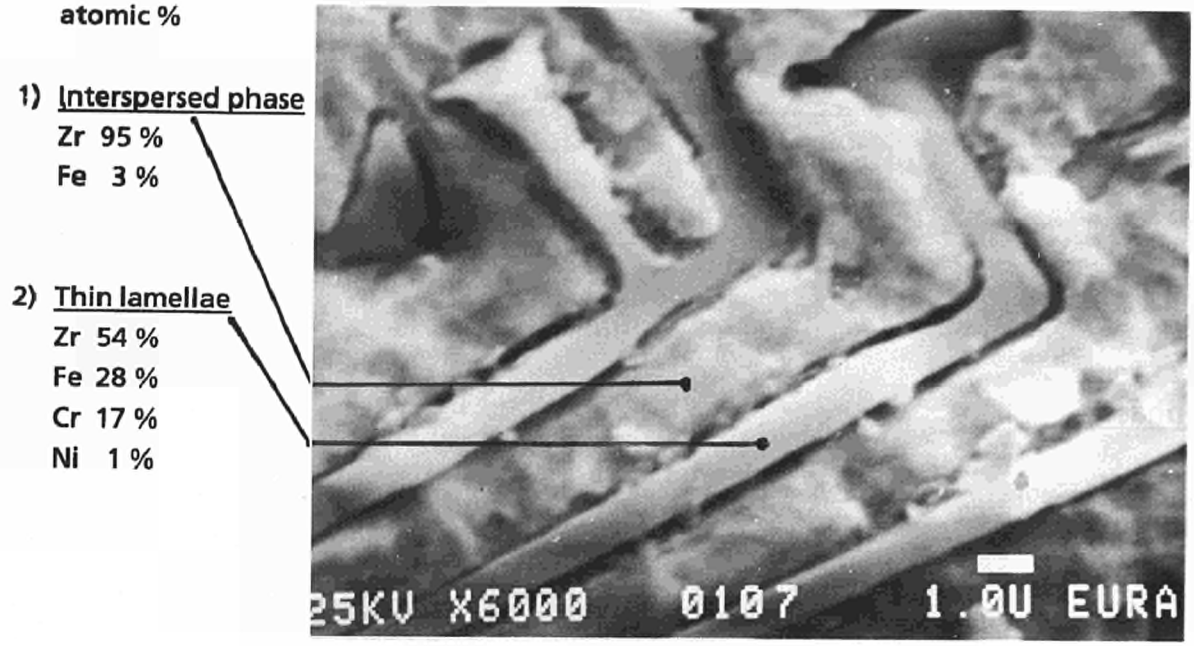

Fig. 4.38 304 stainless steel-zircaloy (304ss-Zry) interaction shows Zr-Cr-Fe and pure Zr lamellae.

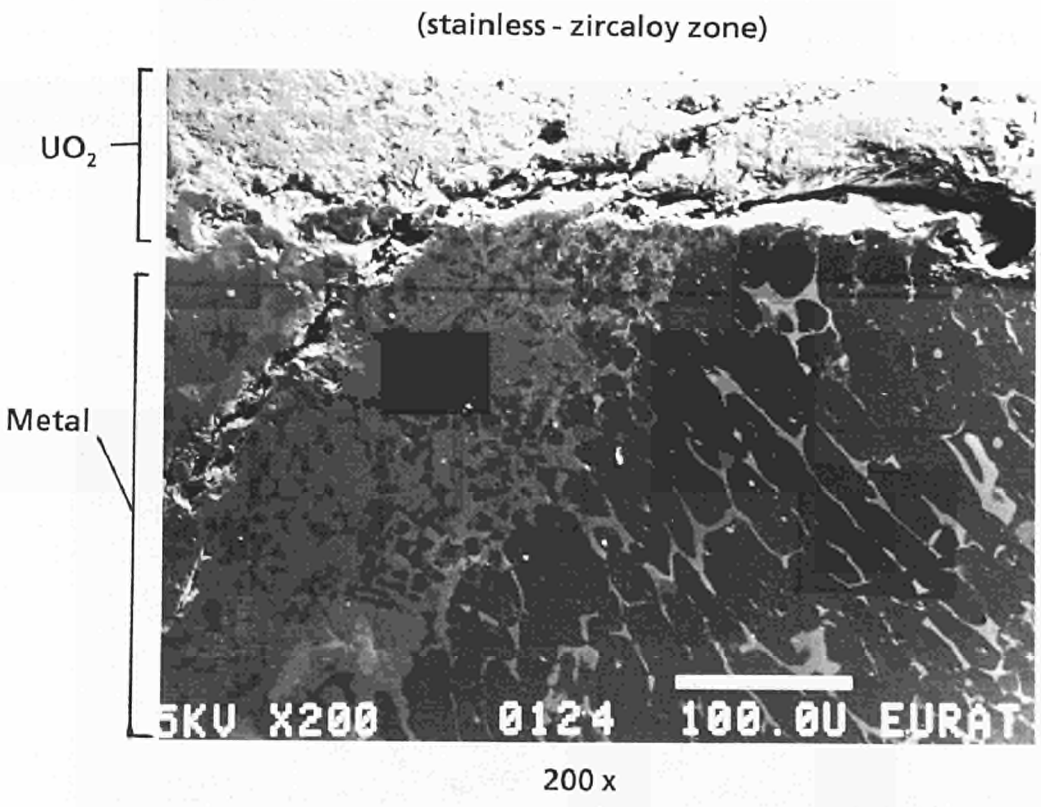

Fig. 4.39 304 stainless steel-zircaloy-UO_2 (304ss-Zry-UO_2) interaction showing the interacted stainless-zircaloy structure adjacent to the UO_2).

The whiter (denser) phase of the two-phase metallic zone is a zirconium-richer phase with Fe and Ni or Fe-Cr present. Sometimes uranium is also present; this indicates that attack of the UO_2 pellet has already commenced. The darker phase is mainly stainless steel (Fe,Cr,Ni) but with reduced nickel content, however, it is close to the main mass of the stainless steel disc.

By contrast the liquefied material that flowed up the side of the UO_2 pellet and reacted with it (see Figs. 4.40a. and b.) shows a melt that is zirconium-dominated (~70 a/o of Zr) and yielded composition of Zr_3(Fe,Ni,Cr) and Zr_2(Fe,Ni,Cr).

atomic %

1) Metallic Zry/ss
Zr 72 %
Fe 19 %
Cr 4 %
Ni 5 %

Zr_3(Fe, Ni, Cr)

Fe:Ni:Cr
= 4:1:1

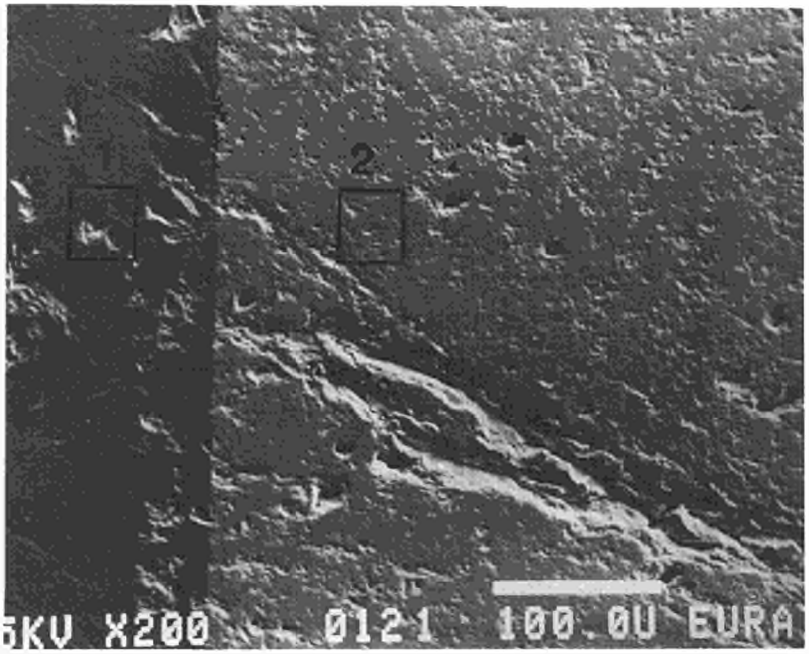

2) UO_2 pellet
U 66 %
Fe 23 %
Cr 7 %
Ni 4 %

200 x

Fig. 4.40a 304 stainless steel-zircaloy UO_2 (304ss-Zry-UO_2) interaction: the liquefied stainless-zry has enveloped UO_2.

4) UO_2 pellet
U 45 %
Zr 35 %
Fe 14 %
Cr 4 %
Ni 2.5 %

3) Metallic Zr/ss

Zr 66 %
Fe 21 %
Cr 9 %
Ni 4 %

Zr_2 (Fe, Ni, Cr)

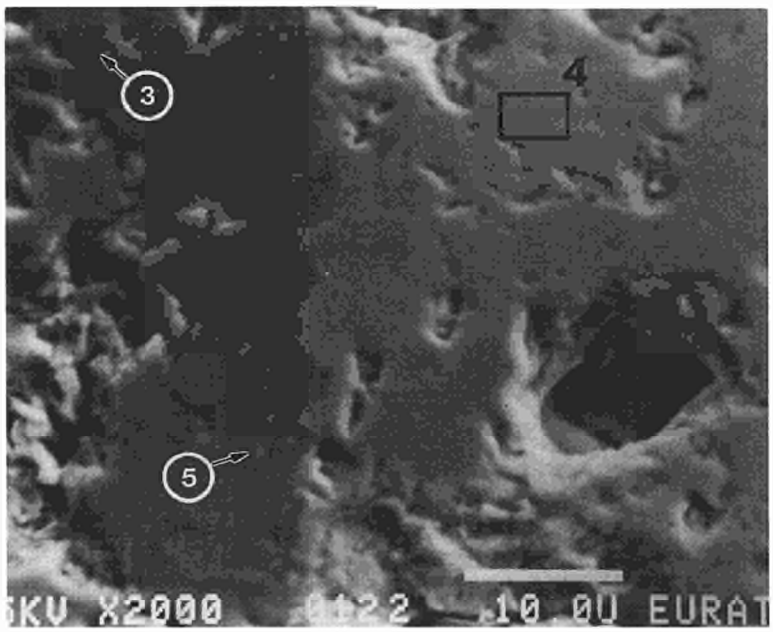

5) White interfacial particles
U 24 %
Zr 39 %
Fe 23 %
Cr 5 %
Ni 2 %
(Au 8 %)

2000 x

Fig. 4.40b 304 stainless steel-zircaloy-UO_2 (304ss-Zry-UO_2) interaction: close up of liquified stainless-zircaloy dissolution of the UO_2.

The melt/ UO_2 interface had small white particles that EDX confirmed were U-rich. These may be the result of uranium precipitating out of solution and would point to a liquefaction of the UO_2. The EDX pellet analyses show considerable presence of other elements e.g. Zr or Fe. Some of this may be impurities introduced during polishing, but may also reflect the inward diffusion or penetration of the melt into the UO_2.

The EDX analyses of the zircaloy-absorber interaction showed that the liquid silver absorber was already slowly dissolving the zircaloy at 900 °C (Ag-15 In-5 Cd

absorber melts at 800 °C). The line analysis going across the zircaloy to the absorber melt showed a descending Zr content with distance from the Zry. Indium was also observed indicating that no extreme temperatures had been reached.

Discussion

The finding of Fe-rich Fe/Ni/Cr-Zr intermetallics e.g. $(Fe,Cr)_3Zr_2$ was mainly restricted to the zones close to the stainless steel discs. In the UO_2/Zry/stainless experiments it was mainly Zr-rich Fe/Cr/Zr intermetallics that were found to be most fluid, usually of a formula $Zr_3(Fe,Ni,Cr)$ and $Zr_2(Fe,Ni,Cr)$. The DTA analysis indicates that both Fe-Zry reactions and Ni-Zry reactions are very exothermic, with Ni-Zry being the most exothermic. These Ni-Zry interactions commence at about ~1100 °C whereas Fe-Zry requires 1330 °C, but once initiated at higher temperatures, it will proceed faster.

The Fe-Zr and Ni-Zr phase diagrams indicate a series of intermetallic compounds. From the Zr-rich side there is $NiZr_2$ (1120 °C) but also Ni-Zr (1260 °C) for Ni-Zr; for Fe-Zr on the Zr-rich side there is Zr_3Fe (928 °C) but also Zr_2Fe and $ZrFe_2$ (~1330 °C). These form the following low melting point eutectics.

Ni Zr_2 - Zr	T_{eut} =	960 °C
Ni Zr - Ni Zr_2	T_{eut} =	1010 °C
Ni_5 Zr - Ni	T_{eut} =	1170 °C
Zr Fe_2 - Zr	T_{eut} =	928 °C

It is seen that both Ni-rich and Zr-rich ends of the Ni-Zr system are capable of forming low melting point eutectics at 1000 - 1200 °C and hence initiating rapid liquefaction at this temperature. However even in the Cr-Zry interaction considerable fluidity of the zircaloy is seen despite only slight attack of the Cr. Thus the effect of all three metals Fe, Ni and Cr to form lower melting point compounds with zirconium is the most important feature.

Conclusions

1) DTA tests carried out on the component elements of the stainless steel in contact with zircaloy have shown the exothermic reactions that occur between Fe + Zry and Ni + Zry to form intermetallic compounds.

2) These intermetallics are seen from the phase diagram to form eutectics between themselves and reactants of relatively low melting points of 1000 - 1200 °C. These are approx. 200 - 300 °C lower than the stainless steel and zircaloy melting points.

3) The Ni-Zry interaction appears to be the most exothermic and to occur at the lowest temperatures of about 1160 °C, while the Fe-Zry interaction occurred at ~1330 °C. Both showed strong interaction/fluxing reactions. Cr-Zry interaction appeared to be at a similar temperature of about 1330 °C but showed lesser attack than Fe-Zry.

4) The 304 stainless steel/zircaloy interaction appears to be dominated by the Fe-Zry interaction since they have similar interaction temperatures of 1330 °C and 1400 °C respectively, although the Ni-Zry interaction also seems to be important as this also has a large heat release.

5) In all cases the original zircaloy samples become most fluid and this indicates that it is the Zr-rich end of the Ni-Zr and Fe-Zr system which is mostly formed and directly influences the fluxing reactions.

6) EDX analyses show that the Zry/Fe-Ni-Cr mixtures such as $Zr_2(Fe,Ni,Cr)$ or $Zr_3(Fe,Ni,Cr)$ can form at 1400 °C and attack the UO_2 within 30 min.. These can result in UO_2 dissolution and diffusion or penetration of Zr, Fe, Ni and Cr into the UO_2 fuel. Ferrous (Fe/Ni/Cr) -rich liquefied material is seen near the stainless samples and this shows that both ends of the phase diagram can contribute to the lowered liquefaction temperatures.

Future Work

In a further stage of investigation the quantitative measurement of the reaction/interaction enthalpy would be important to assess the component element's role. The investigation of the Ni-based alloy Inconel 718 that is used as a spacer grid in the reactor assembly will also be undertaken.

Finally the kinetics of the interaction/reaction will be examined at a constant temperature for different time intervals to assess penetration depths and overall degree of degradation for the couple zircaloy-stainless steel or the component elements (Fe, Ni and Cr) with zircaloy.

References

[1] P. Hofmann, M. Markiewicz, Chemical interactions between as-received and pre-oxidized zircaloy-4 and Inconel-718 at high temperatures, report KfK 4729, June 1994

[2] P. Hofmann, M. Markiewicz, J. Nucl. Mat. 209 (1994) 92-106

[3] S. Hagen, P. Hofmann, "Physical and chemical behaviour of LWR fuel elements upto very high temperatures", report KfK 4104, June 1987

[4] P. Hofmann, M. Markiewicz, "Chemical interactions between as-received and pre-oxidised zircaloy-4 and stainless steel at high temperatures", report KfK 5106, May 1994

4.2.2 Sodium-SUPERFACT fuel compatibility test

Introduction

Laboratory tests were designed to simulate the conditions and analyse the consequences of the potential contact of Na with fuels of the Superfact experiment - $(U,Pu,Am)O_2$, $(U,Pu,Np)O_2$, $(U,Np)O_2$ - should a cladding failure occur during irradiation in a fast breeder reactor.

The aim of the measurements is to determine the extent of the reaction between liquid Na and irradiated SUPERFACT fuel samples, in the temperature range 600-700 °C, and to characterize, chemically and crystallographically, the reaction products formed at different exposure times.

In order to check the experimental installation, a preliminary series of tests was performed with unirradiated fuel using protective glove-boxes in an α - laboratory. Once the tests parameters are defined a final test series will be performed with irradiated fuel samples in hot-cell laboratories.

In previous investigations, the reaction products under conditions of maximum oxygen availability were characterized (TUAR 94, p. 100). Here results of the reaction kinetics between liquid sodium (with low oxygen content, 5 ppm) and MOX fuels containing actinides are reported for the same temperature range (600-700 °C).

Materials

The materials used for the study were Na (Fluka, GmbH) and fuel pellets of the type MO_2 (with $M= U_{1-x-y-z},Pu_x,Am_y,Np_z$), prepared by standard cold pressing and sintering procedures. The fuels used for this study are listed in Tab. 4.15.

Experimental Method

As already reported (TUAR-94, p. 100), a special furnace was designed and constructed (Fig. 4.41), which permits the purification of sodium with an oxygen getter (Zr) before it is brought in contact with the fuel at the reacting temperature.

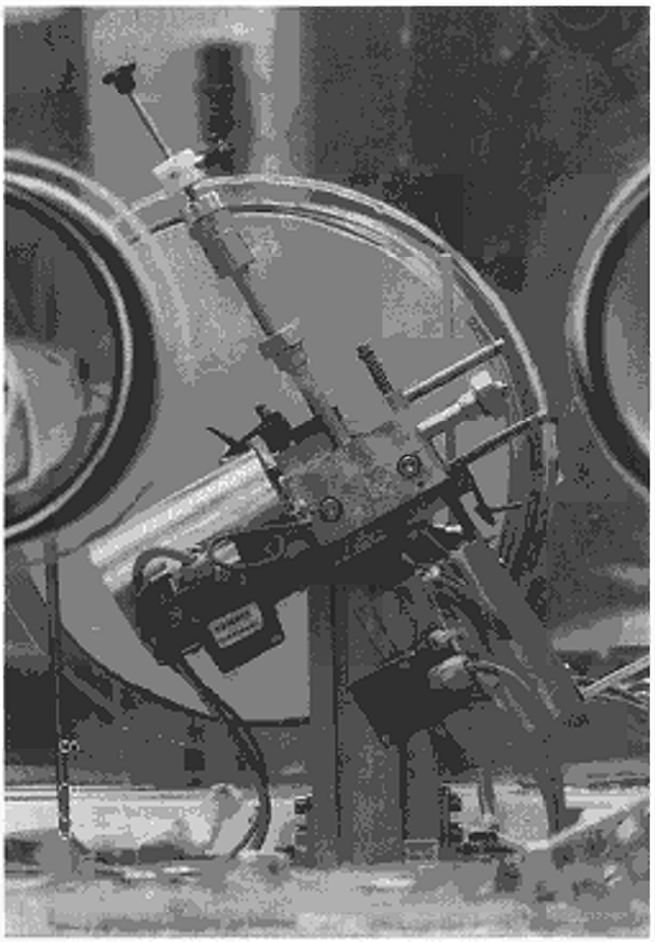

Fig. 4.41 Furnace for compatibility tests of Na with SUPERFACT fuel.

Changes of the initial pellet geometry and dimensions after reaction provide information about the extent reaction at the given temperature-time conditions. To enable a better comparison of the results, the pellets were brought to stoichiometry by thermal treatment, before exposure to liquid sodium. For this purpose the pellets were heated at 850 °C for 6 h in a 10:1 CO/CO_2 gas mixture [1].

After the reaction of sodium with the fuel, residual sodium was extracted with alcohol. Alcohol was chosen as extractant because sodium is highly soluble in it and no dissolution of the reaction products was observed.

The sodium distribution in the pellet was studied by means of EMPA while the morphology of the sodium attack was investigated by metallography and microscopy.

Tab. 4.15 Fuel compositions used for this study.

Fuel
$(U_{0.74}\ Pu_{0.24}\ Am_{0.02})O_2$
$(U_{0.74}\ Pu_{0.24}\ Np_{0.02})O_2$
$(U_{0.55}\ Np_{0.45})O_2$
$(U_{0.8}\ Pu_{0.2})O_2$
UO_2

Results

The volume increase of the pellets was used to indicate the extent of the reaction as a function of time (Tab. 4.16). The behaviour of $(U,Pu)O_2$ was taken as a reference for the comparison with the other fuels (Fig. 4.42).

Tab. 4.16 Dimensional changes of the $(U,Pu)O_2$ fuel.

Time (h)	DL/L %	DD/D %	DV/V %
5	0.15	0.11	0.37
24	0.59	0.69	2.05
48	2.26	1.06	4.44

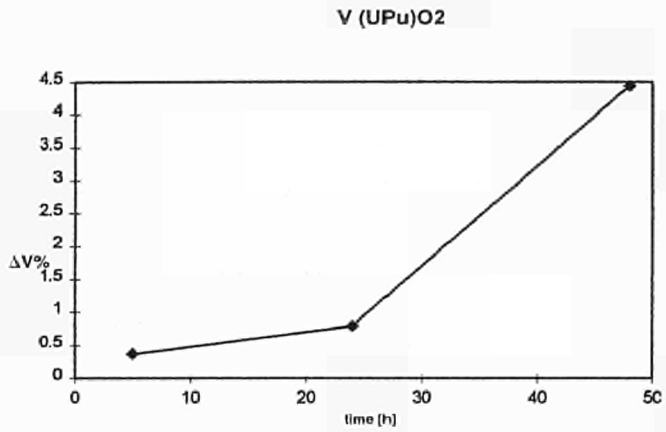

Fig. 4.42 Volume changes of the $(U,Pu)O_2$ pellet after reaction with sodium at 650 °C at different times.

The first series of experiments with the various fuels, carried out at 650 °C for 5 h, indicated no appreciable change of the pellet volumes. The volumes increased, however, with longer exposure times to sodium under these conditions. The results are listed in Tab. 4.17 and plotted in Fig. 4.43.

Tab. 4.17 Volume changes of the fuel used in this study.

Composition	ΔV/V 5h	ΔV/V 48h
$(U_{0.8}\ Pu_{0.2})O_2$	0.37	4.44
$(U_{0.74}\ Pu_{0.24}\ Am_{0.02})O_2$	0.26	6.67
$(U_{0.74}\ Pu_{0.24}\ Np_{0.02})O_2$	0.28	1.73
$(U_{0.55}\ Np_{0.45})O_2$	0	0.98

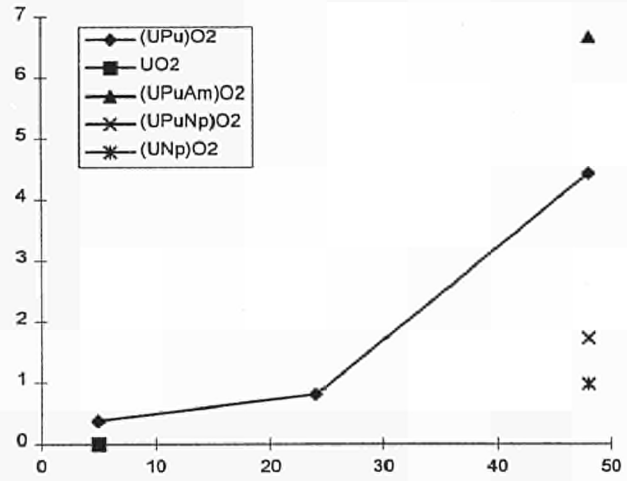

Fig. 4.43 Volume changes of pellets of different fuels after reaction with sodium at 650 °C at different times.

The EMPA results show that sodium remained mainly at the periphery of the pellets, although traces of sodium were always found in the pellet interior. This is an indication that the sodium can diffuse into the fuel. Ceramographic sections of reacted pellets were examined by optical microscopy to determine the extent of the sodium penetration. It appeared that the reaction was not confined to the periphery of the pellet and that, in general, complete penetration had occurred. Ceramographs of reacted pellets are shown in Fig. 4.44.

Fig. 4.44 Ceramographic section of a pellet of $(U,Pu,Am)O_2$ after the reaction with sodium at 650 °C for 5 h; magnification 20 x.

For all materials examined, a typical feature of the reaction was the considerable cracking of the pellets that occurred during the treatment, which makes the determination of the dimensional changes and hence volume swelling difficult. The ceramograph at higher magnification in Fig. 4.45 shows the grey sodium

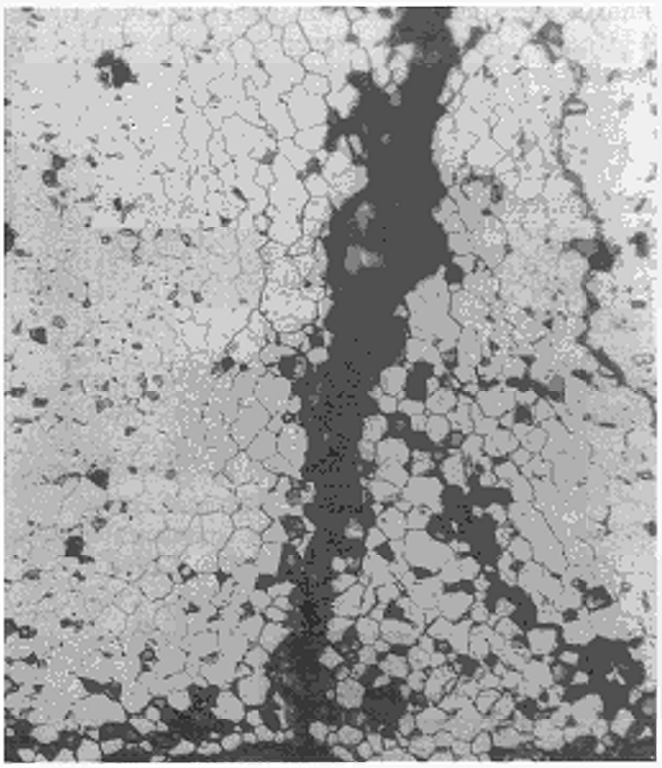

Fig. 4.45 Ceramographic section of a pellet of $(U,Pu,Am)O_2$ after the reaction with sodium at 650 °C for 5 h; magnification 500 x.

urano-plutonate phase formed along the grain boundaries, which causes the pellet swelling.

The pellets containing Am exhibit a larger attack by Na than the pellets of $(U,Pu)O_2$. In contrast, the pellets containing Np exhibit a smaller attack. An increase of the sodium reaction rate and swelling is observed when Am is incorporated in the urania-plutonia lattice. In this case, the intergranular attack is stronger than in the cases of pure $(U,Pu)O_2$ and Np containing fuels. These results are in agreement with the results of volume changes.

A fracture surface from a $(U,Pu,Np)O_2$ reacted pellet was studied by scanning electron microscopy (Fig. 4.46). It shows that a fine film of the product is observed between the grains.

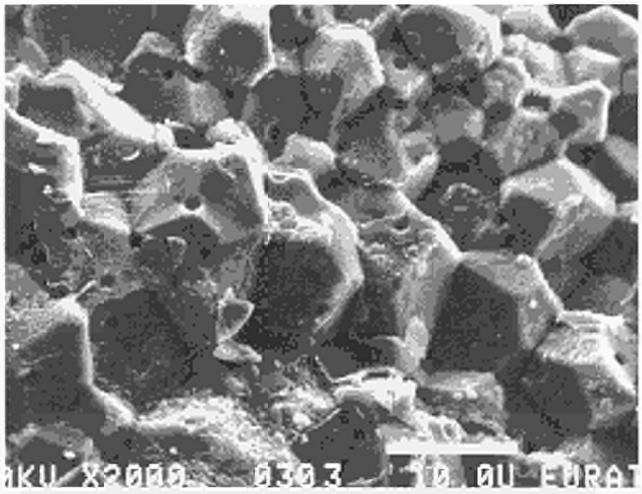

Fig. 4.46 Scanning electron micrographs of a fractured surface of a $(U,Pu,Np)O_2$ pellet after the reaction with sodium at 650 °C for 5 h; magnification 2000x.

An other interesting observation is that in pellets of $(U,Pu)O_2$ a thin band with numerous tangential cracks appears at the pellet edge, with a thickness of about 30 - 40 μm (Fig. 4.47). This structure was not observed in other fuels treated in this way.

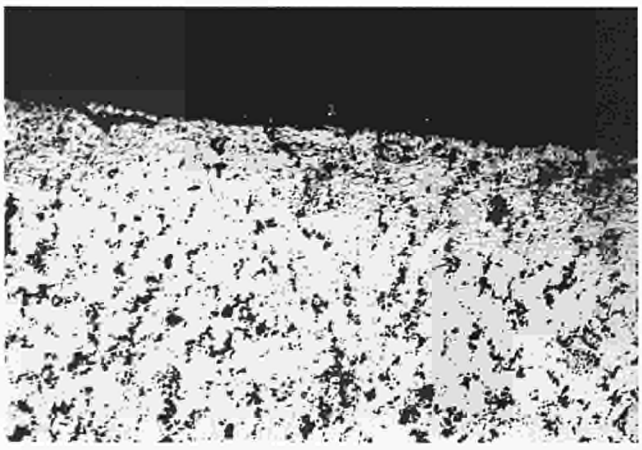

Fig. 4.47 Ceramographic section of a pellet of $(U,Pu)O_2$ after the reaction with sodium at 650 °C for 5 h; magnification 200 x.

An additional Na reaction experiment was performed using a pellet with composition $UO_{2.07}$. In this case the results of EMPA and the ceramographic studies show that the sodium phase appears in the centre of the pellet (Fig. 4.48). This observation is in agreement with the results of Mignanelli and Potter [1], that for hyperstoichiometric uranium the reaction product is found far from the Na-fuel interface.

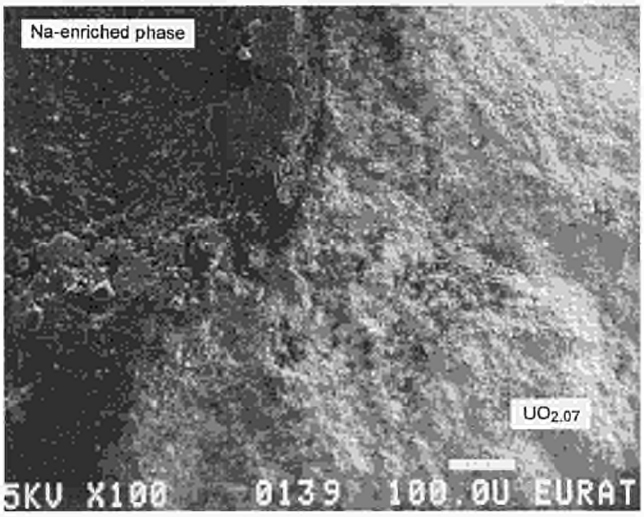

Fig. 4.48 Scanning electron micrographs of a fractured surface of a $UO_{2.07}$ pellet after the reaction with sodium at 650 °C for 5 h ; magnification 200x.

Conclusions

The conclusions can be summarized as follows:

1) The content of actinide in the pellet has an influence on the kinetics of reaction of sodium with the fuel. The reaction rate increases when Am is present and decreases when Np is present.
2) The reaction attack is intergranular.
3) The stoichiometry of the fuel has an influence on the distribution of the sodium found in the pellet.

Future work

Future work will focus on a comparative study of the long term kinetics (≥ 240 hours). In particular, such studies will be performed on irradiated fuels for comparison with the behaviour of fresh fuel. The influence of the stoichiometry of the fuel on the reaction will also be investigated.

References

[1] M. A. Mignanelli, P. E. Potter; J. Nucl. Mater. 125 (1984) 182-201.
[2] M. G. Adamson, E. A. Aitken, R. W. Caputi. M. A. Mignanelli, P. E. Potter; IAEA-SM-236/63 (1979)
[3] M. A. Mignanelli, P. E. Potter; J. Nucl. Mater. 114 (1983) 168-180.

4.3 Non-Destructive Assay of Spent Nuclear Fuel

Introduction

The two main options for the management of spent fuel are direct disposal for isolation of nuclear waste from the biosphere, and reprocessing for retrieval of useful nuclides. Safety considerations, e.g. criticality, fissile material accountancy and inventory of highly toxic radionuclides, require verification of the final burn-up declared by the operators prior to realisation of either of the two waste options. The aim of this work is to demonstrate the verification of (1) the declared burn-up and its axial dependence of a spent fuel and (2) the content of plutonium and curium in the spent fuel.

The build-up of individual nuclides in a spent fuel is inherently consistent. Hence, the analysis of a few nuclides, through their spontaneous fission neutron and characteristic gamma emissions, allow the verification of the predicted evolution of the fuel during irradiation. A methodology, based on Non-Destructive Assay (NDA) complemented by Isotopic Correlations (IC), has been developed to characterize spent fuel in terms of its burn-up and composition. Isotopic correlations are used to extrapolate from the measured neutron and gamma signatures the information sought to characterize the fuel pin. Pellets of the fuel analysed non-destructively, are dissolved for subsequent chemical analyses for the verification of the NDA/IC predictions.

Materials and methods

Fuel analysed

Passive neutron and gamma measurements were carried out along the active length of spent fuels from different reactors and final burn-up: from PWR power stations UO_2 fuel [3.5 and 3.8% enrichment in ^{235}U; declared average burn-up 4.0 to 5.5 a/o] and MOX fuel [U_{nat}, 4% enrichment in Pu_{fiss}, declared average burn-up 4.5 a/o]; and fuel from a fast reactor. The last was comprised of fuels from the SUPERFACT irradiation experiment in which minor-actinide-containing fuels were irradiated in the fast reactor PHENIX [1]. Their compositions were:

(i) 74% U_{nat}, 24% Pu (first generation) and either 2% ^{241}Am or ^{237}Np (declared average burn-up 6.0 a/o);

(ii) 60% U_{nat}, 20% ^{241}Am, 20% ^{237}Np (declared average burn-up 4.0 a/o).

Experimental

NDA techniques, such as passive neutron interrogation (PNI), offer the possibility to analyse spent fuel. A compact counting unit [350 mm x 250 mm x 250 mm height] was employed inside a β-γ hot-cell for the passive neutron interrogation of the spent fuel pins (Fig. 4.49). The fuel pin can be horizontally translated on the metrology bench and in passing through the unit it is scanned. Profiles of the measurements, and hence the required information as a function of distance along the fuel length, are obtained (TUAR-91, p. 108; TUAR-93, p. 128). Destructive assay (DA) was carried out on samples from the spent fuels in order to determine by chemical analysis the final burn-up and isotopic composition achieved during irradiation. These results are then used for the verification of the non-destructive measurements.

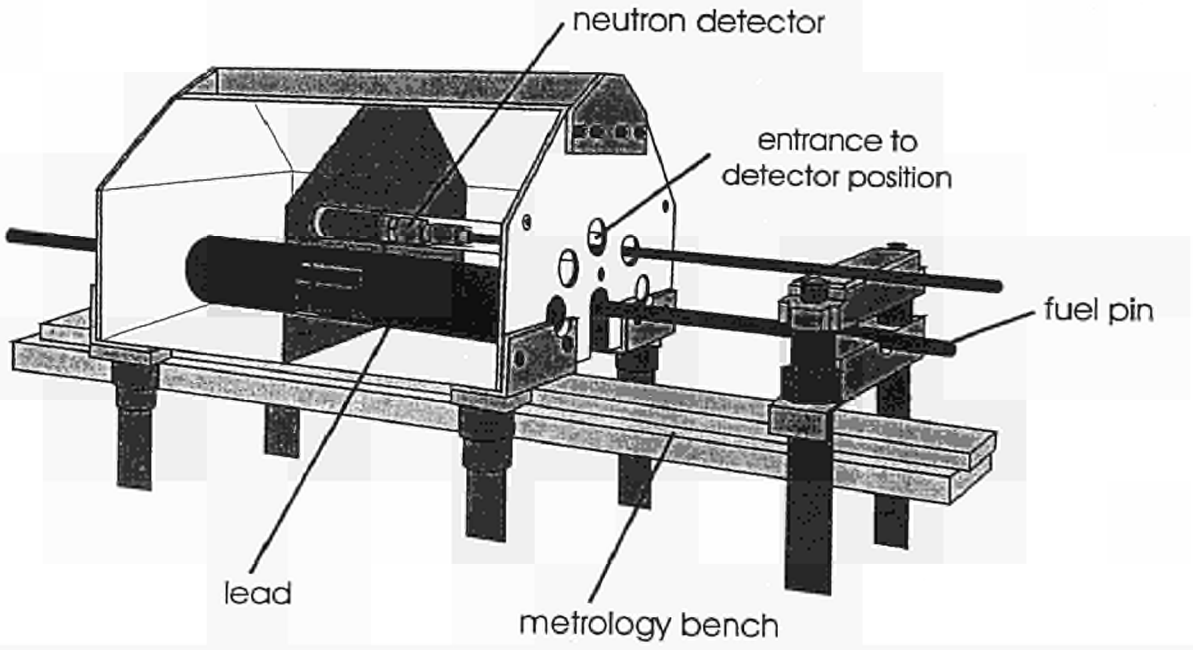

Fig. 4.49 A schematic design of the counting unit with a detector and a spent fuel installed above the metrology bench.

Calculations and correlations

Isotopic correlations [2] suitable for interpretation of the passive neutron interrogation signature were set up applying the computer code KORIGEN [3]. The calculations were coupled with burn-up-dependent cross-section libraries resembling, as close as possible, the type of reactors where the fuel was irradiated. Relationships were thus established which correlated the measured quantities (neutron emission, fission-product activity) with the fuel parameters to be verified (e.g. burn-up, cooling time, fissile content, radiotoxicity potential). The isotopic correlations are fuel- and reactor-dependent. Consequently, they reflect each individual case, relying on the initial enrichment and type of fuel data supplied by the operator of the reactor. Although KORIGEN is consistent within itself, inaccuracies in the nuclear data cause discrepancies in the calculated results. These are localized by the destructive analyses of pellets using high precision analytical techniques and corrected for.

Results and discussion

Neutron emission profiles, as a function of distance along the active length of different PWR spent fuel pins, are shown in Fig. 4.50. The neutron emission effectively reflects, for burn-up higher than 30 GWd/t, the curium formation. ^{242}Cm dominates the neutron emission shortly after discharge and ^{244}Cm at longer cooling times. The shape of these curves reflects the neutron fluence variation along the pin during irradiation in the reactor core. The strong dependence of the neutron emission on the burn-ups renders the passive neutron signature suitable for NDA applications. The sensitivity for the burn-up is further demonstrated in Fig. 4.49, where the profiles from pins differing in average burn-up by about 5 GWd/t are clearly separated.

The neutron profiles in Fig. 4.49 form the basis from which the information required to characterize a fuel is obtained by applying isotopic correlations. Information referring to a single pellet or averaged over the whole pin can be extrapolated from the corresponding local or average neutron emission of the pin. This information includes the burn-up, total and average plutonium and curriculum contents.

The information averaged over the whole pin is used to verify the shipper's declared data. Destructive analyses (DA) of pellets are carried out to verify the local information obtained.

The results obtained through NDA (PNI and IC), the chemical analyses (DA) and the corresponding shipper's declarations are given in Tab. 4.18. The local information given for the pins 1 and 3, refers to pellet positions along the plateau and the slope of the profiles in Fig. 4.49. Otherwise, the information reflects pellets from the middle of the active length of the pin. The total plutonium and curium contents given in Tab. 4.18 have been normalized to the concentration of ^{238}U.

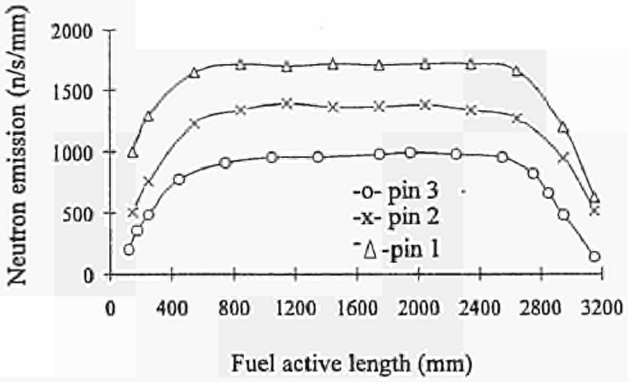

Fig. 4.50 Axial neutron emission profiles from PWR spent fuel.

	Burnup (Gwd/t)		Total Plutonium / ^{238}U		Total Curium / ^{238}U	
Fuel	**NDA**	**DA**	**NDA**	**DA**	**NDA**	**DA**
PIN 1						
local (plateau)	55.8	54.8	0.0133	0.0127	2.0E-4	2.2E-4
local (slope)	46.1	47.0	0.0121	0.0123	-	-
pin average	54.3 [55.0]	-	-	-	-	-
PIN 2						
pin average	50.3 [50.2]	-	-	-	-	-
PIN 3						
local (plateau)	46.5	44.8	0.0122	0.0117	1.12E-4	1.31E-4
local (slope)	29.4	30.5	0.010	0.0113	-	-
pin average	44.9 [44.4]	-	-	-	-	-
MOX thermal	42.7	44.7	0.037	0.038	5.85E-4	6.8E-4
UPu, 2% Np	62.4	62.2	0.33	0.32	-	-
UPu, 2% Am	60.3	62.2	0.31	0.32	1.9E-4	3.3E-4
U, 20%Am 20%Np	41.2	40.3	0.19	0.20	1.4E-3	2.7E-3

[ ] : declared by the operator

Tab. 4.18. Non-destructive (NDA) and destructive (DA) determinations of burn-up and total plutonium and curium (normalized to ^{238}U) in spent fuel.

An agreement within 1.5% is observed between the declared average burn-up of the pins and that measured by NDA. Furthermore, the local burn-up determined by passive assay is within 4% of the destructive (DA) determination. The agreement between the NDA and DA determination of the total plutonium ranges between 2% and 5%. The corresponding total curium agreements are between 10% and 15% for the PWR pins and about 50% for the fast reactor mixed oxide pins.

Passive neutron interrogation, coupled with isotopic correlations, can be extended for the verification of the content of individual nuclides, e.g. the highly toxic radionuclides ^{237}Np and ^{241}Am. An agreement of 5% to 10% is obtained between the NDA and DA determination of the local ^{237}Np and ^{241}Am content in the fast reactor pins. The radiotoxicity potential of the fuel due to these nuclides, or indeed due to any component, is then derived by applying the ICRP-61 (1991) Annual Level of Intake (ALI) values [4].

The nuclear data libraries of neutron reaction cross-sections and fission yields are a major source of the uncertainties resulting from the computation procedures. The cross-section libraries should accurately represent a given reactor-fuel system in order to allow for the changes in the neutron energy spectrum deriving from the evolution in fuel composition. Resonance cross-sections for various nuclides, e.g. ^{238}U, will then be accurately included in the computations. This is particularly important for some of the fuels used in this study, i.e. high burn-up PWR and the minor-actinide-containing fast reactor fuel, for which appropriate libraries are scarce. The adjustment of nuclear data libraries is being treated under separate studies at the Institute.

References

[1] G. Nicolaou, K. Richter, C. Prunier and L. Koch, "Experience with fast Reactor Fuels Containing Minor Actinides: Transmutation Rates and Radiation", Technical Committee Meeting on Safety and Environmental Aspects of Partitioning and Transmutation of Actinides and Fission Products, IAEA Vienna (1993)

[2] C. Foggi and L. Koch; "Isotopic Correlation Technique: a Means for Exploiting the Relationships Inherent in the Fuel Cycle", 4th Annual ESARDA Symposium Specialists Meeting on Harmonisation and Standardization for Nuclear Safeguards, Petten NL (1982)

[3] U. Fischer and H. W. Wiese; "Verbesserte Konsistente Berechnung des Nuclearen Inventars Abgebrannter DWR-Brenstoffe auf der Basis vor Zell-Abbrand-Verfahren mit KORIGEN", Kernforschungszentrum Karlsruhe, KfK- 3014 (1983)

[4] International Commission for Radiological Protection, "Annual Limits on Intake of Radionuclides by Workers based on the 1990 Recommendations", Annals of the ICRP Publication 61, Pergamon Press (1991)

5. Safeguards Research and Development

Introduction

The Institute has used some of its institutional resources to perform research and development in areas not covered by the institutional support programme for DG I and DG XVII. The activities carried out concern essentially initial tests and the establishment of methods for environmental monitoring and improvements of methods for the determination of the origin or transfer routes of seized nuclear materials. In addition, a new miniature cadmium telluride detector was tested for future safeguards applications.

5.1 Analysis of Radionuclide Traces for the Identification of Nuclear Activities

Electron micro-probe analysis and glow-discharge mass-spectrometry of soil and grass containing radioactivity from the nuclear accident at Chernobyl

As reported previously (TUAR-94, p. 171-172), investigations have been performed by glow-discharge mass-spectrometry (GDMS) and electron micro-probe analysis (EMPA) for the direct analysis of the solid samples.

This report presents micro-probe analysis and mass spectrometry results from top-soil and grass contaminated by nuclear fallout from the Chernobyl accident. The material, which was collected in July 1990, was obtained from the International Atomic Energy Agency (IAEA) in Vienna. The soil sample (Ref. IAEA-375) was taken from the Novozybkov district of Bryansk in Russia about 150 km north-east of Chernobyl. The concentration of activity in the soil was 6.5 x 10^3 Bq kg^{-1}. The grass (Ref. IAEA-373) was collected in the Polesskoe district of Kiev in the Ukraine about 100 km south of the reactor. It contained 1.5 x 10^4 Bq kg^{-1}. Caesium-137 is mainly responsible for the radioactivity of both samples, although the material is said to contain one or more hot-particles of fallout origin.

Experimental

Sample preparation

Two different methods of preparation were employed. For GDMS a 500 mg sample of material was compacted into a disc 13 mm in diameter and 2 mm thick using an automatic hydraulic press (3630X, SPEX, USA). A load of eight tons was applied for five minutes. For secondary-ion mass-spectrometry (SIMS) and EPMA about the same amount of material was taken. This was first dried at 50 °C for 24 h and then mixed with epoxy resin. When the mass had hardened after a further 24h, it was introduced into an epoxy mount. The material was then ground and polished using standard techniques. To avoid charging effects the samples were coated with a conducting film of carbon about 20 nm thick.

Glow discharge mass spectrometry (GDMS)

Trace element analysis of the bulk material was carried out using a VG 9000 glow discharge mass spectrometer. The machine which is installed in a glove-box consists of a d.c. glow-discharge ion source coupled to a double-focusing mass-spectrometer of reverse (Nier-Johnson) geometry. A discharge current of 1.2 mA and a voltage of 1.3 kV was used. Ion detection is accomplished by a dual detection system consisting of a Faraday cup for the measurement of large ion currents (typically >10^{-13} A) and a transverse-mounted Daly detector for the measurement of small ion currents.

Glow discharge mass spectrometry was carried out in two steps. First, a full mass spectrum was acquired from each sample at a mass resolution greater than 5000. From this mass spectrum the isotopes of interest were selected. These were then analysed at a mass resolution of 1000. For each isotope 30 scans were made consisting of 50 points measured with dwell times of 160 ms (Faraday cup) and 100 ms (Daly detector). Quantification was made using relative sensitivity factors (RSFs) obtained from other matrices. Prior to analysis, the samples were sputtered for 15 min. to remove any surface contamination. A conducting binder was not employed. To ensure that the samples were conductive a secondary cathode made of tantalum was used.

Secondary ion mass spectrometry (SIMS)

Secondary ion mass spectrometry was used to identify the location of the radionuclides caesium-137, iodine-129 and uranium-238 in the soil and grass samples.

A Cameca IMS 4f secondary ion mass spectrometer was used. This instrument has a double-focusing mass spectrometer which allows rapid switching between masses. It also has micro-focusing ion sources (Cs^+ and duoplasmatron with O_2^+, O^-, Ar^+) which can be used either in the ion-microscope or ion-micro-probe mode.

For the investigation of the soil and grass samples the instrument was used in the microscope mode. An O- primary ion beam was employed at an energy of 6 keV. Positive secondary ions at beam currents of 20-40 nA (typical spot size: 25 µm) were collected from a circular area 60 µm in diameter. The instrument was operated at a mass resolution of 600 with an energy window of 50 eV. Ion images showing the distribution of all the major constituents and the locations of caesium-137, iodine-129 and uranium-238 over areas of 150 and 200 µm square were produced using a standard acquisition time of 300 s. In the case of the grass sample the potassium-39 signal was used to image the individual blades and sheaths of grass.

5

Electron micro-probe analysis

Electron micro-probe analysis was used to identify the different mineral phases in the soil sample. A Cameca MS46 electron micro-probe analyser fitted with a Tracor TN 5500 energy dispersive analyser and installed in a glove-box to permit the analysis of alpha-active materials was employed for this purpose.

A combination of energy and wavelength dispersive analysis was employed. Energy dispersive analysis was used to obtain a comprehensive picture of the sample composition. X-ray spectra were acquired from the different mineral phases at an electron acceleration potential of 15 keV and a beam current of 1 nA. The acquisition time was set at 200 s. For quantification the PRZ option in the standardless analysis (SQ) program was used and the constituent elements were input as stoichiometric oxides.

Wavelength dispersive analysis was used to produce X-ray maps showing the distribution of the different mineral phases in an area 0.4 x 0.3 mm. Regions of interest in the sample were selected using the electron absorbed (specimen current) image, although owing to the similarity in atomic number the individual mineral phases could not be distinguished. The X-ray maps were produced at an electron acceleration potential of 15 keV and a beam current of 50 nA. The acquisition time depended on the signal intensity.

Results

Soil samples

The results of GDMS are shown in Tab. 5.1. It is seen that Si, K and Al were the principal cations in the soil. Most of the radionuclides measured were present in amounts smaller than 1 ppb. Only ^{232}Th, ^{238}U and ^{235}U were found in significant amounts (at the ppm level). The concentrations of U and Th measured were within the range at which these elements occur in nature. For example, 0.03-68 ppm Th and 0.14-45 ppm U are found in common metamorphic rocks and common sedimentary rocks contain up to 80 ppm U [1]. The fact that the concentration of ^{232}Th in the sample was much higher than the concentration of ^{238}U (4950 ppb compared with 2000 ppb) indicates that most of that measured was indeed natural and did not result from the Chernobyl accident. In contrast, it would appear that a large part of the uranium measured came from nuclear fuel. Not only is the measured $^{235}U/^{238}U$ ratio of 0.015 twice as high as that found in nature, but fuel enriched to 1.8% was irradiated in the Chernobyl reactor. The measured $^{235}U/^{238}U$ ratio of 0.015 indicates that the fuel from which the fall-out derived had been irradiated with a low burn-up of 4-5 GWd/tU. At the time of the accident the reactor contained fuel with burn-ups in the range zero to 27 GWd/tU.

Tab. 5.1 Glow discharge mass spectrometry results for the soil sample (figures are in parts per billion unless otherwise indicated).

Element or Radionuclide	Mass Concentration
Si	40.0 %
K	20.0%
Al	12.0%
Na	0.7%
Mg	0.5%
Ca	0.4%
Fe	0.4%
Ti	0.3%
Zr	...a)
Ba	0.1%
O	22.0%
C	3.0%
Sr-90	0.001
Ru-106	...a)
I-129	0.0002
Cs-137	0.002
Th-232	4950
U-234	1.0
U-235	30
U-238	2000
Pu-239	0.001
Pu-240	0.001

a) not detected

The detection of carbon is attributed to organic matter in the soil. The EPMA results are shown in Fig. 5.1. Six different minerals were identified of which quartz and feldspar appeared to be the most abundant. The results of the SIMS investigation are presented in Fig. 5.2. The figure contains ion images for ^{29}Si, ^{129}I and ^{238}U. It can be seen that iodine is present at the same location as silicon. A small particle containing uranium is also revealed. Caesium-137 was not detected in the regions examined by SIMS. The intensity of the ion peak at mass 137 matched the abundance of that isotope in natural barium.

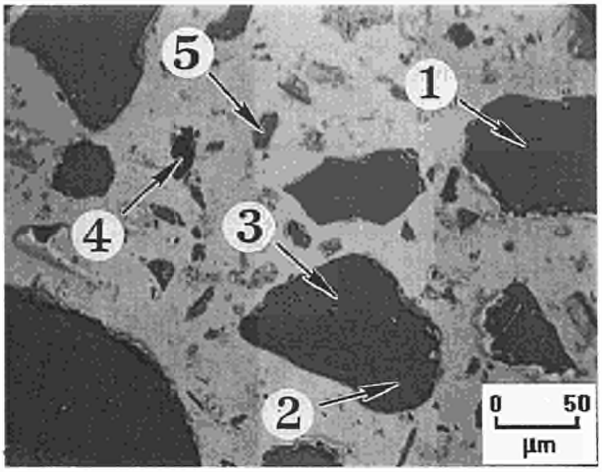

Specimen Current Image

Phase No.	Name	Chemical Formula
1	Quartz	SiO_2
2	Ba-bearing Potassium Feldspar	$(Ba)KAlSi_3O_8$ [a]
3	Potassium Feldspar	$KAlSi_3O_8$
4	Garnet (type Almandine)	$Fe_3Al_2Si_3O_{12}$
5	Plagioclase	$(NaAlSi_3O_8, CaAl_2Si_2O_8)$
	Anatase, Brookite or Rutile [b]	TiO_2

[a] Barium 1.2 wt%
[b] Small inclusions only.

Fig. 5.1 EPMA measurements on soil sample.

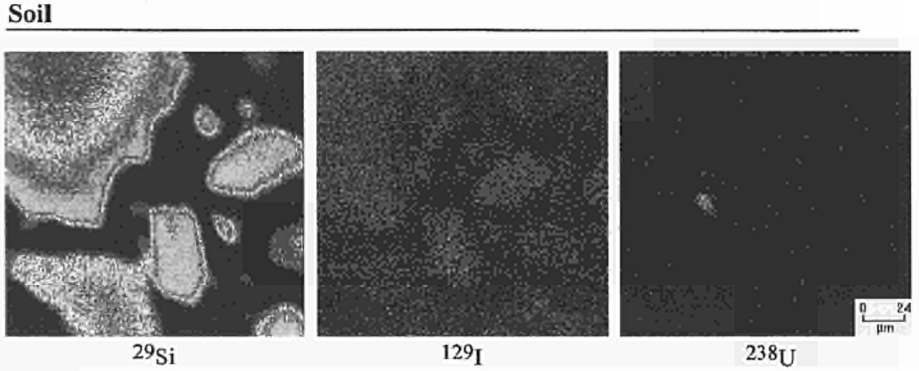

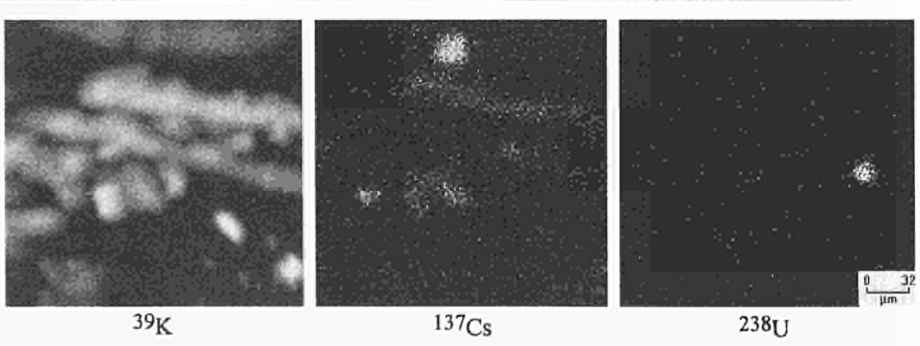

Fig. 5.2 Grass sample: SIMS images.

Grass samples

Glow discharge mass spectrometry results for selected radionuclides are reported in Tab. 5.2. Relatively high concentrations of ^{232}Th, ^{235}U and ^{238}U were measured (50, 5 and 330 ppb, respectively). The measured $^{235}U/^{238}U$ ratio is again ca. 0.015 suggesting that most of the uranium derived from the Chernobyl accident. The level of ^{90}Sr was around 0.001 ppb, and the concentrations of both ^{137}Cs and ^{239}Pu did not exceed 0.005 ppb. Iodine-129 was not detected. Ion images from the SIMS investigation are shown in Fig. 5.2. It is seen that ^{137}Cs was present in the individual blades and sheathes of grass that constituted the sample. It is also evident that two particles of extraneous matter are present in the area studied. One particle contains ^{137}Cs; the other, which is noticeably smaller, contains ^{238}U.

5

Tab. 5.2 Glow discharge mass spectrometry results for the grass sample.

Radionuclide	Concentration, ppb
Sr-90	0.001
Ru-106	...a)
I-129	...a)
Cs-137	0.005
Th-232	50
U-235	5
U-238	330
Pu-239	0.005
Pu-240	0.001

a) not detected

Discussion

GDMS revealed that, in addition to ^{137}Cs, the soil contained 0.0002 ppb ^{129}I (see Tab. 5.1). The SIMS results (Fig. 5.2) indicate that this iodine was incorporated in the silicon containing minerals in the soil. Presumably, the incorporation of iodine in the mineral phases occurred by an ion exchange mechanism. This is a characteristic property of clay. Since X-ray diffraction was not employed, it is not possible to state whether the silicon-containing phases analysed were clays. Certainly, the feldspars identified by EPMA (Fig. 5.1) along with other silicates are clay forming minerals.

The grass from Polesskoe contained about 2.5 times more ^{137}Cs than the soil from Novozybkov (cf., concentrations in Tabs. 5.1 and 5.2). This is consistent with what is known about the behaviour of caesium: that it is absorbed by plants and that it is removed from the top soil at a rate that is dependent on the soil characteristics. Caesium may be removed from top soil by wind and water erosion, by the action of burrowing organisms, such as worms, by leaching and also by plant uptake.

It is probable that most of the caesium measured in the grass sample was incorporated in the plant tissue. The absence of ^{129}I in the sample would suggest that rainfall had washed most of the water-soluble contaminants, including caesium, from the grass surfaces although the relatively high concentrations of ^{238}U and ^{232}Th in the sample and the detection of a particle containing caesium would suggest that some surface contamination was still present when the grass was collected.

Particles of nuclear fuel were an important component of the Chernobyl fallout in Russia and the Ukraine. Particles containing ^{238}U, the principal uranium isotope in UO_2 fuel, were seen in both the soil sample and the grass sample. From the GDMS results it would appear that these particles contained about 1.5 w/o ^{235}U. The GDMS results also indicate that these hot-particles were far more abundant in the soil sample (2000 ppb ^{238}U was measured in the soil compared with 300 ppb in the grass).

Summary

Even though the soil and grass samples were collected roughly 150 and 100 km from the site of the accident, the level of radioactive contamination was such that it could easily be detected by GDMS and SIMS. Caesium-137 was mainly responsible for the radioactivity of both samples, but the grass contained about 2.5 times more ^{137}Cs than the soil. Most of this caesium was evidently incorporated in the plant tissue. The soil sample contained radioactive ^{129}I. This isotope was detected in alkali feldspar and other silicates in the soil sample. It is assumed that the iodine had been incorporated in the crystal lattice of the minerals by an ion exchange process. Particles containing ^{238}U and ^{235}U, the two principal uranium isotopes in UO_2 fuel, were also found in both the soil sample and the grass sample. Far more of these hot-particles were present in the soil, however. The discovery of fuel particles has significance, because they may act as long-term reservoirs of radionuclides, slowly releasing their fission products over many years to the local surroundings.

References

[1] Handbook of Geochemistry, ed. K. H. Wedepobl; (Springer Verlag, Berlin, 1969-78) Vol. 5

5.2 Identification of Nuclear Material with Unknown Irradiation History: a Case Study

Introduction

Assay of nuclear material to verify its declared characteristics, is a fundamental procedure in ensuring that material has not been diverted. Considering that the evolution in nuclide concentration of the nuclear material is dependent on its irradiation and cooling histories, information on the material and its history could also be determined by the assay of the material.

The purpose of this work is to demonstrate the identification of spent fuel in terms of its initial enrichment and final burn-up achieved during irradiation. The content of individual nuclides in a spent fuel is inherently consistent. Hence, the measurement by radiochemical analyses of selected nuclides to determine, for example, the U and Pu isotopic composition, complemented by simulation of the evolution of nuclear material under irradiation, would allow the fuel identification.

Materials and methods

Commercial UOX and MOX spent fuels from BIBLIS-type PWR power stations were considered for the purpose of the study. The initial enrichment and final burn-up of these fuels was declared by the operators. However, in the present study they are considered as nuclear material of unknown irradiation history which has to be predicted through their chemical analyses. The abundances of the U and Pu isotopes were determined by Isotope Dilution Thermal Ionization Mass Spectrometry (IDMS) [1]. The fuels were: UO_2 [enrichment in ^{235}U: 3.5 a/o ('UNKNOWN' 1 and 2); declared average burn-up 47 and 29 GWd/t; enrichment in ^{235}U: 3.8 a/o ('UNKNOWN' 3 to 5), declared average burnup 56, 44 and 67 GWd/t]; MOX [U_{nat}, enrichment in Pu_{fiss}: 4% ('UNKNOWN' 6); declared average burn-up 44 GWd/t].

A databank comprising sets of U/Pu isotopic abundances, for a range of enrichments and burn-ups of UOX and MOX spent fuels, was created using the simulation code KORIGEN [2]. The isotopic composition of the fuel analysed was then compared with each one of the theoretical composition sets in the data bank in search of similarities. The comparison was performed using conventional statistics and also by applying pattern recognition [3], e.g. cluster analysis. The theoretical data set with the highest degree of similarity in burn-up and initial enrichment is searched for.

The calculations performed for this study were coupled with burn-up dependent cross-section libraries resembling, as close as possible, the type of reactors where the fuel was irradiated. They are thus fuel- and reactor-dependent. Consequently, they reflect each individual case, and are based on the initial enrichment and type of fuel data supplied by the operator of the reactor. Calculations were performed for UOX and MOX fuels from PWR power stations: UO_2 [enrichments in ^{235}U: 3.5 a/o and 3.8 a/o; burn-up range: 30 to 55 GWd/t and 40 to 65 GWd/t respectively]; thermal MOX [U_{nat} enrichment in Pu_{fiss}: 4%, burn-up: 40 to 55 GWd/t]. Sixteen sets of uranium and plutonium isotopics, taking into account each enrichment-burn-up combination, formed the data bank for identification purposes. These sets (labelled FUEL 1 to 16) are given in Tab. 5.3.

Tab. 5.3 Spent fuels considered in the formation of the databank.

	Enrichment	Burnup (GWd/t)
FUEL1	3.5 % ^{235}U	30
FUEL2	3.5 % ^{235}U	35
FUEL3	3.5 % ^{235}U	40
FUEL4	3.5 % ^{235}U	45
FUEL5	3.5 % ^{235}U	47
FUEL6	3.5 % ^{235}U	50
FUEL7	3.5 % ^{235}U	55
FUEL8	3.8 % ^{235}U	40
FUEL9	3.8 % ^{235}U	45
FUEL10	3.8 % ^{235}U	50
FUEL11	3.8 % ^{235}U	55
FUEL12	3.8 % ^{235}U	60
FUEL13	3.8 % ^{235}U	65
FUEL14	U_{nat}, 4% Pu_{fiss}	40
FUEL15	U_{nat}, 4% Pu_{fiss}	45
FUEL16	U_{nat}, 4% Pu_{fiss}	50

Statistical treatment of the results was carried out through two approaches, namely conventional and pattern recognition, where the unknown is compared with each set in the bank in turn. The comparison was based on the ratios ($^{235}U/U_{total}$), (U_{total}/Pu_{total}), (Pu_{fiss}/Pu_{total}). The conventional approach is based on the sum of the squares of the differences between the corresponding ratios of a data set and the 'unknown' fuel. This sum acts as a measure of similarity of the unknown and the comparison set. The comparison is repeated for all the sets in the databank. The smallest sum found, i.e. the smallest difference or highest similarity determines the unknown fuel.

Pattern recognition, e.g. cluster analysis [3] was used to display graphically in groups the sets and 'unknowns' in such a manner that any relation between them could be revealed. The graphical representation of the analysis is based on the Euclidean distance coefficient (termed linkage distance) as a measure of comparison. In both cases, the 'unknown' is compared to each one of the comparison sets (termed FUEL 1 to 16) in search for the smallest difference, i.e. highest similarity.

The choice of the ratios $^{235}U/U_{total}$, U_{total}/Pu_{total}, Pu_{fiss}/Pu_{total} was based on the fact that they can be measured with high accuracy. Also ^{235}U and Pu_{fiss} reflect the initial enrichment of the fuel and U_{total} and Pu_{total} indicate whether it is a UO_2 or MOX fuel.

Results

The degrees of similarity between the 'unknown' and databank sets, as obtained from the conventional statistical approach, are given in Tab. 5.4.

The results are presented in the form of the matrix [(UNKNOWN 1 to 6) x (FUEL 1 to 16)]. The [6 x 16] elements of the matrix are the sum of squares from the comparison of each 'unknown' with each of the data bank sets. An 'unknown' is identified as similar to that set from the data bank (FUEL 1 to 16) with which it exhibits the smallest sum of squares. The burn-up and enrichment of that data set can be said to characterize the 'unknown' in terms of these two parameters. The parameters identified for the spent fuel, acting as the material of the 'unknown': burn-up and initial enrichment in this study, are shown in Tab. 5.5. The enrichment and burn-up declared by the operator are included for comparison purposes. It is seen from the table that the 'unknown' fuels are predicted correctly.

The results of the second statistical evaluation approach, i.e. the cluster analysis, is shown in Fig. 5.3. This outcome of this type of analysis is a graphical representation of multivariate statistics, classifying in pairs. Objects were classified in pairs according to their degree of similarity defined by the Euclidean distance, termed here linkage distance.

The resulting pairs are given in Tab. 5.5. The fuels with unknown irradiation history have been paired with isotopic composition sets which predict their burn-up and cooling time.

A major source of error in the calculation of the evolution of a fuel in a reactor is the burn-up-dependence of the cross-sections used. The cross-section libraries should accurately represent a given reactor-fuel system. The data-bank of this study holds strictly for the BIBLIS-type PWR spent fuel since burn-up-dependent cross-sections for such reactors were employed in KORIGEN. However, a general data-bank covering the whole range of reactor types and fuels should contain information such as complete actinide and fission-

Tab. 5.4 Sum of squares totalled over the ratios $^{235}U/U_{total}$, U_{total}/Pu_{total}, Pu_{fiss}/Pu_{total} between the 'unknown' material and the members of the databank.

	FUEL1	FUEL2	FUEL3	FUEL4	FUEL5	FUEL6	FUEL7	FUEL8
UNKNOWN1'	88.91	66.67	43.22	16.74	**8.93**	19.48	66.17	57.96
UNKNOWN2'	**17.74**	40.10	63.43	92.10	104.40	126.10	172.83	48.70
UNKNOWN3'	55.24	33.10	9.55	19.12	31.42	53.12	99.85	24.28
UNKNOWN4'	239.65	217.30	193.96	165.29	152.99	131.30	84.57	208.70
UNKNOWN5'	259.56	237.21	213.87	185.20	172.90	151.20	104.48	228.61
	FUEL9	**FUEL10**	**FUEL11**	**FUEL12**	**FUEL13**	**FUEL14**	**FUEL15**	**FUEL16**
UNKNOWN1'	35.28	15.12	30.68	80.84	148.72	128.32	158.53	194.16
UNKNOWN2'	72.89	100.00	137.33	187.50	255.37	234.98	265.18	300.81
UNKNOWN3'	**5.86**	27.02	64.35	114.52	182.39	162.00	192.20	227.83
UNKNOWN4'	184.51	157.40	120.07	71.25	**6.50**	89.84	57.79	43.41
UNKNOWN5'	204.42	177.31	139.97	89.81	40.53	43.03	**12.12**	26.12

Tab. 5.5 Predicted and declared fuel characteristics.

'UNKNOWN'	Predicted fuel parameters		Declared fuel
	Conventional statistics	Cluster analysis	Characteristics
'UNKNOWN1'	FUEL5 (3.5% ^{235}U/ 47GWd/t)	FUEL4 (3.5% ^{235}U/ 45GWd/t)	(UOX) 3.5% ^{235}U, 47 GWd/t
'UNKNOWN2'	FUEL1 (3.5% ^{235}U/ 30 GWd/t)	FUEL1 (3.5% ^{235}U/ 30 GWd/t)	(UOX) 3.5% ^{235}U, 29 GWd/t
'UNKNOWN3'	FUEL11 (3.8% ^{235}U/ 55 GWd/t)	FUEL11 (3.8% ^{235}U/ 55 GWd/t)	(UOX) 3.8% ^{235}U, 56 GWd/t
'UNKNOWN4'	FUEL9 (3.8% ^{235}U/ 45 GWd/t)	FUEL9 (3.8% ^{235}U/ 45 GWd/t)	(UOX) 3.8% ^{235}U, 44 GWd/t
'UNKNOWN5'	FUEL13 (3.8% ^{235}U/ 65 GWd/t)	FUEL13 (3.8% ^{235}U/ 65 GWd/t)	(UOX) 3.8% ^{235}U, 67 GWd/t
'UNKNOWN6'	FUEL15 (U_{nat} / 45 GWd/t)	FUEL15 (U_{nat} / 45 GWd/t)	(LWR-MOX) U_{nat}, 44 GWd/t

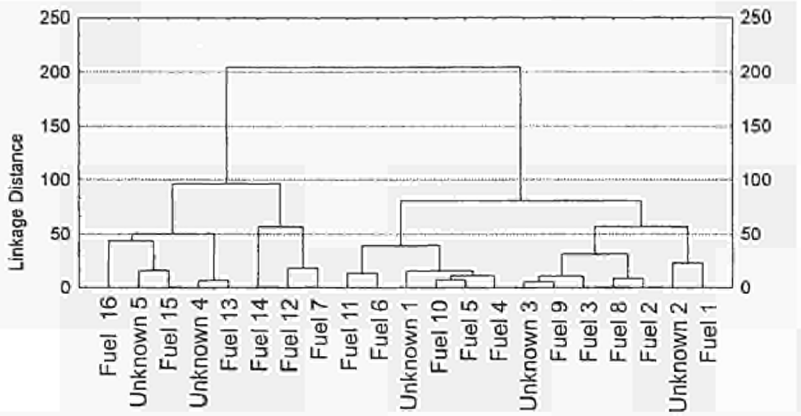

Fig. 5.3 Cluster analysis of 'unknown' fuel with comparison fuels.

product inventories and physical characteristics of the fuels. The feasibility of the procedure described, on a wide range of reactor-fuel types and the criteria on which the comparison will be performed remains to be demonstrated.

References

[1] L. Koch, M. Blumhofer, B. Brandalise, M. de Rossi, R. Wellum, D. Wojnowski, R. Schenkel and H. Wagner; "Conceptual Design of an On-Site Laboratory for Nuclear Materials Safeguards", Proceedings 11th Annual Symposium on Safeguards and Nuclear Material Management, Luxembourg (1989) p. 225-229

[2] U. Fischer and H. W. Wiese; "Verbesserte Konsistente Berechnung des Nuclearen Inventars Abgebrannter DWR-Brennstoffe auf der Basis vor Zell-Abbrand-Verfahren mit KORIGEN", Kernforschungszentrum Karlsruhe, KfK-3014 (1983)

[3] D. Massart and L. Kaufman; "The Interpretation of Analytical Chemical Data by the Use of Cluster Analysis", John Wiley, New York (1983)

5.3 Applications of Environmental Monitoring

Liquid scintillation counting (LSC) for the determination of nuclear signatures

Two samples provided by the IAEA (IAEA SOIL 375 and IAEA GRASS 373) were chosen as reference materials to develop radioanalytical and Liquid Scintillation Counting (LSC) sample preparation techniques for future use in the ARTINA laboratory. A sample of Rhine river water was also collected at Leopoldshafen, Germany, and a small portion was analysed directly by LSC for its tritium content.

Tritium determination

Approximately 1 l of Rhine river upper surface water was collected in a polypropylene bottle near Leopoldshafen. The sample was acidified with dilute nitric acid and LSC was started within 1 hour of collection. Sample preparation for LSC consisted of mixing 8 g of the unfiltered river water with 12 g commercial Optiphase HiSafe 3 LSC cocktail in a 20 ml capacity teflon-coated polypropylene vial. The sample was placed in a "Quantulus 1220" ultra low-level LSC machine (Wallac-Oy) to achieve counting conditions and was counted in cycles of 480 minutes in an optimized tritium window.

A tritium concentration of 7.68 Bq/l was measured and the detection limit of the machine for this isotope is 1.2 Bq/l (3 σ and a counting time of 480 minutes).

Radiocaesium and radon measurements

The IAEA grass and soil reference samples (5 g quantities) were refluxed with water for a set period of time in order to determine the water distilable radioactive components, e.g., tritium, radon. The residue was then subjected to a leaching step with ammonium acetate (1 M) in order to evaluate the ion-exchangeable radioisotopes. The heavily coloured supernatant obtained could not be directly analysed by LSC and had to be chemically treated by a series of precipitations and special techniques before being counted.

The successive leaching was continued on the sample residue by using a nitric acid solution (6 M) to determine the acid-exchangeable component of the sample. Again the supernatant had to be treated before LSC [1].

The liquid fractions were analysed for their beta-emitting and alpha-emitting isotopes. Radiochemistry was performed to separate ^{137}Cs and ^{90}Sr, whose beta spectra overlap. Both samples gave clear ^{137}Cs spectra and some Rn was also observed to be distilled over with water from the soil sample.

Different amounts of ^{137}Cs were leached from the grass and the soil samples with each reagent used. The grass had very large amounts of water soluble Cs and ion-exchangeable components showing that much of the Cs was present as a very fine dispersion on the outer part of the grass and in its easily destroyed organic

structure. A large quantity of Cs was leached from the soil with acid and comparatively little with the ion-exchange solution ammonium acetate thus implying that the Cs is in a more fixed state.

The results of these experiments are not quantitative and it is well established that gamma spectrometry is the preferred analysis method for environmental ^{137}Cs. In these instances, no Cs spikes were used except to determine the counting efficiency of the LSC. However, the experiments do demonstrate that it is possible to analyse Cs by LSC and future work will concentrate on more isotopes including ^{90}Sr, ^{99}Tc and ^{14}C techniques will be further developed and modified. When the methods are fully developed and tested, the LSC apparatus will provide reliable detection levels down to a few Bq and a high sensitivity for many isotopes in many varied sample types.

References

[1] M. Betti, L. C. Jozefowicz, S. Giannarelli and L. Koch; Proceedings of 17th Annual Symposium on Safeguards and Nuclear Materials Management (ESARDA), Aachen, Germany, 9-11 May, 1995, pp. 475-479

5.4 Gamma Spectrometry of Spent Nuclear Fuel Using a Miniature Cadmium Telluride (CdTe) Detector

5

Verification of the burn-up of spent nuclear fuel is an important component of safeguards verification and criticality safety of fuel during transport and storage. Non-destructive assay of the material, by measuring their neutron and gamma emissions, is one of the verification procedures pursued in safeguards [1]. High Resolution Gamma Spectrometry based on germanium detectors has been routinely applied. However, the need to cool the detectors results in bulky devices which are difficult to work with under inspection conditions. There is also an increasing movement towards the use of compact devices for unattended and remote operation. Other semiconductor compounds, e.g. CdTe, CdZnTe, have therefore been explored for gamma spectrometry applications [2]. Their small size, good energy resolution and, above all, ability to be operated at room temperatures, renders such detectors portable and suitable for remote applications on nuclear material under dry or wet conditions.

A planar CdTe crystal (2 mm depth, 4 mm^2 sensitive area) was used in this work (Fig. 5.4). The crystal and preamplification circuitry are incorporated inside a cylindrical probe housing made of aluminium alloy (9 x 90 mm). The crystal is operated at room temperature without the use of cooling. The detector probe and the amplifier were purchased from EURORAD [Strasbourg, France]. The amplifier combines the normal amplification operation with an electronic pulse processing unit (charge loss corrector, CLC) resulting in improved energy resolution, peak-to-Compton and peak-to-valley ratios.

The suitability and ease of application of the CdTe detector was tested on a spent fuel pin stored inside a β-γ hot-cell. The concrete cell wall had a thickness of 1 m. A collimator of lead and tungsten was incorporated into the wall allowing gamma spectrometry of pins with the detector located outside the cell. These measurements were therefore performed in an environment having a normal background. Gamma spectrometry was also carried out at this position using a HPGe detector for comparison.

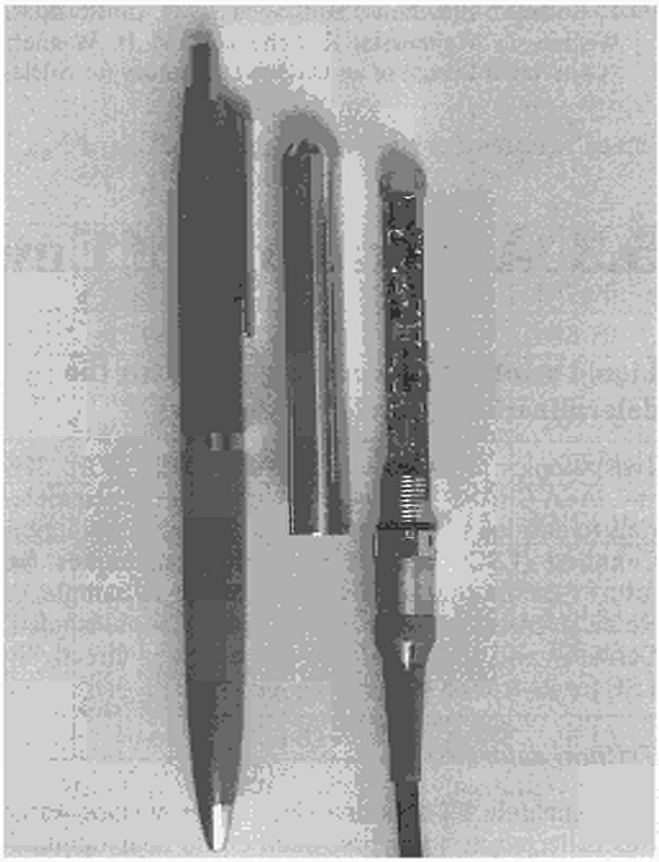

Fig. 5.4 The miniature CdTe detector used in this work.

The resulting gamma spectrum obtained with a CdTe detector, in the energy region 450 keV to 1 MeV, is shown in Fig. 5.5 (spectrum b). The corresponding spectrum with the HPGe detector is also included (spectrum a). The fission products ^{134}Cs and ^{137}Cs and

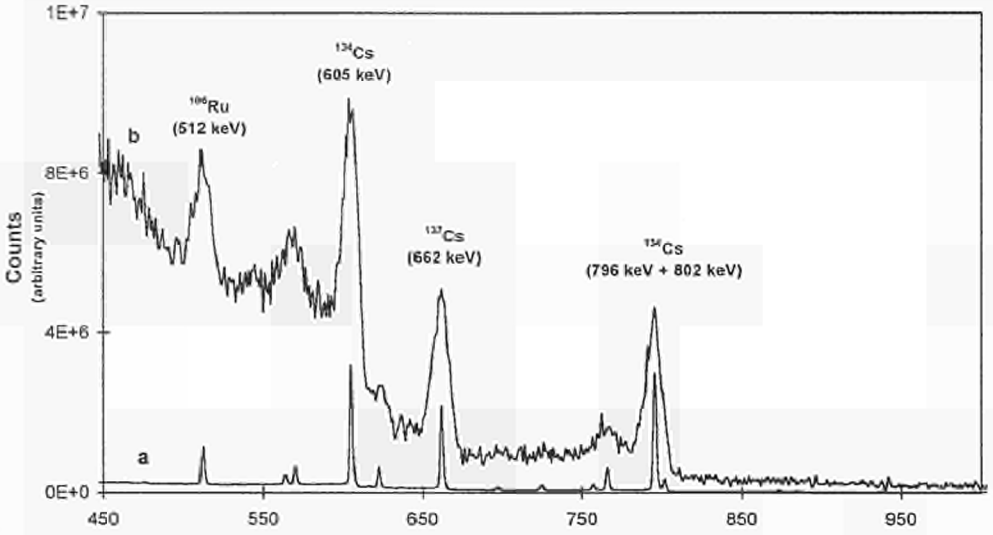

Fig. 5.5 Gamma spectra of spent nuclear fuel pin obtained with the HPGe detector (spectrum a) and with the CdTe detector (spectrum b).

^{106}Ru are visible in the spectrum of the CdTe detector. The 605 keV and 662 keV lines of ^{134}Cs and ^{137}Cs are well resolved and free from interferences. The 796 keV and 802 keV lines of ^{134}Cs are not resolved, which is also the case between the 512 keV of ^{106}Ru and the 511 keV annihilation radiation.

The objective of this work is to demonstrate the usefulness of the CdTe crystal as a gamma detector in the nuclear fuel cycle and its application for the verification of the declared burn-up and cooling time of spent fuels. The isotopic ratio ^{134}Cs/^{137}Cs was used for this purpose (the 605 keV gamma line was used for ^{134}Cs and that at 662 keV for ^{137}Cs).

Isotopic correlations [3] suitable for the interpretation of the gamma spectrometry information were used. They were generated using the point depletion code KORIGEN [4]. The predicted values of burn-up and cooling time were within 10% of those declared by the operator. The uncertainties in the nuclear data in KORIGEN is still a major contributor to the discrepancy in the predictions by the CdTe detector.

The small size of this detector and its capability to operate without cooling make it suitable for remote operation within a compact and transportable device. In this respect, the CdTe detector can be incorporated within a compact measurement device to complement passive neutron interrogation of spent fuel inside a hot-cell. Although not replacing the HPGe, the CdTe can examine spent fuel under conditions where the HPGe would be bulky and prone to saturation.

References

[1] S. Guardini, G. Bignan, R. J. S. Harry, E. Leitner and H. Ottmar; Proceedings 15th ESARDA Symposium on Safeguards and Nuclear Material Management, Rome, 11th-13th May 1993, p. 319

[2] R. Arlt, K. Czock. and D. E. Rundquist; Nucl. Instr. and Meth. A 322 (1992) 575-582

[3] C. Foggi and L. Koch; "Isotopic correlation Technique: a Means for Exploiting the Relationships Inherent in the Fuel Cycle", 4th Annual ESARDA Symposium Specialists Meeting on Harmonization and Standadization for Nuclear Safeguards, Petten NL (1982)

[4] U. Fischer and H. W. Wiese; "Verbesserte Konsistente Berechnung des Nuclearen Inventars Abgebrannter DWR-Brennstoffe auf der Basis vor Zell-Abbrand-Verfahren mit KORIGEN", Kernforschungszentrum Karlsruhe, KfK-3014 (1983)

B. Scientific and Technical Institutional Support Activities

6. Scientific and Technical Support to DG XVII

Introduction

The main activities under support to the European Safeguards Directorate (ESD) are concentrated in essentially four areas:

- Design and setting up of on-site laboratories at the two major reprocessing sites of the European Union. The On-site Laboratory (OSL) at Sellafield demands at present a large effort. Part of this has been for the setting up of the so-called 'Pre-OSL', which consists of the glove-boxes as designed for the application at Sellafield, together with the associated apparatus, installed at the Institute and applied to the measurement of routine Safeguards samples. The design for the Laboratoire sur Site (LSS) at La Hague has also advanced, whereby this laboratory is foreseen one or two years later than the OSL, Sellafield.
- In-field activities, where the analytical staff of the Institute performs verification measurements at, or in relation with, physical inventory ESD inspections.
- Analysis of Safeguards samples and provision of expertise in the framework of the European Communities Safeguards Analytical Measurements (ECSAM) contract, including analysis and evaluation of 'vagabonding' nuclear materials.
- Analysis and development activities related to analytical techniques and provision of training.

In this chapter, progress is reported related to activities performed on behalf of ESD.

6.1 On-site Laboratory at ITU (Pre-OSL)

The European Safeguards Directorate (ESD) has the main responsibility for safeguarding nuclear installations in Europe. Within the overall framework, ESD established a safeguards concept for the new THermal Oxide Reprocessing Plant (THORP) at Sellafield, UK, based on documentation supplied by British Nuclear Fuels (BNFL). Safeguarding this large plant requires a large number of verification samples to be analysed, exceeding the capacity of the existing European Commission's Safeguards Analytical Measurements (ECSAM) laboratories. In order to allow timely verification analysis and to minimize the organization and costs of transporting nuclear materials, ESD has opted for an economically viable On-Site Laboratory (OSL) [1] to be built at Sellafield in co-operation with the Institute.

The OSL [2] is based on the principle of highly automated glove-boxes [3] with equipment for non-destructive (NDA) and destructive analysis (DA). A fully computerized data-management system [4] will allow efficient reporting of the results and quality control of the measurements. To implement the safeguarding of the entire nuclear fuel reprocessing plant, both the incoming material (input, typically solutions of dissolved fuel elements) and the outgoing materials (products, e.g. plutonium dioxide powder and uranium oxide powder) are verified. The NDA techniques will be used to analyse bulk product samples of plutonium, uranium and MOX. DA techniques will be applied for input samples and for approximately 10 to 20% of the product samples.

6.1.1 Pre-on-site laboratory at ITU (pre-OSL)

Concept and objectives

The pre-OSL concept is being implemented at the Institute in order to simulate the future operation of the OSL in Sellafield. The laboratory consists of a similar set of glove-boxes to those to be used in the future OSL. They are conceived as self-standing units which will be operated independently. The pre-OSL set-up is constructed within the existing facilities of the Nuclear Chemistry Department. There will be a laboratory for product samples and another for input samples in line with the OSL concept. The final arrangement of the laboratories and the glove-boxes will differ slightly because of local conditions. All of the analytical techniques of the future OSL will be applied using a complete set of the instrumentation.

The pre-OSL facilities will be extensively used by OSL team members for routine analyses and simultaneously integration and testing of both the OSL equipment and the working methodology, including data management. The pre-OSL installation is a vital assembly to ensure the necessary quality of the analysts for on-site conditions. The teams will be operating in shifts in weekly rotation as they will do in the future OSL. This modus of operation has already been established. The analysts will acquire practical experience with the equipment, and in-house theoretical training will con-

tinue in parallel. Specific managerial functions to comply with BNFL's site licence requirements will be incorporated into the pre-OSL programme early in 1996.

Some of the major components within the pre-OSL are already operational and the complete pre-OSL is scheduled to come on-line in the first quarter of 1996, about two years before the expected start of the OSL.

6.1.2 Description of the pre-OSL

Analytical techniques

To verify the different steps of nuclear fuel reprocessing, the OSL and therefore also the pre-OSL will make use of a variety of analytical techniques for input, intermediate and product samples both in concentrated and diluted form.

Analytical techniques like isotope dilution analysis (IDA), potentiometric titration, alpha-spectrometry. thermal ionization mass-spectrometry (TIMS) have been in routine use at the Institute for some years. Others, especially for product sample analysis by NDA, have been developed more recently. The new techniques are the combined neutron-coincidence counter (NCC) and high resolution gamma-spectrometry (HRGS) [5], product K-edge densitometry (PKED) [6, 7] and combined product-uranium concentration and enrichment assay (COMPUCEA) [8]. They have been described in detail previously (TUAR-93, p. 183, TUAR-94, p. 182). The applications are summarized in Tab. 6.1.

Glove-boxes

The concept of the pre-OSL is based around a set of integrated glove-boxes for the different techniques, set up together as an individual operational unit. It is of fundamental importance that the pre-OSL boxes are representative of the OSL installation to allow realistic training and testing. The various boxes associated with the analytical techniques are indicated in Tab. 6.2.

Certain of the analytical glove-boxes have only been developed recently. The Product box for analysis of plutonium-containing product samples and the Uranium box for the analysis of uranium product samples have been specially designed for the OSL. The Isotope Dilution Analysis (IDA) box for input samples, the MS Turret Preparation box and the MS Loading box have been in use at the Institute for some years. The pre-OSL suite of analytical glove-boxes is completed with a Receipt and a Storage box.

Samples

As the pre-OSL will be a laboratory for routine work, samples sent to Karlsruhe under the ECSAM procedure will be analysed there. The analysis flow is indicated schematically in Fig. 6.1. This figure shows the type and flow of samples, the methods used and the

Method	Application
Neutron Coincidence Counting (NCC) and High Resolution Gamma Spectrometry (HRGS)	Determination of Pu isotopics and concentration in plutonium oxide powders and pellets
Product K-Edge Densitometry (PKED) and High Resolution Gamma Spectrometry (HRGS)	Determination of Pu isotopics and concentration in product sample solutions
Density measurement	Determination of density in Pu or U (product) sample solutions
Potentiometric titration	Determination of Pu and U concentrations
Combined Product-Uranium Concentration and Enrichment Assay (COMPUCEA)	Determination of U-235 and total uranium concentration in uranium product solutions
Alpha spectrometry	Determination of Pu-238 and the concentration of Pu to optimise the robotised filament preparation for MS
Isotope Dilution Mass Spectrometry (IDMS)	Determination of isotopic composition and concentration of Pu and U in input solutions. Determination of isotopic composition of Pu and U in product samples
Thermal Ionisation Mass Spectrometry (TIMS)	Determination of isotopic composition of Pu and U

Tab. 6.1 Methods and applications used in the OSL.

Glove boxes	Analytical techniques
Product box	- Neutron Coincidence Counting (NCC) - Product K-Edge Densitometry (PKED) - High Resolution Gamma Spectrometry (HRGS) - Density measurement - Potentiometric Titration
Uranium box	- Combined Product-Uranium Concentration and Enrichment Assay (COMPUCEA) - Density measurement
IDA box	- U, Pu extraction and separation from fission products - Alpha spectrometry
MS turret preparation and MS loading boxes	- Preparation for the Thermal Ionisation Mass-Spectrometry

Tab. 6.2 Analytical techniques associated with the glove-boxes for OSL.

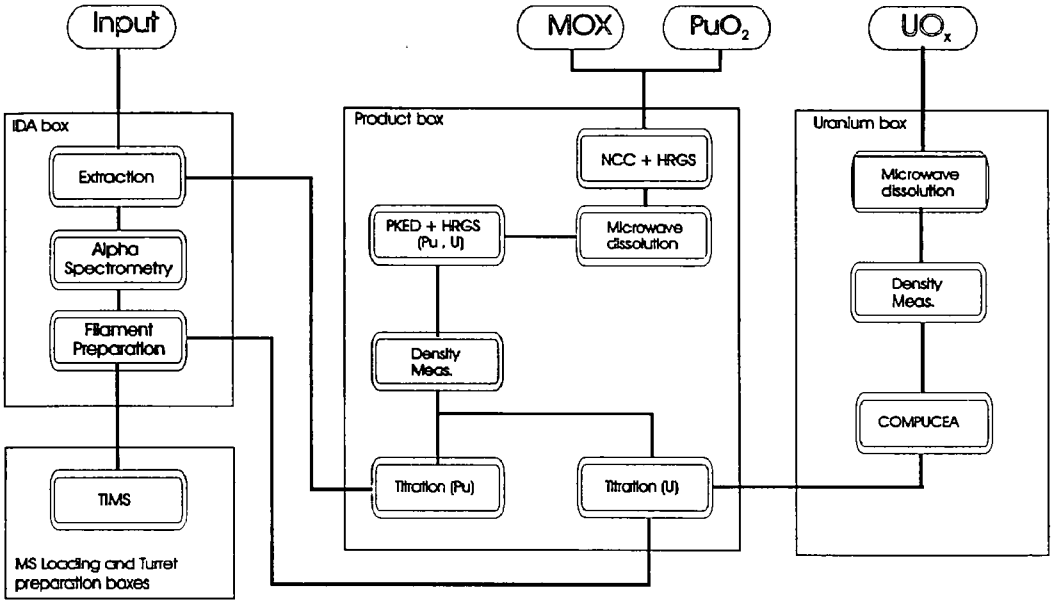

Fig. 6.1 Sample flow of the pre-OSL methods and dedicated glove-boxes.

subdivision of the glove-boxes. Only the major steps are indicated. It is clear that the different processes require several sample conditioning steps, for example dilution, aliquoting, and preparation of alpha planchets.

Some of the typical samples planned to be measured in the OSL cannot be delivered to the Institute at Karlsruhe for measurement in the pre-OSL because of transport regulations, so these sample types will be replaced by simulated samples. The plutonium nitrate samples for example will be simulated by dissolving plutonium oxide in-house.

The greatest number of samples for the pre-OSL comes from requests for analysis from ESD. To comply with the throughput foreseen for the OSL, the total number of samples in the pre-OSL will be increased by adding standards and doing intercomparison tests between the different analytical methods.

Training of operators

A one year general training cycle has been developed and was implemented in 1995 for the members of the OSL. The objective of this training was to provide each team member with general knowledge on the nuclear fuel cycle, emphasizing spent fuel reprocessing, the basis of safeguards activities and an overview of the analytical methods to be used in the OSL. A summary of the training sessions (both lectures and workshops) is given in Tab. 6.3 (the sessions still to be organized in 1996 are marked with '(96)').

The improved understanding of the major aspects of the future working environment for the OSL team

Subject of the training module	Lectures and workshops organised
Introduction to Nuclear Chemistry	Introduction to nucleonics
Nuclear Fuel Cycle	Front end of fuel cycle / Enrichment
	Fuel fabrication and composition / Materials
	Energy production in nuclear reactors / Reactor types
	Back end of fuel cycle / Actinide separation
Spent Fuel Reprocessing	Plutonium and Pu compounds
	Chemical separation of U and Pu
	U/Pu reprocessing, U/Pu/Np complications
Introduction to OSL / Safeguard Activities	Euratom safeguards and objectives of OSL
	Sample types in fuel fabrication and reprocessing
	Laboratory set-up and samples in OSL Sellafield
	Laboratory set-up and samples in OSL La Hague
LIS Analytical Methods	Titration
	Isotopic analysis
	K-edge and Hybrid K-edge
	Alpha spectrometry
	Neutron counting
	Mass spectrometry (96)
	Gamma spectrometry (96)
	Isotope dilution and Robotic treatment (96)
	Inductively Coupled Plasma Mass Spectrometry (96)
Data Treatment and Evaluation	Basis of statistics
	Quality Assurance programme for OSL
	ITU Data processing / Expert systems (96)
Radioprotection and Health Physics	Introduction to Radioprotection and Health Physics
	Units/Detectors/Protective measures in Radioprotection

Tab. 6.3 Training modules for OSL operators.

members, will increase their confidence in their own role and in the understanding of the relation of this work within the overall safeguards approach.

Apart from a series of formal training lectures, on-the-job training is implemented for each OSL member within the working group related to one or more analytical techniques. The routine analysis requests coming from the Safeguards Directorate, Luxembourg are used for this purpose. A team consists of four operators, one for each of the four groups of analytical techniques:

NDA:	Neutron counter; K-edge; gamma-spectrometry; density measurement
Titration:	Dissolution; dilution; titration; dilutions for mass spectrometry
Robot:	Preparation of samples for mass spectrometry, separation, spiking, α-spectrometry
Mass spectrometry:	Isotopic composition determination using one or more mass spectrometers

Each team operates the pre-OSL on a weekly basis. An analysis made to determine the required working procedures and communication requirements to run such an analysis team on a routine basis, resulted in the organization of weekly meetings for sample initialization, problem discussion and solving. The routine work, based on an alternating participation scheme, gives the OSL operators the opportunity to be trained not only in the technical content of the job but also in the work organization. This constitutes an essential element for the success of the OSL.

In the case of special sample requirements or modified analysis sequences, the responsible team members have the possibility to consult experts/scientific advisers for the respective techniques. This has in the past resulted in further development and improvement of several techniques and analysis strategies. The advantage of having the OSL operators involved in this way, is the increased knowledge on the underlying basis of the technique used and the scientific aspects determining the quality of the analysis.

Organization and quality assurance

The organization within the laboratory team of the OSL must be in compliance with BNFL management and local working practices. Some managerial functions need to be covered by the team which are already provided in the Institute's organization by central services, e.g., safety, radioprotection. These functions will be integrated into the organizational planning. As a consequence the training programme will be extended and additional training will be tailored to Sellafield local conditions with the co-operation of BNFL.

The pre-OSL programme is subject to a laboratory quality assurance (QA) regime. The production of results of the highest quality (quality control of results) is the ultimate goal in the pre-OSL and the OSL after the commissioning process. Target values defined by ESARDA [9] concerning precision and accuracy will be controlled by the Quality Control System.

The preparation of a laboratory manual comprised of procedures and working instructions is being completed along with the pre-OSL construction. These procedures and working instructions cover all the aspects of the pre-OSL for the general operation of the laboratory: analysis techniques, measurements, maintenance, quality control and documentation.

The pre-OSL laboratory manual is the result of the combined effort of Institute experts/scientific advisors and the operators concerned and will become the definitive, structured reference document for quality assurance.

Data management

The hardware part of the data management system consists of personal computers and VAX workstations connected via Ethernet. Data are exchanged between the computers using the file transfer protocol TCP/IP. Each computer is independent and conserves its own measured data to make the system resilient. The hardware layout is given in Fig. 6.2.

The data, mainly sample information and analysis results, are collected on a central Micro VAX computer. A data management software system developed in the

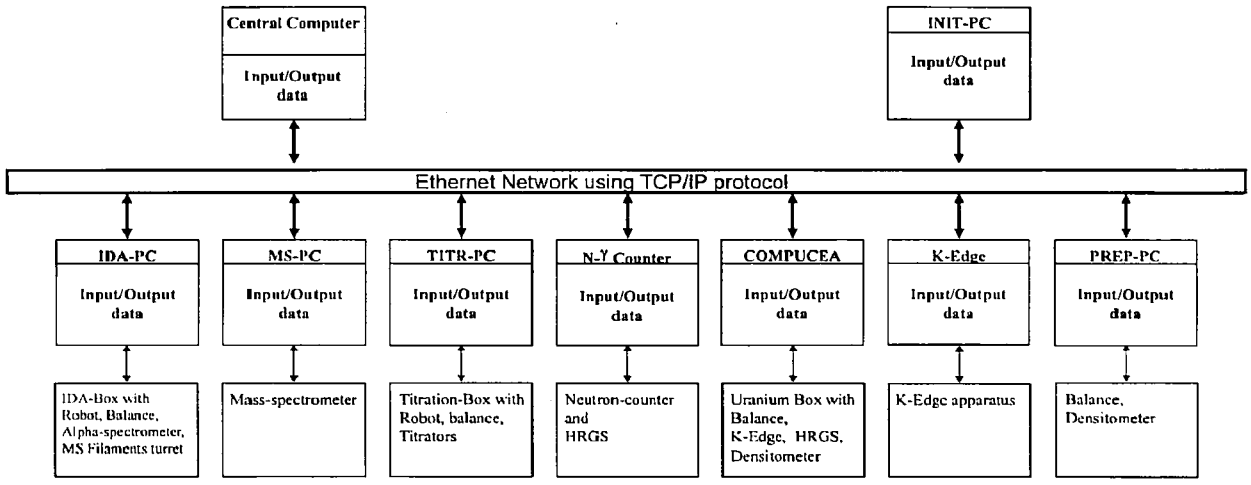

Fig. 6.2 Hardware layout.

Institute collates and calculates the results. This system collects the data, works out the analysis results and prepares the reports which are sent to the requester.

Information on the sample is received in the Institute on a dedicated PC via electronic mail. This PC (the 'initialization PC') is used to transfer data between the Institute and ESD, Luxembourg. Two connections are automatically made each day for exchange of analysis requests and results. A program for this purpose was installed at Luxembourg. The sample information is forwarded from the initialization PC to the central computer together with analytical instructions for the measurement instruments. The decision about which technique to be used is taken at this stage.

The analysis data are collected on individual computers (PCs or VAX workstations) each connected to a measurement instrument. PC programs have been developed in the Institute for each instrument in order to control the flow of data in both directions between the instrument computers and the central data system. A more detailed view of the data flow between the computers is given in Tab. 6.4.

6.1.3 Development status

Glove-box construction and testing

The IDA box for input sample processing along with the MS turret preparation and MS loading boxes are being used for radioactive sample material and have been tested thoroughly.

The product box is installed in the laboratory and the construction is nearly completed. As soon as the density measurement device is included in the design the box will be closed for integrated testing. The individual analytical techniques, the robot and the microwave dissolution have been tested and the test results achieved passed the acceptance criteria. Testing of density measurement will be continued in parallel.

Construction of the uranium box with the COMPUCEA instrument is almost finished. The densitometer is integrated into the design and the box will be assembled and finalized by January next year. Both the COMPUCEA and the microwave dissolution oven have been tested as individual items. Testing of the completed box will then be carried out under pre-OSL conditions. The product and uranium boxes will be subject to glove-box committee approval at the beginning of next year. The receipt and storage boxes are operational but will be replaced in the course of the next year by new boxes completely shielded with lead glass to comply with the radioprotection standards of the future OSL.

Integration and improvements of analytical techniques

Improved data analysis for K-edge densitometry (KEDG)

Some modifications have been developed in the K-edge software to improve the data processing in the analysis of solution samples.

The accurate measurement of the X-ray tube voltage is important especially when the K-edge is coupled with X-ray fluorescence analysis (XRF), as in the Hybrid K-edge instruments installed in the reprocessing plants in La Hague and Sellafield for the measurement of U and Pu concentrations in input solutions. A new method for the calculation of the spectrum endpoint, based on a logarithmic fit of the data below and above the endpoint, will permit better high voltage control. The improvement will be implemented not only on the Hybrid K-edge instruments, which are not a direct part of the pre-OSL, but also on the Product K-edge instrument in the pre-OSL laboratory.

Tab. 6.4 Data flow of the pre-OSL

Computer	Function	Input from	Output data	Destination
INIT-PC	Select type of analysis for each sample and dispatch data and working instructions	DCS-LUX	Sample data	Central Computer IDA-PC PREP-PC
IDA-PC	Prepare working data & instruction for robot, control robot, alpha spec.analysis operations and M.S. filaments. preparation. Manages data coming from the apparatus.	INIT-PC	Weights (Sample + Spike) Alpha spectrometry MS filaments information	Central Computer MS-PC
PREP-PC	Informs operator for dissolution and dilution to be performed, collect and dispatch data	INIT-PC	Weights (Dilution, Dissolution) Density	INIT-PC TITR-PC
MS-PC	Control mass-spectrometry measurements, calculates mass ratios	IDA-PC	Mass Ratios	Central Computer
COMPUCEA	Determines U concentrations and enrichments	INIT-PC	Uranium Concentrations	Central Computer
TITR-PC	Prepare working data & instructions for robot, controls robot and titrator operation. Manages data coming from the apparatus.	PREP-PC	U + Pu Concentrations	Central Computer
K-Edge	Determines Pu and U concentrations	INIT-PC	Pu concentrations	Central Computer
N-γ Counter	Determines effective Pu-240 concentration	INIT-PC	Pu concentrations	Central Computer

A procedure has been implemented and validated for the correction of spectra when known quantities of minor elements are present in the solution (for instance Am in Pu product solutions or Pu in U input solutions). The presence of a secondary heavy element disturbs the analysis of data, since it introduces a small jump due to the minor element K-edge in the fitting regions used for the evaluation of the major element concentration. The method is based on a de-attenuation of the spectrum: the theoretical absorption due to the minor element is computed and then removed leaving a spectrum of a pure solution of the major element. This is possible if the concentration of the minor element is at least approximately known (which is normally the case since the Am/Pu ratio in product solutions is measured by gamma spectrometry and the Pu/U ratio in input solutions by XRF). The analysis proceeds in two steps:

- first a preliminary approximate evaluation of major element concentration with the standard method, coupled with the known element ratio given by the second technique to obtain the minor element concentration,
- then the re-evaluation of major element concentration after spectrum correction.

The validation of this method required a campaign of measurements of solutions of U and Pu which were prepared in our laboratory with U/Pu ratios ranging from 3 to 12. The results were satisfactory, with an accuracy of 0.1-0.2% being obtained compared to 0.3-0.5% by the standard method.

Pu element assay by neutron coincidence counting (NCC)

The non-destructive technique of passive NCC has demonstrated its capability to serve as a reliable and accurate analytical technique for Pu-element assay in gram-sized PuO_2 samples. The impact of all major error contributions for Pu mass determination by neutron coincidence counting has now been quantified. The accuracy depends on the origin of the Pu material (LWR or MAGNOX reactor) as well as its burn-up [10]. The principle design goal of measurement accuracies of between 0.1% and 0.2% for the OSL-counter can be reached under the following conditions:

- Counting times of between 3 and 4 hours for a sample size of 2g PuO_2.
- Reference material of representative isotopic composition certified to 0.1% or better for calibration.
- Application of methods for bias correction as a function of sample variables such as Pu-fissile and (alpha,n) content.
- Precise regular control measurements on suitable reference samples.

The uncertainties for determination of the isotope abundances for ^{238}Pu, ^{240}Pu and ^{242}Pu have to be below the limits given in Tab. 6.5.

Tab. 6.5 Uncertainties of Pu isotope abundances required for isotope correlations.

	^{238}Pu	^{240}Pu	^{242}Pu
LWR samples	1%	0.1%	0.3%
MAGNOX samples	2.5%	0.1%	0.8%

The technique of high-resolution gamma-spectrometry (HRGS) is currently not capable of achieving these limits for ^{240}Pu and ^{242}Pu. The majority - if not all - of the Pu product samples will thus have to be subjected to an additional isotope analysis by mass-spectrometry in order to obtain the values quoted above. A simplified procedure without chemical separation could possibly be employed for this step.

Very promising results were obtained when the measurement data from NCC were combined with carefully measured isotopic data from mass spectrometry [7]. The Pu element content determined in this way for a series of PuO_2 samples agreed to better than 0.1% with results from the standard titration method in the case of MAGNOX plutonium, and to better than 0.3% in the case of LWR plutonium. Further systematic studies will be necessary to allow a fully quantitative description of the neutron response as a function of typical sample variables such as sample mass, isotopic composition and Am content. For example, neutron multiplication due to fast fission has been identified as one of the major measurement variables to be corrected for even for the small sample amounts encountered in the OSL application. Monte Carlo calculations have been carried out with the aim of developing and establishing well-founded analytical expressions for minor bias corrections at accuracy levels down to 0.1%.

Performance of isotopic correlation methods for the determination of ^{242}Pu

The determination of the ^{242}Pu isotope content by Isotopic Correlation Techniques (ICT) is still the limiting factor for the accuracy of non-destructive Pu-element assays. In order to determine the limitations of this method, systematic data analysis and correlation tests have been carried out. In agreement with KORIGEN calculations and previous studies done in the frame of the ESARDA NDA working group the expression $R242 = A \cdot R240^B \cdot R238^C$ was used where R242 stands for the isotopic ratios $^{242}Pu/^{239}Pu$, R240 for $^{240}Pu/^{239}Pu$ and R238 for $^{238}Pu/^{239}Pu$. MAGNOX and LWR material can clearly be distinguished from the position of the Pu isotopic vectors in the R238 vs. R240 plane. Different sets of coefficients A, B, and C were determined for these two cases. The differences between predicted and actual values of the ^{242}Pu content were found to depend strongly on the position in the R238 vs. R240 plane. Different regions or bands were identified which allowed measurements to be flagged as being potentially biased (see Fig. 6.3). It was found that even in the best regions an error component for the ^{242}Pu determination of about 3% has to be accepted, which agrees with other results using slightly

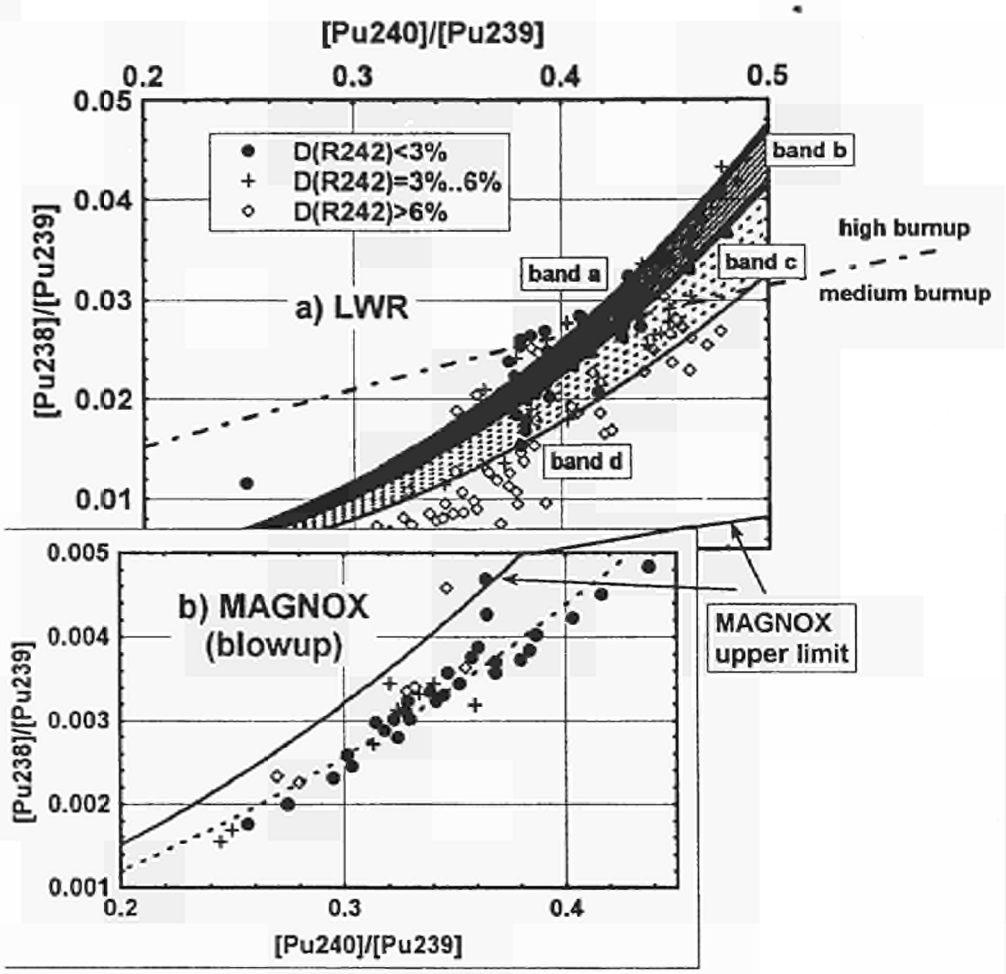

Fig. 6.3 Overview of available isotopic data. Point patterns correspond to three groups of deviations between data and fit in R242, as listed in the legend. A division of the R238 vs. R240 plane into bands and regions is proposed, cf. [3]. (a) typical LWR data; (b) blow-up for MAGNOX data.

different coefficients [11]. The coefficients A, B, and C are not fully independent of each other which allows one coefficient to be fixed with only minor impact on the final performance of the algorithm. The 3% error value can now be regarded as the ultimate limit of any isotopic correlation where more detailed information on the irradiation history of the Pu material cannot be taken into account.

Improvements can be expected from correlations with reactor-specific data, but preliminary results with special fit coefficients determined from small data sets still exhibited standard deviations of 1.3 - 2%. In the situation expected in the future OSL, the performance of the correlation will be tested with sample data from the nuclear installations which correspond to actual reprocessing batches.

The uncertainty of the empirical determination of ^{242}Pu gives rise to a random error component in the final result of combined neutron-gamma counting which depends strongly on the Pu isotopic vector of the sample. For MAGNOX material this component lies between 0.15% and 0.25%. For LWR samples, the ^{242}Pu ICT error completely dominates the final uncertainty and rises nearly linearly from 0.3% for low burn-ups (typically 15 GWd/t) to 0.85% for high burn-ups (around 40 GWd/t). In the latter case an improvement of the ICT performance as suggested above would lower the final error of combined neutron-gamma counting considerably.

COMPUCEA measurements

A COMPUCEA apparatus has been applied in campaign measurements at La Hague and also at Siemens (Hanau) for the measurement of uranium concentrations and enrichment. Such campaigns are extremely valuable for testing the device and for operator training. In many cases, the samples are provided as pellets or powders, which have to be then dissolved ready for measurement.

Together with the Safeguards Directorate, Luxembourg, a joint exercise was carried out to measure uranium product samples by a wide variety of techniques, including IDMS, product K-edge, titration and COMPUCEA. Although the results of this comparison have not yet been finalized, the measurements provided by the COMPUCEA apparatus were satisfactory, reaching the design specifications.

A critical area is the measurement of the ^{235}U enrichment with the COMPUCEA. A set of standard materials is required before the measurement limits can be determined.

The COMPUCEA is at present being incorporated into a glove-box for the pre-OSL. The complete system can then be tested. Software modifications are being carried out at the same time to make the system compatible with the data transfer system of the OSL.

Improvements to data management

Titration analysis management

The purpose of the application is to handle the communication between two RADIOMETER TIM900 titrators, which are installed in a glove-box for the determination of U and Pu concentrations in dissolved product samples, and a Zymark robot in order to be able to perform titration analysis fully automatically. The programs communicate with the three devices, synchronizing their work and collecting their results.

This application, previously written in FORTRAN for a PDP-11 computer, has been completely rewritten in C^{++} for a PC running under OS/2. The structure has been modified in order to perform all the tasks in a single user-friendly program. The program is started by double-clicking on the icon from the OS/2 desktop and navigating through the menus and windows as in the usual OS/2 environment. The data transfer to the Micro VAX is now done using the TCP/IP protocol from within the program. Other improvements are the ability to deal with any number of initialized samples, the possibility to change the analysis list during the run so that the operator can optimize the performances of the two titration systems and the possibility of continuing the analysis after stoppages during a run.

The application consists of a set of programs each performing a different function:

- get sample data from the *preparation* system
- initialize samples for the *titration* system
- supervise the aliquot preparation and the titration cycle
- collect the data from the Robot and from the titrators
- calculate the aliquot concentrations
- handle the various data (aliquot concentrations, standards, iron factors, daily factors) and calculate the analysis results
- send the final data to the Micro VAX

Transfer of data from isotope dilution robot to central VAX

The PDP 11/73 was still being used at the beginning of the year for laboratory applications and data transfer. At present the programs run on the Micro Vax computer and on the PC's running under OS/2 and the data transfer has been reconfigured to work over the Ethernet. This has resulted in a gain of speed and reliability. One application running on the PDP was the communication with the robot program for the IDA glove-box. The purpose of this program is to link the robot with the analysis system and also to the MCA (MultiChannel Analyser) used for alpha spectrometry. It is in fact a set of programs each performing a different function:

- obtain sample data from the expert system
- initialize sample data on the robot
- collect the analysis data during the IDA procedure (weights and alpha spectra)
- calculate the alpha ratio activities from the alpha spectra
- send the data to the Micro VAX for further evaluation

This application, previously written in FORTRAN for the PDP 11/73, has also been completely rewritten in C^{++} for a PC running under OS/2. The data transfer to the Micro VAX is now done using the TCP/IP protocol from within the program. Another welcome improvement is the ability to deal with any number of initialized samples without loss of performance. In the FORTRAN programs a working limit had been set. As the number of analyses for samples and quality control samples increased, this limit had caused frequent problems which have disappeared since the installation of the new program.

In order to give the operator some flexibility, a set of parameters are available which may be changed from run to run. These settings have a direct influence on the robot work. They include alpha counting time (short and long measurements), parameters for peak detection in spectra and guidelines needed for the calculation of the amount to be deposited by the robot on the mass-spectrometry filaments. These parameters were fixed in the old program; the operator did not have access to them.

The program was installed during the reporting period for final testing in the laboratory. During the testing, minor bugs were corrected and modifications as well as improvements proposed by the operator have been included. The program is now in routine use in the laboratory and a users' manual has been written and is available to the operators.

Improvements to the central VAX data system

A series of improvements have been carried out on the analysis system on the Micro VAX, following suggestions from ITU operators and also with the view of the final installation in the OSL at Sellafield.

A special databank was set up for measurements on standard materials for quality control and a program was written to output the measurements as control charts.

A databank, with earlier measurement results, on the central IBM computer of the Forschungszentrum Karlsruhe was ported to the VAX where the data are now available.

The measurement of a sample parameter by more than one technique is now possible. The results are categorized by technique and are selectable from the analysis flow tree.

Corrections for nuclide decay are incorporated into the titration, COMPUCEA, and NCC methods.
Corrections and calculation methods can be incorporated into menu options for later selection.

All communications to the VAX from PC's have been amended to use the TCP/IP protocol with the exception of the transfer of data from the mass spectrometers which is still carried out by serial transfer via a PDP 11 until the mass-spectrometer acquisition program can be successfully run under OS/2 conditions. The disk space has been extended, allowing routine overnight backups of the data.
Further improvements to the system are not foreseen now, as a new laboratory management system (LIMS) is being purchased. All potential changes have to be critically scrutinized for compatibility with the new system.

PREP: A program for sample preparation

As part of the development of the software transfer for the OSL, some programs written in FORTRAN for a PDP 11 have been rewritten and improved in C++ under OS/2. A program for the preparation of samples (i.e. dissolution & dilution) has been developed, installed and is now operational.

The main objective of the program is to help the operators with their daily work at the front-end of the analysis line where samples are prepared for further analysis by K-edge, titration, alpha-spectrometry, IDMS and TIMS.

The program receives the data specifying the samples to be measured and other parameter values from the expert system where new samples are initialized. An up-to-date overview of the workload can be obtained directly by the operator. During the various weighing steps the program accepts data from a balance via a serial interface. The transmission of the weighing data is triggered by a foot switch by the operator.

To help the user to obtain concentrations close to the target values, specific dilution proposals are made by the program and communicated to the operator.

If required, results are sent to the titration station as well as to the expert system, which in turn forwards this information to the central VAX computer, where all analysis data are stored. The flow of data through the system is showed in Fig. 6.4.

6.1.4 Future applications

The pre-OSL will fulfil its purpose as a trial and training medium for the future OSL at Sellafield. ITU will also use it to provide state-of-the-art analytical services to the European Safeguards Directorate. Data acquisition and handling have been developed to match the future needs of the pre-OSL and of the Institute. The pre-OSL demonstrates the high level of design, research and development skills that have been necessary within the many different technical, scientific, informatics and administrational fields involved in this project. The combined system is not only state-of-the-art but is also flexible and has been envisaged in such a way that it can be adapted to the different sample types that may be expected in future. Sample analysis throughput is maximized with the minimum of radiation dose to the operators.

The pre-OSL will become an inherent part of the analytical system accompanying ITU into the 21st. century with dedicated, automated glove-box analytical techniques which are already beginning to supersede previously used manual operations here.

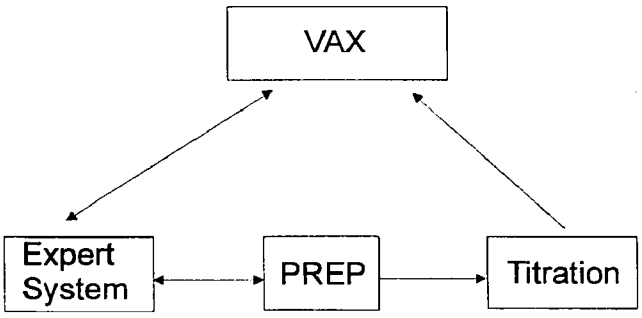

Fig. 6.4 Schematic view of dataflow to program 'PREP'.

References

[1] H. G. Wagner et al, "On-site Analytical Facilities for Euratom Safeguards", ANS Symposium, Albuquerque, New Mexico, 29. Sept.-4 Oct. 1991

[2] L. Koch et al, "Conceptual Design of an On-site Laboratory for Nuclear Material Safeguards", Proceedings of the 11th ESARDA Symposium on Safeguards and Nuclear Material Management pp 225-229, 1989

[3] B. Brandalise et al, "Components for an On-site Safeguards Laboratory", Proceedings of the 13th ESARDA Symposium on Safeguards and Nuclear Material Management, pp 127-129, 1991

[4] D. Wojnowski et al, "Expert System for Preparation of Safeguards Sample Analysis", Proceedings of the 11th ESARDA Symposium on Safeguards and Nuclear Material Management, pp 91-93, 1989

[5] M. C. Miller et al., "The Improved Inventory Sample Counter INVS Mod-III", Los Alamos National Laboratory, LA-12112-M, ISPO-329, May 1991

[6] H. Ottmar et al, "The Hybrid K-edge / K-XRF Densitometer: Principles - Design - Performance", Kernforschungszentrum Karlsruhe, KFK 4590, PWA 01/91, January 1991

[7] O. Cromboom et al., "Qualification of Plutonium Assay Techniques for an On-Site-Laboratory", Proceedings of the 17th ESARDA Symposium on Safeguards and Nuclear Material Management, pp 271-279, 1995

[8] P. Matussek et al., "A Compact K-Edge Densitometer for Uranium", Proceedings of the 13th ESARDA Symposium on Safeguards and Nuclear Material Management, pp 329-335, 1991

[9] ESARDA Bulletin ISSN 0392-30029 No. 23, pp 15-27, March 1994

[10] Ottmar, A. Schubert, O. Cromboom, H. Eberle, "Non-Destructive Assay of Small PuO_2 Samples by Neutron-Gamma Counting - Expectations and Achievements", 5th International Conference on Facilities Operations - Safeguards Interface, Jackson Hole, Wyoming, 25-29 September 1995

[11] Schubert, H. Ottmar, "Empirical Determination of ^{242}Pu in Non-Destructive Assay - Where Are the Limits?", Proc. 17th ESARDA Symposium, Aachen, Germany, 9-11 May 1995

6.2 On-site Laboratory Sellafield

Progress of the on-site laboratory project Sellafield

The main design phase of the OSL project was completed during the reporting period and the main emphasis was then placed on the following topics:

- revision of the infrastructure design
- preparation for setting up the infrastructure
- preparation for integration into the BNFL management structure
- purchasing of equipment and glove-boxes
- quality assurance to ISO 9001
- training of new personnel (see pre-OSL report)

Establishment of detailed design infrastructure

The infrastructure (ventilation, electricity supplies, etc.) of the OSL laboratory will be installed by BNFL Engineering Department at Sellafield, UK. The contracts for undertaking this work were made by DG XVII. The design of the project, which was frozen at the end of 1994, was subject to detailed considerations by BNFL Engineering Department. Subsequently, intense discussions involving all parties, i.e., DG XVII, BNFL and ITU, were carried out for clarification and for resolution of inconsistencies. The alterations are to be integrated into the design by BNFL leading to the agreed final design and this work has almost been concluded.

An integrated work programme has been submitted by BNFL which indicates a period of three months beginning with mid-December 1996 for installation of OSL project equipment. The work programme covers all aspects of construction and installation of the OSL laboratory, including installation checklists which are foreseen to be completed by mid-1997. Installation will then be followed by a 4-month period of mutual acceptance testing of BNFL services and TUI-installed facilities. Hand-over of the operational OSL is anticipated for the end of September 1997.

Quality assurance

Because the laboratory will be subject to quality assurance, the establishment of a QA system was started in 1994 in co-operation with NNC Limited, Risley, England. The system [1] is schematically represented in Fig. 6.5. The QA plan has been finalized and will be submitted to the client, i.e. DG XVII, for approval in December 1995 and will officially take effect then.

Twenty one project procedures have been completed and they are in implementation as far as they apply to ITU. Some of the procedures will only be applicable at Sellafield. The design plan schedules, the design input and output information, and the design verification strategy assure design compliance with the Pre-Commencement Safety Report (TUAR-94, p. 182), regulations, codes and standards. The design plan has been completed and is at the stage of implementation.

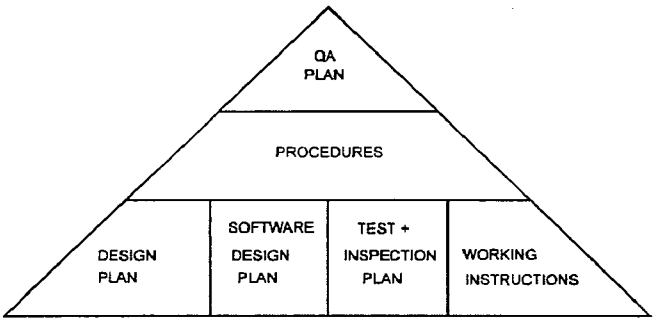

Fig. 6.5 Quality Assurance System.

Development of the software design plan has been started. This plan will be in compliance with ISO 9000-3 and is restricted to safety related robot software. Test and inspection plans have been established wherever testing of either glove-boxes or equipment is to be performed.

Purchase and construction of glove-boxes

In total four reports have been prepared by DG XVII and presented to the "Commission Consultative des Achats et des Marchés" (CCAM) with intensive support of the Institute. Specifications had to be written and call for tenders made representing a total investment of 1.6 MECU. After the committee's approval, material for two of the dossiers was ordered, a good part of which has been delivered to the Institute. The third dossier was approved at the end of November 1995 and the orders have since been placed.

Activities to establish detailed technical drawings of the OSL equipment have been started this year and will be completed in the forthcoming year. These drawings are in compliance with the QA design plan and are the basis for construction and assembly of the OSL equipment.

Integration into BNFL managerial infrastructure

The OSL will be integrated into BNFL's B229 management system which differs to some extent from the system at the Institute. The organization of the OSL must therefore be so harmonized as to allow overall integration. Discussions have been started with B229 management on topics such as safety training, QA for operation, management functions in the laboratory and additional training, laboratory manual and accountability for fissile material. An integrated programme covering all aspects will be established in collaboration with BNFL in the coming year.

References

[1] H. G. Schneider, W. Bartscher; "Quality Asssurance System for the On-Site Laboratory in Sellafield", Proceedings of the 17th Symposium on Safeguards and Nuclear Material Management, (1995), pp. 285-288

6.3 Progress of the 'Laboratoire Sur Site' (LSS) La Hague

The complete 'Avant Projet' of the technical part of the LSS prepared by the firm Société Générale pour les Techniques Nouvelles (SGN) was submitted to the Safeguards Directorate, Luxembourg and the Institute early in the reporting period. It contains all the technical details accumulated during the first part of the project. This 'Avant Projet' has been completed by detailed cost estimates and a time schedule for the completion of the LSS.

The planning includes seven parts corresponding to the following principal tasks:

- preparation of the technical specifications
- call for offers; preparation of the purchase orders
- purchasing of equipment and superstructure requirements
- organization of off-site contractors
- construction of equipment
- inactive tests
- active tests

SGN have estimated a duration of 34 months for the execution of the project, with the assumption of no interruptions. Should the project be paused after the second phase for review and, if necessary for modification, a prolongation for this purpose of five months has been estimated. A delay of six months has already occurred because of budgetary problems. The earliest start for the operation of the LSS is now estimated to be in 1999.

Some technical problems remain to be solved:

- Dissolution of PuO_2 samples: This is normally done in HNO_3 in the presence of a low concentration of HF. The presence of zirconium in waste pipes in the laboratory rules out the use of HF. A change in the dissolution method or a rigorous removal of HF from waste streams is required.
- It is not clear which analytical method can be used in place of titration (which is not acceptable at La Hague) for Pu in dissolved PuO_2 or MOX samples. Gravimetry would only be acceptable for safeguards if a method is available for the analysis of impurities. An alternative method under consideration is to apply a uranium spike and measure by X-ray fluorescence.
- Dilution of input samples for IDMS measurements: To comply with the permitted operator dose level which will be in force at La Hague and which will apply to the isotope dilution glove-box, a dilution factor of 20000 will be required for dissolved input samples, instead of 1000 as assumed up to now. Further tests on alternative analytical methods have to be done to overcome this problem.

6.4 On-Site Verification of Reprocessing Input Samples

During the time period before the on-site laboratories (OSL, LSS) are operative at Sellafield and La Hague, operators from the Institute will travel to these sites to measure samples with the Hybrid K-edge apparatus which is installed there at the hot-cells.

The routine measurements have been reported previously (TUAR-94, p. 187), and the same measurement procedures have been continued during the reporting period. Personnel from the Institute travel to La Hague on a weekly basis. More than 500 samples, from UP3 and UP2-800, have been measured over the last year. Extra work has incurred from the participation of Institute personnel in the measurement of densities of dissolved fuel solutions: this work, like all work at the La Hague hot-cells, is carried out by COGEMA personnel, but it has to be supervised for safeguards' reasons.

An increase in the total number of measurements has arisen from the large number of quality control (QC) samples which are now being included. Problems in the sealing of solutions of standard materials in the optical cuvettes which are used as sample vials in the K-edge devices and also the effect of the severe background radiation dose-levels on the stability of these solutions have had the effect of considerably decreasing their usable lifetime. This situation will have to be addressed in the coming year, because stable samples of standard materials are critical for successful measurements of samples.

The smaller number of samples for measurement at Sellafield has meant that Institute personnel are only required to be there one week per month when maintenance, measurements of samples and standard materials and density measurements are carried out.

6.5 European Commission's Safeguards Analytical Measurements (ECSAM): In-Field Verification Measurements

Introduction

On special request from the European Safeguards Directorate (ESD) Luxembourg, support has been provided for in-field verification measurements. The analytical support consisted of the determination of uranium content by potentiometric titration in dissolved powder and pellet oxide samples taken during various physical inventory campaigns.

The treatment of mainly low-enriched uranium samples under almost 'cold lab' conditions demanded special training of the operators involved. The tight schedule of the measurements required also operational capacity testing of the equipment used. The performance of mobile equipment for titration and the validation of the measurements were subject to preliminary investigations carried out at the Institute.

6

Experimental procedure

In view of the number of samples to be measured on-site (two samples per day), the performance of the standard method had to be critically tested as applied to the bulk analysis of uranium in oxide powders or pellets.

Dissolution

The dissolution of uranium powders and pellets is routinely achieved by wet digestion of the total sample. The amount is usually of the order of 10 g. The procedure is time-consuming and therefore an acceptable sub-sample range was determined assuming that the amount of the dissolution solution was limited to 10 ml of concentrated HNO_3 for the uranium oxide pellets and 10 ml of 8M HNO_3 for powder material.

As can be deduced from Tab. 6.6, significant differences were found by dissolving less than 1 g sample quantities of powder material although the results obtained from the uranium oxide pellets were within the allowed operator-inspector differences.

Tab. 6.6 Uranium concentration as a function of quantity of sub-sample dissolved.

Oxide powder		Oxide pellet	
Quantity dissolved (g)	% U measured	Quantity dissolved (g)	% U measured
0.1179	87.57	0.2059	88.27
0.1459	87.18	0.5818	88.27
1.4672	86.91	1.8723	88.15
7.4333	86.97	6.5101	88.13

Discrepancies of up to 0.7% cannot be explained by weighing or titration errors and therefore oxidation effects or uptake of moisture could be the origin for the heterogeneity of the finely ground powder samples.

Validation of the methodology

Experimental factors

The methodology and the performance data are only valid for the following experimental conditions:

- net (sub)sample weight dissolved: ~1g
- aliquot taken for final measurement: ~1g
- concentration range: 30 - 50 mg U/g aliquot
- $K_2Cr_2O_7$ titrant: 0.05 N

Calculation of the total uncertainty

The error components were calculated for a 95% probability level traceable to international standards by applying error propagation to calculate the overall uncertainty from the following experimental parameters:

- the calibration of the final measurement
- the precision and the accuracy of the analysis
- the uncertainty of the certified reference material used

Precision and accuracy of the analysis

The precision and the accuracy of the methodology is determined by the analysis of a certified reference material which is similar in chemical and physical form to the actual samples. Four certified uranium dioxide pellets were therefore submitted to the complete analytical procedure. The treatment and subsequent analysis of those samples was carried out by the four titration team operators on different days. Each run consisted of three independent measurements.

- Reference material used: NMR-EC-110 uranium dioxide sintered pellet
- Certified uranium content: 881.34 ± 0.13 mg U/g

The certified uranium material was used as an internal quality control standard. Prior to each run two or three standard aliquots were titrated under the same conditions as the sample aliquots. The within-run standard deviation (s_w) reflects the measurement error only while the between-run standard deviation (s_b) defines

the accuracy of both the dissolution step and the final measurement.
The bias of the analysis procedure was calculated as follows:

$$\text{Bias} = (U_{found} - U_{taken}) / U_{taken}$$

If the measured bias is outside the precept control limits, the method is checked for the source of the systematic error. From the mean bias, calculated from the last 20 measurements, an average recovery factor (R) is calculated: This is used to correct all titration results for the residual systematic errors of the titration procedure.

$$R = \text{mean Bias} + 1$$

$$U_{corrected} = U_{measured} \times 1/R$$

Calculation of the total uncertainty

Using the analysis of variance (one way ANOVA) the confidence interval at the 95% probability level is given by:

$$CI_x = (CI^2_{ref} + CI^2_w + CI^2_b)^{1/2} \text{ with } CI = s \cdot t / n^{1/2}$$

where n is the number of replicate measurements on each sample and t is the appropriate student factor.

The coefficient of variation (CV) and the relative standard deviation (RSD) are defined as follows:

$$CV = s / \text{mean and RSD} = CV \times 100 \text{ (percent)}$$

The following uncertainties were calculated from an evaluation of the data obtained:

CI_w = 0.306 mg U
CI_b = 0.905 mg U
CI_{ref} = 0.13 mg U
CI_x = 0.964 mg U
RSD = 0.11%

Acceptable span between duplicate measurements = 0.35%.

Conclusions

Three field exercises were conducted at fuel fabrication plants (ABB (Vasteras, Sweden), ENUSA (Juzbado, Spain) and BNFL (Springfields, GB)). In total, 75 samples were analysed and the measured uncertainties were all within the indicated uncertainty limits of ± 0.14% of international target values for random and systematic uncertainty components in uranium concentration measurements on LEU oxide powders and pellets.

The experience gathered will be included in a Working Instruction in which detailed information will be given for the analysis of uranium samples under in-field conditions.

6.6 Remote Measurement of U and Pu in Nuclear Waste Samples by Laser Ablation Optical Emission Spectroscopy (LA-OES)

Objectives

The reprocessing of spent nuclear fuels to recover uranium and plutonium is always affected by losses in the different process streams as well as in the head-end part before the extraction process itself. Consequently the vitrification of the HLLW raffinate in the tail-end of the process leads to a product which contains non-negligible amounts of fissile U and Pu isotopes. A systematic on-line analysis of the vitrification product is not included in the concept of industrial vitrification plants. Nevertheless in view of intermediate or final storage of vitrified HLLW it could be very useful to have a versatile tool to analyse the U and Pu content and isotopic composition in these glasses. Optical emission spectroscopy (OES) of a plasma produced by laser ablation (LA) is a method, which allows the direct measurement on the waste glass product. No sampling or additional sample preparation is required. However, because of the high activity of real waste glasses, a remote sensing technique has to be applied.

Experimental

A measuring head with special micro-optics has been developed with the dual purpose of focusing the laser beam on the sample and collecting the radiation emitted from the sample (Fig. 6.6).

Optical fibres are used for the light transport from a Nd-Yag laser to the sample and to transport the emission radiation of the plasma to a charge coupled device (CCD) detector connected to a microchannel plate (MCP) amplifier. Suitable absorption lines have to be selected so that the analysis of U and Pu can be achieved with the best possible detection limit and reproducibility. For simulated glasses a U line free of interferences was determined at 591.593 nm. The detection limit was improved to the value of 216 µg/g by using a MCP-CCD camera instead of the previously utilized optical multichannel analyser, mainly due to an improved signal-to-background ratio. The ultimate limit of detection is now limited by interferences from lines emitted by trace components in the glass. The spectra obtained for the German reference waste glass, VG 98/12 (matrix alone) GP 98/12 (matrix + simulated fission products) and GP 98/12 + UO_2 are shown in Fig. 6.7.

Similar results were obtained for the French simulated R7/T7 glass. The method was also used to determine

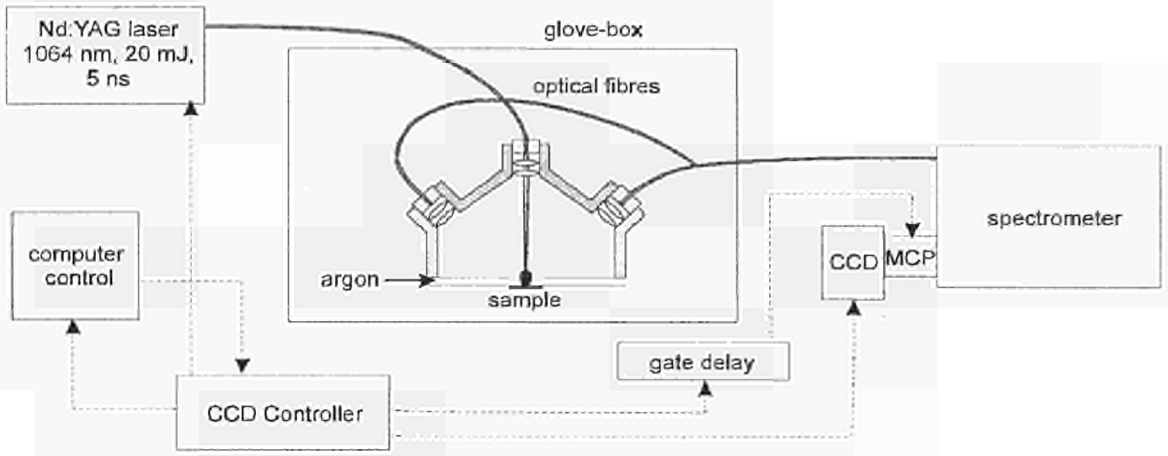

Fig. 6.6 Experimental set-up for LA-OES.

the homogeneity of the materials analysed. Identical equipment has been installed at the Institute where it is being connected to a glove-box in order to determine the Pu content in waste materials.

Conclusions

Based on the encouraging results obtained for U, the method will be extended to the analysis of Pu, to the determination of the isotopic composition for both elements and finally of course to the measurement in real vitrified HLLW. Increased sensitivity of the method and a reduction of the interference from other elements contained in the complex sample could be achieved by the use of laser-induced fluorescence (LIF) applying diode lasers. This technique will furthermore offer the possibility of analysing the isotopic composition of U and Pu.

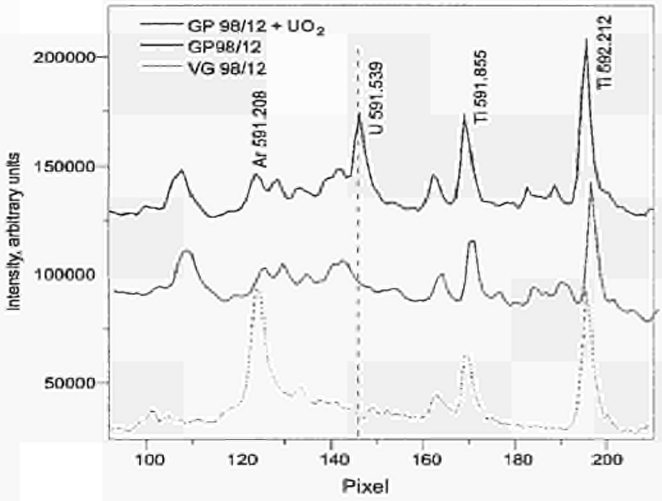

Fig. 6.7 OES spectra for different reference glasses (detection 20 µs, delay 6 µs, 50 laser shots).

6.7 Analysis of Seized Nuclear Materials

Although special nuclear materials are heavily guarded it cannot be excluded that such material be diverted and fall into the hands of sub-national groups, international terrorists or states striving for the possession of nuclear weapons. Indeed, cases of illicit trafficking of nuclear material have recently been observed. Seized material from about 20 cases has been analysed in our institute in order to determine its origin and intended use.

Most of the seized material was not weapons-grade: two batches of non-enriched uranium oxide, four types of CANDU fuel pellets, two metallic ingots of natural uranium - as used in gas-cooled graphite reactors to produce weapons plutonium, six with various pellet types for RBMK and VVER type reactors. Only in one case was highly enriched uranium found. This was a sample of a 2 kg batch that was later seized in Prague (highly enriched uranium: 90%). Three batches consisted of ionization sources with weapons plutonium denaturated by 8% of ^{238}Pu. Finally, there were two spectacular seizures: 363 g plutonium with 87% of ^{239}Pu together with 200 g of 90% ^{6}Li and a sample of about 6 g highly enriched plutonium in so-called 'red mercury'.

Methodology

Forensic analysis that will reveal the origin and intended use of an unknown material has to rely on information from

- the circumstances under which the material was seized,
- cognisance of the intelligence services and
- material analyses.

As in archaeology, hints to the history of a nuclear material can be deduced from the accompanying material (e.g. packaging), contamination of other nuclear material on surfaces and analyses of traces of biological material.

The characteristic signature of trace element concentration in forensic analyses as well as in archaeology (e.g. coins, pottery, etc.), have been often referred to as fingerprints. The analogy to nuclear material reaches further, because the genetic dependence of artificial nuclides contained in a material points to its origin and use.

Material that underwent nuclear processes shows an inherent consistency of its nuclides which in turn - post analysis - point back to the nuclear processes in which the material was involved. Therefore, such **endogenous information** is self-explanatory and needs no verification by comparison with material of established history. As explained below, the histogram (i.e. sequence and date of processing steps), the production mode (burn-up and neutron flux hardness) and intended use (from fuel composition) can be determined.

Other **exogenous** information is engraved in the material by the fabrication processes (e.g. impurities left over or introduced by tools, texture of material) or by the intended use (specification of nuclear materials.)

To link the results of an investigation to a particular production facility or to a nuclear reactor, the corresponding process parameters have to be known. To some extent they can be found in the open literature, but when it comes to material structure or impurities remaining from the fabrication processes, practically nothing has been published. Such databases are common in other fields like archaeology, geology etc., but do not exist for nuclear materials, due to restrictions imposed by commercial interests, national security and to avoid the spread of knowledge that would facilitate the proliferation of nuclear weapons. However there are sufficient characteristics and specific parameters for each of the material types that are not sensitive to any of the restrictions mentioned.

Analysis and evaluation

The analytical tools we use to characterize an unknown nuclear material consist of commercially available equipment which is adapted to the handling of radioactive nuclides and are employed to characterize fuels and actinide materials of our R&D programme as well as to analyse samples in support to the Safeguards' Directorate (Tab. 6.7).

Since the characterization of a sample starts with the measurement of the nuclide abundance, radiometric or mass-spectrometric techniques are used in the first place. α- and γ- spectrometry are easily and non-destructively applied, but they are limited by the specific radioactivity of the nuclides. Mass-spectrometric techniques, however, are far advanced now and one can determine long-lived and stable nuclides with good accuracy. The isotopic composition of uranium and plutonium directly points to the intended use: non-weapons-grade nuclear fuel, weapons-grade material (as used as fuel for certain reactor types) or weapons material. A closer look at the isotopic abundances, complemented - if detectable - with other radionuclides, already suggests the production method of the material, e.g. recycled uranium, plutonium from reactors with different neutron spectra, etc..

Tab. 6.7 Analytical techniques employed in characterization of seized nuclear materials.

Non-destructive analyses	γ-spectrometry
	n-coincidence counting
Destructive analyses	α-spectrometry
	scintillation counting
	titration
	isotope dilution mass-spectrometry
	glow discharge mass-spectrocopy
	inductively-coupled mass-spectrometry
	electron microprobe analysis
	electron microscopy
	secondary ion mass-spectrometry

There is no fixed scheme of analyses for unknown nuclear materials. Rather it is guided by the pattern of information that builds up during the investigation. The selection of further analyses is determined by observations obtained from previous analyses - following the known principle of diagnosis. It is obvious that the scientists evaluating the results must have direct access to the database and auxiliary tools (burn-up codes, etc.).

Another source of information is obtained from the fabrication of nuclear material. Traces of other elements remaining in the material can lead to the processes used. The chemical composition of the material as well as its form points to the intended use, as for example the shape of pellets (Fig. 6.8) for which a comprehensive data collection is available. Also the microscopy structure of the material is typical for a fabrication process and consequently for the intended use.

Traces of nuclides in the material (which are usually not measured during the fabrication, if they are not explicitly specified) can tell the history of a material. The techniques applied to determine these traces are inductively-coupled mass-spectrometry combined with an ion chromatograph and glow-discharge mass-spectrometry. The first technique has a high sensitivity when applied to liquid samples, whereas the second is better for solid samples.

Since the fission yields for the different fission products depend on the fission source and the neutron energy spectrum, analysis of fission products can fix the reactor type. In the case of thermal reactors, the secondary neutron capture in fission products also gives information on the neutron fluence and the burn-up respectively. This follows, of course, also from other fission products, like fission gases contained in the material. The analysis of individual particles will give additional hints of origin and use. For this pur-

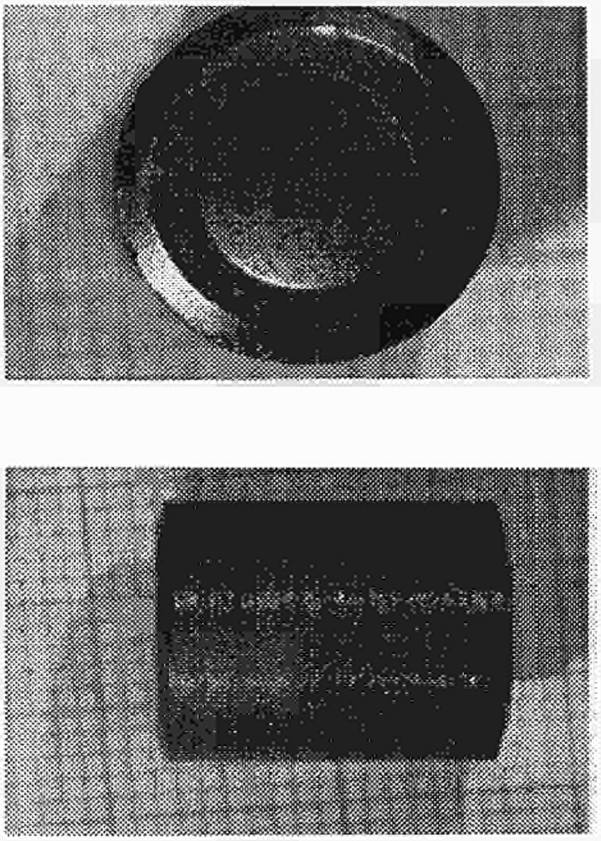

Fig. 6.8 Seized RBMK fuel pellets.

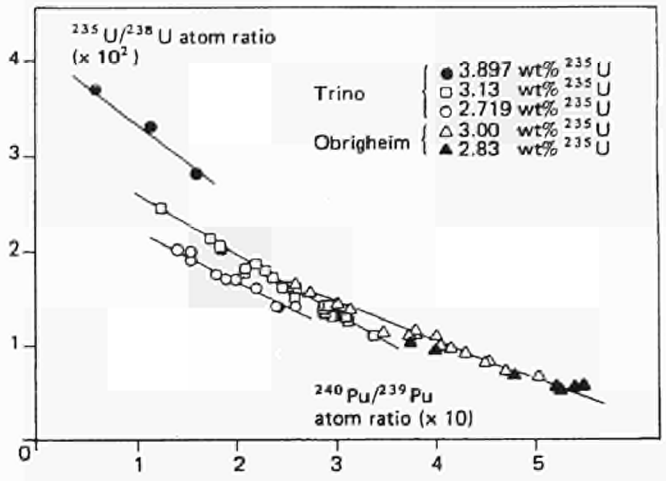

Fig. 6.9 Correlation between $^{235}U/^{238}U$ and $^{240}Pu/^{239}Pu$ atomic ratios for PWR samples.

pose, transmission electron microscopy, ion microprobe analysis, X-ray analysis or secondary ion mass-spectrometry can be applied. In the case of surface contamination of nuclear material, such analyses could lead to the place and date where the material has been diverted (in one of the cases reported above, this surface contamination showed a recent signature of a reprocessing plant. The separated material was therefore older and had been repacked at another facility).

The variety of parent-daughter relations of radionuclides in nuclear materials opens the possibility to date the process steps the material underwent. The grown-in ^{241}Am together with the build-up of ^{236}U and ^{235}U from plutonium decay leads to the date of plutonium separation. The build-up of ^{231}Pa determines the date of uranium conversion after enrichment, which is the same for ^{228}Th for recycled uranium. Similar possibilities offer fission products where a variety of elements exists that can be linked to the different process steps of reprocessing, calcination, precipitation, etc.

Finally, it should be mentioned the wealth of information that is contained in earlier isotope correlation studies showing the typical relations of isotopes in spent fuels as exhibited by the example of Fig. 6.9.

The intended use of a nuclear material follows readily from such investigations, whereas the histogram of the material merely leads to its origins without specifying its location. Here only a comprehensive database listing all potential production facilities with this specification can infer a particular plant from the analytical data. Nevertheless, certainty on the material's identity is only obtained if the 'fingerprint' is connected to the 'finger', i.e. a known material. For this reason the Institute is setting up a databank archive of typical nuclear samples.

For each 'Fund', the Institute has prepared an expert evaluation upon request from the Safeguards' Directorate, Luxembourg. Copies of these evaluations were used as evidence in court, where members of the Institute were also called as expert witnesses. Until the court cases are finished, we are not allowed to report or comment on our findings.

7. Scientific and Technical Support to DG I

Introduction

A number of activities are carried out for the International Atomic Energy Agency (IAEA) under support to DG I. Some are concerned directly with the determination of trace amounts of radioisotopes in the environment. For this reason the ARTINA laboratory, which allows environmental samples to be handled under clean room conditions is being specially constructed (see 7.2 and 7.3 below). Other activities include the application of high-pressure liquid chromatography linked on-line to an ICP mass-spectrometer for the measurement of Pu in high active waste.

7.1 Trace Radioisotopes in Environmental Samples by Glow Discharge Mass Spectrometry

In the last few years Glow Discharge Mass Spectrometry (GDMS) has been recognised to be one of the most powerful method for the analysis of traces in conducting and non-conducting solid samples. In our laboratory many applications for the bulk composition determination of samples of nuclear concern have been performed. Recently, the possibility of the determination in soils, sediments and vegetations of some radioisotopes of caesium, strontium, plutonium, uranium and thorium by GDMS has also been investigated. Appropriate preparation techniques of the samples needed to be optimized. The most appropriate consisted of a combination of the use of a conductive host matrix and a secondary cathode. This procedure decreases the dilution effect of the blending material for trace level determination and allows a stable discharge to be obtained.

Effects of interferences arising from the nature of the conductive host matrix and of the secondary cathode on the sensitivity of the method could be eliminated by a careful choice of the instrumental parameters (e.g. mass resolution and acquisition time). Several matrices were investigated (soils, sediments, vegetations) and detection limits of ppt levels were obtained for an acquisition time of one hour [1].

The results obtained by analysing environmental reference samples obtained from IAEA (Vienna, Austria) and the National Institute of Standards and Technology (NIST, Gaithersburg, USA) showed that GDMS is a helpful technique for the determination of trace radioisotopes in environmental samples. The experimental results obtained by GDMS showed good agreements with the certified values (Tab. 7.1).

Tab. 7.1 Comparison of GDMS results with certified values for accuracy evaluation.

Radioisotope	GDMS value	ref. value (ref. sample)	error %
^{137}Cs	5 pg/g	3.86 pg/g (IAEA 373)	29.5
^{239}Pu	100 pg/g	92* pg/g (IAEA 135)	8.7
^{234}U	1.0 pg/g	1.1 pg/g (IAEA 375)	9.0
^{234}U	1.0 pg/g	1.2 pg/g (IAEA 135)	17.0
^{235}U	25 pg/g	22 pg/g (NIST-4350)	13.6

* value given as $^{239}Pu + ^{240}Pu$

Reference

[1] M. Betti, S. Giannarelli, T. Hiernaut, G. Rasmussen, L. Koch "Detection of trace radioisotopes in soils, sediments and vegetations by glow- discharge mass spectrometry", Fresenius J. Anal. Chem., in press

7.2 Participation in Field Trial of Environmental Monitoring and Analysis

At the end of 1994, the Institute participated in a field trial of environmental monitoring for safeguards purposes in collaboration with the IAEA and three Member States of the European Union, carried out in and around the Urenco centrifuge enrichment facility in Almelo, Netherlands. The sampling campaign lasted two days. During this sampling, specimens of vegetation, soil, water and sediments were taken at locations within the facility and at distances up to 12 km from the site.

Terrestrial samples, were collected at four locations at distances of approximately 1, 3, 5, and 8 km along an axis from the center of the Urenco site and extending to the north east. Samples were also taken inside the Urenco site. In addition, a background sampling location 12 km south west of Almelo was chosen. At all sites, surface soil, moss and pine needles were sampled.

The hydrological samples, grab waters and sediments were taken from a canal at a background site 12 km south west of Almelo, from a roadside ditch 1 km to the east of the facility and from the canal near the center of the Urenco facility. Grab waters and sediments were taken in the storm drain of the site and the sanitary sewer where it exits the site.

Swipe samples were collected in 21 locations in the main process areas: in two operating centrifuge buildings, in a decommissioned centrifuge building, the central services building and a number of other locations.

Part of the samples gathered in this field trial were analysed at the Institute. In particular, swipe samples were analysed by secondary ion mass spectrometry for enriched uranium particles: content and isotopic composition were determined.

The results obtained were found to be in very good agreement with those reported from other laboratories of the IAEA network.

7

7.3 ARTINA (Analysis of Radioisotope Traces for the Identification of Nuclear Activities) Laboratory

The analysis of environmental samples for the identification of nuclear activities is a highly specialized and exacting discipline requiring suitably equipped and designed facilities and a high level of analytical competence. These samples have to be handled so as to avoid any cross-contamination.

As reported previously (TUAR-94, p. 171) the ARTINA laboratory, conceived for this purpose, has been constructed using prefabricated techniques to arrive at a class 100-10 environment. The laboratory has a slightly different function compared to normal clean-laboratories in that its usage is meant for environmental radioactive samples, where cross-contamination from other active materials must be avoided completely. This laboratory will be used for the preparation of samples before the analysis.

The special class 10 environment will be achieved on the working bench where the samples are weighed, ground and sieved for the further dissolution using a special microdigesting system for dissolution. The dissolved samples are then spiked with internal standard solutions, or isotopic standard solutions for subsequent isotopic dilution analysis in a special clean-hood for the handling of very low amounts of radioactive isotopes.

Specimens for the analysis of particles will also be prepared in the ARTINA clean lab. These are generally collected on swipes. The first step is the screening of the sample using a polarized light microscope and then the collection of particles by microtools on special supports for subsequent instrumental analyses. For example, after their identification, the particles will be loaded on filaments for thermal ionization mass-spectrometry, on cathode pins for the examination with glow-discharge mass-spectrometry and on other supports for secondary-ion mass-spectrometry.

The laboratory will be used for the preparation of reference and/or control samples for internal quality purposes and for the preparation and certification of the cleanliness of sampling materials. The kits for the collection of swipes, soil, sediment, water and vegetation in particular will be pre-cleaned in this laboratory, according to well established procedures for trace elements determination [1], then certified and shipped to the users.

All operations will be performed by skilled trace analysts under the supervision of a senior scientist in the field. All tools as well the clothes used by the personnel in the laboratory are specially fabricated for clean laboratory work.

References

[1] M. Betti, P. Papoff; CRC Critical review in Analytical Chemistry 19 (4) (1988) 271-322

7.4 Determination of Plutonium in High Active Liquid Waste (HALW) by Ion-Chromatography Inductively-Coupled-Plasma Mass-Spectrometry Isotopic-Dilution Analysis (IC-ICP-MS-IDA)

During the year, the application of the method [1] for the determination of Pu and selected fission products after chemical separation on HALW samples has been studied and improved. For the analysis of Pu, undiluted samples (c.a. 0.5-1 ml) are treated with solid silver oxide in order to quantitatively oxidize plutonium to Pu(VI). The exact amount of silver oxide and the time necessary to obtain quantitative oxidation has been investigated in detail.

Instead of the 1 M nitric acid previously used as eluent on the cationic-exchange phase CS10, an organic acid/nitric acid mixture (2,3-diaminopropionic acid (DAP), 40 mM + 0.6M HNO_3) was employed. The DAP is a complexant and this improves the separation of plutonium from the isobaric interferences from ^{238}U, ^{241}Am and ^{244}Cm for the case of very low Pu content. The elution conditions of the separation were optimized by varying the eluent flow-rate and the eluent pH according to the Pu intensity signal.

As a test, the method was applied to synthetic solutions having different atomic ratios of Pu/U: (1; 0.1; 0.01) and to active dissolver solutions obtained from the Institute's hot-cell facility. For all three ratios considered the separation of the elements was found to be good. For the solutions from the hot cell the isotopic composition of both Pu and U obtained by IC-ICP-MS method was in satisfactory agreement with the results obtained by thermal-ionization mass-spectrometry (TIMS).

The concentration of Pu is best determined by the method of isotope dilution analysis. The precision of the method determined experimentally for 10 consecutive injections was 3% and the accuracy for the concentration of 1 ng/ml of Pu was better than 10%.

Reference

[1] J. C. Garcia Alonso, F. Sena, Ph. Arboré, M. Betti, L. Koch, J. Anal. Atom. Spectr. 10 (1995) 381

C. Competitive Activities under the Framework Programme

8. Shared Cost Actions

Introduction

In order to strengthen European cooperation in R&D and to further enhance the competitiveness, the 4th Framework Programme of the European Commission permits the participation of the Institute in call for tenders under the different shared cost action (SCA) programmes.

In line with its mission the Institute has limited its participation to the Nuclear Fission Safety Programme. Cooperation in networks of other programmes was considered outside the real competences of the Institute and was also not recommended by the Institute's Advisory Board.

8.1 ITU Participation in the Nuclear Fission Safety Shared Cost Action Programme

During the reporting period, ITU participated in the first call for tender under the above shared cost action programme. Of the twelve projects submitted with other partners from the European Union, eight projects were retained and accepted. The projects are the following:

- Evaluation of partitioning and transmutation strategies
- New partitioning techniques
- Joint EFTTRA experiment on americium transmutation
- Supporting nuclear data for advanced MOX fuels
- Source term for performance assessment of spent fuel
- Revaporisation tests on samples from PHEBUS fp
- Impact of the accelerated based technologies on nuclear fission safety
- Thorium cycles as a nuclear waste management option

Progress in the above projects can not yet be reported as the detailed discussions on the definition of the tasks, the attribution of work to the various partners and contractual aspects continued till the end of 1995.

9. Competitive Support Activities

Introduction

In the framework of technology transfer, Directorate General XIII of the European Commission is supporting cooperative activities between research Institutes and industrial partners on a competitive basis. Such support is given in particular to inventions (patents) originating from the Institute and having a high potential for industrial applications.

9.1 Enhanced Gas Cleaning by Infra-Sonic Agglomeration and Deposition

Initial investigations of the influence of infrasound on aerosols have shown that substantial particle agglomeration and deposition can be achieved [1]. A new project, including the transfer to industrial applications, has been proposed and accepted for funding under the competitive support activities programme administrated by DG XIII. The project entitled 'Enhanced gas cleaning by infra-sonic agglomeration and deposition' foresees detailed investigations and tests of particle agglomeration and deposition processes in a specially designed cavity, whose internal structure will be optimized prior to carrying out tests at an industrial installation. The necessary competence to design and construct the cavity will be supplied by Infrasonic AB (Stockholm, Sweden), while the industrial expertise in flue and process gas cleaning will be provided by Apparatebau Rothemühle (Wenden, Germany).

References

[1] TUAR-94, p. 155

D. Competitive Activities outside the Framework Programme

10. Third Party Work

Introduction

In the following, a short summary of some of the work performed for third parties is given.

That reporting is short and selective due to the commercial character of the work performed. For the Institute, such type of work is beneficial for essentially three reasons:

a) it shows the relevance and competence of the Institute for such work within the nuclear fuel cycle;

b) it increases the know-how of the Institute in areas of industrial applications, where access to material and data would otherwise not be possible;

c) last but not least it provides some financial income which is highly welcome to maintain a functional and safe nuclear infrastructure at the Institute.

10.1 Post Irradiation Examination of Pressurized and Boiling Water Reactor Fuel Rods

Within the frame of the contract with Siemens AG - Bereich Energieerzeugung (KWU) non-destructive and destructive examinations of fuel rods were carried out. The work performed and described in TUAR-91, p. 199, TUAR-92, p. 199, TUAR-93, p. 227, TUAR-94, p. 205 has continued.

A list of the types and number of examinations carried out for 1995 is given in Tab. 10.1.

During 1995, the following fuel rods were transferred to ITU: 12 fuel rods from KKGg (Gösgen), 2 fuel rods from KKP (Philippsburg), 12 fuel rod segments from HFR Petten, 5 fuel rods from KWW (Würgassen) and 7 rods with various Zr-y alloys.

The aim of these post-irradiation examinations was to provide experimental data on the in-pile behaviour of new zirconium alloys, liners, iodine assisted stress corrosion cracking (IASCC) of stainless steels and Ni alloys and, finally, on UO_2 and MOX irradiated under transient conditions.

This work will continue until mid 1996.

Tab. 10.1 Number and types of examination carried out on different fuel rods.

Experiment / Type of analyses	MTS 6	KKGg VII	GKN I III	KKGg VIII	Refab.	KKK (def)	KKK I	KKGg	KKK (def)	KKGg IX	Refab.	HFR	MTS B436	KWO Mox	KKGg hab	TOTAL Exam.
Vis. examination									6	4		4	1			15
Fuel rod length												4				4
Defect detn.									1							1
Gamma Scan.										2	1	1				4
Fission Gas Anal.										5	1	2				8
Free volume detn.										5	1	2				8
Metallography						2	6		2	3		4		3	3	23
Ceramography						4	6		3	2		4		3	3	25
Density		5	4	3						1						13
H_2-detn.	13					5			3	4						25
Vis.Insp. cladding												1				1
SEM-cladding												1				1
Microprobe									1							1
TEM						1										1
Fuel rod refabrication					4											4
Hardness test									3							3
Glow-Discharge-SM								12								12

10.2 Micro-mechanical Testing of High Burn-up Fuels

Within the framework of a cooperation contract with EDF a new experimental programme has been started in our hot-cell laboratories, aiming for a detailed characterization of the mechanical behaviour of high burn-up fuel. Special attention will be paid to the influence of the porous structures formed at the pellet periphery. Because of the heterogeneous nature of the irradiated fuel a thorough characterization of the material requires the determination of the mechanical properties of the different restructuring zones. Due to the small areas involved, the utilization of a micro-indentation technique was required.

The cooperation contract with EDF includes the following points:

- Development and adjustment at ITU of a remote-controlled micro-indentation device. This allows the measurement of properties like $\sigma(\epsilon)$, $\epsilon\sigma$ (t), $\sigma\epsilon$ (t), and the micro-hardness parameters H_V and K_{IC} under controlled atmospheres and at temperatures up to 1000 °C. The sample gauge areas can be as small as 15 x 15 μm^2.
- Non-Destructive Testing (NDT) characterization of a BR3 fuel rod at the hot-cells (BR3-N118) (B_{max} = 69.8 GWd/tM), which will be later utilized for the mechanical tests.
- Development at EDF of a micro-mechanical model computing the strain (stress)-field created around the indenter tip during indentation, from which a correlation with the macroscopic properties of the material will be established.

The state of the project can be summarized as follows:

- The design of the micro-indentation device has been already completed, and the construction of the apparatus has been started.
- The NDT examinations of the BR3-N118 fuel rod has been completed, with evidence of a strong pellet-cladding interaction (PCI) at the maximum power position of the fuel rod. The destructive examinations, including optical microscopy, SEM and EMPA will be performed on the cross-section at the maximum power position.
- For the micro-mechanics model being developed at EDF, a first approach has concentrated on conical indenters. Present studies are now including Vickers-indenters and flat-punch geometries. These models will initially be tested with results obtained on unirradiated materials.

10.3 Matrix Materials for the Transmutation of Actinides

The project between ITU and Electricité de France (EDF) to investigate inert matrices for transmutation of minor actinides was continued. The aim of this investigation is to select suitable matrices for transmutation of Am based on a number of criteria:

- thermal properties (melting point, thermal conductivity)
- compatibility with clad and coolant
- mechanical properties (e.g. Young's modulus)
- solubility of actinides
- radiation stability against α-decay (α-particles and recoil atoms), neutron and fission fragments.

Five matrix materials were selected and fabricated with and without ^{241}Am. Physical properties were measured and experiments to investigate radiation damage effects were started. Fission damage was simulated by ion implantation with 70 MeV iodine ions in cooperation with the Chalk River Laboratories, AECL [1]. The final report will be written in early 1996.

References

[1] Hj. Matzke, P.G. Lucuta, R.A. Verrall; J. Nucl. Mater., in press

10.4 Transmutation of Minor Actinide Containing Alloys in Phénix

As part of a contract with CRIEPI metal fuel pins containing minor actinides are being constructed. The fabrication procedures for sodium bonding and the methods for the final control of the rods for the irradiation experiment in Phenix were adapted and tested. Three glove-boxes for filling and Na-bonding of the pins, equipped with a vacuum furnace, were installed and connected to an existing nitrogen purification bench. Due to problems of high neutron- and γ-emission of the fuel, additional shielding was necessary (steel, polyethylene, Plexiglas ...).

The most important steps are:

- extrusion, just before the filling, of a sodium wire, the necessary quantity being controlled by weighing,
- introduction of the sodium wire and then of the fuel ingots into the cladding tube,
- settling, under vacuum, of the Na-bond in a vertical resistance furnace: the ingots sink, by gravity, into the liquid sodium
- introduction of the end cap and TIG-welding under helium
- final controls: beside the standard controls (He-leak Test, radiography, contamination, ...), an eddy current bench was adapted for the control of the Na-bond.

  3 sets of 3 pins have been fabricated with the alloys UPuZr, UPuZr + 2% MA + 2% RE, UPuZr + 5% MA + 5% RE and UPuZr + 5% MA (MA = minor actinides; RE = rare earths).

  The characterization of the sodium bond and interpretation of the results from the eddy current tests are under way.

10.5 Dissolution Studies on High Burn-up UO_2 and MOX Fuel

The study of the dissolution behaviour of commercial spent nuclear fuels (high burn-up UO_2 and MOX) has continued as part of a contract with CRIEPI. This work is a follow-up of the study presented in TUAR-91, p. 198, where a fuel with very special characteristics was used. Therefore it has been decided to repeat the study with commercial fuels.

An extensive characterization of the fuels by optical and scanning electron microscopy has been carried out. Two samples of each fuel type were dissolved in 4 and 7 molar nitric acid respectively. The residue was separated by centrifugation and filtration and weighed. After a thorough homogenization, aliquots of each residue were prepared for metallographic examination and for dissolution to determine the elemental and isotopic composition. The dissolution was carried out at 200 °C in autoclaves by means of a mixture of nitric, hydrochloric and hydrofluoric acid.

The characterization of the fuel by EPMA with special emphasis on metallic inclusions has started.

10.6 Spent Fuel Characterization for Interim Dry Storage

Work is presently being carried out in the third year of the four year program for a contract with CRIEPI. The studies performed include chemical analyses of fuel pellets over a burn-up range of 55 to 65 GWd/t heavy metal, measurement of density, axial autoradiography, determination of fission gas release during heat treatment (annealing) and dissolution, and SEM and TEM of the rim and pellet regions before and after annealing.

A MOX archive pellet has also been analyzed for isotopic composition (including ^{241}Am) at charge and for Pu concentrations by electron probe micro-analysis in the uranium oxide matrix and in the Pu agglomerates, in order to assess changes due to irradiation through comparisons with the spent MOX fuel.

10.7 The RIM Effect Irradiation

The irradiation of the UO_2-based fuel discs fabricated in 1993 (TUAR-93, p. 227) in the Halden reactor was continued. The peak burnup reached in 1995 was ~ 75 GWd/t. The irradiation will be terminated in May 1996.

As explained in TUAR 93, p. 277, the High Burnup Rim Project is managed by the Central Research Institute of Electric Power Industry (CRIEPI) and the irradiation is performed in the OECD Halden reactor. Small UO_2-disks are used in a matrix of 4 temperatures, 4 burnups and 2 pressures, with control and measurement of temperatures and gas release during the irradiation [1]. The effect of the parameters burnup, temperature, pressure and type of fuel on the polygonization of UO_2 (formation of the rim structure) will be investigated in post-irradiation work planned to be started in TUI towards the end of 1996.

References

[1] M. Kinoshita, T. Matsumura, T. Kameyama, S. Kitajima, E. Kolstad, Hj. Matzke; Extended Halden Project Meeting, Bolkesjø, Norway, paper F 1.9, Nov. 1994

10.8 An Investigation of the Metal-Oxide Interface in Irradiated Zircaloy Cladding Samples by Transmission Electron Microscopy

The investigations of the oxidation of Zircaloy cladding performed under contract with the Paul Scherrer Institute (PSI), as part of their programme with the Nuclear Fuel Industry Research group (NFIR), was continued throughout the reporting period and a second contract involving the investigation of nine more cladding samples has been confirmed by the PSI. A total of 17 cladding samples was examined for the PSI during the reporting period, using TEM, SEM and EDX. Two of these samples came from an additional experiment to test the effects of Li in the cooling water on the cladding corrosion.

Of particular interest is the continuing analysis of the composition and crystalline state of the intermetallic particles as a function of distance into the metal from the oxide-metal interface. This is an investigation which has never been performed previously by any group working on the corrosion of Zircaloy cladding.

10.9 Fabrication and Characterization of MOX Reference Pellets

On request of the IRMM at Geel (Belgium), 350 MOX reference samples in form of MOX pellets were fabricated and characterized by ITU. These samples are foreseen in future to serve as reference material for reliable and accurate analysis of light water reactor MOX fuel in the framework of quality control during their production and safeguards related activities. These samples will be further characterized in a European Certification process by IRMM for both elemental and isotopic composition.

In order to guarantee a perfect homogeneity both within and in between the samples the starting material was prepared by a sol-gel technique from one mother solution. All the material was blended before sample fabrication by pelletizing and sintering technique. The diameter of a pellet is 6.3 mm, the height 5.8 mm, the density 97% TD, the weight about 2 g and the Pu content 4.42 w/o with a Pu-239 content of 64.2%.

The material is single phased, with very sharp peaks of the X-ray pattern, and electron micro-probe analysis (EMPA) confirmed a perfect Pu distribution.

300 samples are ready for transport to Geel. During 1996 another 50 pellets will be fabricated and individually encapsulated at ITU for non-destructive measurements.

10.10 PHEBUS fp Project

The PHEBUS fp project is financed by the French atomic energy authority CEA, the European Commission as well as other non-EU countries such as USA, Canada, Japan and South Korea.

The first test involving the meltdown of trace-irradiated fuel rods took place in December 1994 and the examinations of the degraded bundle and final specimens are currently being completed.

ITU has received one slice of the FPTO bundle at the bottom of the melted zone for post-irradiation examination (PIE) and has also examined samples from the containment vessel (sedimentation coupons and impactor bead beds) as part of the Post Test Analysis (PTA) programme of samples from the simulated primary circuit and containment, in particular, from the vertical line located over the fuel bundle.

ITU has also completed non-destructive testing and destructive characterization on selective fuel rods of four lots of BR3 fuel rods that will be used for the PHEBUS tests. The fifth lot of 25 rods has arrived and will be similarly characterised by ITU for the final PHEBUS test in the course of the coming year.

Finally, ITU has also carried out specialised thermophysical measurements on the zirconia of the thermal shroud of the PHEBUS bundle (thermal capacity, diffusivity and thermal conductivity). ITU will also be involved in separate effects tests of fission product revaporisation from deposits of the PHEBUS FPTO test.

10.11 Tests of Acoustic Agglomeration of Flyash

A one week test on the acoustic agglomeration of flyash was carried out within the framework of a 'work for third parties' contract between the ITU and KEMA.

The 21 kHz sound source of ITU was mounted in the experimental loop constructed by KEMA at their pilot plant in Arnhem. The source remained in these industrial conditions (temperature at 150 - 200 °C) during one week without apparent failure. Aerosol characterization was performed, by KEMA personel, up and downstream of the acoustic module using cascade impactors. A number of agglomeration tests were made and the data are currently being evaluated.

11. Other Community Activities

Introduction

Apart from institutional support to the policy of the European Union, the Institute can participate in other Community activities. Examples are the European Commission's technical assistance programmes to the Eastern countries, like the PHARE and TACIS programmes, or R&D cooperation in the framework of the INTAS programme (International Association for the Promotion of Cooperation with Scientists from the Independent States of the Former Soviet Union).

Another important area is the cooperation with the International Science and Technology Center (ISTC) in Moscow. The objective of this cooperation is to provide support and cooperation to projects financed inter alia by the European Union and which are performed by scientists from sensitive military installations in order to avoid a 'brain drain'.

Below is a short summary of projects, in which ITU is actively involved.

11.1 Assistance to the Bulgarian Academy of Science in Performing Fuel Rod Thermo-Mechanical Simulations and Calculations for Improvements of the Kozloduy NPP Safety and Reliability

The reliable prediction of the fuel performance of the operating Kozloduy NPP Units with VVER-440 and VVER-1000 reactors is an important requirement both for the safety operation and for the computer aided safety analyses. In order to assist the Bulgarian Nuclear Regulatory Authority (i.e. Bulgarian Committee on the Use of Atomic Energy for Peaceful Purposes), the Institute for Nuclear Research and Nuclear Energy (INRNE) of the Bulgarian Academy of Science was requested to perform extensive investigations in the VVER fuel rod behaviour under steady state, transient and accident conditions. In this context the European Institute for Transuranium Elements (ITU) at Karlsruhe, which has proven experience in the field of fuel rod modelling has been requested by the Bulgarian Nuclear Regulatory Authority to assist and qualify INRNE in performing calculational tasks using its thermo-mechanical TRANSURANUS code.

In order to meet the demands for higher safety and the recommendations from international organizations which observe the operation and safety of the Kozloduy NPP and on behalf of the NPP Kozloduy, the INRNE has to perform an extensive investigation in the field of the VVER fuel rod behaviour modelling and its further application for the safe operation of the planned core reloadings including regimes with extended burn-ups.

ITU experts will assist INRNE staff in the following tasks:

- Review of the models and acquirement with the code systems for thermo-mechanical analysis TRANSURANUS and URANUS, and application for different benchmark tasks;
- Development and implementation of alternative mechanistic and empirical models, including Pellet Cladding Interaction (PCI), specific for the VVER fuel rod thermo-mechanical behaviour;
- Preparation of input data and validation of the models and code systems against VVER benchmarks and experimental data;
- Performance of calculations for core design specific loading - and reloading patterns for steady-state and transient operational conditions including regimes with extended burn-up;
- Methodology for evaluation of the failure limits of VVER fuel rods during steady-state and operational transient regimes;
- Application of statistical evaluation methods for fuel rod failure probability and fuel element quality assurance and quality control;
- Exchange of consultations concerning the existing official normative documents related to the PWR and VVER fuel rods and fuel elements.

The project with the acronym FERONIA (Fuel Rod Modelling and Performance) has been entrusted to ITU end of 1995 in the framework of the European Commission's PHARE programme.

11.2 Investigation of the Environmental Impact of Spent Nuclear Fuel and Core Debris of the Destroyed Chernobyl-4 Unit

The state of the core debris of the Chernobyl-4 Unit reactor is still to a great extent unknown. Large masses of lava and, more generally, of fuel containing materials, lie inside the concrete shelter - the so called 'sarcophagus' under rather precarious conditions. An effort is presently being made to determine their physical and chemical properties in view of predicting the hazards of possible further interactions with the environment, and devising preventive countermeasures. Furthermore, the analysis of the state of the various fuel containing materials will provide useful data for reconstructing the reactor accident scenario during the reactivity excursion which led to the catastrophe.

The Ukrainian Minister in charge of the follow up measures associated with the Chernobyl accident requested support in March 1994 for a better understanding of the mechanism and the environmental impact of the Chernobyl accident.

A work programme was defined in cooperation with the Interdisciplinary Scientific and Technical Center 'Shelter' in Chernobyl with emphasis on the aspects described below:

The work will be conducted on samples of fuel containing materials extracted from different premises of the destroyed reactor, as well as on spent nuclear fuel of a similar RBMK reactor.

The analysis is focused on distinct questions concerning the distribution of fission products and actinides:

- obtain information on the transuranium elements contained in the samples,
- measure release rates under laboratory conditions at different temperatures,
- reconstruct the behaviour of the fuel during the accident,
- verify the existing data of the nuclide vector of the 'Chernobyl release', including transuranium elements,
- obtain experimental information on the physical and chemical stability of the samples under different conditions,
- issue a joint publication on the results of this work for further analysis of the environmental impact of the accident.

The experimental work will be performed in three stages:

1. Establishment of present chemical and physical status of various samples
2. Thermochemical stability and release kinetics
3. Fuel dispersion measurements via air-borne particles

This project has been entrusted to ITU end of 1995 in the framework of the European Commission's TACIS programme.

11.3 Construction of the Equation of State of Uranium Dioxide up to the Critical Point

The project 'Construction of the Equation of State of Uranium Dioxide up to the Critical Point' was started in 1995 within the framework of INTAS (International Association for the Promotion of Cooperation with Scientists from the Independent States of the Former Soviet Union). The work is performed at the Institute (Project coordinator), at the High Energy Density Research Centre (HEDRC) of the Academy of Sciences, Moscow, (Russia), at the Physical Technical Institute (PTI) of the Academy of Sciences of Uzbekistan and at the Physics Department of the University Warwick in Coventry (United Kingdom). The objective of this project is to resume the work performed worldwide in this area and to formulate a general theory on the properties of uranium dioxide in the fluid and vapour phases at temperatures from the melting point up to the critical point. The HEDRC has examined the theoretical problem and has proposed a number of possible analytical approaches. In the HEDRC laboratory an experimental programme has been started aimed at measuring the vapour pressure up to the highest reachable temperatures. The radiative property measurements are carried out at PTI and will be used to define physical properties of the liquid uranium dioxide. A critical assessment of the pertinent thermodynamic and thermophysical properties is being developed at the University of Warwick.

11.4 Cooperation of ITU in Projects of the International Science and Technology Center (ISTC) in Moscow

In support of the policy of the European Union to prevent the proliferation of technologies and expertise related to weapons of mass destruction, the Institute is participating in reviewing proposals and as a direct collaborator in projects of the International Science and Technology Center in Moscow.

Based on its competencies, the Institute has chosen to participate essentially in projects related to the nuclear fuel cycle. Some examples are provided below:

- Studies of a fuel cycle with reactor burner of minor actinides
- Radiation characteristics of mixed oxide fuels
- Studies on removal of fission products and minor actinides from irradiated fuel
- Project development for civil and military in Pu utilization in fast and thermal reactors
- Measurements and analysis of the basic nuclear data for minor actinides
- Safe uranium and plutonium storage
- Radioactive and fissionable materials detection

12. Scientific Visitors

During the year 1995, the Institute has welcomed three new doctoral grantees from France and Italy and five new postdoctoral grantees originating from France, Germany, Greece, and Sweden.

The Institute hosted two visiting scientists from Belgium and Greece.

One doctoral grantee from the Institute has obtained his Ph.D. in 1995:

Steve Nicoll, "A computer simulation study of single atoms of Xe, Mo, Ru, Rh and Pd in UO_2" at the University of London.

Six "Stagiaires Visiteurs" came from France, Spain and Japan. They were supported by their organisation of origin. Two scientists from Russia stayed at the Institute in the frame of a collaboration with the High Energy Density Research Center of the Russian Academy of Science in Moscow.

13. Quality Management

In 1993 the decision was taken, to introduce quality management according to ISO 9001 at the Institute (TUAR-93, p. 231). To satisfy immediate demands from customers quality plans and corresponding procedures related to projects for external clients were drawn up in 1994 (TUAR-94, p. 218). The quality measures for post-irradiation examination were satisfactorily audited by the client.

To avoid multiplication of work in setting up quality plans for each customer related project, a quality management system for the whole Institute was built up in 1995. This system shall not only meet the requirements of external clients but also increase the competitivity of the Institute for third party work. As an internal effect the transparency of the Institute organisation and the traceability of weak points shall be improved, procedures will be layed down and consequently the staff motivation, the efficiency and the quality of the activities are expected to future increase.

The quality management system consists of the quality manual and a set of twenty procedures. The quality manual makes statements with respect to each of the twenty elements of ISO 9001 and their implementation in the Institute. The procedures describe the course of realisation of these statements, the responsibilities and the interfaces. If necessary, project specific processes are defined in project procedures.

After the introduction of the system and a test period during 1996 the certification of the quality management system in at least one area is planned for 1997.

Annexes

ANNEX I

Publications 1995

1. Conferences

Conference papers published in 1995 in journals or special conference proceedings volumes may appear also under paragraph 2 (Books and Periodicals)

European Winter Conference on Plasma Spectrochemistry
January 8-13,1995, Cambridge (GB)

Aizpun Fernandez, B., Garcia Alonso, J.I., Koch, L.
Determination of Actinides in Safeguards Environmental Samples by ICP-MS

Barrero Moreno, J.M., Arbore, Ph., Garcia Alonso, J.I., Koch, L.
Characterisation of Spent Nuclear Fuels by Ion Chromatography ICP-MS

Tagung der Deutschen Physikalischen Gesellschaft
March 21, 1995, Berlin (DE)

Koch, L., Schenkel, R., van Geel, J.
Analyse von sichergestelltem Kernmaterial

4. Workshop of the IUCc High Pressure Group on Synchrotron and Neutron Sources
March 22-24, 1995, Tsukuba (JP)

Benedict, U., Dufour, C., Heathman, S., Le Bihan, T., Staun Olsen, J., Gerward, L., Haire, R.G., Vohra, Y.K., Gu, G.
Diffraction Study of Actinides under Pressure
Proceedings High Pressure Research

9th Annual Conference of the Aerosol Society
April 4-6, 1995, Norwich (GB)

Somers, J., Capéran, Ph., Richter, K., Fourcaudot, S.
Acoustic Agglomeration of Titanium Dioxide in the Presence of Stationary Droplets as a Function of the Wave Energy

9. Camus-Treffen (Cameca Users Meeting)
April 5-7, 1995, Baden (CH)

Walker, C.T.
Activities of the ISO Technical Committee 202 on Microbeam Analysis: A Status Report
Proceedings of the Workshop

25. Journées des Actinides
April 7-11, 1995 Aquila (IT)

Amanowicz, M., Rebizant, J., Spirlet, J.C., Vogt, O.
Transport Properties of p-Monochalcogenides

Estrela, P., Goncalves, A.P., Godinho, M., Almeida, M., Spirlet, J.C.
Preparation and Single Crystal Characterisation of $UFe_{10}Mo_2$

Gomez Marin, E., Fournier, J.M., Spirlet, J.C., Wastin, F.
Equipment for High-Temperature Resistivity Measurements

Goncalves, A.P., Paixao, J.A., Amaro, A., Almeida, M., Spirlet, J.C.
Physical Properties of UFe_6Ge_6 Single Crystals

Hiess, A., Resouche, E., Sanchez, J.P., Zwirner, S., Rijkeboer, C., Bednarczyk, E., Wastin, F., Rebizant, J., Lander, G.H.
The Magnetic Structure of $NpBe_{13}$

Ichas, V., Braithwaite, D., Wastin, F., Rebizant, J., Spirlet, J.C., Benedict, U.
Electrical Resistance of NpAs under Pressure up to 27 GPa

Jeandey, C., Sanchez, J.P., Oddou, J.L., Rebizant, J., Wastin, F.
Physical Properties of $Np_4Ru_7Ge_6$ from a Mössbauer Study

Le Bihan, T., Heathman, S., Darracq, S., Abraham. C., Benedict, U., Winand, J.M., Spirlet, J.C.
Synchrotron X-ray Diffraction Study of UX_3 (X=Al,Ga,In,Si,Ge,Sn) at high Pressure

Paolasini, L., Lander, G.H., Shapiro, S., Caciuffo, R., Regnault, L.P., Lebech, B., Fournier, J.M.
Magnetic Response Function of UFe_2 Single Crystal

Pereira, L.C.J., Winand, J.M., Wastin, F., Rebizant, J., Spirlet, J.C.
Synthesis and Crystal Chemistry of Ternary Intermetallic Compounds An_2T_2X (An=Pu), Am X=In, Sn T=Co,Fe,Ir,Ni,Pd, Pt,Rh,Ru)

Pereira, L.C.J., Seret, A., Wastin, F., Hiess, A., Sanchez, J.P., Rebizant, J., Spirlet, J.C.
Electrical Resistivity and Magnetic Susceptibility Measurements on Np_2T_2X Compounds

Prokes, K., Nakotte, H., Havela, L., Sechovsky, V., Pereira, L.C.J., Rijkeboer, C., Seret, A., Spirlet, J.C., Svoboda, P., de Boer, F.R.
Magnetic Anisotropy of U_2PdIn

Wastin, F., Seret, A., Fearon, J., Bednarczyk, E., Rebizant, J.
Studies of $U_{1-x}Np_xPd_2Al_3$ and $U_{1-x}Pu_xPd_2Al_3$ Systems

Watson, G., Gibbs, Doon, Gaulin, B.D., Matzke, Hj., Ellis, W.P.
Magnetic X-ray Scattering on UO_2 Single Crystals

17th Symposium on Safeguards and Nuclear Material Management
May 9-11, 1995, Aachen (DE)

Aaldijk, J.K., Wichers, V.A., Nicolaou, G.
Non-Destructive Assay for Safeguards Purposes of Fuels Containing Minor Actinides
EUR 16290 - Proceedings 17th Annual Symp. 1995, pp. 455-458

Arenz, H., Dossogne, Ph., Kaiser, S., Paternoster, Y., Schenkel, R., Beaudoin, Ph., Molinari, P., Petit, P.
Safeguarding the Melox Fabrication Plant
EUR 16290 - Proceedings 17th Annual Symp. 1995, pp. 199-202

Betti, M., Jozefowicz, L.C., Giannarelli, S., Koch, L.
Liquid Scintillation Counting for the Detection of Nuclear Signatures
EUR 16290 - Proceedings 17th Annual Symp. 1995, pp. 475-479

Betti, M., Giannarelli, S., Lefèvre, O., Walker, C.T., Koch, L.
Detection of Nuclear Signatures in Soil and Sediment Samples
EUR 16290 - Proceedings 17th Annual Symp. 1995, pp. 481-485

Cromboom, O., Koch, L., Mayer, K., De Bievre, P., Ottmar, H., Matussek, P.
Evaluation of Quality Control Measurements - Methods, Experience and Impact
EUR 16290 - Proceedings 17th Annual Symp. 1995 pp. 505-508

Cromboom, O., Eberle, H., Ottmar, H., Schubert, A., Sena, F.
Qualification of Plutonium Assay Techniques for an On-site Laboratory
EUR 16290 - Proceedings 17th Annual Symp. 1995 pp. 271-279

Koch, L.
Identification of Nuclear Material of Unknown Origin
EUR 16290 - Proceedings 17th Annual Symp. 1995 pp. 195-198

Kühn, H., Wellum, R.
Optimisation of Information from the Total Evaporation. Method for Thermal Ionisation Mass-spectrometry
EUR 16290 - Proceedings 17th Annual Symp. 1995 pp. 389-393

Nicolaou, G., Koch, L.
Identification of Nuclear Material with Unknown Irradiation History: a Case Study
EUR 16290 - Proceedings 17th Annual Symp. 1995 pp. 733-736

Nicolaou, G., Abbas, K., Koch, L.
The Use of a CdTe Detector under Dry Conditions on Spent Fuel
EUR 16290 - Proceedings 17th Annual Symp. 1995 pp. 519-521

Schneider, H.G., Bartscher, W.
Quality Assurance System for the On-site Laboratory in Sellafield
EUR 16290 - Proceedings 17th Annual Symp. 1995, pp. 285-288

Schubert, A., Ottmar, H.
Empirical Determination of Pu-242 in Non-Destructive Assay -Where are the Limits?
EUR 16290 - Proceedings 17th Annual Symp. 1995 pp. 426-431

4th European Conference on Modem Developments and Application in Microbeam Analysis (EMAS-4)
May 14-18, 1995, St. Malo (FR)

Lefevre, O., Betti, M., Koch, L., Walker, C.T.
Microbeam Analysis of Soil and Grass Containing Radioactivity from the Nuclear Accident at Chernobyl
Proceedings Mikrochim. Acta

NATO Advanced Research Workshop on "Disposal of Ex-Weapons Plutonium as Waste"
May 14-23, 1995, St. Petersburg (USSR)

Matzke, Hj., van Geel, J.
Incorporation of Pu and other Actinides in Borosilicate Glass and in Waste Ceramics published in:
Proceedings in "Disposal of Weapon Plutonium" Walter Kluwer Academic Publishers (1995) p. 93-105, Editors: E.R. Merz, C.E. Walter

"Surface Canada 95" 15. Canadian Conference on Surface Science
May 25-27, 1995, Waterloo (CA)

Hocking, W.H., Miller, N.H., Lucuta, P.G., Verrall, R.A., Matzke, Hj.
Depth-Profiling Studies of Ion-Implanted Cesium and Rubidium in Uranium Dioxide

Surface X-Ray and Neutron Scattering Conference
June 22-26, 1995 Wisconsin (US)

Watson, G.M., Gibbs, Doon, Lander, G.H., Matzke, Hj., Gaulin, B.D., Berman, L.E., Ellis, W.
Grazing-Incidence X-ray Magnetic Scattering Studies of UO_2(001) Surfaces
Proceedings Physica B

IAEA Technical Committee Meeting on Recycling of Plutonium and Uranium in Water Reactor Fuel
July 3-7,1995, Windermere (GB)

Magill, J., Matzke, Hj., Nicolaou, G., Peerani, P., van Geel, J.
A Once Through Scheme for Weapons Grade Pu Disposition in LWR's: Proliferation and Criticality Aspects
Proceedings IAEA

Walker, C.T., Goll, W,, Matsumura, T.
MOX Fuel Irradiation Behaviour: Results from X-ray Microbeam Analysis
Proceedings IAEA

16th International Conference on Atomic Collisions in Solids (ICACS 16)
July 17-21, 1995, Linz (AT)

Turos, A., Falcone, R., Drigo, A., Sambo, A., Matzke, Hj.
Ion Channeling in Spinel Single Crystals

Annual Meeting of the American Crystallographic Association
July 23-28, 1995, Montreal (CA)

De Ridder, D.J.A.
The Geometry of U-Tris(Cyclopentadienyl-like)-X Compounds

Zuoz Summer School
August 21-25, 1995, Zuoz (CH)

Lander, G.H.
Magnetic Scattering by Neutrons and X-rays
Proceedings published by World Scientific

29. Colloqium Spectroscopicum Internationale (CSI-29)
August 27-September 2, 1995, Leipzig (DE)

Betti, M., Giannarelli, S., Hiernaut, T., Rasmussen, G., Koch, L.
Detection of Trace Radioisotopes in Environmental-Type Samples by Glow Discharge Mass Spectrometry
Proceedings Fresenius Z. Anal. Chem.

14. International Congress on X-ray Optics and Microanalysis
August 29-September 2, 1995, Guangzhou (China)

Walker, C.T.
Application of EPMA to the Problem of Fission Gas Release from Nuclear Fuel
Proceedings of the Conference

4th European Conference on Accelerators in Applied Research and Technology ECAART-4
August 29-September 2, 1995, Zürich (CH)

Turos, A., Matzke, Hj., Drigo, A., Sambo, A., Falcone, R.
Radiation Damage in Spinel Single Crystals
Nucl. Instrum. Methods in Phys. Research B

CSI Post-Symposium: GDS
Analytische Anwendung der optischen und Massenspektroskopie mit Glimmentladung
September 1-4, 1995, Dresden (DE)

Betti, M., Rasmussen, G., Koch, L.
Isotopic Abundance Measurements on Solid Nuclear-Type Samples by Glow Discharge Mass Spectrometry
Proceedings Fresenius Z. Anal. Chem.

5. International Conference on Radioactive Waste Management and Environmental Remediation (ICEM-5)
September 3-9, 1995, Berlin (DE)

Nicolaou, G., Koch, L.
Characterisation of Spent Nuclear Fuel by Non-Destructive Assay
Proceedings of the Conference

25. GDCh-Hauptversammlung
September 10-13, 1995, Münster (DE)

Koch, L.
Beseitigung radiotoxischer Abfälle der Kernenergiegewinnung durch nukleare Umwandlung

International Conference on Chemistry and Migration Behavior of Actinides and Fission Products in the Geospere (Migration 95)
September 10-15, 1995 St. Malo (FR)

Merli, L., Fuger, J.
Thermochemistry of Selected Lanthanide and Actinide Hydroxycarbonates and Carbonates
Proceedings Radiochimica Acta

8th International Conference on Radiation Effects in Insulators
September 11-15, 1995, Catania (IT)

Matzke, Hj.
Radiation Damage in Nuclear Fuel Materials: The "RIM" Effect in UO_2 and Damage in Inert Matrices for Transmutation of Actinides
Proceedings Nucl. Instrum. - Methods in Physics Research B

Global 1995 - International Conference on Evaluation of Emerging Nuclear Fuel Cycle Systems
September 11-14, 1995, Versailles (FR)

Apostolidis, C., Glatz, J.P., Molinet, R., Nicholl, A., Pagliosa, G., Römer, K., Bokelund, H., Koch, L.
Recovery of Minor Actinides from Irradiated Superfact Fuels
Proceedings ANS Topical Meeting, 1995 pp. 1207-1213

Babelot, J.F., Conrad, R., Franken, W.M.P., van Geel, J.Gruppelaar, H., Mühling, G., Prunier, C., Rome, M., Salvatores, M.
Target Development and Transmutation Experiments in the Frame of the EFTTRA European Collaboration
Proceedings ANS Topical Meeting, 1995 pp. 524-529

Babelot, J.F., Bokelund, H., Gerontopoulos, P., Gueugnon, J.F., Richter, K.
New Fabrication Techniques for the Nuclear Fuels of Tomorrow
Proceedings ANS Topical Meeting, 1995 pp. 1663-1666

Boucharat, N., Spirlet, J.C., Cocuaud, N., Fuger, J., Prunier, C.
Metallurgic Study of an Isotropic Structure Technetium Alloy
Proceedings ANS Topical Meeting, 1995 pp. 1675-1682

Casalta, S., Matzke, Hj., Prunier, C.
A Thermodynamic Properties Study of the Americium-Oxygen System
Proceedings ANS Topical Meeting, 1995 pp. 1667-1674

Casalta, S., Richter, K., Prunier, C.
A Study of AmO2-MgO System for Americium Target Transmutation in Fast Reactors
Proceedings ANS Topical Meeting, 1995 pp. 1725-1731

Chauvin, N., Faugere, J.L., Morin, C., Babelot, J.F.
In-Pile Research on Minor Actinide Burning
Proceedings ANS Topical Meeting, 1995 pp. 1691-1699

Glatz, J.P., Song, Ch.Li, Koch, L., Bokelund, H., He, X.M.
Hot Tests of the TRPO Process for the Removal of TRU Elements from HLLW
Proceedings ANS Topical Meeting, 1995 pp. 548-555

Gueugnon, J.F., Richter, K., Mühling, G., Plitz, H.
Design and Fabrication of Fuel Pins for the HFR Experiment TRABANT (Transmutation and Burning of Actinides in TRIOX)
Proceedings ANS Topical Meeting, 1995 pp. 1293-1299

Nicolaou, G., Glatz, J.P., Wellum, R., Koch, L.
Experimental Nuclear Data in Relation to Irradiation Experiments of Minor Actinides Targets in Fast Reactors
Proceedings ANS Topical Meeting, 1995 pp. 1655-1662

European Aerosol Conference
September 18-22, 1995, Helsinki (FI)

Capéran, Ph., Somers, J., Richter, K.
Acoustic Agglomeration of Redispersed Flyash
J. Aerosol. Sci. Vol. 26 Suppl 1 (1995) pp. S275-S276

Capéran, Ph., Somers, J., Richter, K., Fourcaudot, S.
Acoustic Agglomeration of Titanium Dioxide Aggregates as a Function of Acoustic Power
J. Aerosol Sci. Vol. 26 Suppl 1 (1995) pp. S277-278

Capéran, Ph., Somers, J., Richter, K.
On the Time Evolution of Inertia and Inertialess Particle Populations during Acoustic Agglomeration as a Function of Acoustic Power
J. Aerosol Sci. Vol. 26 Suppl. 1 (1995) pp. S925-S926

PSI Workshop on Advanced Fuel Cycles
September 18-19, 1995, Würenlingen (CH)

Koch, L.
International R&D Efforts on Actinide Transmutation
PSI Proceedings 95-01 (1995) 88-95

5. International Conference on Facility Operations - Safeguards Interface
September 24-29, 1995, Jackson Hole, WY (US)

Cromboom, O., Koch, L., van Geel, J., Mayer, K., De Bievre, P., Ottmar, H.
Comparison of DA and NDA Analytical Methods for PuO_2 in Nuclear Material Safeguards
Trans. Am. Nucl. Soc. Suppl. 1 to Vol. 72 (1995) 20-21

Kaiser, S., Paternoster, Y., Dossogne, Ph., Schenkel, R., Beaudoin, Ph., Molinari, P., Regnier, J., Petet, P.
Safeguards in the Melox MOX Fuel Fabrication Plant
Trans. Am. Nucl. Soc. Suppl. 1 to Vol. 72 (1995)

Ottmar, H., Schubert, A., Cromboom, O., Eberle, H.
Non-Destructive Assay of Small PuO_2 Samples by Neutron-Gamma Counting - Expectations and Achievements
Trans. Am. Nucl. Soc. Suppl. 1 to Vol. 72 (1995)

Strongly Correlated Electron Systems '95 (SCES'95)
September 27-30, 1995, Goa (IN)

Wastin, F., Zwirner, S., Seret, A., Waerenborgh, J.C., Pereira, L.C.J., Bednarczyk, E., Rebizant, J.
On the Influence of Transuranium Dilution in well known U Heavy Fermion Compounds
Proceedings Physica B

4. Conference and Exhibition of the European Ceramic Society
October 2-6, 1995, Riccione (IT)

Halton, D., Hiernaut, J.P., Sheindlin, M., Ronchi, C.
Advances in Laser Applications for High Temperature Thermophysical Measurements in Ceramics
Proceedings of the Conference, Elsevier Science Publishers

VIII. Amaldi Conference "Overcoming the Obstacles to Peace in the Post-Cold War Era" October 5-7, 1995, Piacenza (IT)

Koch, L.
Fingerprints of Nuclear Materials and how they can Reveal Origin and Intended Use
Proceedings of the Conference

40. annual conference on magnetism and magnetic materials (MMM-40)
November 6-9, 1995, Philadelphia (USA)

Prokes, K., Nakotte, H., de Boer F.R., Havela, L., Sechovsky, V., Swoboda, P., Winand, J.M., Rebizant, J., Spirlet, J.C., Hu, X., Gortenmulder, T.J.
Electronic properties of U_2Pt_2Sn
J. Appl. Phys. (in press)

Third International CAPRA Seminar
November 7-8, 1995, Lancaster (GB)

Richter, K.
Current Studies on Fabrication and Characterisation of CAPRA Fuel at ITU
Proceedings of the Conference

IAEA Technical Committee Meeting on Advanced Fuels with Reduced Actinide Generation
November 21-23, 1995, Vienna (AT)

Magill, J., Peerani, P., Matzke, Hj., van Geel, J.
A Strategy for Pu Destruction in PWR's
IAEA Proceedings of the Conference

11th French Annual Meeting on Aerosols
December 5-6, 1995, Paris (FR)

Capéran, Ph., Somers, J., Richter, K.
Interaction entre particules de différente taille lors de l'agglomération acoustique d'un brouillard

Tag der Seltenen Erden
December 7-8, 1995, Schönburg (DE)

v. Ammon, R., Apostolidis, C., Dornberger. E., Kanellakopulos, B., Müller, J., Nuber, B., Rebizant, J., Steuernagel, S.
1H- und 13C-NMR-Untersuchungen an Selten-Erd-Hydro-tris (1-pyrazolyl)boraten in Zusammenhang mit ihrer Molekülstruktur

Kanellakopulos, B., Apostolidis, C., Dornberger, E., Nuber, B., Maier, R., Powiezka, B.
Über das ungewöhnliche magnetische Verhalten einer Pr(III)metallorganischen Verbindung; Beobachtung eines Superspins

Maier, R., Apostolidis, C., Kanellakopulos, B., Müller, J., Powietzka, B.
Untersuchungen an 1:1 Addukten von Lanthaoid-tris (cyclopentadienyl)-Verbindungen mit 1,8-bis (dimethylamino)naphtalin (Proton Sponge)

2. Books and Periodicals

(including publications which had been submitted or presented at conferences in 1994 and which appeared in print in 1995)

Auluck, S., Brooks, M.S.S.
Pressure Dependence of Optical Gaps in Graphite
High Pressure Res. 13 (1995) 193-197

Bartscher, W.
Actinides-Hydrogen, Chapter 5 in Solid State Phenomena,
Vol. 49-50: Hydrogen Metal Systems I (Book contribution)
Editors: F.A. Lewis, A. Aladjem; Scitec Publications Ltd., Switzerland (1995) 159-238

Benedict, U.
Comparative Aspects of the High-pressure Behaviour of Lanthanide and Actinide Compounds
J. Alloys Comp. 223 (1995) 216-225

Bonfait, G., Goncalves, A., Spirlet, J.C., Almeida, M.
High Field Magnetoresistance of UFe4Al8
Physica B 211 (1995) 139-141

Brooks, M.S.S.
Band Structure Calculations for f-Electron Systems
Physica B 206 & 207 (1995) 1-7

Brooks, M.S.S., Eriksson, O., Johansson, B.
From the Transition Metals to the Rare Earths - Via the Actinides
J. Alloys Comp. 223 (1995) 204-210

Capéran, Ph., Somers, J., Richter, K., Fourcaudot, S.
Acoustic Agglomeration of a Glycol Fog Aerosol: Influence of Particle Concentration and Intensity of the Sound Field at two Frequencies
J. Aerosol Sci. 26 (1995) 595-612

Cottenier, S., Toye, A., Rots, M., Spirlet, J.C., Winand, J.M.
Perturbed Angular Correlation Study of the Pseudo-Binary System U(IN1-xSnx)3
Physica B 206 & 207 (1995) 492-494

De Ridder, D.J.A.
Comparison of the Frequencies of Crystallographic Space Groups in Organo-Lanthanide and -Actinide Compounds
J. Alloys Comp. 223 (1995) 280-287

Estrela, P., Godinho, M., Concalves, A.P., Almeida, M., Spirlet, J.C.
Magnetic Properties of $UFe_{10}Si_2$ Single Crystal
J. Alloys Comp. 230 (1995) 35-41

Evron, R., Cohen, Y., Eyal, Y., Matzke, Hj., Tinschert, K.
Ion-irradiation Induced Microstructural Damage in the Nuclear Waste Glass GP 98/12
Gesellschaft für Schwerionenforschung (GSI), Scientific Report 1994 94-1 (1995) 195

Fischer, E.O., Apostolidis, C., Dornberger, E., Filippou, A.C., Kanellakopulos, B., Lungwitz, B., Müller, J., Powietzka, B., Rebizant, J., Woth, W.
Carben- und Carbin-Komplexe des Technetiums und Rhenium - Synthese, Struktur und Reaktionen
Z. Nat.forsch. 50b (1995) 1382-1395

Fukushima, T., Matsuyama, S., Kumada, T., Kindo, K., Prokes, K., Nakotte, H., de Boer, F., Havela, L., Sechovsky, V., Winand, J.M., Rebizant, J., Spirlet, J.C.
High-field Magnetization Studies of some U_2T_2X Compounds
Physica B 211 (1995) 142-144

Garcia Alonso, J.I., Sena, F., Arbore, Ph., Betti, M., Koch, L.
Determination of Fission Products and Actinides in Spent Nuclear Fuels by Isotope Dilution Ion Chromatography Inductively Coupled Plasma Mass Spectrometry
J. Anal. At. Spectrom. 10 (1995) 381-393

Gasche, T., Brooks, M.S.S., Johansson, B.
Ground State Properties of Ternary Uranium Compounds. II: Magnetic Properties
J. Phys. Condens. Matter 7 (1995) 9511

Gasche, T., Brooks, M.S.S., Johansson, B.
Ground-State Properties of Ternary Uranium Compounds. I: Hybridization Effects
J. Phys. Condens. Matter 7 (1995) 9499-9510

Gasche, T., Brooks, M.S.S., Johansson, B.
The Kerr Effect from first Principles Theory: Application to HCP/FCC Cobalt
J. Magn. Soc. Jpn. 19 Suppl No S1 (1995) 303-308

Godinho, M., Bonfait, G., Goncalves, A.P., Almeida, M., Spirlet, J.C.
Magnetic Properties of a UFe_4Al_8 Single Crystal
J. Magn. Magn. Mater. 140-144 (1995) 1417-1418

Goncalves, A.P., Bonfait, G., Almeida, M., Estrela, P., Godinho, M., Spirlet, J.C.
Structural and Magnetic Properties of UFexM12-x(M=Al,Mo and Si)
J. Magn. Magn. Mater. 140-144 (1995) 1419-1420

Goncalves, A.P., Estrela, P., Waerenborgh, J.C., Godinho, M. Almeida, M., Spirlet, J.C.
Structural and Physical Properties of $UFe_{10}Mo_2$
J. Alloys Comp. 218 (1995) 183-189

Gouder, T.H., Colmenares C.A.
A surface spectroscopic study of thin layers of U on polycrystalline Pt
Surf. Sci. 341 (1995) 51-62

Gouder, T.H., Colmenares C.A., Naegele, J.R.
A surface spectroscopy study of U overlayers on graphite
Surf. Sci. 342 (1995) 299-306

Havela, L., Sechovsky, V., Svoboda, P., Nakotte, H., Prokes, K., de Boer, F.R., Seret, A., Winand, J.M., Rebizant, J., Spirlet, J.C. et al.
Magnetism in U_2T_2X Compounds
J. Magn. Magn. Mater. 140-144 (1995) 1367-1368

Heathman, S., Le Bihan, T., Darracq, S., Abraham, C., De Ridder, D.J.A., Benedict, U., Mattenberger, K., Vogt, O.
High Pressure Behaviour of TmTe and EuO
J. Alloys Comp. 230 (1995) 89-93

Hiess, A., Boucherle, J.X., Givord, F., Canfield, P.C.
Magnetic Susceptibility and Magnetization Measurements of an $YbAl_3$ Single Crystal for Groundstate Investigations
J. Alloys Comp. 224 (1995) 33-35

Joachim, J.E., Apostolidis, C., Kanellakopulos, B., Meyer, D., Nuber, B., Raptis, K., Rebizant, J., Ziegler, M.
Metallorganische Chemie des Technetiums: Photolytische CO-Substitutionsrekationen von Technetiumtricarbonylverbindungen
J. Organomet. Chem. 492 (1995) 199-210

Kindo, K., Fukushima, T., Kumada, T., de Boer, F.R., Nakotte, N., Prokes, K., Havela, L., Sechovsky, V., Seret, A., Winand, J.M., Spirlet, J.C., Rebizant, J.
Electronic Properties of U_2Ni_2Sn
J. Magn. Magn. Mater. 140-144 (1995) 1369-1370

Koch, L.
Nuklearer Fingerabdruck von Kernbrennstoffen. Methoden zur Identifizierung von Herstellung und Anwendung
Strahlenschutz Praxis 1 No. 1 (1995) 31-33

Koch, L.
Identifizierung von unbekanntem nuklearem Material
Spektrum Wiss. 3/95 (1995) 118-120

Lander, G.H., Burlet, P.
On the Magnetic Structure of Actinide Monopnictides
Physica B 215 (1995) 7-21

Lassmann, K., Walker, C.T., van de Laar, J., Lindström, F.
Modelling the High Burnup UO_2 Structure in LWR Fuel
J. Nucl. Mater. 226 (1995) 1-8

Le Bihan, T., Darracq, S., Heathman, S., Benedict, U., Mattenberger, K., Vogt, O.
Phase Transformation of the Monochalcogenides SmX (X = S, Se, Te) under High Pressure
J. Alloys Comp. 226 (1995) 143-145

Matzke, Hj.
Nuclear Techniques for Analyses of Advanced Materials: Rutherford Backscattering, Channeling, Resonance Scattering, Nuclear Reactions and Elastic Recoil Detection
Materials Challenge 7 (May 1995) 25

Matzke, Hj.
The RIM-Effect in High Burnup UO_2 Nuclear Fuel
Advances in Sci. and Technol. 3D, Techna Srl. 1995 2913-2920

Nicoll, S., Matzke, Hj., Catlow, C.R.A.
A Computational Study of the Effect of Xe Concentration on the Behaviour of Single Xe Atoms in UO_2
J. Nucl. Mater. 226 (1995) 51-57

Nuttall, W.J., Langridge, S., Stirling, W.G., Lander, G.H., Lebech, B., Vogt, O.
Resonant X-ray and Neutron Diffraction Study of $USb_{0.8}Te_{0.2}$
Phys. Rev. B Condens. Matter 52 (1995) 4409-4419

Paolasini, L., Caciuffo, R., Lander, G., Rebizant, J., Keen, D., Sato, N., Komatsubara, T.
Anomalies in the Normal-state Properties of UPd_2Al_3
J. Phys. Chem. Solids 56 (1995) 1323-1329

Pippin, C.G., Gansow, O.A., Brechbiel, M.W., Koch, L., Molinet, R., van Geel, J., Apostolidis, C., Geerlings, M.W., Scheinberg, D.A.
Recovery of Bi-213 from an Ac-225 Cow: Application to the Radiolabeling of Antibodies with Bi-213
Chemist's Views of Imaging Centers, Ed. A.M. Emran Plenum Press (1995) 315-322

Scaffidi, F., Dalle Donne, M., Ferrero, C., Ronchi, C.
Helium Induced Swelling and Tritium Trapping Mechanisms in Irradiated Beryllium: A Comprehensive Approach
Nucl. Eng. Des. 27 (1995) 275-282

Severin, L., Brooks, M.S.S., Johansson, B., Kübler, J.
Calculated Magnetic Properties of Uranium Sulphide under Pressure
J. Magn. Magn. Mater. 140-144 (1995) 1423-1424

Trygg, J., Wills, J.M., Brooks, M.S.S., Johansson, B., Eriksson, O.
Calculation of Elastic Constants in UC, US and UTe
Phys. Rev. B Condens. Matter 52 (1995) 2496-2503

Walker, C.T., Nicolaou, G.
Transmutation of Neptunium and Americium an a Fast Neutron Flux: EPMA Results and KORIGEN Predictions for the Superfact Fuels
J. Nucl. Mater. 218 (1995) 129-138

3. Reports

Gueugnon, J.F., Richter, K.
Project CAPRA - Fabrication of 2 Fuel Pins TRABANT-1 for Irradiation in the HFR/Petten K0295184 (1995)

Nicoll, S., Matzke, Hj.
A Computer Simulation Study of Single Atoms of Xe, Mo, Ru, Rh and Pd in UO_2
K0295183 (1995)

Schenkel, R., Richter, J., Pel, D., Wellum, R. (eds.)
Annual Report 1994 - Institute for Transuranium Elements
EUR 16152 EN (1995)

Syros, C., Ronchi, C.
Advances in Nuclear Physics - Proceedings of the 5th Symposium of Nuclear Physics, 6 and 7 May 1994, Patras
EUR 16302 EN (1995)

4. Patents

a) Patents granted in 1995

Heinz W.
A device for the optical recording of rapid processes with a TV camera
Patent Nr.: 62698, Granting date: 22.02.95, Country: Ireland (IE)

Hiernaut J.P., Werner P.
A method and a device for manufacturing a powder of amorphous ceramic or metallic particles
Patent Nr.: 63224, Granting date: 05.04.95, Country: Ireland (IE)

Magill J., Werner P.
Verfahren zur Dekontaminierung grosser Bodenflächen
Patent Nr.: 88366, Granting date: 01.02.95, Country Luxembourg (LU)

Magill J., Werner P.
Maschine zur Abscheidung von Aerosolteilchen
Patent Nr.: 88387, Granting date: 01.02.95, Country Luxembourg (LU)

Richter K., Magill J., Somers J.
Verfahren zur Entfernung von fein verteilten Stoffen aus einem Gasstrom
Patent Nr.: 88411, Granting date: 05.04.95, Country: Luxembourg (LU)

Ronchi, C., Hiernaut J.P., Beukers R., Heinz W., Selfslag R.
A multiwavelengths pyrometer
Patent Nr.: 64270, Granting date: 26.07.95, Country: Ireland (IE)

van Geel J., Fuger J., Koch L.
A method for producing actinium-225 and bismuth-213
Patent Nr.: 64254, Granting date: 26.07.95, Country: Ireland (IE)

van Geel J., Werner P., Hiernaut J.P., Magill J.
A device for the manufacture of amorphous ceramics materials or metal alloys
Vorrichtung zum Herstellen amorpher Keramikstoffe oder Metallegierungen
Patent Nr.: 64512, Granting date: 21.07.95, Country: Ireland (IE)
Patent Nr.: 2031169, Granting date: 20.03.95, Country: Russia (RU/WO)

b) Patent applications in 1995

Koch L., Babelot J.-F., Niemax K., Hiddemann L.
Fernmessung von U (Pu) in Gläsern
Deposition Nr.: 19531988.5, Deposition date: 30.08.95, Country DE

Koch L., Fuger J., van Geel J.
Verfahren zur Erzeugung von Actinium-225
Deposition Nr.: 88636, Deposition date: 03.07.95, Country LU

Koch L., Fuger J., van Geel J.
Verfahren zur Erzeugung von Actinium-225 und Wismut-213 durch Bestrahlung von Radium-226 mit hochenergetischen Gammanquanten
Deposition Nr. 88637, Deposition date: 03.07.95, Country LU

Magill, J., Matzke Hj., Nicolaou G., Peerani P., van Geel J.
A method for the destruction of plutonium by irradiation in a light water reactor
Deposition Nr.: 95110397.7, Deposition date: 04.07.95, Country EP

Matzke, Hj., Kinoshita M.
Modifizierter Brennstoff
Deposition Nr.: 88668, Deposition date: 05.10.95, Country LU

c) Patent proposals in 1995

Somers J., Capéran P., Richter K., Olsson M., Sandström R.
Particle agglomeration and separation using low frequency sound waves
PP 2478 (20.03.95)

van Geel, J., Capéran P., Somers J., Fortov V., Vetchinin S.
Scavenging of industrial aerosols using electrical discharge induced shock waves
PP 2472 (20.02.95)

Annex II

Collaborations with External Organizations

ARGENTINA

CNEA Buenos Aires: Diffusion in solids (F. Dyment)

AUSTRIA

International Atomic Energy Agency (IAEA), Vienna: Evaluation and automation of techniques for safeguards analysis (K. Lessmon); *Safeguards Directorate:* Environmental analysis (K. Serena); SAL: EURATOM Support Programme (S. Deron)

Technical University of Vienna: resistivity of alloys (E. Gratz)

BELGIUM

Société Belge pour l'Industrie Nucléaire, Brussels: Post irradiation examinations (S. Pilate, M. van den Borck, M. Lippens, J. Basselier, D. Haas)

University of Leuven: Xe-implantation (H. Pattyn)

University of Liège: Single crystal growth, X-ray diffraction, and analysis (J.F. Desreux, L. Martinot, M.R. Spirlet)

BULGARIA

Insitute of Nuclear Research and Nuclear Energy, Bulgarian Academy of Science, Sofia: Fuel rod modelling and performance, FERONIA (S. Stefanova)

CANADA

AECL
Chalk River: Gas release, SIMFUEL production and property studies (I. Hastings, P. Lucuta, R. Verrall);
Whiteshell: Behaviour of Rb and Cs in SIMFUEL (W. Hocking)

McMaster University, Hamilton: Synchrotron X-ray scattering (B. Gaulin)

CZECH REPUBLIC

University of Prague: Magnetic and electrical measurements (V. Sechovsky, L. Havela); Gas release measurements (V. Balek)

DENMARK

Risø National Laboratory: Neutron scattering (B. Lebech)

Technical University Lyngby: High-pressure X-ray diffraction (L. Gerward)

University of Copenhagen: High pressure X-ray diffraction (J. Staun-Olsen)

FRANCE

Commissariat à l'Énergie Atomique (CEA)
CEA, Cadarache: Transmutation of actinides - irradiation experiments: DEC (J.L. Faugère, R. Ginier, Y. Guerin, C. Prunier, D. Warin); DER (A. Lanquille, J. Rouault); DRN (M. Salvatores); TRANSURANUS fuel pin development (J.P. Pages); PHEBUS PF programme, (B. Adroguer): post irradiation examinations (L. Codron, P. von der Hardt)
CEN, Grenoble: Neutron diffraction, magnetic studies, transport properties and Mössbauer studies (P. Burlet, J.P. Sanchez, B. Fåk, D. Braithwaite and F. Bourdarot)
CEN, Saclay: Neutron diffraction (J.M. Mignot); Post-irradiation examinations (J.I. Blanc, F. Couvreur)

CERCA, Romans: MTR fuel development (J.P. Durand, B. Lelievre)

CNRS
Lab. de Cristallographie, Grenoble: Crystallography of phase transitions (J.C. Marmeggi)
Orsay: Basic studies on spent UO_2 fuel (J.C. Dran)

COGEMA
La Hague: On-site laboratory
Branche Combustible Nucléaire, Vélizy: Development of MOX fuels (Mme M. Trotabas)

Électricité de France (EDF)

Septen, Lyon: Transmutation of actinides (M. Rome, D. Deydier), Paris: TRANSURANUS fuel pin code development (B. Salles); RIM effect (M. Baron); Chemical and mechanical interactions fuel/cladding (thermal reactor) and determination of mechanical properties of irradiated UO_2 (M. Baron)

ESRF, Grenoble: Synchrotron studies on actinides (C. Vettier, G. Grübel, M. Wulff)

FRAMATOME, Paris: TRANSURANUS fuel pin code development; Post-irradiation examinations (P. Blanpain)

ILL, Grenoble: Polarized neutron diffraction and neutron inelastic scattering (P.J. Brown, C. Zeyen)

University of Grenoble: Transport measurements (J.M. Fournier)

University of Nantes: (-immunotherapy by Bi-213 (J. F. Chatal)

GERMANY

Apparatebau Rothemühle, Wenden: Acoustic aerosol scavenging (W. Niggeschmidt, N. Seyfert)

Gesellschaft für Schwerionenforschung (GSI) Darmstadt: High energy ion implantation (C. Trautmann, J. Vetter)

Hahn-Meitner-Institut (HMI), Berlin: Ranges of ions in solids, B-profiles in leached glasses (D. Fink, J. Biersack); High-energy ion implantation (S. Klaumünzer)

Forschungzentrum Jülich GmbH (KFA)
Institut für Festkörperforschung: Electrical resistivity under pressure (J. Wittig)

Forschungszentrum Karlsruhe (FZK)
Institut für Kernphysik (IK-III): On-site laboratory training; K-edge densitometry (H. Ottmar, H. Eberle)
Institut für Neutronenphysik und Reaktortechnik (INR): Neutron collar development; Beryllium blanket modelling: ANFIBE-FUTURE (M. Dalle Donne)
Institut für Nukleare Festkörperphysik (INFP): Radiation damage studies, RBS analyses, channeling, ion implantation (O. Meyer, G. Linker)
Institut für Technische Chemie (ITC): Susceptibility and crystal preparation (B. Kanellakopulos)
Projekt Nukleare Sicherheitsforschung (PSF): Irradiation experiment CAPRA-TRABANT (G. Heusener, G. Mühling)

Max-Planck Research Group 'Theory of Complex and Correlated Systems', Dresden:
Theory of the Kerr-effect (P.M. Oppeneer)

Siemens/KWU, Erlangen: Post-irradiation fuel rod examination (R. Manzel)

Technischer Überwachungsverein Bayern, München: TRANSURANUS fuel pin code development (G. Sauer)

Technischer Überwachungsverein Hannover/Sachsen-Anhalt: TRANSURANUS fuel pin code development (D. Märtens)

Technischer Überwachungsverein Norddeutschland, Hamburg: TRANSURANUS fuel pin code development (H. Schmidt)

Technischer Überwachungsverein Südwest, Mannheim, Karlsruhe: TRANSURANUS fuel pin code development (I. Brestrich)

Technische Universität München: Mössbauer and μSR studies (M. Kalvius, W. Potzel, L. Asch)

Universität Stuttgart, IKE: Source term studies (H. Hocke);

VGB-Forschungsstiftung, Essen: Flue gas cleaning (J.P. Jacobs, H. Krüger)

GRECE

University of Patras: Mathematical methods for special diffusion equations (C. Syros)

ISRAEL

Technion, Haifa: Waste glass studies (Y. Eyal)

ITALY

Centro Ceramico Bologna: Leaching studies, Indentation techniques (L. Esposito)

Centro Legnaro/Padova: RBS, Ion implantation, H-analysis on leached waste matrices (G. Della Mea, V. Rigato)

University of Padova: Analysis of glass surfaces (P. Mazzoldi)

University of Trento: Indentation techniques (R. DalMaschio)

University of Ancona: Neutron and bulk magnetization studies (R. Caciuffo);

University of Aquila, Physics Department: Theory of optical properties (P. Monachesi)

JAPAN

Central Research Institute of Electricity Producing Industries (CRIEPI), Tokyo: Preparation and characterization of minor actinide alloys (T. Inoue); Dissolution studies on high burn-up fuel (T. Ohe); Spent fuel characterization (S. Matsumura)

JAERI, Tokai Mura: Basic studies on nitride fuels (T.Ohmichi); DIDPA actinide separation process (Y. Morita); Gas release from oxide fuels (T. Ogawa)

THE NETHERLANDS

Alpha medical, St. Marten: Separation of alpha-emitting nuclides (M. Geerlings)

ECN, Petten: Transmutation of fission products (W. Franken, M. Gruppelaar)

Interfaculty Reactor Institute, Delft: Gas release (A. van Veen)

KEMA, Arnhem: Flue gas cleaning (R. Hunik, R. Tanke)

University of Amsterdam: Low temperature magnetization and resistivity (F. R. de Boer, J. Franse, E. Brück)

POLAND

Institute for Low Temperature and Structure Research, Warsaw: Bulk properties and neutron scattering (R. Troc, W. Suski)

Nuclear Institute, Warsaw: Channeling techniques, Radiation damage studies (A. Turos)

PORTUGAL

LNETI, Sacavem: Physical chemistry of actinides (A. Piros de Matos, M. Almeida)

University of Aveiro, Department of Physics: Kerr effect theory (T. Gasche)

University of Coimbra: Neutron and X-ray studies (J.A. Paixão)

RUSSIA

Academy of Sciences, IVTAN, Moscow: Equation of state of irradiated fuel (I. Iosiliewski); Studies on high-melting materials (A.E. Sheindlin)

Nuclear Power Plant, Leningrad: PIE, non destructive examinations (V.C. Shevchenko)

Radium Khlopin Institute, St.Petersburg: Field testing of a robotized system for safeguards analysis (N. Shulyak)

SPAIN

CIEMAT, Madrid: TRANSURANUS fuel pin code development (J. Lopez Jimenez)

ENRESA: Waste management, leaching tests (J.A. Esteban-Hernandez)

Instituto de Acústica, Madrid: Acoustic aerosol scavenging (J.A. Gallego-Juarez)

SWEDEN

University of Uppsala: Solid state theory of actinides (B. Johansson, O. Eriksson)
Infrasonik AB, Årsta: manufacture of infraphones (M. Olsson)

SWITZERLAND

ETH, Zürich: Single crystal growth, magnetic, optical and transport properties, preparation of U and Th compounds (O. Vogt, P. Wachter, K. Mattenberger)

Paul-Scherrer-Institut, Würenlingen: TRANSURANUS fuel pin code application (C. Ott); Post-irradiation structural investigations by electron microscopy

UKRAINE

Shelter Center Chernobyl: Analysis of the Unit IV Sarcophagus (E.M. Pazukhin)
University of Odessa: Liquid state models (E. Yakub)

UNITED KINGDOM

Birkbeck College: neutron and magnetization studies (K. McEwen)

BNFL, Sellafield: On-site laboratory (R. Strong, J. Reed)

Royal Institute, London: Calculation of fission products in UO_2

University of Liverpool: X-ray and neutron scattering (W.G. Stirling)

University of Warwick: Compton scattering (M.J. Cooper); Equation of state of irradiated fuel (G. Hyland); Radiative properties at high temperatures (G. Hyland)

UNITED STATES OF AMERICA

Argonne National Laboratory: Neutron scattering and X-ray arbsorption spectroscopy (L. Soderholm, S. Kern)

Battelle Pacific Nothwest Laboratories, Richland: Modelling, transfer of the TRANSURANUS burnup model 'tubrnp' (D.D. Lanning)

Brookhaven National Laboratory: High-resolution and magnetic X-ray scattering (D. Gibbs, J. Axe, G. Watson)

Lawrence Livermore National Laboratory: Forensic nuclear analysis (S. Niemeyer)

Los Alamos National Laboratory: Materials preparation and photoemission (B. Cort, A.J. Arko); Radiation damage in ceramics (K. Sickafus)

Memorial Sloan Kettering Cancer Center, New York: (-immunotherapy by Bi-213 (D.A. Scheinberg)

National Institute of Health, Bethesda: (-immunotherapy by Bi-213 (Dr. O.A. Gansow)

Oak Ridge National Laboratory: Material preparation, high pressure X-ray and optical studies (R.G. Haire, J.R. Peterson)

University of New Mexico, Albuquerque: High resolution TEM, radiation damage (R. Ewing, L.M. Wang)

University of W. Virginia, Morgantown, W.- Virginia: Actinide theory (B.R. Cooper)

UZBEKISTAN

Physical Technical Institute, Tashkent: Radiative properties of UO_2 at high temperatures (T. Salikhov)

Annex III

Human Resources

1. Institute's Staff

The evolution of the staff situation in 1995 is given for three reference dates on the table below:

Date	A2-A4	A5-A8	B	C	D	total
01.01.95	20	26	85	63	1	195
01.07.95	20	26	86	63	1	196
31.12.95	19	26	85	62	1	193

2. Visiting Scientists and Scientific Fellows

33 graduate sectorial grantees from the following countries spent in 1995 prolonged periods of time at the Institute:

B	(3)	IR	(2)
D	(3)	NL	(2)
ES	(5)	P	(2)
F	(7)	S	(1)
GR	(2)	UK	(2)
I	(4)		

Annex IV

Organizational Chart

Institute Director	Jacques VAN GEEL
Adviser, acting as Institute Deputy Director	Jean FUGER
Adviser (Programmes)	Roland SCHENKEL
Personnel and Administration	Paul BLAES (until 30.11.95) Gérard SAMSEL (since 01.12.95)
S/T Services:	
- Technical Physics	Michel COQUERELLE
- Applied Physics	Hansjoachim MATZKE
- Nuclear Technology	Karl RICHTER
- Nuclear Chemistry	Lothar KOCH
- Actinide Research	Ulrich BENEDICT (until 31.01.95) Gerard LANDER (acting, since 01.02.95)
S/T-Support:	
- Radiation Protection	Klaas BUIJS
- Technical Services	Gérard SAMSEL

Annex V

Glossary of Acronyms and Abbreviations

AC: Alternating Current
AEA: Atomic Energy Authority (United Kingdom)
AECL: Atomic Energy of Canada Ltd.
ALI: Annual Limits of Intake
amu: atomic mass unit
ANOVA: ANalysis Of VAriance
ANTICORP: Technetium transmutation experiment in Phénix (USA)
ARTINA: Analysis of Radioisotope Traces for the Identification of Nuclear Activity
ATWS: Anticipated Transient Without Scram

BET: Brunauer, Emmett, Teller technique to determine the surface area
BIBLIS: PWR reactor, Biblis/Rhein (Germany)
BNFL: British Nuclear Fuel plc, Springfields (United Kingdom)
BWR: Boiling Water Reactor

C++: Programming Language
CANDU: CANadian Deuterium Uranium reactor
CAPRA: Consommation Accrue de Plutonium dans les Rapides
CCAM: Commission Consultative des Achats et des Marchés, European Commission
CCD: Charged Coupled Device
CEA: Commissariat à l'Énergie Atomique, France
CEN: Centre d'Etudes Nucléaires (Mol, Belgium or Grenoble, France)
CERCA: Compagnie pour l'Étude de la Réalisation de Combustibles Atomiques, Romans (France)
CKED: Compact K-Edge Densitometer
CLC: Charge Loss Corrector
CMD: Count Median Diameter
CNEA: Comision Nacional de Energia Atomica
COGEMA: COmpagnie GEnérale des Matériaux nucléaires, Vélizy (France)
COMPUCEA: COMbined Product-Uranium Concentration and Enrichment Assay
CRIEPI: Central Research Instititute of the Electric Power Company, Tokyo (Japan)
CSA: Cost Shared Action
CV: Coefficient of Variation
CV: Cyclovoltammetry
CW: Continuous Wave

DA: Destructive Assay
DCS: Division Contrôle de Sécurité
DESY: Deutsches Elektronen-Synchrotron, Hamburg (Germany)
DF: Decontamination Factor
DG I: Directorate-General I "Internal Economic Relations" of the European Commission
DG XIII: Directorate-General I "Telecommunication, Information, Market and Exploitation of Research" of the European Commission
DG XVII: Directorate-General "Energy" of the European Commission, Brussels (Belgium), Luxembourg (Luxembourg)
DIDPA: DisoDecylPhosphoric Acid
DIW: DeIonized Water
DTA: Differential Thermal Analysis
DTPA: DiethyleneTriaminoPentaAcetate
DWR: DruckWasser Reaktor

EBR-2: Experimental Breeder Reactor
ECN: Energie Centrum Nederland, Petten (Netherlands)
ECSAM: European Commission's Safeguards Analytical Measurements
EDF: Électricité de France
EDX: Energy-Dispersive X-ray analysis
EDXD: Energy-Dispersive X-ray Diffraction

EFTTRA: Experimental Feasibility of Targets and Transmutation
EFPD: Effective Full Power Days
EMPA: Electron Micro-Probe Analysis (also EPMA)
ENSA: Spanish fuel fabrication plant, Juzbado (Spain)
EOS: Equation Of State
EPMA: Electron Probe Micro-Analysis (also EMPA)
EPRI: Electric Power Research Institute
ERDA: Elastic Recoil Detection Analysis
ESARDA: European SAfeguard Research and Development Association, Rome (Italy)
ESD: European Safeguards Directorate
ESRF: European Synchrotron Research Facility
EFTTRA: Experimental Feasibility of Targets for TRAnsmutation
EURATOM: EURopean ATOMic energy community

FERONIA: fuel rod modelling and performance project
FP: Fission Products
FORTRAN: FORmula TRANslator, Programming Language
FRA: Frequency Response Analyser
FZK: ForschungsZentrum Karlsruhe (Germany)

GDMS: Glow Discharge Mass Spectrometry (Spectrometer)
GSI: Gesellschaft für Schwerlonenforschung, Darmstadt (Germany)
GSP: Gel Supported Precipitation

HALW: Highly Active Liquid Waste
HAW: Highly Active Waste
HBC: High Burn-up Chemistry
HEDRC: High Energy Density Research Centre, Academy of Sciences, Moscow (Russia)
HF: High Frequency
HFR: High Flux Reactor, Petten (Netherlands)
HLW: High Level Waste
HLLW: High Level Liquid Waste
HMI: Hahn Meitner Institut, Berlin (Germany)
HPGe: High Purity low energy Germanium detector
HPLC: High-Pressure Liquid Chromatography
HPXRD: High-Pressure X-Ray Diffraction
HRGS: High Resolution Gamma-Spectrometry
HRTEM: High Resolution Transmission Electron Microscopy

IAEA: International Atomic Energy Agency, Vienna (Austria)
IASSC: Iodine Assisted Stress Corrosion Cracking
IC: Isotopic Correlation
IC-ICP-MS-IDA: Ion Chromatography Inductively Coupled-Plasma Mass Spectrometry Isotopic Dilution Analysis
ICP-AES: Inductively Coupled Plasma Atomic Emission Spectroscopy
ICP-MS: Inductively Coupled Plasma Mass Spectrometry
ICRP: International Commission on Radiological Protection
ICT: Isotope Correlation Techniques
IDA: Isotope Dilution Analysis
ID-ICP-MS: Isotope Dilution ICP-MS
IDMS: Isotope Dilution Mass Spectrometry
ILL: Institut Max von Laue - Paul Langevin, Grenoble (France)
INFP: Institut für Nukleare FestkörperPhysik, FZK (Germany)
INR: Institut für Neutronenphysik und Reaktortechnik, FZK, Karlsruhe, (Germany)
INRNE: Institute for Nuclear Research and Nuclear Energy, Bulgarian Academy of Science
INTAS: INTernational ASsociation for the promotion of Cooperation with Scientists from the Independent States of the former Soviet Union
IRMM: Institute for Reference Materials and Measurements, Geel (Belgium)
ISO: International Standard Organisation
ISIS: ISIS spallation source, Rutherford-Appleton Lab., Rutherford (UK)
ISTC: International Science and Technology Center, Moscow (Russia)
ITC: Institut für Technische Chemie, FZK, Karlsruhe (Germany)
ITU: Institute for Transuranium Elements, Karlsruhe (Germany)
ITN: Instituto Tecnológico e Nuclear

JAERI: Japan Atomic Energy Research Institute
JRC: Joint Research Center

KEDG: K-EDGe densitometer
KEMA: N.V. tot Keuring van Electrotechnische Materialien, Arnhem (Netherlands)
KKGg: KernKraftwerk Gösgen (Germany)
KKI: KernKraftwerk Isar, Eschenbach/Isar (Germany)
KKK: KernKraftwerk Krümmel (Germany)
KKP: KernKraftwerk Philippsburg (Germany)
KORIGEN: FZK development of the ORIGEN code
KRI: Khlopin Radium Institute (Russia)
KWU: KraftWerk-Union (Germany)
KWW: Kernkraftwerk Würgassen/Weser (Germany)

LA: Laser Ablation
LAF: Laser Flash
LA-OES: Laser Ablation Optical Emission Spectroscopy
LET: Linear Energy Transfer
LEU: Low Enriched Uranium
LIF: Laser-Induced Fluorescence
LIMS: Laboratory Information Management System
LSC: Liquid Scintillation Counter
LSS: Laboratoire Sur Site, La Hague (France)
LURE: Laboratoire d'Utilisation du Rayonnement Électro-magnétique, Orsay, (France)
LWR: Light Water Reactor

MA: Minor Actinides (Np, Am, Cm)
MA: Multiple group Analysis
MAGNOX: MAGnesium Non-OXidizing (fuel sheath)
MAGNOX reactor: graphite-moderated, gas cooled reactor type in the United Kingdom
MATINA: MATrices pour INcinération d'Actinides
MCA: Multichannel Analyser
MCP: MicroChannel Plate
MOX: Mixed OXide fuel
MS: Mass Spectrometry
MWd/tM: Megawatt day per (metric) ton of (heavy) Metal
MWd/tU: Megawatt day per (metric) ton of Uranium

NCC: Neutron-Coincidence Counter
Nd-YAG: Neodymium-Yttrium Aluminium Garnet laser
NDA: Non-Destructive Assay (Analysis)
NDT: Non-Destructive Testing
NEA: Nuclear Enery Agency, Paris (France)
NFIR: Nuclear Fuel Industry Research group (EPRI), Palo Alto, (USA)
NIST: National Institute of Standards and Technology, Gaitherburg (USA)
NOC: Normal Operation Conditions
NPP: Nuclear Power Plant
NSLS: National Synchrotron Light Source, Brookhaven, NY (USA)

OCOM: Optimized CO-Milling
OECD: Organization for Economic Cooperation and Development, Paris (France)
OES: Optical Emission Spectroscopy
ORIGEN: Oak Ridge Isotope GENeration and depletion code
ORNL: Oak Ridge National Laboratory, Oak Ridge, TN (USA)
OS/2: Operating System, IBM
OSL: On-Site Laboratory

PADIT: Particle Agglomeration and Deposition In Turbulence
PAGIS: Performance Assessment of Geological Isolation Systems
PCI: Pellet Cladding Interaction
PCMI: Pellet cladding Mechanical Interaction
PDP: Minicomputer (DEC)
PF: Produits de fission
PHARE: Pologne-Hongrie: Aide à la Reconstruction Èconomique

PHEBUS: French test reactor, Cadarache (France)
PHEBUS-fp: Programme to study fission product release and their distribution in the primary circuit
PHENIX: French prototype fast reactor, Marcoule (France)
PIE: Post-Irradiation Examination
PKED: Product K-Edge Densitometer
PNC: Power reactor and Nuclear fuel development corporation (Japan)
PNI: Passive Neutron Interrogation
PRZ: micro-probe metrix correction
PSI: Paul Scherrer Institut, Würenlingen, (Switzerland)
PTI: Physical Technical Institute, Academy of Science of Uzbekistan
PUREX: Plutonium and Uranium Recovery by Extraction
P&T: Partitioning and Transmutation
PWR: Pressurized Water Reactor

QA: Quality Assurance
QC: Qualtity Control

RADONN: Software Package for Radionuclide Analysis, ITU
RBMK: graphite moderated Boiling Water Reactor (BWR), (Russia)
RBS: Rutherford Backscattering Spectroscopy
RIA: Reactivity Induced Accident
RIAR: Research Institute of Atomic Reactors, Dimitrovgrad (Russia)
RSD: Relative Standard Deviation

SAL: Seibersdorf Analytical Laboratory, Vienna (Austria)
SCA: Shared Cost Action
SCK: Studie Centrum voor Kernergie, Mol (Belgium)
SEM: Scanning Electron Microscopy
SGN: Société Générale pour les Techniques Nouvelles
SIMFUEL: SIMulated high burnup FUEL (with major non-volatile fission products)
SIMS: Secondary Ion Mass Spectrometry
SQUID: Superconducting QUantum Interference Device
SUPERFACT: Minor Actinide Irradiation in Phenix

TACIS: Technical Assistance to the Commonwealth of Independent States
TCP/IP: Transmission Control Protocol / Internet Protocol
TEM: Transmission Electron Microscopy
THORP: Thermal Oxide Reprocessing Plant
TIG: Tungsten Inert Gas welding
TIMS: Thermal Ionization Mass Spectrometry
TLC: Thin Layer Chromatography
TRABANT: TRAnsmutation and Burning of Actinides in TRIOX
TRANSURANUS: Fuel behaviour code (ITU), Karlsruhe (Germany)
TRIM: TRansport of Ions in Matter code
TRIOX: HFR irradiation capsule, Petten (Netherlands)
TUAR: Annual Report, Institute for Transuranium Elements (ITU), Karlsruhe (Germany)
TUBRNP: TransUranus BuRNuP model

VAX: Minicomputer (DEC)
VGB: Verein der GroßkraftwerksBetreiber
VVER (WWER): Pressurized Water Reactor (Russia)

WAPD: Westinghouse Atomic Power Division
WWER (VVER): Pressurized Water Reactor (Russia)

XRD: X-Ray Diffraction
XRF: X-Ray Fluorescence analysis

Annex VI

List of Contributors to the Various Chapters

1. Basic Actinide Research

G. H. Lander, , M.S.S. Brooks, S. Darracq, J. Fearon, E. Gómez Marin, T. Gouder, S. Heathman, A. Hiess, E. Higgins, V. Ichas, S. Langridge, T. Le Bihan, L. Paolasini, L. Pereira de Jesus, J. Rebizant, D. De Ridder, J. C. Spirlet, F. Wastin, S. Zwirner, L. Koch, C. Apostolidis

2. Safety of Nuclear Fuels

M. Coquerelle, D. Bottomley, J. Cobos-Sabate, C. Papaioannou, J. Spino, K. Vennix, C. Walker

Hj. Matzke, M. Cheindlin, K. Lassmann, J.P. Hiernaut, I. Ray, C. Ronchi, T. Wiss,

3. Mitigation of Long Lived Actinides and Fission

L. Koch, J.P. Glatz

Hj. Matzke, S. Casalta

K. Richter, J.F. Babelot, K. Buijs, B. Chavane, J.F. Gueugnon, J. Magill

4. Spent Fuel Characterization in View of Long Term Storage

M. Coquerelle, D. Bottomley, J. A. Serrano, M. Juez-Lorenzo, D. Papaioannou, J. Spino, D.H. Wegen

L. Koch, J.-P. Glatz, G. Nicolaou

Hj. Matzke, V. Rondinella

5. Safeguards Research and Development

L. Koch, K. Abbas, M Betti, G. Nicolaou

6. Scientific and Technical Support to DG XVII

L. Koch, O. Cromboom, W. Janssens, H. Ottmar, M. Ougier, P. Peerani, H.-G. Schneider, F. Schiavo, H.G. Schneider, A. Schubert, H. van der Vegt, D. Wojnowski

7. Scientific and Technical Support to DG I

L. Koch, M. Betti, J.-P. Glatz, L. Josefowicz

9. Competitive Support Activities

K. Richter, P. Capéran, J. Somers

10. Work for Third Parties

M. Coquerelle, D. Bottomley, J. Spino, E. Toscano

L. Koch, J. P. Glatz, G. Nicolaou

Hj. Matzke, M. Burghartz, C. Leger

K. Richter, J.F. Babelot, P. Capéran, J.F. Gueugnon, J. Somers

13. Quality Management

W. Bartscher, W. Krischer

Annex VII

Previous Progress Reports of the Institute for Transuranium Elements

TUSR	Period	COM-Nr	EUR-Nr
1	Jan - Jun 1966	1580	
2	Jul - Dec 1966	1522	
3	Jan - Jun 1967	1745	
4	Jul - Dec 1967	2007	
5	Jan - Jun 1968	2172	
6	Jul - Dec 1968	2300	
7	Jan - Jun 1969	2434	
8	Jul - Dec 1969	2576	
9	Jan - Jun 1970	2664	
10	Jul - Dec 1970	2750	
11	Jan - Jun 1971	2833	
12	Jul - Dec 1971	2874	
13	Jan - Jun 1972	2939	
14	Jul - Dec 1972	3014	
15	Jan - Jun 1973	3050	
16	Jul - Dec 1973	3115	
17	Jan - Jun 1974	3161	
18	Jul - Dec 1974	3204	
19	Jan - Jun 1975	3241	
20	Jul - Dec 1975	3289	
21	Jan - Jun 1976	3358	
22	Jul - Dec 1976	3384	
23	Jan - Jun 1977	3438	6475 EN
24	Jul - Dec 1977	3484	7209 EN
25	Jan - Jun 1978	3526	7459 EN
26	Jul - Dec 1978	3582	7227 EN
27	Jan - Jun 1979	3657	7483 EN
28	Jul - Dec 1979	3714	7509 EN
29	Jan - Jun 1980	3822	7857 EN
30	Jul - Dec 1980	3846	8230 EN
31	Jan - Jun 1981	3898	8447 EN
32	Jul - Dec 1981	3927	8777 EN
33	Jan - Jun 1982	3990	9581 EN
34	Jul - Dec 1982	4048	10251 EN
35	Jan - Jun 1983	4094	10266 EN
36	Jul - Dec 1983	4117	10454 EN
37	Jan - Jun 1984	4150	10470 EN
38	Jul - Dec 1984	4165	11013 EN
39	Jan - Jun 1985	4201	11835 EN
40	Jul - Dec 1985	4263	11836 EN

TUSR	Period	COM-Nr	EUR-Nr
86	Jan - Dec 1986	4302	12233 EN
87	Jan - Dec 1987		11783 EN
88	Jan - Dec 1988		12385 EN
89	Jan - Dec 1989		12849 EN
90	Jan - Dec 1990		13815 EN
91	Jan - Dec 1991		14493 EN
92	Jan - Dec 1992		15154 EN
93	Jan - Dec 1993		15741 EN
94	Jan - Dec 1994		16152 EN
95	Jan - Dec 1995		16368 EN

Previous Programme Progress Reports were confidential for a period of two years. Between 1977 and 1987 they had been made freely accessible after that period as EUR-Reports (on microfiches) and since 1988 they have been issued as regular EUR-Reports. They can be ordered from the Office for Official Publications of the European Communities, 2 rue Mercier, L-2985 Luxembourg, Tel. 499 28-1, Telex 1322 PUBOF LU

European Commission

EUR 16368 – Institute for Transuranium Elements – Annual report 1995
Editors: R. Schenkel, J. Richter, D. Pel, R. Wellum
Luxembourg: Office for Official Publications of the European Communities
1996 – 238 pp., – 21.0 x 29.7 cm
Scientific and Technical Research series
ISBN 92-827-6553-9

Abstract

During 1995 the Institute for Transuranium Elements (ITU) continued its research and development activities in the area of basic and applied actinide research, safety of nuclear fuels, mitigation of long lived actinides and fission products, spent fuel characterization in view of long term storage, and safeguards and fissile material management. The Institute participated also in various competitive activities as outlined below.
The overall objective of basic actinide research is to elucidate the electronic structure of the actinides. Important new results have been obtained for the better understanding of uranium based heavy fermion superconductors doped with transuranium ions such as neptunium and plutonium. New results have been obtained in the theory of the interaction between light and solids, in neutron experiments of neptunium compounds and with X-ray synchrotron experiments on uranium oxide single crystals and uranium arsenide crystals.
The Institute has continued its work in the area of measuring and modelling fuel properties and fuel-cladding interactions. Structural investigations of high burn-up fuel continued to be the major activity in 1995. The evolution of the porosity and the grain subdivision process as a function of burn-up was measured with the aid of optical, scanning and transmission electron microscopy.
An important objective of the fuel cycle safety activities is to further minimize the radiotoxicity of spent fuel and highly active waste. Technetium samples, pins with high plutonium and neptunium content and a plutonium-cerium inert matrix based pin were prepared. Extensive studies were done to master fabrication procedures and to measure physical and chemical properties of inert matrix materials for the transmutation of actinides, in particular for americium.
The leaching and corrosion behaviour of uranium and irradiated high burn-up fuel was examined with solutions simulating groundwater and salt brine. The mechanisms of leaching and their kinetics are being explored.
First results on dissolution studies of spent fuel are reported together with the area of high temperature fuel cladding interaction and sodium-SUPERFACT fuel compatibility.
In the area of nuclear safeguards, the Institute has contributed by performing research and development of methods, techniques and instruments, by provision of analytical services and expertise and by direct in-field measurement support. As part of the support to DG XVII, the pre-on-site laboratory at ITU and the on-site laboratory projects for Sellafield and Cap la Hague progressed with the purchasing and testing of major equipment. ITU staff provided significant analytical in-field support to the Safeguards Directorate in reprocessing plants and in fuel fabrication plants. The Institute participated in a field test for environmental monitoring techniques and continued to provide its facilities and expertise in the area of characterization of vagabonding nuclear materials.
The Institute submitted for the first time proposals in the area of the shared cost action programme. Eight projects in the field of nuclear fission safety, established together with different partners from Member States, were accepted.
The Institute has started the two projects under the TACIS/PHARE programme of the European Commission.
Contracts with a volume of 3.4 MECU were signed during 1995, with major contracts in the area of post irradiation examination of irradiated fuels, fabrication and characterization of fuels for transmutation, and examination of high burn-up uranium oxide and mixed oxide fuels for different customers.

15

CG-NA-16368-EN-C

NOTICE TO THE READER

All scientific and technical reports published by the Commission of the European Communities are announced in the monthly periodical **'euro abstracts'.** For subscription (1 year: ECU 63) please write to the address below.

OFFICE FOR OFFICIAL PUBLICATIONS
OF THE EUROPEAN COMMUNITIES

L-2985 Luxembourg

ISBN 92-827-6553-9